

DISS. ETH NO. 19472

SURFACE FUNCTIONALIZING
SUPERPARAMAGNETIC IRON OXIDE
NANOPARTICLES USING NITROCATECHOL
ANCHORS

A dissertation submitted to

ETH ZURICH

for the degree of

Doctor of Sciences

presented by

ESTHER AMSTAD

Material Science ETH

born on June 6, 1983

citizen of Beckenried (NW)

accepted on the recommendation of

Prof. Dr. Marcus Textor, examiner

Prof. Dr. Erik Reimhult, co-examiner

Prof. Dr. André R. Studart, co-examiner

Prof. Dr. Helmuth Möhwald, external co-examiner

2010

*We are trying to prove ourselves wrong as quickly as possible, because only in that way
can we find progress*

RICHARD FEYNMAN

Acknowledgements

Many people spent a lot of time teaching me different essential things during the last 3.5 years. They introduced me into operating procedures of instruments, showed me how to analyze, summarize and present data and how to handle very different scientific and to some extent also more political things. It was very pleasant for me to work and collaborate with so many highly motivated people from all over the world and I am extremely grateful to all these people!

Marcus gave me a lot of freedom to fine-tune the project and to dig deeper in areas I was particularly interested in. He gave me the impression he had confidence in me and encouraged me to communicate and collaborate with many different people. Marcus was always very generous and allowed me to attend many international conferences which I greatly enjoyed and where I learned many different things. At these conferences, I got to meet a lot of people from all over the world and got to see many different ways to scientifically approach problems which was very interesting for me. He often presented this work himself especially during invited talks and made sure, people know what we do which was very helpful for me. Suddenly, people knew me without that I met them thanks to Marcus' presentations and personal communications. This was very motivating for me. He also managed to support me and take away pressure from me by making me understand, that I should worry about science and he was caring about politics that might be related to certain scientific findings and outcomes. This helped me to focus on science and therefore was very valuable for me. He also corrected this thesis timely and in a to me very helpful way. Thank you very much, Marcus, for having me in your group, giving me the possibility, infrastructure and support from yourself and from your whole group! Erik has the unbelievable ability to motivate me for so many different things. He always was there, when I needed help while he managed to give me freedom to do things I wanted to pursue. Whenever I felt unsure, I could ask him and got a honest, helpful and fast answer. He was the one who noticed first when I needed help without that I explicitly asked

for it. He supported me very well during more difficult times which was very valuable for me and helped me carry on science. He taught me very patiently so many essential things such as how to experimentally and theoretically approach scientific questions, how one keeps successful collaborations running, how one presents, writes manuscripts, corrects students works, writes review reports and gradually also let me handle things on my own. It was Erik who taught me that not everything needs to be ready one week before the deadline and by that, made me more relaxed which at the end also allowed me to handle more things in parallel than I would otherwise have been able to do. I still do not have the nerves to prepare things as late as Erik does, but he for sure did a good job in showing me, that I can take things a bit more relaxed and things would work out even if they are not ready well in advance. Furthermore, I also learned from him (at least to a certain extent) how to handle certain political things and how to fight for something important to me even if that meant facing or even provoking tough discussions and disputes. But he also thought me a lot of things which are not directly science related. It is difficult to imagine this PhD thesis without having Erik as a supervisor. It for sure would have been completely different and most likely not so much fun. Thank you very much, Erik, for all your effort and patience, uncountable hours you spent teaching me, answering e-mails from me, correcting manuscripts, presentations, patents and the thesis for me, caring about collaborations which were related to my project and also for the very pleasant hours we spent together with your family and other members of your sub-group somewhere either in Zurich, in Warenmünde or in the pre-Alps!

I am also indebted to Prof. Helmuth Möhwald (MPI Golm) and Prof. André Studart who kindly accepted to be part of my examination committee! Furthermore, I would like to thank Prof. Jörg Löffler for chairing my PhD examination as the head of the Department of Material Science!

There are many people who introduced me to techniques they are experts in. They gave me insights into areas which would otherwise not have been accessible to me, at least not in the given time frame. Elisabeth Müller-Gubler spent many hours with me in front of TEMs teaching me basics on how to operate TEMs and showing me very helpful tricks that made my life in front of the TEM so much easier. She was the one who managed to make me overcome my initial skepticism towards microscopy. After her trainings, I started to highly appreciate all the possibilities electron microscopy has to characterize samples on a nanoscale. Thank you very much, Elisabeth, for all your patience, efforts and commitment! I would also like to acknowledge all the help I got from Roger Wepf and the rest of the EMEZ team. You all were always very helpful and supportive when-

ever I had questions and problems related to electron microscopy. It was a great pleasure for me to have the possibility to be a regular user at EMEZ and get all your support!

Thanks to Joachim Kohlbrecher, I got access to SANS beamtime which was one of the highlights of my PhD. I was fortunate enough to get the possibility to spend multiple times several days at PSI measuring SANS. Joachim always was very helpful, showed me how to measure SANS, gradually let me measure it myself, always under close supervision from him, and very patiently helped me with the data analysis. With his unbelievable experience both in measuring SANS and in analyzing SANS data, he always found a way to solve problems especially if they were related to the data analysis. He never lost patience even though I often needed to ask multiple times how to fit certain data sets because I could not succeed myself. Many thanks, Joachim, for giving me the possibility to do these measurements, for providing so much support during the beamtime and thereafter during data analysis! Without that, I would never have gotten the possibility to get insights into doing SANS experiments and analyzing the obtained data which would have been a shame.

Many people helped me to perform various experiments by introducing me into very different measurement techniques. I very much appreciated to get good introductions into the different techniques from respective experts. I therefore would like to express my gratitude to all these people, namely to Thomas Schweizer, Andreas Gehring, Maxim Yulikov, Håkon Fischer, Giorgia Zandomenighi, Georg Hähner, Conny Schmidt, Christof Baltes, David Rathner, Antony Sánchez-Ferrer, Michaelis Charilaou, Cesare Borgia, Matteo Seita, Idalia Bilecka, Dorota Koziej, Hans Sigg, Philippe Lerch and Barbara Scherrer for all their help and introductions to the various preparation and characterization techniques.

Markus Niederberger allowed me in a very generous way to use his lab to synthesize NPs. He also was open to discussions on how to improve the NP synthesis. He and his group always made me feel welcome in their lab. Thank you, Markus, and your whole group for all your help, generosity and openness!

Patrick Ilg and Martin Kröger helped me developing a theoretical density profile model for dispersants adsorbed on NPs. It was fascinating for me to get some insights into a completely new area and it helped me to understand SANS data. Thank you, Patrick and Martin for your patience and support!

During my PhD, I had the chance to collaborate with many different people from all over the world. In a collaboration with the group of Prof. Georg Wick (University hospital in Innsbruck) we had the chance to test a first generation of our functionalized NPs *in*

vivo in mice and learned important lessons from these studies. Sebastian Schwarz from the group of Prof. Martin Zenke (University of Aachen) tested the uptake of NPs in various cells such as mesenchymal stromal cells (MACS), the influence of the dispersant layer thickness and NP stability on the NP uptake and the fate of NPs inside cells. He is currently continuing these experiments with fluorescently labeled and targeted NPs in Japan and potentially will extend them to *in vivo* studies. Steffi Lehman from the group of Prof. Markus Rudin tested binding of biotinylated NPs *in vitro* on cells that express biotin binding proteins at their surfaces and *in vivo* in mice expressing these biotin binding proteins in tumor sites using MRI. Christian Dose (Miltenyi Biotec, Germany) showed great interest in a collaboration with us where we could explore further functionalization strategies of our NPs with different ligands. Furthermore, he offered to test our NPs for cell separation purposes. Although this collaboration is at the very beginning, it was very nice for me to notice his great interest and I very much hope, this collaboration takes off for real soon, with people from Eriks lab at BOKU in Vienna.

In other collaborations, I got help with a more thorough characterization of NPs. Luc Starman (University of Eindhoven) helped me with quantifying relaxivities of Fe_3O_4 NPs. Michelle Visbal from the group of Prof. Eduardo Juan and in collaboration with Prof. Carlos Rinaldi (University of Puerto Rico) kindly agreed to magnetically characterize our latest generation of NPs. Norbert Buske showed great interest in our NPs and made sure, people especially in the German colloidal society are aware of our work. He also provided us some large iron oxide NPs and showed us where the limits of our dispersants are. Christina Giordano (group leader at MPI, Potsdam) provided us Fe_3C NPs to test our dispersants on. Nico Burns, Jörg Braun and Stefan Egli from Prof. Wolfgang Meiers group (University of Basel) generously provided us block-co-polymer to do feasibility studies on polymersomes that contain hydrophobic iron oxide NPs in their membranes. With the experience they gained in their lab by dealing with polymersomes for many years, they also supported me regarding polymersome assembly. Dermot Brougham (Dublin city University) offered his kind help in measuring relaxivities of liposomes containing hydrophobic iron oxide NPs in their membranes. These collaborations were extremely enriching for me. A big thanks to all of our collaborators!

This work grounds on the use of nitrocatechols. I am extremely grateful to Torben Gillich, who synthesized these anchors for me. Lucio Isa helped me with the core size analysis which was based on TEM images. He also was very interested, motivated and willing to explore the assembly of our core-shell NPs at the liquid-liquid interface. I enjoyed the discussions with him about the assembly of NPs which gave me insights into a more

physical view of the assembly of colloids at interphases. I had the great possibility to start working together with Mirren Charnley. She kindly agreed to test how liposomes affect HeLa cells and measure if liposomes are taken up by cells. These experiments were conducted with the final goal to trigger release of drugs in cell assays and test its effect on the cell viability. Unfortunately, this project was started only shortly before I needed to focus on writing. Therefore, we were forced to stop this project without having it brought to a satisfactory end. However, I very much hope, this project can be carried on in collaboration with Eriks group in Vienna. Additionally, Edmundo Benetti did first trials to graft thermoresponsive PNIPAM dispersants from Fe_3O_4 cores. Despite initial promising results, we could not pursue this project because time was extremely short for both, Eddy and me. However, I greatly enjoyed to work together with Eddy. Torben, Lucio, Mirren and Eddy, thank you so much for your work, interest and good discussions!

I had the chance to work with several co-workers and students during my PhD. This gave me the possibility to get some insights into side-projects and topics not directly related to the core of my thesis but still of great interest to me. I enjoyed to work with all of you, thank you Deborah Studer, Roman Kontic, Sandro Bigler, Ali Arefi, Fabian Fischer and Jens Ammann for having been so motivated and curious! You often made me reflect things, I took for granted, by asking excellent questions. I very much enjoyed and appreciated this!

It was a great pleasure to be a member of Eriks sub-group. I always enjoyed the weekly meetings on Friday afternoons for journal clubs and problem discussions. The fun evenings and weekends we spent together were always a very good and welcome change to the every-day life. Thank you very much, Martina, Stefan, Karthik, Lucio and Mateu for all these good scientific discussions and the fun hours we spent together!

Thanks to our secretary Esther Stähli, administrative things always worked out nicely and timely. This greatly facilitated my work. She was always helpful and never lost patience. Thank you very much for all your assistance and patience, Esther, I very much appreciated all your work you did in the background! And a big thanks also to the whole LSST group. It was fun to work in such a lively group with so many very different people.

I also would like to acknowledge the financial support from the COST Action D43 and ETH Zurich.

Without all the support from my family, I never would have managed to go through all the education including this thesis. My parents were always there, especially during times I struggled. They helped me in a very selfless way and made me understand that they will support me regardless of what would happen. This was and is of immeasurable value and

only thanks to that, I could focus on my work. They together with Helen and Ueli, my sister and brother, accepted my way of life and how I set priorities although I am sure, they did not always understand and appreciate it. Thank you so much for all your support and understanding which opened me up the possibility to do this thesis the way I did it! I also would like to thank the other members of the bigger family and all my friends for very good non-scientific discussions and fun hours. They broadened my horizon during numerous discussions about all sorts of different topics. Thanks to all of you for your understanding especially for the way I prioritized things, for keeping up our contacts by spending time together be it at home, in a restaurant or outside in the mountains and hills!

Abstract

Many material properties change and become size dependent if dimensions are reduced from the micro to the nano scale. These unique, size-dependent properties of nanomaterials render them very interesting for fundamental studies and numerous applications. Nanoparticles (NPs) are a particularly interesting but challenging class of nanomaterials. Biomedical applications of superparamagnetic iron oxide NPs for therapeutic and diagnostic purposes require NPs to be stable under physiologic conditions. This can only be achieved if NPs are sterically stabilized with appropriate dispersants that bind irreversibly to the iron oxide surface. Tight control over the dispersant layer not only prevents NP agglomeration but additionally paves the way to tailor the NP size, charge and the type and density of functionalities presented at the NP surface. These factors are especially important for the *in vivo* performance of NPs, in particular the circulation time, targeting ability and clearance route. With the extremely high surface : volume ratio, surface functionalization becomes a key issue in the endeavor to better understand NP structure-function and structure-toxicity relationship and to explore their unique properties for applications in areas such as material science, biology and medicine. A particularly important aspect related to surface properties is the need for reliable and cost-effective approaches to stabilize and disperse single NPs. Only then can their unique, size-dependent properties be explored, controlled and utilized.

One possibility to appropriately modify NP surfaces is to graft low molecular weight dispersants to these surfaces. Such dispersants typically consist of an anchor which is covalently linked to a spacer. Stabilization of NPs with low molecular weight dispersants relies on high affinity anchors that firmly bind spacers and functionalities to the NP surface at high density. Nevertheless, systematic studies comparing the performance of anchors to graft molecules to magnetite (Fe_3O_4) NPs are missing. Therefore, iron oxide NPs stabilized with low molecular weight are often reported to agglomerate under physiological conditions [1].

Iron Oxide Core Synthesis

The binding affinity of dispersants greatly depends on the NP surface chemistry. To interrogate the influence of dispersants on NP stability, it is therefore of primary interest to control the core stoichiometry, surface chemistry and size. To this end, in chapter 5, different approaches to synthesize Fe_3O_4 NPs were taken, namely aqueous precipitation and non-aqueous sol-gel methods using either microwave (MW) or oil bath heating for nucleation and growth of the NPs. While the core size can be controlled if NPs are synthesized by non-aqueous sol-gel methods, it is difficult to tune if NPs are synthesized by aqueous precipitation. However, iron oxide NPs synthesized in the MW for maximally 1 h had a bimodal size distribution. In contrast, NPs grown in the oil bath for 24 h were monomodally distributed. Therefore, from the synthesis methods investigated in this thesis, the non-aqueous sol-gel method where NPs were nucleated and grown in the oil bath allowed the closest control over the core size and its distribution.

Influence of the Dispersant Anchor on Nanoparticle Stability

To assess the suitability of dispersants to sterically stabilize Fe_3O_4 NPs, dispersants were grafted to Fe_3O_4 NPs with core radii between 2.5 and 6 nm and with varying degrees of polydispersity. A set of 8 different catechol-derived anchors were compared regarding their suitability as dispersant anchors. For this purpose, catechol derived anchors were covalently linked to a linear poly(ethylene) glycol (PEG) spacer. Dispersant binding reversibility and therefore NP stability was investigated with temperature-dependent dynamic light scattering (DLS) measurements and complemented with DLS experiments where excessive dispersants were repeatedly removed. Furthermore, NP stability was correlated with the dispersant packing density on the surface of NPs. It was found that electronegative substituents, namely NO_2 -substituents on the aromatic ring of catechols greatly enhance the binding affinity of such anchors towards Fe_3O_4 surfaces. This led to perfect long-term NP stability in physiologic buffers and at temperatures up to 90°C. Furthermore, NP stability was demonstrated to increase with increasing dispersant packing density. Thus, NPs stabilized with PEG-nitrocatechol dispersants exhibited the highest dispersant packing density and dispersion stability.

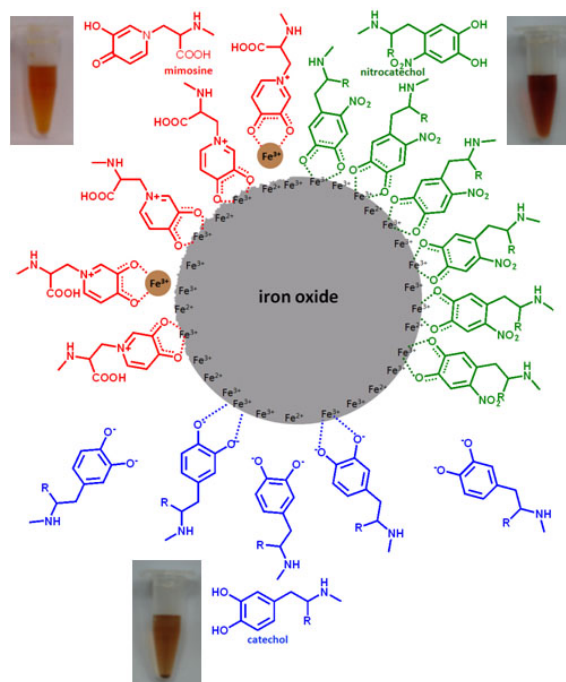


Figure 1: Cartoon of different anchors adsorbed on iron oxide NPs. Iron oxide NPs stabilized with dispersants that contain low binding affinity anchors such as catechols are unstable due to reversible dispersant adsorption. Iron oxide NPs stabilized with anchors that have a too high binding affinity such as mimosine are unstable because mimosine gradually dissolves NPs resulting in mimosine/ Fe^{3+} complexes. If the binding affinity of anchors is optimal, NPs are stable even under dilute physiologic conditions and up to temperatures of $90^{\circ}C$. This is the case *e.g.* for dispersants containing nitrocatechols as anchors.

Electronic Interactions of NitroDOPA with Fe_3O_4 Surfaces

The underlying chemical reactions responsible for the different binding affinities of chemically similar anchors were elucidated with electron paramagnetic resonance (EPR) spectroscopy and complemented with Fourier transform infrared (FTIR) and UV/VIS spectroscopy measurements. Nitrocatechols were found to adsorb to surface-confined Fe(II) ions resulting in a strong electron delocalization between the catechol's delocalized Π^* orbitals and surface Fe(II). This resulted in an increased electron density in nitrocatechol and an electron depletion at the coordinating iron ion which then appeared as Fe^{3+} in EPR. This strong electron delocalization is responsible for the close to optimal binding affinity of nitrocatechols to Fe_3O_4 surfaces. However, it also became clear that binding affinity should not be maximized. A too high binding affinity of anchors to the metal ion leads to gradual NP dissolution, as was shown for mimosine which has a very high complexation constant towards Fe^{3+} ions. Therefore should binding affinities be optimized such that they are high enough to prevent dispersant desorption but below the threshold where NPs start to dissolve (Figure 1).

Influence of the PEG Molecular Weight on Nanoparticle Stability

After anchors that firmly bind molecules to Fe_3O_4 surfaces were discovered, the influence of the PEG molecular weight (M_w) on NP stability, packing density and dispersant density profile was investigated with DLS, small angle neutron scattering (SANS) and thermogravimetric analysis (TGA). PEG M_w s between 5 kDa and 10 kDa were found to be optimal for achieving good long-term NP stability up to 90 °C. DLS measurements indicated that NPs coated with dispersants which had a PEG $M_w < 1.5$ kDa agglomerated under physiologic conditions. These experimental results were well in agreement with theoretical calculations of inter-particle potentials. If the PEG molecular weight was higher than 10 kDa, the dispersant packing density was below the threshold where NPs start to agglomerate. Thus, not only the anchor but also the dispersant molecular weight has to be optimized.

Iron Oxide Nanoparticle Functionalization

Different strategies to functionalize individually stabilized iron oxide NPs were compared. A monolayer of neutravidin was assembled on biotin-presenting iron oxide NPs. Subsequently, these NPs were functionalized with two different biotinylated antibodies. This biotin-avidin functionalization strategy worked well if NPs were used directly after they had been assembled in dilute conditions. However, NPs started to crosslink if functionalized at higher concentrations or if they were stored for prolonged times.

Alternatively, antibodies were covalently linked to acrylate presenting NPs through different coupling reactions. Similarly to what was observed for the functionalization of NPs through the biotin-avidin strategy, NPs started to crosslink during the covalent coupling of antibodies which have multiple amine groups per molecule. However, NPs could readily be functionalized with fluorophores that contained exactly one amine group per molecule. This was achieved by covalently coupling the amine containing fluorophores to acrylate presenting NPs. It resulted in individually stabilized dual labeled contrast agents which were detectable with magnetic resonance imaging (MRI) and fluorescence microscopy.

Assembly of Iron Oxide Nanoparticles into Thermoresponsive Superstructures

Iron oxide NPs can be used as actuators to locally produce heat if subjected to an alternating magnetic field (AMF). Inserted into a thermoresponsive vesicular structure, the

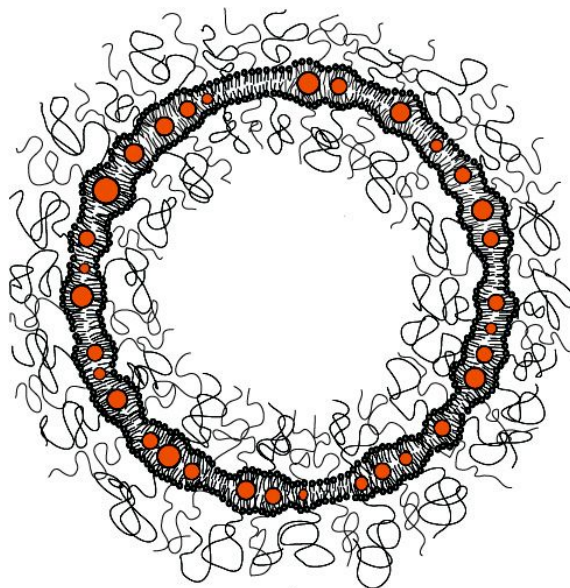


Figure 2: Cartoon of iron oxide NPs assembled in the liposome membrane. Individually stabilized hydrophobic NPs spontaneously assembled into the hydrophobic part of the liposome membrane. These NPs can be used as actuators to trigger release if subjected to an alternating magnetic field. Liposomes were sterically stabilized with PEG to prevent agglomeration if they are stored in the gel phase ($T < T_m$) and to provide stealth properties *in vivo*.

through NP produced heat can be used to trigger release of cargo that had been encapsulated in liposomes. Release will be more efficient if NPs are directly inserted into the thermoresponsive structure. Controlled and stable assembly of NPs into the hydrophobic core of thermoresponsive lipid membranes can only be achieved for NPs with a hydrophobic shell and of sufficiently small size. High affinity anchors pave the way to assemble an irreversibly bound monolayer of palmityl-nitroDOPA on the Fe_3O_4 NP surface. Such individually stabilized hydrophobic NPs were shown to spontaneously assemble into the hydrophobic core of membranes of liposomes (Figure 2).

Liposomes consisting of 1,2-distearoyl-sn-glycero-3-phosphocholine (DSPC) lipids incorporating 2.5 nm core radius NPs in their membrane were prepared through extrusion. The structure of liposomes and the membrane distortions caused by the iron oxide NPs assembled therein, were studied with SANS. Despite that iron oxide NPs significantly distorted the membranes, the membrane phase transition temperature (T_m), determined by differential scanning calorimetry (DSC), was not affected by the presence of iron oxide NPs.

DSPC was chosen because of its T_m of 55 °C which is well above the body temperature. Liposomes are highly impermeable in the gel phase ($T < T_m$) but become permeable at $T \approx T_m$. Application of an AMF could therefore be used to raise the temperature locally in

the liposome membrane, where iron oxide NPs were embedded, to T_m to release cargo. It was indeed shown that release of encapsulated calcein could be more efficiently triggered if hydrophobic NPs were embedded in the liposome membrane rather than if hydrophilic NPs were encapsulated in the liposome lumen.

A comparison between palmityl-nitroDOPA stabilized and oleic acid coated iron oxide NPs revealed that a thin, irreversibly bound hydrophobic dispersant shell surrounding Fe_3O_4 cores also at elevated temperatures was key to this performance. DLS measurements performed before and after exposure of liposomes hosting iron oxide NPs in their membrane revealed that liposomes remained intact during the AMF treatment. Thus, cargo could be gradually released by applying multiple short AMF pulses, which decreased heating of bulk water. In addition to close control over the time and rate at which encapsulated cargo can be delivered, these vesicles thus also allow to efficiently release cargo at bulk temperatures significantly below T_m . This renders Fe_3O_4 NPs functionalized liposomes very attractive delivery vehicles to ferry both, drugs and chemical reagents to desired locations.

Impact of Controlled Surface Modification on Applications

Both the results on functionalized, individually stabilized hydrophilic NPs and on embedded hydrophobic NPs for actuation of liposome membranes demonstrate that high-performance NP applications can only be realized if the NP surface can be modified in a controlled way. Therefore, suitable anchors that firmly bind spacers and functionalities to NP surfaces open up a multitude of possibilities to design multifunctional NPs which meet stringent requirements regarding stability, size and surface functionality. As demonstrated in this thesis they create the opportunity to design NPs and smart materials for so far unobtainable applications.

Zusammenfassung

Viele Materialeigenschaften verändern sich und werden grössenabhängig, wenn die Dimensionen von der Mikro- in die Nanometer Grössenskala verkleinert werden. Die resultierenden einzigartigen Eigenschaften machen Nanomaterialien attraktiv für die Grundlagenforschung und zahlreiche Anwendungen. Ein bedeutendes, aber auch herausforderndes Beispiel solcher Nanomaterialien sind Nanopartikel. Durch das hohe Verhältnis der Oberfläche zum Volumen wird die Oberflächenfunktionalisierung zentral fürs Bestreben zum besseren Verständnis des Einflusses der Struktur auf die Funktion und Toxizität. Zusätzlich ist eine kontrollierte Oberflächenmodifizierung Voraussetzung, damit die speziellen Materialeigenschaften von Nanopartikeln in Bereichen wie der Materialwissenschaft, Biologie und Medizin zum Tragen kommen. Von besonderer Bedeutung ist die rasch zunehmende Nachfrage nach einer kontrollierten, kostengünstigen Möglichkeit, die Nanopartikel individuell stabilisieren und dispergieren zu können. Nur so können die speziellen Materialeigenschaften von Nanopartikeln erforscht, kontrolliert und gezielt ausgeschöpft werden.

Geladene Nanopartikel können elektrostatisch stabilisiert werden, falls diese Nanopartikel in wässrigen Lösungen mit niedrigen Salzkonzentrationen dispergiert werden. Wenn Nanopartikel aber über weite pH Bereiche oder in Lösungen mit hohen Salzkonzentrationen dispergiert werden sollen, müssen sie sterisch stabilisiert sein.

Ein grosses Anwendungsgebiet von Nanopartikeln ist die Biomedizin. Vor allem für die biomedizinischen Anwendungen müssen Nanopartikel auch unter hohen Salzkonzentrationen stabil sein. Diesen hohen Anforderungen können nur sterisch stabilisierte Nanopartikel gerecht werden. Eine gute Kontrolle über die Oberflächenchemie erlaubt es, zusätzlich zur Nanopartikelstabilität die Nanopartikelladung und die Art und Dichte von funktionellen Gruppen, die an der Nanopartikeloberfläche präsentiert werden, an die entsprechende Anwendung anzupassen. Diese Faktoren sind von grosser Bedeutung für *in vivo* Anwendungen, weil sie die Zirkulationszeit und die Route, auf der diese Nanopartikel

ausgeschieden werden, bestimmen. Deshalb ist es entscheidend, Protokolle zu etablieren, die eine kontrollierte, experimentell einfache, vielseitige und kostengünstige Modifizierung der Nanopartikeloberflächen erlauben.

Ein Ansatz dieses Ziel zu erreichen ist die Adsorption von Detergenzien auf der Nanopartikeloberfläche. Diese können aus Ankern bestehen, die kovalent mit Platzhaltermolekülen verbunden sind. Die Strategie der Oberflächenmodifizierung von Nanopartikeln durch niedermolekulare Detergenzien beruht auf Ankern, die Platzhaltermoleküle irreversibel auf die Nanopartikeloberfläche anbinden. Trotz der Wichtigkeit der Anker zur Stabilisierung und Funktionalisierung von Magnetit (Fe_3O_4) Nanopartikeln wurde bisher, unseres Wissens, keine umfassende Studie verfasst, die die Tauglichkeit von verschiedenen Ankern vergleicht. Weil oft suboptimale Anker zur Stabilisierung von Eisenoxidnanopartikeln verwendet werden, agglomerieren solche Nanopartikel unter physiologischen Bedingungen [1].

Eisenoxidnanopartikel Synthese

Die Bindungsaffinität von Ankern hängt stark von der Stöchiometrie der Oberfläche der Nanopartikel ab. Soll der Einfluss von Ankern auf die Nanopartikelstabilität erforscht werden, muss sichergestellt sein, dass die Stöchiometrie der Nanopartikeloberfläche für alle Chargen gleich ist. Zudem sollten Detergenzien, die kommerziell erhältlichen Nanopartikeln zur besseren Handhabung oft zugesetzt werden, vermieden werden.

Um eine bessere Kontrolle über diese Parameter zu bekommen, wurden im Rahmen dieser Dissertation Eisenoxidkerne auf verschiedene Arten synthetisiert, namentlich durch Fällungsreaktionen aus wässrigen Lösungen und durch Sol-Gel Methoden. Nanopartikel, die mittels letzteren Verfahrens hergestellt wurden, entstanden in organischen Lösungsmitteln durch Zersetzungsreaktionen von Präkursoren bei erhöhten Temperaturen, indem entweder mittels Mikrowellen oder im Ölbad geheizt wurde. Die Grösse der Nanopartikel, die durch Fällungsreaktionen in wässrigen Lösungen entstanden, war schwierig zu kontrollieren, im Gegensatz zu Eisenoxidnanopartikeln die mittels Sol-Gel Methoden in organischen Lösungsmitteln synthetisiert wurden. Nanopartikel die mittels der Mikrowelle während maximal 1 h geheizt wurden, zeigten eine bimodale Kerngrößenverteilung. Dem gegenüber stehen Nanopartikel, die im Ölbad produziert wurden und sich als monodispers erwiesen. Von den untersuchten Synthesemethoden erlaubte somit die nichtwässrige Sol-Gel Route, bei der Nanopartikel im Ölbad synthetisiert wurden, die beste Kontrolle über die Kerngrösse und Kerngrößenverteilung.

Einfluss des Ankers auf die Nanopartikelstabilität

Um die Tauglichkeit von verschiedenen Detergenzien zu vergleichen, wurden Detergenzien auf frisch synthetisierte Eisenoxidnanopartikel mit Radien zwischen 2.5 nm und 6 nm adsorbiert. Weil erwartet wird, dass die Anker der Detergenzien einen entscheidenden Einfluss auf die Nanopartikelstabilität haben, wurde zuerst dieser Einfluss untersucht. Die Tauglichkeit von 8 unterschiedlichen Catecholderivaten als Anker für die Stabilisierung von Eisenoxidnanopartikeln wurde verglichen. Zu diesem Zweck wurden die Catecholderivate kovalent zu Poly(ethylen glykol) (PEG) gebunden. Die Nanopartikelstabilität und Bindungsreversibilität der Detergenzien wurden unter anderem mit temperaturabhängigen dynamischen Lichtstreuungsmessungen bestimmt. Zusätzlich wurde die Nanopartikelstabilität mit der Packungsdichte der Detergenzien auf den Nanopartikeloberflächen korreliert. Dabei stellte sich heraus, dass das Einführen eines elektronegativen Substituenten, wie z.B. einer NO_2 -Gruppe, direkt in den aromatischen Catecholring zu einer viel besseren Haftung dieser Anker auf Eisenoxidoberflächen führt, als das für unsubstituierte Catechole der Fall ist. Das zeigte sich in einer deutlich höheren Eisenoxidnanopartikelstabilität unter physiologischen Bedingungen und bis zu Temperaturen von $90^\circ C$. Zusätzlich konnte gezeigt werden, dass die Nanopartikelstabilität mit der Detergenzienpackungsdichte korreliert. Deshalb waren Eisenoxidnanopartikel, die mit PEG-Nitrocatecholen stabilisiert wurden, unter physiologischen Bedingungen deutlich stabiler als Nanopartikel, die mit PEG-Catecholen oberflächenmodifiziert waren.

Elektronische Interaktionen von Nitrocatecholen mit Eisenoxidoberflächen

Die zugrunde liegenden chemischen Reaktionen, die für die stärkere Bindung von elektronegativ substituierten Ankern auf Eisenoxidoberflächen verantwortlich sind, wurden mittels Elektronen-Paramagnetischen-Resonanz-Spektroskopie, Fouriertransformation Infrarot Spektroskopie und UV/VIS Spektroskopie näher untersucht. Dabei wurde festgestellt, dass Nitrocatechole zuerst auf oberflächengebundenen Fe(II) binden. Das ruft eine starke Elektronendelokalisation zwischen dem delokalisierten Π^* -System von Nitrocatecholen und an der Oberflächen gebundenem Fe(II) hervor. Daraus resultiert eine erhöhte Elektronendichte im Nitrocatechol Ring und ein Elektronenmangel am koordinierten Eisenion. Das Letztere zeigte sich in der Elektron-Paramagnetischen-Resonanz-Spektroskopie als Fe^{3+} -Signal. Diese starke Elektronendelokalisation ist für die verglichen mit den unsubstituierten Catecholen erhöhte Bindungsaffinität der Nitrocatechole zu Eisenoxidoberflä-

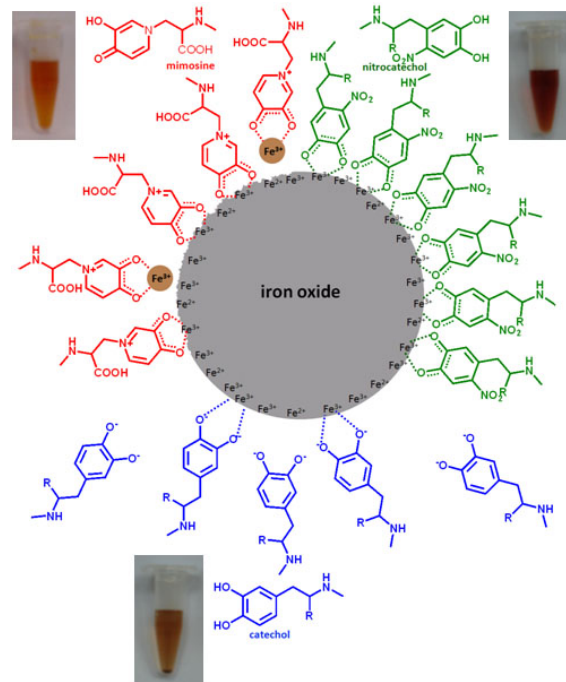


Abbildung 1: Sketch von Eisenoxidnanopartikeln die mit Detergenzien stabilisiert wurden, die verschiedene Anker haben. Eisenoxidnanopartikel, die mit Detergenzien stabilisiert wurden, die einen Anker haben, der eine tiefe Affinität zu Fe_3O_4 Oberflächen hat, agglomerieren, weil die Detergenzien reversibel adsorbieren. Eisenoxidnanopartikel, die mit Detergenzien stabilisiert sind, die einen Anker haben, der zu stark bindet, sind instabil weil der Anker die Nanopartikel auflöst. Dabei werden Anker/ Fe^{3+} Komplexe gebildet. Nur wenn Fe_3O_4 Nanopartikel mit Detergenzien mit Ankern stabilisiert sind, die eine optimale Affinität zu Fe_3O_4 haben, bleiben sie stabil unter verdünnten, physiologischen Bedingungen und bis zu Temperaturen von 90 °C. Nitrocatechol Anker erfüllten diese Kriterien.

chen verantwortlich.

Es stellte sich aber heraus, dass die Bindungsaffinität der Anker nicht maximiert werden sollte. Eine zu hohe Bindungsaffinität führt zu einer kontinuierlichen Auflösung der Eisenoxidnanopartikeln unter Bildung von Anker/ Fe^{3+} -Komplexen. Das wurde bei Mimosin Ankern beobachtet. Die Bindungsaffinität von Ankern muss dementsprechend optimiert werden. Sie sollte gross genug sein, um eine reversible Adsorption von Detergenzien zu verhindern, aber unterhalb der Limite bleiben, bei welcher Anker Eisenoxidnanopartikel aufzulösen beginnen (Abbildung 1).

Einfluss vom PEG Molekulargewicht auf die Nanopartikelstabilität

Nachdem Anker gefunden wurden, die Moleküle irreversibel auf Eisenoxidnanopartikeloberflächen anbinden können, wurde der Einfluss des PEG Molekulargewichts auf die Nanopartikelstabilität, die Detergenzienpackungsdichte und das Detergenziendichteprofil

mittels dynamischer Lichtstreuung, Kleinwinkel-Neutronenstreuung und Thermogravimetrie untersucht. Dabei stellte sich heraus, dass Detergenzien, die PEG mit Molekulargewichten zwischen 5 kDa und 10 kDa enthalten, zu höchster Nanopartikelstabilität führen. Dynamische Lichtstremessungen haben gezeigt, dass Nanopartikel, die mit Detergenzien oberflächenmodifiziert wurden, die PEGs mit Molekulargewichten unterhalb von 1.5 kDa beinhalten, instabil sind. Diese experimentellen Ergebnisse stehen in Einklang mit theoretischen Berechnungen von Potentialen zwischen zwei Partikeln. Wenn das PEG Molekulargewicht 10 kDa überschreitet, ist die Detergenzienpackungsdichte zu gering, was auch zur Agglomeration von Nanopartikeln führt. Deshalb muss nicht nur der Anker, sondern auch das PEG Molekulargewicht optimiert werden, um eine gute Nanopartikelstabilität erzielen zu können.

Funktionalisierung von Eisenoxidnanopartikeln

Weil solche Detergenzien mit dem Anker an die Nanopartikeloberfläche binden, werden die Endgruppen der Platzhaltermoleküle grossteils in der Nähe der Grenzfläche der Nanopartikeln mit der flüssigen Phase sein. Deshalb kann die Funktionalität der Nanopartikel durch Änderung der Endgruppe des Platzhalters beliebig angepasst werden. Unterschiedliche Methoden, Nanopartikel mit Antikörpern zu funktionalisieren, wurden miteinander verglichen.

Biotin-präsentierende Eisenoxidnanopartikel wurden mit einer Monolage von Neutravidin beschichtet. Solche Nanopartikel wurden mit zwei verschiedenen biotinylierten Antikörpern funktionalisiert. Diese Strategie war erfolgreich, wenn die Nanopartikelkonzentration tief gehalten und die Nanopartikel gleich nach der Funktionalisierung getestet wurden. Andernfalls begannen sich solche Nanopartikel über die verschiedenen Biotine, die an einem Antikörper angebunden sind, zu vernetzen. Das Vernetzen führte zu einem Verlust der Kontrolle über Grösse und Stabilität dieser Nanopartikeln.

Als Alternative wurden Antikörper über Amin-Gruppen kovalent an Acrylat-präsentierende Nanopartikel gebunden. In Analogie zu den Nanopartikeln, die via die Biotin-Avidin Bindungsstrategie funktionalisiert wurden, führte auch das kovalente Anbinden von Antikörpern an Nanopartikel wegen den zahlreichen Amin Gruppen, die ein Antikörper besitzt, zur Vernetzung der Nanopartikeln.

Hingegen konnten Acrylat-präsentierende Nanopartikel mit Fluorophoren funktionalisiert werden. Weil Fluorophore nur eine Amingruppe pro Molekül besitzten, vernetzten sich Nanopartikel während der Funktionalisierung nicht. Die resultierenden Nanopartikel

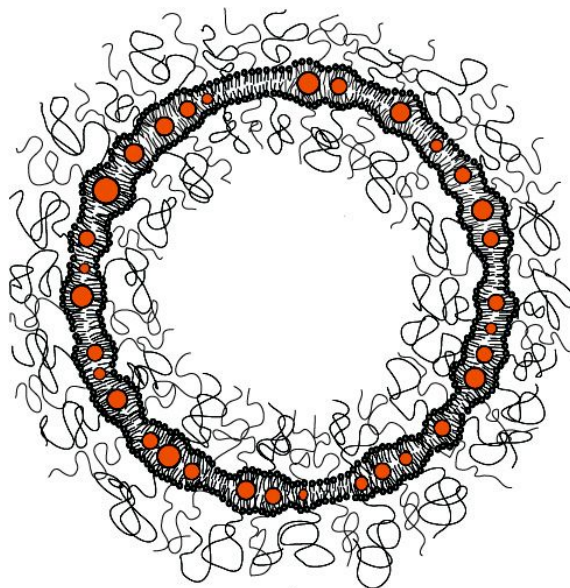


Abbildung 2: Sketch von Eisenoxidnanopartikeln eingebettet in der Membran von Liposomen. Individuell stabilisierte Eisenoxidnanopartikel ordnen sich im hydrophoben Teil der Liposommembran an. Diese Eisenoxidnanopartikel können als Aktuator für eine kontrollierte Freisetzung von Cargo genutzt werden, wenn die Liposome einem alternierenden magnetischen Wechselfeld ausgesetzt werden. Die Liposome wurden mit PEG sterisch stabilisiert damit sie nicht agglomerieren, wenn sie unterhalb ihrer Phasentransformationstemperatur (T_m) aufbewahrt werden.

konnten sowohl mit Magnetresonanz Spektroskopie als auch mit Fluoreszenzmikroskopie visualisiert werden.

Anordnung von Eisenoxidnanopartikeln in Überstrukturen mit temperaturabhängigen Eigenschaften

Eisenoxidnanopartikel generieren lokal Wärme, wenn sie einem alternierenden magnetischen Wechselfeld ausgesetzt sind. Wenn sie in Vesikel eingebettet sind, deren Permeabilität temperaturabhängig ist, kann die durch Eisenoxidnanopartikel lokal generierte Wärme zur Freisetzung von Cargo genutzt werden. Dabei wird Cargo effizienter freigesetzt, wenn die Eisenoxidnanopartikel direkt in der temperaturabhängigen Struktur lokalisiert sind. Eine kontrollierte und stabile Anordnung von Eisenoxidnanopartikeln in Vesikel-Membranen kann nur sichergestellt werden, wenn die Nanopartikel genügend klein sind und vorgängig mit einer irreversibel gebundenen, dünnen hydrophoben Schale bedeckt wurden. Die optimale Bindungsaffinität von Nitrocatecholen zu Fe_3O_4 Oberflächen ermöglichen es, eine Monolage von hydrophoben Detergenzien wie Palmityl-nitroDOPA irreversibel auf die Nanopartikel-Oberfläche zu binden. Es wurde gezeigt, dass sich solch

individuell stabilisierte hydrophobe Nanopartikel in den hydrophoben Teil von Liposommembranen anordnen (Abbildung 2).

Liposome, die aus 1,2-distearoyl-sn-glycero-3-phosphocholine (DSPC) Lipiden bestanden und hydrophobe Eisenoxidnanopartikel in ihrer Membran hatten, wurden durch Extrusion hergestellt. Die Liposomstruktur und das Ausmass der Membrandeformation, die durch die Eisenoxidnanopartikel hervorgerufen wurde, wurden mit dynamischer Lichtstreuung und Kleinwinkel-Neutronenstreuung untersucht. Mittels Differentkalorimetrie-messungen wurde festgestellt, dass trotz grosser Deformationen der Liposommembran die Liposomphasentransformationstemperatur (T_m) durch die Präsenz der Eisenoxidnanopartikel in der Liposommembran nicht beeinflusst wurde.

DSPC wurde wegen seiner T_m von 55 °C, die deutlich über der Körpertemperatur ist, gewählt. Während Liposome in der Gelphase ($T < T_m$) undurchlässig sind, sind sie um T_m herum sehr permeabel. Deshalb konnte mittels eines alternierenden magnetisches Wechselfelds die Temperatur lokal in der DSPC Membran, wo Eisenoxidnanopartikel lokalisiert waren, durch diese Nanopartikel zu T_m erwärmt werden wo Cargo frei gesetzt wurde. Es wurde gezeigt, dass die Freisetzung von Calcein effizienter war, wenn die hydrophoben Eisenoxidnanopartikel in der Membran angeordnet waren, also das für Magnetoliposome der Fall war, die hydrophile Eisenoxidnanopartikel in ihrem Lumen hatten.

Um zu untersuchen, ob Cargo wirklich mittels alternierendem magnetischen Wechselfeld freigesetzt werden kann, wurde Calcein als Modellmedikament in das Liposomlumen geladen. Ein Vergleich zwischen palmityl-nitroDOPA und ölsäure stabilisierten Eisenoxidnanopartikeln hat gezeigt, dass eine dünne, irreversibel gebundene hydrophobe Detergenzienschale, die die Eisenoxidnanopartikel einzeln und auch bei erhöhten Temperaturen stabilisiert, der Schlüssel zur verbesserten Effizienz der Freisetzung von Cargo aus solchen Liposomen ist. Das ist darauf zurückzuführen, dass Nanopartikel, die in der Membran eingebettet sind, die lokal generierte Wärme direkt an die Membran abgeben, ohne das Wasser aufwärmen zu müssen.

Dynamische Lichtstremessungen, die an Liposomen gemessen wurde, bevor und nachdem sie einem alternierenden magnetischen Wechselfeld ausgesetzt waren, zeigten, dass Liposome auch nach der Exposition zum magnetischen Wechselfeld noch intakt sind. Weil nach dem Abschalten des alternierenden magnetischen Feldes kein Cargo mehr freigesetzt wurde, konnte Cargo schrittweise freigesetzt werden, indem Liposome, die Eisenoxidnanopartikel in ihrer Membran haben, mehrmals für kurze Zeit einem alternierenden magnetischen Wechselfeldpuls ausgesetzt wurden. Solche Kapseln erlauben deshalb eine zeitlich und mengenmässig kontrollierte Abgabe von Cargo, ohne dass die Wassertem-

peratur T_m erreicht. Das macht diese Kapselsysteme für biomedizinische und chemische Anwendungen attraktiv.

Der Einfluss einer kontrollierten Oberflächenmodifikation von Eisenoxidnanopartikeln auf deren Anwendung

Die Resultate der funktionsierten, individuell stabilisierten, hydrophilen Nanopartikel und der hydrophoben Nanopartikel, die in Liposomenbranen eingebettet waren, haben zeigt, dass leistungsstarke, spezialisierte Anwendungen von Eisenoxidnanopartikeln nur realisiert werden können, wenn die Nanopartikel mit einer dünnen, irreversibel gebundenen Detergenzienschale umgeben sind. Des Weiteren illustrieren diese Beispiele die Wichtigkeit des Ankers für die Oberflächenmodifizierung von Eisenoxidnanopartikeln. Es ist nur möglich, die Nanopartikel an die spezifischen Anwendungen anzupassen, wenn die Chemie und Funktionalität an der Nanopartikeloberfläche genau kontrolliert werden können. Wie in dieser Doktorarbeit gezeigt, eröffnen geeignete Anker, die Platzhaltermoleküle und funktionelle Gruppen irreversibel an die Eisenoxidnanopartikeloberfläche binden können die Möglichkeit, neue, früher nicht umsetzbare Anwendungen von hydrophilen und hydrophoben Eisenoxidnanopartikeln realisieren zu können.

Contents

1	Background	5
1.1	Size Dependent Material Properties	6
1.1.1	Nanoparticle Size Effects	6
1.1.2	Effects of a High Surface : Volume Ratio	10
1.2	Applications of Optically Active Nanoparticles	10
1.2.1	Optically Active Nanoparticles as Antennas	10
1.2.2	Biomedical Applications of Optically Active Nanoparticles	11
1.3	Applications of Magnetic Nanoparticles	11
1.3.1	Data Storage	11
1.3.2	Ferrofluids Dispersed in Organic Solvents	11
1.3.3	Biomedical Applications of Magnetic Nanoparticles	12
1.4	Biomedical Applications: Diagnostics	13
1.5	Biomedical Applications: Therapeutics	18
1.5.1	Hyperthermia	18
1.6	Biomedical Applications: Drug Delivery	19
1.6.1	Release	19
1.6.2	Triggered Release	20
1.6.3	Requirements for Nanoparticles Intended for Biomedical Applications	25
1.7	Nanoparticle Stability	25
1.7.1	Electrostatic Nanoparticle Stabilization	26
1.7.2	Steric Nanoparticle Stabilization	26
1.7.3	Electrostatic vs. Steric Stabilization	27
1.8	Designing Protein Resistant, Functional Surfaces	27
1.8.1	Protein Resistance	27

1.8.2	Nanoparticle Functionalization	30
1.8.3	Nanoparticle Biodistribution	31
1.9	Surface Modification of Iron Oxide Nanoparticles	32
1.9.1	Steric Stabilization with High Molecular Weight Dispersants . . .	33
1.9.2	Steric Stabilization with Low Molecular Weight Dispersants . . .	35
1.10	Assembly of Nanoparticles in Liposome Membranes	39
1.10.1	Liposomes Containing Nanoparticles in their Membranes	39
1.11	Nanoparticles as Markers and Actuators	43
2	Scope of the Thesis	45
3	Experimental	51
3.1	Dispersant Synthesis	51
3.1.1	Materials for Dispersant Synthesis	51
3.1.2	Synthesis of Anchors	51
3.1.3	PEG-Anchors with PEG $M_w > 1$ kDa	52
3.1.4	PEG-Anchors with PEG $M_w < 1$ kDa	52
3.1.5	Palmityl-nitroDOPA	53
3.2	Preparation of Oxide Substrates	53
3.2.1	Materials for Core Synthesis	53
3.2.2	Iron Oxide Core Synthesis: Aqueous Precipitation	54
3.2.3	Iron Oxide Core Synthesis: Microwave Assisted Synthesis	54
3.2.4	Oil Bath Synthesis	54
3.2.5	Magnetron Sputtering of Flat Iron Oxide Films	56
3.3	Nanoparticle Stabilization	58
3.3.1	Nanoparticles Synthesized with the Aqueous Precipitation Method	58
3.3.2	Nanoparticles Synthesized in Organic Solvents	59
3.3.3	NP Stabilization with Palmityl-nitroDOPA	60
3.3.4	Dispersant Adsorption on Flat Surfaces	60
3.4	Nanoparticle Functionalization	61
3.4.1	Materials for Nanoparticle Functionalization	61
3.4.2	Biotin-Avidin Functionalization	61
3.4.3	Succinimide 4-Formylbenzamide (SFB) - Succinimidyl 6- Hydrazinonicotinamide Acetone Hydrazone (SANH) Coupling .	62
3.4.4	Acrylate-Amine Ligand Coupling	62
3.4.5	Fluorescent Labeling of Nanoparticles	63

3.5	Complexation of Anchors with Iron Ions	63
3.6	Liposomes	64
3.6.1	Materials for Liposomes	64
3.6.2	Liposome Assembly	64
3.6.3	Alternating Magnetic Field Heating of Liposomes	65
4	Methods	67
4.1	Chemical Analysis of Dispersants	67
4.1.1	Microelement Analysis	67
4.1.2	Nuclear Magnetic Resonance (NMR)	67
4.1.3	Mass Spectrometry (MS)	68
4.1.4	Electron Paramagnetic Resonance (EPR)	69
4.1.5	Fourier Transform Infrared Spectroscopy (FTIR)	71
4.1.6	Ultraviolet/Visible (UV/VIS) Spectroscopy	72
4.2	Nanoparticle Core Analysis	73
4.2.1	X-ray Diffraction (XRD)	73
4.2.2	Transmission Electron Microscopy (TEM)	74
4.2.3	X-ray Photoelectron Spectroscopy (XPS)	79
4.2.4	Near Edge X-ray Absorption Fine Structure Spectroscopy (NEX- AFS)	81
4.3	Magnetic Analysis	83
4.3.1	Vibrating Sample Magnetometry (VSM)	83
4.3.2	Magnetic Resonance Imaging (MRI)	84
4.3.3	Specific Absorption Rate (SAR) Determination	88
4.4	Analysis of Core-Shell Nanoparticles	90
4.4.1	Scattering Techniques	90
4.4.2	Thermogravimetric Analysis (TGA)	105
4.4.3	Differential Scanning Calorimetry Analysis (DSC)	106
4.4.4	Quartz Crystal Microbalance with Dissipation Monitoring (QCM-D)	106
5	Iron Oxide Core Synthesis	109
5.1	Background	109
5.2	Aqueous Precipitation	113
5.3	Microwave Assisted Synthesis	113
5.3.1	Core Size	113

5.3.2	Synthesis Parameters that Determine the Nanoparticle Size Distribution	122
5.4	Oil Bath Synthesis	126
5.4.1	Influence of the Reaction Temperature	126
5.4.2	Influence of the Reaction Time	132
5.4.3	Influence of the Temperature Ramping Procedure	135
5.5	Magnetic Properties of Iron Oxide Nanoparticles	136
5.5.1	Saturation Magnetization of Iron Oxide Nanoparticles	136
5.5.2	SAR of Iron Oxide Nanoparticles Synthesized in the Oil Bath	138
5.6	Discussion	141
5.6.1	Influence of Organic Reactions on the Presence of Ultrasmall Nanoparticles	142
5.6.2	Characterization of the Size and Size Distribution of Nanoparticles	146
5.7	Summary	147
6	Anchors for Steric Stabilization of Iron Oxide Nanoparticles	149
6.1	Background	149
6.2	Effect of Anchor on Nanoparticle Stability	151
6.2.1	Influence of Anchor on Nanoparticle Stability at Elevated Temperatures	153
6.2.2	Dispersant Binding Reversibility	155
6.2.3	Dispersant Packing Density	158
6.3	Summary	167
7	Mechanistic Aspects of Anchor-Iron Oxide Interactions	169
7.1	Background	169
7.2	Stability of Fe_3O_4 vs. Fe_2O_3 Nanoparticles	171
7.3	Electronic Changes upon Anchor Adsorption	171
7.3.1	Influence of Anchors on Surface Bound Fe(III) Ions	173
7.3.2	Vibrational Changes in Anchors upon Adsorption on Iron Oxide Nanoparticles	180
7.4	Optimizing Adsorption Conditions	184
7.4.1	Nitrocatechols	188
7.4.2	Catechols	191
7.4.3	Mimosine	191
7.5	Influence of the Anchor Binding Affinity on Fe_3O_4 Nanoparticle Stability	191

7.6	Influence of nitroDOPA on Saturation Magnetization	195
7.6.1	Surface Effects on Saturation Magnetization	197
7.7	Summary	198
8	Iron Oxide Nanoparticle Shell	201
8.1	Background	201
8.1.1	Polymer Density Profile on Flat Surfaces	201
8.1.2	Polymer Density Profile on Highly Curved Surfaces	202
8.2	Calculations of the Inter-Particle Interaction Potential	205
8.2.1	Van-der-Waals Potential	205
8.2.2	Magnetic Potential	206
8.2.3	Electrostatic Potential	207
8.2.4	Steric Potential	207
8.2.5	Total Inter-Particle Potential Using the MWC Theory	209
8.2.6	Total Inter-Particle Potential Using the de Gennes Theory	213
8.3	Experimental Studies on the Dispersant Density Profile	213
8.4	Ultra-Stable Iron Oxide Cores	214
8.4.1	Effect of the PEG M_w on Nanoparticle Stability	214
8.4.2	Effect of the PEG M_w on the Dispersant Packing Density	216
8.4.3	Effect of the PEG M_w on the Core Size Distribution	219
8.4.4	Effect of the PEG M_w on the Dispersant Density Profile	220
8.4.5	Relaxivity of PEG-nitroDOPA Stabilized Nanoparticles	229
8.5	Iron Oxide Nanoparticles that Sedimented During Centrifugation	233
8.5.1	Effect of the PEG M_w on Nanoparticle Stability	233
8.5.2	Effect of the PEG M_w on the Dispersant Packing Density	235
8.6	Summary	237
9	Iron Oxide Nanoparticle Functionalization	239
9.1	Background	239
9.1.1	Biotin-Avidin Functionalization	239
9.1.2	Covalent Functionalization	240
9.2	Functionalization through Biotin-Avidin Coupling	241
9.2.1	Dispersant Packing Density	242
9.2.2	Biotin Quantification	243
9.2.3	Neutravidin Quantification	244
9.2.4	Functionalization with Biotinylated Antibodies	247

9.2.5	Shortcomings of the Biotin-Avidin Coupling Strategy	251
9.3	Nanoparticle Functionalization through Covalent Bonds	252
9.3.1	Succinimide 4-Formylbenzamide (SFB) - Succinimidyl 6-Hydrazinonicotinamide Acetone Hydrazone (SANH) Coupling Strategy	252
9.3.2	Functionalization through Michael Addition	253
9.3.3	Functionalization with Fluorophores	255
9.4	Summary	256
10	Assembly of Iron Oxide Nanoparticles into Thermoresponsive Superstructures	259
10.1	Background	259
10.1.1	Liposomes	259
10.2	Liposome Assembly	263
10.2.1	Hydrophobic Iron Oxide Nanoparticles	263
10.2.2	Assembly of Liposomes	263
10.3	Characterization of Liposomes	264
10.3.1	Influence of Dispersant	264
10.3.2	Loading Efficiency	268
10.3.3	Effect of Nanoparticle Size on Liposome Morphology	268
10.3.4	Effect of Lipid Composition	271
10.3.5	Membrane Distortions Caused by Nanoparticles	271
10.3.6	Influence of Nanoparticles on T_m	276
10.4	Triggered Release	277
10.4.1	Release Mechanism	279
10.4.2	Effect of AMF Sequence	279
10.4.3	Release Efficiency	280
10.5	Summary	281
12	Conclusions	283
13	Outlook	289
13.1	Outlook	289
13.1.1	Fe_3O_4 Nanoparticles	289
13.1.2	Oxide Nanoparticles	290
13.1.3	Liposomes	293

13.1.4	Polymersomes	295
13.1.5	Concluding Remarks	296
	Curriculum Vitae	337
	M Appendix	341
M.1	Effect of Adsorption Conditions on Nanoparticle Stability	341
M.1.1	Effect of Solvent Nanoparticles are Washed With	341
M.1.2	Adsorption Conditions	342
M.2	Replacing Oleic Acid with nitroDOPA	343
M.3	Effect of PEG M_w on the Stability of Bimodally Distributed Iron Oxide Nanoparticles	345
M.3.1	Effect of PEG M_w on Iron Oxide Nanoparticle Stability	345
M.3.2	Effect of PEG M_w on the Dispersant Packing Density	346
M.3.3	Effect of PEG M_w on the Zeta Potential	346
M.3.4	Influence of Solvent Conditions on the Dispersant Layer Thickness	347
M.4	Iron Oxide Nanoparticles Synthesized by Aqueous Precipitation	348
M.4.1	Effect of Dispersant on Nanoparticle Stability	349
M.4.2	Characterization of Nanoparticle Stability	352
M.5	Chemical analysis of PEG(5)-anchors	352
M.5.1	MALDI-ToF	352
M.5.2	Microelement Analysis	353
M.5.3	NMR	356
M.6	Chemical Analysis of Dispersants Containing NitroDOPA as Anchor	358
M.6.1	MALDI-tof	358
M.6.2	Microelement Analysis	358
M.6.3	NMR	361

Abbreviations

A	Hamaker constant
AC	alternating current
AEY	Auger electron yield
AFM	atomic force microscope
AMF	alternating magnetic field
APS	ammonium persulfate
BET measurements	Brunner-Emmett-Teller measurements
BF	bright field
CLION	crosslinked iron oxide nanoparticle
CPMG	Carr-Purcell-Meiboom-Gill
CT	computed tomography
<i>D</i>	distance from the NP surface
DCTB	T-2[3-(4-t-butyl-phenyl)-2-methyl-2-propenylidene]malononitril
DF	dark field
DLS	dynamic light scattering
DLVO theory	Derjaguin-Landau-Verwey-Overbeek theory
DPPC	dipalmitoylphosphocholine
DSC	differential scanning calorimetry
DTGS	deuterated triglycine sulfate
ϵ	radiating energy
EDC	3-(dimethylaminopropyl) carbodiimide
EDX spectroscopy	energy dispersive X-ray spectroscopy
EELS	electron energy loss spectroscopy
EG	ethylene glycol
EPR	electron paramagnetic resonance
EPR	enhanced permeation retention

FACS	fluorescence activated cell sorting
FEG	field emission gun
Fe_3O_4	magnetite
FITC	fluoresceine
FTIR spectroscopy	fourier transform infrared spectroscopy
FWHM	full width of half maximum
γ	gyromagnetic ratio
$\gamma-Fe_2O_3$	maghemite
g	splitting factor
h	Planck constant
HAADF	high angle angular dark field
HOMO	highest occupied molecular orbital
HRTEM	high resolution transmission electron microscopy
HSP	heat shock protein
IEP	isoelectric point
κ^{-1}	Debye length
K	anisotropy constant
k_B	Bolzman constant
L	dispersant layer thickness
l_b	blob size
LSW theory	Lifshitz-Slyozov-Wagner theory
LUMO	lowest unoccupied molecular orbital
M_s	saturation magnetization
M_W	molecular weight
MALDI	matrix assisted laser decomposition/ionization
MBA	N,N^1 -methylene-bis-acrylamide
MLV	multilamellar vesicle
MR	magnetic resonance
MRI	magnetic resonance imaging
MS	mass spectroscopy
MSA	mercaptosuccinic acid
MW	microwave
MWC theory	Milner, Witten, Cater theory
N	number of repeat units of a polymer
NEXAFS	near edge X-ray absorption fine structure spectroscopy

NHS	N-hydroxysuccinimide
NIR	near infrared region
NP	nanoparticle
PAA	poly(acrylic acid)
PC	phosphocholine
PEG	poly(ethylene glycol)
PEI	poly(ethylene imine)
PEM	polyelectrolyte multilayer
PEO	poly(ethylene oxide)
PET	positron emission tomography
PEY	partial electron yield
PLL	poly(L-lysine)
PS	poly(styrene)
PVA	poly(vinyl amine)
PVP	poly(vinyl pyrrolidone)
PZC	point of zero charge
QCM-D	quartz microbalance with dissipation monitoring
QD	quantum dot
r	NP radius
R_F	flory radius
R_G	radius of gyration
$r.u.$	repeat unit
RES	reticuluendothelium system
RF	radio frequency
S/N ratio	signal to noise ratio
SANH	succinimidyl 6-hydrazinonicotinamide acetone hydrazone
SANS	small angle neutron scattering
SAR	specific absorption rate
SAXS	small angle X-ray scattering
SFB	succinimide 4-formylbenzamide
SFC theory	self consistent field theory
SLB	supported lipid bilayer
SPECT	single photon emission computed tomography
STEM	scanning tunnel microscope
τ	relaxation time

T	temperature
T_B	blocking temperature
T_m	liposome membrane transition temperature
TEM	transmission electron microscopy
TEOS	tetraethoxysilane
TEY	total electron yield
TGA	thermogravimetry analysis
Tof	time of flight
TOPO	trioctylphosphinoxide
UV	ultraviolet
ν	viscosity
V	volume
VCAM	vascular cell adhesion molecule
VIS	visible
VSM	vibrating sample magnometry
XPS	X-ray photoelectron spectroscopy
XRD	X-ray diffraction
YAG	yttrium aluminium granat
ζ	zeta potential

CHAPTER 1

Background

Colloids, defined as microscopic gas, liquid or solid objects dispersed in a gas, liquid or solid matrix, are omni-present in our daily life. Examples of well-known colloids are clouds, consisting of solid particles dispersed in a gaseous matrix, emulsions, such as mayonnaise, milk or hand creams that are liquid microscopic droplets dispersed in a liquid medium. Thus, colloids are essential for our daily life.

If the size of colloidal particles is decreased to or below 100 nm, these particles are called nanoparticles (NPs). The concept of NPs is in the general public, in contrast to the above mentioned general term "colloid", rather negatively connoted. This negative sentiment has been fueled by concerned reports about their toxicity and negative impact on our health that were broadcasted by the general media.

The question about long term toxicity of NPs is still not conclusively answered. Nevertheless, solid inorganic NPs are in long term routine use *e.g.* in sun creams, where TiO_2 NPs absorb UV light and therefore protect us from sun burn, in inks and in paints. Hence, even if we are not completely aware of their presence and impact on our daily life, we greatly benefit from their properties.

Metallic NPs were already used in medieval times for staining glass windows (Figure 1.1a). They appeared red if glass was supplemented with Au NPs and yellow if Ag NPs were added [2]. However, the underlying principles of why Au and Ag additives stain glass were not unraveled until last century. Today, the underlying reasons for these special, often size dependent, properties of nanoobjects are at least partially elucidated. They however remain a subject of major interest for both, fundamental studies and numerous applications. The great interest in nanoobject is mainly motivated by the fact, that they are considered to be one of the keys to significantly advance many technologies in very

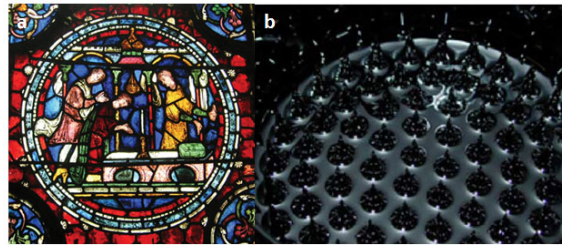


Figure 1.1: Examples of applications of NPs. (a) Plasmonic NPs were used already in medieval times to stain church windows [12] (with permission of Annex Publishing & Printing Inc.). (b) Ferrofluids form peak patterns if an external field is applied perpendicular to the ferrofluid layer [13].

different, for our daily life highly relevant, fields such as building blocks to form dense [3] and porous [4–6] ceramic structures, to reinforce composites [7, 8] and as catalysts [9–11].

1.1 Size Dependent Material Properties

If the size of films and colloids is reduced from the micro- to the nano-scale, bulk material properties often change and become size dependent [14, 15]. The physical principles underlying these size dependent changes of material properties usually are based on quantum physics. However, only with the advent of suitable characterization techniques, dating back to the development of scanning tunneling microscopes [16] followed by other, for modern nanoscience indispensable, characterization instruments and techniques, fundamental studies of these size dependent properties became scientifically accessible.

1.1.1 Nanoparticle Size Effects

Optical Properties

If the size of nanocrystals becomes comparable to the wavelength of the wave function of electrons, optical and electronic properties of metallic and semiconducting NPs start to deviate from those observed in bulk materials and become size dependent [17–19]. In these materials, electrons have been found to not behave as in metallic or semiconducting bulk materials, but show a quantum state behavior as in atoms [20–22].

If anisotropic metallic nanoobjects, so-called antennas, are illuminated with a plane wave

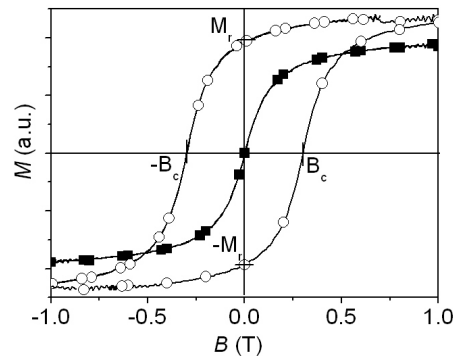


Figure 1.2: *Magnetization curves.* Example magnetization curves of ferro- and ferrimagnetic (-O-) and superparamagnetic (-■-) materials. While superparamagnetic materials have no net-magnetization at $B = 0$ T, ferro- and ferrimagnetic materials have a remnant magnetization M_r . Only if a corecitive field (B_c) is applied, ferro- and ferrimagnetic materials have a zero net-magnetic moment.

of light along their long axis, the conduction electrons form a polarization field that accumulates them at the distal end of the antenna (relative to the incident light). Therefore, the absorption spectra of metallic NPs and nanorods is highly dependent on their size and shape [23].

Optical properties of semiconducting nanocrystals, so-called quantum dots (QDs), of a size comparable to or smaller than the de Broglie wavelength are determined by quantum confinement effects. The quantization of electron levels in QDs greatly affects the luminescence spectra of such nanoobjects. Because the energy gap between the valence and conduction band is dependent on the QD size and shape, luminescent spectra of QDs are highly sensitive to their size and shape [24–26].

Magnetic Properties

Not only optical properties change if the object size is reduced to the nanoscale, but also magnetic properties are altered. Ferro-, antiferro- and ferrimagnetic materials consist of multiple magnetic domains that are separated by domain walls, so-called Bloch walls. The magnetic response of ferro- and ferrimagnetic bulk materials such as magnetite (Fe_3O_4) to externally applied magnetic fields shows hysteresis (Figure 1.2). This hysteresis is caused by multiple magnetic domains present in bulk ferro- and ferrimagnetic materials. Spins within one domain are oriented parallel to each other whereas the spin orientation of different magnetic domains varies. However, if no external magnetic field is applied, but the ferro- and ferrimagnetic material was once subjected to an external magnetic field

strong enough to saturate the magnetization of the bulk material, the orientation of spins in different magnetic domains is no longer equally distributed in all direction. This leads to a net magnetic moment, a so-called remnant magnetization (M_r), even in the absence of an external magnetic field. Only if a magnetic field in the opposite direction to the previously aligned magnetic moment is applied (a so-called corecitive field (B_c)), will such a bulk materials have a zero net-magnetic moment (Figure 1.2) [27–29].

The energy required to flip spins aligned in the external magnetic field by 180 °C is for ferro- and ferrimagnetic materials determined by their remnant magnetization and the corecitive field and proportional to the area of the hysteresis. Therefore, the heat generated by such materials if exposed to an alternating magnetic field (AMF) also scales with the area of the hysteresis [30].

If the size of ferro- and ferrimagnetic objects becomes comparable to or smaller than a magnetic domain, the energy cost for magnetostatic interactions of parallel aligned spins becomes smaller than that for creating Bloch walls [30, 31]. Thus, these nanoobjects consist of a single magnetic domain. However, the size of a magnetic domain does not have to equal that of a crystal domain. NPs that consist of a single crystal domain can have multiple magnetic domains. Thus single crystalline NPs can show ferro- or ferrimagnetic behavior.

The critical size of a magnetic domain, beyond which multiple magnetic domains are energetically favorable, is partially determined by the anisotropy constant K of the material. This anisotropy constant, that describes how easily spins can be aligned along the direction of the magnetic field, is typically much higher for NPs compared to their bulk counterparts. This can be assigned to surface effects that hinder re-alignment of spins [11, 27].

NPs consisting of a single magnetic domain show superparamagnetic behavior at temperatures higher than the blocking temperature T_B . Superparamagnetism is characterized by an initially almost linear increase of the magnetization of nanoobjects with the externally applied magnetic field before the magnetization gradually saturates when all spins are aligned. If the external magnetic field is removed, spins within one NP are oriented in the same direction whereas the alignment of spins of different NPs is randomized. Therefore, superparamagnetic NP assemblies have no net-magnetic moment if $B = 0$ T (Figure 1.2) [15, 32].

Next to the phenomenological difference in the magnetic behavior of small, superparamagnetic NPs compared to their bulk counterparts, the saturation magnetization M_s of the former is below that of the respective bulk materials. Furthermore, M_s decreases with

decreasing core size [33–35]. This decrease was assigned to surface anisotropy effects [36] that start to become increasingly important with increasing surface : volume ratio and thus with decreasing NP size.

The magnetization direction of superparamagnetic materials can easily be switched by applying a static or alternating magnetic field and $T > T_B$. T_B is blocking temperature above which spins re-align within a defined time interval τ of the experiments (equation 1.1) where τ_0 is the relaxation time at $T = 0$ K, k_B the Boltzman constant, T the absolute temperature, K the magnetic anisotropy constant and V the NP volume. τ is typically taken as 100 s [37].

$$\tau = \tau_0 e^{\frac{KV}{k_B T}} \quad (1.1)$$

If an AMF is applied to superparamagnetic NPs, heat can be generated by two processes, namely by Brownian and Néels relaxation. While Brownian relaxation generates heat through friction caused by the Brownian motion and rotation of NPs, Néel relaxation causes spins to re-align in the crystal lattice of NPs without movement of NPs and therefore NP lattices. The contributions of Brownian and Néels relaxations to the total heat generated by superparamagnetic NPs if subjected to an AMF are determined by the relative ratio of the respective relaxation times τ_B and τ_N [38–43]. τ_B is defined as

$$\tau_B = \frac{3\nu V}{k_B T} \quad (1.2)$$

while τ_N is

$$\tau_N = \frac{\sqrt{\pi}}{2} \tau_{0 \text{ att}} \frac{e^{\frac{KV}{k_B T}}}{\sqrt{\frac{KV}{k_B T}}} \quad (1.3)$$

where ν is the viscosity of the medium NPs are suspended in and $\tau_{0 \text{ att}}$ the attempt time, which is typically $\approx 10^{-9}$ s for NPs [15, 31]. The total relaxation time τ is defined as

$$\frac{1}{\tau} = \frac{1}{\tau_B} + \frac{1}{\tau_N}. \quad (1.4)$$

1.1.2 Effects of a High Surface : Volume Ratio

The high surface : volume ratio of NPs not only influences their magnetic properties. Material properties such as the melting temperatures of metals [44] and semiconductors [14] drastically decreases with decreasing NP size [45]. The depression of the melting temperature was assigned to the increasing contribution of energetically more expensive surface atoms to the total number of atoms with decreasing size of nanoscale objects [14]. Yet another example where the high surface : volume ratio of nanoobjects greatly impacts their material properties is the equilibrium crystal phase. Nanoscale objects can have different equilibrium phases at room temperature compared to the respective bulk materials. Prominent examples are Al_2O_3 [46] and ZrO_2 [47, 48] NPs that are in a metastable phase at room temperature compared to bulk materials. Furthermore, for very small NPs (≈ 5 nm) diamond has been reported to be more stable than graphite [49].

The change of the equilibrium phase of these materials is based on the very different surface : volume ratios of bulk materials and NPs respectively, as exemplified on Al_2O_3 . $\alpha-Al_2O_3$ has a lower bulk and higher surface energy compared to $\gamma-Al_2O_3$ [46]. Thus, the high surface : volume ratio of NPs renders the $\gamma-Al_2O_3$ the energetically most favorable phase for NPs whereas $\alpha-Al_2O_3$ is energetically least expensive for bulk materials [46].

1.2 Applications of Optically Active Nanoparticles

1.2.1 Optically Active Nanoparticles as Antennas

If composites consisting of responsive materials are supplemented by optically active, semiconducting or metallic NPs, the latter can serve as actuators and locally couple and amplify externally applied electromagnetic fields. These NPs can thus actuate smart composites [50]. Alternatively, if such NPs are not embedded in a composite matrix but individually dispersed or arranged on a substrate, they can be exploited as antennas to locally generate heat [51, 52] or to *e.g.* harvest energy which is released to drive photosynthetic reactions [53].

1.2.2 Biomedical Applications of Optically Active Nanoparticles

The plasmonic properties of noble metal NPs and nanorods render these nanostructures interesting as a diagnostic tool and for cancer therapy [54, 55]. As described above, the sensitivity can be increased many times if objects under investigation, such as fluorescently labeled proteins, are brought in close proximity to metallic NPs [52]. Field enhancements caused by plasmonic NPs are thought to increase the detection sensitivity *e.g.* of precursors for progressing diseases. This would greatly increase the chances to cure such diseases at early stages. Furthermore, the heat locally generated upon illumination of gold nanoshells was shown to improve the response to radiation therapy of peripheric cancerogenic cells *in vivo* [56, 57].

However, light in the visible range is strongly absorbed by tissues [58, 59]. Thus, applications of NPs < 50 nm [60], that require to be excited outside the optically transparent window of tissues ($\approx 600 - 1000$ nm) [58, 59], are restricted to peripheral locations in the body.

1.3 Applications of Magnetic Nanoparticles

1.3.1 Data Storage

Self-assembled, alloyed *e.g.* FePt NPs are considered to be essential parts of future data storage devices possessing unsurpassed storage density. If such NPs are self-assembled, their spins align. Because alloyed FePt NPs are magnetically hard, meaning they do not easily loose the magnetization upon removal of the external magnetic field, such devices were shown to have a high data storage capacity [61, 62].

1.3.2 Ferrofluids Dispersed in Organic Solvents

Applications of ferrofluids, based on magnetic NPs with diameters ranging from 4 nm up to a few μm , dispersed in organic solvents, were recognized more than 30 years ago (Figure 1.1b). The interest in ferrofluids for a broad field of applications did not cease until now. Ferrofluids are used as hermetic seals, as damper to protect sensitive parts of machines *e.g.* in the textile industry, in robots and machine tools, they are applied in pumps, as valves, bearings and in loudspeakers [63, 64].

Water Purification

Thanks to their high surface : volume ratio, surface modified, magnetic NPs with diameters between 10 and 50 nm, suspended in water, are used to magnetically remove toxic impurities from water [65, 66].

1.3.3 Biomedical Applications of Magnetic Nanoparticles

In the biomedical field, magnetic NPs are primarily applied *in vivo* as diagnostic tools such as magnetic resonance (MR) contrast agents, in therapeutics for hyperthermia applications and as triggers in drug delivery vehicles. Additionally, the ability to magnetically manipulate them allows for *in vitro* tracking and separation of cells and proteins labeled with magnetic NPs [67].

However, these applications rely on non-toxic NPs. Independent on the composition, the high surface : volume ratio of NPs not only affects physical properties as was outlined above, but it has also spawned an ongoing debate about NP toxicity [68]. For example, surface atoms from NPs are thought to potentially abstract electrons from O_2 creating superoxide radicals [69]. Despite the lack of consensus about nanotoxicity issues, especially iron oxide NPs are routinely used in clinics for *in vivo* applications [67].

The lower concerns about toxicity for *in vivo* applications of iron oxide NPs [67, 70, 71] are mainly related to their comparably fast decomposition and clearance in the body through dissolution into Fe^{3+} ions under acidic conditions [15, 72]. The resulting Fe^{3+} ions can be fed into the natural iron storage which is 3-5 g iron for an adult human [15, 72]. Thus the additional amount of iron released from dissolved iron oxide NPs is negligible if iron oxide NP concentrations in the mg range are injected. In contrast, many other magnetic materials, such as Co , have higher M_s compared to iron oxide and would therefore respond more strongly to externally applied magnetic fields, but are toxic. Therefore, the vast body of diagnostic [70, 73] and therapeutic [74–77] applications of magnetic NPs relies on iron oxide NPs.

Biomedicine is one of the important fields of applications for NPs where advanced, surface engineered NPs are key both, for diagnostic and therapeutic purposes. Because of the importance of these application areas of NPs, they are discussed in the following.

1.4 Biomedical Applications: Diagnostics

Chances to cure severe diseases such as cancer or atherosclerosis drastically decrease with increased progression of such often lethal diseases. Therefore, an early and reliable diagnosis is of paramount importance. For this purpose, different diagnostic techniques have been developed and optimized in the past. However, the continued demand for improved sensitivity and spatial resolution of diagnostic tools motivated the development of additional improvements such as contrast agents [15, 78]. In the following, the clinically most often used diagnostic techniques are briefly summarized.

Ultrasound

Ultrasound is a cost effective, easy and fast diagnostic tool where a spacial resolution of 50 - 5000 μm can be achieved. However, the limited penetration depth of ultrasound waves (up to a few cm, depending on the wavelength used) and the poor sensitivity limit the diagnostic value of this technique [79–81].

To increase spatial resolution, ultrasound contrast agents, such as air containing microbubbles and liposomes, were initially used to monitor tissue perfusion. These contrast agents were further developed and functionalized such that they can now be targeted to the desired locations. However, a still unsatisfactorily resolved problem is to bind such large contrast agents to targets on the endothelium [82].

Computed Tomography (CT)

The fast acquisition time and comparably moderate costs of CT renders this technique one of the key diagnostic tools in medicine today. It results in good spatial and anatomic resolution (in the sub-mm range). However, soft tissues are difficult to discriminate with CT due to poor contrast. Furthermore, patients have to be exposed to X-rays. This is considered to be a major disadvantage of CT compared to other imaging modalities [79, 83, 84]. The inherently poor soft tissue contrast often necessitates the use of CT contrast agents if these tissues are to be probed. Typical CT contrast agents consist of liposomes, nanoemulsions, micelles, dendrimers and polymer based NPs that encompass heavy metals such as iodine and optionally drugs. However, their toxicity, mainly induced by the heavy ions required to enhance contrast, is still debated [85].

Fluorescence Microscopy

A comparably high sensitivity and spatial resolution is achieved with optical methods such as fluorescence microscopy. However, the short penetration depth in tissues limits its *in vivo* applicability to peripheral locations. Due to its ease and cost effectiveness, it is, however, often used for *in vitro* investigations and studies on small animals [79, 80, 84]. Next to organic fluorophores or fluorescent proteins used to label objects of interest, NPs such as *Au* NPs or QDs are used *e.g.* to visualize cellular structures and track motions of individual proteins in cells. Such NPs do not photobleach in contrast to organic fluorophores and thus considerably facilitate imaging. The compared to organic fluorophores narrow emission spectra of such NPs significantly reduces the risk of crosstalk of NPs with different absorption and emission wavelengths. Because of the narrow emission range of optically active NPs, that can be tailored by controlling their size, different subpopulations of proteins can be simultaneously labeled with NPs emitting at different wavelengths [72, 86, 87].

Single Photon Emission Computed Tomography (SPECT) and Positron Emission Tomography (PET)

If sensitivity is crucial, SPECT is often the imaging technique of choice. Pharmaceuticals labeled with radioactive tracers are injected into the patient. The γ -ray emitting radiotracers can be detected with a γ -camera resulting in 2D or 3D images. However, injecting radioactive tracers requires justification. Furthermore, because of a very limited lifetime of these radiotracers, appropriate synthesis facilities have to be located reasonably close to the SPECT imaging facility.

Similar to SPECT, PET relies on the detection of radioactive elements. However, in contrast to SPECT, PET tracers are positron emitters. The emitted positrons collide with electrons in the body. This results in two γ -rays that are emitted in opposite directions. The time difference of their arrival at a detector that surrounds the investigated object allows to precisely spatially localize the origin of the γ -rays. This is the reason for the very high spacial resolution of PET. The higher sensitivity obtained with PET, compared to SPECT, however, has to be traded off against the shorter half-life time of PET radiotracers that necessitates a close-by cyclotron where these labels can be synthesized and optionally functionalized with targets. However, this complicates contrast agent handling and timing of experiments [79, 80, 84].

Magnetic Resonance Imaging (MRI)

Complementary to SPECT and PET, MRI measures relaxation times of proton spins oriented in a constant external magnetic field. Therefore, soft tissues, that all contain water, naturally yield MR contrast. Furthermore, MRI does not require radioactive tracers, which facilitates follow-up studies. Despite these benefits, the first MR scans on humans were not published until 1977 [88].

MRI suffers from a limited spacial resolution (in the sub-mm range) and a sensitivity that is $10^6 \times$ lower compared to SPECT or PET. Furthermore, it is a costly diagnostic technique [89] and special care has to be exercised with patients which have metal implants. Despite these shortcomings, the complementarity of the high sensitivity of PET or SPECT with the inherent tissue contrast of MRI renders a combination of MRI with SPECT or PET particularly beneficial for an early, accurate diagnosis of progressive diseases [81, 83, 84]. While the development of a combined PET/MRI instrument started around the same time as a prototype of a combined CT/SPECT instrument was built (1998), technical challenges only allowed to build a combined PET/MRI human scanner prototype in 2007. Thus, this combined imaging method is not yet established [72].

Magnetic Resonance Contrast Agents

Early diagnosis of certain diseases, such as atherosclerosis and cancer, requires molecular sensitivity that currently cannot be achieved with conventional MRI. However, targeted MR contrast agents are believed to indirectly increase the MR sensitivity such that cellular or even molecular resolution is conceivable [90]. If MR contrast agents are functionalized with ligands that specifically bind to early precursors of a disease, accumulation of contrast agents reflects the localization of such markers and thus indicates that the patient suffers from the corresponding disease already at an early stage [80, 91–95].

There are two different MR contrast agent types: Contrast agents that primarily reduce the longitudinal proton relaxation time T_1 lead to a signal enhancement on T_1 -weighted MR images. They are thus called positive MR contrast agents. The most prominent example for positive MR contrast agents is Gd^{3+} . Superparamagnetic contrast agents, that mainly shorten the transverse proton relaxation time T_2 are called negative contrast agents because they lead to a signal loss on conventional T_2 -weighted MR images [73, 96].

Signal losses are most frequently caused by large gradients in susceptibilities between adjacent tissues or local, instrumental based magnetic field inhomogeneities that cannot

be completely shimmed. Therefore, it is easier to assign signal enhancements to the presence of contrast agents. As a consequence, physicians prefer to have positive contrast agents. Gd^{3+} , however, is toxic if it is not strongly complexed. For patients who suffer from chronic renal diseases, Gd^{3+} is toxic even if it is strongly chelated [72, 97, 98]. Therefore, from a toxicologic point of view, iron oxide NPs are the preferred MR contrast agents. Furthermore, it has been shown that, by tuning the MR sequence, negative contrast agents such as iron oxide NPs can also lead to a signal enhancement, thus rendering them attractive as signal enhancing, biocompatible MR contrast agents [99].

Iron Oxide based Magnetic Resonance Contrast Agents

Different types of unfunctionalized iron oxide NPs stabilized with high molecular weight (M_w) dispersants such as dextran, that had previously been used as a plasma expander [95], are already FDA approved. They are used in clinics as negative contrast agents to detect lesions mainly in the liver and spleen where they naturally end up [94]. A comprehensive list of commercially available iron oxide based MR contrast agents was recently published by Laurent *et al.* [100]. However, none of these contrast agents is functionalized with a specific ligand.

Reports where *in vivo* targeting of iron oxide NPs is claimed are numerous [15]. However, NPs were almost exclusively targeted towards the liver, kidney or lymph nodes, locations they naturally end up during clearance. Alternatively, NPs were targeted to cancer cells, where they naturally accumulate due to the enhanced permeation retention (EPR) effect [15, 101–103]. However, studies where such NPs are successfully targeted to specific receptors are scant. The Weissleder group functionalized iron oxide NPs stabilized with crosslinked dextran with a peptide sequence that specifically binds to VCAM-1 receptors. VCAM-1 receptors are up-regulated on endothelial cells in atherosclerotic plaques. They could show that these targeted NPs were more readily taken up by endothelial cells in atherosclerotic regions in mice [104]. However, to the best of our knowledge, studies of targeted NPs that bind to extracellular receptors at sites where monocytes and macrophages, that are part of the reticuloendothelial system (RES) and naturally take up NPs to initiate their clearance, are not up-regulated, are lacking. One of the main reasons for the few successful applications of specifically targeted iron oxide based MR contrast agents is the difficulty to stabilize and functionalize such NPs [15]. Insufficiently stabilized, agglomerated NPs are too large to freely circulate in the body and perfuse through blood vessels. They therefore cannot readily be targeted and bear the risk to provoke

thrombosis. Furthermore, agglomerated NPs are easily detected by the RES and subsequently cleared. This reduces the effectiveness of such contrast agents. Therefore, good NP stability is of prime importance.

On the other hand, it has been shown that NP agglomeration [105–107] and controlled crosslinking of iron oxide NPs through oligonucleotides [108] enhances the T_2 -contrast. In fact, Monte-Carlo studies revealed a power law dependence of T_2^* on the number of NPs that form an agglomerate [107]. This is well in agreement with theory, where relaxivity has been shown to increase with the NP size [109, 110] and NP M_s [92]. Thus, NP stability and therefore good control over NP size, blood circulation time and surface chemistry has to be traded off against high T_2 and T_2^* signals [111].

Iron oxide NPs can be made to multifunctional contrast agents if additional labels such as fluorophores [112–116] or radiotracers [117–121] are irreversibly bound to their surface [72, 122]. A second modality helps to unequivocally locate such contrast agents and differentiate them from imaging artifacts. Second labels can be bound to *e.g.* magnetic cores through organic spacers or the magnetic cores can be coated with inorganic materials such as gold [123], and QD shells (*e.g.* $CdSe$ [124], or $LaF_3 : Ce, Tb$ [125]) [72]. Very recently, iron oxide NPs surrounded by a dielectric polymer layer upon which a Au shell was grown were shown to be both, superparamagnetic and active in the near infrared region (NIR) [126].

However, care must be exercised by combining different imaging modalities. Until recently, successful reports on combining iron oxide NPs with in the NIR active materials and molecules were hampered by the absorption of light caused by the iron oxide cores [126]. In fact, iron oxide, has been reported to quench CY5.5 and FITC if less than two fluorophores were attached to one iron oxide core. Based on the increased fluorescence observed if these fluorophores were cleaved from the iron oxide NP surface, this quenching was assigned to nonradiative iron oxide-fluorophore interactions [112]. Thus, close control over the surface chemistry and therefore the distance between optically active tracers and magnetic cores is key also for assembling multimodal imaging agents.

1.5 Biomedical Applications: Therapeutics

1.5.1 Hyperthermia

Cancer cells have been found to be more prone to cell death at high temperatures (≈ 45 °C) compared to healthy cells [127]. Thus, cancer can be treated if the temperature is increased to a level that it is lethal to malignant cells but at which healthy cells are less affected [128]. Especially in combination with X-ray or drug therapy, hyperthermia is believed to significantly increase the chance to cure cancer [15, 127, 129, 130].

In hyperthermia treatments that are not assisted by NPs, tissue irradiation with high frequency fields leads to an uneven temperature distribution with locally very high temperatures, so-called hot spots. However, the location of these hot spots depends on inhomogeneities of the electrical permittivity and conductivity of tissues, that cannot easily be influenced [131].

Hyperthermia Using Iron Oxide Nanoparticles

Already in 1993, Jordan *et al.* reported the potential of superparamagnetic iron oxide NPs as therapeutic agents for hyperthermia [132]. Since then, much research has been undertaken to analyze and optimize iron oxide NPs for hyperthermia purposes [15]. In contrast to light in the optical range, magnetic fields readily penetrate the body. Therefore, hyperthermia treatments assisted by magnetic NPs are not limited to peripheral locations in the body, whereas light based hyperthermia applications typically are.

By injecting iron oxide NPs that localize preferentially in cancerous tissues, heat can be generated at these sites through the application of an AMF [15]. This reduces the risk of hot spots in other areas of the body. The specific absorption rate (SAR) of iron oxide NPs, that, together with the NP concentration, determines the increase in temperature during a given time at fixed AMF settings, depends on the NP size. It peaks at a NP radius of 7 nm, irrespective of the magnetic field and frequency (in the range of $B = 30 - 90$ mT and $f = 300 - 400$ kHz) [15, 133].

1.6 Biomedical Applications: Drug Delivery

Driven by the large investments in research and marketing of drugs and drug delivery systems, the number of publications on drug delivery systems exploded in the past few years. As early as 1978, investigations on drug delivery systems, consisting of an albumin clusters co-encapsulating Fe_3O_4 NPs and model drugs that could be magnetically targeted and accumulated, have been reported [134]. Encapsulating drugs and vaccines has been shown to be highly beneficial for multiple reasons. Not only is the encapsulated cargo protected from enzymatic degradation, but the surface functionality of the delivery vehicle is adjusted so that drugs can be targeted to certain locations. Therefore, the dose of appropriately encapsulated drugs required to achieve the therapeutic level at the target site can be significantly decreased compared to the free counterparts. With this decrease in the injected drug dose, the risk of adverse side effects or immune responses induced by free drugs is lowered to the benefit and comfort of the patient [135–138]. The assembly of drug delivery vehicles such as liposomes and polymersomes, their efficient loading with drugs and their behavior *in vivo* has been the focus of numerous studies [139, 140].

1.6.1 Release

Cargo is released if delivery vehicles disassemble, degrade, rupture or if their permeability is greatly increased. However, degradation or rupture of these vehicles does not allow to release content over prolonged times. Therefore, it is highly beneficial, if the structure of the delivery vehicles is retained upon cargo release. If the structure of the delivery vehicle is retained, content can be released in any dose ranging from total release in one burst to slow release over prolonged times. This is possible if the permeability of the delivery vehicles can be changed at the desired location for release.

Liposomes

The permeability of liposomes increases drastically around the membrane melting temperature (T_m) [141, 142]. The latter depends on the length of the phospholipid hydrocarbon chains and their configuration (*e.g.* how many unsaturated bonds they contain). This allows to tune the overall T_m by mixing phospholipids with different T_m s [143, 144].

However, the small temperature difference between malignant and healthy tissues renders the design of drug delivery vehicles, that release cargo at malignant sites, difficult. If T_m

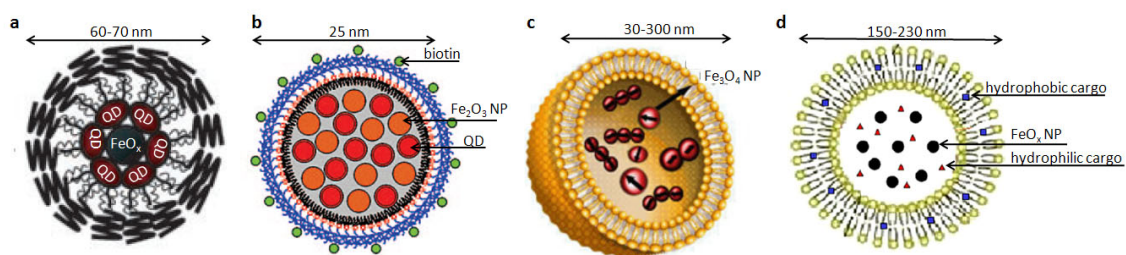


Figure 1.3: Drug delivery vehicles built from amphiphilic molecules and functionalized with NPs. (a) Iron oxide NPs, surrounded by QDs were encapsulated into micelles formed from PEGylated phospholipids [149]. (b) Micelle consisting of amphiphilic molecules that were functionalized with an active chemical group at the hydrophilic head. Fe_2O_3 NPs and QDs were co-encapsulated in these micelles [150]. (c) Magnetoliposomes containing carboxyldextran stabilized iron oxide NPs in their lumen [151]. (d) Magnetoliposomes containing dextran stabilized iron oxide NPs can be loaded with hydrophilic and hydrophobic cargo [152].

of liposomes is only slightly above body temperature, the delivery vehicles are inherently leaky already at body temperature [145, 146]. If, however, T_m is chosen well above body temperature, drug release at malignant sites is inefficient [147, 148]. Thus, the requirements for efficient content release induced from the environment and low passive leakage are incompatible.

1.6.2 Triggered Release

Magnetically Triggered Release of Functionalized Thermoresponsive Polymer Matrices

The inherent problem of a trade-off between leakiness and release efficiency has been addressed by modifying vesicles such that their release can be triggered. Approaches where "natural" triggers such as pH [153–155] or locally at tumor sites accumulated enzymes [156] were used to release drugs, have only been partially successful because release could not be externally controlled but relied on changing environmental conditions at targeted sites. Therefore, external stimuli such as electric fields [157], light [158, 159], ultrasound [160] or chemicals [161] have been used to release drugs.

One of the most successfully applied external trigger is AMF. The application of an AMF as an external trigger was pioneered by Weinstein *et al.* in 1979 [162] and has received increasing attention in recent years [148]. If subjected to an AMF, iron oxide NPs locally increase temperature mainly through Brownian and Néel relaxation (section 1.1.1) [39–42]. Based on the local heating of superparamagnetic NPs used as actuators, a va-

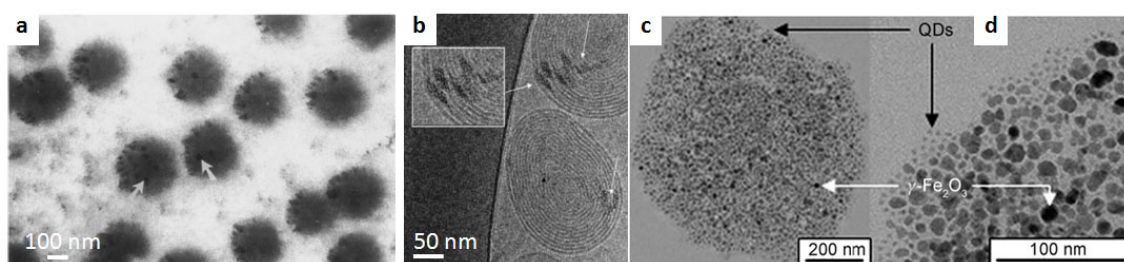


Figure 1.4: TEM micrographs of liposomes containing iron oxide NPs in their lumen. (a) TEM image of dextran coated iron oxide NPs with a hydrodynamic radius of ≈ 20 nm were encapsulated in liposomes [167]. (b) Cryo-TEM image of multilamellar liposomes where iron oxide NPs have been synthesized in these liposomes through coprecipitation of iron salts through diffusion of OH^- through the onion lamella. The iron oxide NPs had an average radius of 2 nm [168]. (c) TEM of liposomes containing TOPO stabilized QDs and citrate stabilized iron oxide NPs in their lumen [74].

riety of different delivery vehicles were designed. These vehicles mostly consisted of a combination of magnetic NPs and drugs or drug mimicking reagents embedded in a polymer matrix or shell. Illustrative examples of such assemblies are silica-coated iron oxide NPs surrounded by a drug loaded poly(vinyl alcohol) (PVA) shell [163, 164] or alternatively agglomerated iron oxide NPs co-embedded with fluorescent, drug mimicking molecules in thermoresponsive polymer beads such as poly (N-isopropylacrylamide) (PNIPAM) [165]. Furthermore, agglomerated 10 nm iron oxide NPs were loaded into a microscopically thick PNIPAM hydrogel where model drugs could be reversibly released from one side of the hydrogel to the other side upon application of an AMF [166].

Magnetically Triggered Release of Liposomes Loaded with Nanoparticles in their Lumen

The possibility to increase temperature through local heating of iron oxide NPs, if subjected to an AMF, allows to design liposomes using a phospholipid composition that has T_m well above the application temperature, and therefore low passive leakage, without compromising drug release efficiency [169].

Liposomes loaded with iron oxide NPs in their lumen [167, 170, 171] or where iron oxide NPs were synthesized inside the liposome lumen through aqueous precipitation methods using Fe^{3+} and Fe^{2+} salts, are known for more than 20 years [172]. Faure *et al.* demonstrated that liposomes containing agglomerated iron oxide NPs in their lumen could magnetically be separated [168]. Furthermore, it was shown that iron oxide NPs and QDs can be simultaneously loaded into the lumen and the liposome bilayer resulting in fluorescent giant magnetoliposomes [74] and micelles [149, 150] (Figure 1.4). Such liposomes

loaded with iron oxide NP could be magnetically moved and deformed to ellipsoids [173]. However, due to steric reasons, only a limited number of iron oxide NPs can be encapsulated into the liposome lumen. Agglomeration of NPs prior to their encapsulation further decreases the encapsulation efficiency. A low iron oxide NP concentration inside the liposome lumen decreases the heating efficiency of iron oxide NPs and necessitates prolonged AMF treatments or the use of higher powers.

Despite the low loading efficiency especially of agglomerated NPs, triggered release of liposomes loaded with drug models and uncoated 8 nm diameter [169] or dextran-coated 3 - 5 nm diameter iron oxide NPs that were agglomerated [152] was demonstrated with AMFs. However, whether NPs were loaded in the liposome lumen, encapsulated in micelles or associated with the liposome membrane remained undetermined [152, 169].

The release efficiency scaled with the concentration of iron oxide NPs associated with liposomes. Because of the poor characterization of liposomes functionalized with iron oxide NPs, increased release efficiency could not be unequivocally assigned to an increased concentration of iron oxide NPs in the liposome lumen. An attempt to quantify the amount of iron oxide NPs with a core radius of 5 nm loaded into the liposome lumen was hampered by the poor iron oxide NP stability and a high affinity of inappropriately surface modified iron oxide NPs to the liposome membrane [151]. Thus, the influence of the concentration of in liposome encapsulated iron oxide NPs on the release efficiency of such delivery vehicles remains unresolved.

In 2010, Nappini *et al.* encapsulated uncoated, ≈ 6 nm $CoFe_2O_4$ NPs into the lumen of liposomes and showed triggered release by applying a low frequency AMF. $CoFe_2O_4$ NP loaded liposomes were larger compared to unloaded counterparts. The release of model drugs upon application of an AMF increased with increasing frequency, $CoFe_2O_4$ NP concentration, $CoFe_2O_4$ NP diameter and exposure time. Because magnetic NPs exposed to low frequency AMFs do not substantially heat, release was thought to be due to mechanical distortions of the liposomes driven by the magnetic NPs [174]. However, liposomes were inherently leaky and leakiness increased with increasing $CoFe_2O_4$ NP size. This can probably be attributed to poor NP stability leading to agglomeration and a corresponding decrease in liposome membrane stability.

Triggered Release of Liposomes containing Nanoparticles in their Membranes

Incorporating NPs directly into membranes (Figure 1.14a) has distinct advantages over delivery vehicles where NPs are loaded into the lumen. NPs embedded in the vesicle

lumen require heating of bulk water before the locally generated heat reaches the vesicle membrane and increases its permeability. In contrast, NPs incorporated in the membrane can directly transfer the locally generated heat into the membrane. Thus, externally triggered release of vesicles bearing optically active or magnetic NPs in their membrane is expected to be more efficient compared to that of vesicles containing these NPs in their lumen.

Paarsonen *et al.* were the first ones to show triggered release of liposomes containing NPs in their bilayers [175]. This was demonstrated with liposomes bearing 2.5 nm hexanethiol stabilized *Au* NPs in their membranes. If the same *Au* cores were coated with mercaptosuccinic acid (MSA), NPs ended up in the liposome lumen. As expected, release of liposomes containing hydrophilic *Au* NPs in the lumen was shown to be less efficient compared to liposomes that had hydrophobic *Au* NPs in their membranes. However, they reported increased non-specific calcein leakage of liposomes that had *Au* NPs incorporated in their membranes as compared to unmodified liposomes.

In 2010, Bothun *et al.* for the first time demonstrated triggered release of liposomes containing iron oxide (Fe_2O_3) NPs in their membranes [176]. They embedded oleic acid stabilized iron oxide NPs into membranes of dipalmitylphosphocholine (DPPC) liposomes and loaded these liposomes with the self-quenching dye carboxyfluorescein. However, these liposomes were inherently leaky [176].

Optically Triggered Release from Polyelectrolyte Membrane (PEM) Microcapsules

Typically, the permeability of PEMs does not change significantly around body temperature. However, if loaded into PEM membranes, NPs can trigger cargo release. Pioneered by the Möhwald group, SiO_2 NPs have been loaded in PEMs assembled on polystyrene latex microspheres [177] and in PEM microcapsules [178]. The size, shape and membrane thickness of these PEM shells could closely be controlled by the choice of the dimensions of the particle template PEMs were assembled on and the number of deposited polyelectrolyte layers [178, 179]. PEMs were further functionalized by introducing catalytically active *Ag* NPs into the PEM [180]. Dissolution of the polystyrene microsphere template resulted in PEM microspheres comprising *Ag* NPs in their walls. These vesicles opened up the possibility to conduct *Ag* catalyzed chemical reactions in the capsule interior [180]. However, similar to liposomes, PEM microcapsules used as drug delivery vehicles or nanoreactors become only truly beneficial, if products synthesized in the PEM microcapsule lumen or cargo loaded into PEM microcapsules can readily be released. Laser

triggered release of fluorescently labeled dextran from the lumen of such PEM vesicles could be demonstrated in cuvettes [181] and in cell assays [182]. Mechanical destabilization of the PEM membrane rather than local temperature increase was found to be the reason for the increased permeability of PEM microcapsules bearing *Au/Co* core-shell NPs in their membranes [183]. Even more advanced, multifunctional PEM microcapsules were assembled by co-embedding *Au* and agglomerated iron oxide NPs into PEM walls. The resulting PEM microcapsules could be magnetically manipulated and laser irradiation destroyed the capsules resulting in complete release of hydrophilic cargo [184].

Magnetically Triggered release from Polyelectrolyte Membrane (PEM) Microcapsules

Similar to liposomes hosting iron oxide NPs in their membranes, PEM microcapsules containing iron oxide NPs in their PEMs could be magnetically manipulated [184–186]. Iron oxide NP loaded PEMs were initially adsorbed on *SiO₂* microspheres [187] before hollow PEM microspheres containing iron oxide NPs in their walls were assembled [188, 189]. However, one of the main drawbacks of PEM microspheres intended for delivery purposes is their leakiness towards small molecules. With the aim to create delivery vehicles that can magnetically be manipulated, the permeability and thus leakiness of hollow PEMs functionalized with iron oxide NPs was decreased by depositing a dense polypyrrole layer onto PEM microcapsules [190].

In 2008, AMF triggered release of PEM microcapsules comprising agglomerated, 5 nm diameter iron oxide NPs embedded in the shell, was experimentally demonstrated. The locally generated heat first induced the formation of pores in PEM membranes resulting in a destruction of the PEM microcapsules [186].

Despite this rapid development of smart PEM microcapsules, their use for biomedical applications might be hampered by several factors. PEM microcapsules typically have diameters in the μm range. Furthermore, they are often charged. However, biomedical applications typically require colloids to be smaller than 100 nm and have good colloidal stability at high salt concentrations and no residual surface charge to avoid non-specific protein adsorption. Furthermore, hydrophobic cargo is difficult to directly encapsulate into PEMs. However, most of the drugs used today are hydrophobic. Thus, PEM microcapsules fail to fulfill several of the requirements imposed on drug delivery vehicles. The flexibility to adjust microcapsules to specific requirements and the ease to assemble these capsules, however, renders them attractive nanoreactors.

Therefore, despite that the principle for triggered release of PEM microcapsules and liposomes comprising superparamagnetic NPs in their membranes is similar, these vesicles most likely will have different applications.

1.6.3 Requirements for Nanoparticles Intended for Biomedical Applications

Common to all applications described above is the requirement for well sterically stabilized NPs surrounded by a dispersant shell that can experimentally easily and cost-effectively be adjusted to the different requirements. The lack of efficiently targeted MR contrast agents, limited efficiency to magnetically trigger release of vesicles functionalized with iron oxide NPs and enhanced leakiness of most of these vesicles is a result of poor control over NP size and stability. Insufficiently stabilized NPs agglomerate and are thus rapidly cleared from the body or cannot be assembled into superstructures like vesicles any more. To gain control over NP stability and therefore size and surface presentation of polymers and functionalities under physiologic conditions, NPs have to be sterically stabilized.

1.7 Nanoparticle Stability

Driven by attractive Van-der-Waals forces, unstabilized NPs tend to agglomerate. The attractive Van-der-Waals potential can in a first approximation be defined as

$$U_{VdW} = -\frac{A}{6} \left(\frac{2r^2}{D(4r+D)} + \frac{2r^2}{(2r+D)^2} + \ln \frac{D(4r+D)}{(2r+D)^2} \right) \quad (1.5)$$

where r is the radius of the spheres, D the interparticle distance and A the Hamaker constant [5].

As can be seen from equation 1.5, smaller NPs result in weaker Van-der-Waals attraction potentials and thus are, at a first glance, less prone to agglomeration compared to larger counterparts. However, the lower Van-der-Waals potential has to be related to the higher surface : volume ratio of the former NPs. The higher surface : volume ratio is energetically expensive and, depending on the solvent, adds additional strong attraction potentials. There are two different approaches to prevent NP agglomeration: NPs can be

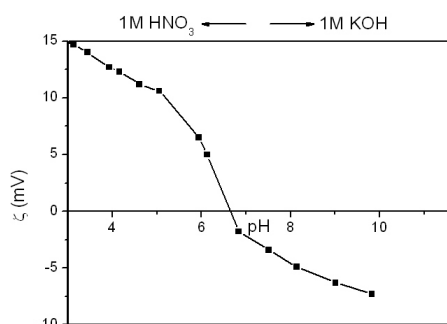


Figure 1.5: Zeta potential of Fe_3O_4 NPs. pH dependence of unstabilized Fe_3O_4 NPs synthesized by the aqueous precipitation method dispersed in Millipore water containing 150 mM NaCl.

electrostatically or sterically stabilized. Optionally, the two stabilization methods can be combined.

1.7.1 Electrostatic Nanoparticle Stabilization

In the absence of a steric stabilization layer, the interparticle interaction potential can be described by the Derjaguin-Landau-Verwey-Overbeek (DLVO) theory, that consists of an attractive Van-der-Waals potential and a repulsive electrostatic potential [191]. The latter is dependent on the zeta potential ζ of NPs which is a function of the pH as can be seen in Figure 1.5 where the pH dependent ζ of Fe_3O_4 NPs is shown.

Because electrostatic stabilization relies on charged surfaces, NPs can be electrostatically stabilized at $pH \ll$ than the isoelectric point (IEP) and $pH \gg$ IEP [192]. However, NPs start to agglomerate if the pH approaches the IEP as ζ of NPs becomes too small. Furthermore, the electrostatic repulsion potential is screened if ions are added. Thus, electrostatic NP stabilization is effective at low salt concentrations and at pHs far above or below the IEP of NPs.

1.7.2 Steric Nanoparticle Stabilization

NPs intended for applications that require NP stability under high salt concentrations and over a wide pH range have to be sterically stabilized [193, 194]. Steric stabilization relies on polymers, so-called dispersants, that surround NP cores. If two sterically stabilized cores approach each other, polymer brushes are confined. This reduces the entropy of

dispersants and increases the osmotic pressure between NPs. The resulting repulsive potential critically depends on the dispersant density profile [195], packing density, binding reversibly and the solvent quality with respect to the dispersants [196].

1.7.3 Electrostatic vs. Steric Stabilization

NP agglomeration can only be prevented if the sum of the attractive Van-der-Waals potential, for magnetic NPs additionally the attractive magnetic potential, the repulsive electrostatic and steric potentials result in an overall repulsive potential barrier at a given interparticle distance that is high compared to $k_B T$. If this condition is fulfilled, NPs do not agglomerate.

Good NP stability at high salt concentration is a stringent requirement especially for biomedical applications. Good NP stability under these conditions can only be ensured if NPs are sterically stabilized. Additionally, dispersants allow to chemically modify surfaces such that they become *e.g.* protein resistant. This possibility, however, is only applicable for sterically and not for electrostatically stabilized NPs. Thus, NPs intended for biomedical use are sterically stabilized.

1.8 Designing Protein Resistant, Functional Surfaces

1.8.1 Protein Resistance

The high surface : volume ratio of NPs renders NP surfaces prone to protein adsorption if these surfaces are not appropriately engineered with so-called stealth molecules that reduce the affinity of proteins to surfaces. If plasma proteins such as opsonins are adsorbed on the NP surface, they induce NP uptake by macrophages, monocytes and dendritic cells and thus initiate NP clearance [15, 136, 197, 198]. Therefore, protein adsorption significantly decreases the circulation time of NPs. Especially if NPs are intended for *in vivo* applications, this severely restricts their use.

One of the most often used polymers to render surfaces stealth is poly(ethylene glycol) (PEG). Attractive Van-der-Waals forces between proteins and PEG-modified surfaces are the smallest, when compared to other well-known water soluble polymers, due to the low refractive index of PEG [199]. Furthermore, it is thought that protein adsorption would lead to confinement of the PEG chains resulting in an energetically unfavorable

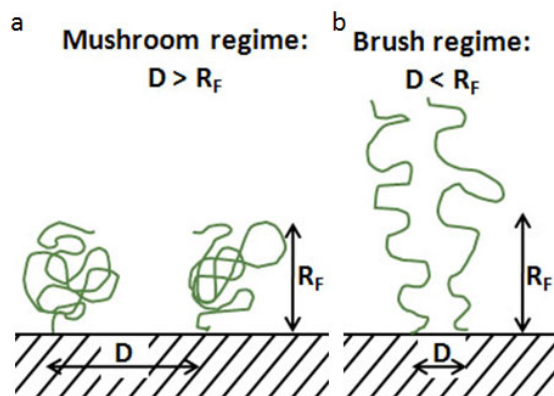


Figure 1.6: Definition of mushroom and brush regime. If the distance D between adjacent polymers is larger than the Flory radius R_F of the polymers, polymers are in the brush regime. However, if $D < R_F$, polymers start to stretch because they sterically repel each other.

entropy decrease [136, 199, 200]. Yet another factor contributing to the ability of PEG to render surfaces protein resistant is the ordering of water around PEG chains [201]. Water molecules that order around PEG chains prevent direct contact of PEG with proteins [202].

Protein adsorption was studied in detail on PEG-modified flat surfaces where different, well-established quantitative surface sensitive characterization techniques such as X-ray photoelectron spectroscopy (XPS) and time-of-flight secondary ion mass spectroscopy (tof-SIMS) are at hand [203–205]. It was found that protein adsorption decreases almost linearly with increasing ethylene glycol (EG) density. If flat surfaces are coated with EG densities $> 15\text{--}30 \text{ nm}^{-2}$, they become protein resistant [203, 204].

Poly(ethylene glycol) (PEG)

The existence of a threshold value for the EG density has direct consequences on the PEG packing densities and M_w s required to render surfaces protein resistant. The higher the PEG M_w , the lower can the polymer packing density be to impart complete protein resistance to PEGylated surfaces. In fact, protein resistance is directly related to the distance of adjacent chains relative to the PEG size. According to de Gennes, one distinguishes between two concentration regimes of polymers. The polymer size can be described by the Flory radius R_F defined as

$$R_F \approx aN^\alpha \quad (1.6)$$

where a is the length of a repeat unit, N is the number of repeat units and α is the Flory exponent that is related to the solvent quality [206, 207].

In the mushroom regime, the distance between adjacent polymer chains D is larger than the Flory radius R_F while for the brush regime $D < R_F$ (Figure 1.6) [208]. The PEG packing density has to be in the mushroom to brush transition or in the brush regime to render surfaces protein resistant. Thus the inter-chain distance has to be smaller than R_F of the respective PEG [209–211].

In fact, a high PEG packing density has been shown to be crucial to prevent adsorption especially of small proteins. The adsorption of large proteins on surfaces was less sensitive to the PEG packing density [205, 210, 212–216].

In line with what has been reported for the protein resistance of surfaces modified with linear PEGs, flat SiO_2 surfaces modified with branched PEG have been found to be protein resistant, provided the density of branched PEGs was such that the distance between two adjacent PEG molecules D was smaller than the protein diameter. Thus, such-modified SiO_2 surfaces were resistant to fibrinogen ($M_w \approx 340$ kDa) adsorption, whereas cytochrome-c ($M_w \approx 12$ kDa) readily adsorbed [210].

PEGylated Nanoparticles

The PEG M_w and the EG packing density were shown to be crucial parameters also for the protein resistance and thus circulation time of NPs. Even though the EG density on NPs might have to be higher to render NP surfaces protein resistant (due to the high surface curvature of NPs that leads to a conically increasing free volume for dispersants starting from the NP surface), the general principle could be expected to hold irrespective of surface curvature.

This was exemplified in a study, where protein resistance of 100 nm diameter poly(lactic acid) (PLA) NPs stabilized with PEG(2 kDa) could only be obtained if the PEG packing density was ≥ 0.2 molecules/ nm^2 [217]. For lower PEG packing densities, circulation time increased with increasing PEG M_w s due to an increased EG density that also yields larger R_F values of PEG [214]. In line therewith, protein adsorption on 200 nm diameter PLA NPs could be significantly decreased if 5 wt% PEG(5 kDa) was added to their surface corresponding to one PEG chain per $2.1 nm^2$ or $D = 1.4$ nm [218] whereas R_F of PEG(5 kDa) = 5.1 nm.

However, because PEG not only should prevent protein adsorption but also has to provide steric stability to NPs, the PEG M_w has to be above a threshold value. In fact, PEG M_w s

between 1.7 and 5 kDa were found to be optimal for surface modifying NPs intended for biomedical applications [209, 213, 219]. NPs stabilized with PEGylated dispersants that fulfill these requirements of high dispersant packing densities and PEG M_w s between 1.7 kDa and 5 kDa showed prolonged circulation times [15, 68, 197, 220–223].

Additionally, also the dispersant conformation influences the ability of these polymers to render surfaces protein resistant. Because branched PEGs with M_w s ≤ 1.7 kDa have a restricted conformational freedom of their chains, protein adsorption results in a much lower entropy penalty as compared to linear PEG chains of comparable M_w s. Hence, protein adsorption is more favorable on NPs modified with branched as compared to linear PEGs. One study claimed that more than twice the amount of proteins were adsorbed on NPs coated with branched PEGs compared to NPs modified with linear PEGs for a PEG $M_w = 1$ kDa [224].

However, because of the importance of the NP stability, PEG packing density and the uniformity of the PEG brush on the NP surface has to be carefully determined in order to make sure that the right conclusions are arrived at from such studies. Results on the protein resistance can only unequivocally be attributed to the PEG conformation if good NP stability and homogeneous dispersant packing density on the NP surface was assured.

1.8.2 Nanoparticle Functionalization

Dispersants adsorbed on sterically stabilized NPs allow for functionalization of NPs, an option that becomes increasingly important for many applications especially in the biomedical field [76, 100, 225]. Potential targeting moieties are antibodies [95, 226, 227], antibody fragments [104], peptides [228–230], aptamers [231], DNA [108] and RNA sequences [100]. They are thought to be able to specifically bind appropriately functionalized NPs to desired locations. However, despite the compared to aptamers and antibody fragments high binding affinity of antibodies to receptors, successful *in vivo* applications of antibody functionalized NPs are scant.

For steric reasons, the large size of antibodies only allows a limited number of these functionalities to be attached to the NP surface. However, the binding affinity of functionalized NPs was greatly enhanced if NPs could bind to receptors through the attachment of multiple ligands compared to NPs functionalized with a low ligand density where statistically only one ligand per NP was able to bind to the receptor [229]. Therefore, the limited number of antibodies that can be immobilized at the NP surface hampers efficient NP targeting. Furthermore, proteins can non-specifically adsorb on antibodies which reduces

the circulation time of antibody functionalized NPs. Additionally, the significant increase in hydrodynamic size of individually stabilized NPs upon functionalization with antibodies prevented cellular uptake of antibody-functionalized NPs [95]. Therefore, ligands that have a lower M_w compared to antibodies might be more promising NP targeting moieties.

1.8.3 Nanoparticle Biodistribution

The fate of NPs in the body is mainly determined by their size [100, 232], shape [232], surface charge [211] and surface chemistry [68]. These properties are greatly dependent on the stability and therefore surface modification of NPs. While particles larger than 200 nm are rapidly cleared by the spleen, NPs smaller than 10 - 50 nm are generally removed from the body through extravasation and renal clearance. The optimal NP size range for *in vivo* applications of intravenously injected NPs that require prolonged blood half-life times is therefore 10 - 100 nm [15, 100].

PEG stabilized iron oxide NPs with a hydrodynamic diameter between 30 - 50 nm have been reported to mainly end up in the liver and spleen if administered in nude mice. Their concentration in the liver and spleen decreased within 72 h by 20 and 50 % respectively. No indication of adverse side effects were reported for PEGylated NPs [222]. However, the clearance of PEGylated NPs was shown to greatly depend on the affinity of dispersant anchors to the NP surface [198, 221]. If PEG was covalently attached to the surface, the NP circulation time was substantially prolonged compared to that of NPs where PEG was just physisorbed to the surface. The fast clearance of the latter NPs was assigned to the fact that proteins could replace physisorbed PEG [214].

Additionally, PEG can reduce NP toxicity. This was exemplified in an empirical study where cell viability remained unaltered if cells were incubated with NPs sterically stabilized with PEG-based dispersants, in contrast to unstabilized Fe_3O_4 NPs that were toxic to cells [67, 233].

Similar to PEG stabilized iron oxide NPs, dextran coated, agglomerated iron oxide NPs accumulated in the liver and spleen. However, the latter were reported to be benign to the body because of their long retention times [234]. Next to the slow clearance and the tendency to agglomerate [234], dextran coated NPs also induced differentiation of monocytes into macrophages [67] and are thus suboptimal for biomedical applications.

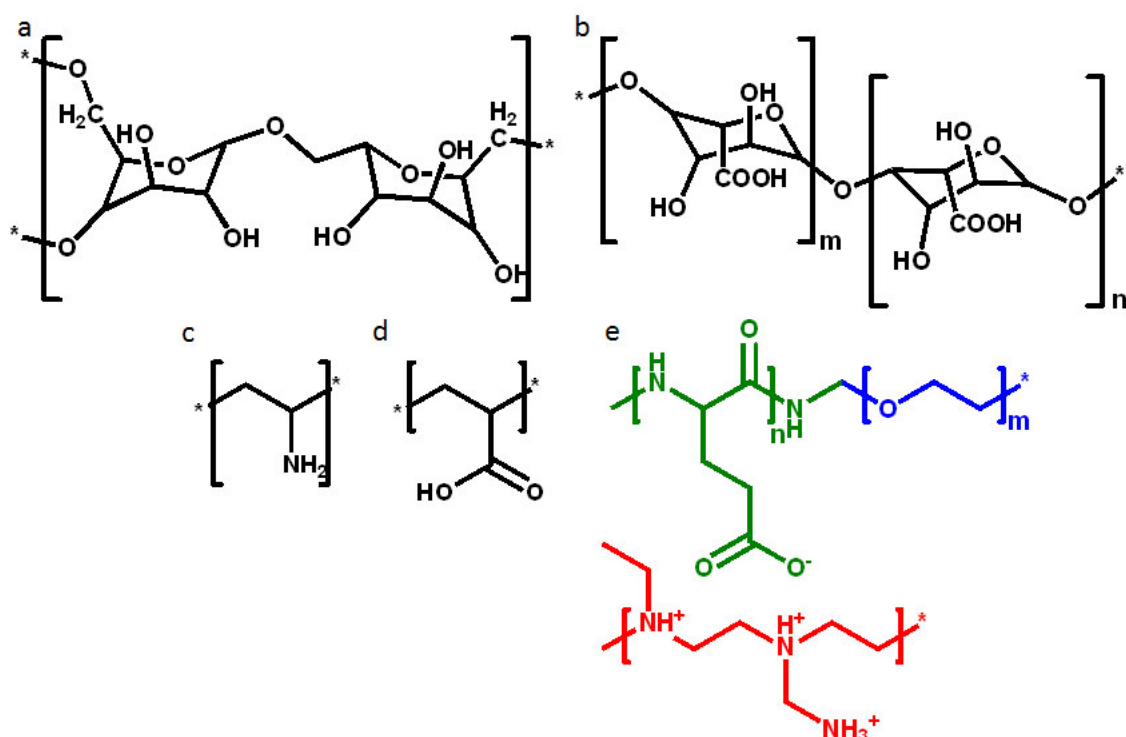


Figure 1.7: *High molecular weight dispersants.* Some of the most frequently used high molecular weight dispersants to stabilize iron oxide NPs are (a) dextran (b) alginate (c) poly(vinyl amine) (PVA), (d) poly(acrylic acid) (PAA) and (e) poly(ethylene imine) where poly(ethylene oxide) (PEO)-poly(glutamic acid) (PGA) is subsequently electrostatically adsorbed to.

1.9 Surface Modification of Iron Oxide Nanoparticles

As indicated above, sterically stabilized iron oxide NPs are often used in the biomedical field for diagnostic purposes [235, 236], for therapeutic purposes in hyperthermia [37, 95, 237], drug delivery [76] and for magnetic cell labeling [115, 238], separation [239] and tracking [240].

The quality and performance of iron oxide NPs, however, crucially depend on NP size, stability, dispersant layer thickness and control over functionalities presented at the NP interface [75, 192]. These parameters are mainly determined by the dispersants that surround NPs. Because of the importance of the dispersant on the NP performance, different approaches typically used to sterically stabilize iron oxide NPs are summarized in the following.

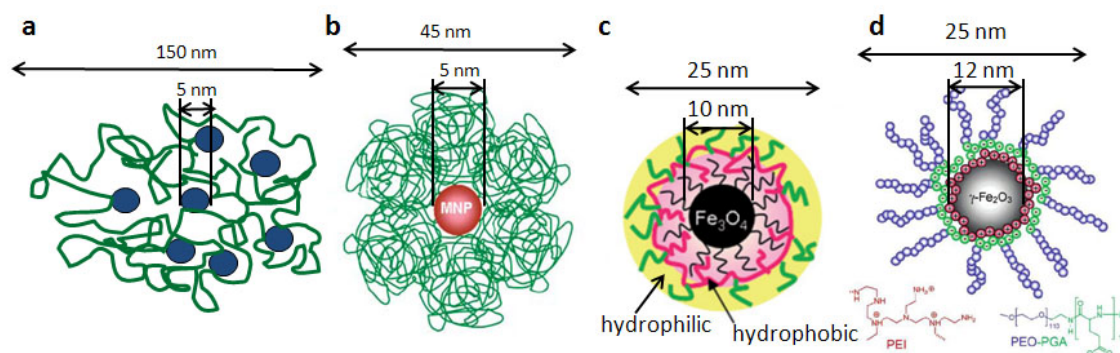


Figure 1.8: Cartoon of iron oxide NPs stabilized with high M_w dispersants. Cartoon of (a) multiple iron oxide cores embedded in physisorbed dextran, iron oxide NPs individually stabilized with (b) crosslinked dextran (CLIONs) [241] Reproduced by permission of The Royal Society of Chemistry <http://dx.doi.org/10.1039/B700091J>, (c) oleic acid and surrounded by pluronics [242] Reproduced by permission of The Royal Society of Chemistry <http://dx.doi.org/10.1039/B902445J> and (d) the polyelectrolytes PEI and PEO-PGA [243].

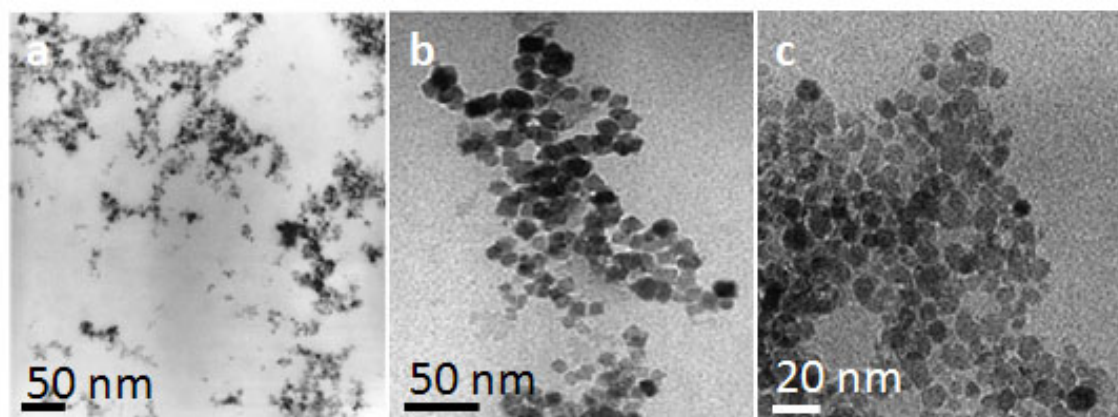


Figure 1.9: Iron oxide NPs stabilized with high M_w dispersants. TEM micrographs of iron oxide NPs stabilized with (a) dextran [244], (b) alginate [245] and (c) PVA [246].

1.9.1 Steric Stabilization with High Molecular Weight Dispersants

Iron oxide NPs used for clinical applications are primarily coated with high M_w dispersants such as dextran [247], alginate [245, 248], poly(vinyl amine) (PVA) [244, 246, 249] or poly(acrylic acid) (PAA) [250] or by electrostatically adsorbing charged polymers like poly(ethylene imine) (PEI) where subsequently a layer of poly(ethylene oxide)-b-poly(glutamic acid) (PEO-PGA) was adsorbed to [243] (Figures 1.7 and 1.8). However, these high M_w dispersants lack a well defined high affinity anchor that could irreversibly couple them to the NP surface [95]. Therefore, high M_w dispersants often encapsulate multiple cores within one cluster (Figure 1.8a). The resulting hydrodynamic cluster radius is many times larger than the radius of individual cores (Figures 1.8 and 1.9)

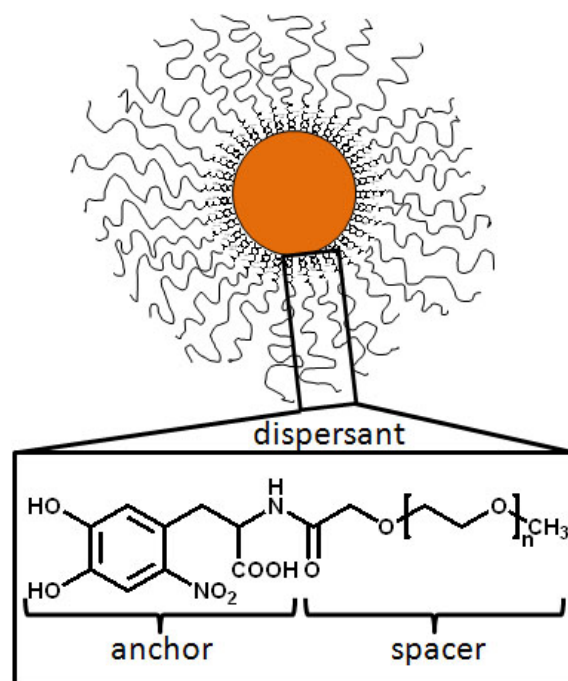


Figure 1.10: Definition of a low M_w dispersant. Cartoon of NPs individually stabilized with low M_w dispersants. These dispersants consist of an anchor group (here nitroDOPA) covalently linked to a spacer (here PEG).

[15, 87, 193, 244, 251, 252]. This hinders NP diffusion and, as described in section 1.8.3, leads to a faster clearance of the large NP clusters.

Reversible dispersant adsorption not only compromises NP stability [194] (Figure 1.9) but proteins have also been shown to replace reversibly adsorbing dispersants leading to a drastically decreased blood circulation time if applied *in vivo* [253]. Needless to say that the resulting poorly defined NP interface prevents controlled functionalization [67].

To prevent desorption of dextran from iron oxide NPs, the Weissleder group crosslinked dextran after it was adsorbed on the NP surface yielding crosslinked iron oxide NPs (CLIONs) (Figure 1.8b) [254, 255]. However, the resulting hydrodynamic radius is large compared to the core radius and control over the dispersant layer thickness difficult. Additionally, epichlorohydrin, the crosslinking agent used to immobilize dextran on the iron oxide NPs, is classified as cancerogenic, mutagenic and reprotoxic. Thus, *in vivo* applications of CLIONs might be hampered by the presence of traces of this chemical [100].

1.9.2 Steric Stabilization with Low Molecular Weight Dispersants

A valuable alternative to high M_w dispersants are low M_w counterparts that consist of one well-defined anchor covalently linked to a spacer (Figure 1.10). Such dispersants can be bound to iron oxide NP surfaces either through the "grafting to" or the "grafting from" technique. For the latter approach, initiators are covalently bound to the NP surface. Spacers, such as PEG described in section 1.8.1, can subsequently be grown *in situ* from on NP surface attached initiators, similar to what has been shown *e.g.* by Muller *et al.* [1]. This approach results in high dispersant packing densities. The limited NP stability reported by Muller *et al.* can likely be ascribed to the reversibly adsorbing anchor, namely dopamine, used to bind initiators to the NP surface. However, even if high affinity anchors are used, which should result in high NP stability, there are some shortcomings to the "grafting from" technique. Dispersant characterization, control over the dispersant polydispersity and layer thickness are difficult. Furthermore, functionalization of stabilized NPs with different ligands or other functional units including a close control over the functionality density presented at the NP interface are challenging.

If low M_w dispersants are synthesized prior to their adsorption on the NP surface, they can easily be characterized with conventional chemical characterization methods. Such low M_w dispersants can be grafted to the NP surface without the requirement for *in situ* chemistry (Figure 1.10). Furthermore, the dispersant layer thickness can be controlled by the spacer configuration and M_w . These NPs can readily be functionalized with a defined density of the functional units by co-adsorbing differently functionalized and unfunctionalized dispersants. However, the polymer grafting density maximally achieved on flat surfaces is lower compared to the "grafting from" approach. The difference in grafting density between surfaces modified through the "grafting from" and the "grafting to" approach is expected to decrease with increasing surface curvature, due to lower steric repulsion of adjacent spacers. Nevertheless, the packing density of dispersants grafted to the NP surface is expected to be lower than that on NP surfaces modified through the "grafting from" approach.

The dispersant packing density critically affects NP stability. However, high dispersant packing densities can only be achieved, if dispersants are firmly adhered to the NP surface through suitable anchors. Despite the importance of good NP stability at elevated temperatures and high ionic strengths, systematic studies of the performance of different anchors and the mechanism underlying the binding of these anchors to iron oxide surfaces are lacking [100].

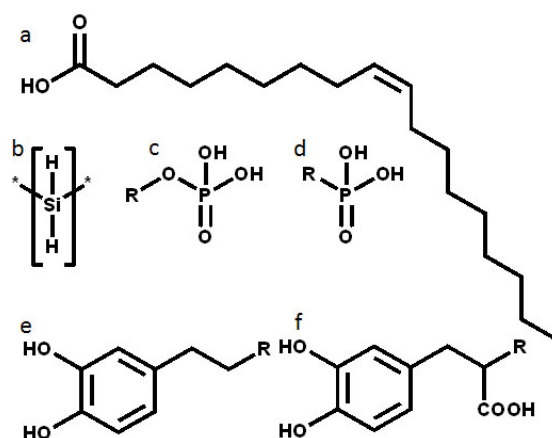


Figure 1.11: Anchors often used for iron oxide NP stabilization. Some of the most frequently used anchors to immobilize dispersants to the NP surface. (a) oleic acid, (b) silane, (c) phosphate, (d) phosphonate, (e) dopamine and (f) DOPA.

Anchors

High affinity anchors that irreversibly bind dispersants to the NP surface are key for good steric NP stability especially if low M_w dispersants are used (Figure 1.10). Because such anchors are not established for most oxides, dispersants have often been immobilized through multiple reversibly adsorbing anchors [204]. Multiple anchors per dispersant decreased the desorption rate of dispersants, provided they were interconnected by flexible linkers that allow these anchors to bind simultaneously to the surface. However, the area, multiple anchors occupy, is considerably larger than that of a single anchor. Thus, multiple anchors might decrease the dispersant packing density on highly curved surfaces where steric repulsion of adjacent spacers is greatly reduced [260]. Therefore, it is more promising to develop individual anchors that have a binding affinity high enough to prevent dispersant desorption.

Anchors frequently used to sterically stabilize especially iron oxide NPs are acids such as oleic acids [100, 261], silanes, phosphates and phosphonates (Figure 1.11) [113, 262–264]. However, especially phosphonates and acids are mainly used to disperse NPs in organic solvents.

Catechols such as L-DOPA, a post-translationally modified amino acid abundantly present in the mussel adhesive protein *Mytilus Edulis* [265], and dopamine have also been used as anchors to sterically stabilize iron oxide [1, 256–259, 266, 267] or iron/iron oxide core-shell [268] NPs in aqueous media (Figure 1.11) (Figure 1.12). Because of the biological relevance of DOPA/ Fe^{3+} and dopamine/ Fe^{3+} complexes, their structure [269–272] and electronic interactions [273, 274] have been studied in detail. Furthermore, the crystallo-

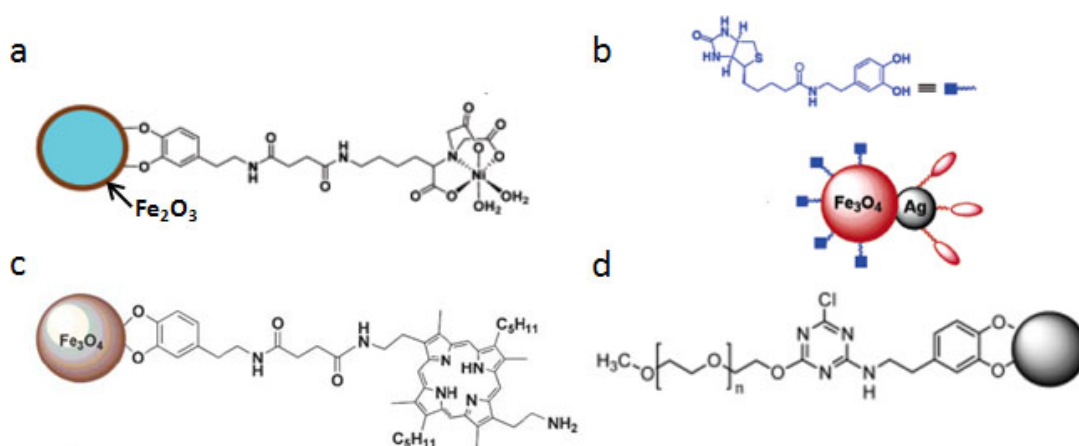


Figure 1.12: Iron oxide NPs stabilized with dopamine anchored low M_w dispersants. Some of the earliest reported examples of iron oxide NPs modified with dopamine anchored low M_w dispersants. (a) Co/Fe_2O_3 or $SmCo_{5.2}/Fe_2O_3$ core-shell NPs were the first reported iron oxide NPs modified with dopamine anchors [256]. (b) In the same year as (a), Fe_3O_4 -Ag heterodimers were surface modified with dopamine containing molecules [257]. (c) The anti-cancer drug porphyrin was bound to Fe_3O_4 NP surfaces through dopamine [258] Reproduced by permission of The Royal Society of Chemistry <http://dx.doi.org/10.1039/B507779F>. (d) Fe_3O_4 NPs stabilized with PEG(2)-dopamine were claimed to be stable under physiologic conditions [259].

graphic and electronic structure of peptides [275], proteins [276] and models for catechol dioxygenases complexed with iron ions [270, 277–279] have been reported.

Based on these studies of catechol/iron complexes and on experimental results of iron oxide NPs stabilized with catechol anchored dispersants, the suitability of catechols as anchors to stabilize iron oxide NPs is debated. Iron is well known to catalyze catechol oxidation which leads to semiquinones, quinones and eventually carboxy-containing products (Figure 1.13) [280–286]. In line therewith, Shultz *et al.* reported oxidative degeneration of dopamine adsorbed on iron oxide NPs resulting in a loss of NP stability [287]. Recently, cryo-TEM images of PEG-dopamine stabilized Fe_3O_4 revealed NP agglomeration [1]. This report further puts into question the suitability of dopamine as anchor for steric stabilization of iron oxide NPs. However, whether surface corrosion of iron oxide NPs is a result of the replacement of oleic acid by the weakly adsorbing dopamine as claimed by Sun *et al.* [259] is questionable. Despite these shortcomings of catechols, they are still often used as anchors to sterically stabilize iron oxide NPs because of a lack of alternative binding groups that directly anchor dispersants to iron oxide NPs.

As a consequence of the still unsolved problem of iron oxide NP stability, such NPs have been coated with a SiO_2 corona [72, 100, 192, 288, 289]. SiO_2 surfaces can readily be functionalized with silanes [290, 291]. Hence, surface modification of these NPs does not require strongly to iron oxide adherent anchors. However, the additional SiO_2 corona

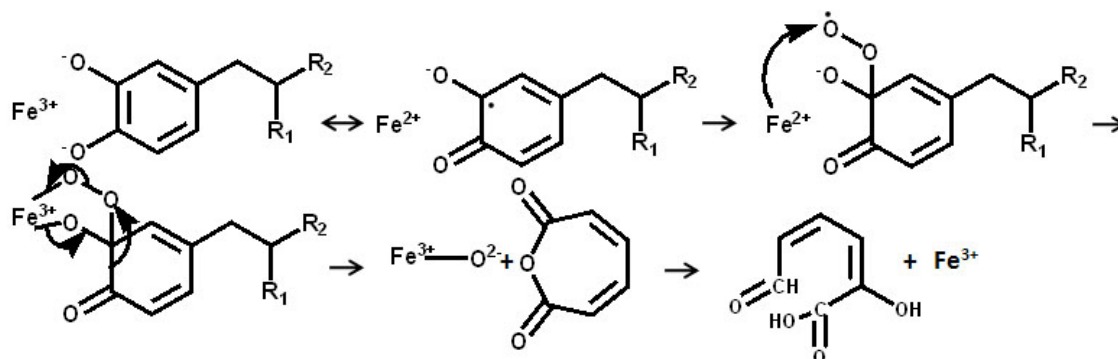


Figure 1.13: Iron catalyzed catechol degradation. Reaction mechanism of iron catalyzed catechol degradation [281, 286].

not only complicates NP synthesis, but also adds a non-magnetic layer to the NP that enlarges the NP core diameter without increasing M_s . Thus, for most applications, it would be desirable to have a suitable chemistry with which the surface of iron oxide NPs could be directly and efficiently modified.

Nitrocatechols

Already in 1976 it was noticed that electronegative substituents strengthen the iron-catechol bond to an extent where bonds between nitro-substituted catechols (so-called nitrocatechols) and iron were claimed to be irreversible. It was speculated that nitrocatechols can act as oxidizing agents which was assumed to be the reason for this exceptionally strong bond [292]. The high affinity of nitrocatechols to Fe^{3+} ions was further supported by the finding that nitrocatechols are strong inhibitors of substrate oxidation that can be induced by non-heme iron dioxygenases such as protocatechuate 3,4-dioxygenase and pyrocatechase. The addition of nitrocatechols to these enzymes, both containing Fe^{3+} , resulted in profound changes in the UV/VIS and electron paramagnetic resonance (EPR) spectra suggesting that nitrocatechols chelate Fe^{3+} ions stronger than these enzymes resulting in ligand exchanges [293]. Despite the high binding affinity of nitrocatechols towards Fe^{3+} ions, the equilibrium constants of nitrocatechols with Fe^{3+} ions are comparable to those of catechol/ Fe^{3+} complexation constants (e.g. $K_1=10^{19.5}$, $\beta_3 = 43.3$ [294] for nitrocatechol/ Fe^{3+} vs. e.g. $K_1=10^{20.01}$, $\beta_3 = 43.7$ [294] for catechol/ Fe^{3+} complexes).

Que *et al.* noticed significant differences in FTIR spectra between the binding of ni-

trocatechols and catechols to Fe^{3+} containing enzymes. However, the origin of these differences was not conclusively elucidated [295]. More detailed studies on the binding of nitrocatechols to iron ions revealed a significantly lower tendency to generate radicals for nitrocatechol/iron compared to catechol/iron complexes [296]. Thus the underlying electron transfer between the nitrocatechol and the Fe^{3+} ions might differ from that of catechols interacting with Fe^{3+} .

More generally, electronegatively substituted catechols such as, nitrocatechols [297] and chlorocatechols [298] were reported not only to bind well to iron oxide surfaces but also to TiO_2 and the former also to Al_2O_3 surfaces. Based on complexation studies of these anchors with Fe^{3+} and Al^{3+} , the increased complexation strength of electronegatively substituted catechols compared to unsubstituted counterparts was related to the increased acidity of the former compounds [299, 300]. As a result of the high binding affinity of nitrocatechols to TiO_2 , PEG-nitrodopamine has proven to be well suited to form polymer brush adlayers on flat TiO_2 surfaces [301].

Spacer

Apart from anchors, suitable spacers are crucial to achieve good steric NP stability (Figure 1.10). The primary task of spacers is to prevent that NPs get into too close proximity, where Van-der-Waals attraction interactions start to predominate. Furthermore, spacers greatly impact the zeta potential and, as outlined in section 1.8.1, the circulation time of such-stabilized NPs if applied *in vivo*. Therefore, the spacer length and configuration are, next to an appropriate anchor, important factors to control the NP stability and performance. For biomedical applications, the most commonly used spacer is PEG [15, 87, 302].

1.10 Assembly of Nanoparticles in Liposome Membranes

1.10.1 Liposomes Containing Nanoparticles in their Membranes

Appropriate surface modification of NPs is not only crucial for applications of individual NPs but also if NPs are assembled in vesicular superstructures. In the latter case,

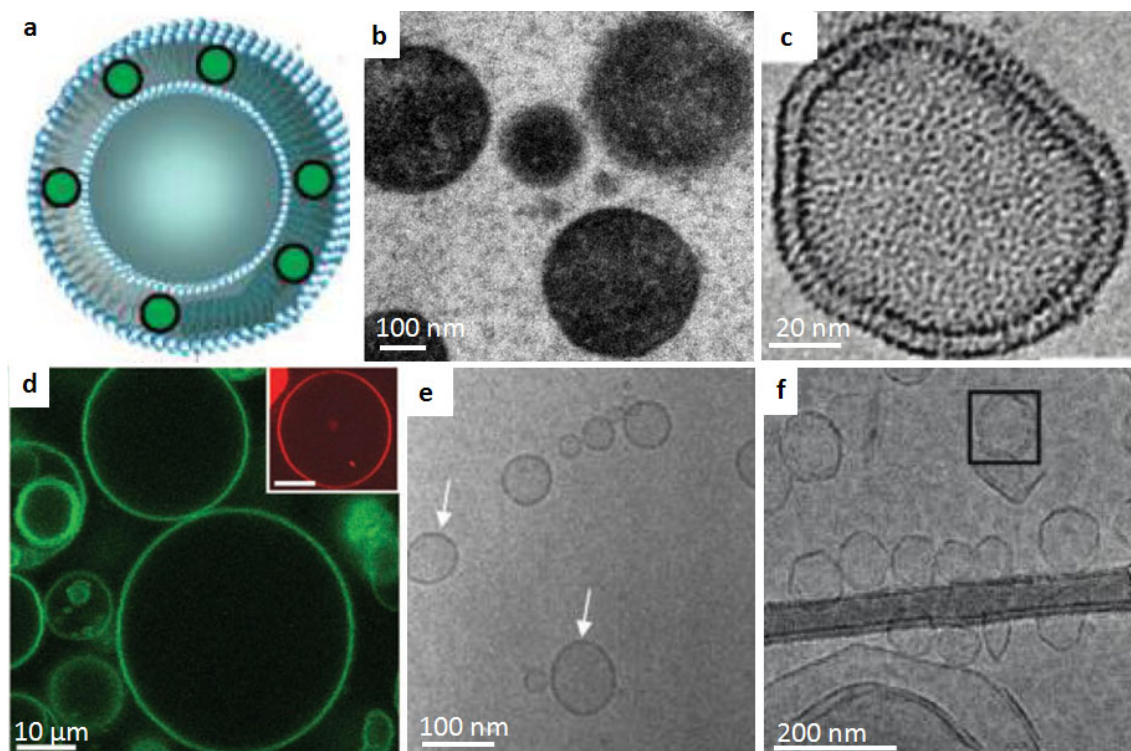


Figure 1.14: Liposomes containing NPs in their membranes. (a) Cartoon of a liposome containing NPs in its membrane [303]. (b) TEM image of sonicated liposomes containing 1.5 - 2 nm core radius Ag NPs, stabilized with stearylamine, in their membranes [304]. (c) Cryo-TEM of extruded liposomes loaded with 1 nm core radius Au NPs. NPs were stabilized with decanethiol [305]. (d) Confocal fluorescence image of giant liposomes loaded with TOPO stabilized CdSe QDs. The radius of stabilized NPs was 2.5 nm. Liposomes were prepared by electroswelling [306]. (e) Cryo-TEM of sonicated liposomes hosting CdSe/ZnS core-shell QDs in their membranes. QDs were 1 nm in radius and stabilized with TOPO [303]. (f) Cryo-TEM of sonicated liposomes. Oleic acid stabilized iron oxide NPs were loaded in these membranes [176].

NP stability greatly influences membrane properties. Encapsulation of NPs in liposome membranes was pioneered by English *et al.* [307]. They sonicated and extruded liposomes that contained octanol surface modified SiO_2 NPs in the membranes and showed unchanged permeability of NP functionalized liposomes compared to their unmodified analogues. Furthermore, fluorescence quenching experiments revealed that a fraction of the SiO_2 NPs was deeply embedded in the liposome bilayers whereas other SiO_2 NPs were in close proximity to the bilayer interface. The latter NPs likely were agglomerated. Incorporation of NPs into liposome membranes causes massive distortions of the membranes. Thus, the influence of NPs on liposome properties were studied by numerous groups and are briefly summarized below.

Influence of Nanoparticles on Membrane Properties

Park *et al.* studied the effect of the incorporation of 3 - 4 nm Ag [304] and Au [308] NPs into liposome bilayers on their fluidity. They found increased lipid mobility in the liquid crystalline phase ($T > T_m$) whereas lipids remained immobile in the gel phase ($T < T_m$) even in the presence of NPs. For these studies, Au and Ag NPs were surface modified with the reversibly adsorbing stearylamine. Whether the increased membrane fluidity in the liquid crystalline phase of liposomes hosting stabilized NPs in their membranes is a result of the NPs or of free stearylamine, that dissociated into the membranes, remains unanswered.

A related and still debated question is the influence of the presence of in liposome membranes embedded NPs and their concentration on T_m . While Gopalakrishnan *et al.* claimed T_m of neutral liposomes to be independent on the NP loading [306], a decrease and broadening in T_m was observed by Bothun *et al.* when they loaded a sufficient amount of NPs into the liposome bilayer [309, 310]. The same group reported that T_m of DPPC liposomes increased with increasing concentration of oleic acid stabilized iron oxide NPs loaded into liposome membranes [176].

Lipid membranes are known to be thicker in the gel phase compared to the fluid phase [311]. The authors assigned the shift of T_m to the assumption, that NPs preferentially embed in thicker membranes. However, experimental evidence for this statement other than DSC curves, that reveal a change in T_m , but do not provide information on the underlying reason for this change, are lacking.

These contradictory findings could partially be caused by the different amounts of NPs in the membrane. Significant changes in T_m were only observed for high NP loadings if incorporated into zwitterionic or if NPs were incorporated in cationic liposome membranes. However, these changes could also be related to partial NP agglomeration caused by a poor binding affinity of the dispersant used to modify the surface of NPs or the direct influence of dissociated dispersants on the membrane lipid mobility.

Influence of Nanoparticles on Liposome Size and Shape

Next to the influence of NPs on the membrane properties, NPs also affect the overall liposome size and shape. Based on cryo-TEM investigations of liposomes containing tri-octylphosphinoxide (TOPO) coated QDs, it has been claimed that high concentrations of QDs forced liposome membranes to open up forming pockets, where QDs were accumu-

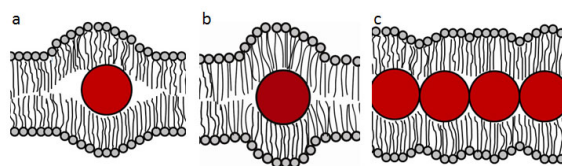


Figure 1.15: *Cartoon of NPs incorporated into SLBs.* (a) NPs incorporated into SLBs require that SLBs open up free space. Opening up of the liposome membrane creates "empty space". This "empty space" is against principles in nature where "empty spaces" are avoided. (b) Liposome hosting NPs in their membrane core are highly curved around NPs. Through this high curvature "empty space" can be avoided. (c) If NPs are assembled in close proximity in SLBs, the energy penalty for incorporating NPs in SLBs is claimed to be lowered.

lated in. This is opposed to the case of liposomes hosting only a low concentration of perfectly spherical QDs in their membranes (Figure 1.14) [303].

Not only the vesicle shape but also their size is influenced by NPs. Binder *et al.* incorporated TOPO-stabilized *CdSe* QDs and hexanethiol stabilized *Au* NPs (both cores had a diameter of ≈ 2 nm) into liposome and polymersome bilayers, respectively. Polymersomes consist of amphiphilic block-co-polymers that assemble into a vesicular structure. Compared to liposomes, polymersomes are less susceptible to traces of organic solvent and thus more robust [140]. They reported significantly smaller sizes of polymersomes containing NPs in their membrane compared to unmodified polymersomes [312]. In contrast, oleic acid stabilized iron oxide NPs were reported to increase the overall size of DPPC liposomes if the lipid : NP ratio was below 25000 : 1 [176].

Membrane Distortions

In 2010, 2 nm core diameter *Au* NPs were embedded into liposomes through extrusion or detergent removal techniques [305]. Cryo-TEM investigations of the resulting liposomes revealed that liposomes in the same sample were either completely loaded with 2 nm core diameter, dodecanethiol stabilized *Au* NPs or they did not contain any *Au* NPs (Figure 1.14). That no liposomes were observed that were loaded with an intermediate amount of *Au* NPs was assigned to the energy penalty that has to be paid if NPs are embedded in the membranes. NPs embedded in membranes necessitate that phospholipid bilayers open up more free space (Figure 1.15). In the proposed picture, this creates empty space within the bilayer, that is energetically expensive. If NPs cluster, this energy penalty can be reduced because the membrane does not have to deform equally with each subsequent addition of NPs if NPs pack closely [305] (Figure 1.15).

Membranes have to open up more free space in the membranes, the larger the NP size

is. Theoretical studies revealed that it is energetically favorable to incorporate NPs into the liposome membrane only if the NP diameter is < 6.5 nm. Larger hydrophobic NPs are preferentially surrounded by a phospholipid monolayer [313]. This finding is experimentally supported by the observation of Vogel and co-workers. They demonstrated the feasibility of incorporating TOPO-stabilized *CdSe* QDs with a core diameter of 3 nm (resulting in a total diameter of 5 nm) into liposomal membranes where the liposome diameter ranged from 50 nm to a few tens of μm . However, they failed to incorporate 8 nm diameter QDs into such membranes [306]. Furthermore, simulations revealed that charged NPs embedded in lipid membranes promote the formation of micelles that separate themselves from the bilayer leading to rupture of the membranes [314]. Hence, only uncharged, hydrophobic NPs with a diameter < 6.5 nm can successfully be embedded in liposome bilayers.

1.11 Nanoparticles as Markers and Actuators

As described above, applications of iron oxide NPs especially in the biomedical field are diverse. Individually stabilized NPs can serve as contrast agents and markers *e.g.* for cell separation purposes. Stabilized NPs can also be assembled in thermoresponsive materials where they can actuate these smart materials *e.g.* by triggering release of content encapsulated in vesicular structures. Common to all these applications is the requirement to closely control NP size, stability and surface presentation of functional groups. Key to meet these requirements are dispersants that sterically stabilize NPs and allow to modify their surface according to specific needs.

CHAPTER 2

Scope of the Thesis

Iron oxide NPs are increasingly used *in vitro* for tracking and manipulating purposes and *in vivo* for diagnostic and therapeutic applications. However, published results and concepts about NP preparation and properties such as stability and *in vivo* performance is still debated and often non-conclusive. The contradictory literature is to a large extent the result of poor NP stability and characterization. Despite the tremendous amount of work and money invested in research in this area and the consensus about the importance of surface chemistry and NP stability for their performance, surface functionalization of oxide NPs with hydrophilic dispersants can still not be controlled to the level required especially for biomedical applications. The fast developments of new diagnostic and therapeutic techniques routinely used in the biomedical field require increasingly close control over NP surface properties and surface-presentation of functionalities. Additionally, many of these applications demand that the NP surface can flexibly, experimentally easily and cost-effectively be custom modified. It is the aim of this thesis to achieve sufficient control over the stability, assembly and surface-presentation of functionalities of iron oxide NPs. This aim can be summarized in three main objectives.

Objective I

Objective I of this thesis is to optimize low molecular weight (M_w) dispersants for iron oxide NP stabilization. These studies encompass three parts: the NP core, the dispersant anchor and the dispersant spacer. If the influence of the dispersant anchor on the NP stability is to be elucidated, iron oxide NPs should present a capping agent free, defined surface. Therefore, different protocols to synthesize iron oxide NPs in the absence of

capping agents are compared regarding their control over core size and size distribution. Subsequently, the binding affinity of dispersant anchors is correlated to the iron oxide NP stability and dispersant grafting density. This includes an in-depth investigation of electronic interactions of selected anchors with iron oxide NP surfaces. Finally, the influence of the spacer M_w on the shell thickness, dispersant packing density and dispersant density profile is related to the NP stability.

Objective II

Iron oxide NPs intended for biomedical applications are often required to present ligands and second functionalities on their surface. It is the second objective of this thesis to compare different strategies to immobilize functionalities on the surface of individually stabilized core-shell NPs. This comparison is focused on the influence of ligands and functionalization methods on the control of the NP size, stability and functionality.

Objective III

Iron oxide NPs can be used as actuators of thermoresponsive materials. They generate heat if subjected to an alternating magnetic field (AMF). It is the third objective of this thesis to design and characterize liposomes carrying hydrophobic iron oxide NPs in the hydrophobic core of their membranes for triggering changes in the liposome permeability. Liposomes, that have a greatly enhanced permeability enhanced around their melting transition temperature, can be used as delivery vehicles and nanoreactors. Due to size restrictions of liposome membranes, only individually stabilized hydrophobic NPs of the size comparable to the membrane thickness can be assembled in these membranes. Thus, it is aimed to stabilize iron oxide NPs individually using hydrophobic dispersants and to subsequently assemble these NPs into the liposome bilayer. Emphasis is put on the characterization of the liposome structure and the mechanism with which cargo release can be triggered using an AMF.

Structure of the Thesis

The thesis is structured following the core-shell structure of NPs starting from the innermost part of NPs, the core (Figure 2.1). The experimental part (chapter 3) describes the

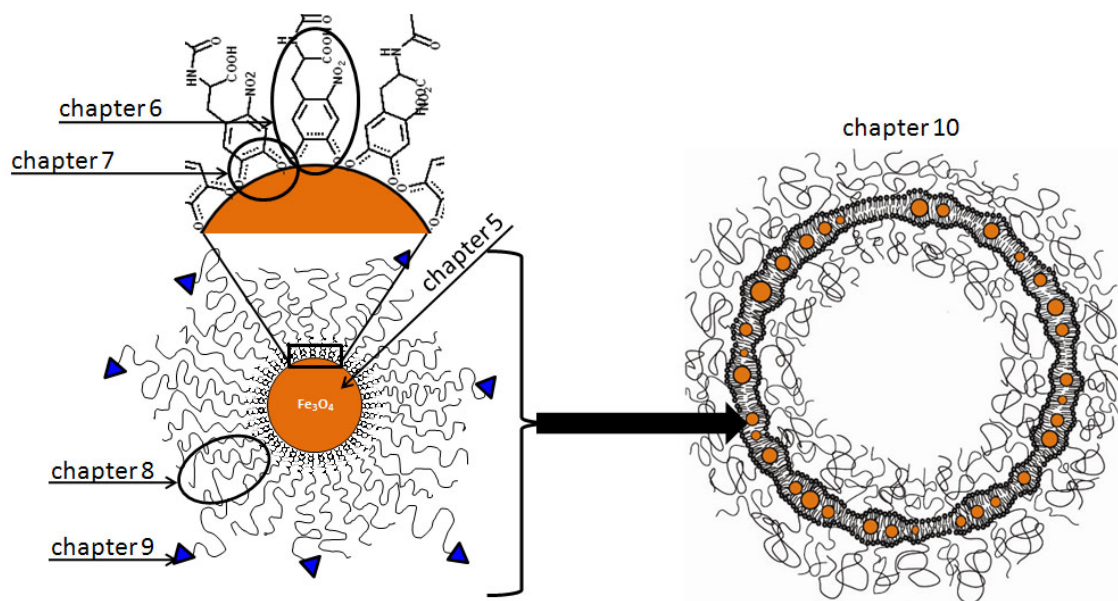


Figure 2.1: Cartoon of the structure of the thesis. This thesis is structured like a core-shell NP. It starts from the core synthesis and subsequently describes the different building blocks of a sterically stabilized NP. It ends with the assembly of a superstructure which is responsive to alternating magnetic fields.

synthesis of dispersants, cores, the NP stabilization and functionalization. The different methods used to characterize NPs are summarized in chapter 4.

Iron Oxide Core Synthesis (Chapter 5)

Control over the iron oxide core size and size distribution is crucial for applications that require good magnetic responses. Furthermore, for fundamental studies it is critical to minimize the core size distribution. Iron oxide NPs with narrow size distributions are typically synthesized using oleic acid as a capping agent. However, oleic acid binds to the iron oxide NPs rendering them hydrophobic. To avoid the hydrophobic oleic acid layer presented at the NP surface, the influence of the synthesis conditions on the iron oxide core shape, size and size distribution was first assessed for capping agent-free synthesis routes. Iron oxide NPs were synthesized with three different methods, namely by aqueous precipitation and by two non-aqueous sol-gel methods. The non-aqueous sol-gel syntheses were conducted at elevated temperatures using the microwave (MW) and oil bath as energy sources, respectively. The non-aqueous sol-gel method, where NPs were grown in the oil bath for prolonged times, yielded the best control over NP size and the narrowest size distribution. Parts of these results are summarized in publications (Isa *et al.* CHIMIA, 2010, Amstad *et al.* in preparation).

Anchors for Steric Stabilization of Iron Oxide Nanoparticles (Chapter 6)

The suitability of catechol anchors, often used to sterically modify iron oxide NPs, is debated. To shed light on the influence of anchors on the NP stability and the suitability of catechol anchors to immobilize molecules on iron oxide NPs, eight different catechol derived anchors were compared. As-synthesized iron oxide NPs were stabilized with low M_w dispersants which consisted of anchors covalently linked to PEG spacers. Stability of iron oxide NPs was investigated with dynamic light scattering (DLS). It was found that nitrocatechols are well suited as anchors to surface modify iron oxides. They vastly outperformed the well-known (unsubstituted) catechols. The results of these studies have been summarized in a publication (Amstad *et al.*, Nano Letters, 2009).

Mechanistic Aspects of Anchor-Iron Oxide Interactions (Chapter 7)

To gain a better understanding of the mechanism of how anchors bind to iron oxide surfaces, the underlying electron interactions between selected catechols with iron oxide surfaces were studied. Such a deeper understanding paves the way to further optimize anchors and potentially allows to theoretically predict the suitability of anchors to bind to different oxides. It was found that electronegative ring substituents such as NO_2 facilitate electron delocalization between the catechol derivative and surface bound iron. This electron delocalization leads to an increased electron density at the electronegatively substituted catechol and an electron deprived iron center which showed up as Fe^{3+} in the electron paramagnetic resonance (EPR) spectra. The facilitated electron delocalization is responsible for the higher affinity of electronegatively substituted compared to unsubstituted catechols. These studies are reported in two publications (Amstad *et al.* accepted in Journal of Physical Chemistry C and Amstad *et al.* submitted).

Iron Oxide Nanoparticle Shell (Chapter 8)

The dispersant shell determines NP stability. Furthermore, calculations of interparticle interaction potentials require knowledge about the dispersant density profile at the NP surface. Therefore, this chapter focuses on the influence of the PEG M_w on the NP stability, dispersant layer thickness, packing density and the dispersant density profile. It was shown that iron oxide cores with radii between 2.5 nm and 5 nm are most stable if the PEGs with a M_w between 5 kDa and 10 kDa are used as spacers. Small angle neutron

scattering (SANS) results indicate that the density profile of these dispersants decays following an exponential function. Parts of these results are summarized in two publications (Isa *et al.* CHIMIA, 2010 and Amstad *et al.* in preparation).

Iron Oxide Nanoparticle Functionalization (Chapter 9)

Many different strategies to immobilize additional functionalities and ligands on iron oxide NPs are known. However, a thorough characterization of NPs functionalized with ligands such as antibodies including a direct comparison of the performance of NPs functionalized through different linking strategies is elusive. Advantages and disadvantages of some often used coupling strategies to functionalize individually stabilized core-shell NPs with antibodies and fluorophores were elucidated. Biotinylated NPs that were functionalized with biotinylated antibodies through an avidin monolayer crosslinked during functionalization and consequently agglomerated. Similar crosslinking reactions were observed if antibodies were covalently linked to acrylate presenting NPs through amine groups. However, fluorophores containing exactly one amine group per molecule could easily be covalently linked to acrylate presenting NPs. The resulting multimodal NPs could be visualized with MRI and fluorescence microscopy. Parts of these results have been published (Amstad *et al.* Small, 2009).

Assembly of Iron Oxide Nanoparticles into Thermoresponsive Superstructures (Chapter 10)

Thus far, only noble metal and semiconductor NPs could successfully be incorporated into liposome bilayers. It was the goal of this chapter to individually stabilize NPs using hydrophobic dispersants, such that they could be assembled into vesicular superstructures. The dispersants consisted of the same catechol derived anchor used in chapters 8 and 9, but covalently coupled to a hydrophobic tail. NPs individually stabilized with a thin hydrophobic dispersant monolayer self-assembled into the hydrophobic part of the liposome membrane. The liposome morphology and size was analyzed with transmission electron microscopy (TEM), DLS and SANS. The influence of NPs on membrane properties such as membrane deformation and liposome melting temperature were studied using SANS and differential scanning calorimetry (DSC). It was found that iron oxide NPs embedded in liposome membranes can locally increase T to T_m during exposure to an AMF leading to cargo release. Triggering efficiency of liposomes hosting iron oxide NPs in their

membranes was much higher than that of magnetoliposomes that contained iron oxide NPs in their lumen. This work will be reported in a future publication (Amstad *et al.* in preparation).

Conclusions and Outlook (Chapters 12 and 13)

Following the conclusions, preliminary results and future directions on different topics are summarized in the outlook. First results on the affinity of nitroDOPA to different oxides and its implication for their stability are presented. The outlook is concluded with preliminary SANS data indicating that hydrophobic iron oxide NPs can also be embedded in polymersome membranes.

Appendix

The effect of different parameters used during stabilization of iron oxide NPs on their stability is presented in section M.1. Section M.2 summarizes preliminary results on the ability of nitroDOPA to replace oleic acid on the iron oxide NP surface. Furthermore, the effect of the PEG M_w on the stability of bimodally distributed NPs is summarized (section M.3). Potential deficiencies in the commonly used characterization of NP stability intended for *in vivo* applications are discussed in section M.4. Finally, the results of the chemical analysis of the dispersants used in this thesis are compiled in section M.5.

3.1 Dispersant Synthesis

3.1.1 Materials for Dispersant Synthesis

Methoxy-terminated, biotin and acrylate terminated PEG-NHS was purchased from Jenkem (Allen, TX) and palmityl-NHS (purity > 90%) from Fluka (Switzerland). DOPA (purity = 99%), hydroxydopamine (purity = 99 %) were bought from Acros, 3-hydroxytryamine-hydrochloride (purity >98.5%), mimosine (purity = 98%), N-hydroxysuccinimide ester (palmityl-NHS), ethan-1,2-diamine, benzylalcohol, N, N-dimethyl formamide (DMF), NaCl, 4-(2-hydroxyethyl)-1-piperazineethanesulfonic acid (HEPES) and Sephadex G75 (superfine), rhodamine 110 chloride (purity \geq 99 %) from Sigma and Triphenylphosphine-3,3',3''-trisulfonic acid trisodium salt hydrate (Tris) from Alfa Aesar.

3.1.2 Synthesis of Anchors

Nitrodopamine and nitroDOPA were synthesized according to Napolitano *et al.* [315]. Starting from kojic acid hydroxypyridine was synthesized by replacing the aliphatic alcohol by chlorine according to Ma *et al.* [27] followed by a removal of chlorine [316]. The aromatic alcohol was protected with benzyl [27] before the aromatic oxygen was substituted with ethylenediamine [316].

Hydroxypyronone was synthesized starting from kojic acid. The aliphatic alcohol was replaced by chlorine [27] and subsequently by azides [317] before it was converted to kojic amine [318].

3.1.3 PEG-Anchors with PEG $M_w > 1$ kDa

PEG(1.5)-NHS, PEG(5)-NHS, PEG(10)-NHS, PEG(20)-NHS, acrylate-PEG(5)-NHS, acrylate-PEG(7.5)-NHS and biotin-PEG(3.6)-NHS were coupled to anchors according to a slightly modified protocol from Zurcher *et al.* [319]. Because of different solubilities of the anchors, mimosine, nitroDOPA and nitrodopamine were coupled to PEG-NHS in borate buffer whereas the remaining anchors were coupled in a mixture of ethanol and chloroform.

1 mol *equ* of the respective anchor (0.2 mmol anchors) was dissolved in 20 ml sodium borate buffer (pH = 8.4) before 1 mol *equ* PEG-NHS was added to reactions conducted in sodium borate buffer. For reactions conducted in organic solvents, 0.2 mmol anchors were dissolved in 20 ml ethanol before it was mixed with 1 mol *equ* PEG-NHS dissolved in chloroform (0.02 mmol PEG-NHS was dissolved in 5 ml chloroform). For the latter reaction, PEG-NHS was activated by adding 1 mol *equ* morpholine. After 24 h reaction at room temperature under constant magnetic stirring, the solution was acidified with concentrated HCl. It was extracted with chloroform before it was precipitated in diethylether and vacuum dried. Typical yields were between 70 and 90 wt%. Dispersants were analyzed with matrix assisted laser desorption/ionization time of flight (MALDI-TOF), microelement analysis and 1H - and ^{13}C -NMR.

The coupling efficiency of reactions conducted in sodium borate butter was considerably lower compared to those conducted in organic solvents because PEG-NHS partially hydrolyzed in borate buffer before it reacted with amines of the anchor groups (section M.5). To increase the yield, coupling of *e.g.* nitrocatechols to PEG-NHS could be done in DMF instead of sodium borate buffer. In this case, 1 mol *equ* morpholine needed to be added to DMF to activate PEG-NHS.

3.1.4 PEG-Anchors with PEG $M_w < 1$ kDa

PEG(0.8)-anchor dispersants were synthesized similarly to what has been described for the other PEG-anchor dispersants (section 3.1.3). However, PEG(0.8) is liquid at room

temperature, and did not precipitate in diethyl ether as a powder. Therefore, nitroDOPA was coupled to PEG(0.8)-NHS in sodium borate buffer at a molar ratio of PEG-NHS : nitroDOPA = 1 : 1 (0.57 g nitroDOPA was dissolved in sodium buffer before 2 mg PEG(0.8)-NHS was added). The reaction was conducted at room temperature for 24 h under constant magnetic stirring. PEG-nitroDOPA (and hydrolyzed PEG-COOH) were extracted in chloroform. Chloroform was evaporated using a rotary evaporator before it was completely dried in vacuum. The yield was ≈ 75 wt% (see section M.5).

3.1.5 Palmityl-nitroDOPA

1 mol *equ* nitroDOPA (1.8 g) was dissolved in 60 ml DMF. 1 mol *equ* palmityl-NHS was added and activated with 1 mol *equ* morpholine. The reaction was magnetically stirred for 20 h at room temperature before it was acidified with concentrated HCl. Palmityl-nitroDOPA was extracted in dichlormethane. After dichlormethane was partially evaporated using a rotary evaporator, palmityl-nitroDOPA was precipitated with Millipore water ($R = 18.2 \Omega$, TOC < 6 ppb). The dispersion was thoroughly washed with Millipore water to ensure complete removal of unreacted nitroDOPA before the filtrate was freeze-dried. The yield was ≈ 60 wt%. Identical to the other dispersants, palmityl-nitroDOPA was analyzed with MALDI-tof, microelement analysis and 1H - and ^{13}C -NMR. For the latter analysis, palmityl-nitroDOPA was dissolved in deuterated methanol.

pK_a Determination

2 mM of the respective anchor was dissolved in Millipore water containing 160 mM NaCl. These solutions were titrated with 0.1 M HCl and NaOH respectively using a SevenMulti pH meter (Mettler Toledo, Switzerland).

3.2 Preparation of Oxide Substrates

3.2.1 Materials for Core Synthesis

$Fe(ac)_2$ (batch 517933 and 51933, Lot 03901JJ), $Mg(OC_2H_5)_2$, $Fe(acac)_3$, $Al(acac)_3$, $Mn(ac)_2$, $Mn(acac)_2$, $TiCl_4$, Al_2O_3 NPs, Sephadex G75 superfine and 25% ammonia

solution were purchased from Fluka (Switzerland). For the MW assisted NPs synthesis batch 517933 (Lot 03901JJ) was used whereas NPs synthesized in the oil bath were made from batch 51933. Chloroform was bought from Acros, benzylalcohol, pyrrolidone, ethanol and diethyl ether from Sigma and Si oil (A12728) for the oil bath from Alfa Aesar. All solvents were purity grade and used as-received.

3.2.2 Iron Oxide Core Synthesis: Aqueous Precipitation

To synthesize iron oxide NPs by aqueous precipitation methods the protocol established by Massart was followed [320]. A typical batch was synthesized out of 198.8 mg (1.2 mmol) $FeCl_2$ and 540.6 mg (2.3 mmol) $FeCl_3$. Black precipitates indicated the immediate iron oxide NP formation after the pH was shifted > 10 using concentrated NaOH. The resulting NPs were neutralized by washing them with 10 mM HEPES solution. To accelerate NP agglomeration especially at high pH, where NPs were electrostatically stabilized, 160 mM NaCl was added to the HEPES buffer.

3.2.3 Iron Oxide Core Synthesis: Microwave Assisted Synthesis

A protocol established by Bilecka *et al.* [321] was followed for the MW assisted iron oxide cores synthesis. Unless stated otherwise, 1 mmol (173 mg) $Fe(ac)_2$ or 1 mmol (353 mg) $Fe(acac)_3$ was dissolved in 5 ml benzylalcohol or pyrrolidone respectively under Ar atmosphere. Depending on the targeted mean core size, the dispersion was heated for 30 s up to 1 h at 180°C in Ar atmosphere in a MW (Discover S-class, CEM, NC, USA). However, the actual temperature inside the reaction vial differed between different MWs of the same type and bought from the same company. Thus, temperature dependent NP size determinations might not be directly translated to the NPs synthesized in other MWs. As-synthesized NPs were washed once with 10 ml ethanol before they were re-dispersed in 10 ml fresh ethanol resulting in an iron oxide NP concentration of ≈ 10 mg/ml.

3.2.4 Oil Bath Synthesis

Iron Oxide Nanoparticle Synthesis

1 mmol (173 mg) $Fe(ac)_2$ was dissolved in 5 ml benzylalcohol. To dissolve the precursor, the dispersion was magnetically stirred in an oil bath under atmospheric conditions

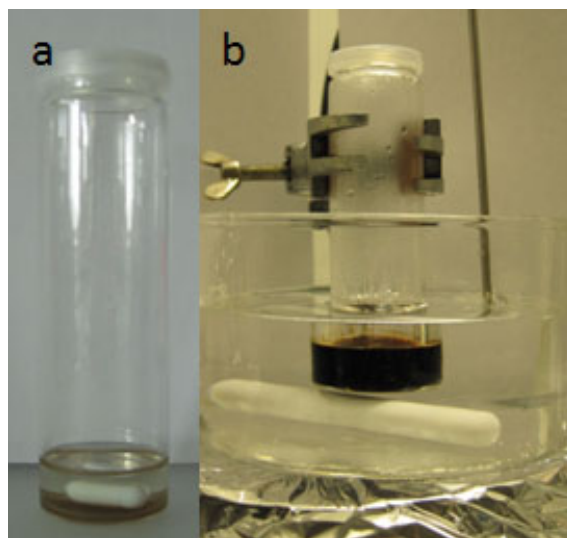


Figure 3.1: Oil bath synthesis of Fe_3O_4 NPs. (a) $Fe(ac)_2$ was dissolved in benzylalcohol before (b) Fe_3O_4 NPs were grown at temperatures between 150 and 180 °C.

for 1 h at 70 °C before the temperature was increased to 150 °C, 165 °C or 180 °C. Unless stated otherwise, NPs were grown at the respective temperature for 24 h under constant magnetic stirring (Figure 3.1). The resulting black dispersion was mixed with 5.5 ml ethanol, centrifuged for 10 min at 14'000 rpm (MiniSpin, Vaudaux Eppendorf, Switzerland) before the supernatant was exchanged with 10 ml ethanol. These NPs were washed two more times with twice 10 ml ethanol before they were stabilized.

TiO_2 Nanoparticle Synthesis

TiO_2 NPs were synthesized following the protocol of Kotsokechagia *et al.* [322]. Briefly, 1 ml $TiCl_4$ was slowly added to 5 ml ethanol followed by the addition of 20 ml benzylalcohol. The solution was heated to 80 °C using an oil bath and magnetically stirred at this temperature for 12-16 h. NPs were precipitated with 100 ml diethyl ether and washed twice with 2×100 ml ethanol.

SiO_2 Nanoparticle Synthesis

SiO_2 NPs were synthesized according to Busbee *et al.* [323, 324]. 120 ml ethanol, 1.1 ml Millipore water, 3.4 ml 25 % ammonia solution and 3 ml tetraethoxysilane (TEOS) were magnetically stirred at room temperature for 9 h. The resulting NPs were dialyzed against

2 l Millipore water for 1 week using dialysis tubes with a cut-off of 25 kDa (Spectra/Por dialysis membrane, spectrum labs, Netherlands). Water was exchanged twice a day.

$Mg(OH)_2$ Nanoparticle Synthesis

To synthesize $Mg(OH)_2$ NPs, 1 mmol (114 mg) magnesium ethoxide ($Mg(OC_2H_5)_2$) was dissolved in 5 ml acetophenone. This dispersion was heated to 180 °C and kept at this temperature for 1 h. The synthesis was performed under Ar atmosphere. NPs were washed twice with 2×10 ml fresh ethanol.

MnO Nanoparticle Synthesis

MnO NPs were synthesized according to a slightly modified protocol of Bilecka *et al.* [321]. 1 mmol of $Mn(ac)_2$ or $Mn(acac)_2$ respectively was added to 5 ml benzylalcohol. This suspension was heated in Ar atmosphere in the MW to 180 °C for 1 h. Benzylalcohol was exchanged with 10 ml ethanol before these NPs were washed once with 10 ml fresh ethanol. However, according to XRD analysis, both precursors, $Mn(ac)_2$ and $Mn(acac)_2$ resulted in MnO NPs in contrast to what has been reported by Bilecka *et al.* where $Mn(acac)_2$ yielded Mn_3O_4 NPs [321].

MnO_2 Nanoparticle Synthesis

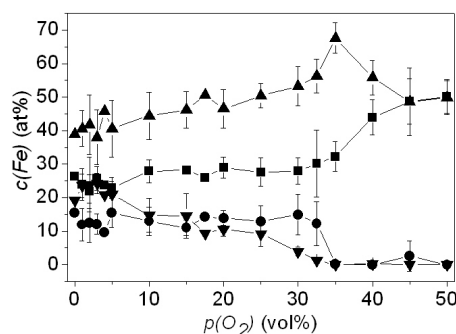
MnO_2 NPs were synthesized according to the protocol of De Guzman *et al.* [325]. 589 mg $KMnO_4$ and 880 mg $MnSO_4 \times H_2O$ were dissolved in 10 ml and 3 ml Millipore water respectively. The two solutions were combined before 0.3 ml concentrated nitric acid was added. The solution was magnetically stirred under reflux for 24 h at 100 °C. NPs were washed twice with Millipore water.

3.2.5 Magnetron Sputtering of Flat Iron Oxide Films

Thin iron oxide films were magnetron sputtered (PVD products, MA, USA) onto one side polished $10 \times 10 \text{ mm}^2$ Si wafers (Silicon materials, Germany). Metallic Fe targets (purity 99.9%, Kurt J. Lesker, UK) were reactive sputtered at $P = 200$ W for 10 min at $p = 5$ mtorr. The influence of $p(O_2)$ during reactive sputtering on the resulting iron oxide

Table 3.1: Parameters used to fit the XPS Fe $2p_{3/2}$ peak of iron oxide films.

	BE (eV)	FWHM (eV)	% gauss	tail parameter
Fe^{3+}	710.2 ± 0.1	2.4	45	0.0
Fe^{2+}	709.0 ± 0.1	2.4	45	0.0
$FeOOH$	711.5 ± 0.1	3.4	45	0.0
Fe_{met}	706.6 ± 0.1	1.5	85	0.9

**Figure 3.2:** Oxidation state of iron in iron oxide films. The atomic percentage of Fe^{3+} (\blacksquare), Fe^{2+} (\bullet), $FeOOH$ (\blacktriangle) and $Fe(met)$ (\blacktriangledown) of thin reactive magnetron sputtered iron oxide films could be controlled by adjusting the oxygen partial pressure during magnetron sputtering.

stoichiometry was investigated with XPS (Figure 3.2 and Table 3.1). The atomic Fe^{3+} percentage rose significantly if $p(O_2)$ was 30 at% whereas the atomic Fe^{2+} percentage decreased, indicating an oxidation of Fe^{2+} to Fe^{3+} . The amount of metallic iron decreased with increasing $p(O_2)$. No metallic iron was detectable at $p(O_2) > 35$ vol%. The $Fe2p_{3/2}$ spectra measured by XPS were fitted with four gaussian/lorenzian convoluted peaks with the parameters shown in Table 5.1 after a Shirley background had been subtracted. These fit parameters are in the range of reported values [326].

It was found that an atmosphere consisting of 20 vol% O_2 and 80 vol% Ar resulted in thin Fe_3O_4 films. Thus, substrates used for investigations of the influence of anchors on the PEG brush density on flat surfaces and for NEXAFS studies were reactive sputtered under these conditions.

Table 3.2: Stabilization of oxide NPs.

oxide	ethanol (ml)	dispersant (mg)	NP dispersion (ml)
Fe_3O_4 , oil bath	0.5	8	0.5
Fe_3O_4 , microwave	0.9	8	0.1
Fe_2O_3 , microwave	0.9	8	0.1
TiO_2	0.5	8	0.5
SiO_2	0	8	1
$Mg(OH)_2$	0.5	8	0.5
Al_2O_3	0.9	8	0.1
MnO	0.5	8	0.5
MnO_2	0.9	8	0.1

3.3 Nanoparticle Stabilization

3.3.1 Nanoparticles Synthesized with the Aqueous Precipitation Method

As-synthesized NPs were stabilized within 4 h after the synthesis was completed. To a typical batch of iron oxide NPs resulting from 1.2 mmol $FeCl_2$ and 2.3 mmol $FeCl_3$, 24 μmol , of PEG(0.55)-gallol or PEG(5)-gallol dissolved in 25 ml Millipore water was added. NPs were dispersed in this solution by pulsed sonication (5 min, $P = 105 \text{ W/cm}^2$, pulse frequency = 1 s on, 1 s off, UP260s, Hirschler GmbH). To stabilize NPs with a mixture of biotin-PEG(3.4)-gallol and mPEG(0.55)-gallol, 25 ml Millipore water containing 2.4 μmol of the former dispersant was added to uncoated NPs before they were sonicated and back-filled with 21.6 μmol mPEG(0.55)-gallol. NPs were sonicated a second time according to the above described procedure. Excessive dispersants were removed by ultracentrifugation using a filter with a cut-off of 30 kDa (vivaspin, Epsom). The filter cake was re-suspended in Millipore water before the dispersion was freeze-dried (dryer ALPHA 1-2 / LDplus, Kuhner LabEquip, Switzerland). NPs were re-suspended in PBS, HEPES or Millipore water, sonicated for 30 min, and centrifuged for 10 min at 25'000 g (Eppendorf centrifuge 5417R) to eliminate agglomerates. The dispersed NPs in the supernatant were freeze-dried a second time.

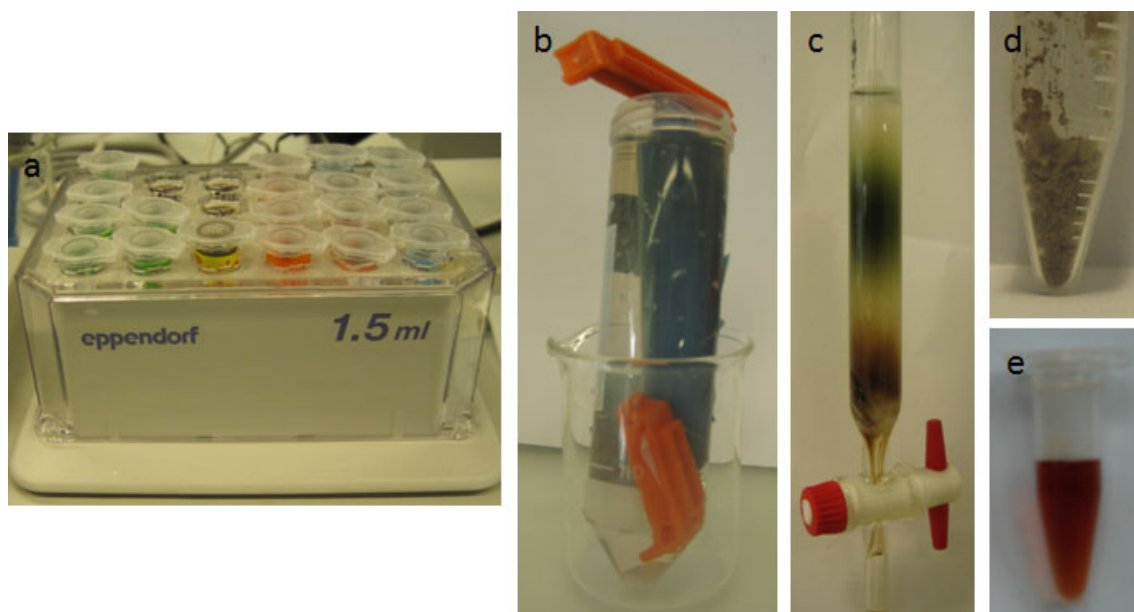


Figure 3.3: Stabilization of Fe_3O_4 NPs. (a) Dispersants were adsorbed on as-synthesized Fe_3O_4 NPs before (b) ethanol was exchanged with Millipore water and excessive dispersants were removed by dialysis. (c) Freeze-dried NPs were re-dispersed in water and remaining free dispersants were removed by column separation before these NPs were freeze dried a second time. NPs were stored (d) as a powder or (e) in aqueous solutions.

3.3.2 Nanoparticles Synthesized in Organic Solvents

As-synthesized NPs were stabilized within 6 h after completion of the NP synthesis. Unless stated otherwise, NPs were stabilized in ethanol. Because especially PEG-based dispersants are poorly soluble in ethanol, they were first aliquotted in DMF at a concentration of 100 mg/ml. This dispersant solution was pipetted into an eppendorf tube containing ethanol or DMF respectively before NP dispersions were added at concentrations summarized in Table 3.2. NPs were stabilized at 50 °C for 24 h under constant mechanical stirring (Thermomixer comfort, Vaudaux-Eppendorf, Switzerland) (Figure 3.3a).

NPs which were functionalized *e.g.* with biotin or acrylate terminated dispersants were first incubated with the functionalized dispersants (unless stated otherwise 10 mol%) at 50 °C for 30 min under constant mechanical stirring at 500 rpm. Unfunctionalized dispersants were added to this dispersion and NPs were incubated for another ≈ 23.5 h at 50 °C under constant mechanical stirring at 500 rpm (Thermomixer comfort, Vaudaux-Eppendorf, Switzerland).

To exchange ethanol with water and to partially remove excessive dispersants, stabilized NPs were dialyzed for 24 h against Millipore water (Figure 3.3b). Approximately 5 ml NP dispersion was dialyzed against 50 ml Millipore water and the Millipore water was

exchanged twice. Fe_3O_4 NPs synthesized in the MW were dialyzed using 14-16 kDa cut-off dialysis tubings whereas the other NPs were dialyzed with 25 kDa cut-off of the dialysis tubings (Spectra/Por dialysis membrane, spectrum labs, Netherlands). NPs other than iron oxide were dialyzed for 1 week. Millipore water was exchanged twice a day. Iron oxide NPs, however, were only dialyzed for one day. Dialyzed NPs were freeze dried.

To ensure complete removal of agglomerates and free dispersants, Fe_3O_4 NPs synthesized in the oil bath were further purified. Agglomerates and NPs that were coated to less than full dispersant coverage were removed by centrifuging stabilized Fe_3O_4 NPs for 60 min at 13'400 rpm (MiniSpin, Vaudaux Eppendorf, Switzerland). The supernatant was freeze dried before these NPs were re-dispersed at a concentration > 10 mg/ml in Millipore water. To ensure complete removal of free dispersants, NPs were run through a Sephadex column (Sephadex G75, superfine) using Millipore water as eluent (Figure 3.3c). NPs were freeze-dried a second time before they were stored as a powder (Figure 3.3d) or re-dispersed in an aqueous media at the desired concentration (Figure 3.3e).

3.3.3 NP Stabilization with Palmityl-nitroDOPA

As-synthesized NPs were stabilized within 6 h after the NP synthesis was completed. 6 mg palmityl-nitroDOPA dissolved in DMF at a concentration of 100 mg/ml was added to 0.5 ml ethanol before 0.5 ml of the Fe_3O_4 NPs synthesized in the oil bath at, unless stated otherwise, 150 °C was added. Palmityl-nitroDOPA was adsorbed for 24 h at 50 °C under constant mechanical stirring at 500 rpm (Thermomixer comfort, Vaudaux-Eppendorf, Switzerland). To remove excessive dispersants, NPs were washed three times by centrifuging them for 30 min at 14'000 rpm (MiniSpin, Vaudaux Eppendorf, Switzerland) before the supernatant was exchanged with 1 ml fresh ethanol. NPs were centrifuged a fourth time where ethanol was exchanged with 1 ml Millipore water before these NPs were freeze-dried.

3.3.4 Dispersant Adsorption on Flat Surfaces

As sputtered Fe_3O_4 substrates were cleaned for 30 min by UV/ozone (UV clean Model 135500, BEOKEL, PA, USA) before they were inserted into a DMF based solution containing 100 μ g/ml dispersants or anchors respectively. Dispersants or anchors were ad-

sorbed for 24 h at 50°C before the substrates were thoroughly rinsed with Millipore water and dried with N_2 .

3.4 Nanoparticle Functionalization

3.4.1 Materials for Nanoparticle Functionalization

D_2O , Sephadex G75 (superfine) and phosphate buffered saline (PBS) (pH=7.4) tablets, rhodamine 110 chloride (purity $\geq 99\%$), 6-aminofluorescein and ethan-1,2-diamine from Sigma, ethanol (absolute) from Scharlau and chloroform from ESCA. Triphenylphosphine-3,3',3''-trisulfonic acid trisodium salt hydrate (Tris) was obtained from Alfa Aesar. L- α -Phosphatidylcholine (egg-PC) and 1,2-Dipalmitoyl-sn-Glycero-3-Phosphoethanolamine-N-(Cap Biotinyl) (biotin-PE) were purchased from Avanti Polar Lipids, protein A, neutravidin, bovine serum albumin (BSA) and PBS (containing 2.67 mM KCl, 1.47 mM KH_2PO_4 , 137.93 mM NaCl and 8.5 mM Na_2HPO_4) from Invitrogen, serum (Precinorm U) from Roche, Feridex from Berlex, recombinant human vascular cell adhesion molecule (VCAM)-1 chimera and biotinylated human anti-E-selectin antibodies from R & D systems, biotinylated anti-human CD106 (VCAM-1) from Lubio science. Succinimide 4-formylbenzamide (SFB) and succinimidyl 6-hydrazinonicotinamide acetone hydrazone (SANH) was purchased from SoluLink (CA, USA). Fc-tagged human E-cadherin was a kind gift from Prof. Deborah E. Leckband. PLL-g(3.5)-PEG(2) was purchased from SuSoS (Switzerland).

3.4.2 Biotin-Avidin Functionalization

Iron oxide NPs synthesized by the aqueous precipitation method and stabilized with mPEG(550)-gallol and biotin-PEG(3.4)-gallol were functionalized with anti-human-vascular cell adhesion molecule-1 (anti-human VCAM-1). Functionalization was done at RT. 50 μg iron oxide NPs dispersed in 500 μl HEPES containing 160 mM NaCl were further coated with 23 μg neutravidin (corresponding to 7 μmol (neutravidin)/mg(iron oxide)), where neutravidin was aliquotted at 1 mg/ml in Millipore water. Unless stated otherwise, 7.5 μg biotinylated anti-human VCAM-1 antibodies, aliquotted at 1 mg/ml in HEPES containing 160 mM NaCl were added to neutravidin pre-coated NPs. Binding experiments were performed within 1 h after antibodies were added to the NPs.

3.4.3 Succinimide 4-Formylbenzamide (SFB) - Succinimidyl 6-Hydrazinonicotinamide Acetone Hydrazone (SANH) Coupling

Iron oxide NPs stabilized with 50 mol% acrylate-PEG(5)-nitroDOPA and backfilled with PEG(5)-nitroDOPA were modified with ethane-1,2-diamine. NPs dispersed at 1 mg/ml in Millipore water were mixed with ethane-1,2-diamine at a molar ratio of ethane-1,2-diamine : acrylated dispersants = 100 : 1 for 3 h at 30 °C under constant mechanical stirring. To remove excessive ethane-1,2-diamine, NPs were run through a Sephadex column before they were freeze-dried.

SFB and SANH were aliquotted in DMF at 10 mg/ml. Heat shock protein 60 (HSP60)-antibodies were incubated in PBS at RT for 2 h with SANH using a weight ratio of SANH : HSP60 antibody = 1 : 6. Excessive SANH was removed by filter centrifugation with a cut-off of 50 kDa.

SFB was coupled to acrylated NPs that had previously been modified with ethane-1,2-diamine, at a molar ratio of amine functionalized dispersants adsorbed on NPs : SFB = 1 : 10. Coupling was done in PBS at 30 °C for 2 h.

SANH functionalized HSP60 antibodies were coupled to SFB functionalized NPs at a molar ratio of HSP60 antibodies : NPs = 15 : 1 in PBS where they were mechanically stirred (Thermomixer comfort, Vaudaux-Eppendorf, Switzerland) at 37 °C for 3 h. Excessive antibodies were removed by centrifuging NPs for 10 min at 13'400 rpm (MiniSpin, Vaudaux Eppendorf, Switzerland). HSP60-antibody functionalized NPs were analyzed within one hour after completion of the functionalization.

3.4.4 Acrylate-Amine Ligand Coupling

Antibodies and second labels were covalently linked to acrylate functionalized iron oxide NPs through a slightly modified protocol of the Michael addition reported by Surendra *et al.* [327]. MW synthesized iron oxide NPs were stabilized with a mixture of 30 mol% acrylate-PEG(5)-nitroDOPA and 70 mol% PEG(1.5)-nitroDOPA. Freeze dried NPs were re-dispersed in Millipore water at 1 mg/ml. 140 µg HSP60 antibodies (dispersed in PBS at 1.7 mg/ml) were added to 0.5 ml of the NP dispersion, which corresponds to ≈ 20 antibodies per NP. NPs were incubated with these antibodies at 30 °C for 3 h under constant mechanical stirring at 500 rpm (Thermomixer comfort, Vaudaux-Eppendorf, Switzerland). Excessive antibodies were removed by centrifuging NPs at 13'400 rpm for 30 min (MiniSpin, Vaudaux Eppendorf, Switzerland) and exchanging the supernatant

with PBS buffer. However, NPs could not be readily re-dispersed and were strongly agglomerated. NPs that could be re-dispersed after centrifugation agglomerated with time if kept at RT due to an ongoing reaction between amine groups of on NP coupled antibodies and acrylate terminated dispersants adsorbed on other NPs. If NPs were not centrifuged, they agglomerated within 7 h after they had been mixed with HSP60-antibodies. NP agglomeration prevented reproducible binding studies of individually stabilized, antibody functionalized NPs.

3.4.5 Fluorescent Labeling of Nanoparticles

Iron oxide NPs synthesized in the oil bath, stabilized with 30-50 mol% acrylate-PEG(5)-nitroDOPA and back-filled with PEG(5)-nitroDOPA or PEG(1.5)-nitroDOPA were fluorescently labeled with FITC- NH_2 and rhodamine respectively. This was achieved by coupling the fluorophores to the acrylate terminated dispersants that had been adsorbed on the NP surface. 5.3 mg stabilized, freeze-dried iron oxide NPs were dispersed in Millipore water at a concentration of 1 mg/ml. 0.265 mg FITC- NH_2 and 0.278 mg rhodamine (corresponding to ≈ 2000 fluorophores per iron oxide core) dispersed in Millipore water at 10 mg/ml were added to 1 ml solution. NPs were incubated with fluorophores for 3 h at 30 °C under constant mechanical stirring. To remove excessive fluorophores freeze-dried NPs were re-dispersed in 1 ml Millipore water and run through a Sephadex column using Millipore water as an eluent. To ensure complete removal of unbound fluorophores, NPs were freeze dried and column separated two more times before they were freeze-dried again and stored as a powder.

3.5 Complexation of Anchors with Iron Ions

For FTIR and UV/VIS investigations, 0.137 μmol anchors were added to 0.137 μmol $FeCl_2$ and $FeCl_3$ respectively which was dissolved in 1 ml Millipore water ($R = 18.2 \Omega$, TOC < 6 ppb), 1 ml 10 mM Tris containing 160 mM NaCl, EtOH and DMF respectively. For EPR investigations 40 $\mu\text{mol/ml}$ nitroDOPA was complexed with Fe^{3+} and Fe^{2+} at a molar ratio of nitroDOPA : iron ion = 3 : 1 and 1 : 1 respectively in Millipore water. Unless stated otherwise, these solutions were left at RT for 1 h before they were analyzed with UV/VIS spectroscopy or freeze dried for FTIR and EPR investigation.

3.6 Liposomes

3.6.1 Materials for Liposomes

1,2-distearoyl-sn-glycero-3-phosphocholine (DSPC), 1-stearoyl-2-oleoyl-sn-glycero-3-phosphocholine (SOPC), 1-palmitoyl-2-oleoyl-sn-glycero-3-phosphocholine (POPC) and 1,2-Dioleoyl-sn-Glycero-3-Phosphoethanolamine-N-[Methoxy(Polyethylene glycol)2000] (Ammonium Salt) (PEG(2)-PE) were purchased from Avanti Polar Lipids (Alabama, USA). Calcein was obtained from ABCR (Kahlsruhe, Germany), D_2O , N-N dimethylformamide (DMF), Sephadex G75 (superfine) and phosphate buffered saline (PBS) (pH = 7.4) tablets from Sigma, ethanol (absolute) from Scharlau and chloroform from esca chemicals.

3.6.2 Liposome Assembly

886 μg PEG(2)-PE dissolved in $CHCl_3$ at a concentration of 25 mg/ml was added to 5 mg DSPC, SOPC or POPC respectively dispersed in 0.5 ml $CHCl_3$ before optionally 1.5 mg palmityl-nitroDOPA stabilized iron oxide NPs, dispersed in 150 μl $CHCl_3$ was added. A thin film of lipids optionally mixed with hydrophobic NPs was formed by slowly evaporating $CHCl_3$ under a constant N_2 stream. To ensure complete removal of $CHCl_3$, the lipid film was further dried for 1 h under a constant N_2 stream.

The lipid film optionally functionalized with iron oxide NPs was swollen in 1 ml Millipore water, PBS or PBS containing 3 mg/ml calcein. Liposomes that were loaded with PEG(1.5)-nitroDOPA stabilized iron oxide NPs were swollen in PBS containing calcein and PEG(1.5)-nitroDOPA stabilized iron oxide NPs where the iron oxide concentration was kept constant at 0.5 mg/ml. To prevent filter clogging by oversaturated calcein solutions, calcein dispersed in PBS at 3 mg/ml was filtered using syringe filters with a cut-off of 200 nm (Sartorius, Germany) before it was added to the dried lipid film.

The lipid film was swollen for 1 h at 65 °C before it was sequentially extruded 10 \times through 200 nm and 31 \times through 100 nm polycarbonate filters using a hand extruder (Avestin, Mannheim, Germany). Extrusion was performed at 65 °C. As-extruded liposomes could be stored at 4 °C for at least 4 weeks. Liposomes where calcein or PEG(1.5)-nitroDOPA stabilized iron oxide NPs were embedded in the lumen were run through a Sephadex column (Sephadex G75) using PBS as an eluent to remove not encapsulated

fluorophores and NPs respectively and were analyzed within 4 h after column separation to avoid passive leakage.

3.6.3 Alternating Magnetic Field Heating of Liposomes

1.5 ml calcein loaded liposomes dispersed at a liposome concentration of ≈ 0.5 mg/ml in PBS were treated with an AMF (Easyheat (1.2 kW), Ambrell). AMF was induced by running 450 A through a 3.5 cm diameter coil which had 6 loops at a frequency of 230 kHz. The sample was localized within only 2 loops. Unless stated otherwise, samples were treated for 6×5 min with 1 min equilibration between each cycle. Fluorescence was quantified using a fluorispectrometer at an excitation and emission wavelength of 488 nm and 520 nm respectively. The fluorescence was normalized to the fluorescence of samples which were not exposed to an AMF and to the volume the vesicle lumen measured with SANS. Statistics was measured on 3-6 independent identical batches. Calcein loaded control liposomes with and without palmityl-nitroDOPA stabilized NPs embedded in their membranes were externally heated at a heating rate of 1 °C/min.

4.1 Chemical Analysis of Dispersants

4.1.1 Microelement Analysis

In microelement analysis, organic compounds are heated in a combustion chamber to $T > 1000\text{ }^{\circ}\text{C}$ in an oxygen/helium atmosphere. The decomposition products of the resulting catalyzed flash combustion are swept through a reduction chamber which contains helium as a carrier gas and are analyzed by gas chromatography, infrared spectroscopy or thermal conductivity measurements [328].

Experimental

Microelement analysis of the dispersants used here was performed in the Microlaboratory of organic chemistry at ETH Zurich.

4.1.2 Nuclear Magnetic Resonance (NMR)

NMR is one of the most often used techniques to chemically characterize especially organic compounds. All stable isotopes which have an odd number of protons and/or neutrons possess a net spin quantum number $\neq 0$ and thus can be detected with NMR. Due to their abundance in organic chemistry, the most often analyzed elements are ^1H and ^{13}C isotopes. Spins of these isotopes align either parallel or antiparallel to the applied external

magnetic field. They precess around the magnetic field axis with the Larmor frequency $\vec{\omega}$ defined as

$$\vec{\omega} = \gamma \vec{B}, \quad (4.1)$$

where γ is the gyromagnetic ratio and \vec{B} the magnetic field. However, the local magnetic field \vec{B} depends on the chemical environment of nuclei. Nuclei are surrounded by electrons which possess magnetic moments that typically align antiparallel to the external magnetic field. By applying a pulsed magnetic field at an angle $\neq 0$ to B_0 , spins are flipped. NMR measures how quickly these spins re-align along the axis of the external magnetic field [329].

Experimental

Dispersants used in this thesis were characterized with ^1H -NMR and ^{13}C -NMR on a Bruker 500 MHz NMR spectrometer where they were dispersed, unless stated otherwise, in D_2O .

4.1.3 Mass Spectrometry (MS)

The molecular weight distribution of dispersants was quantified using Matrix Assisted Laser Decomposition/Ionization (MALDI)-time of flight (tof). MALDI is a soft ionization technique often used in biology and to investigate large, fragile polymers. Polymers are embedded in a matrix which absorbs most of the laser energy, thus preventing polymer degradation by the direct laser beam [330]. Samples are typically illuminated using a pulsed Yttrium aluminum granat (YAG)-laser. Laser illumination primarily ionizes the matrix. Even though the exact mechanism is still debated, the matrix is thought to ionize the polymer which subsequently can be analyzed using *e.g.* tof [331]. The through MALDI generated ions are accelerated in an electromagnetic field where the final velocity of the polymer is analyzed. The velocity of the polymer fragments depends on the m/z ratio where m is the mass and z the net charge of the fragment [329].

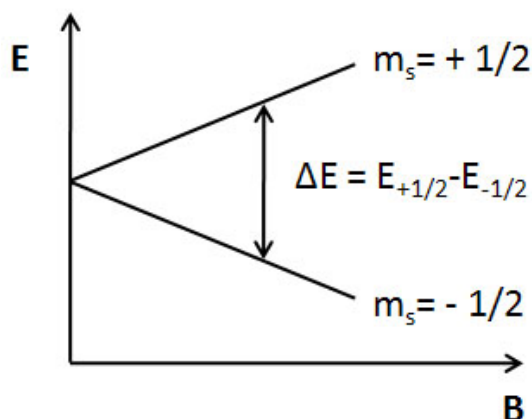


Figure 4.1: Zeemann effect. Energy splitting of unpaired electron spins if an external magnetic field B is applied

Experimental

MALDI-tof on dispersants was measured by the MS service of the organic chemistry laboratory at ETH Zurich. It was done on a Bruker Daltonics Ultraflex II equipped with a YAG Laser (pulse rate = 50 ps). The matrix consisted of a mixture of T-2-[3-(4-t-butyl-phenyl)-2-methyl-2-propenylidene]malononitril (DCTB) + Na of 1:10:1.

4.1.4 Electron Paramagnetic Resonance (EPR)

Electron paramagnetic resonance (EPR) spectroscopy is a technique to study species with unpaired electrons. The energy difference between electrons which are in the magnetic spin state $m_s = - 1/2$ and those which have $m_s = + 1/2$ is

$$\Delta E = g\mu_B B_0 \quad (4.2)$$

where g is the splitting factor, μ_B is the Bohr magneton and B_0 is the applied magnetic field (Figure 4.1).

Electrons occupy the spin states $m_s = - 1/2$ and $m_s = + 1/2$ according to Boltzmann statistics (equation 4.3)

$$\frac{n_{upper}}{n_{lower}} = e^{-\frac{\Delta E}{k_B T}}, \quad (4.3)$$

where n_{upper} and n_{lower} are the number of electrons which populate the spin state $m_s = +1/2$ and $-1/2$ respectively, ΔE is the energy difference between the $m_s = +1/2$ and $-1/2$ states, k_B is the Boltzmann constant and T the absolute temperature. According to equation 4.3, electrons of samples which are subjected to magnetic fields more likely populate the $m_s = -1/2$ spin state. However, they can flip between the two spin states by absorbing and radiating the energy ε (equation 4.4).

$$\varepsilon = \nu h, \quad (4.4)$$

where ν is the frequency of the electromagnetic radiation and h the Planck constant. Therefore, if the frequency of the external magnet is kept constant and the magnetic field is swept, electrons absorb energy if equation 4.5 is fulfilled

$$\nu h = g\mu_B B_r, \quad (4.5)$$

where B_r is the resonance magnetic field [332].

In a typical EPR graph, the first derivative of the measured energy absorption is plotted as a function of the applied field B . Because of the well-defined, sharp transition between the $m_s = -1/2$ and $+1/2$ state of free electrons, they result in a sharp characteristic EPR signal with $g = 2.00$ unless there is hyperfine coupling which broadens the signal slightly [333, 334].

Spin transitions measured with EPR are sensitive to distortions in the atom ligand field. Therefore g -values of atoms which have unpaired electrons, such as paramagnetic Fe^{3+} ions, depend on the coordination of Fe^{3+} ions. Uncomplexed Fe^{3+} ions absorb energy at $g = 2.0$ [332]. However, depending on the distortion of their ligand field, the g -values can be shifted up to $g = 9$ [335]. Thus, EPR spectra yield information on the ligand field of complexed paramagnetic species such as Fe^{3+} ions.

If paramagnetic ions are part of a superparamagnetic ensemble (*e.g.* Fe^{3+} in iron oxide NPs), strong magnetic coupling between these Fe^{3+} ions significantly broaden EPR peaks. Therefore, superparamagnetic NPs result in broad EPR peaks centered at $g \approx 2$. Dipole-dipole interactions between different NPs lead to further broadening of the line width [333, 336].

Experimental

In this work, 2-3 mg unstabilized, PEG(5)-nitroDOPA, PEG(5)-dopamine and PEG(5)-mimosine stabilized freeze-dried iron oxide NPs synthesized in the MW and 7-12 mg nitroDOPA/iron complexes respectively were analyzed with EPR. Reproducibility was checked on 2-3 independent identical samples. EPR measurements were done on a Bruker EMX spectrometer at a frequency of ≈ 9.86 GHz and a power of 2.04 mW at room temperature. The sum of 3 scans is shown. The resonance equation 4.2 was used to calculate the g -values. These values correspond to the resonance field B_r which is defined as B at maximum absorption, i.e. zero crossing of the first derivative of the absorption spectrum. N,N-diphenylpicrylhydrazyl (DPPH) with $g = 2.0036$ was used as internal standard. The ratio of the derived intensity peaks was determined based on the total height of the discontinuity resulting from free electrons at $g = 2.0$ and the height of the Fe^{3+} signal at $g = 3.9$ with respect to the baseline. Heat treatment was performed in EPR glass tubes. Samples were heated to $T > 200$ °C for 10 min before they were analyzed with EPR.

4.1.5 Fourier Transform Infrared Spectroscopy (FTIR)

FTIR is an often used technique to characterize especially organic molecules because it can identify molecular vibrations. Organic species absorb light in the mid-infrared region (typically between ≈ 400 and 4000 cm^{-1}) where the molecular bonds are excited and thus start vibrating. The wavelength, where molecules absorb energy is characteristic for the bond type (and the electron density of the bond) and can therefore be used to identify organic molecules [329, 337].

Experimental

200 μg of NPs synthesized in the MW at 180 °C for 3 min were added to 1 ml DMF or EtOH containing 3.85 μmol of the respective anchor. Pure anchors, rather than PEG-anchors, were chosen for FTIR in order to minimize the interference from the C-O and C-C stretching bands of the PEG moieties with vibrations from anchors. Anchors were adsorbed for 24 h at 50 °C while they were constantly mechanically mixed at 500 rpm (Thermomixer comfort, Vaudaux-Eppendorf, Switzerland). Iron oxide NPs coated with anchors were purified by washing them 10 times with Millipore water through centrifugation for 10 min at 13400 rpm. Purified NPs were freeze-dried (freeze dryer ALPHA 1-2 /

LDplus, Kuhner LabEquip, Switzerland).

FTIR spectra of freeze dried NPs coated with anchors were measured as KBr tablets where the weight ratio of KBr : sample was $\approx 100 : 1$. Spectra were recorded from 400 to 4000 cm^{-1} at a resolution of 4 cm^{-1} at room temperature and a pressure of < 2 mbar. Spectra were acquired on a Bruker IFS 66v FTIR spectrometer using a deuterated triglycine sulfate (DTGS) detector where the sum of 64 scans was shown.

4.1.6 Ultraviolet/Visible (UV/VIS) Spectroscopy

While FTIR is used to excite molecular bonds, UV/VIS spectroscopy can measure electronic transitions within molecules and complexes. Because the amount of absorbed light linearly scales with the number of molecules which underwent electron transitions at a specific wavelength, concentrations of compounds can easily be quantified using the Lambert-Beer law (equation 4.6)

$$\frac{I}{I_0} = e^{-\epsilon c L} \quad (4.6)$$

where I_0 and I are the intensities of the incident and transmitted beam, ϵ the extinction coefficient, c the concentration and L the path length of light in the sample.

Especially metal ions complexed by chelators often result in characteristic strong absorptions in the UV/VIS region. This renders UV/VIS spectroscopy attractive to identify the presence and determine the concentration of metal ions by adding an appropriate chelator. Furthermore, UV/VIS spectroscopy can be used to *e.g.* investigate electronic transitions involved in the complexation of ligands to metal ions [329].

Experimental

In this thesis, electron transitions between anchors and iron ions were studied with UV/VIS spectroscopy. For this purpose, UV/VIS spectra were recorded on 0.505 μM anchor containing solutions where optionally iron ions were added. Spectra were acquired at room temperature on a Cary 1E UV/VIS spectrometer (Varian) between 200 and 800 nm.

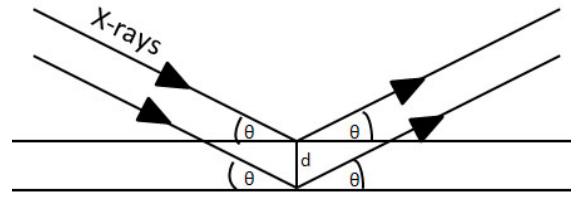


Figure 4.2: Bragg equation. Illustration of the Bragg equation where d is the lattice spacing.

4.2 Nanoparticle Core Analysis

4.2.1 X-ray Diffraction (XRD)

XRD is a non-destructive technique to analyze the crystallographic structure and phase purity of crystalline materials. Reflected, monochromatic X-rays only constructively interfere with each other at angles Θ defined in Figure 4.2, where the Bragg equation

$$n\lambda = 2d\sin(\Theta), \quad (4.7)$$

with n being an integer, λ the X-ray wavelength and d the lattice spacing, is fulfilled. The full width of half maximum (FWHM) of observed Bragg peaks are influenced by instrumental factors, internal stresses and small crystallite sizes. Whereas small crystallite sizes result in a peak broadening τ_{size} which can be described with the Scherrer formula (equation 4.8) where β_{τ} is the FWHM of this diffraction peak, the peak broadening caused by internal stresses τ_{int} has an angle dependence according to equation 4.9 with ϵ being a parameter for the internal stresses [338, 339].

$$\tau_{size} = \frac{\lambda}{\beta_{\tau}\cos(\Theta)} \quad (4.8)$$

$$\tau_{int} = \epsilon\tan(\Theta) \quad (4.9)$$

Therefore, an average volume weighted crystallite size, which for single crystalline NPs corresponds to the NP size, can be determined based on XRD measurements. However, the average diameter of single domain NPs determined with XRD is volume weighted. It thus cannot be directly compared to the number weighted core diameters *e.g.* obtained by analyzing TEM micrographs.

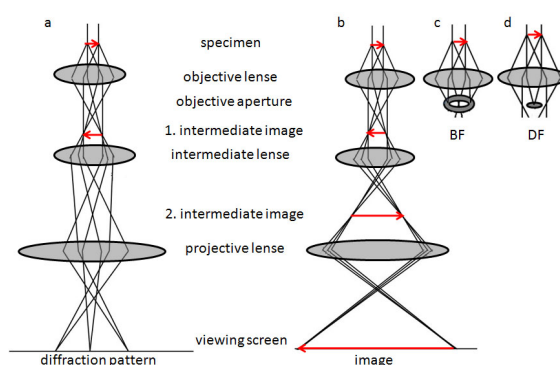


Figure 4.3: Schematic of electron path in TEM. Schematics of the electron path in the (a) diffraction and (b) direct imaging mode. If imaged in the direct mode, either (b) all the electrons are transmitted, or a lens is added to the electron beam that only lets pass the (c) undiffracted electrons resulting in bright field (BF) images or (d) the diffracted electrons resulting in dark field (DF) images.

According to equation 4.7 the location of the diffraction peaks depends on the lattice distance d and the crystal structure. Materials like Fe_3O_4 and $\gamma-Fe_2O_3$, where $\gamma-Fe_2O_3$ is a defect structure of Fe_3O_4 which has additional oxygen vacancies, have very similar lattice distances and identical crystal structures [340–342]. Therefore, it is very difficult to tell these structures apart based on XRD measurements. If small NPs are analyzed which, according to equation 4.8, lead to a significant line broadening, such structures cannot unequivocally be distinguished with XRD.

Experimental

To analyze the crystal structure and phase purity of oxide NPs investigated in this work, XRD was measured on as-synthesized and PEG(5)-nitroDOPA stabilized NPs. As-synthesized NPs, dispersed in ethanol or PEG(5)-nitroDOPA stabilized NPs dispersed in Millipore water were dried onto plane sapphire substrates. XRD was measured between 20 and 90 ° on a Philips PW 1800 instrument in the reflection mode using a Cu $K\alpha$ radiation. The diffractometer was equipped with a postsample monochromator.

4.2.2 Transmission Electron Microscopy (TEM)

Two main imaging modes have to be distinguished: conventional TEM and scanning TEM (STEM). For TEM the electrons enter the specimen in the form of a plane wave, while in STEM a focused beam is scanned over the sample.

Imaging Contrast

In TEM electrons that are transmitted through the sample are detected. Electrons enter the specimen as a plane electron and are scattered or absorbed by the sample. If an image is formed with these electrons, different mechanisms have to be considered to explain the observed image contrast. The most simple contrast is mass-thickness contrast. The darkness of the image (reflecting the amount of absorbed electrons) directly scales with the sample thickness and atomic number of the elements. However, because TEM samples are thin, contrast most often arises from phase shifts. Due to lense aberrations, different phase shifts, which mainly depend on the angle the electron had been scattered at, add up (contrast transfer function). This leads to an interference pattern of scattered and unscattered electron waves that depend on the focussing conditions. Crystalline materials lead to additional and specific contrast formation (for details see [343]). Contrast can be enhanced with an aperture inserted into the diffraction plane (Figure 4.3). The aperture selectively absorbs electrons scattered at angles other than a specific angle. This increases the signal : noise ratio of images.

If a so-called objective aperture is inserted into the back focal plane of the objective lens directly below the sample, forward scattered or diffracted electron waves can be selectively chosen (Figure 4.3). In the bright field (BF) imaging mode, the aperture is centered around the primary, undeflected beam. Therefore, objects which weakly scatter are preferentially imaged in the BF mode. In contrast, only diffracted electrons are used for image formation in the dark field (DF). Electron dense objects thus yield high contrast and are easily visualized in the DF mode. If the Bragg conditions are fulfilled, the BF and DF modes are basically complementary.

Independent of the relevant contrast mechanism, the resulting TEM micrograph is a modified 2D projection of the crystal potential of the specimen [343–345].

Experimental

In this work, the NP core size, morphology and crystallinity was investigated with conventional TEM whereas liposomes containing iron oxide NPs in their membrane were also studied with cryo-TEM. PEG-anchor stabilized iron oxide NPs were dispersed in Millipore water at 1 mg/ml. To form free spanning membranes, 3.5 μ l of the NP dispersion was dried on a carbon coated Cu-grid (300 mesh) where the carbon support had holes with a diameter of 3.5 μ m (Quantifoil Micro Tools GmbH, Germany). For size evaluations,

300 mesh Cu-grids (Ted Pella Inc, Pelco International) were coated with 10 nm carbon. 3.5 μl of 1 mg/ml NP solution was dried on this grid. Alternatively, 3.5 μl drops were deposited on a paraffin film. Hydrophobic carbon coated Cu-grids were glow discharged for 30 s (Emitech K 100X) to render them hydrophilic. These grids were placed onto the NP dispersion drop and particles were adsorbed for 1 min. The latter method resulted in a lower NP loading where NPs were arranged randomly, in stark contrast to grids, where the NPs dispersion was completely dried on the grid.

Transmission electron micrographs were taken on a Philips CM12 microscope operated at 100 kV while HRTEM was performed on a Philips CM30 and a Tecnai F30 (FEI), both operated at 300 kV. While the Philips CM30 had a LaB_6 filament as an electron source, the Tecnai was equipped with a Schottky field emission gun (FEG) which results in a more coherent electron beam. Diffraction patterns were analyzed using jems (ems java version 3.2927U2008 software, P. Stadelmann, EPFL, Switzerland).

Scanning Transmission Electron Microscopy (STEM)

In contrast to conventional TEM, where full images are acquired simultaneously *e.g.* in a parallel data acquisition mode, a convergent electron beam is scanned over a certain area in the STEM mode. STEM can be acquired in the BF, DF or high angle angular dark field (HAADF) mode. The HAADF mode detects electrons that are mainly incoherently forward scattered under a high angle. The intensity of incoherently scattered electrons almost linearly scales with sample thickness and is $\propto z^2$ where z is the atomic number. The HAADF mode is thus highly sensitive to z of the atoms and therefore yields chemical contrast [343–345].

Diffraction

Crystallographic information of the sample can be gathered if the back focal plane of the objective lens instead of the intermediate imaging plane is projected (Figure 4.3a). The resulting diffraction pattern reveal information on the crystallinity and crystal periodicity including lattice plane distances of the imaged sample. Diffraction is a collective interference phenomenon of electrons scattered at the periodic potential of a crystal.

The spacial resolution is mainly defined by the diameter of the plane incident electron beam. In TEM, this diameter can be made small enough to extract local crystallographic information of individual NPs, given the NP has enough crystal planes for effective

diffraction. Thus, depending on the diameter of the electron plane wave, local or averaged crystallographic information can be retrieved. This is in stark contrast to *e.g.* XRD where an averaged diffraction pattern over a large number of NPs is measured. The main advantage of diffraction patterns acquired in the TEM over *e.g.* XRD is that the local crystallographic information can be directly correlated to a real space image [343–345]. However, if highly accurate, quantitative information of bulk materials is sought, XRD is a more appropriate technique to analyze the overall crystalline structure of a material.

Chemical Analysis by TEM

In electron energy loss spectroscopy (EELS) inelastically scattered electrons are analyzed. Some of the transmitted electrons are inelastically scattered *e.g.* because they lift electrons of the sample from the ground state into higher energy orbitals. During these elastic electron interactions, the beam electrons lose kinetic energy. These energy losses of transmitted electrons are specific for atomic species with which the beam has inelastically interacted. With sufficient energy resolution, EELS can provide local information on the atomic species and its bonding state (*e.g.* the oxidation state of elements).

The spacial resolution is limited by the electron beam diameter and the localization of the respective crystal electron. However, spacial resolution needs to be traded off with the signal to noise (S/N) ratio of the acquired signal that scales with the amount of material contributing to the EELS signal [346].

An alternative to EELS is energy dispersive X-ray (EDX) spectroscopy. EDX is based on X-rays which are emitted by excited electrons that relax into their ground state. Thus the wavelength of X-rays, which are emitted by relaxing electrons, is element specific. However, while elements can be identified, the energy resolution is too poor to distinguish different oxidation states with EDX. Furthermore, EDX is a semi-quantitative technique at best. Re-absorption of X-rays in the sample or the microscope column and subsequent re-emission also contribute to the detected EDX signals and prohibit an accurate quantification of the sample composition. Nevertheless, by combining the different imaging modes, TEM cannot only provide information about size, shape and crystal structures of materials but also yields chemical information [343–345].

TEM on Biological Samples

Biological samples almost exclusively consist of light elements such as *C*, *N*, *O* and *S*. Therefore, they cause only small amplitude and phase shifts of the transmitted electron waves resulting in poor contrast even in the BF mode. To enhance contrast, these samples often are stained with a heavy metal such as uranyl acetate.

Furthermore, to minimize sample preparation artifacts of biological samples like vesicles induced *e.g.* through air-drying, these samples can be fixed with trehalose or frozen *e.g.* in liquid ethane to preserve their native shape. If frozen in liquid ethane, the cooling rate of water is too fast to allow for crystallization. Therefore, water vitrifies and these samples can be imaged at liquid N_2 temperatures (≈ -162 °C). However, the poor absorption contrast of organic samples such as vesicles necessitates that such vesicles are imaged in underfocus. This enhances their contrast according to [347]

$$I(x) = 1 + \frac{\Delta\lambda}{2\Pi} \Phi''(x) \quad (4.10)$$

where Δ is the distance of the image plane, λ the wavelength of electrons and $\Phi''(x)$ the second derivative of the phase shift function. Because these images are acquired in underfocus, an accurate quantification of distances is only possible if appropriate calibrations are done under identical focussing conditions.

Experimental

Cryo-TEM was performed on Millipore based 5 mg/ml liposome dispersion. 2 μ l drops of these solutions were adsorbed Quantifoil holey carbon films R3.5/1 (Electron Microscopy Sciences, PA, USA), dried for 10 s and plunged in liquid ethane using a Vitrorobot (FEI). Samples were blotted for 6 s at an offset of -2. These samples were analyzed on a Philips CM12 microscope operated at 100 kV at liquid N_2 temperatures (≈ -162 °C).

Conventional was done on liposomes that were fixed with 1 wt% trehalose and air dried on a Quantifoil holey carbon films R3.5/1 (Electron Microscopy Sciences, PA, USA) using a Philips CM12 microscope operated at 100 kV.

Millipore water based liposome dispersions were freeze dried on a TEM grid which was supported by a 8 nm thick, glow discharged carbon film. These samples were chemically analyzed in a STEM (Hitachi).

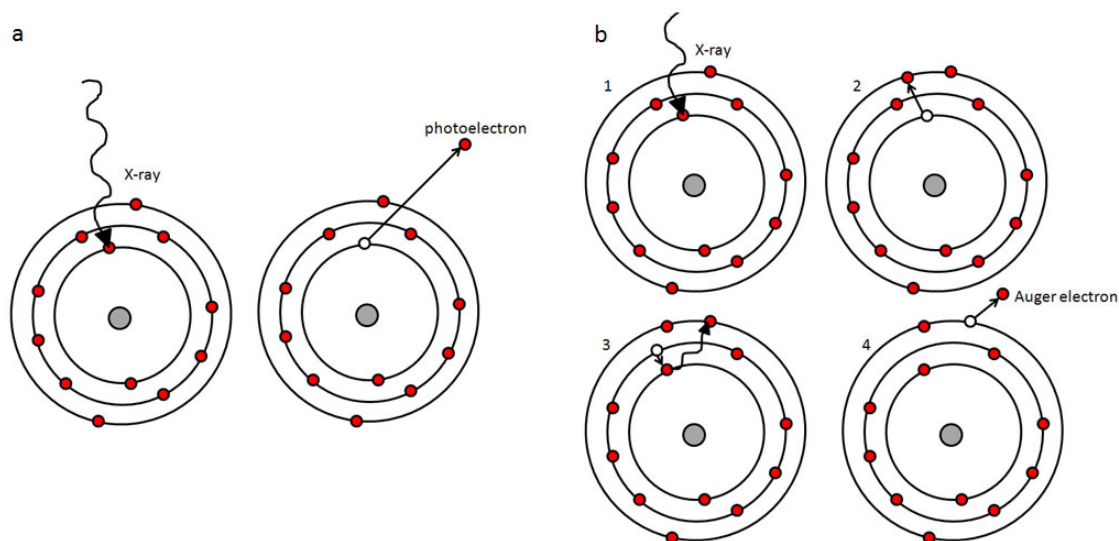


Figure 4.4: XPS. (a) Photoelectrons are generated through absorption of X-rays (b) Auger electrons are generated through (1) the absorption of X-rays which (2) excite an electron. (3) The electron hole in the inner electron shell is filled by a relaxing outer shell electron. The free energy resulting from electron relaxation is converted into X-rays. (4) These X-rays generate an Auger electron that can be detected.

4.2.3 X-ray Photoelectron Spectroscopy (XPS)

X-ray photoelectron spectroscopy (XPS) is a quantitative surface sensitive technique to determine the elemental composition and oxidation states of the top ≈ 10 nm of substrates. Samples are irradiated with X-rays. X-ray interaction with the sample yields photo- and Auger electrons. While photoelectrons are electrons which were set free by absorbing energy from X-rays (Figure 4.4a), Auger electrons are generated in a three step process. X-rays first excite electrons from an inner electron shell. The resulting hole is filled by electrons of an outer electron shell which relaxes into the hole. The released energy is converted into X-rays which subsequently are absorbed by electrons from outer electron shells. These electrons are emitted from the sample can be analyzed (Figure 4.4b) [348]. The kinetic energy (E_{kin}) of photo- and Auger electrons is element specific and depends on the oxidation state of atoms. While E_{kin} of photoelectrons depends on the energy of the incoming X-ray, E_{kin} of Auger electrons is independent on the X-ray energy. Thus, these two electron types can be distinguished by analyzing their kinetic energy with two different X-ray sources which yield different X-ray energies.

The kinetic energy of photoelectrons is analyzed *e.g.* with a hemispherical analyzer. The binding energy (E_{bin}) can be calculated according to equation 4.11.

$$E_{bin} = h\nu - E_{kin} - \Phi, \quad (4.11)$$

where ν the wavelength of the incident X-ray and Φ the work function which is instrument specific. The latter can be determined by measuring calibration standards.

The peak area of a graph where the number of electrons detected per time is plotted as a function of the binding energy, can be used to quantify the relative amounts of different elements. This quantification is achieved by correcting the area I_A for the ionization photoelectron cross section σ_A , the inelastic mean free path of electrons λ_A , the instrument specific transmission function T_A and the take-off angle of analyzed electrons Θ_A according to [348]

$$N_A = \frac{I_A}{\sigma_A T_A \lambda_A \sin(\Theta_A)}. \quad (4.12)$$

Equation 4.12 holds for flat, homogeneous layers. However, quantification of flat NP films is more daunting. The spherical shape of NPs and their core-shell structure significantly influence Θ_A . Furthermore, pressing NPs into pellets for analysis result in non-homogeneous samples. Therefore, especially if the amount of carbon residues on the NP surface is to be quantified, equation 4.13 needs to be applied.

$$I = \frac{\kappa d + \lambda}{d + \lambda} e^{\frac{d}{\lambda}} \pi \lambda^3 \left(\left(\frac{r}{\lambda} \right)^2 + \frac{\left(\frac{2r}{\lambda} + 1 \right) e^{-\frac{2r}{\lambda}} - 1}{2} \right), \quad (4.13)$$

where

$$\kappa = \frac{\beta_1 \left(\frac{r}{\lambda} \right)^2 + \beta_2 \frac{r}{\lambda} + 1}{\beta_1 \left(\frac{r}{\lambda} \right)^2 + \beta_3 \frac{r}{\lambda} + 1} \quad (4.14)$$

r is the core radius, d the dispersant layer thickness assuming it is homogeneous on NP surfaces, λ the electron inelastic mean free path. $\beta_1 = 0.00289$, $\beta_2 = 0.05135$ and $\beta_3 = 0.45982$ are fitting constants which were empirically obtained [349].

Experimental

XPS measurements presented in this thesis were performed on a Sigma Probe (Thermo Scientific, MA, USA), using an Al $K\alpha$ source operated at 200 W. Photoelectrons were detected with a hemispherical analyzer at a pass energy of 25 eV at 90° take-off angle. Data were analyzed using the CasaXPS software (CasaXPS software Version 2.3.15dev52, Software Ltd, UK). A Shirley background was subtracted before the peak areas were

integrated and corrected for the ionization photoelectron cross section using the Scofield factors [350], inelastic mean free path, attenuation length [351] and the energy dependent transmission function which is instrument specific according to equation 4.12.

The dispersant packing density on flat surfaces was calculated based on the atomic $C : Fe$ ratio measured on flat Fe_3O_4 coated with dispersants. For this purpose, the two layer model was taken into account. Because iron oxide substrates absorb light, the dispersant thickness could not be quantified with ellipsometry. Therefore, the dispersant layer thickness was calculated by relating the intensities of the Fe2p and Fe3p peaks [352] assuming a PEG density of 1.1 g/cm^3 [353]. Furthermore, to check the ability of dispersants to replace aliphatic contaminations the C 1s was deconvoluted into three peaks. These C 1s peaks were fitted with peaks which had a 30 % gaussian and 70 % lorentzian shape. The resulting peaks with a binding energy (BE) of $268.6 \pm 0.1 \text{ eV}$, 288.6 ± 0.1 and $284.9 \pm 0.1 \text{ eV}$ were assigned to C_{PEG} , $C_{aliphatic}$ and $C_{COOH \text{ or } OH}$ respectively.

To investigate the oxidation state of iron oxide NPs, XPS was performed on freeze dried, PEG(5)-nitroDOPA stabilized NPs. For the quantification of the amount of dispersants adsorbed on NPs, 5 mg stabilized, freeze-dried NPs were re-dispersed in 0.5 ml Millipore water for 24 h before they were centrifuge filtered with Microcon filters with a cut-off of 30 kDa (Millipore). Filter cakes were re-dispersed in Millipore water and freeze-dried a second time. NPs were pressed into cavities of an Al sample holder where the cavities had a diameter of 10 mm or alternatively pressed onto vacuum compatible sticky tape where it was made sure that the compressed NP layer was thicker than the XPS penetration depth of $\approx 10 \text{ nm}$. Spectra were acquired with the same instrumental parameters as described above. Data were analyzed similarly to what has been described for the XPS data analysis on flat surfaces. Additionally the 3D shape of NPs was taken into account for quantifying the atomic $C : Fe$ ratio (equation 4.13) [349].

4.2.4 Near Edge X-ray Absorption Fine Structure Spectroscopy (NEXAFS)

NEXAFS is a complementary analytical technique to XPS. It measures unoccupied electron orbitals and is thus very sensitive to the number of valence electrons and their spin configuration. Furthermore, it gives insights into the symmetry and coordination number of a unit cell of transition metal compounds [354]. This information is obtained by measuring the energy region from the absorption edge to about 50 eV above the absorption edge [348, 355]. Upon excitation of electrons with monochromatic X-rays at an energy

slightly lower than the energy needed to create photoelectrons, electrons are lifted into higher unoccupied orbitals. Electrons which are in energetically higher orbitals relax into the resulting hole under emission of X-ray fluorescence. The latter can subsequently create Auger electrons [355]. In NEXAFS, one can either detect the fluorescence that is emitted through the relaxation of electrons or Auger electrons. Depending on the detection mode, NEXAFS is more bulk or surface sensitive [355, 356].

If fluorescence is measured, NEXAFS can probe structures as thick as 200 nm. In contrast, the limited penetration depth of Auger electrons (2-10 nm) is responsible for the high surface sensitivity of NEXAFS if the latter detection method is applied [354, 355]. Emitted Auger electrons positively charge the analyzed surface where the surface charge linearly scales with the number of emitted electrons. The electron emission can be quantified by measuring the surface potential in the total electron yield (TEY), partial electron yield (PEY) or Auger electron yield (AEY) mode. These different modes require increasingly more elaborate experimental setups [355].

In the TEY mode, photoelectrons and Auger electrons are detected simultaneously. Therefore, it is the experimentally easiest quantification mode. Photoelectrons have a higher kinetic energy than Auger electrons. Because the electron inelastic mean free path is dependent on the kinetic energy of electrons, the TEY is thus less surface sensitive compared to the PEY or AEY mode [355, 356].

In the PEY, the number of emitted electrons is limited by applying a retardation voltage. However, because Auger and photoelectrons (even if they are inelastically scattered) are detected as long as their kinetic energy is higher than the retardation voltage potential, the two electron types cannot be discriminated [355, 356].

The AEY is experimentally most difficult and most surface sensitive detection mode. Auger electrons are detected exclusively by setting the energy analyzer at a specific Auger transition energy. This excludes that photoelectrons are simultaneously detected [355, 356].

Because electrons can be most effectively excited if the X-ray incidence is parallel to the electron orbital whereas no electrons are excited if the X-rays are oriented perpendicular to the electron orbital, the orientation of *e.g.* aromatic compounds adsorbed on molecularly flat surfaces can be quantified with NEXAFS [355–357].

Experimental

NEXAFS spectra of the *O* K-edge and the *Fe* L-edge presented here were acquired under normal X-ray incidence at the PolLux beamline at PSI Villigen (Switzerland) in total electron yield (TEY) mode. The resolution was ≈ 0.1 eV. The pressure was kept below 2×10^{-4} mbar. Spectra were recorded on at least two independent samples for each anchor. The *O* K pre-edge was normalized to 530 eV while the *Fe* K-pre-edge was normalized to 710 eV [354].

4.3 Magnetic Analysis

4.3.1 Vibrating Sample Magnetometry (VSM)

Paramagnetic, superparamagnetic and ferromagnetic materials align their spins along the axis of an external magnetic field. The resulting magnetic dipole moment of the sample creates an additional magnetic field \vec{B} around the sample, a so-called stray field. According to Faraday's laws, the magnetic stray field changes, if the sample is moved inside an external static magnetic field. The changing magnetic field induces electric fields which can be detected by pick-up coils. These electric fields can be related to the magnetic moment of the sample using Faraday's law of induction (equation 4.15)

$$\Phi_B = \Sigma(t) \int \vec{B}(\vec{r}, t) d\vec{A} \quad (4.15)$$

where Φ_B is the magnetic flux, Σ the surface the magnetic flux \vec{B} penetrates and $d\vec{A}$ the area element of the moving surface Σ . Thus, the magnetization of such samples can be measured as a function of the strength of the external, static magnetic fields [358, 359]. The resulting magnetization curve can be fitted with a Langevin function according to

$$L(\xi) = \coth(\xi) - \frac{1}{\xi}, \quad (4.16)$$

with

$$\xi = \frac{\mu_0 M_s H V_M}{k_B T \Phi}, \quad (4.17)$$

where $\mu_0 = 4 \pi \times 10^{-7} \text{ TmA}^{-1}$, M_s is the saturation magnetization, H the magnetic field, V_M the NP core volume and Φ the volume fraction of NP. Magnetization curves thus provide information about the saturation magnetization and susceptibility. Additionally, they also contain information on an averaged volume weighted core radius if fitted with equation 4.16 [15, 32].

Experimental

The magnetization of Fe_3O_4 NPs was measured on 1-3 mg freeze dried PEG(5)-nitroDOPA stabilized and unstabilized NPs. These NPs were weighted into plastic capsules. To minimize NP motion during the measurements, NPs were confined by filling the empty space of the capsule with 20-30 mg cotton. An average of 3 hysteresis scans with a resolution of 100 Oe was measured on a *MicroMagTM* VSM (Princeton Measurement Cooperation, NJ). The measured magnetization was normalized to the amount of Fe_3O_4 quantified with TGA. However, because of the limited precision of the balance (Mettler Toledo, Switzerland) which added uncertainty to TGA and VSM measurements, the accuracy and reproducibility of VSM measurements as performed here was limited.

4.3.2 Magnetic Resonance Imaging (MRI)

Because MRI was derived from NMR spectroscopy (section 4.1.2), those two techniques are based on the same principles. The former, however, is mainly used for diagnostic purposes in medicine whereas NMR is mainly used to characterize organic compounds and to analyze structures of large molecules such as proteins.

MR contrast comes from differences in relaxation times typically of protons which precess with the Larmor frequency $\vec{\omega}$ defined in equation 4.1.

If a RF pulse is superimposed to the static magnetic field at an angle $\Theta \neq 0$ to the axis of the static magnetic field, spins are flipped into the direction of the RF pulse. After removing the RF pulse, spins gradually relax. There are two types of relaxation times: the longitudinal T_1 and the transverse T_2 relaxation time (Figure 4.5). T_1 describes how fast spins re-align in the direction of the external magnetic field (Figure 4.19). Because $\vec{\omega}$ depends on the magnitude of the local magnetic field, protons precess with slightly different frequencies depending on their surrounding. T_2 describes, how fast spins dephase in the plane perpendicular to the static magnetic field after the RF pulse is terminated (Figure 4.19) [96].

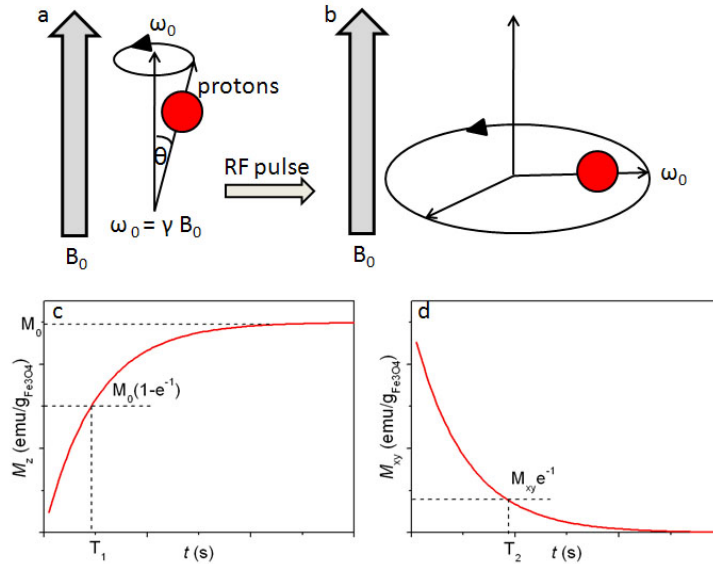


Figure 4.5: MRI principles. (a) Proton spins precess around the static magnetic field. (b) Upon application of an RF pulse, spins are flipped. After the RF pulse is terminated, the spins relax (c) longitudinally, with a relaxation time T_1 and (d) transverse with a relaxation time T_2 [73].

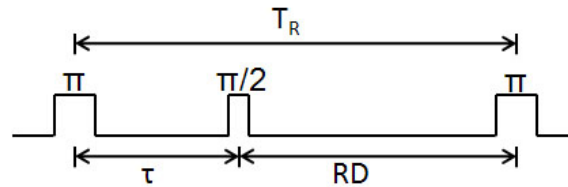


Figure 4.6: Inversion recovery sequence. T_1 is typically measured using an inversion recovery sequence that consists of a 180° pulse, followed by a 90° pulse. The time τ between these two pulses is the inversion recovery time while RD is the recovery delay and T_R the repetition time of the whole sequence. T_1 is measured by varying τ and fitting the obtained data using equation 4.18.

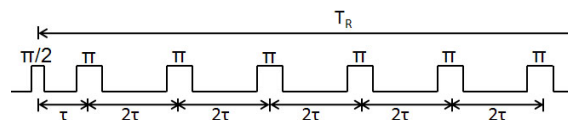


Figure 4.7: Carr-Purcell-Meiboom-Gill (CPMG) MRI sequence. A MRI sequence often used to determine T_2 is the CPMG sequence. It consists of a 90° pulse where spins originally aligned in the $+z$ direction are flipped into the xy plane. This 90° pulse is followed by 180° pulses where the phase of spins is changed. After the echo time $T_E = 2\tau$, spins are refocused and a spin echo is measured. The decay of this echo determines T_2 which can be fitted according to equation 4.19. T_R is the repetition time.

$$\vec{M}_z(t) = \vec{M}_{z, equ} (1 - e^{-\frac{t}{T_1}}) \quad (4.18)$$

$$\vec{M}_{xy} = \vec{M}_{xy}(0) e^{-\frac{t}{T_2}} \quad (4.19)$$

MR contrast agents are classified depending on their influence on T_1 and T_2 respectively. T_1 -contrast agents are typically paramagnetic ions such as Gd^{3+} and markedly decrease T_1 which enhances signals on MR images. Thus, they are defined as positive contrast agents. Contrast agents with a comparably high net-magnetic moment such as iron oxide NPs, decrease T_2 . They lead to signal losses on T_2 -weighted MR images and are defined as negative contrast agents [15, 73].

T_1 is proportional to the number of H_2O molecules in immediate proximity to paramagnetic ions during a given time. Thus ions and very small NPs are more effective T_1 contrast agents compared to larger NPs. Furthermore, because magnetic interactions between electrons from the T_1 -contrast agents and protons are proportional to D^6 , where D is the distance between the electron from the T_1 contrast agent and the proton, only protons which are in close proximity (e.g. the innermost water shell surrounding the T_1 contrast agent) yield contrast. Thus the shorter the residence time of H_2O molecules in close proximity to the NP, the stronger is the MR contrast evoked by the T_1 contrast agent [15].

Because T_2 is directly related to differences in $\vec{\omega}$ of proton spins and $\vec{\omega} \propto \vec{B}$ (equation 4.1) and therefore very sensitive to magnetic field inhomogeneities, superparamagnetic objects like iron oxide NPs significantly decrease T_2 . Magnetic field inhomogeneities, however, can have many different reasons. They can result from external sources and tissue inherent factors. External sources are mainly inhomogeneities of the static magnetic field which cannot properly be shimmed and magnetic objects, such as iron oxide NPs. However, local magnetic field gradients caused by differences in the magnetic susceptibility of adjacent tissues also decrease T_2 . Therefore, typically the total relaxation time T_2^* is defined as

$$\frac{1}{T_2^*} = \frac{1}{T_2} + \frac{\gamma \Delta B_0}{2} \quad (4.20)$$

where ΔB_0 is the variations of the magnetic field [15, 37].

Experimental

The relaxivities r_2 and r_2^* , and thus the performance of Fe_3O_4 NPs as MR contrast agents, were tested *in vitro* with MRI. PEG-nitroDOPA stabilized, oil bath synthesized Fe_3O_4 NPs, dispersed in Millipore water were embedded in a hydrogel to mimic their binding to tissue *in vivo*. Therefore, NPs were dispersed in Millipore water at a final Fe_3O_4 concentration of 20-100 $\mu\text{g/ml}$. A hydrogel was formed by radical initiated polymerization of methacrylates [360]. From a Millipore water based 100 mg/ml N,N^1 -methylene-bis-acrylamide (MBA) and ammonium persulfate (APS) stock solutions, 10 mg MBA and 5 mg APS were added to eppendorf containing Millipore water based Fe_3O_4 NP solutions. The total volume of Millipore water was 0.5 ml. The radical reaction was initiated by adding 7 μl N,N,N^1,N^1 -tetramethylethylenediamine (TMEDA). Eppendorfs containing NP loaded hydrogels were inserted into a 50 ml Falcon tube which was filled with Millipore water to avoid discontinuities of the permeability of the hydrogels at the interface of the eppendorf tubes which could cause artifacts in MRI and thus influence the measured relaxivities. As a comparison, PEG-nitroDOPA stabilized in the oil bath synthesized NPs dispersed in PBS were analyzed.

MRI on in hydrogels embedded NPs was measured on a 4.7 T Bruker instrument using a volume resonator coil with a diameter of 31 mm. A field of view of 3.5 cm \times 4.0 cm was imaged. The repetition time was 5000 ms where spins were flipped 90° with an echo spacing of 6 ms. 16 echos were measured per repetition. r_2^* measurements as a function of the PEG molecular weight were performed on 3 independent identical samples at room temperature.

The MRI experiments performed on PBS based PEG-nitroDOPA stabilized in the oil bath synthesized NPs dispersions were conducted on a Bruker Minispec mq60 (1.41 T) NMR analyzer at 20 °C. Longitudinal relaxation rates r_1 were obtained using an inversion recovery sequence with four averages. The inversion recovery sequence consists of a 180° pulses where spins aligned in the +z direction are flipped into the -z direction. After the inversion time τ , a 90° pulse is applied which rotates spins in the xy-plane. After the recovery delay (RD), the pulse sequence is repeated (Figure 4.6). T_1 is measured by varying τ [361]. Here, ten different inversion times ranging from 5 ms to at least $5 \times T_1$, where more than 98.5% of all the spins of the solution are re-aligned along the +z axis, were used. The 180° pulse was 4.4 ms whereas the 90° pulse was 2.2 ms. The relaxation delay was at least $5 \times T_1$ of the solution. T_1 was determined by fitting the data points to equation 4.18.

Transversal relaxation rates r_2 were obtained using a Carr-Purcell-Meiboom-Gill (CPMG) sequence with 16 averages. The CPMG sequence consists of a 90° pulse which flips spins originally aligned in the +z direction into the xy plane. The 90° pulse is followed by multiple 180° pulses (Figure 4.7). Spins aligned in the xy plane precess with a frequency determined by the local magnetic field. This gives rise to a free induction decay T_2^* . After a delay τ , spins are flipped 180° in the xy plane which changes the phase of the spins. They thus start to refocus which yields in an echo at the echo time $T_E = 2\tau$. Thus, this sequence is called a spin echo sequence. If multiple 180° pulses are applied, the amplitude of the echoes decays. This decay is solely determined by T_2 because static magnetic field inhomogeneities cancel if this pulse sequence is measured [361]. In measurements presented here, the 90° pulse was 2.2 ms, the 180° pulses were 4.4 ms. The relaxation delay was at least $5 \times T_1$ of the solution, the time interval τ between the 90° and 180° was 1 ms. Depending on T_2 of the iron oxide NP dispersions, between 512 and 2048 points were acquired. T_2 was determined by fitting the data points to equation 4.19.

4.3.3 Specific Absorption Rate (SAR) Determination

If NPs are subjected to an AMF, their spins follow the magnetic field by flipping 180° if the frequency of the magnetic field is below or in the range of the relaxation time of spins. As described in the background, spins can follow the AMF by Brownian or Néels relaxation [15]. The power P which is dissipated from these relaxations can be described as

$$P = f\Delta U = \mu_0\pi\chi''fH_0^2, \quad (4.21)$$

where f is the frequency, ΔU the difference in the internal energy, χ'' the imaginary part of the magnetic susceptibility and H_0 the magnetic field.

χ is defined as

$$\chi = \frac{\omega\tau}{1 + (\omega\tau)^2}\chi_0 \quad (4.22)$$

where $\omega = 2\pi f$ and τ is the relaxation time.

The ratio of power dissipated by Brownian and Néels relaxation respectively depends on the relaxation times τ_B and τ_N defined in equations 1.2 and 1.3 [15, 38, 133]. The total relaxation time τ of a NP is defined as [100, 133]

$$\frac{1}{\tau} = \frac{1}{\tau_B} + \frac{1}{\tau_N}. \quad (4.23)$$

The effectiveness of NPs to dissipate power and thus generate heat if subjected to an AMF can be described with the specific absorption rate (SAR). It is defined as [100]

$$SAR = C_e \frac{\Delta T}{\Delta t} = 4.1868 \pi \mu_0^2 \frac{\phi M_s^2 V}{1000 k_B T} H_0 f^2 \chi \quad (4.24)$$

where C_e is the specific heat capacity, ΔT the temperature difference caused by the absorption of electromagnetic radiation followed by its dissipation as heat within the measurement time. The SAR is typically measured in calories per kg which adds the numerical factor in the second expression in equation 4.24 to convert it into SI units [100].

If the heat capacity C_e is known, the SAR can be measured by monitoring the temperature increase (ΔT) as a function of the time Δt exposed to the AMF Δt using the first expression in equation 4.24. The SAR value can then be used to calculate the total relaxation time τ of the NPs. To distinguish Néels relaxation contributions from those contributions caused by Brownian relaxation, NPs can be embedded in a matrix such as agarose which prevents NP motion. The SAR of in this matrix embedded NPs therefore exclusively results from Néels relaxation and thus can be compared with the SAR determined from NPs dispersed in solution where they can freely rotate. In the latter case, Néels and Brownian relaxation contribute to the total relaxation time [362–364].

Experimental

SAR values presented in this work were measured on iron oxide NPs synthesized in the oil bath for 24 h at 150 °C, 165 °C and 180 °C respectively. They were stabilized with PEG(5)-nitroDOPA. SAR values were measured for magnetic fields H 16.56 kA/m $< H$ < 51.56 kA/m and at frequencies 2.32×10^5 Hz $< f$ $< 2.39 \times 10^5$ Hz. The SAR was calculated according to equation 4.24.

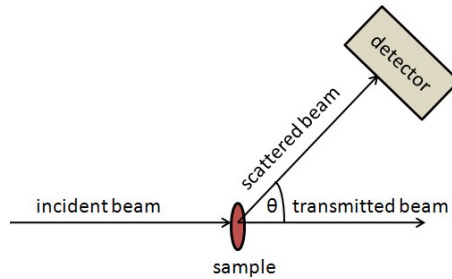


Figure 4.8: Principle of scattering techniques. An incident beam is scattered by a sample. The scattered beam is detected at an angle Θ relative to the transmitted beam.

4.4 Analysis of Core-Shell Nanoparticles

4.4.1 Scattering Techniques

The basic principle of all scattering techniques is a monochromatic beam which is scattered by the sample. The intensity of the scattered radiation is measured as a function of the angle Θ as defined in Figure 4.8. The most important variable for scattering experiments is the wave vector \vec{q} defined as

$$\vec{q} = \frac{4\pi \sin(\frac{\Theta}{2})}{\lambda} \quad (4.25)$$

where λ is the wavelength of the radiation source [365].

Dynamic Light Scattering (DLS)

Dynamic light scattering (DLS) is also known as photon correlation spectroscopy (PCS). It is an experimentally easy technique that does not require large facilities such as neutron or X-ray sources and is readily available in many labs. It is most suited to probe structures > 10 nm. A laser illuminates a defined sample volume. Laser light is scattered by objects such as NPs because of differences in the refractive index between objects under investigation and the solvent.

In DLS, the scattering interference pattern $I(t)$ measured at time t is correlated with that taken at $t + \tau$. The correlation coefficient $G(\tau)$ defined by

$$G(\tau) = \int_0^{\infty} I(t)I(t+\tau) dt \quad (4.26)$$

equals 1 if the scattering patterns are identical and 0 if there is no correlation between the two scattering patterns [366]. Because the scattering pattern changes when NPs move, $G(\tau)$ decays faster the faster NPs move. Thus, the diffusion coefficient D_{diff} of NPs can be obtained by fitting $G(\tau)$. One often used method to fit $G(\tau)$ is the cumulant analysis (equation 4.27), which assumes that scattering objects are optically isotropic and small compared to the wavelength of the incoming light [367]

$$G(\tau) = A(1 + Be^{(-2\Gamma\tau + \mu_2\tau^2)}) \quad (4.27)$$

where

$$\Gamma = D_{\text{diff}}q^2 \quad (4.28)$$

\vec{q} is defined in equation 4.25 and D is the diffusion coefficient. A , B , Γ and μ_2 are fitting parameters. According to the Stokes Einstein equation 4.29, the diffusion coefficient can be translated into a hydrodynamic radius R_H , assuming NPs are spherical, have a uniform density and a smooth surface [366].

$$R_H = \frac{k_B T}{6\pi\eta D_{\text{diff}}} \quad (4.29)$$

where η is the viscosity of liquid. The polydispersity index (PDI) can be calculated according to

$$PDI = \frac{\mu_2}{\Gamma^2}. \quad (4.30)$$

The resulting hydrodynamic radius is intensity weighted. Because intensity weighted averages scale with r^6 , DLS is very sensitive to large objects. If the refractive index is known, intensity weighted averages can be converted into volume weighted averages (which scale with r^3) using the Mie theory [368, 369]. However, this conversion is strictly only applicable for spherical particles which have a homogeneous density. This is not the case for core-shell NPs [370, 371].

Large objects mainly scatter in forward direction. Thus, if backward scattering is correlated, DLS measurements are less sensitive to dust. However, forward scattering is more sensitive to the onset of NP agglomeration. Thus, if forward and backward scattering is

measured with DLS, NP size and the onset of agglomeration can be quantified more reliably than if only one scattering direction is evaluated.

As can be seen from equations 4.27 and 4.29, DLS measures the diffusion coefficient and not the particle radius. Thus, if DLS is measured on concentrated samples, where NPs interact with each other, their size determination becomes inaccurate. If particles attract each other, the measured diffusion coefficient decreases with increasing NP concentration. Thus, the particle radius is overestimated. If, however, particles are repulsive, they diffuse faster than NPs which do not interact with each other. Consequently, their size is overestimated [366, 371].

Furthermore, if DLS is measured on concentrated samples, multiple scattering influences the interference pattern. This affects the correlation function and leads to an underestimation of the NP size [366]. Therefore, DLS should be measured on diluted samples where electrostatic particle interactions are screened with salts.

Experimental

DLS measurements of NPs shown here were performed on Tris and HEPES based NP dispersions. Both solutions were buffered to pH = 7.4 and contained 160 mM NaCl. NP dispersions were filtered with 200 nm cut-off Minisart syringe filters (Sartorius, Germany) prior to the measurements. The NP concentration was varied between 50 and 100 $\mu\text{g/ml}$. In this concentration range, DLS results were independent of the NP concentration. Too low NP concentrations lead to poor correlation functions whereas too high NP concentrations lead to multiple scattering. Unless stated otherwise, measurements were performed in the backscattering mode (scattering angle = 173°) using a Zetasizer NS (Malvern, UK). To check reproducibility, each measurement was repeated three times on the same sample. 5-10 independent identical samples were analyzed with this method.

For temperature dependent measurements, samples were equilibrated for 10 min at the desired temperature prior to the measurement. Temperature was increased from 25°C to 90°C in 5°C steps.

To investigate long-term stability, NP dispersions were kept in covered plastic cuvettes and their size was measured weekly with DLS. However, despite that plastic cuvettes were covered, water evaporation over a period of 1-2 months could not be completely avoided. Therefore, Millipore water was regularly added to the samples to keep the total sample volume constant at 1 ml.

To check dispersant adsorption reversibility, NPs were either dialyzed against Millipore

water or subjected to multiple centrifugation filtration steps. If the dispersant binding reversibility was checked with dialysis, the hydrodynamic radius of stabilized iron oxide NPs was checked daily during the first week of dialysis and subsequently weekly with DLS. However, it was found that dialysis does not efficiently remove excessive dispersants. NPs were stable for more than one month even if the anchor bound reversibly to iron oxide NP surfaces. Therefore, dispersant binding reversibility was additionally tested with more stringent centrifugation filtration experiments. HEPES based 100 $\mu\text{g/ml}$ NP dispersions were centrifuge filtered using 100 kDa cut-off filters (Millipore Microcon filters, Millipore, MA). NPs were re-dispersed in 1 ml HEPES, equilibrated for 24 h before their hydrodynamic radius was measured with DLS. This was repeated on 10 subsequent days. Fe_3O_4 NPs stabilized with reversibly adsorbing dispersants were investigated until the count rate was below 10 % of the initial count rate.

Because intensity weighted diameters scale with r^6 and thus large particles predominate the scattering pattern, volume weighted size distributions which scale with r^3 [368] are shown even though the conversion of intensity to volume weighted averages assumes a homogeneous object, a requirement which is not fulfilled for core-shell NPs. However, the average hydrodynamic radius was calculated using the cumulant analysis (equation 4.27) which results in intensity weighted hydrodynamic radii. The difference between intensity and volume weighted average radii is indicative of the polydispersity of the NPs.

Liposomes dispersed in PBS or Millipore water respectively were analyzed at a concentration of 50 $\mu\text{g/ml}$ without that they were filtered prior to DLS analysis. Data were analyzed using the multiple narrow modes evaluation incorporated into the Malvern software.

Small Angle X-ray Scattering (SAXS)

In contrast to DLS, where scattering is caused by differences in the refractive index, X-rays are scattered by electrons and thus sensitive to changes in the electron density. The upper limit of λ of X-rays useful for SAXS studies is about 0.2 nm because X-rays with larger λ are strongly absorbed by the sample. Therefore, the optimum size range, where features can be probed with SAXS is between 1 nm and 1 μm . Thus, SAXS is an excellent technique to investigate *e.g.* NP cores consisting of high atomic number elements [365]. The scattering intensity $I(\vec{q})$ is defined as

$$I(\vec{q}) = (\rho_p - \rho_m)^2 N_p V_p F(\vec{q}) S(\vec{q}) \quad (4.31)$$

where ρ_p and ρ_m are the scattering densities of the particle and matrix (solvent) respectively, N_p is the number of particles, V_p the particle volume, $F(\vec{q})$ the particle form factor and $S(\vec{q})$ the structure factor. $F(\vec{q})$ depends on the NP size, size distribution and shape. If NPs interact with each other $S(\vec{q}) \neq 1$. $S(\vec{q})$, which is an oscillatory function, therefore can provide information on the particle arrangement of concentrated dispersions. $S(\vec{q}) = 1$ for diluted dispersions where NPs do not interact with each other. Thus, to determine the form factor $F(\vec{q})$, NPs should be evaluated under dilute conditions where scattering contributions from the structure factor can be neglected [365].

SAXS requires a monodisperse, high intensity source. While SAXS instruments with regular X-ray sources are available in some of the labs [372], SAXS experiments are often performed at synchrotron sources. If SAXS is performed at a synchrotron source, it offers a spacial and temporal resolution in the nm and ms range respectively [373, 374]. Even though typical SAXS measurements on colloids are very fast if performed at the synchrotron, in stark contrast to SAXS measurements performed on laboratory scale SAXS instruments, it is difficult to get access to beamtime at synchrotron. Thus, these measurements, although very valuable in their scientific content, are not generally accessible.

Experimental

SAXS measurements shown here were performed on a Anton-Paar SAXSess diffractometer with a line focus sealed Cu tube (PANalytical PW3830) using a pin hole geometry and a ^3He gas detector. Data were fitted with the sasfit software (J. Kohlbrecher, PSI, Switzerland) assuming a lognormal size distribution. PEG-nitroDOPA stabilized 2.5 nm and 5 nm core radius NPs synthesized in the oil bath and Fe_3O_4 NPs heated for 3 min in the MW were analyzed. Because the SAXS scattering contrast of iron oxide is many times higher compared to that of the PEG shell, only cores contribute to SAXS scattering. Thus, unless stated otherwise, PEG(5)-nitroDOPA stabilized 2.5 and 5 nm core radius NPs were analyzed. To check for structure factor contributions different NP concentrations, namely 0.1, 0.05 and 0.01 vol% NPs for 2.5 nm core radius NPs and 2.5, 0.5, 0.1 and 0.02 vol% for 5 nm core radius NPs (calculated based on the hydrodynamic radius), were measured. Samples were measured for 12 h.

Small Angle Neutron Scattering (SANS)

Features like size, size distribution and spacial correlation of structures in the range of 1 nm to 150 nm can be analyzed with SANS where neutrons typically have a wavelength between 0.1 and 2 nm. However, in contrast to X-rays, neutrons are scattered by protons rather than electrons. Therefore, SANS is independent on the atomic number and thus better suited for the analysis of light elements and to investigate structures which consist of different elements with similar atomic numbers.

Isotopes such as 2D and 1H have different scattering cross sections. Neutron scattering contrast depends on the difference in the scattering cross sections of the sample and solvent. Therefore, the scattering contrast of samples can be adjusted *e.g.* by deuterating certain protons to enhance scattering contrast within the sample. Alternatively, the scattering contrast can be varied by adjusting the solvent (*e.g.* the ratio of $H_2O : D_2O$). Such, contrast variation experiments can be very valuable to investigate *e.g.* core-shell structures. By matching the cross-section of the core and shell independently (*e.g.* by using appropriate mixtures of $H_2O : D_2O$), scattering contributions of the core can be separated from scattering contributions of the shell [365]. This allows to quantify the core sizes, core size distribution, the shell thickness and the dispersant density profile of sterically stabilized, dispersed core-shell NPs.

Furthermore, in contrast to X-rays, neutrons also possess a magnetic moment which allows to not only investigate nuclear but also magnetic scattering. If an external magnet is applied, magnetic scattering depends on the spin state σ of the neutrons (*e.g.* whether neutron spins are aligned parallel or antiparallel to the external magnetic field). The scattering intensity is proportional to $(F_{nuc} \pm F_{mag})^2$ where F_{nuc} and F_{mag} are the nuclear and magnetic form factors respectively.

If polarized neutrons are used, they can be aligned either parallel or antiparallel to the external magnetic field. The form factors can then be described as $(F_{nuc} + F_{mag})$ and $(F_{nuc} - F_{mag})$ respectively. Thus, if SANS data are acquired with both spin polarizations, they can be subtracted. The resulting cross term defined in equation 4.32 might reveal information on magnetic scattering contributions which cannot be assessed otherwise. Depending on the sample, magnetic scattering contributions are much weaker than nuclear scattering contributions. Thus, weak magnetic scattering contributions might only surface in the crossterm of with polarized neutrons measured SANS data.

$$\frac{d\sigma_-}{d\Omega}(\vec{q}) - \frac{d\sigma_+}{d\Omega}(\vec{q}) = 4\tilde{F}_{mag}(\vec{q})F_{nuc}(\vec{q})\sin(\varepsilon)^2S(\vec{q}) \quad (4.32)$$

$F_{mag}(\vec{q})$ and $F_{nuc}(\vec{q})$ are the magnetic and nuclear form factors respectively, $\frac{d\sigma_-}{d\Omega}(\vec{q})$ and $\frac{d\sigma_+}{d\Omega}(\vec{q})$ the cross sections for samples measured with neutron spins aligned antiparallel and parallel to the external static magnetic field respectively and ε the azimuthal scattering angle. As can be seen in equation 4.32 the crossterm has a characteristic $\sin(\varepsilon)^2$ dependence if the intensity of scattered neutrons are detected on a 2D detector [375]. However, SANS measurements can exclusively be performed at spallation sources. Because it is difficult to get beamtime at such large-scale facilities, only a limited amount of samples can be characterized with SANS. Thus, although very valuable information about core size, shell thickness, dispersant density profiles and magnetic properties of NPs can be obtained with SANS, it is not a technique with which samples routinely can be characterized.

Experimental

SANS measurements shown in this thesis were performed on SANS I at SINQ (PSI, Switzerland). Spectra of PEG-nitroDOPA stabilized iron oxide NPs were recorded at detector distances of 2 m, 6 m and 15 m where the neutron wavelength was 0.5 nm.

2.5 and 5 nm core radius Fe_3O_4 NPs synthesized in the oil bath and stabilized with PEG-nitroDOPA where the PEG molecular weight was ranged from 1.5 and 10 kDa were investigated. Alternatively, PEG(5)-nitroDOPA stabilized Fe_3O_4 NPs heated for 3 min in the MW were analyzed. The total volume percentage of 5 nm core radius NPs synthesized in the oil bath was kept constant at 5 vol% independent on the PEG molecular weight (resulting in a core volume fraction of concentration of 0.2, 0.3 and 0.6 vol% for PEG(10)-, PEG(5)- and PEG(1.5)-nitroDOPA respectively). Similarly, the total volume fraction of 2.5 nm core radius NPs synthesized in the oil bath and stabilized with PEG-nitroDOPA was kept constant at 5 vol%. Unless stated otherwise, SANS was measured on NPs dispersed in D_2O .

To distinguish magnetic objects from non-magnetic ones, some of the SANS measurements were performed with polarized neutrons. The sum of the SANS measurements performed with neutrons polarized parallel and antiparallel to the external magnetic field equals scattering patterns measured with unpolarized neutrons. The difference between these two spectra reveals the crossterm of the magnetic and nuclear scattering factor as defined in equation 4.32. Thus, while the difference pattern reveals information about the size and size distribution of Fe_3O_4 cores, the sum contains information about nuclear scattering of the cores and dispersants.

SANS measurements on liposomes were also performed at SANS-I at the Paul-Scherrer-Institute (PSI, Villigen, Switzerland). For SANS experiments, liposomes were extruded in D_2O . Samples were analyzed at a liposome concentration of 5 mg/ml, corresponding to 0.6 vol% liposomes assuming liposomes have a diameter of 76 nm at 25 °C. Data were acquired on a two dimensional 3He detector at distances of 2 m, 6 m and 15 m and a neutron wavelength of 0.5 nm. Additionally, the neutron wavelength was increased to 1.3 nm at 15 m detector distance covering a q -range of $0.02 \text{ nm}^{-1} < q^{-1} < 3 \text{ nm}^{-1}$.

SANS Data Analysis

After correcting the data for background, empty cell scattering and detector efficiency, data obtained with unpolarized neutrons and the sum of the spectra acquired with neutrons polarized parallel and antiparallel to the magnetic field were radially averaged. The difference spectra of the SANS data acquired with polarized neutrons were averaged using the $\sin(\varepsilon)^2$ dependence of the isotropic scattering pattern. For form factor which allowed it, the sum and difference SANS spectra acquired with polarized neutrons were fitted simultaneously. With this procedure, it was tried to extract information about the dispersant packing density, shell thickness and dispersant density profile.

Form Factor for Iron Oxide Nanoparticles

The sum spectra of SANS data acquired with polarized neutrons were fitted with form factors which assume a core-shell structure. The dispersant density profile is assumed to decay differently, namely exponentially, according to a Gauss curve where the mean was translated such that it coincided with the NP surface and with a step-function decay profile. The dispersants are assumed to undergo a self avoiding walk.

Gaussian Dispersant Density Profile

Assuming a core-shell model, where the dispersant density profile decays with a Gaussian profile, the scattering intensity $I_{\text{Gauss}}(q)$ is fitted as [376–378]

$$I_{\text{Gauss}}(q) = n_{\text{agg}}^2 \rho_c^2 F_c^2(q, r) + n_{\text{agg}}^2 \rho_s^2 F_s^2(q, R_G) + n_{\text{agg}}(1 - n_{\text{agg}}) \rho_s^2 F_{ss}^2(q) + 2n_{\text{agg}}^2 \rho_c \rho_s F_{cs}^2(q) \quad (4.33)$$

with

$$F_c(q, r) = 3 \frac{\sin(qr) - qr \cos(qr)}{(qr)^3} \quad (4.34)$$

$$F_s(q, R_G) = \sqrt{2 \frac{e^{-R_G^2 q^2} - 1 + R_G^2 q^2}{R_G^4 q^4}} \quad (4.35)$$

$$F_{ss}(q) = \Psi(q, R_G) \frac{\sin(q(r + R_G))}{q(r + R_G)} \quad (4.36)$$

$$F_{cs}(q) = \sqrt{\Psi(q, R_G) \Phi(q, R_G) \frac{\sin(q(r + R_G))}{q(r + R_G)}} \quad (4.37)$$

$$\Psi(q, R_G) = \frac{1 - e^{-q^2 R_G^2}}{q^2 R_G^2}. \quad (4.38)$$

n_{agg} is the dispersant packing density, q the scattering vector, r the radius of the NP core, R_G the radius of gyration of the dispersant, ρ_s and ρ_c the scattering length of the shell and core respectively. The latter are defined as $V_s (v_{\text{shell}} - v_{\text{solvent}})$ and $V_c (v_{\text{core}} - v_{\text{solvent}})$ respectively, where V_s and V_c is the volume of the shell and core, v the scattering length density.

Step-function Dispersant Density Profile

If a step-function density profile $\Phi(l)_{\text{brush}}$ according to de Gennes is assumed it can be described as

$$\Phi(r) = \begin{cases} \Phi(l)_{\text{core}} & \text{for } 0 < l < r \\ n_{\text{agg}} & \text{for } r < l < r + d \\ 0 & \text{for } l > r + d \end{cases} \quad (4.39)$$

The scattering intensity $I(q)$ can, in general for exponentially decaying density profiles, be described as

$$I(q) = n_{\text{agg}}^2 \rho_c^2 F_c^2(q, r) + n_{\text{agg}}^2 \rho_s^2 F_s^2(q, R_G) + n_{\text{agg}} (1 - n_{\text{agg}}) \rho_s^2 F_s^2(q) + 2n_{\text{agg}}^2 \rho_c \rho_s F_c(q) F_s(q). \quad (4.40)$$

The form factor of the core can be described with equation 4.34 identical to the Gaussian profile. The form factor for the shell is given by [378]

$$F_s(q, r, t) = \frac{1}{C_{\text{norm}}} \int_r^{r+d} 2\Pi r^2 r^{-\alpha} \frac{\sin(qr)}{qr} dr \quad (4.41)$$

with

$$C_{\text{norm}} = \begin{cases} \frac{4}{3-\alpha} \Pi \left((r+d)^{3-\alpha} - r^{3-\alpha} \right) & \text{for } \alpha \neq 2 \\ 4\Pi \ln \left(\frac{r+d}{r} \right) & \text{for } \alpha = 2 \end{cases} \quad (4.42)$$

For the de Gennes model $\alpha = 0$.

Exponential Dispersant Density Profile

If an exponential decay of the dispersant density profile is assumed, the density profile $\Phi(l)$ as a function of the distance from the core center l can be described as

$$\Phi(l) = \begin{cases} \Phi(l)_{\text{core}} & \text{for } 0 < l < r \\ \Phi_{\text{shell}} \left(\frac{l-r}{D} \right) & \text{for } r < l < r+d \\ 0 & \text{for } l > r+d \end{cases} \quad (4.43)$$

with

$$\Phi_{\text{shell}}(x) = \begin{cases} (1 - \Theta) (V_s v_s - \rho_s x e^{|1-x|\alpha}) & \text{for } \alpha < 0 \\ (1 - \Theta) \rho_s (1-x) e^{-x\alpha} & \text{for } \alpha \geq 0 \end{cases} \quad (4.44)$$

Θ is the percentage of solvent adsorbed on the NP surface.

The scattering intensity is given by [378]

$$I_{\text{exp}}(q) = \int_0^{\infty} 4\pi r^2 \frac{\sin(qr)}{qr} \Phi_{\text{shell}}(r) dr. \quad (4.45)$$

Structure Factor for Iron Oxide Nanoparticles

If the NP concentration is high such that NPs start to interact with each other, contributions from the resulting structure factor $S(q)$ need to be taken into account. In this thesis it was done by multiplying the size averaged form factor with the structure factor [378]

$$I(q) = \langle F^2 \rangle(q) S(q) \quad (4.46)$$

Hard Spheres

The potential of the structure factor that assumes hard sphere interactions can be described with [378]

$$U(l) = \begin{cases} \infty & \text{for } 0 < l < \sigma \\ 0 & \text{for } l > \sigma \end{cases} \quad (4.47)$$

σ is the hard sphere radius and l the distance from the core center. The structure factor for hard spheres $S_{\text{HS}}(q)$ is defined as [378]

$$S_{\text{HS}}(q, \sigma, f_p) = \frac{1}{1 + 24f_p \frac{G(\sigma, f_p)}{\sigma q}} \quad (4.48)$$

with

$$G(\sigma, f_p) = \alpha \frac{\sin(A) - A \cos(A)}{A^2} + \frac{\gamma [-4A^4 \cos(A) + 4[(3A^2 - 6) \cos(A) + (3A - 6) \sin(A) + 6]]}{A^5} \quad (4.49)$$

$$A = 2\sigma q \quad (4.50)$$

$$\alpha = \frac{(1+2f_p)^2}{(1-f_p)^4} \quad (4.51)$$

$$\beta = -6f_p \frac{\left(1 + \frac{f_p}{2}\right)^2}{(1-f_p)^4} \quad (4.52)$$

$$\gamma = \frac{\alpha f_p}{2} \quad (4.53)$$

f_p is the volume fraction of NPs in solution.

Hard Sticky Spheres

The hard sticky sphere structure factor has a potential of [378]

$$U(l) = \begin{cases} \infty & \text{for } 0 < l < \sigma \\ \ln\left(\frac{12\tau\Delta}{\sigma+\Delta}\right) & \text{for } \sigma < l < \sigma + \Delta \\ 0 & \text{for } l > \sigma + \Delta \end{cases} \quad (4.54)$$

It can be calculated by approaching Δ to 0.

The structure factor $S_{\text{HSS}}(q, \sigma, f_p, \tau)$ is defined as [378]

$$S_{\text{HSS}}(q, \sigma, f_p, \tau) = \frac{1}{1-C(q)} \quad (4.55)$$

with

$$\begin{aligned} C(q) = & 2\frac{v\lambda}{\kappa} \sin(\kappa) - 2\frac{v^2\lambda^2}{\kappa^2} (1 - \cos(\kappa)) - \\ & [\alpha\kappa^3 (\sin(\kappa) \kappa \cos(\kappa)) + \beta\kappa^3 (2\kappa \sin(\kappa) - (\kappa^2 - 2) \cos(\kappa) - 2) + \\ & \frac{v\alpha}{2} ((4\kappa^3 - 24\kappa) \sin(\kappa) - (\kappa^4 - 12\kappa^2 + 24) \cos(\kappa) + 24)] 24 \frac{v}{\kappa^3} \end{aligned} \quad (4.56)$$

$$\alpha = \frac{(1+2v-\mu)^2}{(1-v)^4} \quad (4.57)$$

$$\beta = -\frac{3\nu(2+\nu)^3 - 2\mu(1+7\nu+\nu^2) + \mu^2(2+\nu)}{2(1-\nu)^4} \quad (4.58)$$

$$\mu = \lambda\nu(1-\nu) \quad (4.59)$$

$$\lambda = \frac{6}{\nu} \left(\varepsilon - \sqrt{\varepsilon^2 - \gamma} \right) \quad (4.60)$$

$$\varepsilon = \tau + \frac{\nu}{1-\nu} \quad (4.61)$$

$$\gamma = f_p \frac{1 + \frac{\nu}{2}}{3(1-\nu)^2} \quad (4.62)$$

$$\nu = f_p \left(\frac{2\sigma + \Delta}{2\sigma} \right)^3 \quad (4.63)$$

$$\kappa = 2q\sigma \quad (4.64)$$

τ is the stickiness parameter that describes the affinity of two adjacent NPs.

A contribution from the hard sticky sphere structure factor was included in fits where a broad NP core size distribution was assumed (Figure 8.15).

Dispersant Packing Density

The dispersant packing density which results from fits obtained using an exponential dispersant density profile (section 4.4.1) can be calculated using

$$4\Pi \int_r^{r+d} r^2 \Phi(r) dr = 4\Pi r^2 n_{\text{agg}} V_{\text{molecule}} \quad (4.65)$$

where $\Phi(r)$ is defined similar to equation 4.43 as

$$\Phi(l) = \begin{cases} 1 - \frac{l-r}{d} e^{(1-\frac{l-r}{d})\alpha} & \text{for } \alpha < 0 \\ \left(1 - \frac{l-r}{d}\right) e^{-\frac{l-r}{d}\alpha} & \text{for } \alpha \geq 0 \end{cases} \quad (4.66)$$

d the shell thickness and V_{molecule} is the molecular volume. The latter was calculated assuming a cylindrical shape of a ethylene glycol (EG) repeat unit ($r.u.$) with a C-C, C-H and C-O bond length of 0.133 nm, 0.110 nm and 0.143 nm [379] and an angle between the different $r.u.$ of 109° . This yielded a cylinder radius $r_{r.u.}$ of 0.149 nm and a height $h_{r.u.}$ of 0.431 nm. Hence, the volume of a molecule was calculated

$$V_{\text{molecule}} = \Pi r_{r.u.}^2 h_{r.u.} N \quad (4.67)$$

where N is the number of repeat units.

Assuming a lognormal core size distribution, equation 4.65 can be re-written as

$$\int_0^\infty \left(\int_r^{r+d} l^2 \Phi(l) dl \right) \frac{1}{r} e^{-\frac{\ln(\frac{r}{\bar{r}})^2}{2\sigma^2}} dr = n_{\text{agg}} N \alpha^3 \int_0^\infty e^{-\frac{\ln(\frac{r}{\bar{r}})^2}{2\sigma^2}} r dr. \quad (4.68)$$

This equation can be solved analytically. For $\alpha < 0$, n_{agg} is

$$n_{\text{agg}} = \frac{d e^{-\frac{9s^2}{2}}}{3\alpha^4 r^3 V_{\text{molecule}}} (d^2 (\alpha(18 + \alpha(9 + \alpha(3 + \alpha)))) - 18(-1 + e^\alpha)) + 3\alpha d e^{\frac{s^2}{2}} (4 + \alpha(4 + \alpha(2 + \alpha)) - 4e^\alpha) r + 3\alpha^2 e^{2s^2} (1 + \alpha + \alpha^2 - e^\alpha) r^2. \quad (4.69)$$

where d (shell thickness) and α (decay rate of the dispersant density profile) are fitting parameters.

For $\alpha \geq 0$, n_{agg} is

$$n_{\text{agg}} = \frac{d e^{-\alpha - \frac{9s^2}{2}}}{\alpha^4 r^3 V_{\text{molecule}}} (d^2 (6 + 4\alpha + \alpha^2 + 2(-3 + \alpha)e^\alpha) + 2\alpha d e^{\frac{s^2}{2}} (2 + \alpha + (-1 + \alpha)e^\alpha) r + \alpha^2 e^{2s^2} (1 + (-1 + \alpha)e^\alpha) r^2). \quad (4.70)$$

Liposomes

Data measured on liposomes were analyzed by combining a form factor for vesicles and one that describes scattering of a core-shell NP. To account for the agglomeration of DSPC

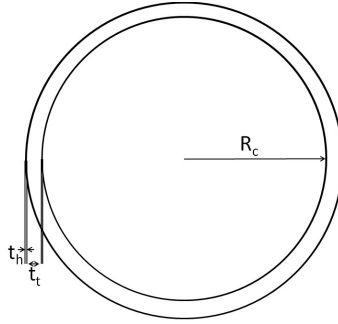


Figure 4.9: Definition of the vesicle dimensions of the SANS form factor. The definition of the thickness of the head group t_h , the tail length t_t of the bilayer and the vesicle core radius R_c which are used to calculate the vesicle form factor used to fit SANS data.

liposomes measured at RT, a constantly increasing background with a slope of -3.5 was assumed. Furthermore, a contribution from the structure factor for hard sticky spheres was added.

The scattering intensity of a vesicle was described with equation 4.71

$$I_{\text{vesicle}} = (K(q, R_c, \eta_{\text{solv}} - \eta_t) + K(q, R_c + t_t, \eta_t - \eta_h) + K(q, R_c + t_t + t_h, \eta_h - \eta_t) + K(q, R_c + 2t_t + t_h, \eta_t - \eta_{\text{solv}}))^2 \quad (4.71)$$

where

$$K(q, R, \Delta\eta) = \frac{4}{3} \pi r^3 \Delta\nu_3 \frac{\sin(qR) - qR \cos(qR)}{(qr)^3} \quad (4.72)$$

q is the scattering vector, r the inner radius of the liposome, t_t the head group thickness and t_h the thickness of the hydrophobic region of the bilayer as defined in Figure 4.9 and η is the scattering length density.

Scattering from core-shell NPs was fitted using [378]

$$I_{\text{core}}(q, R_c, \Delta\eta) = K^2(q, R_c, \Delta\eta) \quad (4.73)$$

and

$$I_{\text{shell}}(q, R_c, \Delta R, \Delta\eta_1, \Delta\eta_2) = [K(q, R_c + \Delta R, \Delta\eta_2) - K(q, R_c, \Delta\eta_2 - \Delta\eta_1)]^2. \quad (4.74)$$

SANS data acquired on PEGylated liposomes were fitted using an extended form factor from equation 4.71 where additional polymers were assumed to surround the vesicle bilayer.

4.4.2 Thermogravimetric Analysis (TGA)

One possibility to quantify the amount of dispersants adsorbed on NPs is TGA. Organic dispersants are typically thermally degraded to volatile products between 200 and 500 °C. The resulting weight loss is measured as a function of the temperature and can be used to quantify the weight percentage of organic compounds on oxide NPs [380]. The volatile decomposition products can further be analyzed *in situ* by connecting the TGA to a MS or FTIR. This technique is especially valuable because it does not rely on model assumptions. However, care must be exercised that free dispersants are completely removed before these NPs are analyzed. Furthermore, to determine the packing density of dispersants on stabilized NPs, not only impurities and non-adsorbed dispersants need to be thoroughly removed but also particle agglomerates.

Experimental

To quantify the amount of dispersants on the NP surface, 1-3 mg stabilized iron oxide NPs were analyzed per run on a NETZSCH STA 449 C Jupiter, which for some experiments was coupled to a NETZSCH QMS 403 Aeolos MS (NETZSCH Geraetebau GmbH, Austria). Samples were heated from 35°C to 600 °C at 10 °C/min using a flow rate of 47.4 sccm Ar and 12.6 sccm O_2 where TGA and DSC spectra were recorded simultaneously. TGA analysis of liposomes containing iron oxide NPs was performed on a TA Q500 instrument (TA instruments). Millipore based liposome solutions, extruded at a lipid concentration of 5 mg/ml where the liposome concentration was increased by partially evaporating water under a constant N_2 flow were analyzed. 50 μ l liposome dispersions were analyzed at a time. Water was evaporated *in situ* at 50 °C before the sample was heated at 20 °C/min to 600 °C in a N_2 atmosphere. Statistics was done on 2-4 independent identical samples.

4.4.3 Differential Scanning Calorimetry Analysis (DSC)

Differential scanning calorimetry measures the difference in heat flow needed to heat the sample and reference at the same rate. If the sample undergoes an exothermic reaction, less external heat is required to maintain a constant heating rate of the sample compared to a reference sample which does not undergo any reaction in this temperature range. Endothermic reactions in the sample require more external heat to keep the heating rate constant. If DSC is measured simultaneously with TGA, mass losses measured in TGA can be assigned to endo- or exothermic reactions. Thus DSC helps to assign mass changes measured with TGA to chemical reactions. Furthermore, phase transformations and re-crystallization processes often cannot be detected with TGA whereas they often can clearly be seen with DSC. Thus, while TGA reveals information about mass changes involved in phase transformations and/or thermal degradations, DSC provides information about the amount of energy involved in such reactions and phase transformations [381].

Experimental

DSC of liposomes was measured on a Perkin Elmer instrument (Perkin Elmer). The same Millipore water based liposome solutions as analyzed with TGA were used to measure DSC. Samples were analyzed from 25 °C to 80°C before they were cooled to 25 °C using a heating and cooling rate of 10 °C/min. This temperature cycle was repeated twice. 40 μ l liposome solution was analyzed at the time. Statistics was done on 2-6 independent identical samples.

4.4.4 Quartz Crystal Microbalance with Dissipation Monitoring (QCM-D)

QCM-D is a label-free *in situ* biosensing technique which provides real time quantitative information on mass adsorbed on a QCM-D crystal as well as the viscoelasticity of the adsorbed layers [382]. Adsorption of molecules induce changes in the resonance frequency Δf of the quartz crystal oscillating freely in shear thickness mode. Δf can be translated into the adsorbed masses Δm using the Sauerbrey equation for homogeneous thin films without losses [383]

$$\Delta m = \frac{C}{n} \Delta f \quad (4.75)$$

where $C = 17.7 \text{ ng}/(\text{cm}^2 \text{ n})$ and n is the overtone of the resonance frequency or by applying theoretical models which account for limitations of the Sauerbrey equation such as losses due to viscoelasticity [384] or hydrodynamics [385]. Simultaneously to monitoring changes in frequency, the decay rate of the amplitude of the quartz crystal after the excitation voltage is turned off is measured. The decay time constant is inversely proportional to the energy dissipation. Changes in the dissipation ΔD are recorded to obtain information on the viscoelasticity of the adsorbed layer. Whereas rigid, dense layers such as supported lipid bilayers (SLBs) result in small ΔD values [386, 387], the adsorption of proteins or NPs can cause large increases in ΔD . Thus QCM-D allows to *in situ* observe how *e.g.* targeted NPs bind to specific surfaces and might therefore be used as a tool to measure binding kinetics and specificity of functionalized NPs towards protein surfaces or cell membrane mimics.

Experimental

To measure the binding kinetics of biotinylated NPs synthesized by the aqueous precipitation method and stabilized with PEG-gallol, QCM-D studies were performed at room temperature in HEPES containing 160 mM NaCl under static conditions. To form an anti-VCAM presenting surface, 400 ng/cm² protein A was adsorbed on SiO₂-coated QCM-D crystals followed by the addition of 5 μg/ml recombinant human VCAM-1 chimera before 100 μg/ml anti-VCAM-1 antibody functionalized NPs were injected. Between every step, the system was rinsed with buffer. For control experiments, recombinant human VCAM-1 chimera was exchanged by Fc-tagged E-cadherins. Alternatively, neutravidin coated NPs were functionalized with biotinylated anti-human E-selectin antibodies instead of biotinylated anti-human VCAM-1 antibodies. A concentration of 100 μg/ml NPs was used. For control experiments with human serum, the latter was immobilized on Au-coated QCM-D crystals before functionalized NPs were injected into the QCM-D chamber.

Binding kinetics of biotinylated NPs synthesized by non-aqueous sol-gel routes was tested by forming a supported lipid bilayer (SLB) from 100 μg/ml 50 nm radius extruded POPC vesicles containing 3 mol% biotin-PE vesicles [386, 387]. After 50 μg/ml neutravidin was injected into the QCM-D chamber, the neutravidin presenting surface was rinsed

with 1 ml Tris at a flow rate of 50 $\mu\text{l}/\text{min}$ to remove excessive neutravidin. In the following, binding of 100 $\mu\text{g}/\text{ml}$ NPs dispersed in HEPES buffer containing 160 mM NaCl was monitored.

To test binding kinetics of NPs functionalized with HSP60 antibodies, where functionalization was done through the biotin-neutravidin linkage, 5 $\mu\text{g}/\text{ml}$ HSP60 receptor was immobilized on SiO_2 QCM-D crystals before the surface was back-filled with 100 $\mu\text{g}/\text{ml}$ PLL-g(3.5)-PEG(2). To these surfaces, 50 $\mu\text{g}/\text{ml}$ functionalized NPs were added.

The binding kinetics and specificity of NPs functionalized with HSP60 antibodies through covalently linking them to the acrylate terminated dispersants, 250 $\mu\text{g}/\text{ml}$ protein A was immobilized on SiO_2 QCM-D crystals followed by the injection of functionalized NPs. The concentration of functionalized NPs was unknown due to NP agglomeration. Functionalization was done at a NP concentration of 200 $\mu\text{g}/\text{ml}$. Functionalized NPs were subsequently filtered with syringe filters which have a cut-off of 200 nm prior to their injection into the QCM-D chamber. All functionalization studies where HSP60 antibodies were involved were performed in Tris containing 160 mM NaCl under static conditions where solutions were exchanged at a flow rate of 50 $\mu\text{l}/\text{min}$.

5.1 Background

To facilitate the handling and re-suspension, commercially available iron oxide NPs are often coated with unknown stabilizers. However, studies on the influence of dispersants and anchors on the NP stability require uncoated, as-synthesized NPs with a defined surface chemistry. To have better control over the NP composition and size distribution, and to eliminate the uncontrolled influence of detergents added to commercially available NPs either during or after synthesis, all iron oxide NPs used in this work were synthesized in our lab. Therefore, different NP synthesis routes were compared regarding the resulting core size and size distribution and are described in the following chapter.

Motivated by the versatility of NP applications, much research has been devoted to the NP synthesis. The NP synthesis protocol determines their size, shape and size distribution [192, 302, 388]. These factors are crucial for the NP performance because, as outlined in chapter 1, they determine physical properties such as the absorption and emission wavelength for NPs used for optical purposes or the magnetic properties of magnetic NPs [33, 389].

Due to the high scientific and technological interest on iron oxide NPs, numerous synthesis routes for these NPs have been developed [100]. Already in 1981, Massart reported a capping agent-free aqueous precipitation method. Precipitation of iron oxide NPs could be induced through the addition of a base to a supersaturated solution containing Fe^{2+} and Fe^{3+} ions [320, 390]. Even though the average size can to a certain extent be tuned by controlling the pH, the molar ratio of $Fe^{2+} : Fe^{3+}$, adding additional cations and using different bases, the size distribution is broad and its control limited [100, 391–393].

Non-aqueous sol-gel processes are thought to be less susceptible to small changes in synthesis protocols. This renders them more reproducible and robust compared to aqueous systems [394]. Furthermore, NP size and morphology can be controlled by adjusting solvents, precursors, synthesis temperature and time if NPs are synthesized by the non-aqueous sol-gel route compared to the aqueous precipitation methods [394]. The closer control over NP size and shape allowed to synthesize monodisperse NPs through sol-gel methods where nucleation was separated from the slow NP growth [390, 395].

The superior control over morphology, size and size distribution of NPs synthesized by non-aqueous sol-gel as compared to aqueous precipitation methods might at least partially be related to the fact, that the aqueous and non-aqueous synthesis routes rely on different chemical principles. Iron oxide NPs synthesized by aqueous precipitation methods are precipitated from a supersaturated salt solution. If NPs are synthesized by non-aqueous sol-gel methods, which are typically conducted at elevated temperatures, organic reactions between the precursors and the solvent are responsible for nucleation and growth of NPs [394, 396].

There are many different methods to heat precursor/solvent dispersions. Next to conventional methods such as the oil bath where synthesis can be done under inert atmosphere [397] or reflux [398] and in the autoclave [399], MW synthesis has become increasingly popular. The homogeneous heating and fast nucleation induced by MWs was reported to result in monodisperse noble metal NPs such as *Au* and *Ag* NPs through a reduction of Au^+ and Ag^+ ions if dispersed in DMF in the presence of poly(vinyl pyrrolidone) (PVP) [400] or *Pt* NPs through the reduction of *Pt* ions [401]. However, the presence of $\approx 3\%$ 15-20 nm radii *Ag* NPs was reported in batches that otherwise consisted of 1.5 and 2 nm core radii *Ag* NPs. Nevertheless, control over the NP size was claimed to be superior if these noble metal NPs were synthesized in the MW compared to NPs synthesized under reflux [402]. The closer size control and the short synthesis time is considered as the main advantage of the MW synthesis route compared to older heating methods. NPs of many different compositions and shapes such as QDs [400], semiconductor rods [403], *Ni* NPs [404], *Ag* nanorods [405], tungstates [406], *PbTe* and *PbSe* nanocubes, [407] $LaPO_4 : Ce, Tb$, [408] *ZnO* needles, [409] TiO_2 NPs [410–412], $BaTiO_2$ [413] and oxide NPs [321] were synthesized in the MW.

Irrespective of the heating method, the core size can be reduced and the control over the NP shape increased if capping agents such as citrates are added [414]. The most prominently used capping agent for the synthesis of iron oxide NPs, namely oleic acid, has been shown to narrow the core size distribution if added to the precursor dispersion prior

to NP synthesis [395, 415]. However, complete replacement of capping agents with hydrophilic dispersants is challenging, mainly due to a lack of dispersants which have high affinity anchors. Incomplete displacement of capping agents, however, compromises NP stability in aqueous media. To avoid having to displace and replace hydrophobic capping agents, Lei *et al.* reported a one pot reaction where iron oxide NPs were synthesized by a thermal decomposition reaction in the presence PEG-COOH [416]. Because PEG-COOH and oleic acid have the same anchor, the influence of PEG-COOH on the NP size and size distribution might be similar to that of oleic acid. However, the resulting NP size distribution was considerably broader compared to NPs synthesized in the presence of oleic acid. Furthermore, based on TEM micrographs and the lack of data on the hydrodynamic radius of PEG-COOH stabilized NPs, stability of the resulting PEG-coated iron oxide NPs is questionable.

A drawback of most of these synthesis methods is their limited batch sizes. However, a non-aqueous sol-gel synthesis route similar to the one described by Sun *et al.* [395] was shown to be suited to up-scale. Monodisperse iron oxide NPs in batch sizes of 40 g were obtained [415]. This is especially valuable for industrial applications. However, in this thesis, NPs were synthesized in small batch sizes only.

To investigate the influence of the anchor, dispersant M_w and core radius on NP stability, dispersant packing density and dispersant packing density profile, cores should have a monomodal, ideally monodisperse size distribution. Therefore, three different synthesis protocols, namely an aqueous precipitation method and two non-aqueous sol-gel methods where the precursor suspensions were heated in the MW and oil bath, respectively, were compared regarding the control over the core size and size distribution. The aqueous precipitation method yielded in poor control over the NP size. The core size of NPs synthesized by the non-aqueous sol-gel method could be controlled by adjusting the synthesis time and temperature. However, iron oxide NPs heated in the MW for maximally 1 h had a bimodal size distribution whereas NPs synthesized in the oil bath for 24 h were monomodally distributed. The bimodal size distribution of NPs synthesized in the MW also significantly influenced their magnetic properties as was measured with polarized neutrons in SANS experiments.

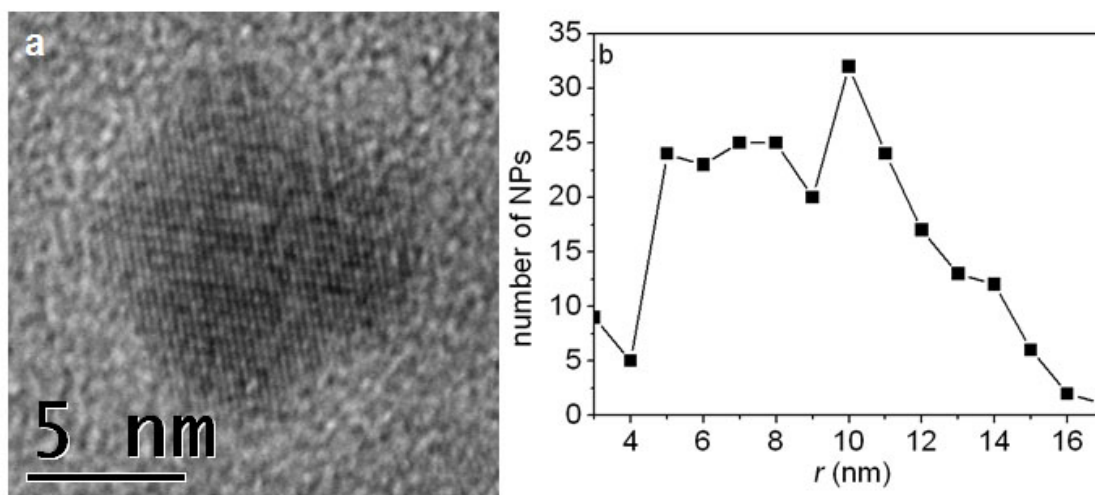


Figure 5.1: Iron oxide cores synthesized by aqueous precipitation of iron ions. HRTEM of mPEG-gallol stabilized iron oxide NPs revealed single domain NPs with an Fe-Fe distance of $3.0 \pm 0.3 \text{ \AA}$ in the (221) direction. (b) Analysis of TEM micrographs revealed an iron oxide core size of $9 \pm 2 \text{ nm}$ (measured on 240 particles).

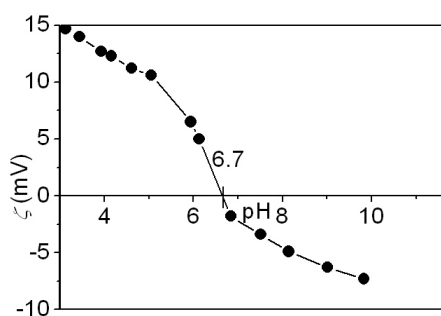


Figure 5.2: Zeta potential of iron oxide cores synthesized by aqueous precipitation of iron ions. The zeta potential by aqueous precipitation synthesized iron oxide NPs dispersed in Millipore water containing 160 mM NaCl measured as a function of pH revealed a PZC of iron oxide of 6.7.

5.2 Aqueous Precipitation

Aqueous precipitation is an experimentally simple synthesis route that yields single domain iron oxide NPs as can be seen in Figure 5.1 for NPs synthesized according to the procedure described in section 3.2.2. The single domain NP seen on the HRTEM micrograph in Figure 5.1a is oriented in the (221) direction and has an Fe-Fe distance of 3.0 ± 0.3 Å in good agreement with what has been previously reported for magnetite [417] and maghemite [342]. The BET-surface area of uncoated powder was $88 \text{ m}^2/\text{g}$. This area was lower than expected for an average NP radius of 4.5 nm obtained from TEM analysis. However, during centrifugation of stabilized, freeze-dried and re-dispersed NPs, larger NPs were removed and thus excluded from the core size evaluations of re-dispersed NPs performed by TEM while they were included in BET measurements. This discrepancy between core sizes obtained by TEM and the one calculated from the BET surface area is a consequence of the broad NP size distribution.

5.3 Microwave Assisted Synthesis

To investigate the influence of the dispersant shell thickness and the dispersant density profile on NP stability, the size distribution of iron oxide NPs should be narrow. Therefore, NP synthesis was performed by a non-aqueous MW assisted sol-gel method.

5.3.1 Core Size

The mean core size of iron oxide NPs synthesized in the MW according to the protocol of Bilecka *et al.* [321] described in section 3.2.3 was evaluated with XRD using the Scherrer formula (equation 4.8). It linearly depended on the time the $Fe(ac)_2$ precursor (dissolved in benzylalcohol) was kept at 180 °C (Figures 5.3 and 5.4), well in agreement with what has previously been reported [321]. Additionally, the core size distribution was analyzed based on TEM images for iron oxide NPs synthesized at 180 °C for 3 and 30 min (Figure 5.5). Despite the short synthesis time, the cores were highly crystalline and single domain (Figure 5.6).

As expected, freshly in the MW synthesized, unstabilized iron oxide NPs had an inverse spinel structure that can be assigned to Fe_3O_4 (ICDD PDF No. 00-019-0629) or to γ -

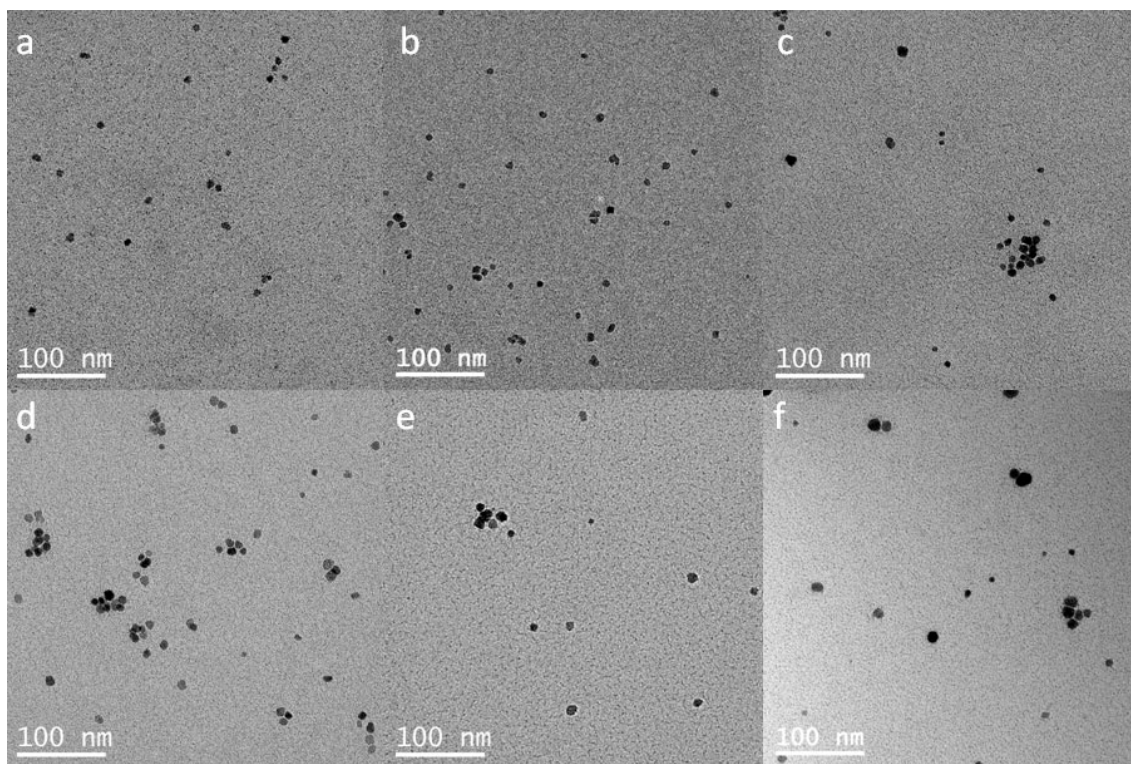


Figure 5.3: TEM images of NPs synthesized in the MW as a function of synthesis time. $Fe(ac)_2$, dissolved in benzylalcohol has been heated with the MW to 180 °C for (a) 30 s, (b) 3 min, (c) 10 min, (d) 15 min, (e) 20 min and (f) 30 min. Iron oxide NPs were stabilized with PEG(5)-nitroDOPA, dispersed in Millipore water and air dried on a TEM grid.

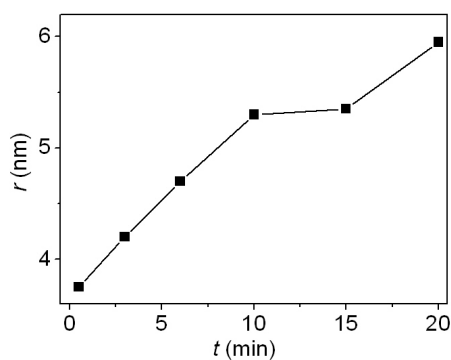


Figure 5.4: Dependence of the size of the fraction of large NPs synthesized in the MW on the synthesis time. $Fe(ac)_2$ dispersed in benzylalcohol was heated in the MW for different times. The resulting size of the fraction of the large cores of the bimodally distributed NPs was analyzed with XRD using the Scherrer formula.

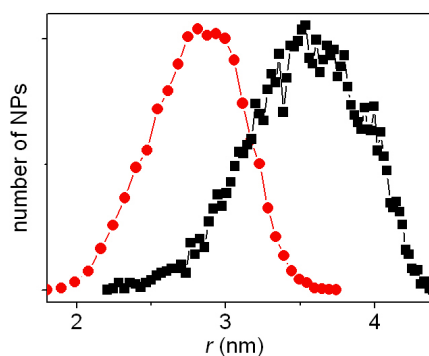


Figure 5.5: Size distribution of iron oxide NPs synthesized in the MW. The core size distribution of the NP fraction where the mean size was analyzed with XRD in Figure 5.4 was analyzed based on TEM images for Fe_3O_4 NPs synthesized in the MW where they were kept at 180 °C for 3 min (-●-) and 30 min (-■-) respectively. If the size distributions were fitted with a Gaussian curve, their mean radii were 2.8 nm and 3.6 nm and their size distributions 0.7 nm and 0.8 nm respectively.

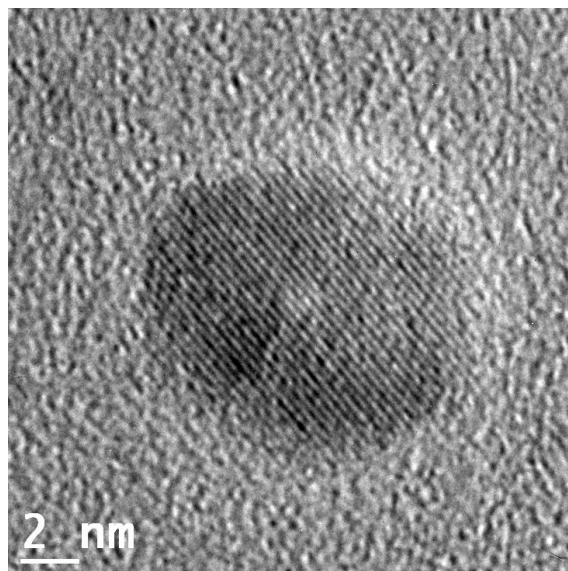


Figure 5.6: HRTEM image of Fe_3O_4 NPs synthesized in the MW. HRTEM of NPs grown from $Fe(ac)_2$, dissolved in benzylalcohol for 3 min in the MW stabilized with PEG(5)-nitroDOPA. The lattice spacing is 0.25 nm.

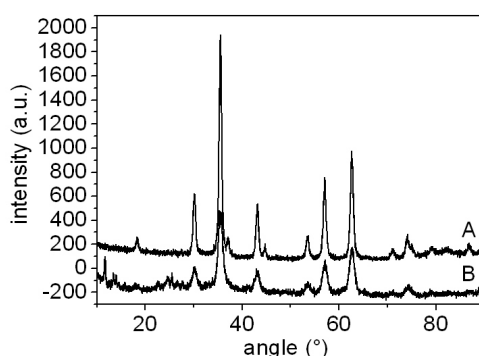


Figure 5.7: XRD of iron oxide NPs synthesized in the MW. XRD of unstabilized iron oxide NPs that were grown for (A) 30 min and (B) 3 min in the MW. The diffraction patterns could be assigned either to Fe_3O_4 (ICDD PDF No. 00-019-0629) or γ - Fe_2O_3 (ICDD PDF No. 00-039-1346).

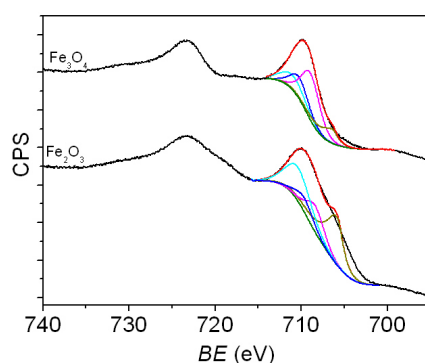


Figure 5.8: XPS of iron oxide NPs. Fe 2p XPS spectra of (A) as-synthesized Fe_3O_4 and (B) 4 months in ethanol stored, oxidized NPs. The red line shows the fit obtained by a convolution of the $FeOOH$ (cyan), Fe^{3+} (blue), Fe^{2+} (magenta) and Fe (metallic) (dark yellow) peaks where the binding energy and FWHM were constrained using parameters summarized in Table 5.1

Fe_2O_3 (ICDD PDF No. 00-039-1346) irrespective whether cores were grown for 3 or 30 min (Figure 5.7).

Iron Oxide Nanoparticle Stoichiometry

The iron oxidation state of as-synthesized iron oxide NPs and those stored for 4 months in ethanol at 4 °C was investigated with XPS (Figure 5.8). The $Fe\ 2p_{3/2}$ XPS peak of freshly synthesized iron oxide NPs could be deconvoluted into four peaks assigned to Fe^{3+} , Fe^{2+} , $FeOOH$ and metallic Fe by restricting the binding energy and FWHM of these peaks with parameters listed in Table 5.1. The atomic ratio of $Fe^{2+} : Fe^{3+}$ was close to 1 : 1. This ratio is higher than expected for Fe_3O_4 NPs. These NPs were synthesized under Ar at-

Table 5.1: Parameters used to fit the XPS Fe $2p^{3/2}$ peak of iron oxide films.

	BE (eV)	FWHM (eV)	% gauss	tail parameter
Fe^{3+}	710.2 ± 0.1	2.4	45	0.0
Fe^{2+}	709.0 ± 0.1	2.4	45	0.0
$FeOOH$	711.5 ± 0.1	3.4	45	0.0
Fe_{met}	706.6 ± 0.1	1.5	85	0.9

mosphere, vacuum dried and analyzed directly thereafter with XPS. The high $Fe^{2+} : Fe^{3+}$ ratio might indicate that less than 2/3 of the Fe^{2+} ions were oxidized to Fe^{3+} during synthesis in benzyl alcohol. The exposure time to air after NP synthesis but prior to their XPS analysis might then have been too short to further oxidize sufficient Fe^{2+} ions to yield a molar ratio of $Fe^{3+} : Fe^{2+}$ ions = 2 : 1.

In contrast, the Fe $2p_{3/2}$ peak of iron oxide NPs that had been stored at 4 °C for 4 months prior to XPS analysis could not be properly deconvoluted if the peak locations were restricted to the binding energies and FWHM summarized in Table 5.1 (Figure 7.2b). Furthermore, the Fe $2p_{1/2}$ peak of the aged iron oxide NPs was convoluted with a strong Fe^{3+} satellite peak centered at 719 eV [418, 419]. This indicates that storage of iron oxide NPs for 4 months in ethanol lead to their oxidation to Fe_2O_3 . In contrast, the Fe^{3+} satellite of as-synthesized NPs was significantly weaker and convoluted with the Fe^{2+} satellite at 715 eV [418, 419] supporting fitting results of the $Fe2p_{3/2}$ peak where significant amounts of Fe^{2+} and Fe^{3+} ions were found for as-synthesized NPs.

Iron Oxide Nanoparticle Size Distribution

PEG(5)-nitroDOPA stabilized NPs dispersed in Millipore water were air-dried on a carbon coated Cu TEM grid where the carbon film had 3.5 μm diameter holes. Next to individually stabilized NPs, NPs that agglomerated from drying were seen (Figure 5.9a). Furthermore, PEG-nitroDOPA, the dispersant used to stabilize as-synthesized NPs, was found to span 3.5 μm diameter holes, as control experiments revealed. However, surprisingly, many of the 3.5 μm diameter holes in the carbon film were spanned with a film of 0.5 - 1 nm core radius NPs surrounded by a polymer matrix (Figure 5.9b). These ultrasmall NPs could only unequivocally be identified as NPs if embedded in films that spanned holes. If iron oxide NPs were deposited on a ≈ 10 nm thick carbon film supported on a Cu TEM grid, as is conventionally done, contrast from the carbon film was similar to that of 0.5 - 1 nm radius NP cores. Thus, these ultrasmall NPs could not be detected. The minuscule size of the ultrasmall NPs also complicates their detection with

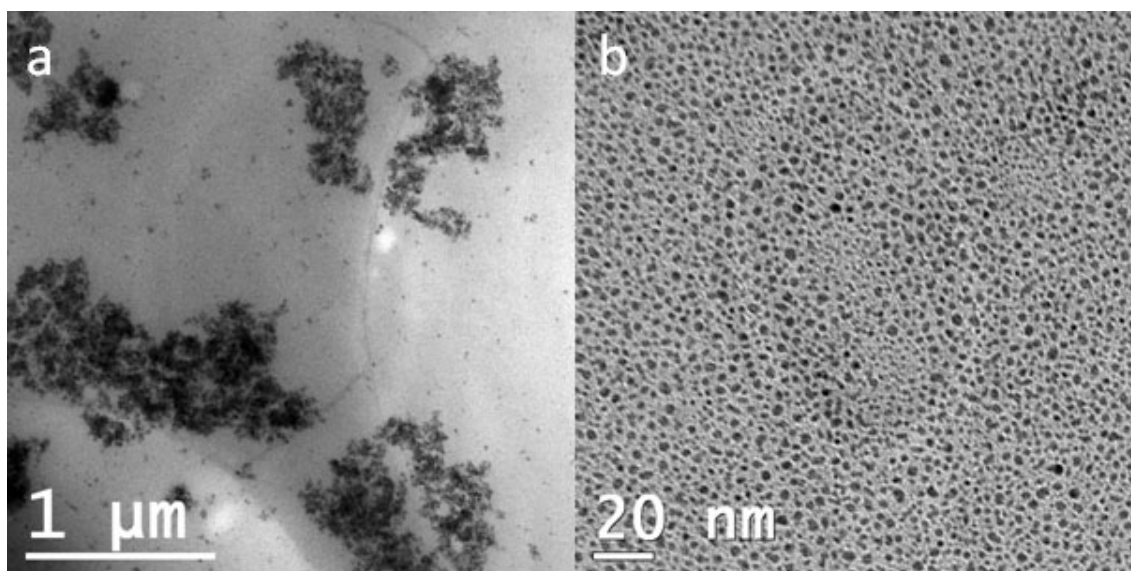


Figure 5.9: TEM of iron oxide NPs synthesized in the MW. a) Overview and b) detail TEM micrograph of iron oxide NPs synthesized from $Fe(ac)_2$ in benzylalcohol. The precursor solution was heated in the MW to 180 °C where NPs were grown for 30 min. As-synthesized NPs were stabilized with PEG(5)-nitroDOPA and air-dried on a carbon supported Cu-grid where the carbon film had 3.5 μm diameter holes.

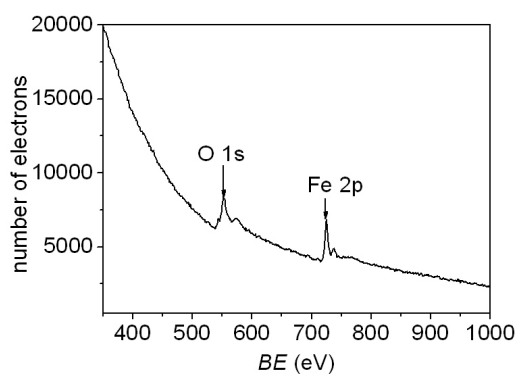


Figure 5.10: EELS spectra of spanning films. EELS analysis of films that spanned the 3.5 μm holes in the carbon film such as shown in Figure 5.5b revealed the presence of iron and oxygen. This demonstrates that the NPs seen in TEM are iron oxide NPs.

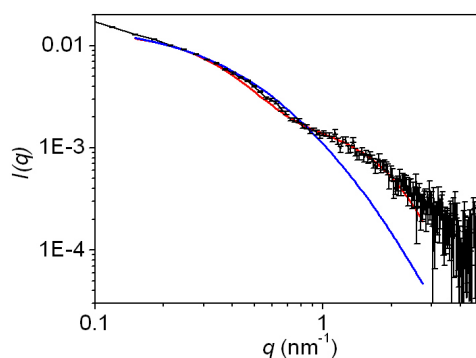


Figure 5.11: SAXS on NPs synthesized in the MW. SAXS was measured on PEG(5)-nitroDOPA stabilized iron oxide NPs which had been synthesized in the MW (black line). The red line is the best fit obtained assuming a bimodal NP size distribution where the NPs were lognormally distributed. The larger NP fraction had a mean radius of 4.0 nm and a size distribution of 0.27 while the smaller fraction had a mean radius of 0.9 nm and a size distribution of 0.23. The small NPs were $1700 \times$ more numerous than the larger NPs. The blue line corresponds to the best fit obtained a monomodal lognormally distributed size distribution where the core radius was 4.1 nm while the size distribution was with 0.66 extremely high.

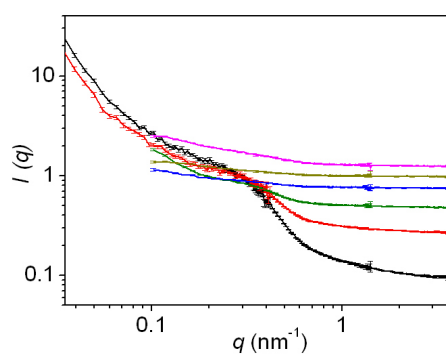


Figure 5.12: SANS on PEG(5)-nitroDOPA stabilized NPs synthesized in the MW. Contrast variation SANS experiments were performed on PEG(5)-nitroDOPA stabilized iron oxide NPs synthesized in the MW where the volume ratio of D_2O and H_2O was 100 : 0 (black), 80 : 20 (red), 60 : 40 (green), 40 : 60 (blue), 20 : 80 (yellow) and 0 : 100 (magenta). PEG yields highest SANS scattering contrast in D_2O and its contrast is matched if it is dispersed in a mixture of 84 vol% H_2O and 16 vol% D_2O . The iron oxide cores would scatter best in H_2O and least in D_2O . Because hardly any scattering can be seen if PEG(5)-nitroDOPA stabilized iron oxide NPs were dispersed in a mixture of 80 vol% of H_2O and 20 vol% of D_2O , which is close to the matching point of PEG, the vol% of cores must be very low. The PEG concentration is however high, given the good scattering of PEG in D_2O .

conventional diffraction techniques such as XRD. The crystallite size is too small to result in clear diffraction peaks if analyzed with XRD. For similar reasons, no clear diffraction peaks could be detected with TEM if such samples were analyzed in the reciprocal space. Moreover, due to attractive Van-der-Waals forces and the high surface : volume ratio, NPs will agglomerate if they are not stabilized. Once agglomerated, these ultrasmall NPs cannot be detected any more. Therefore, an appropriate sample preparation protocol and characterization technique is required if these ultrasmall NPs have to be detected.

To assure that these dots were iron oxide NPs rather than contaminations introduced during the sample preparation, EELS was performed on films spanning $3.5 \mu\text{m}$ holes in the carbon film supported TEM grids. This analysis unequivocally revealed the presence of iron and oxygen demonstrating that the NPs comprised of iron oxide (Figure 5.10). These ultrasmall iron oxide NPs must therefore be a byproduct of the NP synthesis or alternatively be generated during the stabilization process.

Air-drying of Millipore water-based NP dispersions can induce size-based NP segregation. TEM images acquired on these samples can therefore not be used to quantitatively determine the relative fraction of the bimodal size distribution. However, these TEM images allow to qualitatively determine if the core size distribution is monomodal or bimodal. To estimate the fraction of ultrasmall NPs in solution, SAXS measurements were performed on Millipore water based PEG(5)-nitroDOPA stabilized NPs that had been synthesized in the MW at 180°C for 3 min (Figure 5.11). SAXS data could only be fitted assuming two lognormally distributed populations of cores, one with a mean radius of 4 nm and the other had a mean radius of 0.9 nm. The 0.9 nm core radius NPs were 1700 times more abundant compared to the 4 nm radius cores (resulting in a weight fraction of 98 wt% and 2 wt% of small and large NPs respectively) (Figure 5.9). The standard deviations for the larger and smaller cores were 0.27 and 0.23 respectively.

The consequences of the predominance of the ultrasmall NPs for NP characterization and physical properties of these dispersions was exemplified in SANS measurements which were performed on the same batch of NPs as used for the SAXS measurements. As can be seen in Figure 5.12, no scattering was detected for NPs dispersed in 84 vol% H_2O and 16 vol% D_2O whereas scattering was maximal if NPs were dispersed in D_2O . Considering that the scattering contrast of PEG is maximal in D_2O and its scattering cross section is matched if they are dispersed in a mixture of 84 vol% H_2O and 16 vol% D_2O , these contrast variation experiments evidenced that neutron scattering was limited to scattering from PEG. Iron oxide cores of the ultrasmall fraction were with a radius of 0.9 nm considerably smaller than the radius of gyration (R_G) of PEG(5) which is 2.9 nm [200].

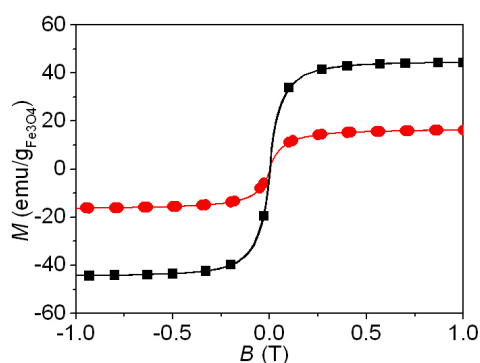


Figure 5.13: VSM measurements on iron oxide NPs synthesized in the MW. VSM measurements were performed on uncoated iron oxide NPs heated in the MW to 180 °C for 3 min (●) and 30 min (■) respectively. The amount of organic impurities was quantified with TGA and VSM data were normalized accordingly.

Furthermore, one core is surrounded by multiple PEG chains. Thus, for ultrasmall NPs stabilized with PEG(5)-nitroDOPA, PEG is expected to scatter stronger even if the scattering contrast of PEG and that of the core was identical. That no scattering from 4 nm radius cores can be seen with SANS despite that scattering contrast scales with r^6 and thus renders SANS sensitive to larger objects, supports SAXS data where the concentration of ultrasmall cores was much higher compared to that of larger cores.

Ultrasmall NPs were seen in SAXS but not in SANS because X-rays are scattered by electrons and the electron density in the Fe_3O_4 cores is more than five times higher compared to that of the PEG shell. Scattering in SANS relies on differences in the scattering cross section between the solvent and the scatterer, which is determined by the nucleus. Depending on the solvent (if H_2O or D_2O are used) scattering contrast from PEG or that from the core predominates. However, the volume fraction of ultrasmall NPs was too low to be detected with SANS even if they were dispersed in H_2O which yields highest scattering contrast of Fe_3O_4 cores (Figure 5.12).

Magnetic Properties

Despite that 4 nm radius iron oxide cores synthesized in the MW were, according to VSM measurements, superparamagnetic (Figure 5.13), no clear magnetic scattering, which would result in an anisotropic 2D scattering pattern in Figure 5.14c, could be observed with polarized neutrons. This apparent contradiction is likely due to the large fraction of ultrasmall NPs in solution. Disordered spins at the NP surface are thought to cause a \approx

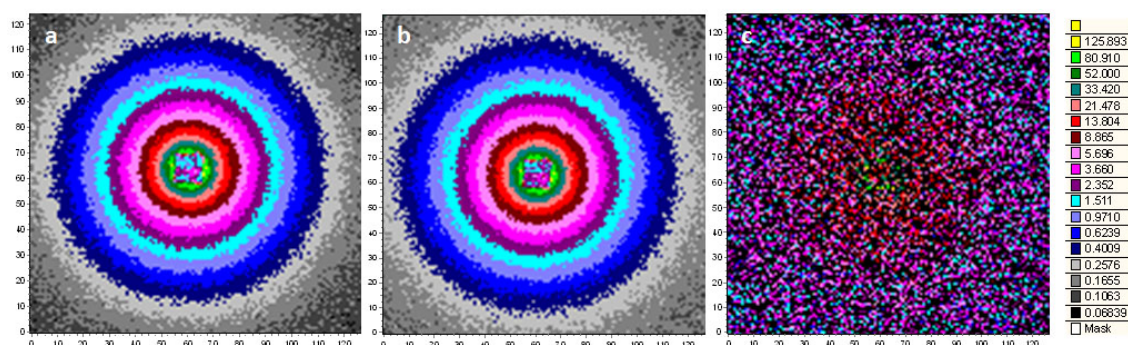


Figure 5.14: SANS measurements performed with polarized neutrons on PEG(5)-nitroDOPA stabilized NPs synthesized in the MW. 2D SANS data of PEG(5)-nitroDOPA stabilized iron oxide NPs synthesized in the MW at 180 °C for 3 min acquired with polarized neutrons. Neutrons were polarized (a) parallel and (b) antiparallel to the static magnetic field. (c) The difference spectra of (a) - (b) is close to zero indicating that these samples do not magnetically scatter. The logarithmic color scale indicates scattering contrast.

0.2-1.5 nm thick non-magnetic shell [35, 36, 420, 421] which will be further discussed in chapter 7. Therefore, the contribution of well-dispersed ultrasmall NPs to magnetic properties of the dispersion is most likely negligible. This might be one of the reasons for the low saturation magnetization (M_s) especially of cores where the larger fraction had a radius of 4 nm.

5.3.2 Synthesis Parameters that Determine the Nanoparticle Size Distribution

Solvent, precursor, precursor concentration and synthesis time are known to influence the NP size and size distribution [394]. Therefore, the influence of these parameters on the size distribution of iron oxide NPs synthesized in the MW were investigated. Because, as described above, ultrasmall NPs could be visualized with TEM if embedded in PEG-nitroDOPA films spanning 3.5 μm holes of carbon film supported TEM grids, this technique was mainly used to characterize the core size distribution as a function of synthesis conditions.

Influence of Precursor and Precursor Concentration and Solvent

The large NP fraction synthesized from Fe^{3+} acetylacetonate ($\text{Fe}(\text{acac})_3$), the most abundantly used precursor to synthesize iron oxide NPs by non-aqueous sol-gel methods, was

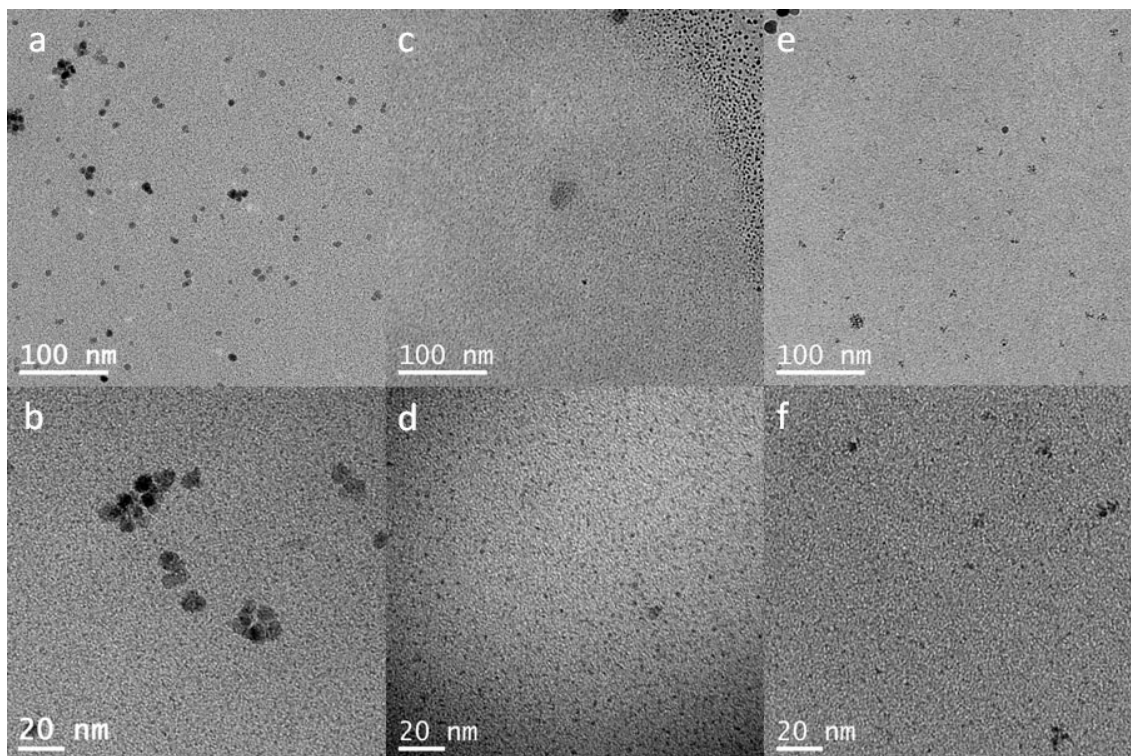


Figure 5.15: TEM of iron oxide NPs synthesized in benzylalcohol in the MW. (a), (b) 1 mmol $Fe(ac)_2$ and (c), (d) 0.1 mmol $Fe(ac)_2$ and (e), (f) 1 mmol $Fe(acac)_3$ dissolved in benzylalcohol has been heated in the MW to 180 °C for 3 min. Iron oxide NPs were stabilized with PEG(5)-nitroDOPA, dispersed in Millipore water and air dried on a TEM grid. Images were taken in regions where PEG(5)-nitroDOPA/NP films span the 3.5 μm holes.

smaller compared to that of iron oxide NPs synthesized from Fe^{2+} acetate ($Fe(ac)_2$) (Figure 5.15). However, ultrasmall NPs were seen irrespective whether $Fe(ac)_2$ or $Fe(acac)_3$ was used as a precursor (Figure 5.15 c and d).

The influence of the solvent on the size distribution of iron oxide NPs was investigated by comparing NPs synthesized from $Fe(ac)_2$ and $Fe(acac)_3$ dispersed in benzylalcohol and pyrrolidone respectively. Pyrrolidone based precursor dispersions were heated in the MW to 180 °C and kept at this temperature for 30 min. Especially the larger core fraction of NPs synthesized from $Fe(ac)_2$ was smaller if NPs were synthesized in pyrrolidone compared to those synthesized from $Fe(ac)_2$ in benzylalcohol (cf. Figure 5.16a and 5.15a). This likely is due to a high affinity of pyrrolidone especially to Fe^{3+} [422].

NPs synthesized and stored in pyrrolidone were colloidal stable. This likely is related to the high affinity of pyrrolidone to Fe^{3+} . Because of the good colloidal stability if dispersed in pyrrolidone, NPs could not be precipitated even if they were centrifuged for 2 h at 40'000 rpm. Thus these NPs were not washed with ethanol prior to stabilization.

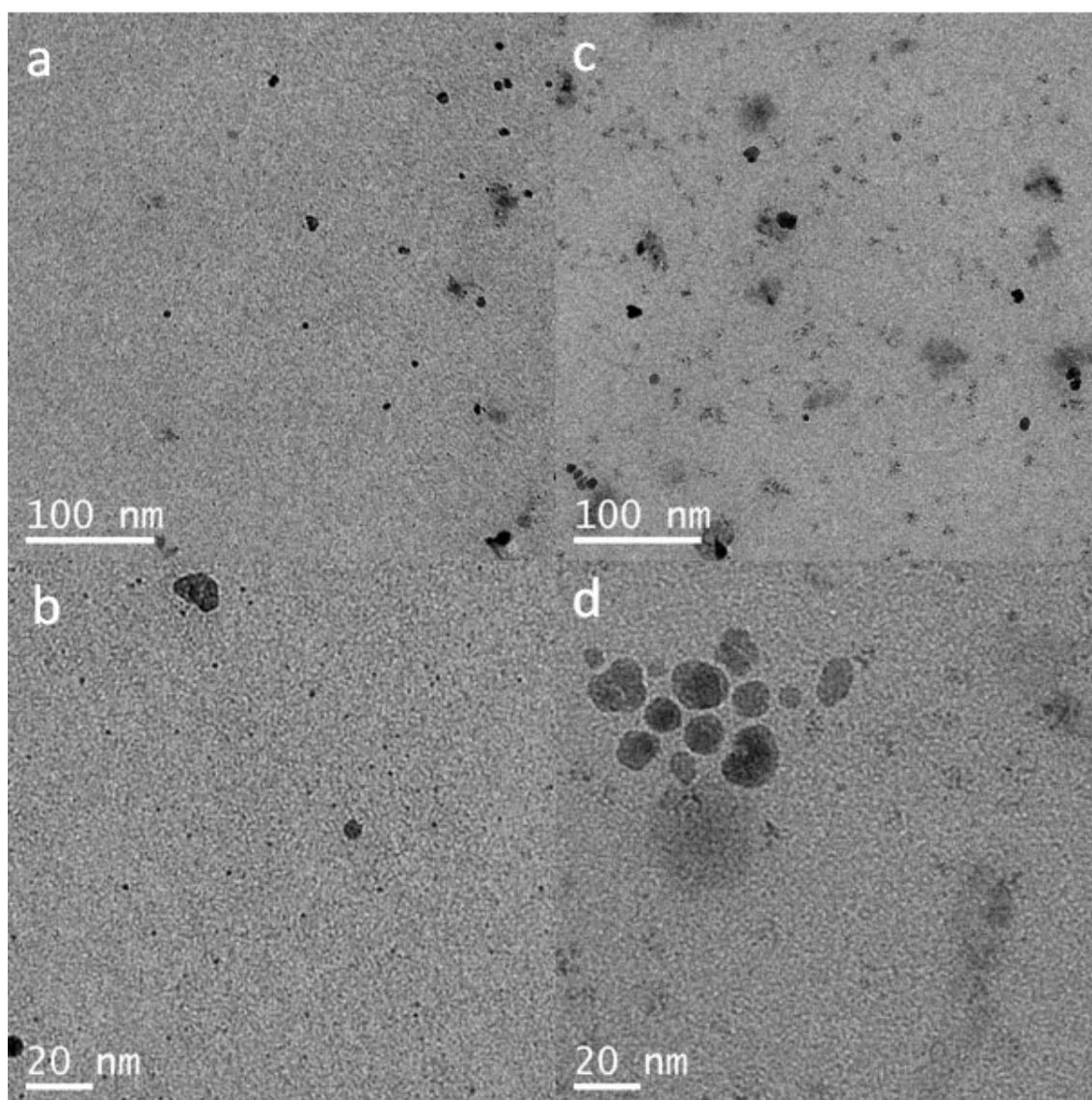


Figure 5.16: TEM images of NPs synthesized in pyrrolidone in the MW. (a), (b) $Fe(ac)_2$ and (c), (d) $Fe(acac)_3$ dissolved in pyrrolidone has been heated to 180 °C for 3 min using the MW. Iron oxide NPs were stabilized with PEG(5)-nitroDOPA, dispersed in Millipore water and air dried on a TEM grid.

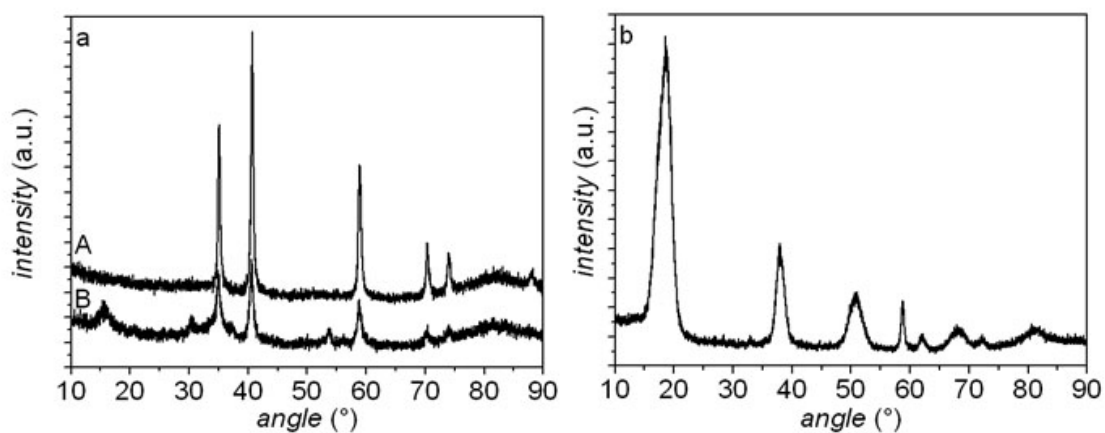


Figure 5.17: XRD of MnO and $Mg(OH)_2$ NPs. (a) XRD of MnO NPs (ICDD PDF No. 01-075-0625) synthesized in the MW from (A) $Mn(ac)_2$ and (B) $Mn(acac)_2$ precursors dissolved in benzylalcohol and (b) $Mg(OH)_2$ NPs (ICDD PDF No. 01-074-2220) synthesized from magnesium ethoxide dissolved in acetophenone.

The good stability of as-synthesized NPs in pyrrolidone was in strong contrast to NPs synthesized in benzylalcohol. The latter agglomerated and readily sedimented if stored unstabilized in benzylalcohol or ethanol. They thus could easily be washed with ethanol prior to stabilization.

MnO and $Mg(OH)_2$ Nanoparticles Synthesized in the Microwave

To check, if ultrasmall NPs were a feature of iron oxide NPs, MnO and $Mg(OH)_2$ NPs were grown in the MW and stabilized with PEG(5)-nitroDOPA. Dispersions of $Mn(ac)_2$ and $Mn(acac)_2$ dissolved in benzylalcohol and magnesium ethoxide ($Mg(OC_2H_5)_2$) dissolved in acetophenone were heated to 180 °C and grown at this temperature for 1 h. $Mn(ac)_2$ and $Mn(acac)_2$ precursors dissolved in benzylalcohol both resulted in MnO NPs as was confirmed by XRD (ICDD PDF No. 01-075-0625). That $Mn(acac)_2$ resulted in MnO NPs rather than Mn_2O_3 is in contrast to what has previously been reported [321]. However, this discrepancy was not further investigated. $Mg(OC_2H_5)_2$ dissolved in acetophenone resulted in $Mg(OH)_2$ NPs as was confirmed with XRD (ICDD PDF No. 01-074-2220) (Figure 5.17).

Similar to iron oxide NPs synthesized in the MW, a tentatively large fraction of ultrasmall NPs were also found for PEG(5)-nitroDOPA stabilized MnO and $Mg(OH)_2$ NPs as can be seen in Figure 5.18.

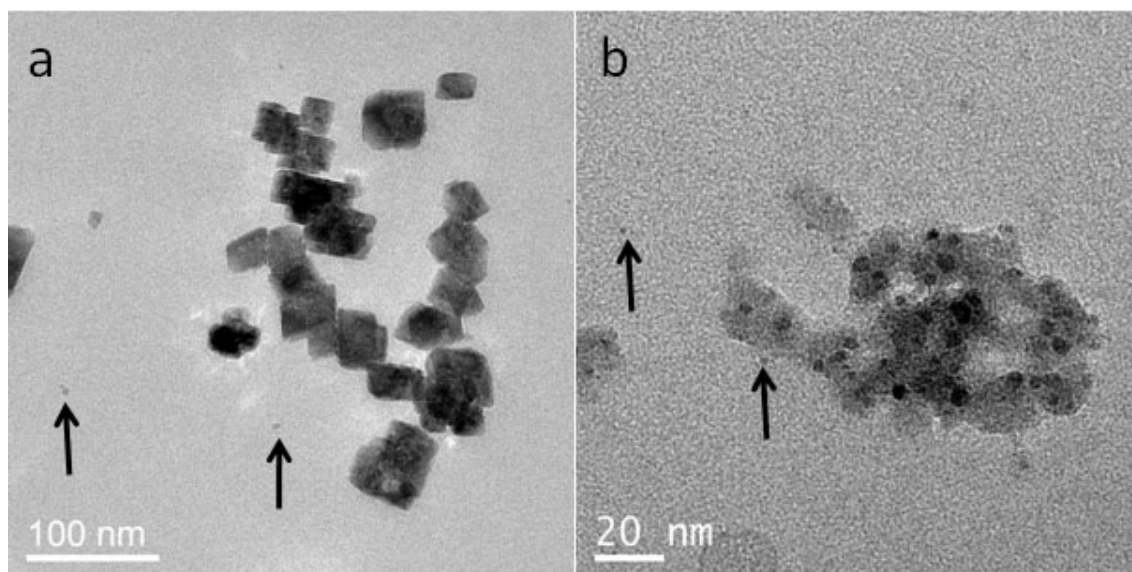


Figure 5.18: TEM micrographs of oxides NPs other than iron oxide synthesized in the MW. (a) MnO NPs were synthesized starting from $Mn(ac)_2$ dissolved in benzylalcohol and (b) $Mg(OH)_2$ NPs were synthesized from magnesium ethoxide in acetophenone. NPs were heated with the MW to $180\text{ }^\circ\text{C}$ and kept at this temperature for 30 min. They were washed, stabilized with PEG(5)-nitroDOPA and dispersed in Millipore water before they were air dried on a TEM grid.

5.4 Oil Bath Synthesis

To check the influence of the energy source on the NP size distribution, the precursor solution, namely $Fe(ac)_2$ dispersed in benzylalcohol, was prepared identically to those precursor solutions used for the MW protocols. However, these precursor solutions were heated in the oil bath instead of the MW. Because the MW is known to greatly accelerate NP formation and growth [396] NPs synthesized in the oil bath were grown for considerably longer times than those in the MW. Studies on iron oxide NPs grown in the oil bath focused on the influence of temperature and synthesis time on the NP size distribution.

As can be seen in Figure 5.19, PEG(5)-nitroDOPA stabilized iron oxide NPs grown in the oil bath also spanned $3.5\text{ }\mu\text{m}$ holes. However, the density of large cores was significantly higher compared to NPs synthesized in the MW. Furthermore, no ultrasmall NPs could be detected inside these hole spanning films, in stark contrast to NPs synthesized in the MW.

5.4.1 Influence of the Reaction Temperature

NP morphology became more spherical with increasing synthesis temperature. However, while NPs synthesized at temperatures $< 180\text{ }^\circ\text{C}$ were single domain (Figure 5.21), some

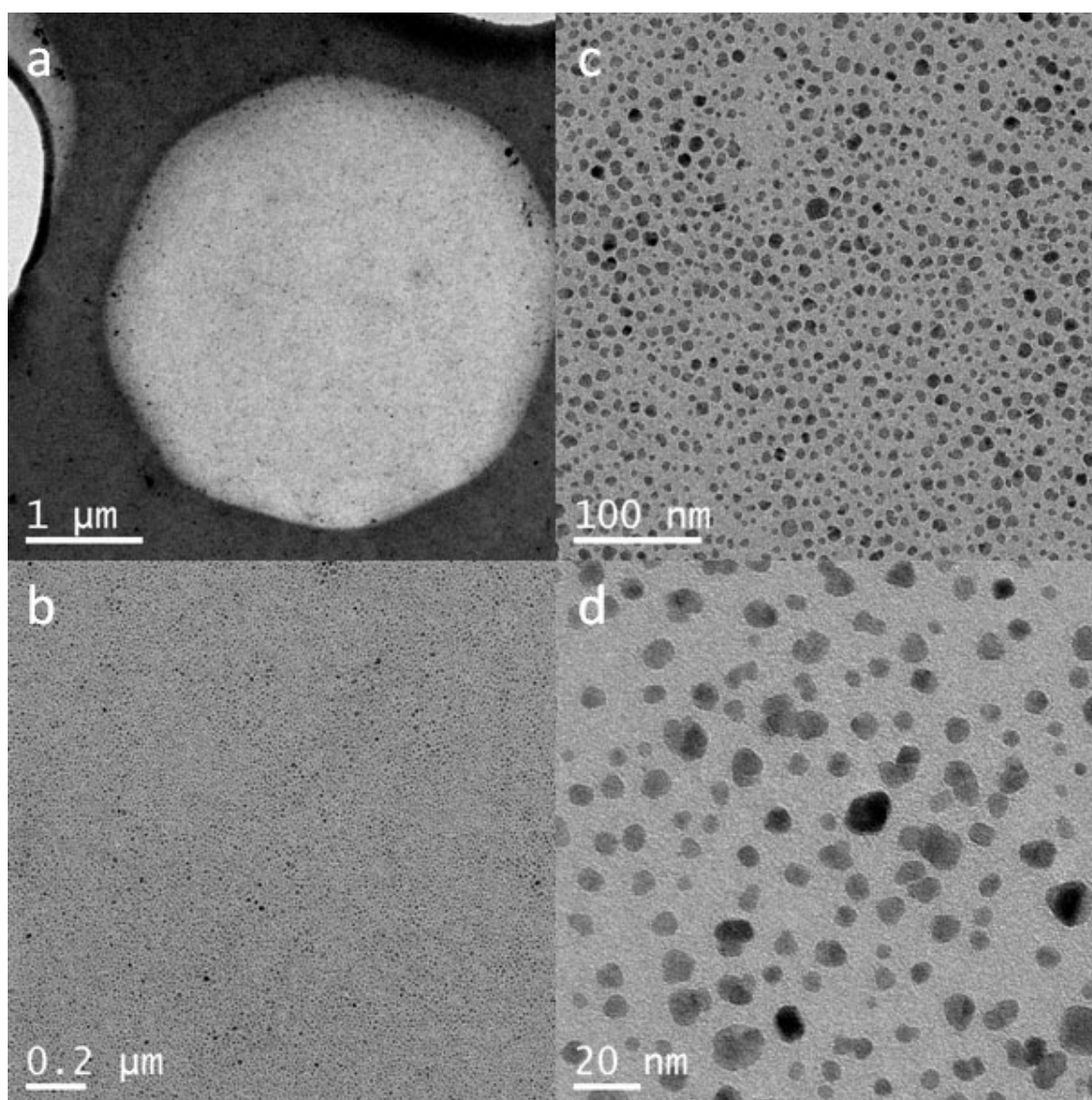


Figure 5.19: TEM images of iron oxide NPs synthesized in the oil bath. Iron oxide NPs were synthesized from $Fe(ac)_2$ dissolved in benzylalcohol. They were heated to 180 °C in the oil bath where they were grown for 24 h. As-synthesized NPs were stabilized with PEG(5)-nitroDOPA, dispersed in Millipore water and air-dried on a carbon film supported on Cu-grid where the carbon film had 3.5 μm diameter holes. The 3.5 μm holes were spanned with a monolayer of PEG(5)-nitroDOPA stabilized NPs as can be seen on the images taken at the same place with different magnifications. However, in contrast to iron oxide NPs grown in the MW, no ultras small NPs could be seen even at 100'000 \times magnification (image d).

Table 5.2: Comparison of iron oxide core radii obtained by different techniques.

technique	r_{180} 180 °C cores (nm)	s_{180} 180 °C cores (r_{180})	r_{150} 150 °C cores (nm)	s_{150} 150 °C cores (r_{150})
SAXS	5.6	0.3	2.4	0.3
XRD	6.7		3.1	
TEM	5.0		2.2	

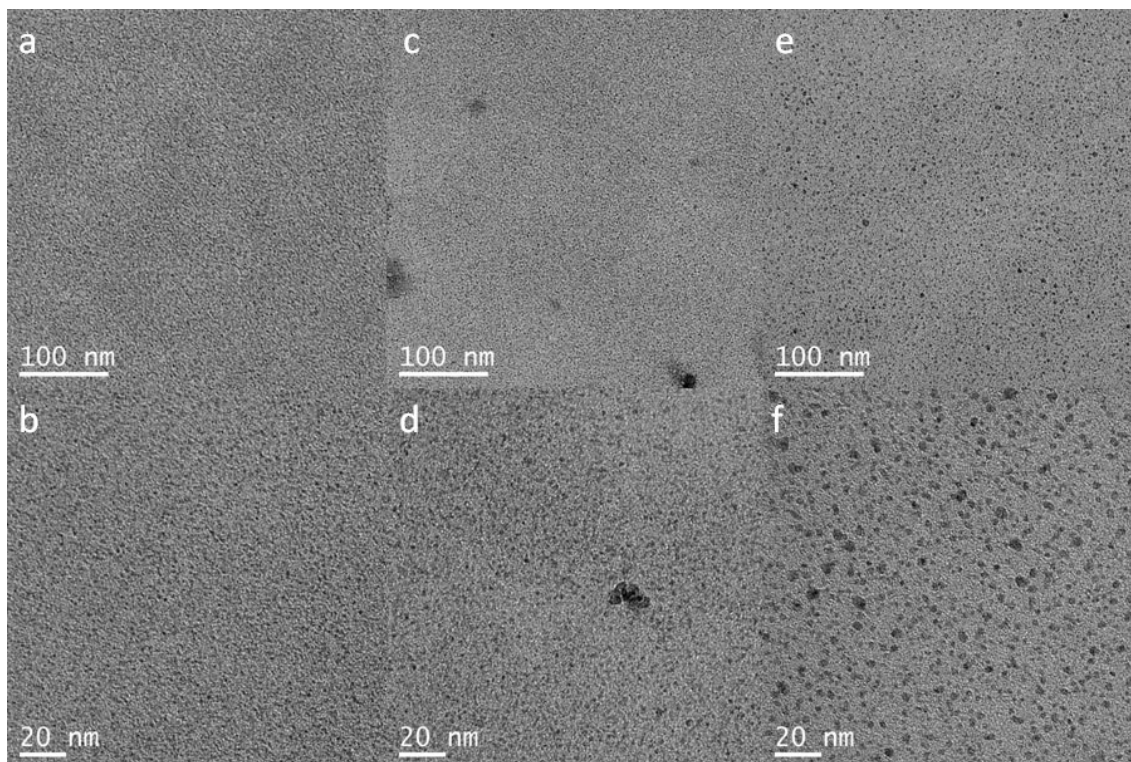


Figure 5.20: TEM micrographs of Fe_3O_4 NPs synthesized in the oil bath as a function of the synthesis temperature. NPs were grown from $Fe(ac)_2$ dispersed in benzylalcohol in the oil bath at (a), (b) 140 °C, (c), (d) 160 °C, (e), (f) 180 °C for 24 h. They were washed, stabilized with PEG(5)-nitroDOPA and re-dispersed in Millipore water before they were air dried on a carbon coated Cu TEM grid. While the synthesis conducted at 140 °C yielded exclusively ultrasmall NPs that were only seen at 100'000 \times magnification (b) but not at 40'000 \times magnification (a) NPs grown at 160 °C were considerably larger and could already be detected at a magnification of 40'000 \times (e). However, especially the NPs grown at 140 °C and 160 °C could only be detected within the spanning membranes. If they were adsorbed on a carbon film, the contrast from the carbon film was too big to allow for detection of these NP.

of the NPs synthesized at 180 °C were multi-domain NPs (Figure 5.22).

Furthermore, NPs grown at 140 °C for 24 h had a core radius similar to what was seen for MW synthesized ultrasmall NPs. However, in contrast to NPs synthesized in the MW, NPs synthesized in the oil bath had a monomodal core size distribution (Figure 5.20). The core radius increased with increasing temperature up to ≈ 5 nm for NPs grown at 180 °C as demonstrated with TEM and SAXS (Figures 5.20a, 5.21, 5.23, 5.26 and Table 5.2).

Core sizes were additionally evaluated on PEG(5)-nitroDOPA stabilized NPs with SAXS. To, see whether SAXS scattering is limited to the scattering of individual NPs (form factor) or if it is convoluted by scattering contributions from the structure factor, PEG(5)-nitroDOPA stabilized iron oxide cores were measured at different concentrations. Despite the low NP concentrations, NP interactions that lead to a structure factor $\neq 1$. Therefore, the structure factor still contributed to the scattering curves of 5 nm core radius NPs as

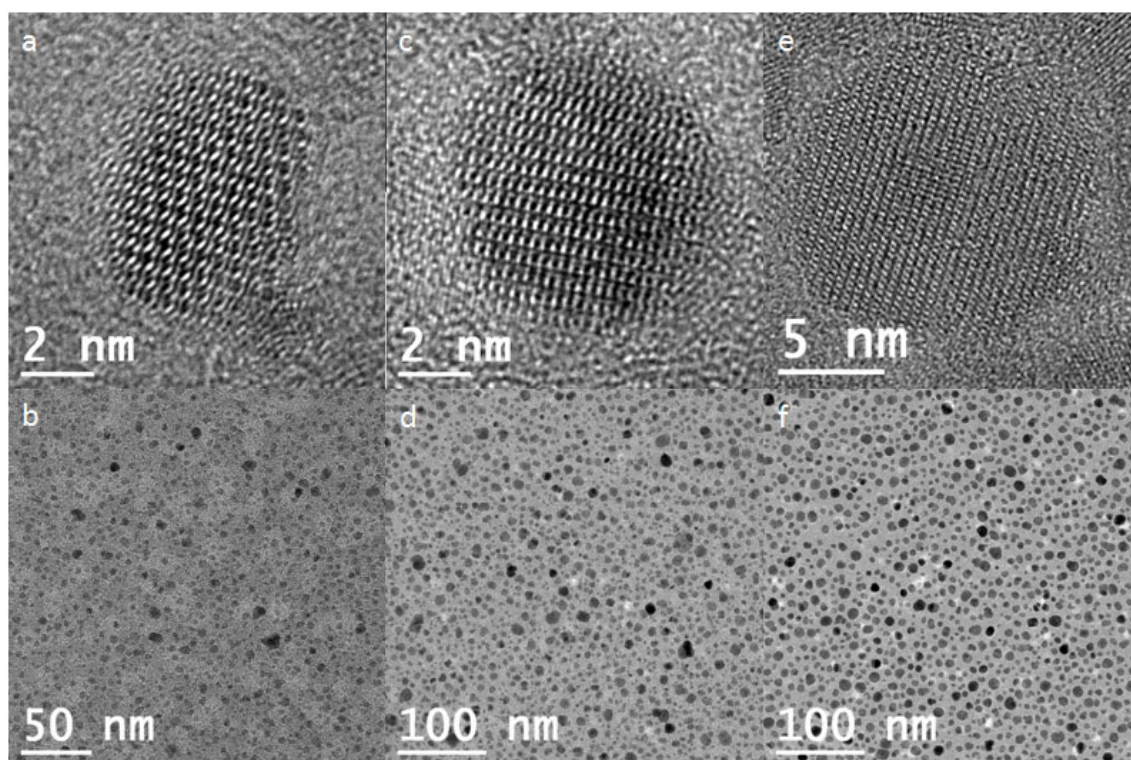


Figure 5.21: HRTEM and TEM micrographs of iron oxide NPs mainly used in this thesis. Based on the results shown in Figure 5.20 three different NP core sizes were mainly used. NPs synthesized at (a), (b) 150 °C, (c), (d) 165 °C and (e), (f) 180 °C. While the NPs synthesized at 150 °C and 165 °C were single domain NPs, some of the NPs synthesized at 180 °C were multidomain (Figure 5.22).

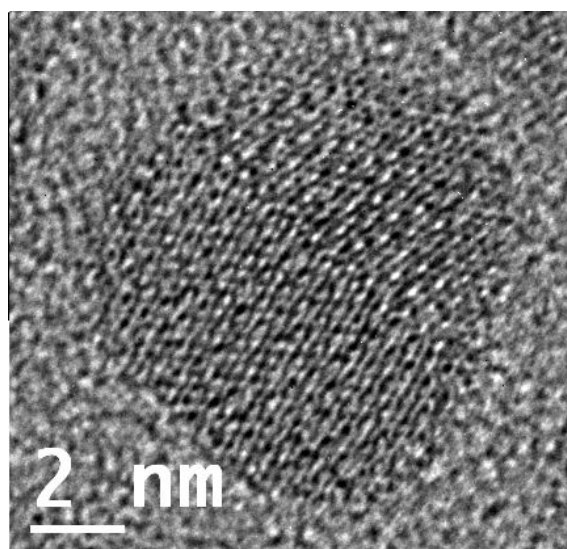


Figure 5.22: HRTEM of Fe_3O_4 NPs synthesized at 180 °C for 24 h. HRTEM of an Fe_3O_4 NP stabilized with PEG(5)-nitroDOPA air-dried on a carbon film supported TEM grid. While most of these NPs were single domain as seen in Figure 5.21, some consisted of two domains.

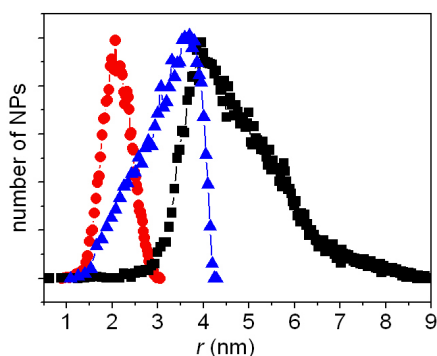


Figure 5.23: Size distribution of iron oxide NPs synthesized in the oil bath for 24 h. The size distribution of iron oxide NPs grown for 24 h at 150 °C (-●-), 165 °C (-▲-) and 180 °C (-■-) was evaluated based on TEM micrographs. Size analysis was done on 16'000, 14'000 and 20'000 NPs respectively. If these size distributions were fitted with a Gaussian curve, their average radii were 2.1 nm, 3.4 nm and 4.5 nm while the standard deviations were 0.7 nm, 1.1 nm and 1.9 nm for NPs synthesized at 150 °C and 180 °C respectively.

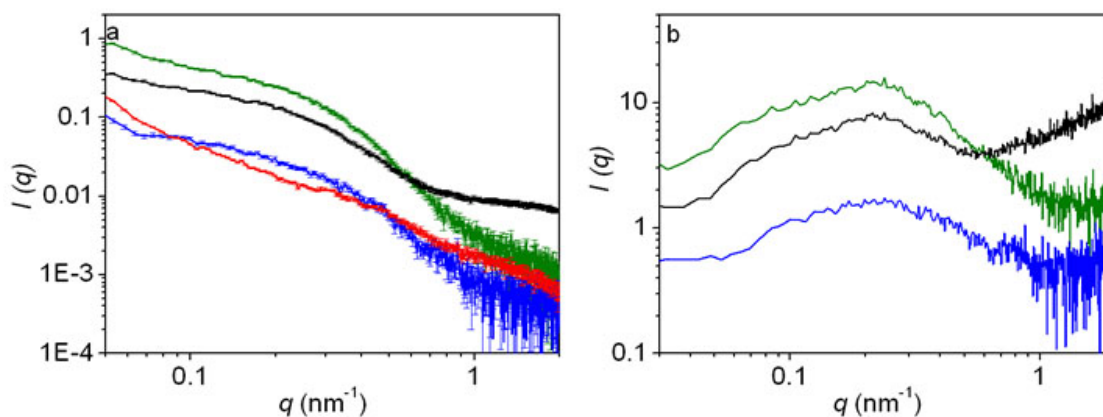


Figure 5.24: SAXS of PEG(5)-nitroDOPA 5 nm core radius iron oxide NPs synthesized in the oil bath. (a) PEG(5)-nitroDOPA stabilized iron oxide NPs were dispersed in Millipore water at a concentration of 2.5 vol% (green), 0.5 vol% (black), 0.1 vol% (blue) and 0.02 vol% (red) where the vol% corresponds to the hydrodynamic volume of the NPs. Spectra were corrected for background scattering by subtracting the water spectrum. (b) Spectra shown in (a) were divided by the SAXS spectrum measured on 0.02 vol% NP. They revealed a structure factor indicating that NPs interacted with each other at the measured concentrations.

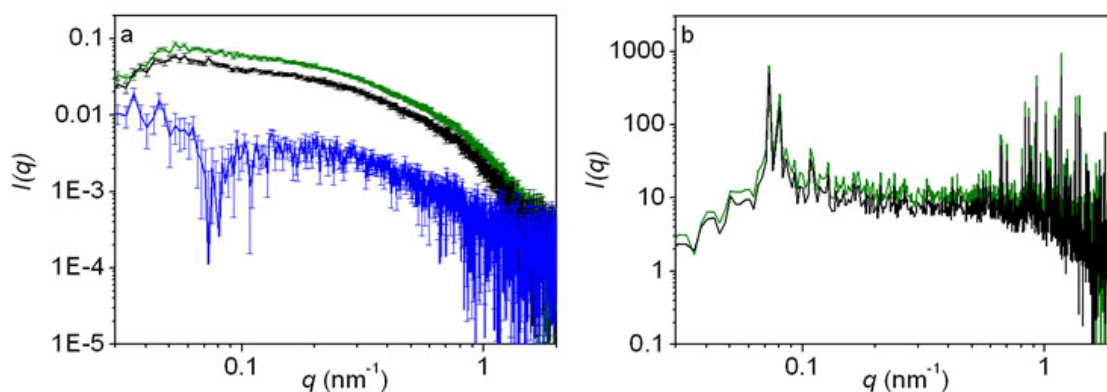


Figure 5.25: SAXS of PEG(5)-nitroDOPA 2.5 nm core radius iron oxide NPs synthesized in the oil bath. (a) PEG(5)-nitroDOPA stabilized iron oxide NPs were dispersed in Millipore water at a concentration of 1 vol% (green), 0.5 vol% (black) and 0.1 vol% (blue) where the vol% corresponds to the hydrodynamic volume of the NPs. Spectra were corrected for background scattering by subtracting the water spectrum. (b) Spectra shown in (a) were divided by the SAXS spectrum measured on 0.1 vol% NP. They indicate that NPs did not interact with each other as can be seen by the absence of a contribution from the structure factor.

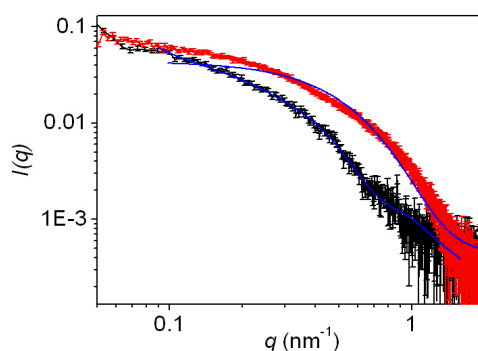


Figure 5.26: SAXS measurements on PEG(5)-nitroDOPA stabilized iron oxide NPs synthesized in the oil bath. SAXS measurements were performed on PEG(5)-nitroDOPA stabilized iron oxide NPs synthesized in the oil bath for 24 h at 180 °C (black) and 150 °C (red). Stabilized iron oxide NPs were dispersed in Millipore water at a concentration of 0.1 vol%. The best fits assuming a lognormal distribution are shown in blue. According to these fits, NPs synthesized at 180 °C and 150 °C have a mean radius of 4 nm and 2.5 nm with a size distribution s of 0.2 respectively.

can be seen in Figure 5.24b. The structure factor peaked at a q -value corresponding to ≈ 40 nm which is slightly larger than twice the hydrodynamic radius measured for PEG(5)-nitroDOPA stabilized 5 nm core radius NPs of 14 ± 3 nm. The decrease of the SAXS curves at low q -values hints to a repulsive interparticle potential. No contribution from a structure factor could be measured for PEG(5)-nitroDOPA stabilized 2.5 nm core radius NPs (Figure 5.25b).

SAXS data were fitted assuming a lognormal core size distribution. Additionally, the structure factor of 5 nm core radius iron oxide NPs was assumed to have a square well potential form with a repulsive energy of $3.8 k_B T$ (Figure 5.26). As was shown in Figure 5.25, no structure factor contribution had to be taken into account for fitting SAXS data of PEG(5)-nitroDOPA stabilized 2.5 nm core radius iron oxide NPs. The resulting mean core radii are summarized in Table 5.2.

SAXS core radii obtained from fitting results shown in Figure 5.26 were in good agreement with values obtained from analyzing TEM data (Table 5.2). The considerably larger core radii obtained by XRD compared to values obtained from SAXS and TEM measurements (Table 5.2) might be related to the fact, that NPs were measured at different stages during the NP stabilization process. XRD was performed on unstabilized NPs. Stabilization might alter the core size distribution. According to equation 1.5, smaller NPs are easier to stabilize if a dispersant with a sufficiently high M_w such as PEG(5)-nitroDOPA is used. It is therefore possible, that the larger NPs sedimented during centrifugation due to lower NP stability and larger gravity and were thus excluded from the analysis. The good agreement between core sizes obtained by TEM and SAXS - despite that TEM yields number weighted averages (which scale with r) and SAXS yields intensity weighted averages (which scale with r^6) - indicates that the core size distribution is relatively low.

5.4.2 Influence of the Reaction Time

The growth of iron oxide NPs synthesized from $Fe(ac)_2$ in benzylalcohol at $180^\circ C$ was followed by taking fractions of the synthesis dispersion at different time points. As can be seen in Figure 5.27, the mean NP size steadily increased up to NPs synthesized for 24 h. Longer synthesis times were not investigated. However, differences in the mean size between NPs grown for 8 h and those grown for 24 h were significantly smaller compared to the difference in the mean core size of NPs grown for 6 h and 8 h. This indicates that the NP growth rate decreased after 8 h. Furthermore, the concentration of large cores in the spanning membranes increased with increasing synthesis time as

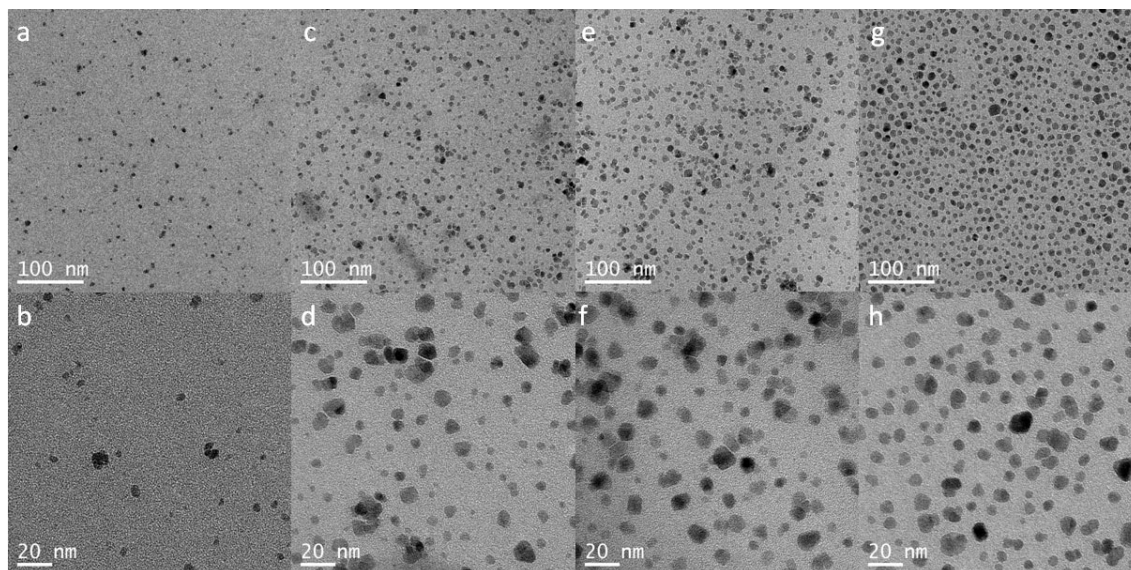


Figure 5.27: TEM images of Fe_3O_4 NPs synthesized in the oil bath at 180 °C as a function of the reaction time. $Fe(ac)_2$ dispersed in benzylalcohol was grown to iron oxide NPs in the oil bath at 180 °C for (a), (b) 1 h, (c), (d) 4 h, (e), (f) 8 h and (g), (h) 24 h. They were stabilized with PEG(5)-nitroDOPA, re-dispersed in Millipore water and air dried on a carbon coated Cu TEM grid.

indicated by TEM images (Figure 5.27). These TEM images could be misleading for judging the concentration of NPs because of size dependent NP segregation. To minimize such bias, all samples were prepared identically. Thus, differences seen on these TEM images should not only be assigned to segregation effects. More likely, differences in concentrations of large cores were related to the fact that fractions taken after 1 h and 4 h synthesis still contained ultrasmall NPs as can be seen on the TEM images taken with a $100'000 \times$ magnification (Figure 5.27b and d). These ultrasmall NPs were not visible at lower magnifications and made the NP concentration appear low (Figure 5.27a-d). Only very few if any of these ultrasmall NPs were visible in batches where NPs were grown at 180 °C for 24 h (Figure 5.27h).

Similar trends were observed for NPs synthesized at 160 °C (Figure 5.28). However, compared to NPs grown at 180 °C which reached core radii of ≈ 5 nm within 24 h, those grown at 160 °C had to be grown for ≈ 4 days until similar core radii were obtained. Because crystal growth is a thermally activated process, that can be described with an Arrhenius equation [423], it was expected that NPs grow slower at 160 °C than at 180 °C.

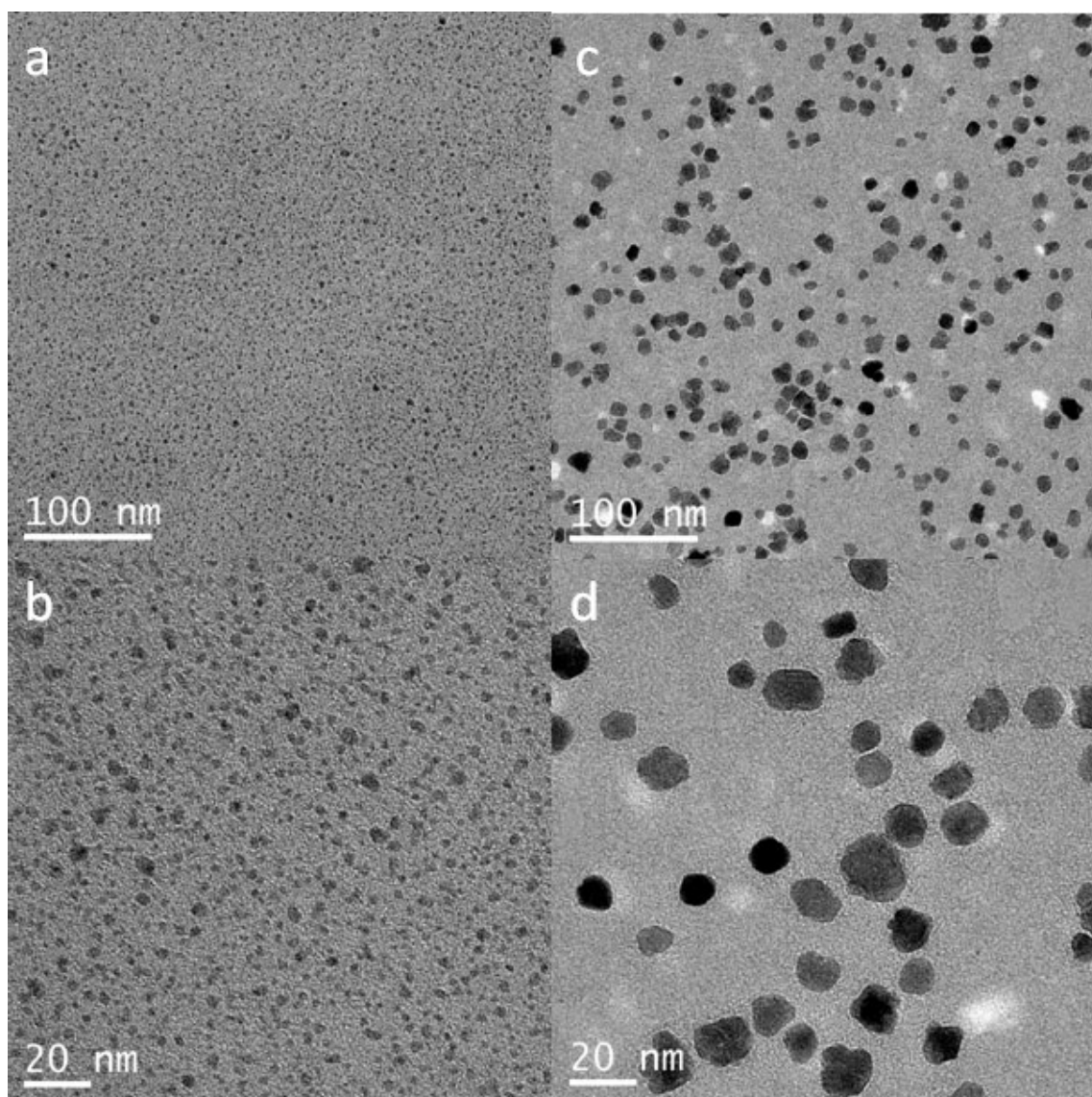


Figure 5.28: TEM images of Fe_3O_4 NPs synthesized in the oil bath at 160 °C as a function of synthesis time. $Fe(ac)_2$ dispersed in benzylalcohol was heated in the oil bath to 160 °C for (a), (b) 24 h and (c), (d) 4 d. They were stabilized with PEG(5)-nitroDOPA and re-dispersed in Millipore water before they were air dried on a carbon coated Cu TEM grid.

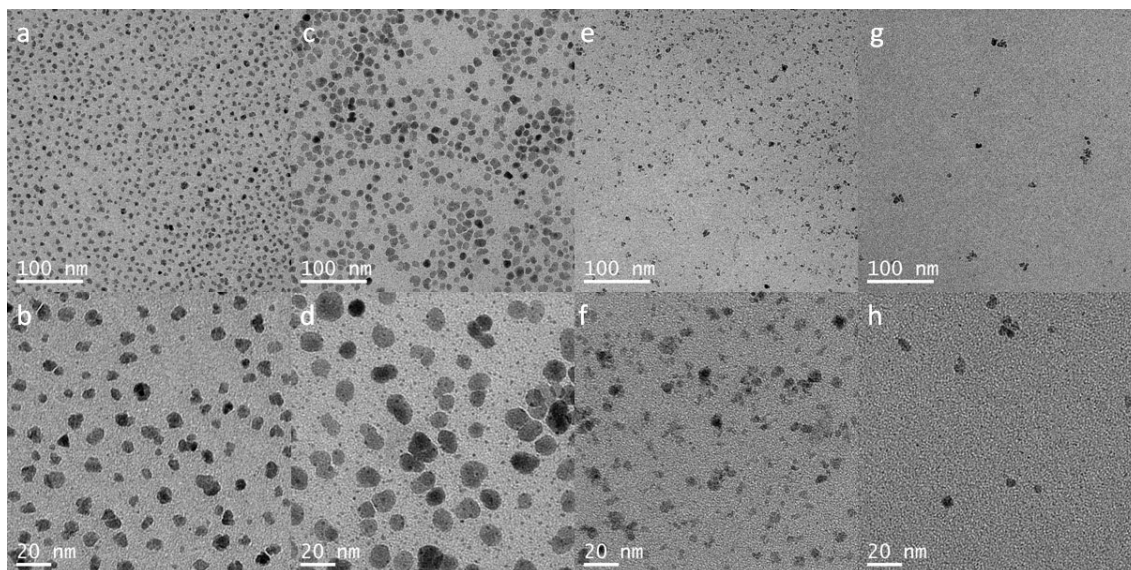


Figure 5.29: TEM images of iron oxide NPs synthesized from two different precursors. (a)-(d) $Fe(ac)_2$ and (e)-(h) $Fe(acac)_3$ was dispersed in benzylalcohol and heated for 1 h to 140 °C before the temperature was raised to (a), (b) and (e), (f) 160 °C and (c), (d) and (g), (h) 180 °C where the NPs were grown for 4 h before they were stabilized with PEG(5)-nitroDOPA and re-dispersed in Millipore water and air dried on a carbon coated Cu TEM grid.

5.4.3 Influence of the Temperature Ramping Procedure

Because $Fe(ac)_2$ is not well soluble in benzylalcohol at room temperature, the precursor/benzylalcohol dispersion was magnetically stirred at 70 °C for 1 h before the temperature was raised. This procedure was previously suggested to decrease the NP core size distribution [321]. The onset of NP growth could visually easily be followed by the color change from a brown precursor/benzylalcohol dispersion to a black iron oxide NP dispersion.

However, if benzylalcohol based $Fe(ac)_2$ or $Fe(acac)_3$ dispersions were kept at 140 °C for 1 h before they were heated to 180 °C to grow NPs, a bimodal NP size distribution was observed after growing NPs for 4 h (Figure 5.29 b, d, f and h). This indicates that ultrasmall NPs serving as nuclei were efficiently formed at 140 °C, however, the system did not reach equilibrium after 4 h reaction time.

Table 5.3: Saturation magnetizations of uncoated Fe_3O_4 NPs synthesized with the non-aqueous sol-gel method.

heating method during synthesis	r_{core} (nm)	M_s (emu/g Fe_3O_4)
MW	4.0	16.3
MW	7.0	44.4
oil bath	2.5	43.5
oil bath	5	47.5

5.5 Magnetic Properties of Iron Oxide Nanoparticles

5.5.1 Saturation Magnetization of Iron Oxide Nanoparticles

Most of the applications of iron oxide NPs make use of their magnetic properties. One essential parameter that describes magnetic properties of a material is its saturation magnetization (M_s). The higher the M_s of NPs is, the easier they can be magnetically separated and ferried to desired locations. Furthermore, a high M_s of NPs locally induces higher magnetic field gradients if dispersed in solutions and subjected to an external homogeneous magnetic field. These magnetic field perturbations are responsible for changed relaxivities r_2 measured in MRI. Thus, the higher the NP M_s , the more effective are MR contrast agents. M_s of iron oxide NPs was thus measured with VSM as described in section 4.3.1.

The M_s of uncoated 2.5 nm core radius NPs synthesized in the oil bath was 8% below the M_s of 5 nm core radius NPs (Figure 5.30 and Table 5.3). Furthermore, the M_s of NPs with core radii of $\approx 4 - 5$ nm was almost three times lower if they were synthesized in the MW compared to those synthesized in the oil bath (Table 5.3 and Figure 7.22). The low M_s of iron oxide NPs synthesized in the MW likely is related to the large fraction of ultrasmall NPs. Because of their minuscule size, ultrasmall NPs hardly contribute to the overall M_s [34, 421].

As described in chapter 1, the M_s of superparamagnetic NPs is considerably below that of the respective bulk material [35]. Furthermore, well in agreement with literature [33, 34], the M_s of NPs measured in this thesis decreased with decreasing iron oxide core radius irrespective whether NPs were synthesized in the oil bath or MW. The decrease in M_s with decreasing NP size might be related to surface anisotropy effects [36] that become more pronounced with decreasing core radius due to an increased surface : volume ratio. Such surface effects will be discussed in more details in chapter 7.

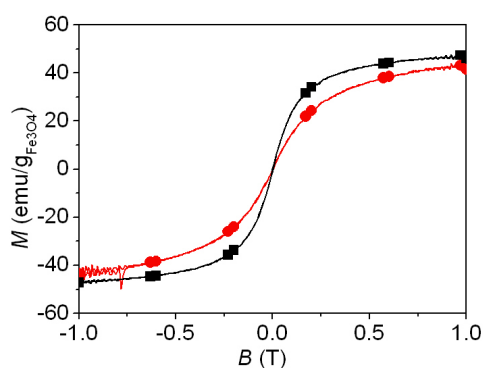


Figure 5.30: Magnetization of iron oxide NPs synthesized in the oil bath measured with VSM. Iron oxide NPs synthesized in the oil bath for 24 h at 150 °C (●) and 180 °C (■) were superparamagnetic. However, the M_s of the smaller, 2.5 nm core radius NPs synthesized at 150 °C was 8% below that of 5 nm core radius NPs synthesized at 180 °C.

Magnetic Neutron Scattering

As a result of the monomodal core size distribution and the higher M_s of iron oxide NPs synthesized in the oil bath compared to those synthesized in the MW, the former NPs yielded anisotropic SANS scattering patterns if analyzed with polarized neutrons as can be seen in Figures 5.31 and 5.32. The magnetic scattering of 2.5 nm core radius NPs, seen as anisotropic 2D scattering pattern in Figures 5.31a and 5.32a and d and a non-zero difference spectra in Figures 5.31c and 5.32c and 5.32f was considerably weaker compared to the 5 nm cores. Furthermore, PEG(1.5)-nitroDOPA stabilized 2.5 nm core radius NPs showed a more pronounced anisotropic 2D scattering pattern compared to that of PEG(5)-nitroDOPA stabilized 2.5 nm cores. Scattering techniques are sensitive to the vol% rather than the number of scatterers. Therefore, the total vol% NPs was kept constant at 5 vol%. However, as will be shown in chapter 8, the dispersant layer thickness decreases with decreasing PEG molecular weight. Therefore, the core concentration of 2.5 nm core radius NPs stabilized with PEG(5)-nitroDOPA was with ≈ 0.02 vol% more than two times lower compared to that of PEG(1.5)-nitroDOPA stabilized 2.5 nm core radii analogues (≈ 0.05 vol%).

The weaker magnetic scattering of the PEG(1.5)-nitroDOPA stabilized 2.5 nm core radius NPs compared to PEG(5)-nitroDOPA stabilized 5 nm core radius NPs likely is related to the lower vol% of cores and the lower M_s of the former NPs (Table 5.3). However, especially the difference in the magnetic scattering of 2.5 nm core radius NPs stabilized with PEG(5)-nitroDOPA and PEG(1.5)-nitroDOPA respectively (cf. Figure 5.32c and f) illustrates the importance of the core concentration on the magnetic scattering measured

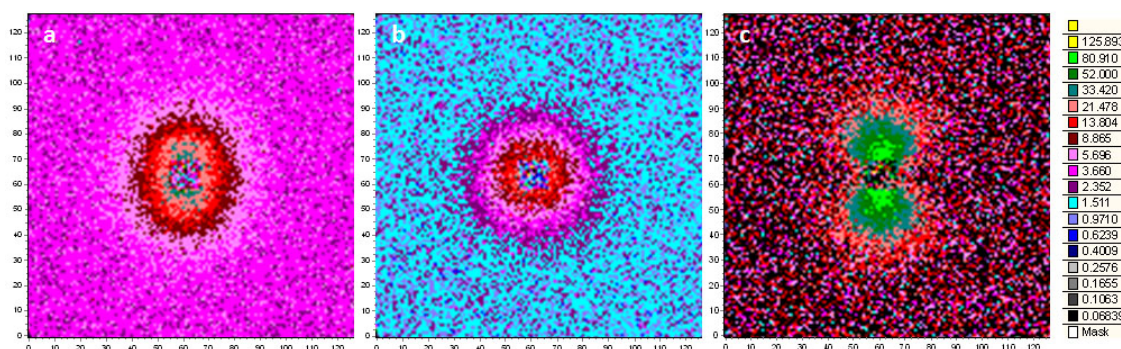


Figure 5.31: 2D SANS data of PEG(5)-nitroDOPA stabilized 5 nm core radius iron oxide NPs synthesized in the oil bath. PEG(5)-nitroDOPA stabilized 5 nm core radius iron oxide NPs were analyzed with polarized neutrons similar to PEG(5)-nitroDOPA stabilized iron oxide NPs which were synthesized in the MW (Figure 5.14). PEG(5)-nitroDOPA stabilized iron oxide NPs were dispersed in D_2O at a total concentration of 5 vol% yielding a core concentrations of 0.3 vol%. Neutrons were polarized (a) parallel and (b) antiparallel to the static magnetic field. (c) The resulting anisotropic difference spectra, that shows a $\sin(\Psi)^2$ dependence, can be attributed to magnetic scattering caused by the Fe_3O_4 cores.

with polarized neutrons. Thus, the core concentration of 4 nm core radius iron oxide NPs synthesized in the MW was, because of the predominance of ultrasmall NPs, likely too low to yield magnetic scattering (Figure 5.7).

5.5.2 SAR of Iron Oxide Nanoparticles Synthesized in the Oil Bath

The specific adsorption rate (SAR) determines how effectively NPs generate heat if they are exposed to an alternating magnetic field (AMF). This is of paramount importance if such NPs are to be used as antennas in hyperthermia treatment or to actuate thermoresponsive materials. Therefore, SAR values of NPs synthesized in the oil bath were measured as described in section 4.3.3.

The SAR values measured for PEG(5)-nitroDOPA stabilized Fe_3O_4 NPs are in the range of reported values for iron oxide NPs of comparable size [27, 364]. According to Figure 5.30, Fe_3O_4 NPs investigated in this thesis are superparamagnetic. Thus, the SAR of NPs in an AMF field can be attributed to Néels and eventually Brownian relaxation [27, 424].

Dependence of the SAR on the Core Size

As can be seen in Figure 5.33, the SAR of 2.5 nm radius Fe_3O_4 NPs was considerably smaller than that of 4 nm and 5 nm core radius Fe_3O_4 NPs respectively. However, the

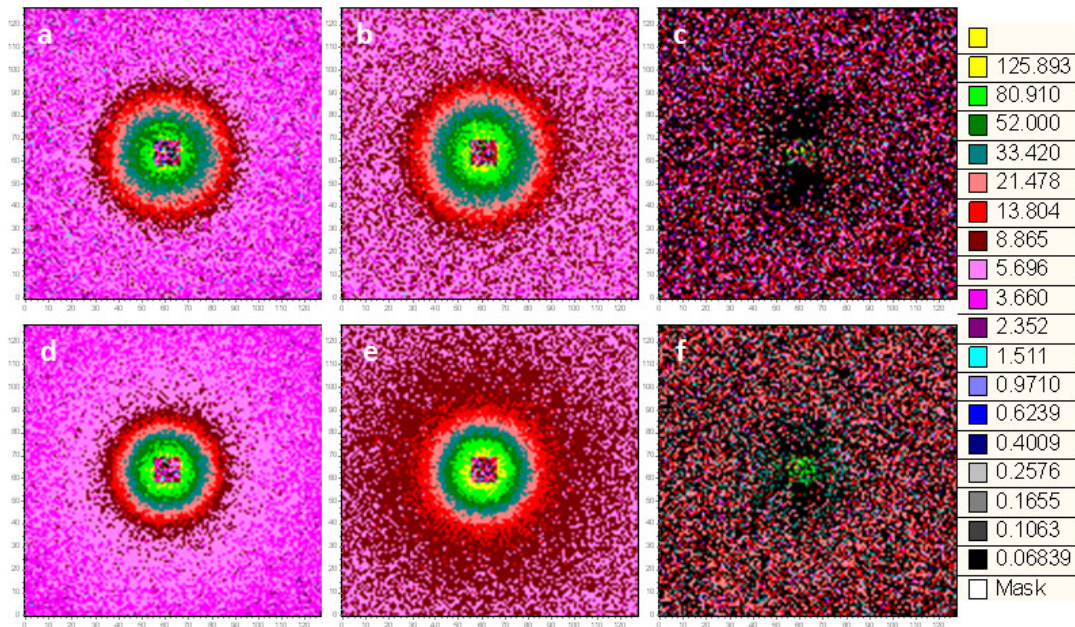


Figure 5.32: 2D SANS data of PEG-nitroDOPA stabilized 2.5 nm core radius iron oxide NPs. SANS was measured on 2.5 nm core radius iron oxide NPs synthesized in the oil bath and stabilized with PEG(1.5)-nitroDOPA (a-c) and PEG(5)-nitroDOPA (d-f) dispersed in D_2O with polarized neutrons. Neutrons were polarized parallel (a, d) and antiparallel (b, e) to the external magnetic field. (c) and (f) are the resulting difference spectra. The difference spectra show a weak $\sin(\Psi)^2$ dependence that can be attributed to magnetic scattering caused by the Fe_3O_4 cores. The total volume percentage of the samples was kept constant at 5 vol%. Because PEG(1.5)-nitroDOPA yields in a lower brush thickness, and thus the core volume percentage is higher for PEG(1.5)-nitroDOPA stabilized NPs (≈ 0.05 vol%), their scattering pattern was more anisotropic compared to that of PEG(5)-nitroDOPA stabilized NPs (core concentration ≈ 0.02 vol%). This illustrates the influence of core concentration on the magnetic scattering. The color code indicates how strongly neutrons were scattered and is given in a logarithmic scale.

SAR did not increase with increasing core radius but peaked for 4 nm core radius NPs. That the SAR has a maximum at an optimum core size is well known from literature [27, 28, 425]. According to equation 4.24, the SAR for small NPs is $\propto M_s^2 V$. Because M_s increases with increasing NP core radius (Figure 5.30), the SAR increases accordingly. If NPs become ferromagnetic, hysteresis losses are the predominate heat source. Hysteresis losses are proportional to the coercive field B_c (Figure 1.2). They are caused by domain wall (so-called Bloch wall) motions. It was shown that $B_c \propto r^6$ for NPs $< r_{crit}$. For these NPs, Bloch wall motions are hindered due to pinning effects at the NP surface. However, if NPs are $> r_{crit}$, pinning effects become smaller with increasing NP size. In the latter case, B_c is $\propto r^{-1}$. Therefore B_c and the SAR peak at a NP size of r_{crit} . r_{crit} for Fe_3O_4 NPs was calculated to be 13.5 nm [27].

However, experimental results on unstabilized, agglomerated NPs yielded a maximum in

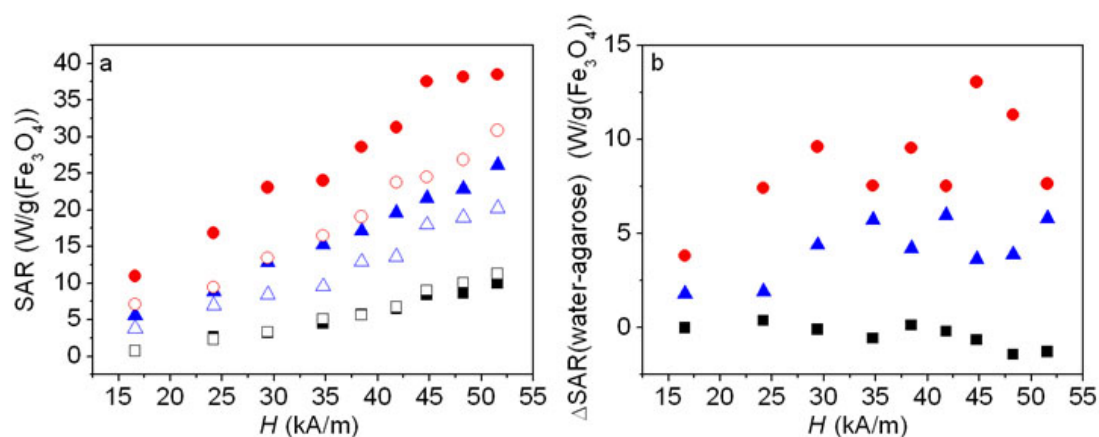


Figure 5.33: SAR measurements of PEG(5)-nitroDOPA stabilized Fe_3O_4 NPs synthesized in the oil bath. (a) SAR measurements performed at room temperature and frequencies between 2.3×10^5 and 2.4×10^5 Hz. Fe_3O_4 NPs with core radii of 2.5 nm (■), 4 nm (●) and 5 nm (▲) were stabilized with PEG(5)-nitroDOPA and dispersed in water (filled symbols) and embedded in agarose (empty symbols). While NPs dispersed in water can heat through Néels and Brownian relaxation if subjected to an AMF, NPs embedded in agarose can generate heat only through Néels relaxation. (b) The difference of SAR values measured in water and agarose respectively are shown as a function of the applied magnetic field. They can be assigned to losses caused by Brownian relaxations.

SAR at a core radius of 23 nm [27]. The SAR of iron oxide NPs surface modified with Pluronic peaked at a NP radius of 7 nm [425]. The maximum SAR obtained in this thesis was measured on 4 nm core radius NPs (Figure 5.33). The large differences in NP sizes where the SAR peaked might be attributed to differences in NP stability.

Néels vs. Brownian SAR Contributions

No significant difference in the SAR of 2.5 nm core radius NPs was measured whether they were dispersed in water or embedded in agarose (Figure 5.33). It strongly suggests, that the SAR of these NPs is almost exclusively related to Néels relaxations. This is in contrast to Fe_3O_4 NPs that had a core radius of 4 nm and 5 nm. The SAR of the latter NPs was significantly higher if they were stabilized with PEG(5)-nitroDOPA and dispersed in water compared to being embedded in agarose. The difference in SAR of NPs dispersed in water and embedded in agarose (Δ SAR) can be attributed to contributions from Brownian relaxation. 4 nm core radius NPs, that had the highest SAR values, also had the highest Δ SAR values (Figure 5.33b).

However, well in agreement with literature reports on Néels and Brownian contributions for NPs of similar sizes [43], Néels relaxation was the main contribution to the SAR for all investigated core radii. This is especially beneficial for applications where Fe_3O_4 are

used as antennas to locally deliver heat to actuate smart materials or treat diseases. For these applications, NPs ideally are immobilized in materials or firmly bound to desired sites. Thus, NP rotation, leading to Brownian relaxation losses, is hampered or might even be destructive to the scaffold material in question. The SAR of such immobilized superparamagnetic NPs should thus mainly rely on Néels relaxation contributions.

5.6 Discussion

Iron oxide NPs synthesized by aqueous precipitation had a broad core size distribution that was difficult to control. The core size of iron oxide NPs synthesized by the non-aqueous sol-gel method could be controlled by adjusting the synthesis temperature and time. However, NPs synthesized in the MW had a bimodal core size distribution where the fraction of ultrasmall NPs vastly dominated the fraction of larger cores. In contrast, iron oxide cores synthesized in the oil bath were monomodally distributed.

Because the surface area of ultrasmall NPs seen especially in batches synthesized in the MW completely dominates the total surface area, the bimodal core size distribution not only influences magnetic properties and scattering results as exemplified with SANS and SAXS measurements, but the strongly increased surface area severely influences NP characterization in general. It is also questionable whether the relative ratio between ultrasmall and larger cores is reproducible. This ratio is expected to change if synthesis conditions such as synthesis time are changed. Moreover, even if both NP size fractions are well stabilized by adding high amounts of dispersants, the influence of ultrasmall NPs on NP stability (*e.g.* through depletion effects) is unknown and has to be investigated separately. Although it would be interesting to study the influence of ultrasmall core-shell NPs on the stability of larger core-shell NPs, a better understanding of core-shell NPs that have a defined monomodal size distribution *e.g.* as a function of the dispersant anchor, layer thickness and packing density is required before more complex *e.g.* bimodal core size distributions can be understood in detail. Additionally, most of the applications aim for maximal magnetization of NPs, which is, as shown with SANS experiments, severely reduced by the presence of ultrasmall NPs. Thus, it is highly desirable for this work to synthesize monomodally distributed NPs.

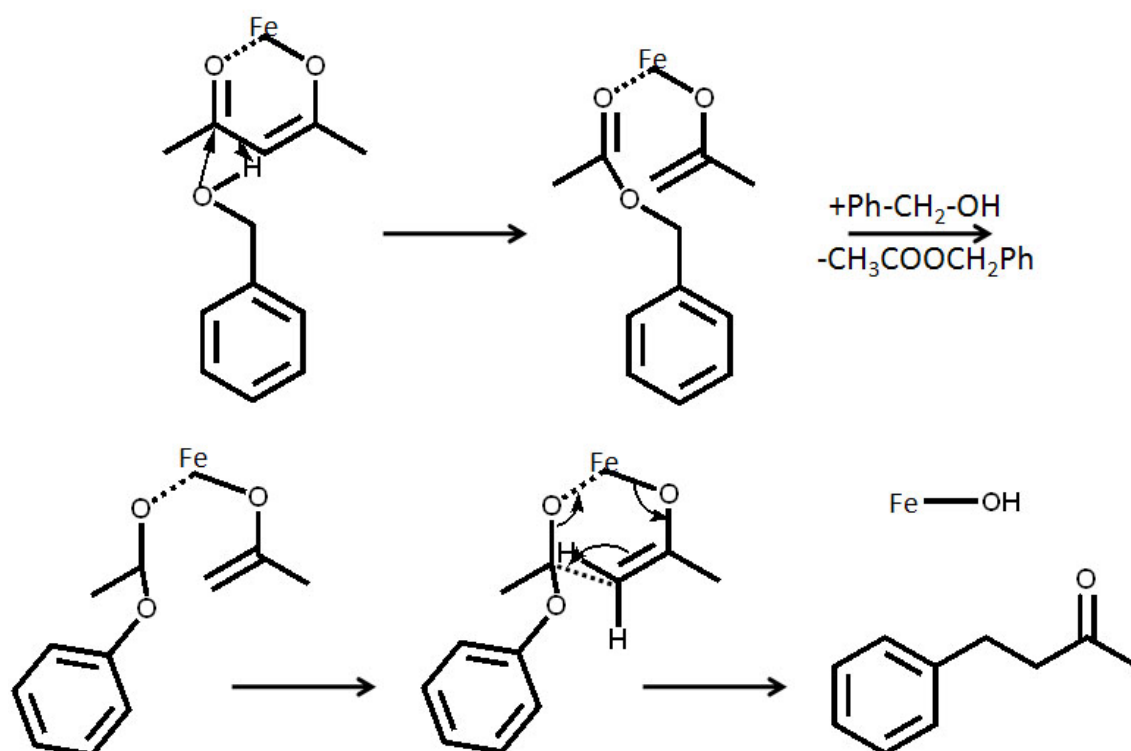


Figure 5.34: Reaction mechanism of $Fe(acac)_3$ with benzylalcohol. The suggested reaction mechanism for the non-aqueous synthesis iron oxide NPs starting from $Fe(acac)_3$ dissolved in benzylalcohol under inert atmosphere [394].

5.6.1 Influence of Organic Reactions on the Presence of Ultrasmall Nanoparticles

The non-aqueous sol-gel NP synthesis relies on organic reactions between precursors and solvents. Such organic reactions involved in the iron oxide NP formation have been reported for the most abundantly used precursor, namely $Fe(acac)_3$, if dispersed *e.g.* in pyrrolidone [426] and benzylalcohol [394].

If $Fe(acac)_3$ is dispersed in pyrrolidone, it is thought that 1/3 of the Fe^{3+} ions of $Fe(acac)_3$ are reduced through thermal decomposition of pyrrolidone under the formation of carbon monoxide yielding Fe_3O_4 NPs [426].

However, the yield of stable iron oxide NPs synthesized from $Fe(acac)_3$ and surface modified with PEG(5)-nitroDOPA was considerably lower than that of NPs synthesized from $Fe(ac)_2$ counterparts which were identically surface modified. As will be shown in chapter 7, PEG(5)-nitroDOPA binds primarily to surface bound Fe(II). The fact that iron oxide NPs synthesized from $Fe(acac)_3$ could not be well stabilized with PEG(5)-nitroDOPA might indicate that the oxidation of Fe^{3+} ions during the synthesis was in-

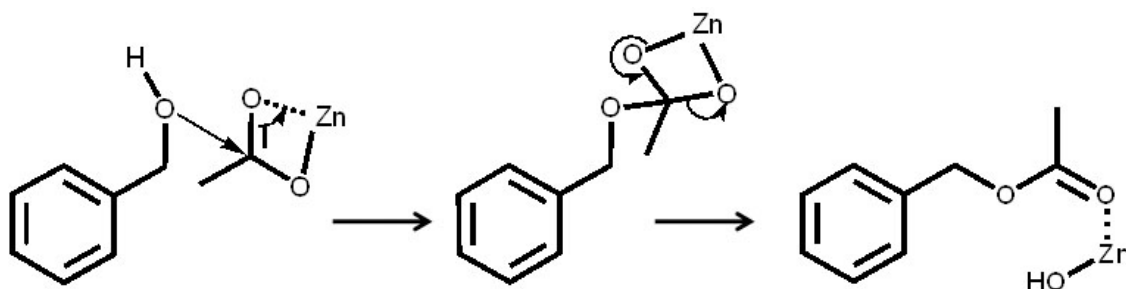


Figure 5.35: Reaction mechanism of $Zn(ac)_2$ with benzylalcohol. This scheme suggests a reaction mechanism for the non-aqueous synthesis of ZnO NPs starting from $Zn(ac)_2$ dissolved in benzylalcohol under inert atmosphere [396]. A similar reaction mechanism might also apply to iron oxide NP formation if synthesized from $Fe(ac)_2$.

complete.

If $Fe(acac)_3$ is dispersed in benzylalcohol, it is thought to react with benzylalcohol according to Figure 5.34. Benzylalcohol nucleophilically attacks one of the carbonyl groups of acetylacetonate leading to alcoholysis. In a following ligand exchange reaction, benzyl alcohol coordinates the Fe center followed by the release of benzyl acetate. The coordinated benzyl alkoxide is attacked by the enolate resulting in a release of 4-phenyl-3-butene-2-one. The Fe bound hydroxy group can bind another Fe center resulting in small clusters that serve as nuclei. If Fe_3O_4 NPs are synthesized from $Fe(acac)_3$, one third of the Fe^{3+} centers of $Fe(acac)_3$ are reduced to Fe^{2+} during the synthesis. It is suggested that 4-phenyl-3-butene-2-one is oxidized to 4-phenyl-2-butanone while two iron centers are reduced [394].

In contrast, the reaction of $Fe(ac)_2$ in benzylalcohol is, to the best of our knowledge, unpublished. However, a reaction mechanism for the formation of ZnO starting from $Zn(ac)_2$ in benzylalcohol has been described (Figure 5.35) [396]. A similar reaction mechanism might apply to the synthesis of iron oxide NPs from $Fe(ac)_2$ in benzylalcohol. During the NP synthesis, $2/3$ of the Fe^{2+} ions have to be oxidized to obtain Fe_3O_4 NPs. However, Fe^{2+} readily oxidizes to Fe^{3+} if traces of O_2 are present. Thus, this oxidation might occur spontaneously without the addition of oxidation agents as the resulting NPs clearly have a spinel structure (Figure 5.7) and present Fe(II) ions at the surface, as well be shown in chapter 7. Thus, NPs synthesized from $Fe(ac)_2$ consist of Fe_3O_4 .

Influence of Reaction Temperature on Nanoparticle Size

Because NP growth is a thermally activated process, NP size is known to increase with synthesis temperature and time [397, 399, 427]. This is in good agreement with our findings for NPs grown in the oil bath (Figure 5.23) and for the increased size for the fraction of larger NPs grown in the MW (Figure 5.4).

Nanoparticle Morphology

The morphology of iron oxide NPs was found to depend on the precursor irrespective whether they were heated in the MW or in the oil bath. Iron oxide NPs synthesized from $Fe(ac)_2$ in benzylalcohol were closer to spheres compared to NPs synthesized from $Fe(acac)_3$ (Figure 5.15 and 5.29). However, the majority of the reported non-aqueous synthesis routes start from $Fe(acac)_3$ and result in nicely shaped iron oxide NPs [395]. This is likely related to the fact, that no oleic acid was added to the precursor dispersion during the synthesis of Fe_3O_4 NPs in this thesis. Because one of the primary aims of this thesis was to study the influence of anchor groups on the NP stability, synthesis protocols that do not rely on capping agents were preferred. Consequently, the effect of oleic acid on the NP size and size distribution was not further investigated.

The ill-defined shape of iron oxide NPs synthesized from $Fe(acac)_3$ in benzylalcohol is also related to the type of solvent used during synthesis. NPs synthesized from $Fe(acac)_3$ were more spherical compared to those synthesized from $Fe(ac)_2$ if pyrrolidone was used instead of benzylalcohol. This is likely due to the known high affinity of pyrrolidone to Fe^{3+} which makes pyrrolidone a capping agent similar to oleic acid. Capping agents are known to result in a more spherical NP morphology and a greatly reduced NP size distribution [395].

Nanoparticle Size Distribution

Despite that the synthesis of oxide NPs from $Fe(ac)_2$ and $Fe(acac)_3$ involves different organic reactions and influences the morphology of NPs, ultrasmall NPs were seen in batches synthesized in the MW irrespective whether they were formed from $Fe(ac)_2$ or $Fe(acac)_3$ and for batches synthesized in benzylalcohol or pyrrolidone. However, ultrasmall NPs were not always seen for iron oxide NP batches synthesized in the oil bath. Thus, it is unlikely, that these ultrasmall NPs are directly related to the organic reactions

involved in the NP formation. Furthermore, that ultrasmall NPs were also seen in batches of PEG(5)-nitroDOPA stabilized MnO and $Mg(OH)_2$ NPs synthesized in the MW indicates that the observed bimodal size distribution is not restricted to iron oxide.

All NPs investigated were stabilized with PEG(5)-nitroDOPA. NPs had to be stabilized because ultrasmall NPs could only be detected with TEM if they were embedded in spanning films formed by PEG(5)-nitroDOPA. However, we believe that formation of ultrasmall NPs is not a result of the NP stabilization process, because ultrasmall NPs were absent in batches synthesized in the oil bath from $Fe(ac)_2$ in benzylalcohol for 24 h at $T > 140$ °C. Hence, their presence must be related to the synthesis procedure.

It has been shown that the precursor concentration in a supersaturated solution influences r_{crit} of nuclei above which they start to grow. Thus, the precursor concentration influences the final NP size if the system is in equilibrium [416, 423, 428]. If the precursor concentration is decreased, the iron ion concentration in solution should decrease which would lead to slower nucleation and growth. However, if the solution gets depleted of iron ions, NPs smaller than the critical radius should dissolve to feed the growth of larger cores. Thus, less ultrasmall NPs would be expected to form at low precursor concentration. This, however, was not observed experimentally for NPs synthesized in the MW. All batches of NPs synthesized in the MW contained ultrasmall NPs irrespective of the precursor concentration (Figure 5.15 a and b). Thus, NPs grown in the MW for maximally 1 h are unlikely to be in a thermodynamic equilibrium.

If the synthesis time is sufficiently long, oxide NPs grow by Ostwald ripening. Ostwald ripening describes an equilibrium situation, where NPs with radii (r) smaller than a critical value (r_{crit}) are dissolved to feed the growth of NPs with $r > r_{crit}$. The large surface curvature and the high surface : volume ratio of ultrasmall NPs renders them thermodynamically unstable resulting in their dissolution [428, 429]. The dissolved atoms then drive growth of NPs with $r > r_{crit}$ [423, 428–431]. Thus, in equilibrium, NPs have a monomodal, ideally monodisperse size distribution where all NPs are larger than r_{crit} .

Reaction Kinetics

The presence of ultrasmall NPs in all investigated NP systems synthesized in the MW and the fact that ultrasmall NPs were seen irrespective of the precursor concentration indicate, that those systems are not in a thermodynamic equilibrium. The MW synthesis route has been reported to massively increase reaction kinetics compared to conventional synthesis routes [396]. This increased reaction kinetics combined with the shortened synthesis time

might not allow the system to reach a thermodynamic equilibrium.

Ester elimination is one of the organic reactions responsible for nucleation and NP growth of ZnO NPs starting from benzylalcohol based $Zn(ac)_2$ dispersions. This reaction has been reported to be more than 10 times faster in the MW compared to dispersions heated in the oil bath. Furthermore, NP growth was almost 3 times faster if NPs were synthesized in the MW compared to oil bath synthesized counterparts [396]. Because nucleation is 10 times more accelerated and NP growth only 3 times if the synthesis is performed in the MW rather than in the oil bath, the ratio of nuclei : growing NPs is likely to be higher for batches synthesized with the former process, resulting in excessive nuclei with $r < r_{crit}$. NPs synthesized in the oil bath, where nuclei were formed at 140 °C and NPs were subsequently grown at 180 °C, showed a bimodal core size distribution which evidenced that Ostwald ripening was not completed after 4 h. In analogy, Ostwald ripening might not be completed for NPs synthesized in the MW for 30 min - 1 h considering that NP growth is 3 times faster in the MW compared to conventional methods like oil bath heating [396]. Furthermore, NPs synthesized in the MW for 30 min had a considerably higher M_s compared to those synthesized for 3 min. This might indicate that the fraction of ultrasmall NPs, that have a very small magnetic moment [15], decreases with increasing synthesis time. Thus, the size distribution of NPs grown in the MW is expected to become monomodal if NPs were grown considerably longer than 1 h.

5.6.2 Characterization of the Size and Size Distribution of Nanoparticles

Core sizes quantified with different characterization methods cannot directly be compared to each other. While scattering techniques such as SANS, SAXS and DLS yield intensity weighted averages ($\propto r^6$), XRD results in volume weighted ($\propto r^3$) and TEM in number weighted ($\propto r^1$) core sizes. Especially if the core size distribution is broad or bimodal, different weightings result in different mean values.

Furthermore, certain techniques have poor sensitivities towards a certain size fraction and all techniques have detection limits. Because of the limited lattice planes ultrasmall NPs have, these NPs could not be detected with diffraction techniques such as XRD or analyzed in the reciprocal space with TEM. Furthermore, because contrast in TEM increases with sample thickness, larger NPs are easier to visualize compared to ultrasmall, individually stabilized NPs. Because of the constraints and limits of each characterization technique, a combination of different, complementary techniques is required to properly

characterize NP sizes. Only if results obtained with the different characterization techniques agree with each other, is the system well characterized. Especially if techniques used to characterize NP sizes are sensitive towards different sizes (*e.g.* TEM which yields number weighted and SAXS providing intensity weighted averages) are in agreement with each other, it can be assumed that the whole system and not only a fraction thereof is characterized.

5.7 Summary

The composition and average size of iron oxide cores determine their M_s and SAR values. This is particularly important for applications. However, for more fundamental studies such as investigations of the influence of the dispersant layer thickness and packing density on NP stability, a monomodal, ideally narrow core size distribution and close control over the NP composition are crucial. Therefore, the NP core synthesis, that determines the mean core size, its distribution and composition, is crucial both for scientific investigations and industrial applications.

While aqueous precipitation methods result in a rather broad core size distribution, non-aqueous sol-gel methods generally allow close control over the mean core size and its distribution. Precursors such as $Fe(ac)_2$ and $Fe(acac)_3$ and solvents were shown to influence NP morphology and the average NP size. However, NPs synthesized in the MW for less than 1 h were bimodally distributed independent on the precursor, precursor concentration and solvent used. In batches of iron oxide NPs grown from $Fe(ac)_2$ in benzylalcohol for 3 min, the fraction of ultrasmall, 0.9 nm core radius NPs thousandfold exceeded the fraction of 4 nm core radius NPs. In contrast to the MW assisted NP synthesis, a benzylalcohol based dispersion of $Fe(ac)_2$ resulted in a monomodal iron oxide core size distribution if heated in the oil bath for at least 24 h. For the latter synthesis route, the average core radius could be controlled by adjusting the synthesis temperature.

Ultrasmall NPs greatly increase the surface : mass ratio and make a quantitative characterization of surface related properties difficult. Because this quantification is a main goal of this thesis, most of the NPs used in this thesis were synthesized from $Fe(ac)_2$ dispersed in benzylalcohol and heated in the oil bath. However, ultrasmall NPs present in batches synthesized in the MW were not detected until SANS and SAXS measurements on individually stabilized NPs were performed. Only after SANS and SAXS measurements indicated the presence of ultrasmall NPs where TEM sample preparation protocols

adjusted and optimized so that ultrasmall NPs could be directly visualized with TEM. Therefore, some parts of this thesis will deal with NPs synthesized in the MW. The fact, that these ultrasmall NPs were only noticed after NPs could be well sterically stabilized and therefore characterized with a large range of colloidal size sensitive techniques might be one of the main reasons why these ultrasmall NPs have not been previously reported despite that many different people have worked with oxide particles synthesized under similar conditions in the MW.

Anchors for Steric Stabilization of Iron Oxide Nanoparticles

6.1 Background

As outlined in chapter 1, good NP stability under physiologic conditions combined with a controlled surface presentation of functionalities are stringent requirements for successful applications of NPs especially in the biomedical field. This can only be achieved if NPs are sterically, rather than electrostatically stabilized. An attractive strategy to gain control over NP stability and interfacial chemistry is to sterically stabilize NPs with low M_w dispersants. There are two different ways to surface modify NPs with low M_w dispersants: these dispersants can be grafted from or grafted to the NP surface (Figure 6.1).

Grafting Dispersants From Surfaces

If dispersants are grafted from the surface, initiators are first firmly immobilized on the NP surface. After monomers have been added, a chemical reaction is initiated where dispersants are grown *in situ* [1]. While the grafting from strategy can yield high dispersant packing densities, control over the dispersant layer thickness is comparably difficult due to a relatively high dispersant polydispersity. Furthermore, because these chains are grown *in situ*, there is limited control over the surface functionality of the resulting dispersants (Figure 6.1a) [432].

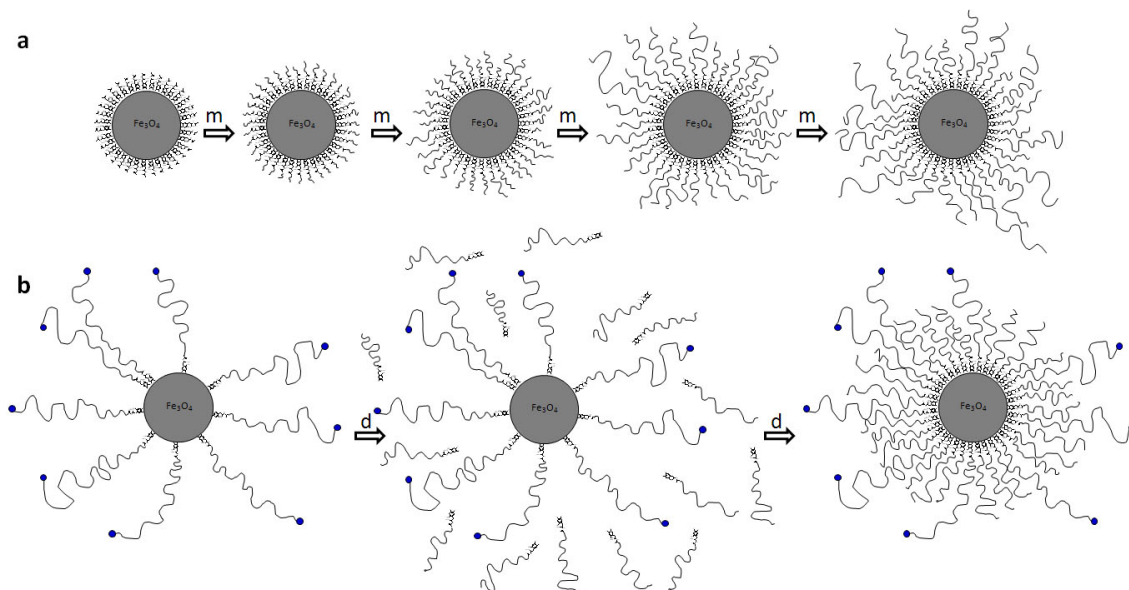


Figure 6.1: Approaches to sterically stabilize NPs using low molecular weight dispersants. (a) If NPs are stabilized through the "grafting-from" strategy, initiators are immobilized on the NP surface before monomers (m) are added to the solution and the reaction is initiated. "Grafting-from" strategies are able to yield higher packing densities. However, the control over the dispersant layer thickness is limited and the polydispersity of the resulting dispersants high. (b) An alternative route is the "grafting-to" method where dispersants (d) are synthesized prior to their adsorption on the NP surface. This allows for close control over the dispersant layer thickness by controlling the dispersant M_w and configuration and the surface-presentation of functional groups. The latter can be tuned by co-adsorbing differently functionalized dispersants.

Grafting Dispersants to Surfaces

The alternative grafting to technique is based on pre-synthesized and characterized multifunctional dispersants that spontaneously assemble through a suitable anchor to the surface. The advantage of such self-organizing approaches is that they are cost effective, have a high reproducibility and are easy to up-scale. They are widely used to functionalize flat (2D) and NP (3D) surfaces [256, 258, 259]. The grafting density of polymer brushes assembled on flat surfaces is lower compared to those obtained by grafting polymers from the surface [432]. However, the polymer layer thickness and presentation of functional groups can easily be tailored by choosing appropriate polymer molecular weights and architectures. A particular advantage of the grafting to approach (for both flat and NP surfaces) is the feasibility to tailor the density of one or multiple surface-presented (bio)ligands by co-adsorbing differently functionalized dispersants in one or several subsequent assembly steps (Figure 6.1b).

Anchors

Irrespective whether dispersants are grafted to or from the surface, they have to be firmly adherent to the NP surface through suitable anchors. Ideally, the binding affinity of anchors is not only high enough to strongly bind spacers to uncoated NPs but it should also be able to replace hydrophobic capping agents such as oleic acid which are often used to synthesize monodisperse Fe_3O_4 NPs [395]. Naturally, anchors that meet these stringent requirements for coupling dispersants to NPs can perform the same function to graft non-fouling polymer brushes to planar substrates and to immobilize initiators on a surface to graft polymers from these substrates. Despite its importance and to the best of our knowledge, no systematic study has been performed on the influence and optimization of anchors, which determine the binding affinity and adsorption reversibility of dispersants on iron oxide NP surfaces.

To this end, eight different catechol derivatives and the carboxy group (-COOH), an anchor often used to stabilize iron oxide NPs in organic solvents *e.g.* with oleic acid [433, 434], were selected to shed light on the design principles for optimized anchors for dispersants to sterically stabilize iron oxide NPs. To selectively test the influence of the eight anchors, the latter were covalently linked to a PEG with a molecular weight of 5 kDa (PEG(5)). PEG was chosen because of its good biocompatibility already described in chapter 1. The choice of the PEG molecular weight is explained in chapter 8.

6.2 Effect of Anchor on Nanoparticle Stability

Despite that dopamine and DOPA are often used anchors to sterically stabilize iron oxide NPs for numerous biomedical applications [267, 435, 436], successful *in vivo* applications of individually stabilized iron oxide NPs using these anchors are scant. This might partially be related to the stringent requirements such as a high binding affinity and low reversibility even at elevated temperatures and physiologic salt concentration inflicted on anchors if applied in biomedical applications. We found a nitro-substituted catechol derivative anchor which meets these requirements *in vitro* and vastly outperforms the well known catechols if used to immobilize low M_w dispersants to iron oxide NP surfaces. The *in vivo* performance of nitroDOPA as anchor to sterically stabilize iron oxide NPs is currently tested in collaborations with the University Hospitals in Aachen and Innsbruck. Thus, novel dispersants containing this optimized anchor might allow new, more advanced applications of such NPs.

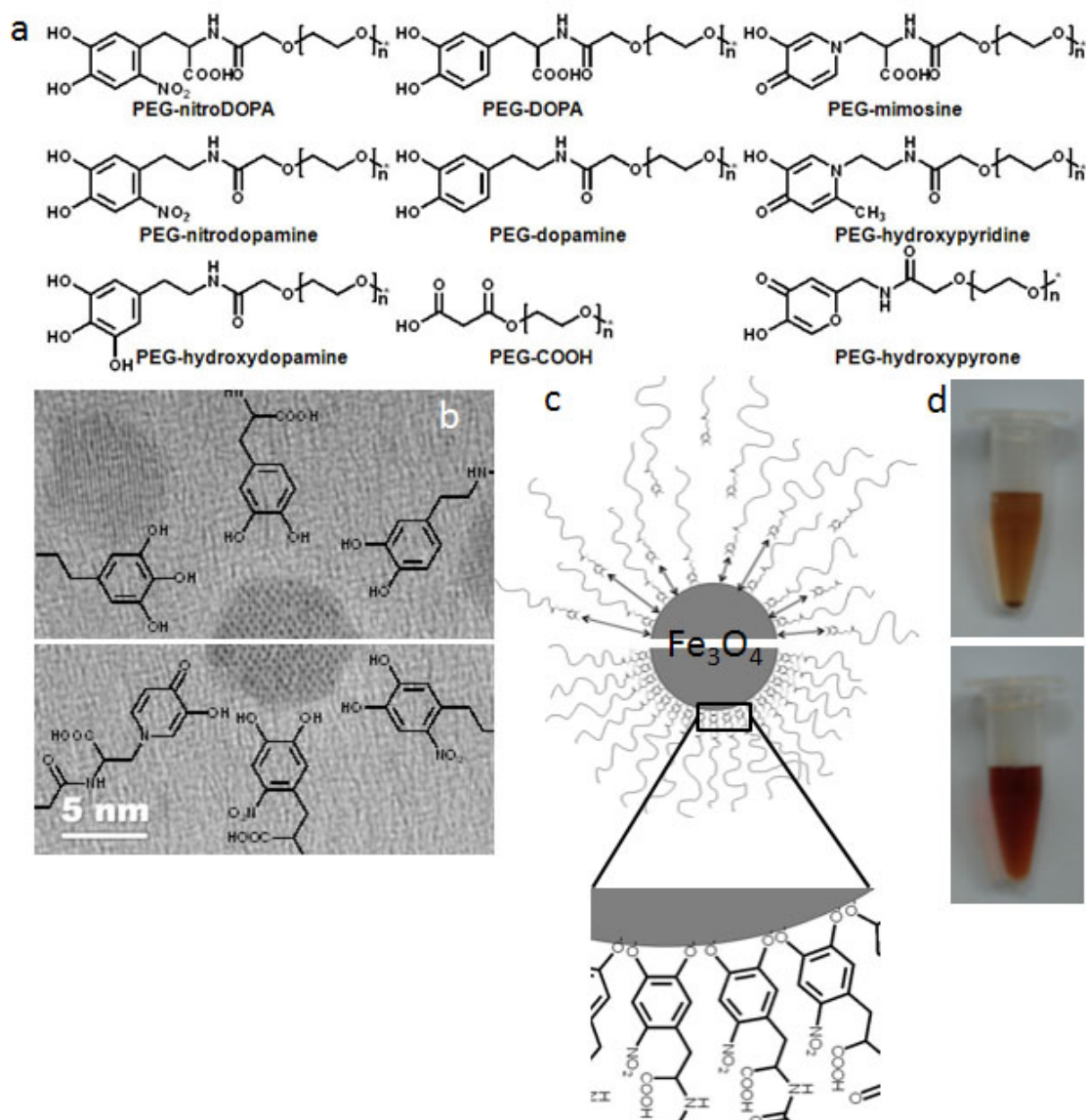


Figure 6.2: Stabilization of iron oxide NPs. (a) Chemical structures of investigated dispersants with a degree of polymerization of $n \approx 114$ for PEG(5). (b) HRTEM of iron oxide NPs air-dried on a carbon supported Cu-grid. The hexagonal pattern of the inverse spinel structure of Fe_3O_4 oriented in the (010) direction is clearly visible proving the high crystallinity of these NPs. Dispersants with different anchors have been grafted to as-synthesized iron oxide NPs. (c) Stabilization of iron oxide cores with PEG(5)-dopamine which adsorbed reversibly (top) and the irreversibly adsorbing PEG(5)-nitroDOPA (bottom). (d) While PEG(5)-dopamine stabilized NPs agglomerated and thus visibly precipitated (top), PEG(5)-nitroDOPA coated NPs were stable even after having kept them in HEPES for 20 h at 90 °C (bottom). The initial NP concentration was 1 mg(iron oxide)/ml. Thus, the color difference between PEG(5)-dopamine and PEG(5)-nitroDOPA stabilized NP dispersions is a result of the precipitation of PEG(5)-dopamine stabilized NPs.

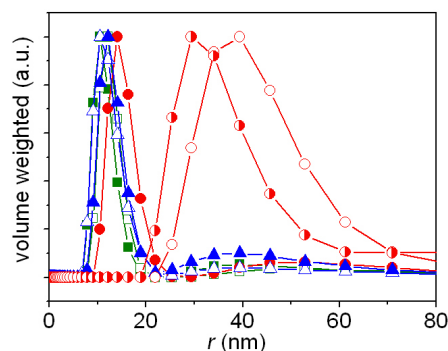


Figure 6.3: DLS of PEG(5)-anchor stabilized iron oxide NPs synthesized in the MW. The volume weighted hydrodynamic radius of iron oxide NPs synthesized by MW heating to 180 °C for 3 min, and stabilized with PEG(5)-nitroDOPA (-■-), PEG(5)-nitrodopamine (-□-), PEG(5)-DOPA (-●-), PEG(5)-dopamine (-○-), PEG(5)-hydroxydopamine (-◐-), PEG(5)-mimosine (-▲-) and PEG(5)-hydroxypyridine (-△-) dispersed in HEPES containing 150 mM NaCl (pH = 7.4) at room temperature shows the influence of the anchor on NP stability.

6.2.1 Influence of Anchor on Nanoparticle Stability at Elevated Temperatures

The nine different PEG-based dispersants investigated are shown in Figure 6.2. Among these anchors, in addition to dopamine [256, 258, 259], also L-DOPA [267] has been reported to lead to good iron oxide NP stability. Carboxy groups are often used as anchors to synthesize and stabilize iron oxide NPs in organic solvents [395, 433, 434]. In addition, dopamine and DOPA, and other investigated catechol derivatives chemically differ only in one carboxy group. Hence, PEG(5)-COOH was included in this study to elucidate the effect of the carboxy group on the binding of anchors.

Single domain Fe_3O_4 cores prepared by the MW assisted non-aqueous sol gel route [321] as described in chapters 3 and 5 had a radius of 3 ± 0.5 nm and were stabilized with the different dispersants through a simple grafting to method (Figure 6.2). As-synthesized iron oxide NP cores were added to a DMF-based dispersant solution. Dispersants were adsorbed at 50°C for 24 h before excessive dispersants were removed and DMF was exchanged through 24 h dialysis against Millipore water. Stabilized iron oxide NPs were freeze-dried and re-dispersed in the desired media at appropriate concentrations.

PEG(5)-hydroxypyridone and PEG(5)-COOH stabilized iron oxide NPs did not pass filters with a cut-off of 200 nm. This demonstrated that these NPs instantaneously agglomerated to clusters larger than 200 nm in diameter. NP agglomeration was caused by too low anchor affinity. Consequently, no reliable DLS could be performed in this case.

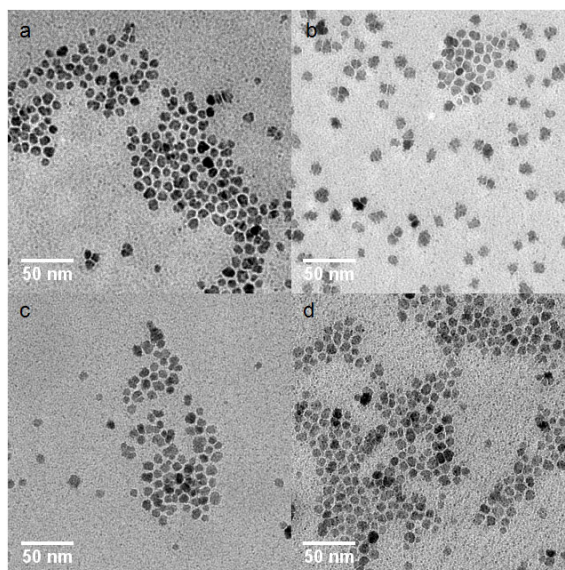


Figure 6.4: Overview TEM micrographs of iron oxide NPs. Iron oxide NPs stabilized with (a) PEG(5)-nitroDOPA, (b) PEG(5)-nitrodopamine, (c) PEG(5)-mimosine and (d) PEG(5)-DOPA air dried on a 10 nm thick carbon film supported Cu grid.

The average volume-weighted hydrodynamic radius of iron oxide NPs individually stabilized with PEG(5)-nitroDOPA, PEG(5)-nitrodopamine, PEG(5)-mimosine, PEG(5)-DOPA, and PEG(5)-hydroxypyridine, respectively, and dispersed in HEPES containing 150 mM NaCl (pH=7.4) at room temperature was 11.5 ± 1 nm whereas that of PEG(5)-dopamine and PEG(5)-hydroxydopamine stabilized NPs was considerably larger, indicating superior stability of NPs stabilized with the former dispersants (Figure 6.3). Especially the hydrodynamic radius of PEG(5)-nitroDOPA and PEG(5)-nitrodopamine stabilized iron oxide NPs dispersed in HEPES at 40°C was considerably lower (11.5 nm) and the NP size distribution narrower when compared to previously reported PEG(5)-silane stabilized iron oxide NPs at room temperature (41 nm [437] and 44 nm [438] respectively) and PEG(3)-dopamine (≈ 25 nm) and PEG(6)-dopamine (≈ 35 nm) stabilized iron oxide NPs dispersed in phosphate buffered saline (PBS) [266] despite similar iron oxide core radii. An average dispersant shell thickness of 8.5 nm was calculated as the difference between the iron oxide core radius of 3 nm and the hydrodynamic radius of 11.5 nm.

PEG-nitroDOPA stabilized iron oxide NPs could be freeze-dried, stored as a powder for at least 3 months or alternatively re-dispersed in Millipore water and stored for at least 4 months without noticeable change in particle stability and hydrodynamic radius after re-dispersing and diluting them in HEPES containing 150 mM NaCl. Stabilized iron oxide cores dispersed in Millipore water and dried on a carbon supported TEM Cu grid were clearly separated from each other. Because the dispersant shell is invisible on these TEM

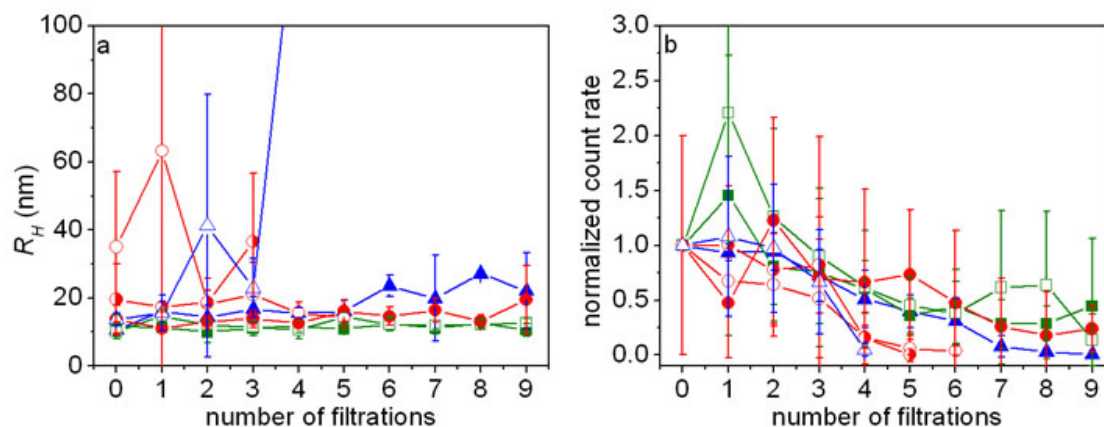


Figure 6.5: Binding reversibility of dispersants. The binding reversibility of dispersants was measured by successive filtrations of iron oxide NPs, synthesized in the MW by growing them at 180 °C for 3 min, stabilized with PEG(5)-nitroDOPA (-■-), PEG(5)-nitrodopamine (-□-), PEG(5)-DOPA (-●-), PEG(5)-dopamine (-○-), PEG(5)-hydroxydopamine (-●-), PEG(5)-mimosine (-▲-) and PEG(5)-hydroxypyridine (-△-). The system was equilibrated at room temperature for 24 h between every filtration step before the (a) hydrodynamic radius and (b) normalized count rate of these NPs was measured. Statistics was done on 6 independent samples.

image due to poor TEM contrast of PEG especially if adsorbed on a 10 nm thick carbon support, cores are expected to be separated by the invisible PEG shell. That cores are not agglomerated even though they were air dried on a carbon supports indicates that these cores are individually stabilized by a dispersant layer surrounding the iron oxide cores (Figure 6.4).

6.2.2 Dispersant Binding Reversibility

Nanoparticle Stability Under Dilute Conditions

The binding reversibility of these dispersants adsorbed on iron oxide NPs was tested by successive centrifuge filtrations and re-dispersions of HEPES containing 150 mM NaCl based NP dispersions. Thereby, free dispersants could efficiently be removed with centrifuge filters resulting in NP agglomeration if dispersants were reversibly bound to the NP surface. However, the same NPs remained stable if dialyzed for 30 days against Millipore water. This apparent discrepancy is due to hindered diffusion of free dispersants during dialysis despite that the dialysis tubes had a cut-off of 12-14 kDa, more than twice the M_w of dispersants investigated here. Therefore, centrifuge filtration is a more suitable method to remove excessive dispersants and test dispersant binding reversibility compared to dialysis.

Based on NP stability at elevated temperatures and dispersant binding reversibility, dispersants could be grouped into three categories, namely good, intermediate and poor dispersants. While NPs stabilized using poor (PEG-dopamine, PEG-hydroxydopamine, PEG-hydroxypyridine, PEG-hydroxypyronone and PEG-carboxyl) and intermediate (PEG-mimosine and PEG-DOPA) dispersants agglomerated within 0-3 and 5-7 filtrations, respectively, as can be seen in the increase in hydrodynamic radius and an increase followed by a decrease in count rates, NPs stabilized with dispersants containing good (PEG-nitroDOPA and PEG-nitrodopamine) dispersants, remained stable for more than 9 filtrations (Figure 6.5). The derived count rate increased if NPs agglomerate due to stronger scattering of larger agglomerates (the intensity of scattered light scales with r^6 [368]) before it decreases upon sedimentation of those agglomerates. Because iron oxide NP suspensions analyzed here had been equilibrated for 24 h after each filtration before DLS was measured, larger agglomerates could sediment and thus were not analyzed by DLS any more.

Even though the standard deviations in Figure 6.5b were large, the normalized derived count rates of PEG(5)-dopamine, PEG(5)-hydroxydopamine and PEG(5)-hydroxypyridine stabilized iron oxide NPs decreased faster compared to those stabilized with PEG(5)-nitroDOPA, PEG(5)-nitrodopamine, PEG(5)-DOPA and PEG(5)-mimosine, well in agreement with the change in hydrodynamic radius that increased more rapidly for iron oxide NPs stabilized with the former dispersants. The change in count rate is a very good and sensitive measure of agglomeration and sedimentation reducing the artifact of looking only at the change of the hydrodynamic radius of stable NPs remaining in solution.

Except of NPs stabilized with PEG(5)-dopamine, PEG(5)-hydroxydopamine and PEG(5)-hydroxypyridine, the hydrodynamic radii of stabilized NPs did not change even after NPs have been filtered 9 times (Figure 6.5a). However, the count rate of PEG(5)-mimosine stabilized NPs decreased faster compared to those stabilized with PEG(5)-nitroDOPA (Figure 6.5b). This apparent contradiction can be related to the fact, that only the stable, not sedimented NP fraction was analyzed with DLS. Thus, if NPs agglomerate to sizes that sediment within 24 h, the hydrodynamic radius of the dispersed NPs does not change whereas the count rate decreases. If, however, agglomerates form but are too small to sediment during 24 h, the count rate increases because it scales with r^6 . Thus, by comparing changes in count rates and in the hydrodynamic radius, one can capture both effects, namely NP agglomeration and sedimentation.

In summary, these DLS results indicated essentially irreversible binding of nitroDOPA

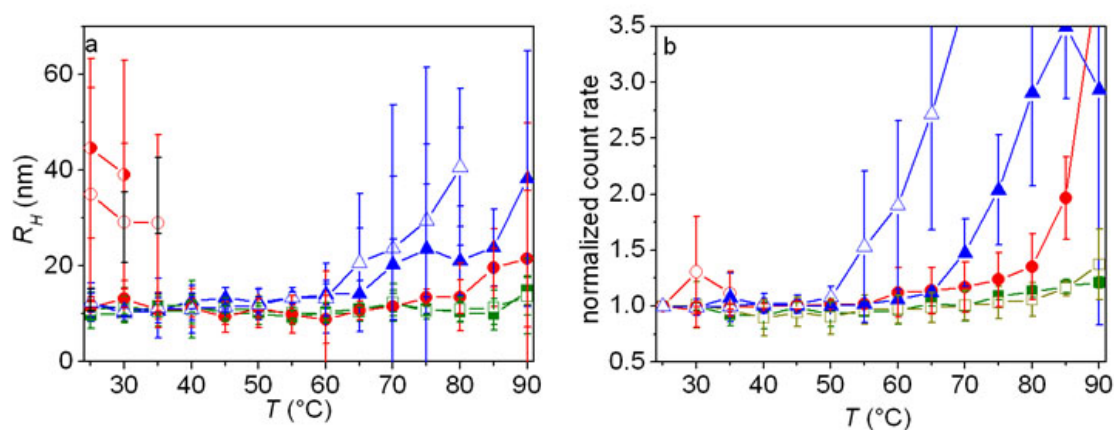


Figure 6.6: DLS of PEG(5)-anchor stabilized iron oxide NPs synthesized in the MW. Temperature dependence of the (a) hydrodynamic radius and (b) normalized count rate of iron oxide NPs synthesized in the MW by growing them at 180 $^{\circ}\text{C}$ for 3 min stabilized with PEG(5)-nitroDOPA (-■-), PEG(5)-nitrodopamine (-□-), PEG(5)-DOPA (-●-), PEG(5)-dopamine (-○-), PEG(5)-hydroxydopamine (-●-), PEG(5)-mimosine (-▲-) and PEG(5)-hydroxypyridine (-△-). Statistics was done on 5 - 7 identical independent samples.

and nitrodopamine to iron oxide NPs under physiologic conditions, in contrast to other investigated anchors. However, NPs stabilized through intermediate anchors agglomerated considerably slower compared to those stabilized through poor anchors. This can be seen by the faster decay of the count rate and the rapid increase in the hydrodynamic radius of the latter NPs.

Temperature Dependent Nanoparticle Stability

If dispersants adsorb reversibly, the dispersant desorption rate k_{off} is expected to increase with increasing temperature. Therefore, agglomeration of NPs stabilized with reversibly adsorbing dispersants is expected to be faster at elevated temperatures. In agreement with these expectations, individually stabilized iron oxide NPs dispersed in HEPES containing 150 mM NaCl started to irreversibly agglomerate below body temperature if they were stabilized with dispersants containing poor anchors. NPs stabilized with intermediate dispersants agglomerated between 60 and 80 $^{\circ}\text{C}$, as indicated by an increase in the hydrodynamic radius and an increase followed by a decrease in the derived count rate due to NP agglomeration and sedimentation, respectively (Figure 6.6). On the other hand, NPs stabilized with PEG(5)-nitroDOPA and PEG(5)-nitrodopamine (called PEG(5)-nitrocatechols) could be repeatedly heated up to 90 $^{\circ}\text{C}$ without noticeable agglomeration or changes in the derived count rates. That PEG(5)-nitrocatechol stabilized NPs did not agglomerate up to 90 $^{\circ}\text{C}$ demonstrates that NP agglomeration was not caused by a collapse of the

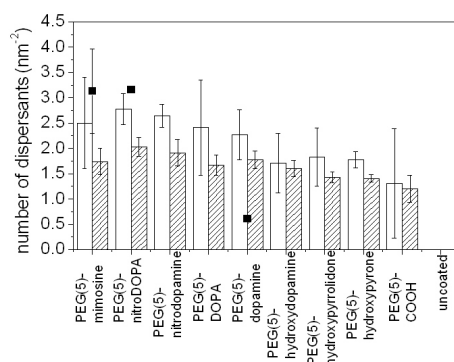


Figure 6.7: PEG-anchor packing densities on iron oxide NPs synthesized in the MW. The dispersant packing densities of iron oxide NPs stabilized with 8 mg(dispersant)/mg(NP) obtained by TGA (empty bars) are compared with those obtained from XPS analysis (dashed bars). Data points (■) correspond to the dispersant packing density calculated from the TGA results of stabilized NPs dispersed in Millipore water which had been externally heated to 90 °C for 1 h before excessive dispersants were removed. Statistics was done on 3-5 identical samples.

PEG shell (PEG has an inverse solubility/temperature relationship [439, 440]) but rather by desorption of reversibly binding dispersants. This supports results obtained from the NP filtration experiments where dispersants could be categorized into three groups (Table 6.1). PEG(5)-nitrocatechol stabilized NPs were considerably more stable than those stabilized with the well-known PEG(5)-DOPA and PEG(5)-dopamine. That NPs stabilized with the latter dispersant already agglomerated below body temperature might be one of the reasons why successful *in vivo* studies of iron oxide NPs which were individually stabilized with PEG-dopamine are elusive.

6.2.3 Dispersant Packing Density

Table 6.1: The dispersant packing density on NPs measured by TGA and XPS respectively has been compared with that measured on flat surfaces. Statistics was done on 3-6 independent samples.

dispersant	anchor quality affinity	$\frac{\text{dispersant}}{\text{nm}^2}$ on NPs (TGA)	$\frac{\text{dispersant}}{\text{nm}^2}$ on NPs (XPS)	$\frac{\text{dispersant}}{\text{nm}^2}$ on flat surfaces (XPS)	$\frac{EG}{\text{nm}^2}$ on NPs	$\frac{EG}{\text{nm}^2}$ on flat surfaces
PEG(5)-nitroDOPA	good	2.8±0.3	2.5±0.2	0.31±0.01	296±27	36±2
PEG(5)-nitrodopamine	good	2.6±0.2	2.5±0.4	0.26±0.01	290±40	30±1
PEG(5)-mimosine	intermediate	2.5±0.9	2.2±0.3	0.32±0.01	247±37	36±1
PEG(5)-DOPA	intermediate	2.4±0.9	1.8±0.4	0.26±0.00	210±50	30±0
PEG(5)-dopamine	poor	2.3±0.5	2.2±0.2	0.22±0.01	254±25	25±1
PEG(5)-hydroxydopamine	poor	1.7±0.6	2.2±0.2	0.15±0.00	254±26	17±0
PEG(5)-hydroxypyridine	poor	1.8±0.6	1.7±0.1	0.22±0.01	197±16	25±1
PEG(5)-hydroxypyrrone	poor	1.8±0.2	2.1±0.1	0.11±0.00	244±13	13±0
PEG(5)-COOH	poor	1.3±1.1	1.4±0.3	0.10±0.00	162±37	11±0

The dispersant packing density on iron oxide NPs was quantified by TGA and XPS (Figure 6.7 and Table 6.1). While the atomic $C_{\text{PEG}} : \text{Fe}$ ratio was determined by accounting for the ionization cross section, inelastic mean free path and transmission function for flat surfaces (equation 4.12), the spherical NP shape had to be considered when quantifying the $C_{\text{PEG}} : \text{Fe}$ ratio of dispersants adsorbed on NPs (equation 4.13). The obtained percentage weight losses measured between 200 and 400 °C by TGA (Figure 6.11a) were converted into dispersant packing densities assuming spherical iron oxide NPs with the core radius distribution shown in Figure 5.5 and an Fe_3O_4 density of 5.18 g/cm³ [379]. The ethylene glycol (EG) density was calculated based on the dispersant packing density measured by XPS for NPs and flat surfaces respectively (Table 6.1).

As a result of the unknown amount of ultrasmall NPs which were not taken into account for calculations of the dispersant packing density, values reported in Figure 6.7 and Table 6.1 are upper limits of dispersant packing densities. However, because different dispersants were adsorbed on identical NP batches, the relative differences in packing densities should still hold, irrespective of the concentration of ultrasmall NPs. A comparison between Figure 6.7 and Table 6.1 reveals that as the dispersant packing density increases, NP stability increases. It is highest for NPs stabilized with PEG(5)-nitrocatechols. To test the dispersant desorption at elevated temperatures, NPs dispersed in Millipore water had been externally heated to 90°C, before excessive dispersants were removed by filtration. The packing densities of PEG(5)-nitroDOPA and PEG(5)-mimosine stabilized NPs remained in the range of packing densities of as-stabilized NPs. However, that of PEG(5)-dopamine stabilized NPs decreased to 26% of the initial packing density. This correlated well with the filtration experiments shown in Figure 6.5 where k_{off} of on iron oxide NPs adsorbed PEG(5)-dopamine was markedly higher than that for PEG(5)-mimosine and PEG(5)-nitroDOPA. Thus, binding reversibility, dispersant packing density and NP stability are closely related to each other and strongly depend on the binding affinity of anchors to iron oxide NP surfaces.

Influence of the Mass Ratio Dispersant : Nanoparticle During Stabilization

To test the influence of the dispersant packing density on NP stability, temperature dependent DLS measurements were performed on Fe_3O_4 NPs stabilized with different amounts of PEG(5)-nitroDOPA (Figure 6.8). Even if dispersants were bound to NPs surfaces with high affinity anchors such as nitroDOPA, NPs were only stable up to 90 °C if coated with ≥ 6 mg(dispersant)/mg(NP) (Figure 6.8). This indicates that a high dispersant packing

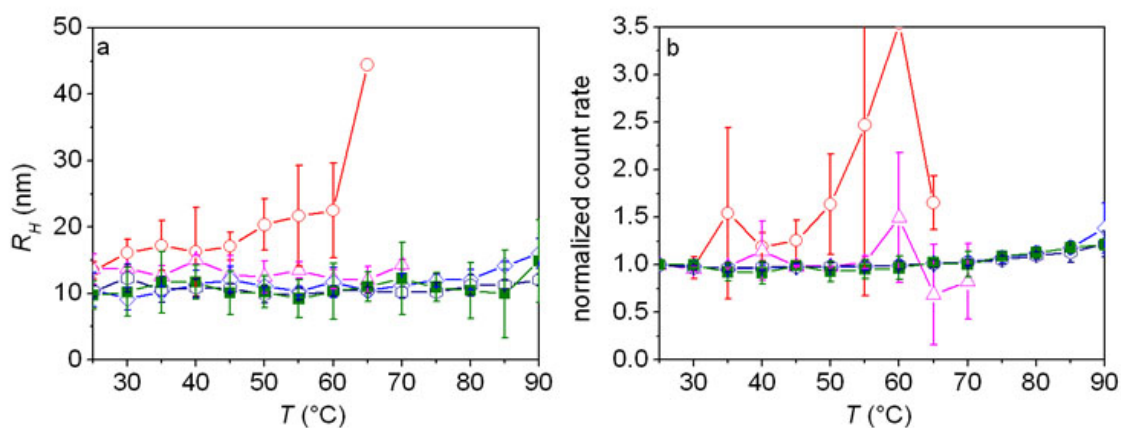


Figure 6.8: DLS of PEG(5)-nitroDOPA stabilized iron oxide NPs synthesized in the MW. The (a) hydrodynamic radius and (b) normalized count rate of iron oxide NPs grown in the MW at 180 °C for 3 min stabilized with 1 mg/mg(NP) (-○-), 2 mg/mg(NP) (-△-), 4 mg/mg(NP) (-◇-), 6 mg/mg(NP) (-□-) and 8 mg/mg(NP) (-■-). Statistics was done on 3-7 identical samples.

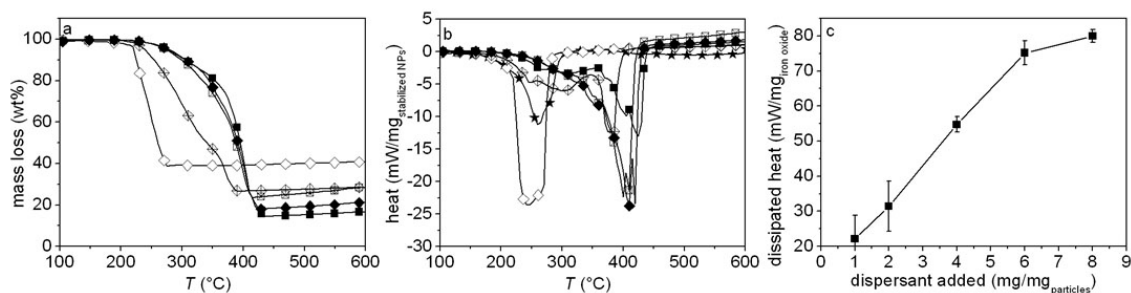


Figure 6.9: TGA and DSC of with PEG(5)-nitroDOPA coated iron oxide NPs synthesized in the MW. (a) TGA and (b) DSC graphs of PEG(5)-nitroDOPA stabilized iron oxide NPs synthesized in the MW by growing them at 180 °C for 3 min. NPs were stabilized with 1 mg(dispersant)/mg(NP) (-◇-), 2 mg(dispersant)/mg(NP) (-◇-), 4 mg(dispersant)/mg(NP) (-□-), 6 mg(dispersant)/mg(NP) (-◆-), 8 mg(dispersant)/mg(NP) (-■-), respectively, and uncoated iron oxide NPs (-★-). (c) The heat dissipated during temperature induced decomposition of the organic part of iron oxide NPs stabilized with different amounts of dispersants was measured by DSC. The dissipated heat was normalized to the iron oxide core weight. Statistics was done on 3-6 independent samples.

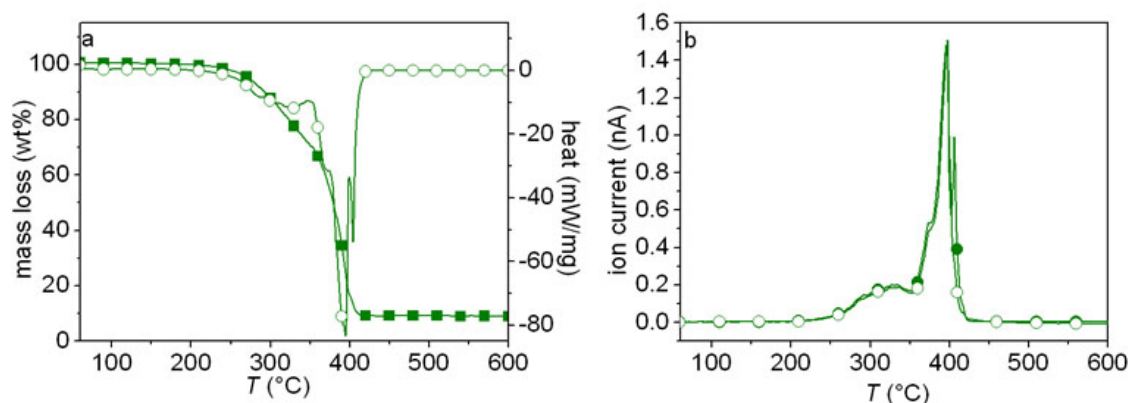


Figure 6.10: TGA and DSC measurements coupled to a MS of PEG(5)-nitroDOPA stabilized iron oxide NPs synthesized in the MW. (a) TGA (-■-)/DSC (-□-) measurements and (b) MS of the volatile products CO_2 (-●-) and H_2O (-○-) produced by TGA on PEG(5)-nitroDOPA stabilized iron oxide NPs. NPs were synthesized in the MW by heating them to 180 °C and growing them for 3 min. Statistics was done on 3-6 independent samples.

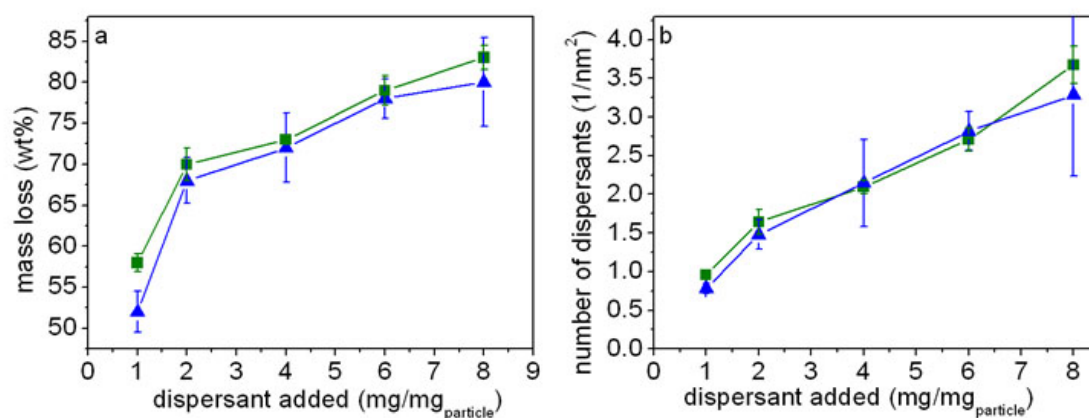


Figure 6.11: Quantification of the dispersant packing density on iron oxide NPs synthesized in the MW. Iron oxide NPs synthesized in the MW by growing them at 180 °C for 3 min were coated with different amounts of PEG(5)-nitroDOPA (-■-) and PEG(5)-mimosine (-▲-). Curve (a) shows the relative weight loss measured between 200 and 400 °C in the TGA. (b) The calculated numbers of dispersants adsorbed per nm^2 are shown. Statistics was done on 3-5 identical samples.

density is crucial for good NP stability especially at elevated temperatures.

To correlate NP stability to the dispersant packing density, simultaneous TGA and DSC measurements were performed on iron oxide NPs which were stabilized with different amounts of PEG(5)-nitroDOPA. The exothermic reaction around 255 °C (Figure 6.9b) seen in DSC measurements for uncoated NPs coincided with a mass loss of 20 wt% in TGA (Figure 6.9a). This is attributed to a decomposition of weakly physisorbed impurities (Figure 6.9). A similar exothermic peak was measured for iron oxide NPs stabilized with only 1 mg(PEG(5)-nitroDOPA)/mg(NP). If NPs were coated with 2 mg(dispersant)/mg(NP), two exothermic reactions around 255 °C and 380 °C were observed in DSC while two distinct slopes were measured with TGA. The onset of the mass loss was slightly shifted towards higher temperatures compared to NPs stabilized with 1 mg(dispersant)/mg(NP). The onset of the mass loss of NPs stabilized with 4-8 mg(dispersant)/mg(NP) coincided with that of NPs stabilized with 2 mg(dispersant)/mg(NP). However, considerably less mass was lost between 240 and 360 °C for NPs stabilized with 4-8 mg(dispersant)/mg(NP) compared to NPs stabilized with only 2 mg(dispersant)/mg(NP) whereas more mass was lost between 360 and 440 °C for the former NPs. Because the first reaction measured for NPs stabilized with 1 mg(dispersant)/mg(NP) coincided with that measured for uncoated NPs, it was assigned to the decomposition of impurities or the decomposition of PEG adsorbed on the iron oxide NP surface at a low packing density. The second exothermic reaction, which coincided with the main mass loss and consisted of equal amounts of CO_2 and H_2O measured *in situ* with MS (Figure 6.10), was assigned to the decomposition of PEG. For NPs stabilized with at least 4 mg(dispersant)/mg(NP), hardly any exothermic peak could be seen at 250 °C whereas the exothermic decomposition of PEG around 410 °C was evident. These results indicate that nitroDOPA replaced physisorbed impurities if NPs were stabilized with a sufficient amount of dispersants. The absence of nitrogen containing fragments in the mass spectra acquired during TG analysis further indicated quantitative removal of DMF during particle processing (Figure 6.10).

The mass loss and thus dispersant packing density started to level off at a mass ratio of dispersants : NPs = 6 : 1 (Figure 6.11). This indicates that the maximum dispersant packing density obtainable with the grafting to strategy was reached for iron oxide NPs synthesized in the MW and stabilized with PEG(5)-nitroDOPA. These TGA/DSC results are in good agreement with DLS findings where only NPs stabilized with at least 6 mg(dispersant)/mg(NP) NPs remained stable up to 90 °C (Figure 6.8). However, care should be exercised with the quantitative ratio of dispersants : iron oxide NPs required

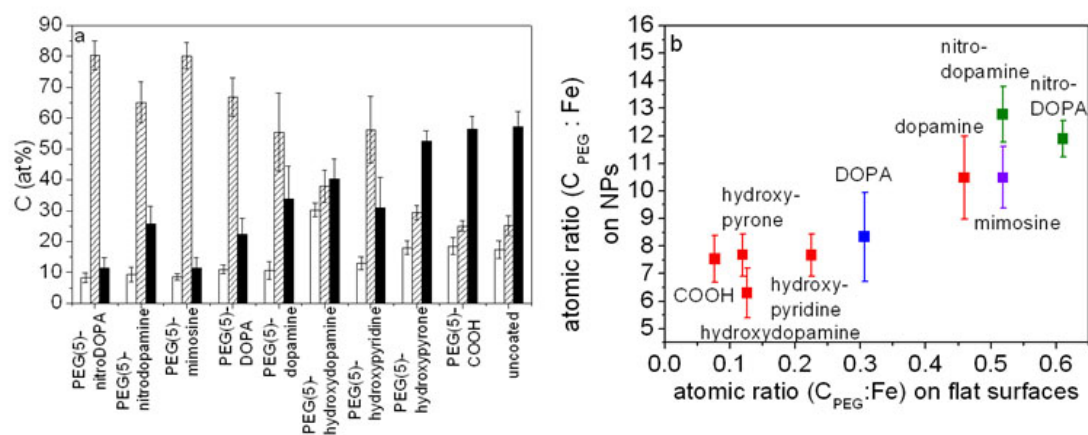


Figure 6.12: XPS studies of dispersants adsorbed on flat 2D and NP surfaces. (a) The atom percentage of C of PEG (C-O, empty), aliphatic C (C-C, C-H, dashed) and OH-conjugated carbons (C-OH and COOH, filled) of dispersants adsorbed on flat Fe_3O_4 surfaces was determined from XPS analysis. (b) The atomic ratio of $C_{PEG} : Fe$ of dispersants adsorbed on flat Fe_3O_4 surfaces correlates well with that of dispersants adsorbed on iron oxide NPs and indicates that the ability of dispersants to replace aliphatic contaminations is independent on surface curvature whereas the dispersant packing density is considerably higher on NPs as compared to flat surfaces. Statistics was done on 3-6 independent samples.

to completely sterically stabilize these NPs. Because of the large unknown fraction of ultrasmall NPs, it is likely that the larger cores were stable already at considerably lower ratios of dispersants : iron oxide NPs if they were monomodally distributed.

Influence of Surface Curvature on Dispersant Packing Density

To investigate the influence of the surface curvature on the dispersant packing density, PEG(5)-anchors were adsorbed on flat (2D) surfaces and on Fe_3O_4 NPs (3D) synthesized in the MW. The NPs had a core radius comparable to the dispersant layer thickness which yields a high surface curvature on the length scale of the dispersant dimensions. Because iron oxide absorbs light, the dispersant layer thickness on 2D surfaces could not be determined with ellipsometry. Thus, the dispersant coverage was estimated based on the intensity of the $C1s : Fe2p$ peaks measured with XPS. As a comparison, the same XPS analysis was also performed on iron oxide NPs stabilized with PEG(5)-anchors.

The $C1s$ peaks acquired with XPS on flat Fe_3O_4 substrates modified with dispersants were deconvoluted into three components. The peaks with a binding energy (BE) of 286.6 ± 0.1 eV, 288.6 ± 0.1 and 284.9 ± 0.1 eV were assigned to C_{PEG} , $C_{aliphatic}$ and C_{COOH} or OH respectively. All peaks had a full width of half maximum (FWHM) of 1.9 ± 0.1 eV. Fe was quantified based on the area of the $Fe2p_{3/2}$ peak. The atomic ratio of $C_{PEG} : C_{aliphatic}$,

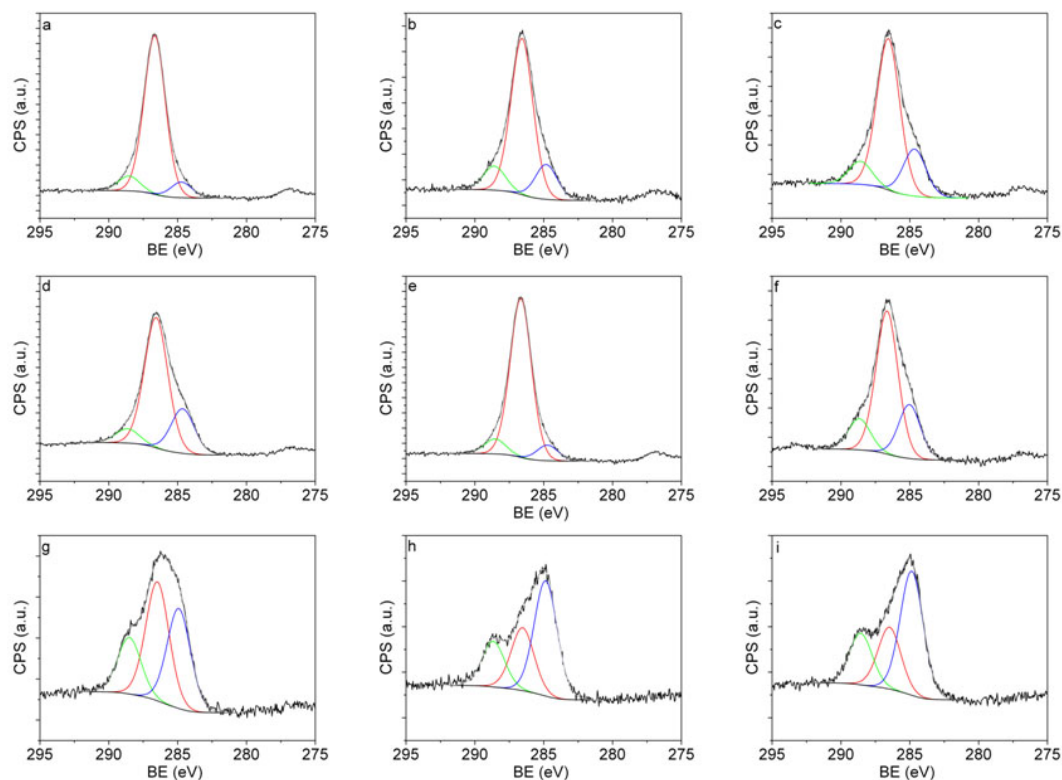


Figure 6.13: *C1s* peak of dispersants adsorbed on flat surfaces measured by XPS. *C1s* peak of (a) PEG(5)-nitroDOPA, (b) PEG(5)-nitrodopamine, (c) PEG(5)-DOPA, (d) PEG(5)-dopamine, (e) PEG(5)-mimosine, (f) PEG(5)-hydroxypyridine, (g) PEG(5)-hydroxydopamine, (h) PEG(5)-hydroxypyrrone and (i) PEG(5)-COOH adsorbed on flat magnetron sputtered iron oxide surfaces. Three peaks have been fitted to the *C1s* peak. They correspond to PEG (red), aliphatic contaminations (blue) and anchoring groups, COOH or OH conjugated contaminations (green).

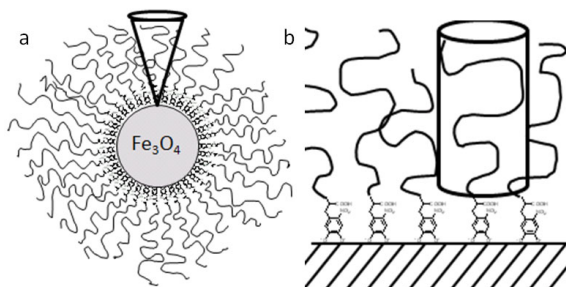


Figure 6.14: *Cartoon of the free volume available for PEG grafted to highly curved and flat surfaces.* The free volume PEG can occupy if grafted to (a) highly curved NP surfaces and (b) flat surfaces is many times larger for the former case. Because of the considerably smaller steric interchain repulsions of PEGs adsorbed on NPs compared to those adsorbed on flat surfaces, the PEG packing density on highly curved surfaces likely is higher.

derived from the deconvoluted XPS C1s spectra (Figures 6.12 and 6.13), in combination with the atomic ratio of $C_{\text{PEG}} : Fe$ (Figure 6.11) were taken as a measure of the binding affinity of the dispersants. These ratios reflected the ability of dispersants to replace aliphatic carbon contaminations. The atomic ratios of $C_{\text{PEG}} : C_{\text{aliphatic}}$ and $C_{\text{PEG}} : Fe$ increased from poor dispersants to good dispersants (Figures 6.12 and 6.13) and supported DSC results where PEG-nitroDOPA was shown to replace weakly physisorbed carbon contaminations while poor dispersants failed to do so. Moreover, good dispersants had higher $C_{\text{PEG}} : Fe$ ratios which translates into higher dispersant packing densities compared to poorly anchored dispersants (Table 6.1). The reasonably good linear correlation of the XPS atomic $C_{\text{PEG}} : Fe$ ratios between catechol-based dispersants adsorbed on flat surfaces and on NPs (Figure 6.12), respectively, indicates that the binding affinity of anchors is independent on surface curvature. This is in contrast to the packing density which was found to be considerably higher on NPs than on flat surfaces (Table 6.1).

The extremely high dispersant packing density obtained especially for PEG-nitrocatechols appears, at first glance, to be too high for a grafting to immobilization process that requires diffusion of large polymers through a brush of already adsorbed polymers to reach completion. However, account must be taken of the high curvature of the NPs. The conical volume that can be occupied by each immobilized PEG chain will significantly reduce steric inter-chain repulsion. It leads at saturation coverage to a different chain density profile and thus different dispersant packing densities on highly curved surfaces of NPs compared to flat surfaces (Figure 6.14). Similar conclusions were recently drawn for the dependence of the DNA-SH packing density on *Au* NPs with different diameters [441]. Furthermore, the thiol packing density has been reported to be up to 2.2 times higher for poly(ethylene oxide)-thiols (PEO-SH) and 23 times for polystyrene-thiols (PS-SH) if adsorbed on *Au* NPs compared to 2D *Au* surfaces [260].

The observed correlation of the XPS $C_{\text{PEG}} : Fe$ atomic ratios between dispersants adsorbed on flat, 2D surfaces and on 3D NPs (Figure 6.12) demonstrates the feasibility of screening the relative affinity of dispersants on 2D surfaces where more surface sensitive and quantitative characterization techniques are at hand. The obtained results can then likely be translated into the performance of these dispersants to stabilize NPs of the same composition as the flat surfaces.

6.3 Summary

Essentially irreversible binding of low M_w dispersants allows for controlled and efficient surface modification of individual oxide NPs that withstand agglomeration under physiologically relevant conditions. The anchor affinity was shown to not only determine the dispersant desorption rate and therefore NP stability but also to strongly correlate with dispersant packing density. Nitrocatechols were found to irreversibly anchor low M_w PEG-based dispersants to Fe_3O_4 NPs and vastly outperform the well-known catechols. If PEG-based low M_w dispersants were anchored to the NP surface through an irreversibly binding group such as nitrocatechols, NPs could be freeze-dried and re-dispersed at the desired concentration and solution conditions, which facilitates NP handling considerably. Furthermore the stability of PEG(5)-nitrocatechol surface modified Fe_3O_4 NPs was greatly enhanced compared to previously reported similar NPs, especially at low concentrations, elevated temperatures and ionic strengths. This greatly increases chances for successful biomedical applications of iron oxide NPs individually stabilized with low M_w dispersants. Close control over NP stability, hydrodynamic radius and interfacial chemistry are key issues for applications of iron oxide NPs *e.g.* as MR contrast agents.

Mechanistic Aspects of Anchor-Iron Oxide Interactions

7.1 Background

As discussed in the previous chapter, stability of NPs sterically stabilized with low molecular weight dispersants through the grafting to method relies on anchors which irreversibly bind spacers to the NP surface. It was empirically shown in chapter 6 that nitrocatechols vastly outperform the well known catechols if used as anchors to stabilize Fe_3O_4 NPs despite their close chemical similarity.

Based on the results presented in chapter 6, it can be noted that a mere increase in the number of hydroxyl groups on the catechol ring does not significantly increase the affinity of the anchor, suggesting that binding occurs with the ring oriented orthogonal to the substrate. Thus, it is unlikely that differences in binding affinities of these different catechol derived anchors originate in differences in the number of binding sites per anchor.

The striking difference in binding affinities more likely is at least partially related to different pK_a values. While nitroDOPA, nitrodopamine [442] and mimosine, the three anchors which lead to highest NP stability, all have one of their pK_a values around 6.5 close to the point of zero charge (PZC) of iron oxide NPs (6.7) (Figure 5.2), DOPA, dopamine and hydroxydopamine have $pK_a > 9$ (Figure 7.1) [443–446].

The binding affinity of catechols and catechol derivatives towards TiO_2 has been shown to scale with their Brønstead acidity [447] and thus with the pK_a that is influenced by the carboxy group. This is likely one of the reasons for the higher affinity of DOPA compared to dopamine towards iron oxide. Furthermore, the aromatic nitrogen of mimosine and hydroxypridine enhances the Brønstead acidity of these anchors compared to DOPA and dopamine, respectively, which might result in higher packing densities of dispersants

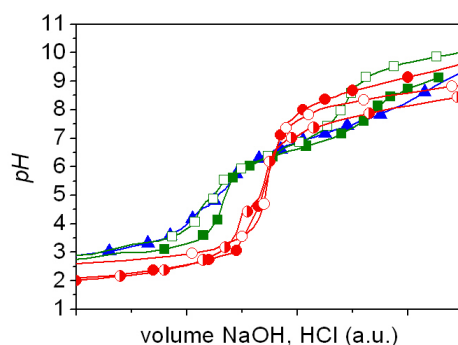


Figure 7.1: pK_a determination of anchors. Titration curves of nitroDOPA (-■-), nitrodopamine (-□-), mimosine (-▲-), DOPA (-●-), dopamine (-○-) and hydroxydopamine (-◐-). These titration curves were measured in Millipore water based solutions containing 150 mM NaCl.

containing pyridine-based anchors compared to their catechol-based counterparts.

To the best of our knowledge, no similar mechanistic studies of interactions of catechol based anchors with iron oxide surfaces and its influence on magnetic properties of NPs have been conducted. However, interactions primarily of dopamine and L-DOPA with Fe^{3+} ions were studied in detail mainly in view of their biological relevance [270, 277, 278]. It was found that Fe^{3+} promotes an oxidative degeneration of these catechols to semiquinones and eventually to quinones [279, 281, 282, 286]. In line with these reports, Shultz *et al.* found that dopamine gradually degrades if adsorbed on Fe_3O_4 NP surfaces [287]. Despite of all these reports, catechols are often used as anchors to sterically stabilize iron oxide NPs [1, 256, 258, 259, 266–268].

The aim of this chapter is to elucidate the reasons for the very different affinities of catechol derivatives to iron oxide surfaces. To approach questions about mechanistic binding aspects of catechol derivatives towards iron oxide surfaces, gain more insights into parameters influencing binding affinities and to relate insights into mechanistic binding aspects to their suitability as anchors for iron oxide NP stabilization, interactions between iron ions or iron oxide surfaces and five different anchors, namely nitroDOPA, nitrodopamine, DOPA, dopamine and mimosine and iron ions or iron oxide surfaces are compared in this chapter. Changes of the electronic structure upon adsorption of the anchors to as-synthesized and oxidized Fe_3O_4 NPs and upon complexation with Fe^{2+} and Fe^{3+} ions were investigated with EPR, FTIR and UV/VIS spectroscopy.

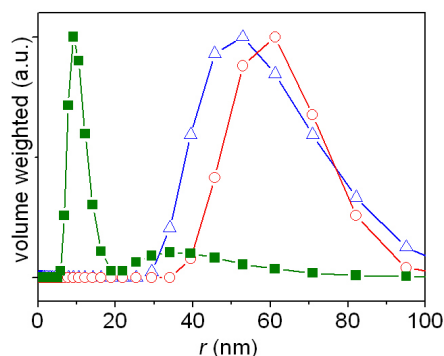


Figure 7.2: Iron oxide NP stability. DLS measurements of iron oxide NPs stabilized with PEG(5)-nitroDOPA 4h (-■-), 3 weeks (-○-) and 7 weeks (-□-) after Fe_3O_4 NPs have been synthesized. DLS was measured at room temperature.

7.2 Stability of Fe_3O_4 vs. Fe_2O_3 Nanoparticles

Fe_3O_4 NPs, that present Fe^{2+} and Fe^{3+} ions at the surface, could be individually stabilized with PEG(5)-nitroDOPA as was shown in chapter 6. However, NPs stored unstabilized in ethanol for 4 months before stabilization with PEG(5)-nitroDOPA were significantly less stable as was found with DLS (Figure 7.2).

The striking difference in NP stability between freshly synthesized Fe_3O_4 and NPs that were stored in ethanol for 4 months was observed irrespective of whether iron oxide NPs were stabilized with PEG(5)-nitroDOPA in ethanol or DMF. Storage of iron oxide NPs for 4 months in ethanol was shown by XPS to result in oxidation of NPs (Figure 5.8) which then present exclusively Fe^{3+} at the surface.

7.3 Electronic Changes upon Anchor Adsorption

Catechols in solution are known to bind preferentially to Fe^{3+} [448, 449]. Therefore, they are expected to bind better to oxidized compared to as-synthesized Fe_3O_4 NPs. However, as is shown in Figure 7.2, freshly synthesized Fe_3O_4 NPs are much more stable compared to oxidized iron oxide NPs surface modified with PEG(5)-nitroDOPA. To investigate this apparent contradiction, the coordination properties of Fe(III) in iron oxide NPs stabilized with PEG(5)-nitroDOPA, PEG(5)-dopamine and PEG(5)-mimosine were analyzed with EPR measurements.

EPR spectra of as-synthesized Fe_3O_4 NPs stabilized with PEG(5)-nitroDOPA, PEG(5)-

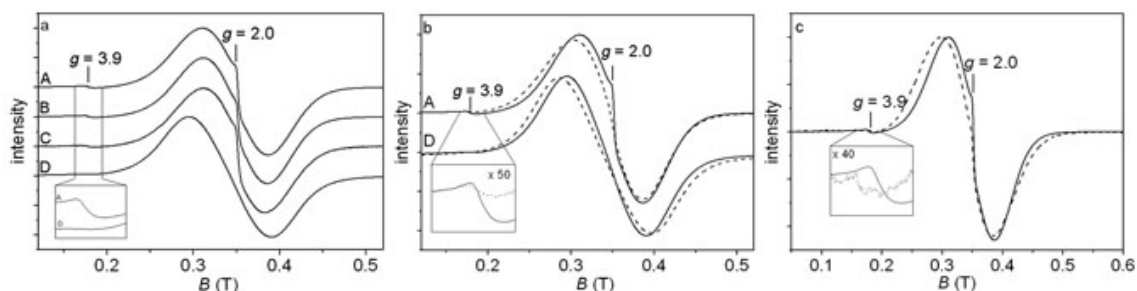


Figure 7.3: EPR spectra of iron oxide NPs synthesized in the MW coated with different dispersants. (a) Overview of EPR spectra of iron oxide NPs stabilized with (A) PEG(5)-nitroDOPA, (B) PEG(5)-dopamine, (C) PEG(5)-mimosine and (D) uncoated Fe_3O_4 NPs that had residual precursors and physisorbed impurities on their surface. (b) EPR spectra of (A) PEG(5)-nitroDOPA and (D) uncoated Fe_3O_4 NPs before (solid line) and after (dashed line) dispersants were decomposed by subjecting NPs to $T > 200^\circ C$. (c) PEG(5)-nitroDOPA stabilized Fe_3O_4 (solid line) and to Fe_2O_3 surface oxidized (dashed line) NPs.

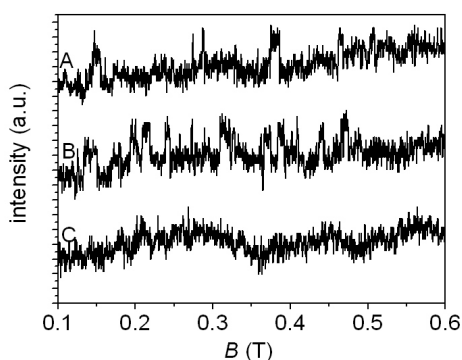


Figure 7.4: EPR spectra of dispersants. Reference EPR measurements of (A) PEG(5)-nitroDOPA, (B) PEG(5)-dopamine and (C) PEG(5)-mimosine.

dopamine, PEG(5)-mimosine and unstabilized Fe_3O_4 NPs were dominated by a near-isotropic signal with $g = 2.06$ ($B_r = 343$ mT), characteristic for NPs in a superparamagnetic state (Figure 7.3) [336]. The line width $\Delta B = 73 \pm 4$ mT of the superparamagnetic signal of PEG(5)-anchor stabilized NPs was found to be considerably lower compared to that of unstabilized Fe_3O_4 NPs ($\Delta B = 92 \pm 6$ mT). The lower ΔB indicates less dipole-dipole inter-particle interactions between stabilized as compared to unmodified Fe_3O_4 NPs [336, 450].

Moreover, the stabilized NPs revealed two additional signals at $B_r = 352$ mT (resulting in $g = 2.0$) and $B_r = 180$ mT ($g = 3.9$). The sharp signal at $g = 2.0$ is characteristic for "free electrons". Such signals were only found if dispersants were adsorbed on Fe_3O_4 NPs but not for pure dispersants (Figure 7.4). The low field resonance at $B_r = 180$ mT ($g = 3.9$) can be assigned to rhombohedrally distorted, magnetically decoupled Fe^{3+} [332, 451].

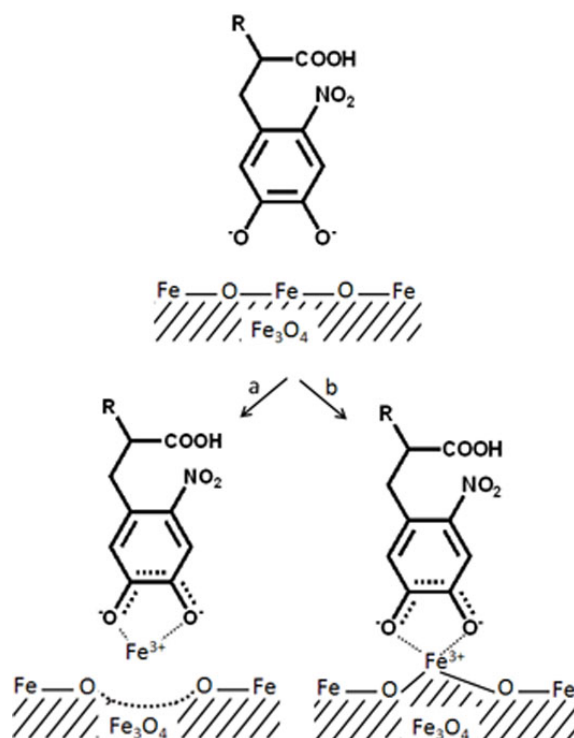


Figure 7.5: Cartoon of nitroDOPA interaction with a Fe_3O_4 surface. Cartoon of possible nitroDOPA interaction with a Fe_3O_4 surfaces where it (a) removes Fe^{3+} from the surface and (b) distorts the Fe_3O_4 surface.

Although the two signals occur simultaneously, their relative intensity, deduced from their peak heights, were different. The relative intensity ratio of free electrons ($g = 2.0$) to Fe^{3+} ($g = 3.9$) was highest for PEG(5)-nitroDOPA stabilized NPs. This ratio decreased by $14 \pm 5\%$ for PEG(5)-mimosine and $32 \pm 1\%$ for PEG(5)-dopamine compared to PEG(5)-nitroDOPA stabilized Fe_3O_4 NPs. Therefore, electron delocalization is suggested to be highest for PEG(5)-nitroDOPA stabilized NPs.

7.3.1 Influence of Anchors on Surface Bound Fe(III) Ions

The occurrence of a $g = 3.9$ signal associated with magnetite NPs indicates that Fe(III) is magnetically decoupled from the bulk material [452]. However, the ligand field of Fe(III) resulting in $g = 3.9$ is less distorted compared to Fe^{3+} complexed with three catechols per ion, for which g -values of 4.2-4.3 have been reported [273, 276, 278, 279, 451]. At $T < 239$ K, a signal at $g = 4.3$ has also been found for polystyrene co-butadiene-co-methyl methacrylate stabilized 4.5 nm radius Fe_3O_4 NPs. This signal was ascribed to paramagnetic Fe(III) in a rhombohedral crystal field [450]. However, the signal observed here

for PEG(5)-nitroDOPA stabilized NPs appears already at room temperature and is shifted towards higher fields. Thus, the signal at $g = 3.9$ is unlikely to have the same origin as the one reported by Noginov *et al.* at $g = 4.3$ [450]. A second possible explanation for the $g = 3.9$ signal would be that it is a half-field signal of the superparamagnetic peak. The intensity of the half-field signal of Fe_3O_4 NPs is about 8×10^{-4} times lower than the superparamagnetic signal [450]. The intensity of the $g = 3.9$ signal measured here, however, is only 6.6×10^{-3} times lower than the superparamagnetic signal and it is not observed at all for uncoated Fe_3O_4 NPs. Assignment of the $g = 3.9$ signal as the half-field signal of the superparamagnetic peak can therefore be excluded.

Because no free electrons were found for pure PEG(5)-nitroDOPA (Fig. 7.4), it is most likely that the simultaneous occurrence of free electrons and the Fe^{3+} signal at $g = 3.9$ for PEG(5)-nitroDOPA stabilized SPIONs is due to interactions of nitroDOPA with the iron oxide surface. The appearance of distorted Fe^{3+} coordination can be explained by two different mechanisms. Depending on the complexation strength, PEG(5)-nitroDOPA could partially dissolve or strongly bind to Fe_3O_4 NP surfaces (Figure 7.5). In the first case, removing surface Fe^{3+} ions would lead to free PEG(5)-nitroDOPA/ Fe^{3+} complexes. In the second case, adsorption of PEG(5)-nitroDOPA on iron oxide surfaces would result in strong interactions of nitroDOPA with surface Fe(III) ions causing structural and electronic distortions at the Fe_3O_4 surfaces (Figure 7.4).

NitroDOPA/Iron Ion Complexes

EPR spectra of freeze-dried nitroDOPA/ Fe^{3+} molecular complexes assembled in solution with a molar ratio of 1 : 1 and 3 : 1 are shown in Figure 7.6. A molar ratio of 1 : 1 was taken for steric reasons, because Fe(III) at the Fe_3O_4 surface can interact only with one nitroDOPA. In contrast, catechols form complexes with free Fe^{3+} ions at a molar ratio of 3 : 1 [276, 453]. Irrespective of the Fe^{3+} concentration, the spectra exhibited three features (Figure 7.6). The broad absorption around $g \approx 2$ is most likely caused by nonspecific Fe^{3+} configurations with strong dipole-dipole interactions, the sharp signal at $g = 2.0$ is due to free electrons and the signal at $g = 4.3$ originates from Fe^{3+} in a rhombohedrally distorted ligand field [273, 276, 278, 279, 451].

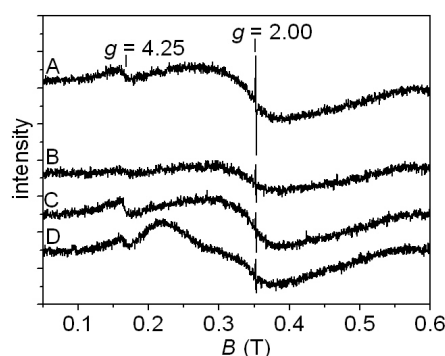


Figure 7.6: EPR spectra of nitroDOPA/iron complexes. EPR spectra of (A) nitroDOPA/ Fe^{2+} complexed in a molar ratio of 1 : 1, (B) nitroDOPA/ Fe^{2+} complexed in a molar ratio of 3 : 1, (C) nitroDOPA/ Fe^{3+} complexed in a molar ratio of 1 : 1, (D) nitroDOPA/ Fe^{3+} complexed in a molar ratio of 3 : 1. NitroDOPA was complexed with iron ions in Millipore water for 1 h before complexes were freeze dried and analyzed with EPR.

Thermal Degradation of NitroDOPA

NitroDOPA/Iron Complexes

To elucidate the influence of nitroDOPA on the rhombohedrally distorted Fe^{3+} signals, nitroDOPA/ Fe^{3+} complexes in a molar ratio of 3 : 1 and PEG(5)-nitroDOPA stabilized Fe_3O_4 NPs were subjected to $T > 200$ °C for 10 min. FTIR spectra revealed that this treatment degraded nitroDOPA as indicated by the disappearance of the C-C ring vibration centered at ≈ 1500 cm^{-1} [447] (Figure 7.7). For nitroDOPA/ Fe^{3+} complexes, the concentration of EPR active Fe^{3+} ions coordinated in a rhombohedrally distorted ligand field markedly *increased* upon heating. In contrast, heat treatment of Fe_3O_4 NPs stabilized with PEG(5)-nitroDOPA resulted in a drastic *decrease* of the $g = 3.9$ signal intensity (Figure 7.3b). The differences in g -value and change in response to nitroDOPA decomposition of nitroDOPA/ Fe^{3+} complexes and PEG(5)-nitroDOPA stabilized Fe_3O_4 NPs strongly suggests that the signal in the latter case originates from complexed surface bound Fe^{3+} .

A paramagnetic EPR response of Fe(III) associated with a ferrimagnetic solid phase has rarely been described since magnetic coupling below the Curie temperature leads to collective behavior. An example was reported to occur during dehydroxidation of γ - $FeOOH$ and the formation of superparamagnetic γ - Fe_2O_3 . The generation of a $g = 4.2$ signal was explained by the enhanced distortion of FeO_6 octahedra due to dynamic rearrangements of oxygen and hydrogen atoms [452]. In analogy, the occurrence of Fe(III) in a

distorted ligand field due to the adsorption of PEG(5)-nitroDOPA onto Fe_3O_4 NPs could be explained by re-arrangements of surface-coordinated iron.

NitroDOPA Adsorbed on Iron Oxide Nanoparticles

To verify that the $g = 2.06$ signal assigned to free electrons and the $g = 3.9$ assigned to Fe(III) in a rhombohedral ligand field are directly related to each other, PEG(5)-nitroDOPA stabilized Fe_3O_4 NPs were subjected to $T > 200$ °C for 10 min. This heat treatment should thermally remove dispersants from the NP surface. Thus EPR spectra similar to those of uncoated Fe_3O_4 NPs would be expected. Indeed, after heat treating PEG(5)-nitroDOPA and uncoated Fe_3O_4 NPs, the signal arising from superparamagnetic NPs exhibited a similar, broad line width for all samples. The broadening for the coated NPs is due to an increase in magnetostatic interactions [336]. It clearly shows that the thermal treatment decomposed the coating which was further supported by FTIR measurements (Figure 7.7a). A comparison of XRD spectra of PEG(5)-nitroDOPA stabilized Fe_3O_4 NPs before and after they were subjected to $T > 200$ °C revealed no significant peak shifts or the appearance of new peaks after NPs had been heat treated (Figure 7.8). This indicates that the inverse spinel structure of the iron oxide cores was retained after exposing the cores to elevated temperatures. The reduced signal : noise ratio of heat treated compared to as-synthesized samples is because of the lower amount of powder analyzed for heat treated samples. Upon heating, both signals at $g = 2.0$ and $g = 3.9$ disappeared (Figure 7.3b). The correlated appearance and loss of the EPR signals of free electrons and magnetically decoupled Fe(III) ions upon adsorption and removal of dispersants on Fe_3O_4 NPs demonstrates that these two signals are related to each other. Hence adsorbed nitroDOPA is preferentially bound to Fe(III) rather than to Fe(II) which is not directly detectable with EPR [454].

Electronic Interactions of NitroDOPA with Fe_3O_4 Surfaces

As shown above, nitroDOPA/ Fe^{3+} complexes lead to a signal at $g = 4.3$. Thus, the $g = 3.9$ signal cannot be assigned to nitroDOPA/ Fe^{3+} complexes, but must arise from surface bound Fe(III). That a signal at $g = 3.9$ is apparent for as-synthesized Fe_3O_4 NPs stabilized with PEG(5)-nitroDOPA but is absent for unstabilized NPs indicates that strong interactions of nitroDOPA with surface bound Fe(III) ions must significantly distort the Fe(III) ligand field. Furthermore, electron delocalization is significantly stronger and the signal

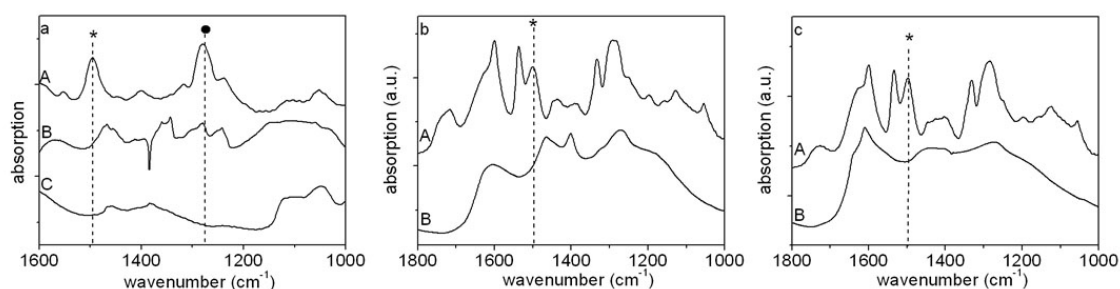


Figure 7.7: Influence of heat treatment. FTIR spectra of (a) nitroDOPA adsorbed on iron oxide NPs, nitroDOPA complexed with (b) Fe^{2+} and (c) Fe^{3+} at a molar ratio of 3 : 1 (A) before and (B) after heat treatment to $T > 200$ °C for 10 min. The vibration indicated with * can be assigned to the C-C ring vibration while (●) was assigned to C-O stretch vibrations [447].

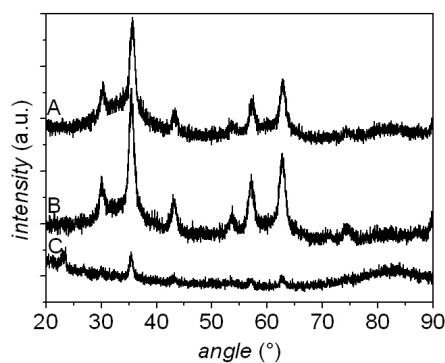


Figure 7.8: Influence of heat treatment. XRD of (A) uncoated (B) nitroDOPA coated iron oxide NPs before and (C) after thermal treatment.

at $g = 3.9$ more pronounced if as-synthesized Fe_3O_4 NPs are modified with PEG(5)-nitroDOPA than if PEG(5)-dopamine is used as a dispersant (Figure 7.3a). These results indicate, that the magnetically decoupled Fe(III) signal with $g = 3.9$ is a result of strong interactions of the nitroDOPA with Fe(III) ions at the NP surface.

Upon adsorption of nitroDOPA on Fe_3O_4 NPs, nitroDOPA can interact with Fe(II) or Fe(III). If nitroDOPA initially binds to Fe(III) ions, the simultaneous appearance of free electrons and a magnetically decoupled Fe(III) signal would not be expected, since the charge transfer to create free electrons is unaccounted for. On the other hand, if the electron density in the conjugated electron system in nitroDOPA is increased by binding to Fe(II) and oxidation to Fe(III) occurs (see suggested reaction in Figure 7.10a), the simultaneous appearance of a magnetically decoupled Fe(III) signal and free electrons would be expected. In literature, a reduction of nitrobenzenes [455] and facilitated oxidation of Fe^{2+} to Fe^{3+} in the presence of chelates which strongly bind to Fe^{2+} have already been reported [456, 457].

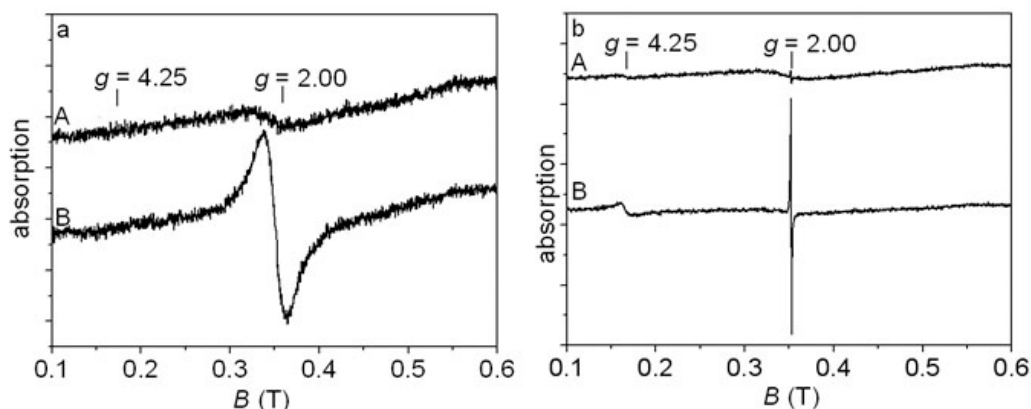


Figure 7.9: Influence of heat treatment on nitroDOPA/iron complexes. EPR spectra of (a) nitroDOPA/ Fe^{2+} and (b) nitroDOPA/ Fe^{3+} complexes (A) before and (B) after heat treatment at $T > 200$ °C for 10 min. Iron was complexed with nitroDOPA in Millipore water for 1 h at a molar ratio of 1 : 3 before complexes were freeze dried.

Interactions of NitroDOPA with Fe^{2+} and Fe^{3+}

PEG(5)-nitroDOPA stabilized oxidized NPs revealed a significantly weaker signal at $g = 2.0$ compared to PEG(5)-nitroDOPA stabilized freshly synthesized Fe_3O_4 NPs. This supports the interpretation that the change in EPR spectra is a result of strong electron delocalization between nitroDOPA and Fe(II) ions. Furthermore, no clear decoupled Fe(III) signal at $g = 3.9$ could be detected for stabilized oxidized NPs (Figure 7.3c). This provides clear evidence for weaker interaction of nitroDOPA with oxidized compared to freshly synthesized Fe_3O_4 NPs.

Further evidence that nitroDOPA initially binds to Fe(II) if adsorbed on Fe_3O_4 NPs is given by EPR studies of freeze-dried nitroDOPA complexed in solution with Fe^{2+} and Fe^{3+} ions (Figure 7.6). The intensity ratios of the peak heights resulting from delocalized electrons at $g = 2.0$ to Fe^{3+} ($g = 4.2$) are 6 ± 1 and 8 ± 1 for molar ratios of nitroDOPA : $Fe^{2+} = 1 : 1$ and $3 : 1$ respectively. These are considerably higher than those of nitroDOPA/ Fe^{3+} complexes (2 ± 0 and 3 ± 1 for molar ratios of nitroDOPA : $Fe^{3+} = 1 : 1$ and $3 : 1$ respectively) despite that the signal : noise ratio of the Fe^{3+} signal is comparable for these complexes. The Fe^{3+} signal of nitroDOPA/ Fe^{2+} complexes at $g = 4.2$ further indicates that Fe^{2+} , which is not directly observable with EPR [454], is oxidized to EPR active Fe^{3+} if complexed with nitroDOPA. More importantly, it shows that interactions of nitroDOPA with Fe^{2+} lead to stronger electron delocalization compared to nitroDOPA/ Fe^{3+} complexes. The enhanced electron delocalization of nitroDOPA/ Fe^{2+} complexes thus likely results from a redox reaction between nitroDOPA and Fe^{2+} , in sup-

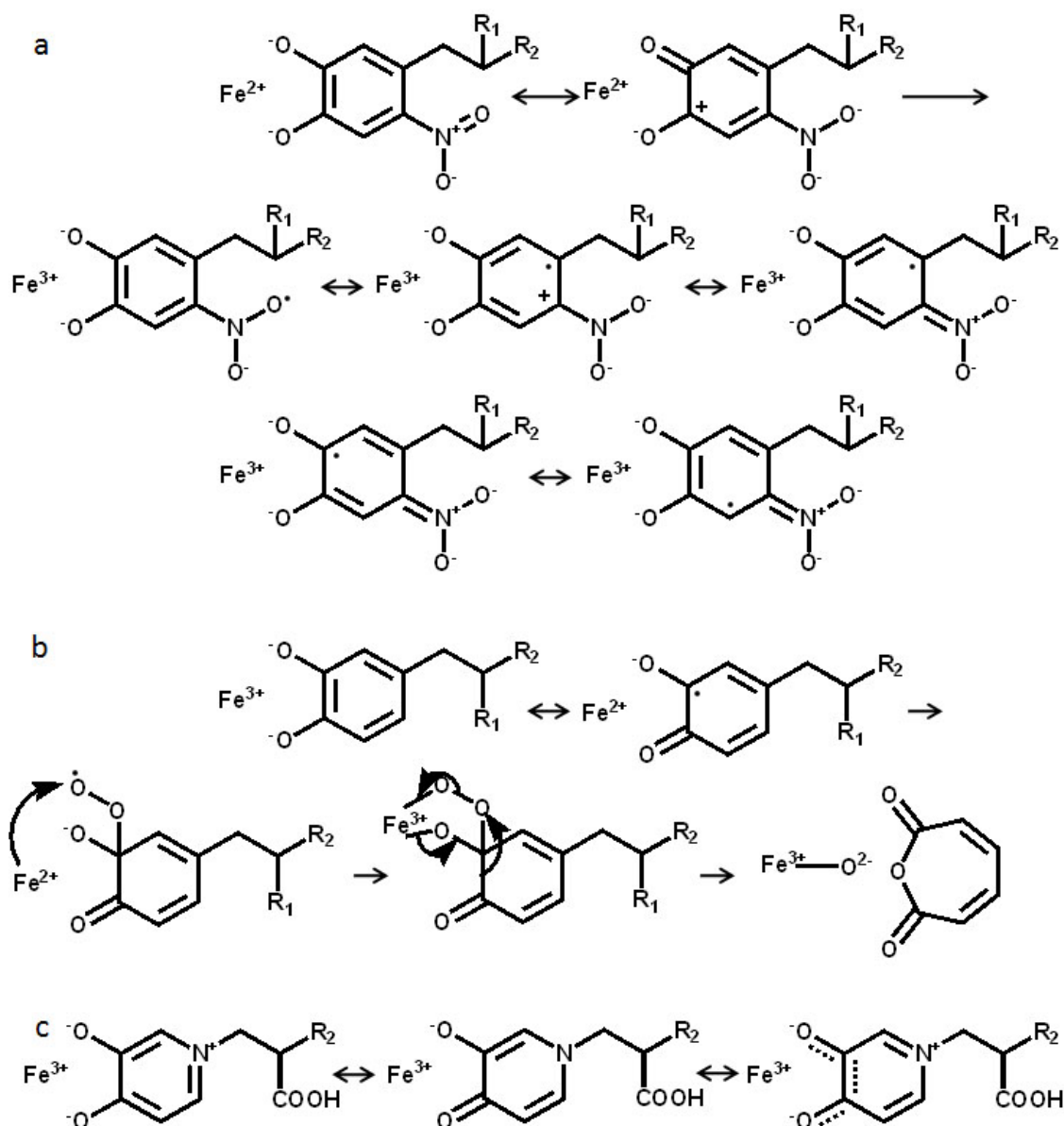


Figure 7.10: Suggested mechanism for the binding of anchors to Fe_3O_4 NPs. (A) Reduction reaction of nitrocatechol complexed with Fe^{2+} ions. (B) Iron catalyzed catechol degradation. Fe^{3+} complexed catechols are oxidized to semiquinones while Fe^{3+} is reduced to Fe^{2+} before semiquinones are further degraded through reactions with O_2 [282]. (C) Mimosine complexed with Fe^{3+} . $R_1 = H$ for dopamine and $COOH$ for DOPA whereas R_2 were amines for pure feet and PEG(5) for dispersants used to stabilize NPs.

port of the similar observations and conclusions described above for the surface bound iron ions.

7.3.2 Vibrational Changes in Anchors upon Adsorption on Iron Oxide Nanoparticles

To further investigate vibrational changes that occur upon anchor adsorption on iron oxide, FTIR studies were performed on nitroDOPA, nitrodopamine, DOPA, dopamine and mimosine adsorbed on Fe_3O_4 NPs. Additionally, FTIR spectra of anchors adsorbed on Fe_3O_4 NPs were compared to spectra of anchors complexed with Fe^{2+} and Fe^{3+} ions. FTIR spectra revealed two pronounced peaks, one at $\approx 1280\text{ cm}^{-1}$ assigned to in-plane C-O stretching vibrations and one at 1496 cm^{-1} assigned to tangential normal C-C vibration modes of the aromatic ring [447], upon adsorption of anchors to Fe_3O_4 NPs (Figure 7.11).

Nitrocatechols

Changes in the C-C ring vibration of nitrocatechols upon complexation with iron ions or adsorption on Fe_3O_4 NPs were small (Figure 7.11). However, shifts of the C-O stretch vibrations from 1290 to 1281 cm^{-1} for nitroDOPA and from 1294 to 1277 cm^{-1} for nitrodopamine upon adsorption on Fe_3O_4 NPs were close to that of nitrocatechols complexed with Fe^{2+} (1284 cm^{-1} for nitroDOPA and 1277 cm^{-1} for nitrodopamine) in contrast to nitrocatechol/ Fe^{3+} complexes (1292 cm^{-1} for nitroDOPA and 1290 cm^{-1} for nitrodopamine). Moreover, the C-O ring vibrations of Fe^{2+} -complexed nitrocatechols were gradually shifted towards lower wavenumbers with time (Figure 7.12). The good agreement of the C-O ring vibrations of Fe^{2+} -complexed nitrocatechols with that of nitrocatechols adsorbed on Fe_3O_4 NPs and the time dependent shift towards even closer agreement further support the conclusions from the EPR results of initial binding of nitroDOPA to Fe(II) accompanied by a strong electron delocalization between nitroDOPA and Fe(II). The FTIR spectra also display marked shifts for the symmetric and asymmetric NO_2 vibrations upon adsorption of nitrocatechols on Fe_3O_4 NPs (e.g. 1319 cm^{-1} and 1554 cm^{-1} for symmetric and asymmetric NO_2 vibrations of nitroDOPA) [458] compared to reference spectra ($\approx 1331\text{ cm}^{-1}$ and 1535 cm^{-1}) (Figure 4a, b). This indicates that the electron transfer to nitroDOPA results in an increased electron density on the nitro group (Figure 7.10a). Increased electron density in the lowest unoccupied molecular

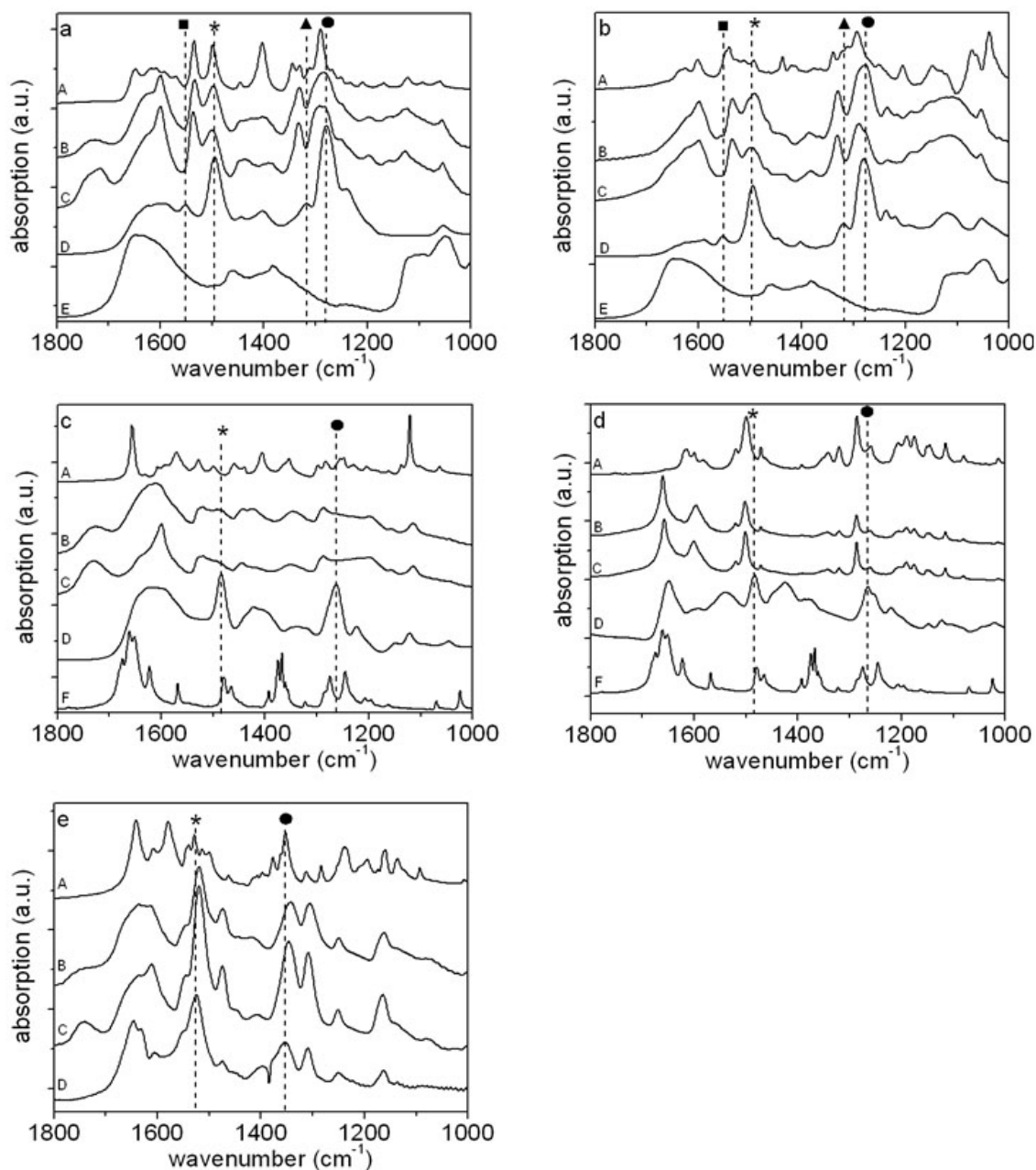


Figure 7.11: FTIR of anchors complexed with iron ions and adsorbed on iron oxide NPs. FTIR spectra of (A) pure anchors were compared to those of anchors complexed with (B) Fe^{2+} and (C) Fe^{3+} ions in Millipore water at a molar ratio of anchor : iron ion = 1 : 1. Complexes were kept for 24 h at $50^{\circ}C$ before they were freeze-dried. Furthermore, anchors were adsorbed on (D) Fe_3O_4 NPs. (E) Uncoated Fe_3O_4 NPs and (F) benzoquinones are shown as references. The investigated anchors were (a) nitroDOPA, (b) nitrodopamine, (c) DOPA, (d) dopamine and (e) mimosine. The most apparent vibrations measured on anchors adsorbed on Fe_3O_4 NPs were the C-C ring out of plane vibration (*), the C-O stretch vibrations (●) and for nitrocatechols asymmetric (■) and symmetric (▲) NO_2 vibrations.

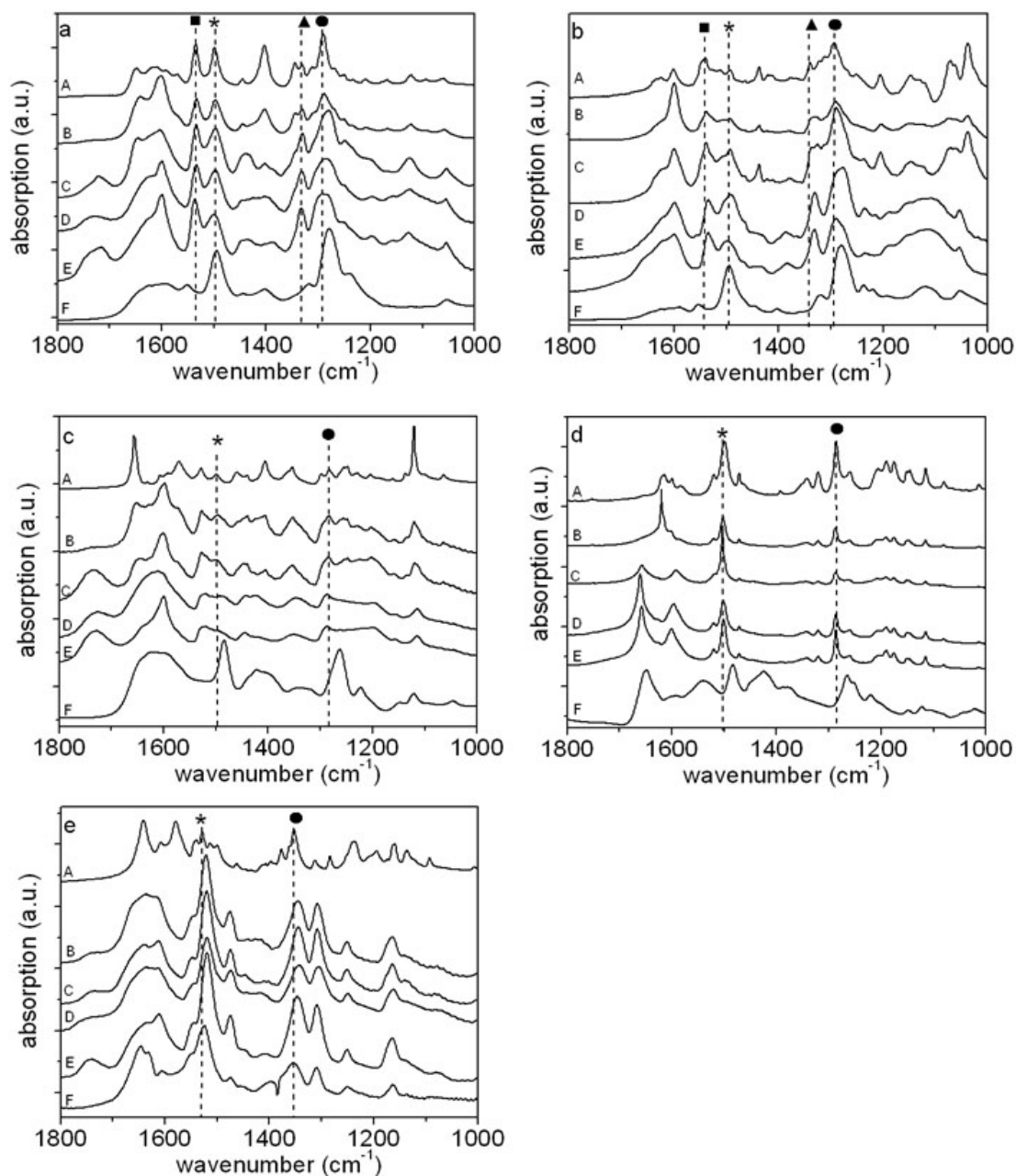


Figure 7.12: FTIR of anchor/iron complexes. FTIR spectra of (A) pure anchors, anchors complexed with (B) Fe^{2+} and (C) Fe^{3+} kept for 1 h at RT, (D) Fe^{2+} and (E) Fe^{3+} kept for 24 h at 50°C and (F) anchors adsorbed on Fe_3O_4 NPs for (a) nitroDOPA, (b) nitrodopamine, (c) DOPA, (d) dopamine and (e) mimosine. The molar ratio of the anchor : iron complexes was always 1 : 1. * was assigned to the C-C ring vibration while (●) was assigned to C-O stretch vibrations [447].

orbital (LUMO) upon deprotonation has already been calculated [458]. It agrees with the observed increased electron density in the LUMO upon binding of nitroDOPA to Fe_3O_4 NPs observed here.

Catechols

Differences in FTIR spectra of catechols complexed with Fe^{2+} and Fe^{3+} and that of catechols adsorbed on Fe_3O_4 NPs were more pronounced relative to those of nitrocatechols (Figure 7.11). Whereas the C-C ring vibrations of nitrocatechols were only slightly shifted towards higher wavenumbers if adsorbed on Fe_3O_4 NPs, marked shifts towards the position of benzoquinones were recorded for (unsubstituted) catechols if adsorbed on Fe_3O_4 NPs (Figure 7.11c, d). The similarity of FTIR spectra of dopamine adsorbed on Fe_3O_4 NPs with the reference spectra of benzoquinone is striking. Therefore, the peak at 1487 cm^{-1} measured for catechols adsorbed on Fe_3O_4 NPs can likely be assigned to a C-O stretching vibration of semiquinones [459–461].

The absence of an electronegative NO_2 group on catechols compared to nitrocatechols renders catechols more prone to oxidation [296, 462]. Moreover, iron catalyzed catechol degradation, which results in semiquinones, quinones and eventually in carboxy containing species, has been thoroughly described in literature (Figure 7.10b) [279, 281, 282, 286]. It can explain the weak C-C ring and C-O stretch vibrations of catechols compared to nitrocatechols seen on FTIR spectra. Furthermore, carboxy groups, that can be the result of iron catalyzed catechol degradation [286], were shown to poorly bind to Fe_3O_4 NPs in chapter 6. This might account for the considerably worse stability of PEG(5)-catechol compared to PEG(5)-nitrocatechol stabilized Fe_3O_4 NPs (see *e.g.* Figures 6.5 and 6.6).

Mimosine

In contrast to catechol/iron and nitrocatechol/iron complexes, FTIR spectra of mimosine/iron complexes did not change significantly with complexation time and temperature (Figure 7.12e). This indicates a fast reaction between mimosine and iron resulting in stable complexes. It might be due to the low pK_a values of mimosine [463]. Similar to nitrocatechols, the location of the C-C ring vibration did not change significantly upon adsorption of mimosine on Fe_3O_4 NPs (Figure 7.11e). However, the C-O ring vibration of mimosine and nitrocatechols complexed with Fe^{2+} was shifted towards lower

Table 7.1: Locations of HOMO → LUMO transition UV/VIS peaks of uncomplexed and with Fe^{2+} and Fe^{3+} ions complexed nitrocatechols dissolved at different pHs and in organic solvents respectively where the molar ratio of nitrocatechols : iron = 1 : 1.

	pH = 5	pH = 7.4	pH = 12	ethanol	DMF
nitroDOPA	352	422	499	355	364/441
nitroDOPA/ Fe^{2+}	353	414		382	369
nitroDOPA/ Fe^{3+}	391	406		372	366
nitrodopamine	351	422	501	356	346
nitrodopamine/ Fe^{2+}	353	418		353	421
nitrodopamine/ Fe^{3+}	390	405		345	363

Table 7.2: Peak locations of electron transition UV/VIS peaks of uncomplexed and with Fe^{2+} and Fe^{3+} ions complexed anchors dissolved at different pHs and in solvents, respectively. The molar ratio of anchors : iron ions is 1 : 1. Some of the peaks are convoluted and only appear as shoulders (s).

	pH = 5	pH = 7.4	ethanol	DMF
nitroDOPA/ Fe^{2+}				406
nitroDOPA/ Fe^{3+}	644	broad	667	420/s
nitrodopamine/ Fe^{2+}		broad		520/s
nitrodopamine/ Fe^{3+}	466	broad	739	637
DOPA/ Fe^{2+}		574		
DOPA/ Fe^{3+}	402/742	573	356/739	359
dopamine/ Fe^{2+}		575		471/602
dopamine/ Fe^{3+}	405/744	561	356	364
mimosine/ Fe^{2+}	396/463	395/452		
mimosine/ Fe^{3+}	4513	448	363	361

wavenumbers compared to the respective reference spectra. Interestingly, in contrast to nitrocatechols, the C-O ring vibration of mimosine adsorbed on Fe_3O_4 NPs was closer to that of mimosine complexed with Fe^{3+} compared to mimosine/ Fe^{2+} complexes. This indicates that mimosine binds directly to Fe^{3+} (Figure 7.10c).

7.4 Optimizing Adsorption Conditions

To elucidate the role of adsorption conditions on the binding kinetics of these anchors to Fe_3O_4 NPs, UV/VIS spectroscopy measurements on complexes of anchors with free iron ions were performed (Figures 7.13, 7.14, 7.15 and Tables 7.1 and 7.2). Primarily electron transitions between the highest occupied molecular orbital (HOMO) and the LUMO were investigated because these electron transitions provide insight into anchor-iron interac-

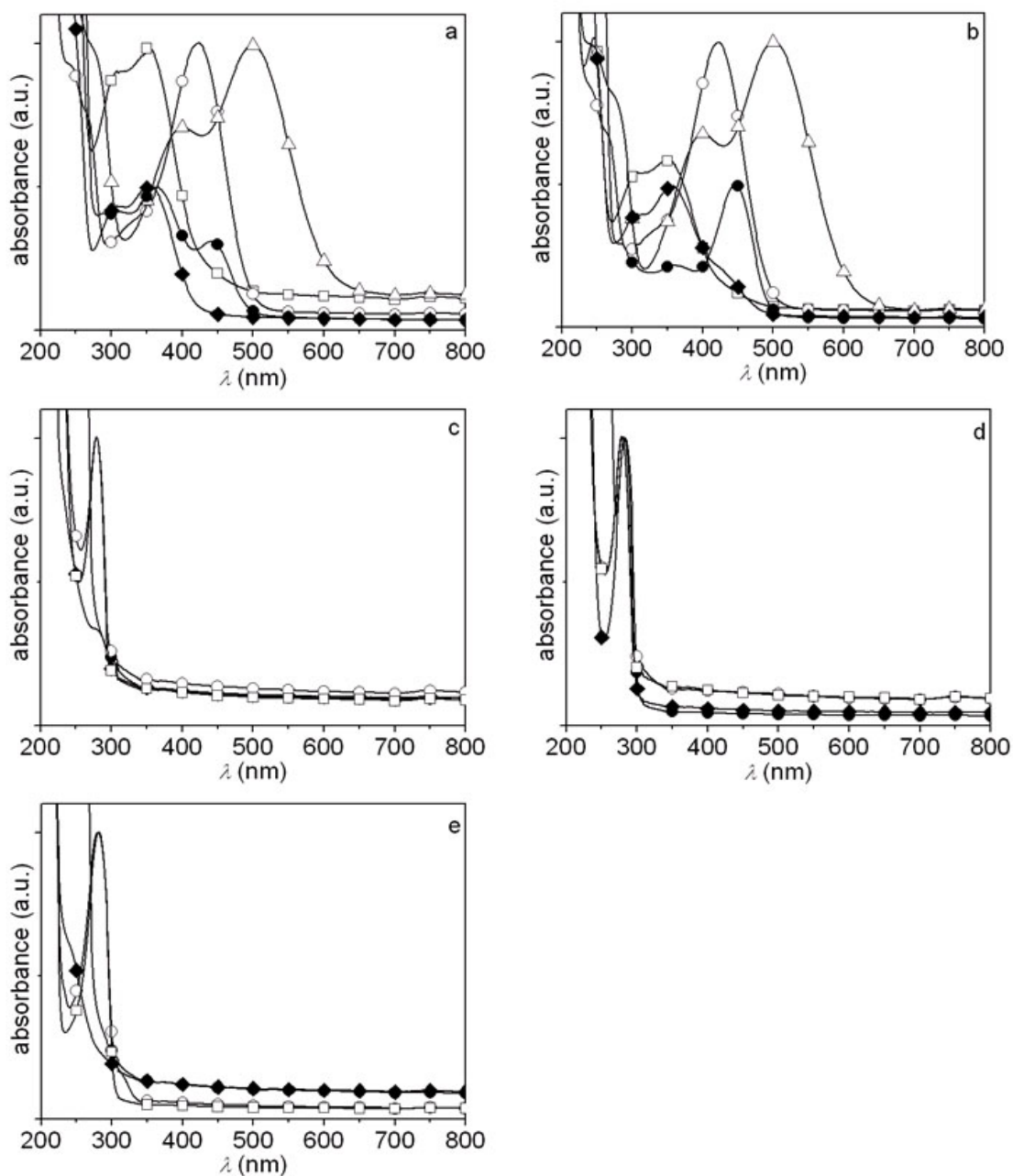


Figure 7.13: UV/VIS spectra of anchors. Reference UV/VIS spectra of (a) nitroDOPA (b) nitrodopamine (c) DOPA, (d) dopamine and (e) mimosine dissolved in Millipore water (pH around 5) (\square), Tris buffer at pH= 7.4 (\circ), Tris buffer at pH=12 (\triangle), ethanol (\blacklozenge) and DMF (\bullet) respectively.

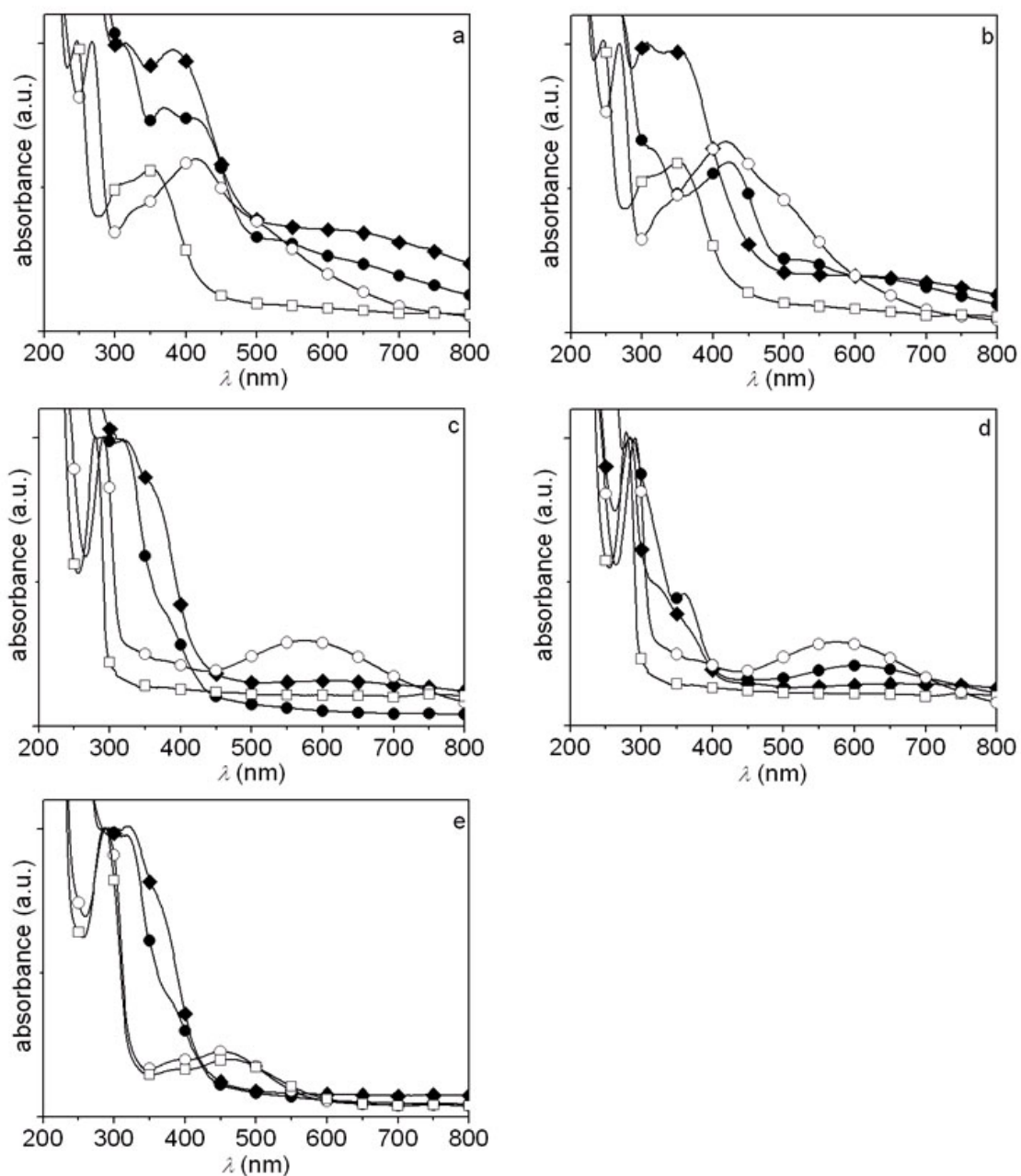


Figure 7.14: UV/VIS spectra of anchor/ Fe^{2+} complexes. (a) nitroDOPA (b) nitrodopamine (c) DOPA, (d) dopamine and (e) mimosine complexed with Fe^{2+} Millipore water ($-\square-$), Tris buffer ($-\circ-$), ethanol ($-\diamond-$) and DMF ($-\bullet-$) respectively. The molar ratio of anchors : iron ions was 1 : 1. UV/VIS spectra were measured 1 h after complexation.

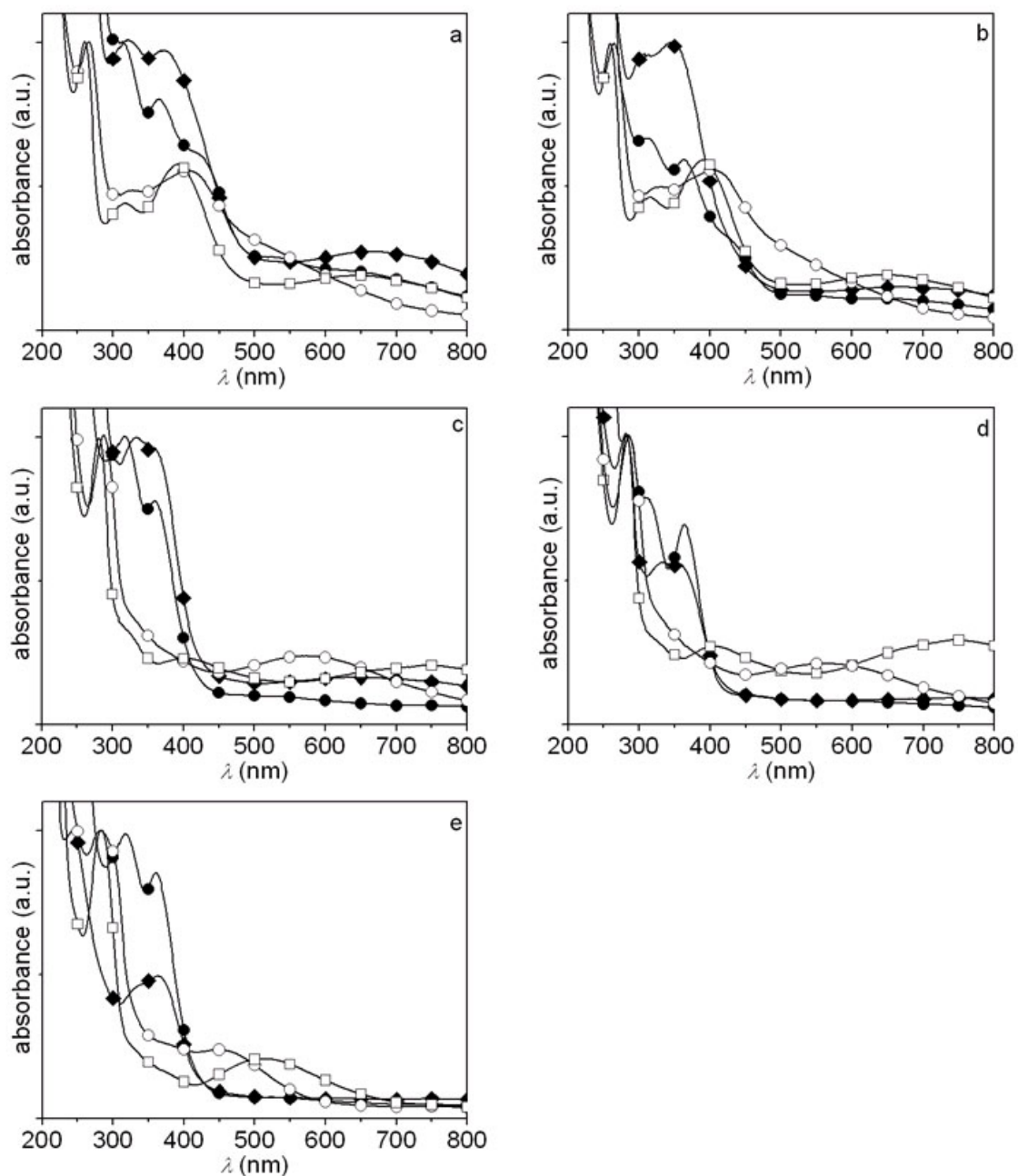


Figure 7.15: UV/VIS spectra of anchor/ Fe^{3+} complexes. (a) nitroDOPA (b) nitrodopamine (c) DOPA, (d) dopamine and (e) mimosine complexed with Fe^{3+} Millipore water (empty square), Tris buffer (-○-), ethanol (-◇-) and DMF (-●-) respectively. The molar ratio of anchors : iron ions was 1 : 1. UV/VIS spectra were measured 1 h after complexation.

tions. Reference spectra were compared to UV/VIS spectra of anchors complexed with Fe^{2+} and Fe^{3+} ions at different pHs and in organic solvents respectively.

The pH of Millipore water based complex solutions varied between 3 and 5. Tris has been reported not to interfere with iron ions [449] and was chosen to buffer the solutions to pH = 7.4. Furthermore, anchors were complexed with iron in organic solvents, namely ethanol and DMF, because iron oxide NPs presented in chapter 6 were stabilized in these solvents.

7.4.1 Nitrocatechols

The prominent peak located between 350 and 500 nm was assigned to the HOMO \rightarrow LUMO transition resulting from a charge transfer of the HOMO localized on the aromatic ring of nitrocatechols to the LUMO mainly localized on the nitro group. The wavelength of the HOMO \rightarrow LUMO transition peak maxima increased from 350 nm at pH \approx 5 to 420 nm at pH \approx 7.4 and 500 nm at pH \approx 12. Considering the pK_a values of nitrocatechols ($pK_{a1} \approx 6.5$, $pK_{a2} \approx 10$) [442] (Figure 7.1), these peaks were assigned to the fully protonated, once deprotonated and twice deprotonated state of nitrocatechols, respectively. A comparison of the pH-dependent reference spectra of nitrocatechols aliquotted in aqueous solutions to reference spectra of nitrocatechols dissolved in ethanol and DMF reveals that nitrocatechols were fully protonated if dissolved in ethanol whereas a significant fraction of nitrocatechols was once deprotonated if aliquotted in DMF. While the peak locations of nitroDOPA and nitrodopamine aliquotted in DMF were identical, relative peak intensities differed markedly indicating that a higher amount of nitrodopamine was partially deprotonated compared to nitroDOPA (Figure 7.13).

Nitrocatechol/Iron Complexes

1 h after complexation, changes in the HOMO \rightarrow LUMO transition peak of Millipore water based nitrocatechol/ Fe^{2+} complex solutions compared to the reference (free) nitrocatechol spectra were negligible (Table 7.1 and cf. Figure 7.13 and 7.14). This is in contrast to nitrocatechols complexed with Fe^{3+} where nitrocatechol/ Fe^{3+} interactions were seen already 1 h after complexation (Figure 7.15). Well in agreement with FTIR results, a significant broadening of the HOMO \rightarrow LUMO peak became apparent 24 h after nitrocatechols were complexed with Fe^{2+} . No further change in the UV/VIS spectra

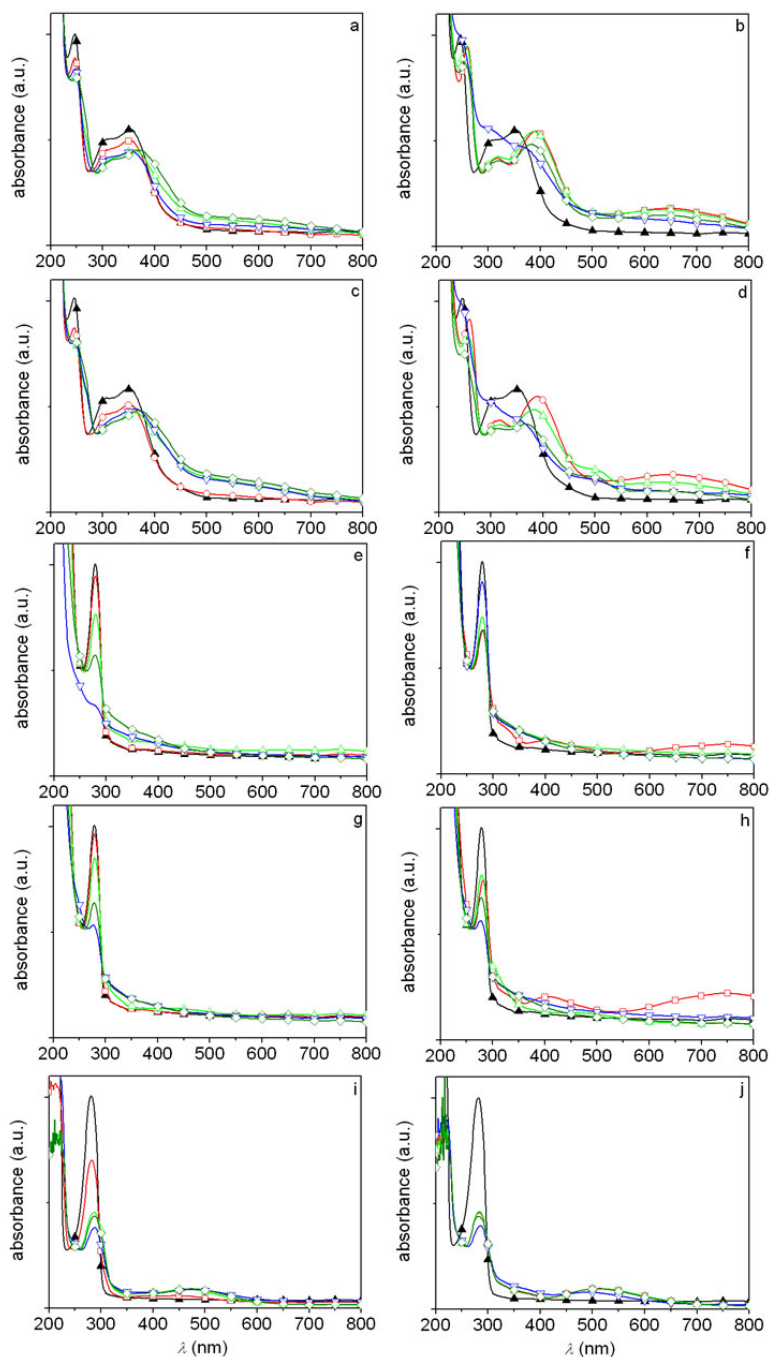


Figure 7.16: Time and temperature dependence of anchor/iron complexes. UV/VIS spectra of (a) nitroDOPA/ Fe^{2+} , (b) nitroDOPA/ Fe^{3+} , (c) nitrodopamine/ Fe^{2+} , (d) nitrodopamine/ Fe^{3+} , (e) DOPA/ Fe^{2+} , (f) DOPA/ Fe^{3+} , (g) dopamine/ Fe^{2+} , (h) dopamine/ Fe^{2+} , (i) mimosine/ Fe^{2+} , (j) mimosine/ Fe^{3+} complexes dispersed in Millipore water after 1 h (\square), 1 d (\triangle) and 8 d (\diamond) if kept at RT and after 1 d kept at 50°C (∇) respectively. Uncomplexed anchors (\blacktriangle) are shown as reference.

of nitrocatechol/ Fe^{3+} complexes was measured if these complexes were kept in Millipore water at RT for 24 h compared to spectra taken 1 h after complexation (Figure 7.16). These results indicate that fully protonated nitrocatechols interacted faster with Fe^{3+} compared to Fe^{2+} . However, fully protonated nitrocatechols started to interact with Fe^{2+} within 24 h.

The different UV/VIS and FTIR peak locations and shapes of nitrocatechol/ Fe^{2+} and nitrocatechol/ Fe^{3+} complexes indicate different interactions of nitrocatechols with Fe^{2+} and Fe^{3+} . Thus, time dependent changes in the UV/VIS spectra of nitrocatechol/ Fe^{2+} complexes cannot be assigned to a nitrocatechol-independent oxidation of Fe^{2+} to Fe^{3+} but should be ascribed to a slow reaction between nitrocatechols and Fe^{2+} which is absent if nitrocatechols are complexed with Fe^{3+} as suggested in Figure 7.10a.

Nitrocatechol Protonation State

HOMO \rightarrow LUMO transition peaks of nitrocatechol/iron complexes were considerably broader and shifted towards higher wavelengths already 1 h after complexation if once deprotonated nitrocatechols were complexed with Fe^{2+} compared to fully protonated nitrocatechol/ Fe^{2+} complexes (Table 7.2, Figure 7.14). Because deprotonated nitrocatechols interacted faster especially with Fe^{2+} ions compared to the fully protonated nitrocatechols, their binding to Fe_3O_4 surfaces can be accelerated by choosing appropriate solvents for their adsorption.

Furthermore, nitrocatechol adsorption on Fe_3O_4 NPs in a fully protonated form from ethanol and in a partially once deprotonated form from DMF resulted in equal EPR and FTIR spectra. Therefore it can be concluded that adsorption of nitrocatechols on Fe_3O_4 surfaces in a fully protonated form slows down their binding but does not prevent or alter the nitrocatechol-iron interactions after adsorption is completed.

Deprotonation of nitrocatechols upon adsorption to iron oxide NPs is well in agreement with literature where protons from alcohols of catechols have been reported to dissociate upon adsorption on TiO_2 [464–468]. As is shown here, adsorption of catechol derivatives is facilitated if these anchors are at least partially deprotonated already prior to adsorption. The NO_2 group lowers pK_{a1} values of nitrocatechols to 6.7 [463] compared to that of catechols ($pK_{a1} > 8.5$) [444]. Therefore, nitrocatechols can more readily bind to iron ions and adsorb on iron oxide surfaces in a pH range between 6.5 and 9 compared to catechols.

7.4.2 Catechols

No differences between reference spectra of catechols were seen whether they were aliquotted in Millipore water or Tris buffer respectively, indicating that they are protonated under these conditions (Figure 7.13). This was expected considering their pK_a values ($pK_a > 8.5$) [444]. Furthermore, the absence of electron transfer peaks of Millipore water based catechol/ Fe^{2+} complex solutions points to negligible interactions of catechols with Fe^{2+} ions if dispersed in Millipore water irrespective of complexation time (Figure 7.14 and 7.16), well in agreement with what has been reported [453].

While UV/VIS spectra of nitrocatechols and mimosine complexed with iron ions did not change significantly if kept at RT even after 8 d, the intensity of the $\pi \rightarrow \pi^*$ transitions located at ≈ 280 nm of complexed catechols decreased markedly if kept for 8 d at RT indicating slow catechol degradation. This is well in agreement with FTIR results (Figure 7.16). Moreover, catechol degradation was accelerated if kept at 50°C , where no $\pi \rightarrow \pi^*$ transition was seen after 1 d.

7.4.3 Mimosine

While UV/VIS spectra of Tris and Millipore water based mimosine/ Fe^{3+} complexes were independent of the complexation time and temperature, the electron transfer peak of mimosine/ Fe^{2+} complexes shifted towards that of the respective mimosine/ Fe^{3+} complexes with increasing complexation time (Figure 7.16e). This might indicate oxidation of Fe^{2+} to Fe^{3+} and hints to strong mimosine/ Fe^{3+} interactions but a low affinity of mimosine to Fe^{2+} which is in stark contrast to nitrocatechols.

7.5 Influence of the Anchor Binding Affinity on Fe_3O_4 Nanoparticle Stability

Whereas nitrocatechols have a high affinity to iron [469] and lead to good Fe_3O_4 NP stability as was shown in chapter 6, catechols have been reported to undergo iron catalyzed degradation [287] and thus lead to poor Fe_3O_4 NP stability. However, mimosine is known to have a high affinity towards Fe^{3+} [470] but only leads to intermediate Fe_3O_4 NP stability if used as an anchor for grafting low M_w dispersants to NPs (chapter 6). To elu-

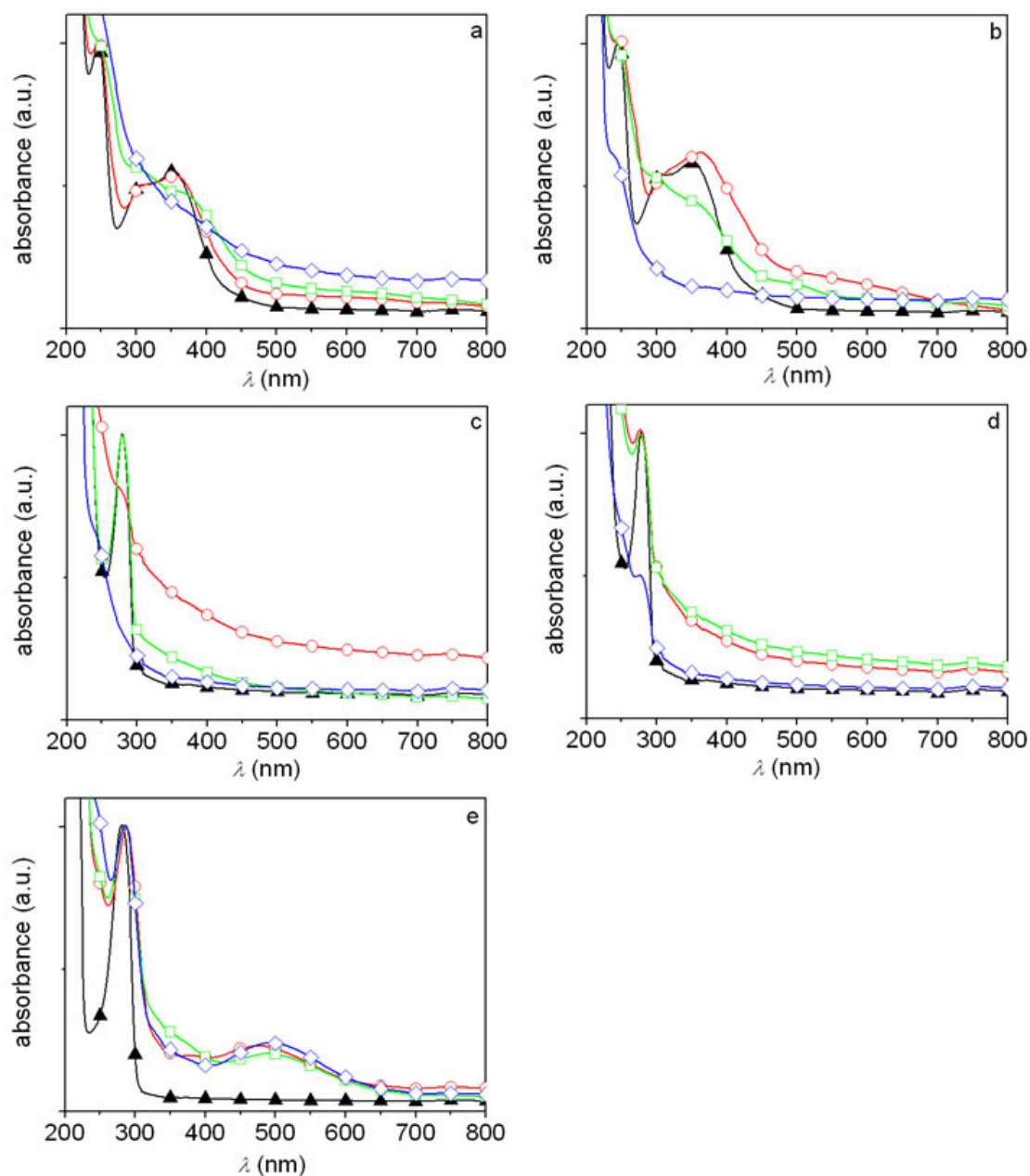


Figure 7.17: UV/VIS of supernatant of PEG-anchor stabilized iron oxide NPs. UV/VIS spectra of the supernatant of (a) PEG(5)-nitroDOPA, (b) PEG(5)-nitrodopamine, (c) PEG(5)-DOPA, (d) PEG(5)-dopamine and (e) PEG(5)-mimosine stabilized iron oxide NPs (\diamond) and as a comparison respective uncomplexed (\blacktriangle), Fe^{2+} (\circ) and Fe^{3+} (\square) complexed anchors. All solutions were Millipore water based and the molar ratio of anchors:iron ions was 1 : 1.

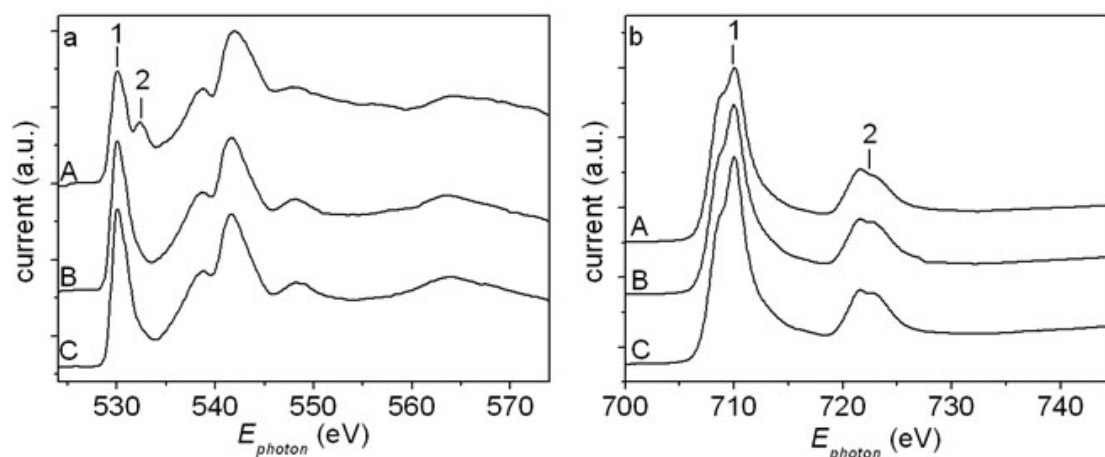


Figure 7.18: NEXAFS spectra of flat iron oxide surfaces coated with anchors. NEXAFS spectra of the (a) O K-edge and (b) Fe L-edge of (A) mimosine and (B) DOPA adsorbed on flat Fe_3O_4 surfaces. (C) Reference spectra of uncoated Fe_3O_4 surfaces.

to elucidate this apparent contradiction, UV/VIS spectra of anchor/iron complexes were compared to spectra taken from supernatants of Fe_3O_4 NPs stabilized with PEG(5)-anchors and dispersed in Millipore water. UV/VIS spectra revealed a charge transfer peak in supernatants of Fe_3O_4 NPs stabilized with PEG(5)-mimosine identical to Millipore based mimosine/ Fe^{3+} complexes (Figure 7.17). This close similarity suggests that the strong complexation of PEG(5)-mimosine rips out Fe^{3+} ions from the NP surface. As a result, PEG(5)-mimosine/ Fe^{3+} complexes are free in solution which leads to a loss of dispersants from the NP surface and a gradual Fe_3O_4 NP dissolution. This likely is the reason for only intermediate stability of PEG(5)-mimosine stabilized NPs. No such PEG(5)-anchor/iron ion complexes were found in supernatants of PEG(5)-nitrocatechol or PEG(5)-catechol stabilized Fe_3O_4 NPs (Figure 7.17).

Further evidence for iron oxide dissolution upon adsorption of mimosine is given by NEXAFS recorded on flat, magnetron sputtered Fe_3O_4 surfaces coated with mimosine and DOPA, respectively. NEXAFS spectra of the O K-edge and Fe L-edge of DOPA coated flat Fe_3O_4 surfaces closely resembled those of uncoated reference samples (Figure 7.18). This indicates that no significant change of iron oxide surfaces occurred upon adsorption of DOPA. However, clear differences were apparent for mimosine coated Fe_3O_4 surfaces.

The decrease in intensity of the peak at 530 eV (1) and the appearance of the peak at 532 eV (2) in the O K-edge NEXAFS spectra of mimosine coated Fe_3O_4 surfaces was evidence for a change in the iron oxide stoichiometry and suggested the appearance of an oxide species with a lower electron density (Figure 7.18a) [471–473]. The more pro-

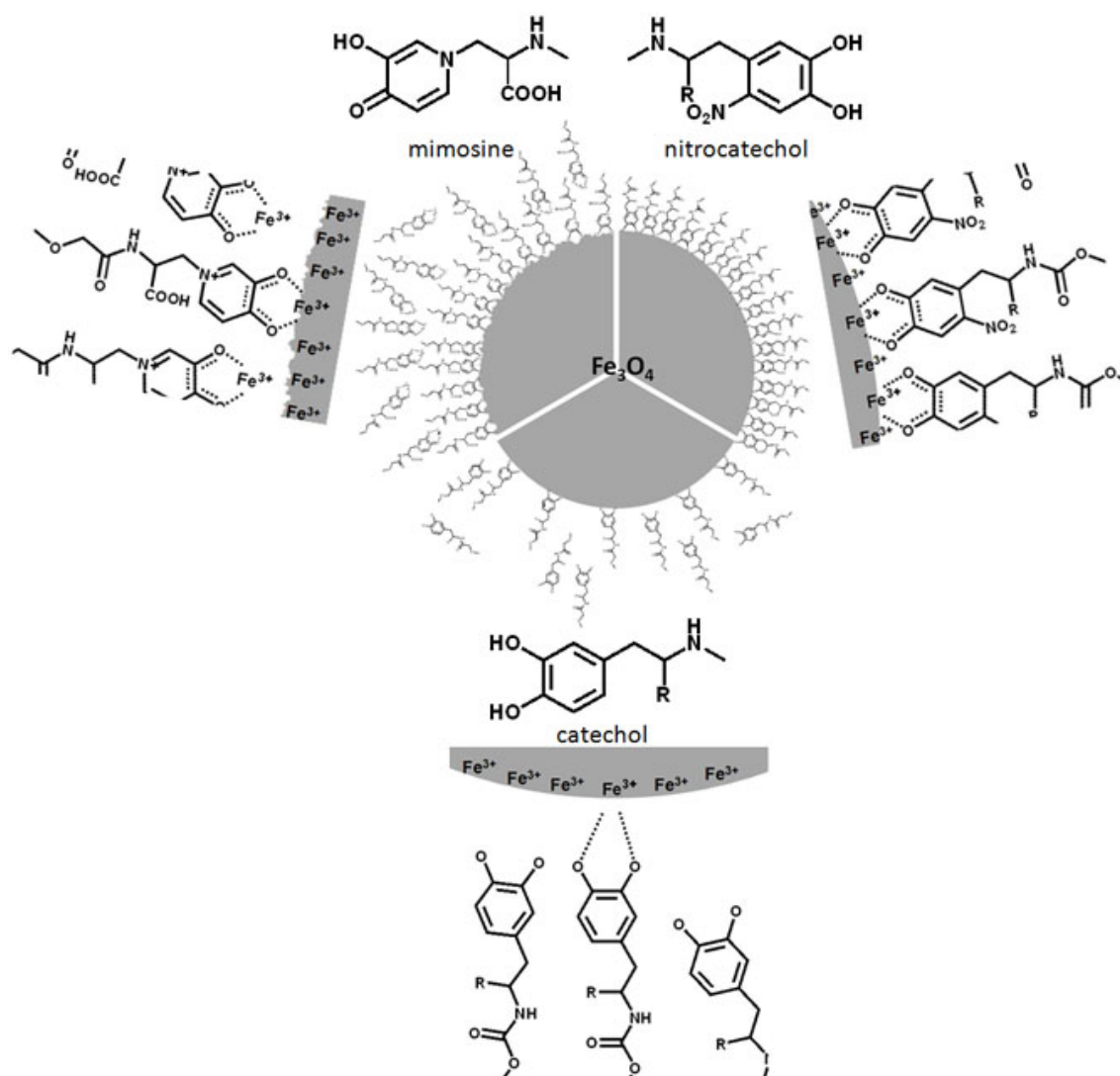


Figure 7.19: Cartoon of binding of different anchors to Fe_3O_4 NPs. While catechols bind weakly and reversibly to iron oxide NPs, the binding affinity of mimosine is high enough to remove Fe^{3+} ions through complexation which gradually dissolves iron oxide NPs. Nitrocatechols have an intermediate affinity to iron oxide NPs and strongly adsorb on Fe_3O_4 NPs without dissolving them. R = H for dopamine and nitrodopamine and R = COOH for DOPA and nitroDOPA respectively.

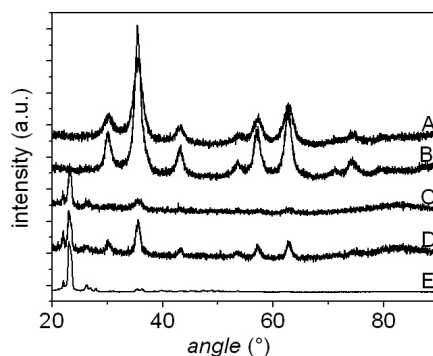


Figure 7.20: XRD of iron oxide NPs synthesized in the oil bath. As-synthesized iron oxide NPs synthesized in the oil bath with a mean radius of (A) 5 nm and (B) 13 nm. (C) 5 nm and (D) 13 nm NPs after stabilization with PEG(5)-nitroDOPA. As a reference, (E) PEG(5)-nitroDOPA is shown.

nounced shoulder at the *Fe* L-edge at 710 eV (1) and the different ratios of the two convoluted peaks around 722 eV (2) indicated that some surface iron atoms had a higher electron density after the adsorption of mimosine compared to reference Fe_3O_4 surfaces (Figure 7.18b). If mimosine partially dissolved iron oxide surfaces by removing Fe^{3+} , the remaining surface would be depleted of iron ions. The resulting excess of electrons would increase the electron density at the remaining surface iron atoms. This could explain the changes at the *Fe* L-edge of mimosine coated iron oxide surfaces observed in Figure 7.18b. Thus NEXAFS results are well in agreement with UV/VIS results where dissolution of iron oxide surface upon adsorption of mimosine was shown (Figure 7.17). These NEXAFS results further indicate that the iron oxide dissolution induced by mimosine adsorption is independent of the surface curvature, which is high on NPs and very low on flat surfaces. Thus, as already indicated above, the binding affinity of anchors to Fe_3O_4 cannot be maximized as this leads to a gradual degradation of the Fe_3O_4 surface. The anchor binding affinity rather has to be optimized such that it is high enough to prevent reversible dispersant adsorption but it is still should be below the threshold where anchors start to dissolve Fe_3O_4 surfaces (Figure 7.19).

7.6 Influence of nitroDOPA on Saturation Magnetization

As described in section 5.5.1, the saturation magnetization of superparamagnetic NPs is considerably below that of the respective bulk material [35]. This might partially be assigned to surface anisotropy effects [36]. However, it has often been reported that the sat-

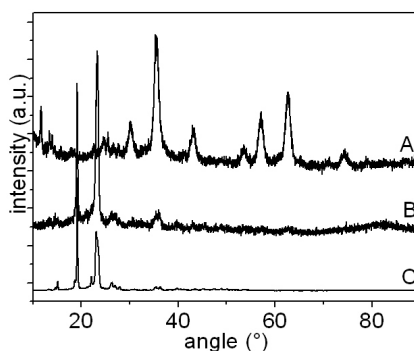


Figure 7.21: XRD of iron oxide NPs synthesized in the MW. The XRD spectra of (A) as-synthesized and (B) PEG(5)-nitroDOPA stabilized iron oxide NPs heated in the MW for 3 min. (C) PEG(5)-nitroDOPA is shown as a reference.

Table 7.3: Saturation magnetizations (M_s) of Fe_3O_4 NPs synthesized with the non-aqueous sol-gel method.

heating method during synthesis	r_{core} (nm)	M_s of uncoated NPs ($\text{emu}/g_{Fe_3O_4}$)	M_s of PEG(5)-nitroDOPA stabilized NPs ($\text{emu}/g_{Fe_3O_4}$)
MW	4.0	16.3	10.5
MW	7.0	44.4	29.9
oil bath	2.1	43.5	31.5
oil bath	4.5	47.5	38.8

uration magnetization of superparamagnetic iron oxide NPs further decreases upon steric stabilization [35, 474]. The decreased saturation magnetization for sterically stabilized NPs might at least partially be attributed to the interactions between anchors and surface iron ions. According to EPR results, nitroDOPA magnetically decouples surface Fe(III) (Figure 7.3). To see, if these distortions of surface Fe(III) ions affect the saturation magnetization of PEG-nitroDOPA stabilized NPs, the magnetization of PEG(5)-nitroDOPA stabilized Fe_3O_4 NPs was compared to that of the respective uncoated NPs. To check, if potential differences in the magnetization curves of PEG(5)-nitroDOPA stabilized and unstabilized iron oxide NPs can be related to stabilization effects rather than to changes in the crystal structure of the iron oxide cores, XRD spectra of stabilized NPs were compared to those of unstabilized counterparts.

As can be seen in Figures 7.20 and 7.21, the inverse spinel structure of Fe_3O_4 NPs is retained upon stabilization with PEG(5)-nitroDOPA. The additional peak at 23° seen for NPs stabilized with PEG(5)-nitroDOPA can be assigned to scattering of PEG(5)-nitroDOPA. The sensitivity of XRD, however, is too low to detect changes in the surface

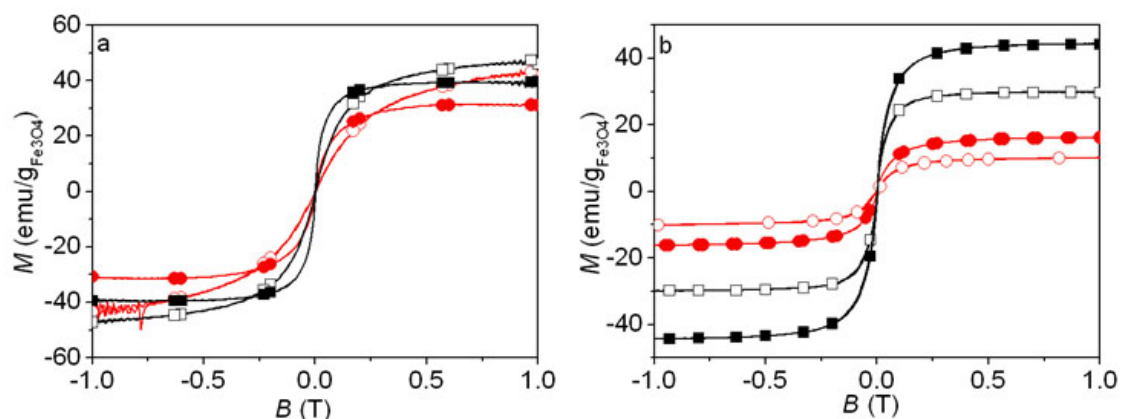


Figure 7.22: VSM measurements of iron oxide NPs. VSM was measured on iron oxide NPs (a) synthesized in the oil bath with a core radius of 5 nm (■) and 2.5 nm (●) and (b) in the MW with an average core radius of the larger fraction of 7 nm (■) and 3 nm (●) on uncoated (filled symbols) and PEG(5)-nitroDOPA stabilized (empty symbols) iron oxide NPs.

layers of these NPs, which might occur upon adsorption of PEG-nitroDOPA. Therefore, potential differences in magnetic properties of stabilized compared to unstabilized NPs are most likely related to surface effects induced through the adsorption of nitroDOPA on the iron oxide surface. Additionally, changes in magnetic interactions might also be assigned to decreased interparticle interactions because stabilized NPs are spatially separated from each other, in contrast to as-synthesized NPs. However, a phase transition of the iron oxide cores from Fe_3O_4 to $\gamma-Fe_2O_3$ cannot be excluded based on these XRD measurements.

The saturation magnetization of iron oxide NPs synthesized in the MW decreased by 37 % and 33 % for 4 and 7 nm core radius NPs upon stabilization with PEG(5)-nitroDOPA whereas that of iron oxide NPs synthesized in the oil bath decreased by 28 % and 18 % for 2.5 and 5 nm core radius NPs (Table 7.3). The resulting saturation magnetizations are in the range reported by Gupta *et al.* for sterically stabilized NPs [233] but well below values reported by others for iron oxide NPs with similar core size iron oxide NPs (70 $emu/g(Fe_3O_4)$ for oleic acid stabilized [475] and ≈ 60 $emu/g(Fe_3O_4)$ for PMAA coated [474]).

7.6.1 Surface Effects on Saturation Magnetization

If it is assumed that the decrease in saturation magnetization can be solely assigned to surface effects, the non-magnetic layer of NPs synthesized in the oil bath would be 0.3

nm, irrespective if PEG(5)-nitroDOPA was adsorbed on 2.5 nm or 5 nm core diameter NPs. Considering that magnetite has an inverse spinel structure with a lattice constant of 0.8397 nm [476], the magnetically dead layer would correspond to $\approx 1/3$ of a lattice constant or approximately the distance between two adjacent Fe centers in the [221] direction [342].

However, the density of iron ions at the surface greatly exceeds that of nitrocatechols. Thus, not all surface iron ions interact with nitrocatechols. Furthermore, for these calculations, NPs were assumed as spheres. Considering the irregular shape of the NPs and their surface roughness, the actual surface area was underestimated in these calculations. Therefore, the average thickness of a magnetically dead layer as it was calculated here can only be taken as a rough estimate. Nevertheless, the decreased saturation magnetization of Fe_3O_4 NPs upon stabilization with PEG(5)-nitroDOPA supports EPR results where strong interactions of nitroDOPA with iron oxide surfaces was shown. This strong interaction not only distorts surface Fe(III) ions as was shown in this chapter (Figure 7.3), but also influences the magnetic properties of the outermost atomic layers of PEG(5)-nitroDOPA Fe_3O_4 cores.

7.7 Summary

The addition of electronegative groups such as a NO_2 to the catechol ring greatly enhances electronic interactions between these anchors and iron ions in solution as well as, importantly, to Fe_3O_4 NP surfaces. As a result, catechol derivatives that are electronegatively substituted lead to greatly enhanced Fe_3O_4 NP stability if covalently linked to a spacer molecule such as PEG. NitroDOPA (and nitrocatechols in general) was shown to bind to Fe(II) leading to strong electron delocalization. As a result of these electron delocalizations, the electron density was increased on the nitrocatechols, as was shown with EPR and FTIR, whereas the electron density at surface iron sites was reduced. As a result of the firm adhesion of nitroDOPA to Fe_3O_4 surfaces, a magnetically decoupled, rhombohedrally distorted Fe(III) signal with $g = 3.9$ was measured with EPR upon adsorption of PEG(5)-nitroDOPA to Fe_3O_4 NP surfaces. The magnetic decoupling is also believed to be one of the reasons for the observed decreased saturation magnetization of PEG-nitroDOPA stabilized NPs compared to unstabilized counterparts.

The significance of this strong electron delocalization on the binding affinity of said anchors and thus on the NP stability was illustrated when comparing Fe_3O_4 and Fe_2O_3 NPs.

In the latter case, no Fe(II) was available for donating electrons to undergo strong electron delocalization reactions between surface bound Fe(II) ions and nitroDOPA. Thus, no rhombohedrally distorted Fe(III) signal at $g = 3.9$ was measured with EPR and the corresponding stability of PEG(5)-nitroDOPA coated NPs was poor.

The addition of an electronegative NO_2 group to the catechol ring enlarges the conjugated electron system of the resulting nitrocatechols compared to the unsubstituted catechols. This facilitates electron transfer reactions with surface iron ions. The facilitated electron transfer reactions are responsible for exceptionally strong binding of nitrocatechols to Fe_3O_4 surfaces.

Furthermore, electronegatively substituted catechols are less prone to oxidation compared to catechols. Oxidative degradation of catechols to semiquinones leads to a poor binding affinity of the degraded anchors to Fe_3O_4 . However, no such reaction was seen for nitrocatechols adsorbed on Fe_3O_4 surfaces. In summary, electronegative aromatic ring substituents such as NO_2 enhance their binding affinity towards Fe_3O_4 surfaces through both, a facilitated electron delocalization between the anchors and surface iron ions, and by preventing an oxidative degradation of anchors.

Catechol derivatives interact faster and stronger with iron ions, if they are partially deprotonated prior to their adsorption or complexation. Furthermore, it has been shown that they adsorb best if the IEP of the oxide is close to the pK_{a1} of the catechol derivative [301]. Electronegative substituents such as NO_2 , which are directly bound to the catechol ring, lower their pK_{a1} value to ≈ 6.5 [442]. Thus, nitrocatechols bind faster if they are adsorbed at $6.5 < \text{pH} < 9$ or in organic solvents such as ethanol, where they were shown to be partially deprotonated.

Important in the context of optimization of dispersant anchors for steric stabilization of NPs, our findings demonstrate that there is an optimal (rather than maximal) binding affinity of anchors towards the metal ion of iron oxide NPs. Whereas low binding affinities of anchors to iron oxide surfaces lead to reversible adsorption and thus poor NP stability, too high binding affinity resulted in gradual Fe_3O_4 NP dissolution as was exemplified for mimosine. In the latter case mimosine/ Fe^{3+} complexes were found in the supernatant of PEG(5)-mimosine stabilized Fe_3O_4 NPs. Thus, the affinity should be high enough to ensure essentially irreversible adsorption in the salt, temperature and pH range in which sterically stabilized NPs will be applied, but below the limit that causes substrate dissolution through complex formation. NitroDOPA was shown to fulfill these requirements for the conditions relevant for biomedical and biotechnologic applications.

8.1 Background

Apart from the choice of suitable anchors, spacers are a key aspect for the stability of sterically stabilized NPs. While anchors have to firmly bind molecules to the NP surfaces, spacers have to prevent that NPs get into too close proximity where attractive Van-der-Waals forces become predominant and drive their agglomeration.

It would greatly facilitate the design and optimization of sterically stabilized core-shell NPs if inter-particle potentials could be calculated. Such calculations, however, require knowledge of the dispersant layer thickness, packing density and the dispersant density profile [195, 477]. To this end, these parameters were investigated as function of the spacer molecular weight (M_w), in our case the M_w of PEG on two different core sizes, with DLS, TGA and SANS and are presented in this chapter.

8.1.1 Polymer Density Profile on Flat Surfaces

Numerous theoretical [208, 478, 479, 481, 482] and experimental studies have been published on the density profile of polymers adsorbed on flat surfaces. De Gennes used scaling theories to predict the density profile of polymers adsorbed on flat surfaces. He assumed that all chain ends are located at the interface resulting in a step-function polymer density profile (Figure 8.1) [208]. Based on such profiles, an inter-particle potential, that takes Van-der-Waals attraction and steric repulsion potential into account, has been shown to result in a logarithmic decay with inter-particle distance [477].

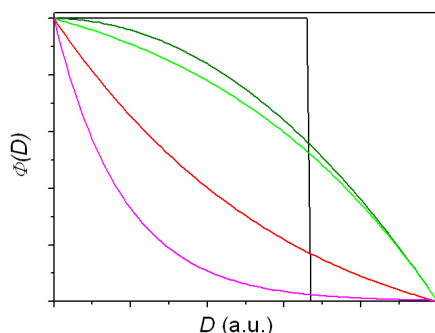


Figure 8.1: *Dispersant density profiles.* Different dispersant density profiles are compared, namely the step-function profile predicted by de Gennes *et al.* [208] (black), the parabolic density profile (green) calculated from the MWC theory [478, 479], the density profile of chain ends that decays like a Gaussian curve (magenta) if the maximum of the latter is translated to $D = 0$ predicted by Dan *et al.* [480] and an exponential dispersant density decay where the exponent α is ≥ 0 (red) and < 0 (light green).

Theoretical self-consistent field (SFC) theory calculations were used to refine this step profile by relaxing the stringent requirement that chain ends are located at the interface. This resulted in the Milner, Witten, Cater (MWC) theory where a parabolic polymer density profile was found (Figure 8.1) [478, 479, 482]. Shim and Cates further refined this model by taking into account the finite extensibility of the polymer chains and extended it to high polymer coverages. Based on these refined models it was found that with increasing surface coverage, the density profile changes from a parabolic to a step-function profile for tightly packed, highly stretched polymers [483]. More than 10 years later, a Monte-Carlo simulation revealed deviations from the parabolic density profile namely that the density profile has a smooth tail and a depletion zone close to the surface if PEG is dissolved in a good solvent [484].

8.1.2 Polymer Density Profile on Highly Curved Surfaces

If the dispersant layer thickness is much smaller than the core diameter, steric repulsion potentials of NPs can be derived from those of flat surfaces based on scaling theories and the Derjaguin approximation. However, this theory fails if the dispersant chain dimensions approach or exceed the core diameter [480, 485, 486], conditions usually met if NPs are sterically stabilized in aqueous media. As a result, the Derjaguin approximation has been adapted for polymers adsorbed on curved surfaces. Nevertheless, it is most accurate for core sizes that largely exceed the dimensions of dispersants [487].

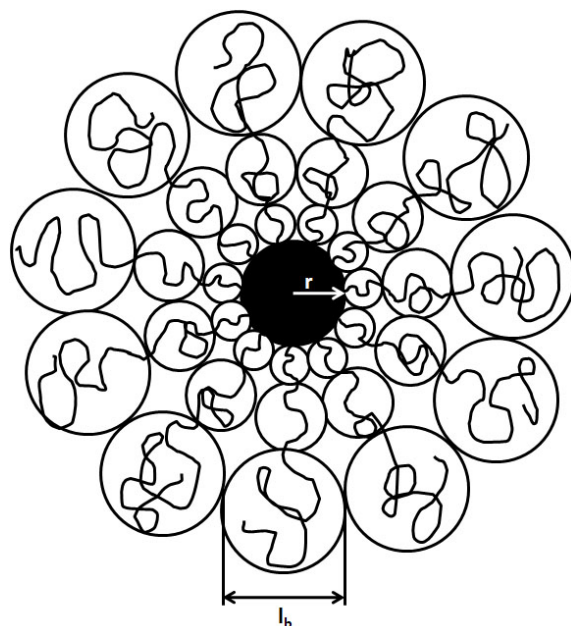


Figure 8.2: Cartoon of the blob model assumed in the scaling theory. In the scaling theory, polymers adsorbed on a NP with radius r are divided into so-called blobs with the blob size l_b .

Scaling Theory

Scaling theory describes the behavior of semidilute polymer solutions where the polymer chain is divided into so-called blobs with a length l_b that increases with increasing distance to the NP core (Figure 8.2). Within a blob, the polymer chains undergo self-avoiding walk. Blobs are assumed to act as hard spheres that do not allow adjacent chains to interact [208, 487]. The scaling theory predicts the dependence of the layer thickness from the solvent quality, polymer chain length and stiffness [196]. A very early study reported by Alexander claimed that the density profile of non-interacting chains adsorbed on NPs decayed exponentially. Furthermore, the brush thickness was reported to linearly depend on the polymer M_w [488]. Thus, this and follow-up studies provided evidence that the density profile of dispersants adsorbed on the NPs obtained from scaling theories differs from that of polymers adsorbed on flat surfaces [489].

Self-Consistent Field Theory

While the scaling theory is comparably easy to apply, it does not reveal insights into inter-chain interactions [196] and results in a qualitatively wrong density profile [490]. If more detailed information about the dispersant density profile on NPs is warranted, a

self-consistent field (SCF) theory such as the MWC theory has to be applied [487]. Ball *et al.* who used the SCF theory [491] and Li *et al.* who compared the SCF theory to exact solutions obtained by minimizing the free energy [490] found that in the limit of low dispersant packing densities and high dispersant M_w s, the density profile close to the NP interface is depleted from free polymer chain ends. The thickness of this depletion layer described by Li *et al.* [490] was well in agreement with that found by Monte Carlo simulations [485].

Next to the fact that the depletion zone of free polymer chain ends was neglected, all models established for the polymer density profile on flat surfaces assumed negligible interchain penetration. While this assumption holds for long chains and low packing densities, short chains significantly interpenetrate adjacent chains. This chain interpenetration leads to a parabolic density profile that asymptotically decays to zero at the end. For polymer chains shorter than 1000 repeat units, this change in the polymer density profile leads to an earlier and gradual onset of repulsive inter-particle forces compared to a parabolic polymer density profile [492]. It is thus of significance for the prediction of inter-particle forces.

Furthermore, the asymptotic decay of the polymer brush becomes increasingly important with decreasing core radius. According to a modified SCF theory, the dispersant density profile decreases faster and thus the dispersant layer thickness becomes thinner with decreasing NP core radius [487, 493]. The faster decay of the dispersant density profile with decreasing core radius was confirmed by Monte Carlo simulations [485]. Dan *et al.* claimed the density profile of free chains to decrease like a Gaussian curve when the maximum of the Gaussian curve is translated to $D = 0$ nm (denoted as Gaussian profile) (Figure 8.1) if the dispersant layer thickness approached the core radius [480]. Later, this density profile has been revised. It was predicted that the dispersant density profile undergoes a smooth change from a parabolic decay at low surface curvatures and for small or stiff dispersants to a power law decay similar to that of star polymers if dispersants are adsorbed on highly curved surfaces or if dispersants are flexible [196, 487].

In summary, despite the numerous theoretical [494, 495] studies on the density profile of polymers adsorbed on highly curved surfaces and experimental investigations of the density profile of block-co-polymers and star-polymers [496–498] the density profile of polymers adsorbed on highly curved surfaces is still debated. One of the main reasons for the in-conclusive literature might be the lack of experimental data on dispersants irreversibly grafted to highly curved surfaces. Reversible dispersant adsorption is likely to change the dispersant density profile as the latter is dependent on the dispersant packing

density. Moreover, dispersant density profiles often are investigated with scattering techniques [496–498]. However, desorbed dispersants also scatter and therefore contribute to the total scattering curve measured for core-shell NPs. These desorbed dispersants thus hamper the analysis of scattering data.

As was shown in chapters 6 and 7, nitroDOPA can irreversibly bind dispersants to Fe_3O_4 NP surfaces. Thus, this anchor potentially allows to experimentally assess the dispersant density profile on Fe_3O_4 NPs. This would be highly interesting because, as will be shown below, the dispersant density profile critically affects inter-particle potentials and therefore NP stability. The design of sterically stabilized core-shell NPs could be greatly facilitated and improved if one could theoretically calculate the inter-particle potential and therefore NP stability prior to the assembly of NPs. A simple approach to calculate inter-particle interaction potentials is described next.

8.2 Calculations of the Inter-Particle Interaction Potential

Generally, the inter-particle potential of magnetic NPs is composed of four main contributions, namely the attractive Van-der-Waals potential (U_{VdW}), the attractive magnetic potential (U_{mag}), the repulsive electrostatic potential ($U_{electrostatic}$) and the repulsive steric potential (U_{steric}) [499–501]

$$U_{tot} = U_{VdW} + U_{mag} + U_{electrostatic} + U_{steric}. \quad (8.1)$$

8.2.1 Van-der-Waals Potential

The attractive inter-particle Van-der-Waals potential is based on permanently and temporarily induced dipolar interaction potentials and a dispersion interaction potential. The latter is a measure of the energy change if an object interacts with the solvent rather than with itself [206].

In contrast to the Van-der-Waals attraction energy between molecules that decays with D^{-6} , where D is the inter-particle distance, the Van-der-Waals attraction energy between two NPs is $\propto D^{-2}$ (equation 8.2). To account for longer range attractive inter-particle interactions, the retarded Van-der-Waals interaction potential can be calculated [499, 500]

$$U_{VdW} = -\frac{A_{\text{eff}}}{6} \left(\frac{2r^2}{D(4r+D)} + \frac{2r^2}{(2r+D)^2} + \ln \frac{D(4r+D)}{(2r+D)^2} \right) \quad (8.2)$$

where A_{eff} is the retarded Hamaker constant defined as

$$A_{\text{eff}} = \frac{4}{3} k_B T \left(\frac{\epsilon_{\text{Fe}_3\text{O}_4}(0) - \epsilon_{\text{water}}(0)}{\epsilon_{\text{Fe}_3\text{O}_4}(0) + \epsilon_{\text{water}}(0)} \right)^2 + \frac{3hf}{16\sqrt{2}} \frac{(n_0^2 \text{Fe}_3\text{O}_4 - n_0^2 \text{water})^2}{(n_0^2 \text{Fe}_3\text{O}_4 + n_0^2 \text{water})^{\frac{3}{2}}} F(H) \quad (8.3)$$

where

$$F(H) \approx \left(1 + \left(\frac{\pi H}{4\sqrt{2}} \right)^{\frac{3}{2}} \right)^{-\frac{2}{3}} \quad (8.4)$$

and

$$H = n_0 (n_0^2 \text{Fe}_3\text{O}_4 + n_0^2 \text{water})^{\frac{1}{2}} \frac{Df}{c} \quad (8.5)$$

r the core radius, $\epsilon(0)$ the dielectric constant which is 20'000 for Fe_3O_4 [502] and 80 for water [499], n_0 the refractive index taken as 1.970 for Fe_3O_4 and 1.333 for water [230], f the frequency of the dominant relaxation in the UV region (1.88×10^{16} rad/s), H the Hamaker constant and c the speed of light.

The Van-der-Waals forces of core-shell NPs have been shown to be significantly influenced by the attraction forces of the shell given that the dielectric properties of the shell are sufficiently different from those of the media NPs are dispersed in. However, they usually do not contribute significantly to the overall inter-particle potential [503, 504]. Because the dielectric properties of PEG ($n = 1.36$) [505] are close to those of water ($n = 1.33$), the Van-der-Waals attraction potential of the shells was neglected for the following calculations as was suggested by Bevan *et al.* [503].

8.2.2 Magnetic Potential

The magnetic inter-particle potential can be quantified using [499–501]

$$U_{\text{mag}} = -\frac{8\pi\mu_0 r^6 M_s^2}{9(D+2r)^3} \quad (8.6)$$

where μ_0 is the permeability of free space and M_s the saturation magnetization.

8.2.3 Electrostatic Potential

The electrostatic potential can be described as [500]

$$U_{\text{electrostatic}} = 2\pi r \epsilon_r \epsilon_0 \zeta^2 \ln(1 + e^{-\kappa(D-L)}) \quad (8.7)$$

where the Debye length κ is defined as

$$\kappa^{-1} = \sqrt{\frac{\sum \rho_{\infty i} e^2 z_i^2}{\epsilon \epsilon_0 k_B T}} \quad (8.8)$$

ζ is the zeta potential, L the dispersant layer thickness, e the electron charge, z the valency of the ions and $\rho_{\infty i}$ the ion concentration.

8.2.4 Steric Potential

As described above, the steric repulsion potential qualitatively and quantitatively depends on the dispersant density profile [195]. Therefore, inter-particle potentials arising from the two most often used packing density profiles, the de Gennes step-function and the parabolic packing density profile, are compared.

Steric Potential According to the de Gennes Theory

Because of the simplicity of the de Gennes step-function density profile [208], it is often used to calculate inter-particle interactions despite the consensus that the boundary condition where all chain ends are presented at the NP interface is inappropriate.

Using the de Gennes model, the dispersant layer thickness can be approximated as

$$L = \left(\frac{5}{3}\right)^{\frac{1}{2}} R_G \quad (8.9)$$

where R_G is the radius of gyration of the polymer [500] defined as [200, 207]

$$R_G = \sqrt{\frac{1}{N} \sum_{i=1}^N \langle |\vec{r}_i - \vec{r}_c|^2 \rangle}. \quad (8.10)$$

\vec{r}_i is the position of the polymer segment and \vec{r}_c the center of gravity of this polymer. The steric repulsion potential can then be calculated with [500, 506]

$$U_{\text{steric}} = \begin{cases} \frac{5}{18} f(r)^{\frac{3}{2}} \left(-\ln \left(\frac{D}{L} + \frac{1}{1 + \frac{\sqrt{f(r)}}{2}} \right) \right) & \text{for } D < L \\ \frac{5}{18} f(r)^{\frac{3}{2}} \frac{1}{1 + \frac{\sqrt{f(r)}}{2}} \frac{L}{D} e^{\frac{\sqrt{f(r)}(D-L)}{2\sigma}} & \text{for } D > L \end{cases} \quad (8.11)$$

$f(r)$ is the number of dispersants per NP defined as

$$f(r) = 4\pi r^2 n_{\text{agg}} \quad (8.12)$$

with n_{agg} being the dispersant packing density.

Steric Potential According to the SCF Theory

In the SCF theory, the dispersant layer thickness can be calculated based on the MWC theory using [479]

$$L = \left(\frac{8}{\pi^2} \right)^{\frac{1}{3}} N a^{\frac{5}{3}} n_{\text{agg}}^{\frac{1}{3}} \left(\frac{v_e}{a^3} \right)^{\frac{1}{3}} \quad (8.13)$$

where N is the number of repeat units, a the length of one repeat unit (r.u.) (0.38 nm for PEG) [507, 508] and $\eta_E = a^3$ the free volume of a r.u. [479].

The resulting steric potential is defined as [495, 501]

$$U_{\text{steric}} = \begin{cases} \infty & \text{for } D < 2r \\ U_0 \left(-\ln(y) - \frac{9}{5}(1-y) + \frac{1}{3}(1-y^3) - \frac{1}{30}(1-y^6) \right) & \text{for } 2r < D < 2(r+L) \\ 0 & \text{for } D > 2(r+L) \end{cases} \quad (8.14)$$

where

$$y = \frac{D-2r}{2L} \quad (8.15)$$

and

$$U_0 = \left(\frac{\pi^3 L n_{\text{agg}} k_B T}{12 N p^2} \right) a L^2 \quad (8.16)$$

8.2.5 Total Inter-Particle Potential Using the MWC Theory

As can be seen in Figure 8.3 the inter-particle potential of PEG(5)-nitroDOPA stabilized NPs is dominated by the steric repulsion potential at inter-particle distances larger than 1 - 4 nm, dependent on the core size. These potentials were calculated using the parameters summarized in Table 8.1. As expected, the electrostatic potential of these NPs, which are surrounded by a PEG(5)-nitroDOPA monolayer that effectively screens the surface charge, is negligible. The magnetic interaction potential of Fe_3O_4 NPs with a core radius of 5 nm is more negative and protrudes farther from the NP surface compared to the Van-der-Waals potential, in stark contrast to the 2.5 nm core radius NPs.

A comparison between PEG-nitroDOPA stabilized 2.5 nm and 5 nm core radius NPs reveals that the latter are more difficult to stabilize (Figures 8.4 and 8.5). Not only is the Van-der-Waals attraction potential more negative for 5 nm core radius NPs but also the magnetic attraction potential of 5 nm core radius NPs is more attractive than that of 2.5 nm NPs. The latter is due to the higher M_s of the 5 nm compared to the 2.5 nm core radius NPs. Thus, achieving good stability, especially of magnetic NPs, gets increasingly difficult with increasing core size and requires higher dispersant packing densities and $M_{w,s}$. While PEG(0.8)-nitroDOPA stabilized NPs are expected from Figure 8.4a to be unstable irrespective of the dispersant packing density for both core sizes, PEG(1.5)-nitroDOPA stabilized NPs might temporarily be stable at room temperature (Figure 8.4b). However, the energy barriers of iron oxide NPs stabilized with 3 PEG(1.5)-nitroDOPA molecules/ nm^2 are with 14 $k_B T$ and 52 $k_B T$ for 5 nm and 2.5 nm core radius NPs relatively low. Therefore, NP agglomeration is expected if they are stored for prolonged times even if PEG(1.5)-nitroDOPA is densely packed at the NP surface (Figures 8.4 and 8.5). However, NPs stabilized with PEG(5)-nitroDOPA and PEG(10)-nitroDOPA are expected to be stable also at elevated temperature if the dispersant packing density is > 1 molecule/ nm^2 (Figures 8.4 and 8.5).

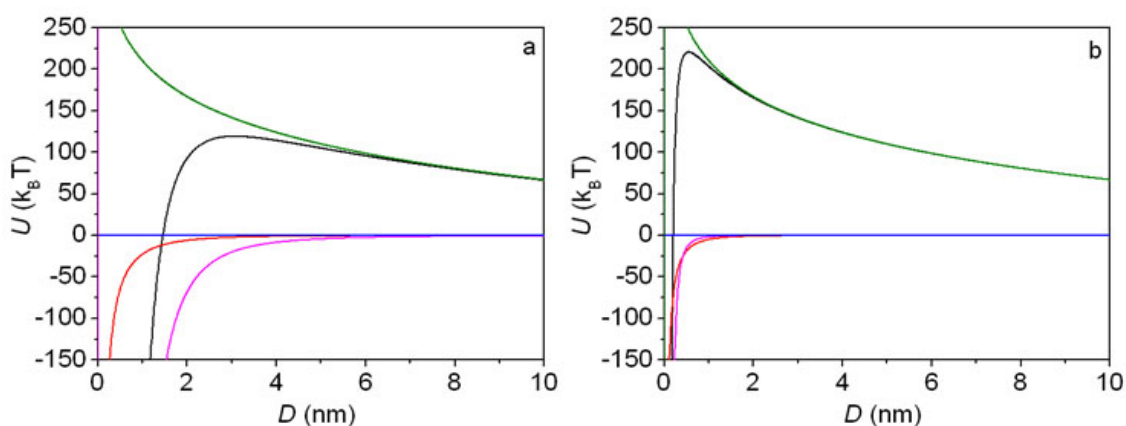


Figure 8.3: Inter-particle potential calculated with the SCF theory for PEG(5)-nitroDOPA stabilized NPs. The total inter-particle potential (black) is shown as the sum of the Van-der-Waals potential (red), magnetic potential (magenta), steric potential (green) and electrostatic potential (blue). These potentials were calculated for (a) 5 nm core radius and (b) 2.5 nm core radius Fe_3O_4 NPs stabilized with 1 molecule/nm² PEG(5)-nitroDOPA.

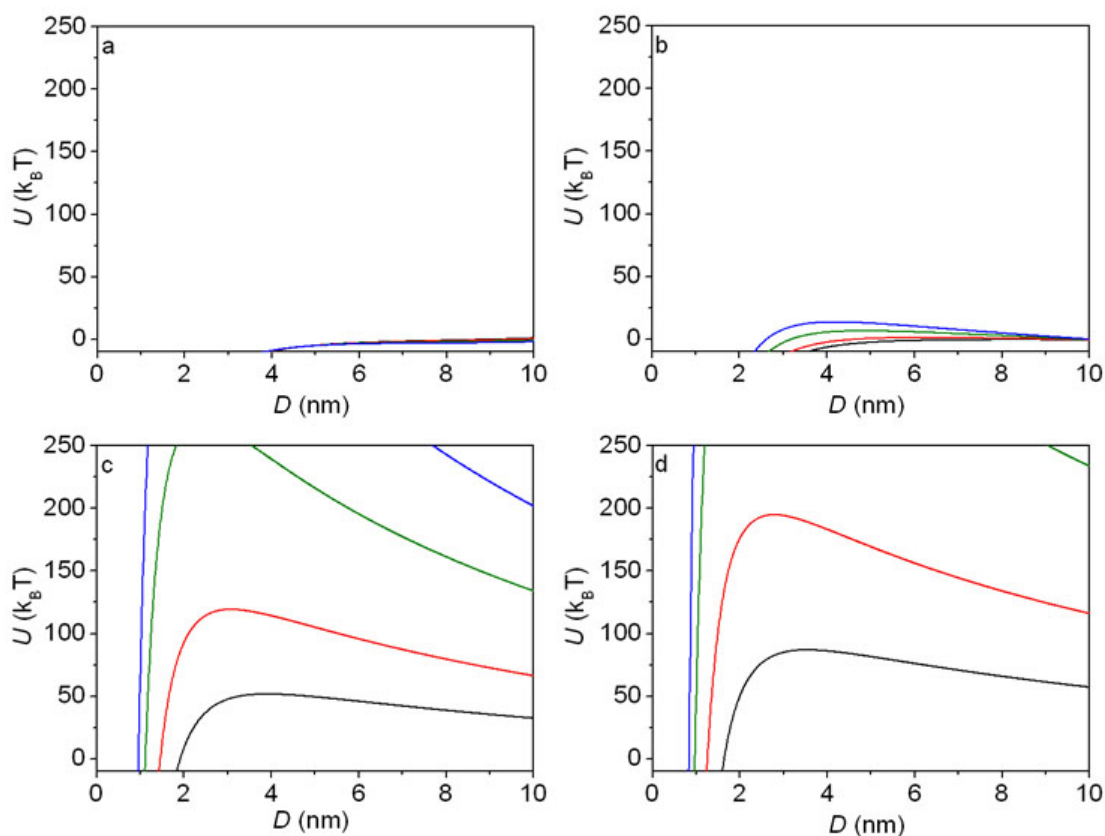


Figure 8.4: Inter-particle potential calculated with the SCF theory for 5 nm core radius NPs. The inter-particle potential calculated using the SCF theory of 5 nm core radius iron oxide NPs stabilized with (a) PEG(0.8)-nitroDOPA, (b) PEG(1.5)-nitroDOPA, (c) PEG(5)-nitroDOPA and (d) PEG(10)-nitroDOPA for dispersant packing densities of 0.5 molecule/nm² (black), 1 molecule/nm² (red), 2 molecules/nm² (green) and 3 molecules/nm² (blue).

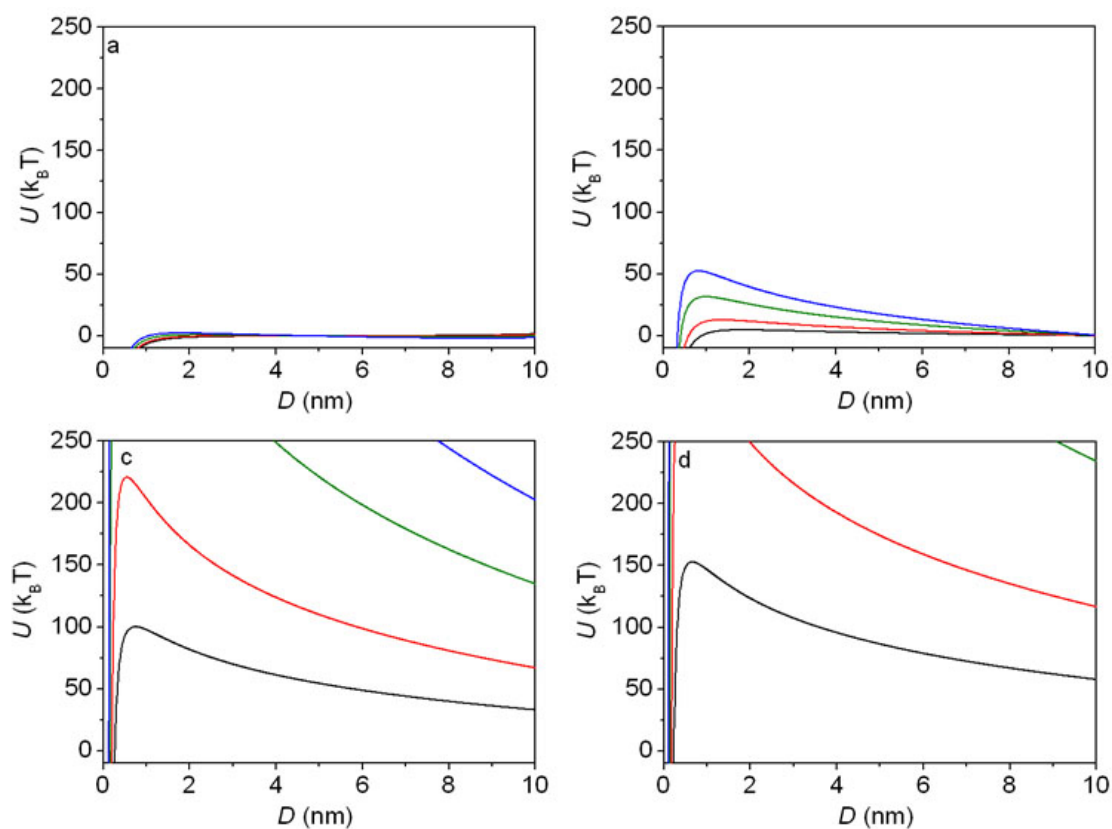


Figure 8.5: Inter-particle potential calculated with the SCF theory for 2.5 nm core radius NPs. The inter-particle potential calculated using the SCF theory of 2.5 nm core radius iron oxide NPs stabilized with (a) PEG(0.8)-nitroDOPA, (b) PEG(1.5)-nitroDOPA, (c) PEG(5)-nitroDOPA and (d) PEG(10)-nitroDOPA for dispersant packing densities of 0.5 molecule/nm² (black), 1 molecule/nm² (red), 2 molecules/nm² (green) and 3 molecules/nm² (blue).

Table 8.1: Parameters used to calculate the inter-particle potentials.

core radius (nm)	PEG of nitroDOPA (M_w (kDa))	M_s ($\frac{A}{m}$)	ζ (mV)	L (MWC theory) (nm)	R_F (nm)
2.5	0.8	1.4×10^5	-2	2.8	2.2
2.5	1.5	1.4×10^5	-0.7	5.1	3.2
2.5	5	1.4×10^5	-1.2	14.8	6.7
2.5	10	1.4×10^5	-0.2	20.5	10.1
5	0.8	2.0×10^5	-2	2.8	2.2
5	1.5	2.0×10^5	-0.7	5.1	3.2
5	5	2.0×10^5	-1.2	14.8	6.7
5	10	2.0×10^5	-0.2	20.5	10.1

8.2.6 Total Inter-Particle Potential Using the de Gennes Theory

In contrast to the inter-particle potential calculated using the SCF theory, the inter-particle potential calculated according to the scaling theory, that assumes a step-function dispersant density profile, ends rather abruptly at inter-particle distances slightly larger than R_F of the dispersants (Figure 8.6). This is a consequence of the dispersant density profile that implies an abrupt ending of the dispersant layer and thus of the steric repulsion potential. Given the opinion that the density profile of polymers adsorbed on NPs cannot be described with the de Gennes theory, the abrupt decay of the inter-particle potential is rather unrealistic. Nevertheless, dispersant density and NP interaction profiles are still often discussed in the framework of the de Gennes theory. However, the large differences in inter-particle potentials calculated using the SCF and de Gennes theory, respectively (*cf.* Figures 8.4 and 8.6), illustrates the importance of the dispersant density profile for calculating the inter-particle potentials. These potentials are of high interest for many applications especially for ferrofluids.

8.3 Experimental Studies on the Dispersant Density Profile

Experimental studies of the dispersant density profile have often been performed on star polymers [506], block-co-polymers [494] and on core-shell NPs where the shell consisted of high M_w dispersants that had no well defined high affinity anchor [500, 501]. However, reversible dispersant adsorption will alter the dispersant density profile and reduces NP stability as was shown in chapters 6 and 7.

The irreversible binding of nitroDOPA to Fe_3O_4 allows to experimentally investigate the influence of the dispersant M_w on the dispersant packing density, layer thickness, density profile and its consequences for the NP stability. For this purpose, Fe_3O_4 NPs with core radii of 2.5 nm and 5 nm respectively, synthesized by the non-aqueous sol-gel method in the oil bath (section 3.2.4), were stabilized with PEG-nitroDOPA where the PEG M_w was varied between 0.8 kDa and 20 kDa (section 3.3.2).

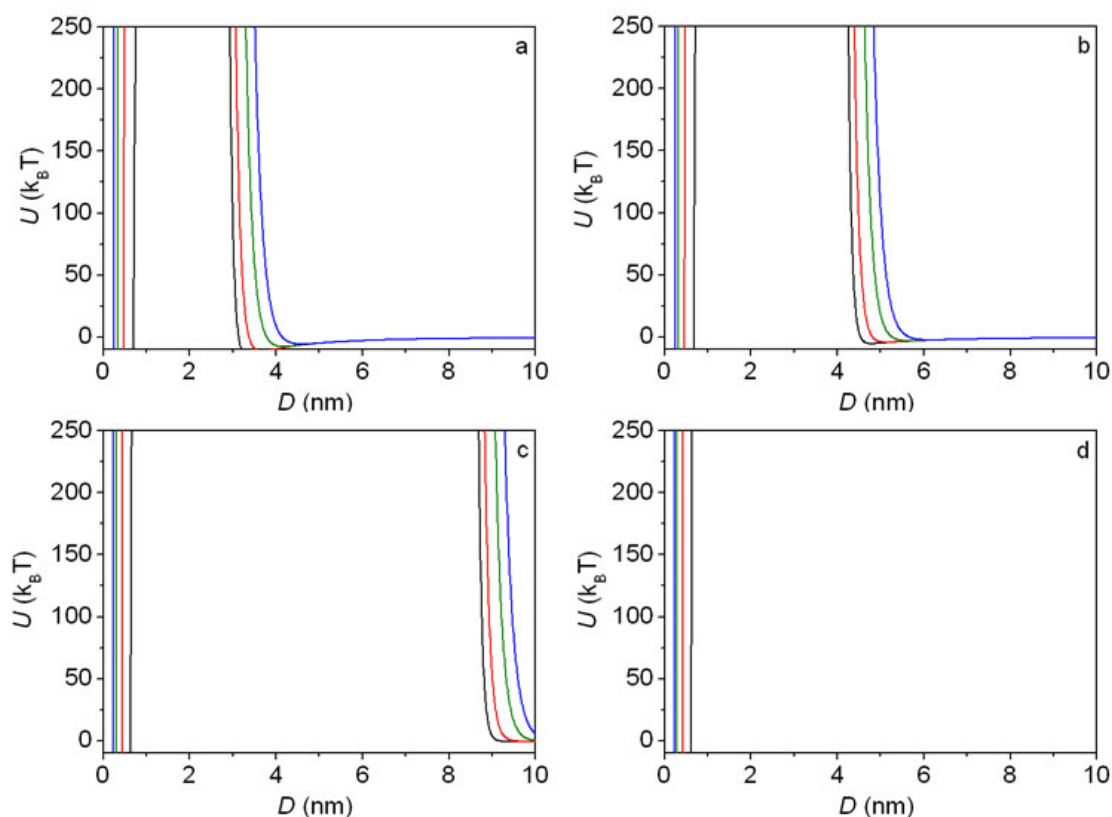


Figure 8.6: Inter-particle potential calculated with the scaling theory. The inter-particle potential of 5 nm core radius iron oxide NPs stabilized with (a) PEG(0.8)-nitroDOPA, (b) PEG(1.5)-nitroDOPA, (c) PEG(5)-nitroDOPA and (d) PEG(10)-nitroDOPA for dispersant packing densities of 0.5 molecule/nm² (black), 1 molecule/nm² (red), 2 molecules/nm² (green) and 3 molecules/nm² (blue).

8.4 Ultra-Stable Iron Oxide Cores

8.4.1 Effect of the PEG M_w on Nanoparticle Stability

As can be seen in Figure 8.7, the hydrodynamic radius of iron oxide NPs synthesized in the oil bath and stabilized with PEG-nitroDOPA increased with increasing PEG M_w irrespective whether the core radius was 2.5 nm or 5 nm. The small hydrodynamic radii and good correlation between the increase in hydrodynamic radius with increasing dispersant M_w indicate that, with one exception, NP cores could be individually stabilized. The exception are PEG(0.8)-nitroDOPA stabilized 2.5 nm core radius NPs. The similar hydrodynamic radii of PEG(0.8)-nitroDOPA and PEG(1.5)-nitroDOPA stabilized 2.5 nm radius cores suggest that PEG(0.8)-nitroDOPA stabilized NPs were slightly agglomerated already at room temperature. The free volume available to one dispersant increases by a

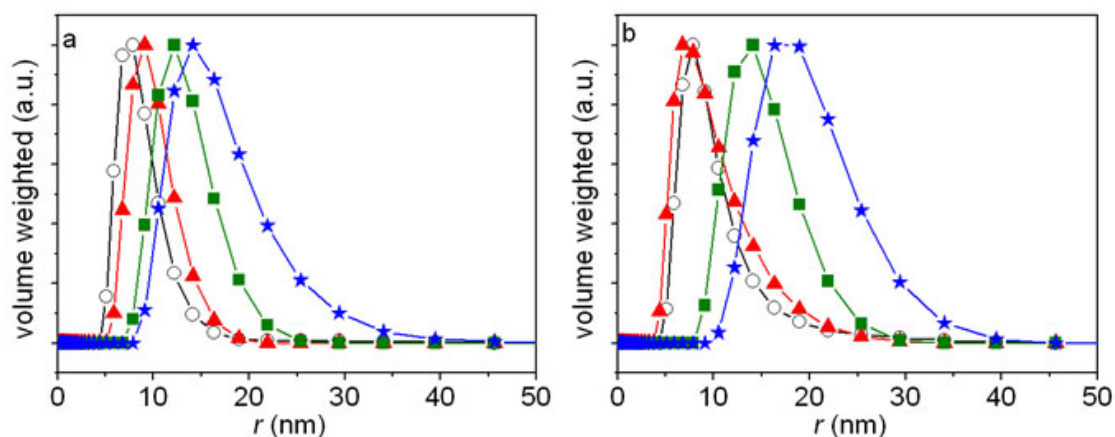


Figure 8.7: Volume weighted size distribution of iron oxide NPs stabilized with PEG-nitroDOPA. Iron oxide NPs with a core radius of (a) 5 nm and (b) 2.5 nm were stabilized with PEG(10)-nitroDOPA (-*-*), PEG(5)-nitroDOPA (-□-), PEG(1.5)-nitroDOPA (-▲-) and PEG(0.8)-nitroDOPA (-○-) and dispersed in Tris containing 160 mM NaCl.

factor of two at a distance of 0.6 nm from the NP surface. Therefore, steric inter-chain repulsions, that would lead to a partial stretching of the chain and thus to a thicker dispersant layer, are most likely negligible. Thus, the low M_w of PEG(0.8) likely results in a too thin dispersant layer, not able to prevent NP agglomeration. On the other hand, PEG(20)-nitroDOPA stabilized NPs did not pass 200 nm cut-off filters indicating that they instantaneously agglomerated. Thus, these NPs could not be further characterized.

Differences in NP stability for different PEG M_w s became even more apparent at elevated temperatures. While NPs remained stable in Tris buffer containing 160 mM NaCl up to 90 °C if coated with PEG(5)-nitroDOPA and PEG(10)-nitroDOPA, they started to agglomerate around 80 °C and 60 °C respectively if 5 nm core radius iron oxide NPs were stabilized with PEG(1.5)-nitroDOPA and PEG(0.8)-nitroDOPA and around 65 °C and 35 °C respectively if 2.5 nm core radius iron oxide NPs were stabilized with PEG(1.5)-nitroDOPA and PEG(0.8)-nitroDOPA (Figure 8.8). The decrease in NP stability with decreasing dispersant M_w is well in agreement with the theoretical predictions (Figures 8.4 and 8.5).

That 2.5 nm core radius NPs start to agglomerate at lower temperatures compared to the 5 nm core radius counterparts might be related to the stabilization protocol. Irrespective of the core radius, the weight ratio of NPs : dispersant was kept constant at 1 : 6 (section 3.3.2). However, assuming that the NP surface is smooth, this results in a ≈ 10 times higher NP surface area per mg NPs for 2.5 nm compared to 5 nm core radius NPs. Furthermore, TEM images indicated a rougher surface and less spherical shape of the 2.5 nm compared to the 5 nm cores (Figure 5.21). Both effects further increase the effective

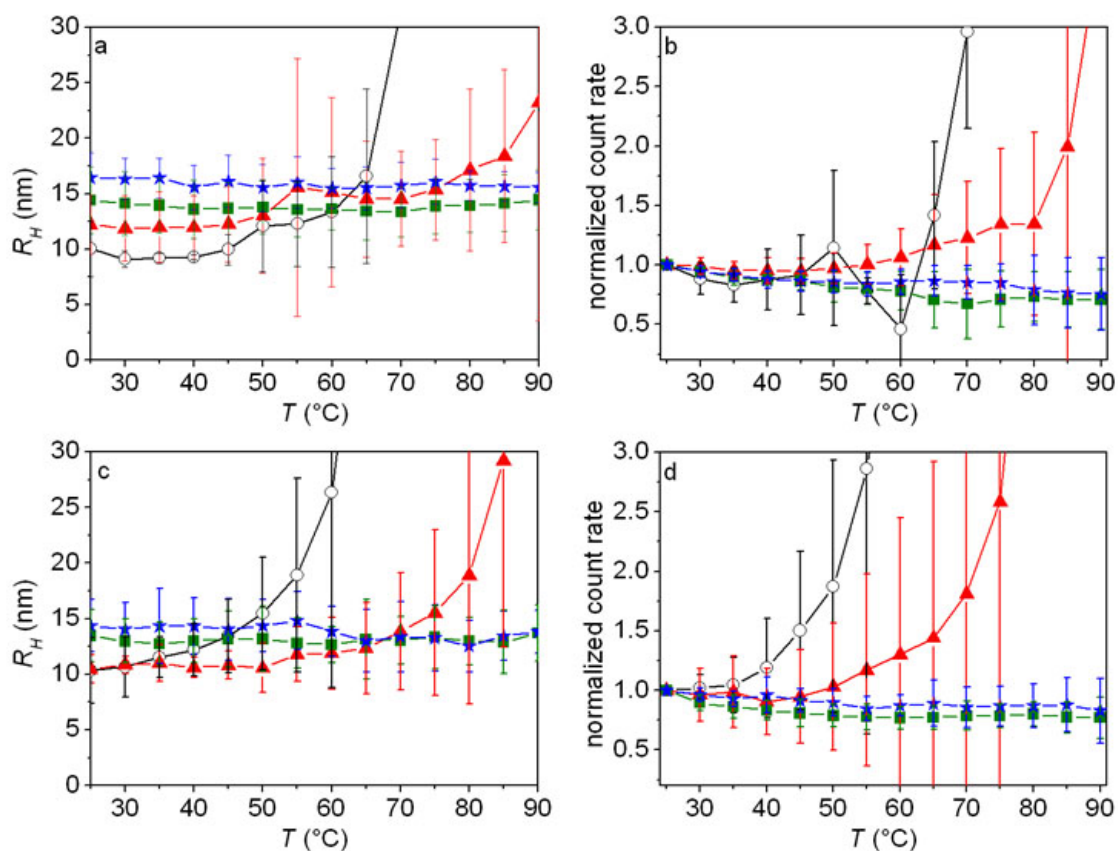


Figure 8.8: DLS of PEG-nitroDOPA stabilized iron oxide NPs as function of temperature. The (a), (c) hydrodynamic radius and (b), (d) the corresponding normalized count rates of (a), (b) 5 nm and (c), (d) 2.5 nm core radius iron oxide NPs stabilized with PEG(10)-nitroDOPA (-*-), PEG(5)-nitroDOPA (-■-), PEG(1.5)-nitroDOPA (-▲-) and PEG(0.8)-nitroDOPA (-○-) dispersed in Tris containing 160 mM NaCl. After stabilization, iron oxide NPs were dispersed in Millipore water and centrifuged for 1 h at 13'400 rpm. DLS was measured on the NP fraction that did not sediment during centrifugation. Statistics was done on 4-7 samples.

surface area of the 2.5 nm core radius NPs. Thus, the surfaces of 2.5 nm core radius NPs might not have been saturated with dispersants during stabilization. The lower dispersant packing density might then be the reason for the inferior stability of 2.5 nm compared to 5 nm core radius NPs. To relate the NP stability to the dispersant packing density, the dependence of the dispersant packing density on the core size and M_w PEG, quantified with TGA, is described next.

8.4.2 Effect of the PEG M_w on the Dispersant Packing Density

According to TGA, and in view of the large scattering of experimental data, the PEG-nitroDOPA packing density (PEG chains/ nm^2) on 5 nm core radius NPs is within the

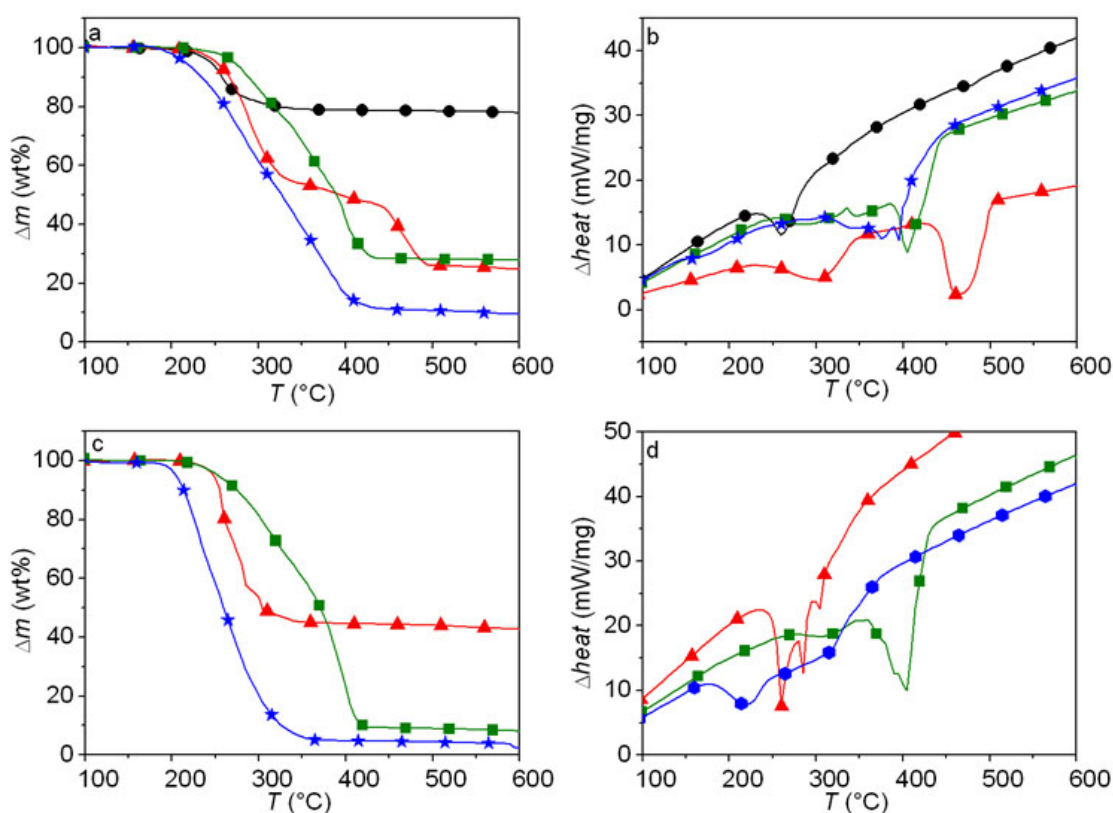


Figure 8.9: TGA and DSC measurements of iron oxide NPs synthesized in the oil bath and stabilized with PEG-nitroDOPA. (a), (c) TGA and (b), (d) DSC measurements of (a), (b) 5 nm core radius and (c), (d) 2.5 nm core radius iron oxide NPs synthesized in the oil bath stabilized with PEG(10)-nitroDOPA (-*-), PEG(5)-nitroDOPA (-■-), PEG(1.5)-nitroDOPA (-▲-) and PEG(0.8)-nitroDOPA (-○-).

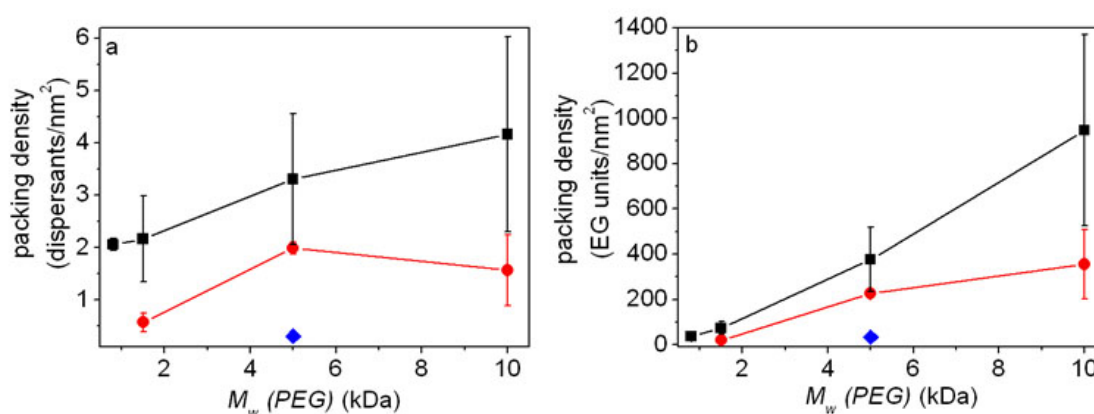


Figure 8.10: Packing density of PEG-nitroDOPA adsorbed on iron oxide NPs synthesized in the oil bath. The (a) PEG-nitroDOPA and (b) ethylene glycol packing density adsorbed on 5 nm core radius (-■-) and 2.5 nm core radius (-●-) iron oxide NPs synthesized in the oil bath was quantified with TGA as a function of the PEG M_w . Statistics was done on 2-10 samples. As comparison the density of PEG(5)-nitroDOPA adsorbed on flat iron oxide surface reported in Table 6.1 is shown (◆).

experimental error independent on the PEG M_w in a range of $1.5 \text{ kDa} < M_w < 10 \text{ kDa}$ ($2.2 \pm 0.8 \text{ nm}^{-2}$, $3.3 \pm 1.3 \text{ nm}^{-2}$ and $4.2 \pm 1.9 \text{ nm}^{-2}$ for PEG(1.5)-, PEG(5)- and PEG(10)-nitroDOPA). However, it is significantly lower for PEG(1.5)- compared to PEG(5)- and PEG(10)-nitroDOPA stabilized 2.5 nm core radius NPs ($0.6 \pm 0.2 \text{ nm}^{-2}$, $2.0 \pm 0.1 \text{ nm}^{-2}$ and $1.6 \pm 0.7 \text{ nm}^{-2}$ for PEG(1.5)-, PEG(5)- and PEG(10)-nitroDOPA) (Figures 8.9 and 8.10a). This is in contrast to what was reported in literature for flat surfaces where the PEG packing density was shown to decrease with increasing PEG M_w s. Packing densities of 0.9, 0.5 and 0.3 chains/ nm^2 were achieved for PEG(1), PEG(2) and PEG(5) if PEG was immobilized through poly (L-lysine) (PLL) on Nb_2O_5 surfaces [203] and 1.7 and 0.4 molecules/ nm^2 for PEG(2)-SH and PEG(5)-SH on Au surfaces [509].

The PEG-nitroDOPA packing densities on iron oxide NPs measured here were not only many times higher than the maximum PEG packing densities on flat surfaces but also greatly exceeded those reported for PEG-silanes adsorbed on Fe_3O_4 NPs (0.3 and 0.8 molecules/ nm^2 for PEG M_w s between 0.1 and 0.35 kDa) [262]. However, the PEG(5)-nitroDOPA packing density measured on iron oxide NPs synthesized in the oil bath was well in agreement with what was found for NPs synthesized in the MW (*cf.* Figure 8.10 and Table 6.1).

As a consequence of the weak dependence of the dispersant packing density on the PEG M_w , the EG density increased almost linearly with increasing PEG M_w (Figure 8.10b). This is in stark contrast to ethylene glycol densities of densely packed PEG chains measured on flat surfaces that were shown to be independent on the PEG M_w [203]. These different trends are likely related to the high surface curvature of NPs which significantly decreases steric repulsion potentials between adjacent dispersants. A decreased steric repulsion can be expected from the rapid increase of the free volume available to dispersants with increasing distance from the NP surface. In contrast, the free volume remains constant if adsorbed on flat surfaces (Figure 6.14).

The larger curvature of the smaller compared to the larger NPs should lead to a higher dispersant packing density. However, the dispersant packing density determined with TGA for 2.5 nm core radius NPs was below that of 5 nm core radius counterparts (Figure 8.9). This agrees well with the lower NP stability of 2.5 nm compared to 5 nm core radii NPs stabilized with PEG-nitroDOPA (Figure 8.8). It might be related to the fact that surfaces of 2.5 nm core radius NPs were not saturated with dispersants as was detailed above. A depletion of dispersants during stabilization of 2.5 nm core radius NPs is possibly also one reason for the leveling off of the EG packing density for these NPs observed in Figure 8.10b.

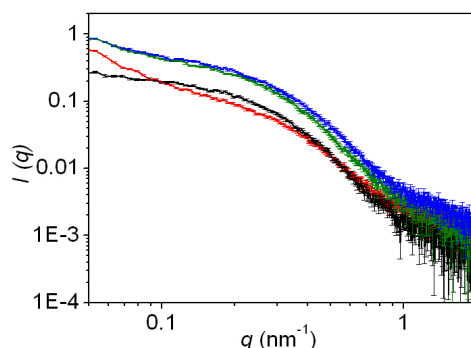


Figure 8.11: SAXS measurements of 5 nm core radius iron oxide NPs synthesized in the oil bath and stabilized with PEG-nitroDOPA. SAXS was measured on 5 nm core radius iron oxide NPs synthesized in the oil bath stabilized with PEG(1.5)-nitroDOPA and dispersed at 0.5 vol% (red), PEG(5)-nitroDOPA stabilized NPs dispersed at 0.5 vol% and 2.5 vol% (green) and PEG(10)-nitroDOPA stabilized NPs dispersed at 4 vol% (blue).

8.4.3 Effect of the PEG M_w on the Core Size Distribution

Because iron oxide cores have a rather broad size distribution as was shown in chapter 5, dispersants could preferentially adsorb on a certain size fraction of these cores, depending on the dispersant M_w . This could lead to selective losses of certain core size fractions during NP stabilization and purification and thus skew the NP core size distribution. If we intend to compare packing densities and PEG density profiles, it has to be ensured that the core size and size distribution is identical for NPs stabilized with dispersants that have different PEG M_w s. For this purpose, SAXS measurements were performed on 5 nm core radius iron oxide NPs stabilized with PEG(1.5)-nitroDOPA, PEG(5)-nitroDOPA and PEG(10)-nitroDOPA.

As can be seen in Figure 8.11, SAXS scattering curves of PEG-nitroDOPA stabilized iron oxide NPs where the PEG M_w ranged from 1.5 kDa to 10 kDa, closely resembled each other. This indicates that the stabilization does not result in a dispersant M_w dependent size selection of the iron oxide cores. Thus, these measurements justify the assumption that the core size and size distribution are independent on the PEG-nitroDOPA M_w which NPs are stabilized with. They therefore allow to directly assign measured differences in the hydrodynamic radius, NP stability and dispersant packing densities of stabilized iron oxide NPs to effects of the different dispersant M_w s.

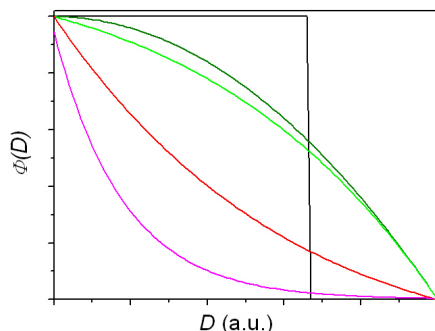


Figure 8.12: Theoretically calculated dispersant packing density profiles. Theoretically calculated dispersant profiles on NPs with core radii of 5 nm, namely a step-function (black), parabolic (green), exponential with negative α (light green), exponential with positive α (red) and Gaussian (magenta) profile as a function of the distance D from the NP surface.

8.4.4 Effect of the PEG M_w on the Dispersant Density Profile

To assess the density profile of PEG-nitroDOPA adsorbed on iron oxide NPs, SANS was performed on PEG(10)-nitroDOPA, PEG(5)-nitroDOPA and PEG(1.5)-nitroDOPA stabilized 5 nm and 2.5 nm core radius iron oxide NPs using polarized neutrons. Because neutrons possess a magnetic moment and iron oxide cores are superparamagnetic, these NPs yield an anisotropic scattering pattern if analyzed with polarized neutrons. The total scattering intensity measured with polarized neutrons is the sum of the nuclear and magnetic scattering of the core-shell NPs (equation 8.17)

$$I_{\text{tot}}(\vec{q}) = (F_{\text{nuc}}(\vec{q}) \pm F_{\text{mag}}(\vec{q}))^2 \quad (8.17)$$

where $F_{\text{nuc}}(\vec{q})$ and $F_{\text{mag}}(\vec{q})$ are the nuclear and magnetic scattering contributions respectively. The + or - sign in equation 8.17 correspond to nuclei spins that are aligned parallel (spin up) and antiparallel (spin down) to the external magnetic field respectively. As described in chapter 5, information about magnetic scattering originating from the iron oxide cores can be retrieved if SANS spectra acquired with polarized neutrons are subtracted from each other. If SANS spectra acquired with the two different neutron polarizations are summed up, the cross term consisting of the product of the nuclear and magnetic scattering cancels and the nuclear scattering is the vastly predominant contribution.

Nuclear forward scattering is proportional to the number of scattering centers, in this case predominantly dispersants. The magnetic scattering contains information about the number and size of NP cores. Therefore, the dispersant packing density can be evaluated by

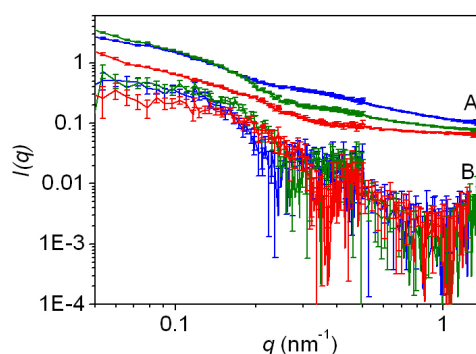


Figure 8.13: SANS measurements on 5 nm core radius iron oxide NPs stabilized with PEG-nitroDOPA. The (A) sum and (B) difference spectra of SANS experiments performed with polarized neutrons on 5 nm core radius iron oxide NPs synthesized in the oil bath and stabilized with PEG(10)-nitroDOPA (blue), PEG(5)-nitroDOPA (green) and PEG(1.5)-nitroDOPA (red) are shown.

simultaneously fitting the difference and sum SANS spectra acquired with polarized neutrons.

To elucidate the dispersant density profile, SANS curves were fitted with form factors that assume a core-shell structure of NPs where the dispersant packing density profile decays like a step-function profile, exponentially and according to a Gauss curve that is translated such that the mean of the Gauss curve coincides with the NP surface (denoted as Gauss curve) (Figure 8.12). By comparing how the qualitatively different density profiles fit the acquired scattering data, at least the qualitative shape of the dispersant density profile on the NPs can be estimated.

Dispersant Density Profile on 5 nm Core Radius Nanoparticles

The sum and difference spectra of SANS data acquired with polarized neutrons on PEG-nitroDOPA stabilized iron oxide NPs with core radii of 5 nm are shown in Figure 8.13. The total NP concentration was kept constant at 5 vol%. Because the shell thicknesses and thus the hydrodynamic radius of NPs was dependent on the PEG-nitroDOPA M_w , the core concentration of the three different samples varied. They are summarized in Table 8.2.

De Gennes and Gaussian Density Profiles

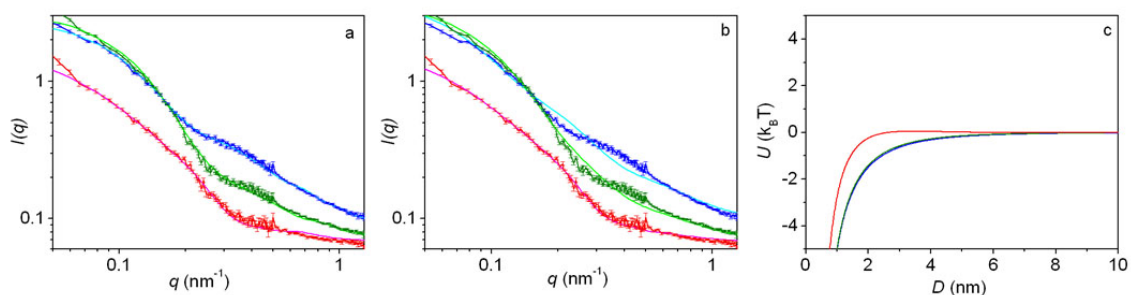


Figure 8.14: SANS measurements on 5 nm core radius iron oxide NPs stabilized with PEG-nitroDOPA. The sum spectra of SANS experiments performed with polarized neutrons on 5 nm core radius iron oxide NPs stabilized with PEG(10)-nitroDOPA (blue), PEG(5)-nitroDOPA (green) and PEG(1.5)-nitroDOPA (red) are shown. These SANS data were fitted with a (a) step-function dispersant density profile according to de Gennes and (b) Gaussian dispersant density profile assuming the core dimensions evaluated with SAXS (Table 5.2). The resulting dispersant layer thickness and packing density are summarized in Table 8.2. These data were fitted assuming a structure factor for hard spheres for PEG(10)- and PEG(5)-nitroDOPA stabilized and a structure factor for hard sticky spheres for PEG(1.5)-nitroDOPA stabilized NPs. (c) The NP interaction potential was calculated using the SCF theory and the parameters of Table 8.2.

Table 8.2: Dispersant layer thickness (d) and packing densities (n_{agg}) obtained by fitting SANS data displayed in Figure 8.14.

PEG M_w (kDa)	core concentration (vol%)	molecular volume (nm^3)	length of extended dispersant (nm)	R_F (nm)	R_G (nm)	d (de- Gennes) (nm)	n_{agg} (de- Gennes) (nm^2)	d (Gauss) (nm)	n_{agg} (Gauss) (nm^2)
10	0.2	16	68	10.4	4.2	20	0.03	14.2	0.04
5	0.3	10	34	6.9	2.9	15	0.07	9	0.09
1.5	0.6	2.5	10	3.3	1.5	5.5	0.3	10	0.2

Because the step-function density profile is often used to calculate layer thicknesses and inter-particle potentials, SANS data were fitted assuming this dispersant density profile. Additionally, the dispersant density profile can decay according to a parabolic or power law function. Because the Gaussian profile decays qualitatively similar to a power law decay (Figure 8.1), SANS data were also fitted using this profile.

To limit the number of free fitting parameters, cores were assumed to be lognormally distributed with an intensity weighted average core radius of 5.6 nm and a standard deviation of 0.3 as was evaluated with SAXS on the same NP batch (Figure 5.26 and Table 5.2). The dispersant layer thickness d should be within $R_F < d <$ extended length of the dispersants. R_F values were calculated according to Szleifer *et al.* (equation 1.6) assuming the length of a ethylene glycol repeat unit a of 0.38 nm and $\alpha = 3/5$ (assuming D_2O is a good solvent for PEG) [213].

For scattering experiments, the radius of gyration R_G is often a more appropriate measure to describe the size of polymers compared to R_F . R_G defined in equation 8.10 describes the average distance of a polymer segment to the center of gravity of the entire polymer. R_G was used as a fixed parameter to fit SANS data with the dispersant density profile that had Gaussian decay (using the form factors described in equations 4.33-4.38) and to calculate inter-particle potentials according the SCF theory.

Having the core size, size distribution and R_G fixed, the dispersant packing density n_{agg} and the dispersant layer thickness d were fitted. The constraints of d described above were used to check if fitting results were physically possible.

Assuming a step-function or Gaussian dispersant density profile, the curves could only be fitted if unreasonably low dispersant packing densities were assumed (Table 8.2). Moreover, even if such low dispersant packing densities were assumed, data could not be fitted well with a dispersant density profile that decays according to a Gaussian curve (Figure 8.14b). Fits were decent if a step-function density profile was assumed (Figure 8.14a). However, values of n_{agg} obtained with these fits were too low for NPs to be colloidally stable under physiologic conditions (*cf.* Table 8.2 and Figure 8.4). This is in contradiction to DLS data where these NPs were shown to be stable in aqueous solutions and under physiologic conditions (see e.g. Figure 6.6). Thus, it is unlikely, that these two models for the dispersant density profile are appropriate for NPs investigated in this thesis.

Table 8.3: Fitting parameters obtained from evaluating SANS data of Figure 8.15 assuming an exponential dispersant density decay. The number weighted r_{core} was found to be 5.0 nm with a variance $\sigma = 0.3$.

PEG M_w (kDa)	d (nm)	α	$\Theta_{solvent}$ (%)	n_{agg} (nm^{-2})	$U_{barrier}$ ($k_B T$)
10	10.2	11.9	0	0.026	0
5	3.6	-2.8	5.4	0.22	0
1.5	2.7	-1.6	0	0.46	0

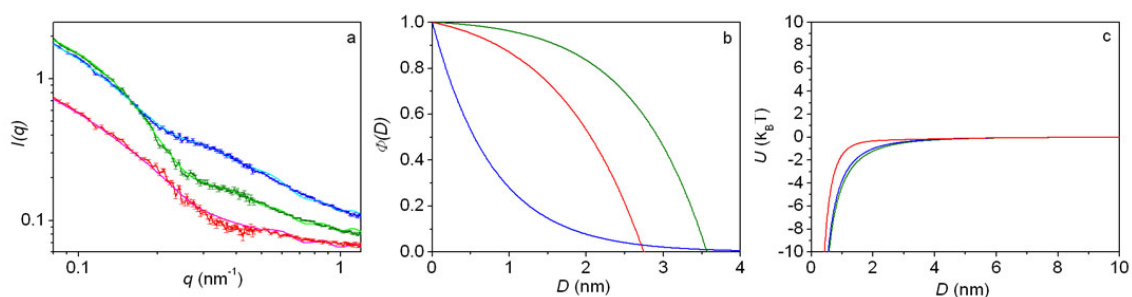


Figure 8.15: Evaluations of SANS data measured on 5 nm core radius iron oxide NPs stabilized with PEG-nitroDOPA assuming an exponential dispersant density decay. (a) The sum spectra of SANS experiments acquired with polarized neutrons on 5 nm core radius iron oxide NPs stabilized with PEG(10)-nitroDOPA (blue), PEG(5)-nitroDOPA (green) and PEG(1.5)-nitroDOPA (red) were fitted with a core-shell form factor that assumes the dispersant density profile to decay exponentially (equations 4.43-4.45). The core radius was assumed to be lognormally distributed. According to these fits, the intensity weighted core radius was 8.9 nm with a standard deviation of 0.3 nm. (b) The to (a) corresponding dispersant density profiles $\Phi(D)$ are shown as a function of the distance from the NP core surface D . (c) The inter-particle potentials calculated according to equations 8.1 - 8.16 using the SCF theory.

Exponential Density Profile

Because, as shown above, the dispersant density profile is unlikely to decay with a Gaussian profile or assume a step-function profile, SANS curves were fitted with a form factor assuming an exponential dispersant density decay where α could be < 0 , resembling a parabolic profile or $\alpha > 0$, resembling a Gaussian profile (Figure 8.1). As outlined in section 8.1, the former is often described in literature as the most appropriate density profile. The shell thickness d and α , the parameter that describes the decay rate of the dispersant density profile were fitted. However, because the obtained fits were superior to the ones obtained using form factors that describe a Gaussian or step-function density profile (*cf.* Figures 8.14 and 8.15), fits were robust. Therefore, the core size and standard deviation could also be fitted. To limit the number of free fitting parameters, scattering curves of 5 nm core radius NPs stabilized with PEG(10)-, PEG(5)- and PEG(1.5)-nitroDOPA were fitted simultaneously using the core size and size distribution as global fitting parameters. To further improve fits especially in the region of low q -values ($q < 0.15 nm^{-1}$), a

contribution of the structure factor describing hard sticky sphere interactions was added (section 4.4.1).

Fits of the core size and size distribution, which was assumed to be lognormally distributed, yielded an intensity weighted R_G of 6.9 nm and a standard deviation of 0.3. The resulting core radius r , defined as

$$r = R_G \sqrt{\frac{3}{5}}, \quad (8.18)$$

is 8.9 nm, assumed the cores are spherical. The corresponding number weighted core radius is 5.0 nm, well in agreement with number weighted core radii obtained from TEM image analysis (Figure 5.23 and Table 5.2).

The undulations in the fits at $0.5 \text{ nm}^{-1} < q < 1 \text{ nm}^{-1}$, that are not seen in the experimental data, indicate that the core size distribution is higher than assumed, NPs have a rough surface or are not perfectly spherical. According to TEM images (see *e.g.* Figure 5.21), NPs are not spherical and have rough surfaces. Thus, NP shape and surface roughness likely smoothed the experimental curves such that the fits are not perfect in this q -range (Figure 8.15a).

Interestingly, the dispersant density profile qualitatively changes if the PEG M_w is increased from 5 kDa to 10 kDa (Figure 8.15b). This likely is related to the unrealistically low dispersant packing density obtained from these fits using equation 4.69 (Table 8.3). The low dispersant packing densities result in inter-particle potentials that are attractive if they are calculated with parameters for the shell thickness and dispersant packing density obtained from these SANS fits (Table 8.3) using equations 8.2 - 8.16.

These inter-particle potentials would result in immediate NP agglomeration. NP agglomeration is, however, not observed as good NP stability was shown using DLS (Figure 8.8). Furthermore, dispersant packing densities quantified with TGA are many times higher compared to those calculated based on SANS fitting results (*cf.* Figure 8.10 and 8.3). Thus, the dispersant packing density is likely considerably underestimated in quantifications done based on SANS analysis.

One possibility for the quantitatively unrealistic results obtained from these SANS fits would be a wrong model for the dispersant density decay profile. Fits obtained with a form factor that assumes an exponentially decaying profile are superior to those obtained with a step-density or Gaussian profile (*cf.* Figures 8.14 and 8.15). Furthermore, if α is < 0 , the exponential profile resembles that of a parabolic profile (Figure 8.1). Thus, all dispersant density profiles that are commonly reported were tested. It is unlikely that

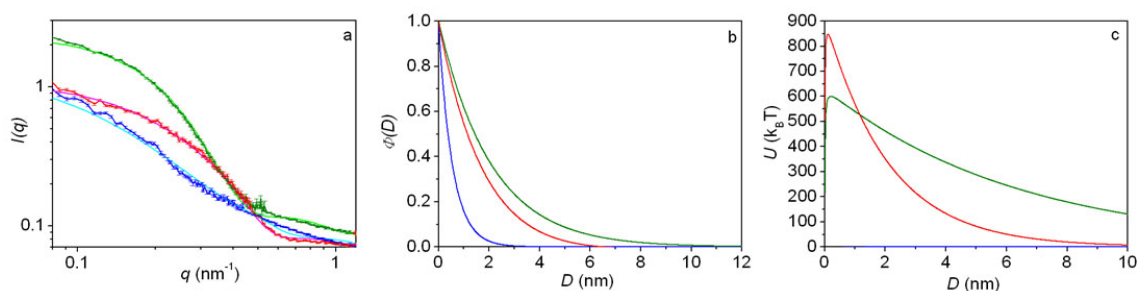


Figure 8.16: Evaluation of SANS measurements on 2.5 nm core radius iron oxide NPs stabilized with PEG-nitroDOPA. (a) The sum spectra of SANS experiments acquired with polarized neutrons on 2.5 nm core radius iron oxide NPs stabilized with PEG(10)-nitroDOPA (blue), PEG(5)-nitroDOPA (green) and PEG(1.5)-nitroDOPA (red) are shown. The curves were fitted with a core-shell form factor that assumes the dispersant density profile to decay exponentially (equations 4.43 - 4.45). According to these fits the intensity weighted core radius was 2.9 nm with a deviation of 0.3, if a lognormal core size distribution was assumed (Table 8.4). (b) The to (a) corresponding dispersant density profiles $\Phi(D)$ are shown as a function of the distance D from the NP core surface. (c) The inter-particle potentials calculated according to equations 8.1 - 8.16 using the SCF theory.

none of them would qualitatively resemble the actual density profile.

Another possibility for the unrealistically low dispersant packing densities would be that additional objects contributed to the scattering. If this was the case, scattering curves would have to be fitted with multiple form factors. To check, if non-magnetic objects contributed to the scattering, difference spectra acquired with polarized neutrons could be simultaneously fitted with sum spectra (Figure 8.13). Non-magnetic objects do not contribute to the difference spectra but they do contribute to the sum spectra (equations 8.17 and 4.32). Thus, simultaneous fitting of difference and sum spectra of SANS data acquired with polarized neutrons allow to trace scattering contributions from non-magnetic objects. However, to do this simultaneous fitting, the form factor that describes the exponentially decaying density profile has to be extended to account for the magnetic scattering of the cores. This is work in progress. In summary, the deviation of SANS results leading to unphysically low dispersant packing density from the results obtained with DLS and TGA remains to be determined.

Dispersant Density Profile on 2.5 nm Core Radius Nanoparticles

Because the exponential density profiles yielded best fits for PEG-nitroDOPA stabilized 5 nm core radius NPs, 2.5 nm core radius NPs stabilized with PEG-nitroDOPA were only fitted using the exponential dispersant density profile. Furthermore, the exponential density profile can qualitatively approximate the parabolic ($\alpha < 0$), step-function ($\alpha = 0$) and

Table 8.4: Fitting parameters obtained from evaluating SANS data of Figure 8.16 assuming an exponential dispersant density decay with a number weighted $r_{core} = 2.2$ nm with a variance $\sigma = 0.3$.

PEG M_w (kDa)	d (nm)	α	$\Theta_{solvent}$ (%)	n_{agg} (nm^{-2})	$U_{barrier}$ ($k_B T$)
10	10.3	3.1	25.8	0.26	0
5	19.9	8.6	74.7	1.0	600
1.5	6.5	2.8	0	1.7	850

Gaussian ($\alpha > 0$) dispersant density profile (Figure 8.12). It therefore covers qualitatively all possibilities for dispersant density profiles described in literature.

Similar to SANS data acquired with polarized neutrons on 5 nm core radius NPs, spectra acquired with polarized neutrons on PEG-nitroDOPA stabilized 2.5 nm iron oxide NP cores could be fitted assuming an exponentially decaying dispersant density profile (Figure 8.16a). R_G of the cores obtained from these fits was 2.9 nm with a standard deviation of 0.3, resulting in an intensity weighted core radius of 3.7 nm corresponding to a number weighted core radius of 2.2 nm. This compares well with values obtained from TEM image analysis and SAXS fits (Table 5.2).

In contrast to 5 nm core radius NPs, dispersant density profiles obtained from fits of PEG-nitroDOPA stabilized 2.5 nm core radius NPs decayed with $\alpha < 0$ irrespective of the PEG M_w (Figure 8.16b and Table 8.4). The faster decay of the PEG(10)-nitroDOPA density profile, compared to that of PEG(5)- and PEG(1.5)-nitroDOPA, is a result of the much lower dispersant packing density obtained for the former dispersant (Table 8.4).

In addition to providing good fits of the scattering spectra of 2.5 nm core radius NPs, the choice of exponentially decaying profiles also resulted in dispersant packing densities for PEG(1.5)- and PEG(5)-nitroDOPA stabilized NPs that are comparable to those values obtained with TGA (*cf.* Figure 8.10 and Table 8.4). Consequently, the energy barrier of the inter-particle potential calculated based on the values quantified with SANS indicate good stability of NPs modified with PEG(1.5)- and PEG(5)-nitroDOPA (Figure 8.16c and Table 8.4). This is well in agreement with DLS data (Figure 8.8).

According to these quantifications, PEG(10)-nitroDOPA stabilized NPs should readily agglomerate. The poor NP stability and the very low dispersant packing density for this dispersant are again in contradiction to DLS (Figure 8.8) and TGA (Figure 8.10) data. Furthermore, the higher dispersant packing density on 2.5 nm compared to 5 nm core radii NPs (*cf.* Table 8.3 and 8.4) strongly disagrees with what was found with TGA (Figure 8.10) and the inferior stability of the former NPs (Figure 8.8).

However, the trend towards lower dispersant packing densities with higher PEG M_w s is in

Table 8.5: Relaxivities measured on the stable fraction of PEG-nitroDOPA stabilized iron oxide NPs synthesized in the oil bath: MRI measurements were conducted at 20 °C and 1.5 T.

NP core radius (nm)	PEG M_w (kDa)	r_1 ($\frac{1}{mM(Fe)s}$)	r_2 ($\frac{1}{mM(Fe)s}$)	$\frac{r_2}{r_1}$
2.5	10	13	77	6.0
2.5	5	12	82	6.8
2.5	1.5	12	76	6.4
5	10	17	157	9.4
5	5	18	204	11.4
5	1.5	15	140	9.1

agreement with the fact, that PEG(20)-nitroDOPA stabilized NPs strongly agglomerated such that they did not pass 200 nm cut-off filters. Furthermore, it is in line with studies done on flat surfaces [203, 509]. Thus, the quantitative disagreement of SANS results likely is based on a systematic error or inappropriate model assumption used to evaluate SANS data. Therefore, the validity of the numbers obtained from SANS fits will be checked by simultaneously fitting difference and sum spectra of SANS data acquired with polarized neutrons, similar to what was described for 5 nm core radii NPs.

8.4.5 Relaxivity of PEG-nitroDOPA Stabilized Nanoparticles

Table 8.6: Relaxivities of iron oxide NPs reported in literature measured at 0.47 T at 37-39 °C.

NP name	NP core radius (nm)	hydro-dynamic radius (nm)	dispersant	r_1 $\left(\frac{1}{mM(Fe)_s}\right)$	r_2 $\left(\frac{1}{mM(Fe)_s}\right)$	$\frac{r_2}{r_1}$	reference
Feridex/Endorem	2.4	114	dextran	25	151	5.9	[510]
Resovist	2.1	31	carboxy-dextran	24	107	4.5	[511]
individually stabilized iron oxide NPs		5.7	dextran	22	44	2.0	[236]

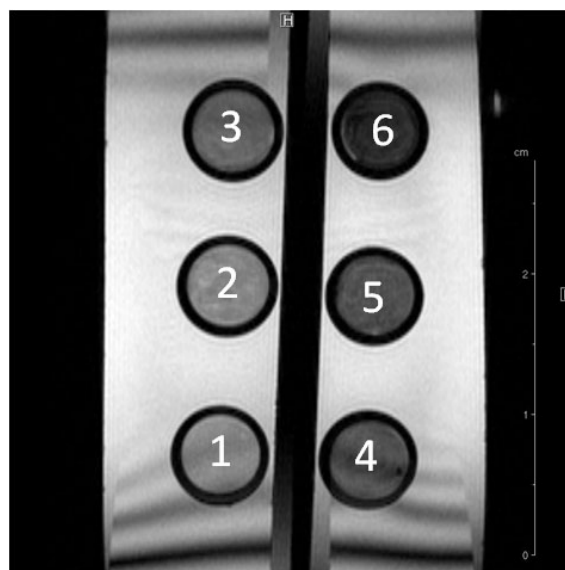


Figure 8.17: T_2^* -weighted MRI of PEG(5)-nitroDOPA stabilized NPs synthesized in the oil bath. T_2^* -weighted MRI scans of PEG(5)-nitroDOPA stabilized 5 nm core radius Fe_3O_4 NPs embedded in a hydrogel at Fe_3O_4 concentrations of (1) 20 $\mu\text{g/ml}$, (2) 30 $\mu\text{g/ml}$, (3) 40 $\mu\text{g/ml}$, (4) 50 $\mu\text{g/ml}$, (5) 60 $\mu\text{g/ml}$ and (6) 70 $\mu\text{g/ml}$. To prevent susceptibility discontinuities at the edge of the vials, these vials were inserted into tube filled with Millipore water that yielded the white background contrast. The repetition time T_R was 5000 ms, the echo time T_E was 9.8 ms.

To assess the suitability of these individually stabilized NPs as MR contrast agents, their relaxivities as a function of the PEG-nitroDOPA M_w and the core size were quantified. T_2 and T_2^* relaxation times are dependent on the M_s of cores [96]. Because the M_s depends on the core size (Table 5.3), T_2 and T_2^* were shown to also depend on the core radius [73, 96, 512]. T_1 is mainly determined by the exchange rate of water molecules in the first hydration shell of NPs. Thus, it depends on the accessibility of the iron oxide core surface to water molecules. Whether the dispersant shell slows down the water exchange rate in the first hydration shell of the core and therefore influences T_1 or not is an ongoing debate [513]. Therefore, relaxivities of 2.5 nm and 5 nm core radius NPs stabilized with PEG-nitroDOPA where the PEG M_w was varied between 1.5 kDa and 10 kDa were compared.

The MR contrast induced by PEG(5)-nitroDOPA stabilized iron oxide NPs embedded in hydrogels at different concentrations is exemplified in Figure 8.17. The relaxivities r_1 and r_2 , defined as $1/(T_1 c)$ and $1/(T_2 c)$ respectively, where c is the NP concentration, were larger for PEG-nitroDOPA stabilized 5 nm core radius compared to 2.5 nm core radius NPs (Table 8.5). This is well in agreement with literature [29, 109, 110] and can be assigned to the higher M_s of the former NPs (Figure 7.22a).

T_1 -Contrast

r_1 values were below reported values for commercially available iron oxide NP based contrast agents (*cf.* Table 8.5 and 8.6). Commercially available iron oxide NPs are coated with the reversibly adsorbing dextran that allows water to readily exchange also in close proximity to the NP surface. However, the strong binding and dense packing of PEG-nitroDOPA on the Fe_3O_4 NP surface likely reduced the number of H_2O molecules that can get into direct contact with the NP surface during a given time. r_1 values of individually PEG-nitroDOPA stabilized NPs were therefore lower than the values measured for dextran stabilized NPs.

T_2 -Contrast

r_2 values of PEG-nitroDOPA stabilized 2.5 nm core radius NPs were below values of commercially available dextran stabilized iron oxide NPs with comparable core sizes. However, individually dextran stabilized NPs have a significantly lower r_2 compared to Feridex, Sinerem and the PEG-nitroDOPA stabilized NPs studied in this thesis. Feridex and Sinerem are the most prominent commercially available iron oxide based negative MR contrast agents. The higher r_2^* values of these commercially available contrast agents are likely due to their structure of multiple iron oxide NPs embedded in a dextran matrix leading to partial agglomeration of the cores [100, 108]. Agglomerated NPs yield higher r_2^* values than individually stabilized analogous [108].

r_2 values of PEG-nitroDOPA stabilized 5 nm core radius NPs were significantly higher compared to the commercially available iron oxide based contrast agents (*cf.* Tables 8.6 and 8.5). The core radius of PEG-nitroDOPA stabilized NPs is with 5 nm two times higher than the core radius of Feridex. However, the increased core radius only insignificantly increased the hydrodynamic radius of the former NPs (Figure 8.7). In contrast, dextran stabilized iron oxide NPs had a hydrodynamic radius many times larger than the respective core radius (*cf.* Tables 8.6). Thus, even though PEG-nitroDOPA stabilized 5 nm core radius NPs had a slightly larger core radius, their overall size was still many times lower than that of NPs individually stabilized with dextran (*cf.* Figure 8.7 and Table 8.6). Therefore, PEG-nitroDOPA stabilized iron oxide NPs with core radii ≥ 5 nm are potentially effective negative MR contrast agents that allow to control NP size and surface presentation of functional groups and have higher T_2 values compared to commercially available iron oxide based MR contrast agents.

Dependence of Relaxivities on the PEG M_w

The relaxivities r_1 and r_2 were found to be independent on the PEG-nitroDOPA layer thickness as a comparison between iron oxide NPs stabilized with PEG(10)-, PEG(5)- and PEG(1.5)-nitroDOPA reveals (Table 8.5). This is in contrast to what has been previously reported [110, 513]. While r_2 reported by Duan *et al.* did not vary systematically with the hydrodynamic NP radius [110], La Conte *et al.* reported a decrease in r_2 with increasing hydrodynamic radius [513].

NPs investigated by La Conte *et al.* were stabilized with phospholipids that formed a micellar structure around the iron oxide cores [513]. Duan *et al.* coated NPs with poly(ethylene imine) (PEI), PEI-g-PEG and a mixture of polymaleic anhydride and octadecene [110]. Interestingly, a decrease in r_2 with increasing dispersant layer thickness was observed for PEG M_w s ranging from 0.55 kDa to 1 kDa. However, r_2 remained stable if higher PEG M_w s were used [513]. As was shown in this chapter, PEG M_w s < 1.5 kDa resulted in partial NP agglomeration even if they were firmly adherent to the NP surface. r_2 is known to increase with NP size [109] and upon NP agglomeration [108]. Thus, the discrepancy on the dependence of the relaxivity on the dispersant layer thickness observed here and by others [110, 513] is likely a consequence of partial NP agglomeration.

8.5 Iron Oxide Nanoparticles that Sedimented During Centrifugation

A large fraction of the stabilized NPs which sedimented during centrifugation could be re-dispersed in Millipore water and passed 200 nm cut-off filters. This demonstrates that they were only weakly agglomerated. The differences in NP properties of the sedimented vs. the non-sedimented fraction was investigated with DLS, TGA and DSC.

8.5.1 Effect of the PEG M_w on Nanoparticle Stability

DLS measurements revealed that the majority of the re-suspended NPs were individually stabilized (Figure 8.18). However, in contrast to NPs which did not sediment during centrifugation, the hydrodynamic radius of sedimented NPs did not systematically increase with increasing PEG-nitroDOPA M_w . Furthermore, a second broad peak around 60 nm

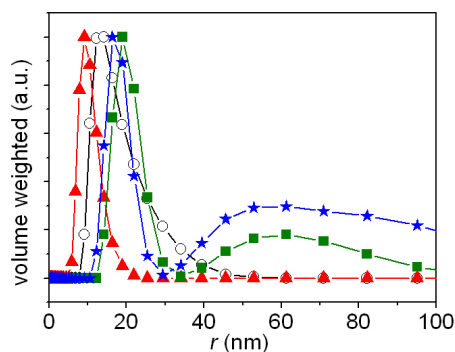


Figure 8.18: DLS of the iron oxide NP fraction that sedimented during centrifugation stabilized with PEG-nitroDOPA. The volume weighted size distribution of 5 nm core radius iron oxide NPs stabilized with PEG(10)-nitroDOPA (-*-), PEG(5)-nitroDOPA (-■-), PEG(1.5)-nitroDOPA (-▲-) and PEG(0.8)-nitroDOPA (-○-) dispersed in Tris containing 160 mM NaCl. After stabilization, iron oxide NPs were dispersed in Millipore water and centrifuged for 1 h at 13'400 rpm. DLS was measured on the sedimented fraction after agglomerates > 200 nm had been removed by filtration.

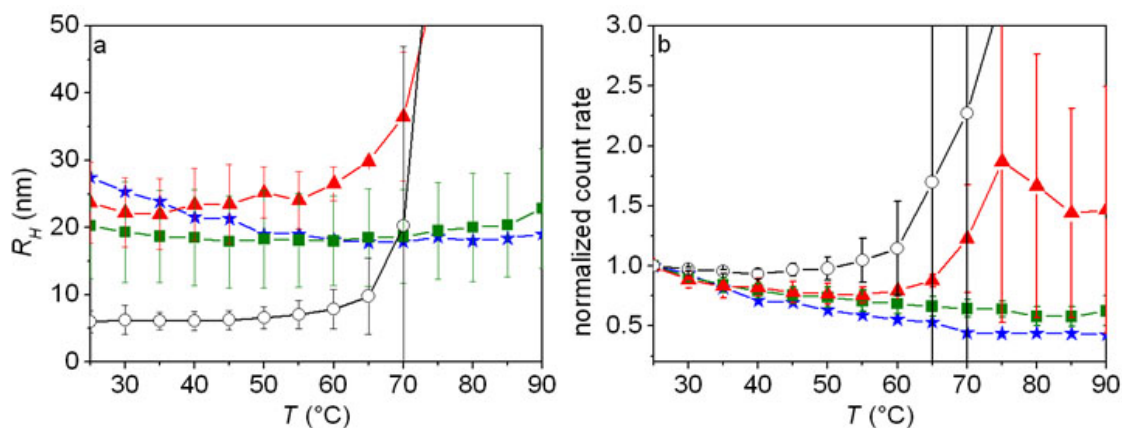


Figure 8.19: Temperature dependence of hydrodynamic radius of the fraction of iron oxide NPs stabilized with PEG-nitroDOPA which sedimented during centrifugation. The (a) hydrodynamic radius and (b) normalized count rate of iron oxide NPs with a core radius of 5 nm stabilized with PEG(10)-nitroDOPA (-*-), PEG(5)-nitroDOPA (-■-), PEG(1.5)-nitroDOPA (-▲-) and PEG(0.8)-nitroDOPA (-○-). After stabilization, these NPs were dispersed in Millipore water and centrifuged for 1 h at 13'400 rpm. DLS was measured on the iron oxide NP fraction, which sedimented during centrifugation after agglomerates > 200 nm were removed by filtration. NPs were dispersed in Tris containing 160 mM NaCl. Statistics was done on 2-7 independent samples.

was measured for PEG(5)-nitroDOPA and PEG(10)-nitroDOPA stabilized NPs, in stark contrast to what was seen for NPs that did not sediment (*cf.* Figures 8.7 and 8.18). That the hydrodynamic radius does not scale with the PEG-nitroDOPA M_w and especially the appearance of a second, larger peak are strong indications that these NPs were partially agglomerated. However, the fraction of agglomerates was low as volume weighted radii scale with r^3 and thus, larger agglomerates predominate the scattering pattern and therefore DLS analysis.

Despite that these NPs were partially agglomerated, trends of the dependence of the NP stability on the PEG-nitroDOPA M_w (Figure 8.19) were similar to the stable NP fraction (Figure 8.8). NPs stabilized with PEG(5)-nitroDOPA and PEG(10)-nitroDOPA did not show further agglomeration up to 90 °C, as can be seen in the constant hydrodynamic radius and slow decrease in the normalized count rate (Figure 8.19). Furthermore, in analogy to what was observed for NPs that did not sediment during centrifugation, the sedimented fraction of PEG(1.5)-nitroDOPA and PEG(0.8)-nitroDOPA stabilized NPs started to further agglomerate at 65 °C and 55 °C respectively. These results are in good agreement with theoretical predictions where the repulsive steric interaction potentials are below $10 k_B T$ if the dispersant packing density is below 0.5 molecules/nm² (Figures 8.4 and 8.5).

8.5.2 Effect of the PEG M_w on the Dispersant Packing Density

TGA measurements revealed that the wt% of dispersants adsorbed on iron oxide NPs that sedimented during centrifugation was less than half of what was measured on NPs that did not sediment during centrifugation (Figure 8.20) independent on the PEG M_w (Figure 8.21 and *cf.* Table 8.7 and Figure 8.10). Furthermore, the main endothermic peak measured with DSC was around 250 °C. DSC curves of NPs that did not sediment during centrifugation peaked at 400 °C (Figure 8.9). The endothermic peak around 250 °C coincided with the one observed for as-synthesized, unstabilized iron oxide NPs and NPs modified with PEG-anchor dispersants at a low dispersant packing density. This endothermic peak seen in Figure 8.20 thus indicates, that a lot of organic contaminants were adsorbed on the surface of the NP fraction which sedimented during centrifugation. This is well in agreement with results presented in chapter 6 where a high PEG-nitroDOPA packing density was required to displace organic contaminations from the NP surface.

However, even if the amount of dispersants used to stabilize as-synthesized NPs was doubled, the unstable NP fraction, which sedimented during centrifugation, could not be

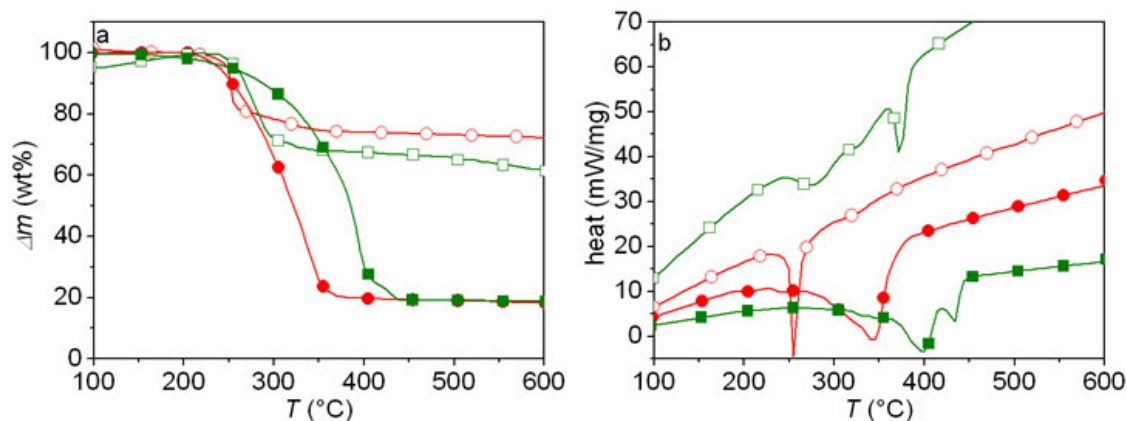


Figure 8.20: DSC and TGA measurements of 5 nm core radius iron oxide NPs synthesized in the oil bath and stabilized with PEG(5)-nitroDOPA. PEG(5)-nitroDOPA stabilized iron oxide NPs synthesized in the oil bath which had core radii of 2.5 nm ($-\circ-$) and 5 nm ($-\square-$). Stabilized iron oxide NPs were dispersed in Millipore water and centrifuged for 1 h at 13'400 rpm. The fraction that sedimented during centrifugation (empty symbols) and the NPs which remained in the supernatant (filled symbols) were subsequently analyzed with (a) TGA and (b) DSC.

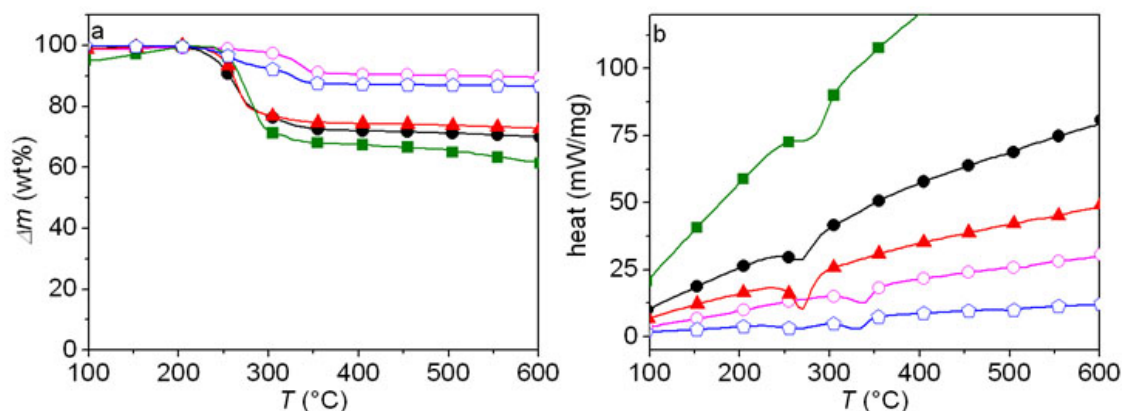


Figure 8.21: DSC and TGA measurements of 5 nm core radius iron oxide NPs synthesized in the oil bath stabilized with PEG-nitroDOPA. 5 nm radius iron oxide cores synthesized in the oil bath and stabilized with PEG(20)-nitroDOPA ($-\diamond-$), PEG(5)-nitroDOPA ($-\square-$), PEG(1.5)-nitroDOPA ($-\triangle-$), PEG(0.8)-nitroDOPA ($-\circ-$) and uncoated NPs ($-\circ-$). After stabilization, NPs were dispersed in Millipore water and centrifuged for 1 h at 13'400 rpm. The sedimented NP fraction was re-dispersed in Millipore water, filtered through 200 nm cut-off filters, freeze dried and analyzed with (a) DSC and (b) TGA.

Table 8.7: Comparison of the wt% of dispersants adsorbed on iron oxide NPs that sedimented during centrifugation. Statistics was done on 2-5 independent samples.

PEG M_w (kDa)	5 nm cores (wt%)	2.5 nm cores (wt%)
20	15 ± 2 ¹	
5	38 ± 4	25 ± 3
1.5	29 ± 2	30 ± 23
0.8	31 ± 3	24 ± 1

eliminated. Therefore, the low surface dispersant packing density of the unstable NP fraction cannot be caused by a lack of dispersants during stabilization. It more likely is related to surface properties of these NPs.

A possible reason for the lower NP stability of this sedimented fraction might be that a fraction of NPs was already surface oxidized prior to stabilization with PEG-nitroDOPA. NitroDOPA was shown to have a significantly lower affinity to surface oxidized iron oxide which resulted in poor NP stability of such oxidized NPs (see chapter 7). Thus, the yield of ultra-stable NPs might be increased if oxidation of as-synthesized NPs prior to their stabilization can be prevented. This might be achieved if NPs are synthesized, washed and stabilized in an inert atmosphere where surface oxidation can be prevented.

8.6 Summary

Next to an anchor, that firmly binds dispersants to the NP surface, the spacer length is crucial to achieve good NP stability. Linear PEG spacers with $M_w < 1.5$ kDa yield too thin shells to prevent NP agglomeration especially at elevated temperatures. PEG M_w s > 10 kDa result in low dispersant packing densities (≤ 0.1 dispersant/nm² for PEG(20)-nitroDOPA if adsorbed on 5 nm core radius NPs), detrimental to NP stability. Such NPs agglomerated instantaneously. These trends were observed irrespective of core size and size distribution for the cores investigated here. Thus, to achieve good stability of NPs with core radii between 2.5 nm and 5 nm, the PEG M_w should be between 5 kDa and 10 kDa.

SANS data indicate an exponentially decaying dispersant density profile that strongly depends on the dispersant packing density and core size. The obtained dispersant packing densities for PEG(1.5)- and PEG(5)-nitroDOPA stabilized NPs with a core radius of 2.5 nm are in agreement with TGA values. However, dispersant packing densities obtained

¹NPs could not be filtered prior to freeze drying because they did not pass 200 nm cut-off filters.

for 5 nm core radius NPs and PEG(10)-nitroDOPA stabilized 2.5 nm core radius NPs are unphysically low and in contradiction to TGA and DLS results. Therefore, model assumptions used to analyze SANS data have to be checked by relating the magnetic scattering of the cores to the total scattering mainly caused by the PEG-shell.

The magnetic relaxivities r_1 and r_2 , relevant for magnetic contrast agent properties, were found to be independent of the PEG M_w , given NPs were individually stabilized. In contrast, as expected, the smaller 2.5 nm radius cores yielded significantly lower contrast compared to the 5 nm core radius NPs. Thus, if individually stabilized iron oxide NPs are intended for use as MR contrast agents, 5 nm radius cores are superior to cores with radii = 2.5 nm. The former have higher relaxivities but only a marginally larger size and equal NP stability if the cores are coated with PEG-nitroDOPA with a PEG M_w between 1.5 kDa and 10 kDa.

Iron Oxide Nanoparticle Functionalization

9.1 Background

As outlined in chapter 1, many biomedical applications rely on iron oxide NPs functionalized with ligands or second labels. Suitable ligands have usually been bound to NPs either through the biotin-avidin coupling strategy [514, 515] or by covalently linking them to the dispersant shell [95, 255, 516, 517].

9.1.1 Biotin-Avidin Functionalization

The avidin-biotin bond is one of the highest non-covalent bonds, with a dissociation constant of $K_d \approx 10^{-15}$ M [518, 519]. For practical purposes, this is an essentially irreversible bond, at least in the absence of external forces. Because many ligands are commercially available in a biotinylated form, this functionalization method is often used for research purposes.

Individually stabilized NPs functionalized through the biotin-avidin coupling strategy possess a layer-by-layer build-up. The different layers are modularly interchangeable and allow to firmly attach active ligands to NP cores. Thus, such NPs are well suited for *in vitro* applications, that require only dilute NP dispersions, and where NPs do not have to be stealth.

9.1.2 Covalent Functionalization

NPs can be rendered stealth by grafting stealth dispersant like PEG to their surface [136, 199, 200]. However, these stealth properties are lost if NPs are surrounded by an additional avidin monolayer required for the biotin-avidin coupling strategy [519]. The avidin monolayer can be omitted by covalently linking ligands and second labels directly to the dispersant shell. In this case, specific and non-specific protein adsorption to NPs are assumed to be limited to the added ligands. Thus, properties imposed to NPs through dispersants are at least partially retained if ligands are covalently linked to the dispersant shell. This likely increases the circulation time of NPs functionalized with covalently bound ligands. It thus renders those NPs more attractive especially for *in vivo* applications compared to NPs functionalized through the biotin-avidin coupling strategy.

Any coupling strategy known from chemistry can be applied to covalently link functionalities to NPs, provided the ligands and NPs withstand the synthesis conditions [95, 255, 516, 517]. Therefore, although covalent coupling of ligands to the NP surface requires *in situ* chemistry, it is versatile.

However, covalent binding of functionalities to the NP shell requires control over the surface presentation of chemically active groups. It is crucial that dispersants, and with that functionalities, are irreversibly bound to the NP surface. Only then, desorption of functional units from NP surfaces can be prevented. Desorbed functional units could block receptors, NPs should be targeted to, before functionalized NPs reach these locations. Furthermore, if NPs are functionalized with second labels, desorption leads to large non-specific background signals.

Low M_w dispersants consisting of a high affinity anchor such as the in the previous chapters detailed nitrocatechols, covalently linked to a spacer to which functionalities can be attached, are promising candidates for further NP modification. Because these dispersants adsorb in a well defined way to the NP surface, the interfacial chemistry of such stabilized NPs can easily be tailored by grafting combinations of differently end-functionalized dispersants to NPs. The exposure of ligands to the surrounding can partially be controlled by varying the ratio of the spacer M_w s of functionalized and unfunctionalized dispersants. Furthermore, the ligand density can be tuned with the molar ratio of functionalized to unfunctionalized dispersants that are grafted to the NP surface. This is in stark contrast to iron oxide NP surfaces coated with high M_w dispersants where the serpentine, constantly changing conformation prevents efficient addition and controlled presentation of ligands at the NP interphase [193].

Covalent Linking Strategies

Many different linking strategies have been reported. Most commonly, amine or carboxy groups presented at the NP interphase were used to covalently couple ligands and second labels to the NP shell [95]. Ligands which have previously been activated *e.g.* with N-hydroxysuccinimide (NHS) can easily be linked to amine presenting NPs while carboxy groups bearing NPs can be activated *e.g.* with 3-(dimethylaminopropyl)carbodiimide (EDC) rendering them reactive towards amine bearing ligands. These reactions can be performed under close to physiologic conditions and are thus suited for coupling biologic entities to NP surfaces.

An alternative covalent functionalization strategy is the thiol-ene reaction. The thiol-ene coupling strategy has gained increasing interest because it can be performed under mild conditions without the need for potentially toxic catalysts. Furthermore, it is insensitive to moisture and oxygen [520]. Most antibodies possess a limited number of cysteins on their surface through which these moieties can be coupled to NPs. Furthermore, short ligands such as DNA, RNA and peptide sequences can easily be supplemented with a cystein group at one of their terminals. This significantly simplifies their controlled coupling to the NP surface.

In the following, advantages and disadvantages of different strategies to couple functionalities to sterically stabilized NP surfaces will be discussed. The biotin-avidin functionalization strategy will be compared to different methods to covalently link antibodies and fluorophores to iron oxide NPs. For these studies, iron oxide NPs synthesized in different ways were stabilized with PEG-nitroDOPA or PEG-gallol. The dispersants were partially end-functionalized with biotins or acrylates. After dispersants were grafted to the iron oxide NP surface, further functionalities such as avidins, antibodies or fluorophores were coupled to these iron oxide NPs.

9.2 Functionalization through Biotin-Avidin Coupling

One of the experimentally easiest and most versatile ways to functionalize NPs is the biotin-avidin strategy. Biotinylated ligands can be immobilized on biotinylated NPs through an avidin derivative intermediate layer. However, good control over the NP stability and surface presentation of functionalities, requires thorough characterization of the layer-by-layer structure of these core-shell NPs. Thus, the number of biotin and neutra-

vidin sites presented at individually stabilized iron oxide NPs were quantified. Furthermore, consequences of this widely used functionalization strategy on the size and stability of individually stabilized iron oxide NPs are presented. These studies were conducted on iron oxide NPs synthesized by aqueous precipitation as described in section 3.2.2. They were stabilized with methoxy-PEG(0.55)-gallol (mPEG(0.55)-gallol), methoxy-PEG(5)-6-hydroxy-dopamine (mPEG(5)-gallol), biotin-PEG(3.4)-6-hydroxy-dopamine (biotin-PEG(3.4)-gallol) or mixtures thereof. Even though 6-hydroxy-dopamine is not a direct derivative of gallic acid (it has no acidic group on the phenol ring), it is called gallol in this thesis for simplicity because it has three hydroxy groups directly linked to the phenol as is the case for gallic acid. Gallol is less prone to oxidation than dopamine and DOPA and thus better suited to anchor dispersants to NPs [449, 521]. By the time of investigations using the biotin-avidin coupling, the comparison of the different anchors had not been conducted. Thus, we were not aware of the superior performance of nitrocatechols compared to gallol.

Biotinylated NPs stabilized as described in section 3.3.1 were further functionalized with biotinylated anti-human vascular cell adhesion molecule 1 (VCAM-1) antibodies through neutravidin. Neutravidin is a deglycosylated derivative of avidin, that shows lower non-specific adsorption compared to streptavidin or avidin [519]. VCAM-1 is considered to be a well-suited target for MR contrast agents because it is up-regulated at the endothelial cell periphery of lesion prone sites [522, 523]. It thus is an early marker of atherosclerosis and an attractive receptor for targeting of *e.g.* MR contrast agents [104].

9.2.1 Dispersant Packing Density

TGA-FTIR was performed on PEG-gallol stabilized NPs to validate the presence and quantify the amount of PEG-gallol on the NP surface. The weight loss measured between 200 and 400 °C during TG analysis could be assigned to the decomposition of PEG by FTIR spectroscopy, proving that PEG-gallol was adsorbed on the NPs. The weight loss between 200 and 400 °C measured by TG analysis for mPEG(0.55)-gallol, mPEG(0.55)-gallol/biotin-PEG(3.4)-gallol and mPEG(5)-gallol stabilized NPs was 11 wt%, 15 wt% and 50 wt% respectively. Based on these values, approximately 235 molecules were adsorbed per NP (≈ 194 to $198 \mu\text{mol/g}(\text{iron oxide})$). This corresponds to an average contact area of 0.74-0.76 nm^2 per molecule for all PEG-gallol dispersants tested, independent on PEG M_w if the wt% of dispersants adsorbed on NPs is related to the BET surface area [524]. Assuming the maximum surface coverage is 74%, the packing density of gallol at

the NP surface is 40% of the theoretical maximum if one refers to the reported theoretical cross-sectional anchor group area perpendicular to the benzyl ring of 0.223 nm^2 [355]. The corresponding PEG density is $1.3 \text{ PEG}(5)/\text{nm}^2$. This is more than three times higher than the maximum PEG(5) density reported ($0.4 \text{ PEG}(5)/\text{nm}^2$) for mPEG(5)-(DOPA)₃ adsorbed onto flat TiO_2 surfaces [204] but clearly below what has been obtained by the same technique for PEG(5)-nitrocatechol coated NPs as was shown in chapter 6. However, care must be exercised if dispersant packing densities on NPs synthesized according to different protocols are compared. NP size distribution plays a pivotal role for these calculations. As was shown in chapter 5, depending on the synthesis route, there might be impurities and ultrasmall NPs which significantly contribute to the total surface area, but are difficult to detect by TEM and might thus remain unnoticed.

9.2.2 Biotin Quantification

The molar ratio of biotin-PEG(3.4)-gallol : mPEG(0.55)-gallol could be calculated by comparing the difference in mass losses measured with TGA of mPEG(0.55)-gallol and mPEG(0.55)-gallol/biotin-PEG(3.4)-gallol stabilized NPs assuming that the dispersant packing is independent on the PEG M_w . This is, as was shown in chapter 8, a questionable assumption. Therefore, this method provides a lower limit for the number of biotin sites per NP. Based on these calculations, the dispersant shell surrounding the iron oxide core consisted of 9 mol% biotin-PEG(3.4)-gallol and 91 mol% mPEG(0.55)-gallol. The iron oxide cores were stabilized by modifying uncoated NPs with 10 mol% biotin-PEG(3.4)-gallol and back-filling the NP surface with 90% mPEG(0.55)-gallol. Thus, the estimated molar ratio of biotinylated to unfunctionalized dispersants on the NPs was close to the percentage of the dispersants NPs had been modified with. Assuming NPs were perfectly spherical and had a core radius of 4.5 nm, this equaled 20 biotin sites per NP.

Binding Affinity of Biotinylated NPs to Neutravidin Presenting Surfaces

To check the binding affinity of biotinylated NPs to neutravidin presenting surfaces, binding kinetics of 5 nm core radius iron oxide NPs synthesized by the non-aqueous sol-gel method in the MW and stabilized with a mixture of biotin-PEG(3.4)-nitroDOPA and PEG(1.5)-nitroDOPA was followed *in situ* using QCM-D (Figure 9.1). PEG(1.5)-nitroDOPA rather than PEG(5)-nitroDOPA was chosen to back-fill NP surfaces due to its lower M_w compared to biotin-PEG(3.4)-nitroDOPA. This minimizes the risk that biotin

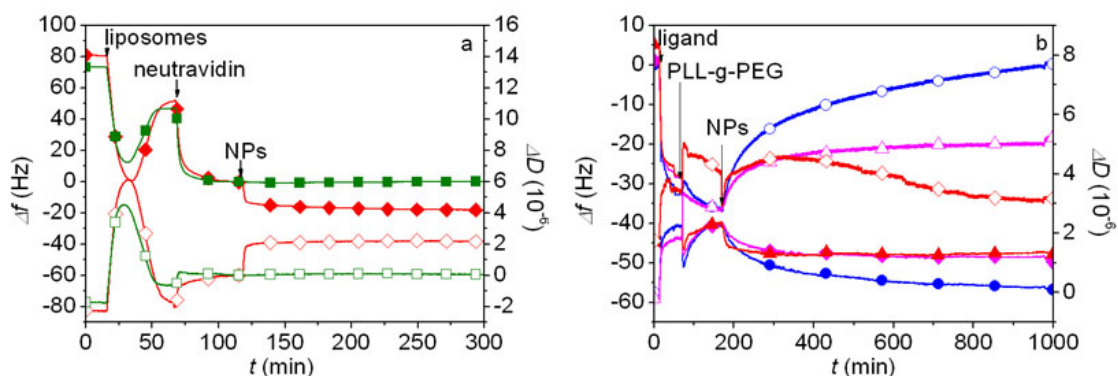


Figure 9.1: Binding kinetics of biotinylated NPs. (a) The binding kinetics of iron oxide NPs synthesized in the MW and stabilized with 10 mol% biotin-PEG(3.4)-nitroDOPA and 90 mol% PEG(1.5)-nitroDOPA (-◇-) to biotin presenting surfaces was compared to that of mPEG(1.5)-nitroDOPA stabilized NPs (-■-) using QCM-D where frequency (filled symbols) and dissipation changes (empty symbols) were monitored. (b) Binding of biotinylated NPs (-◇-), biotinylated NPs coated with neutravidin (-▲-) and NPs functionalized with biotinylated HSP60 antibody immobilized on the biotinylated NPs through a neutravidin linkage (-○-) towards surfaces presenting HSP60 receptors was measured with QCM-D.

sites are buried inside the dispersant shell. However, control measurements revealed that binding kinetics of biotinylated NPs are comparable irrespective whether these NPs were back-filled with PEG(5)-nitroDOPA or PEG(1.5)-nitroDOPA.

For these QCM-D studies neutravidin was immobilized on a SiO_2 coated quartz crystal through biotinylated supported lipid bilayers (SLBs). The biotinylated SLBs prevented non-specific adsorption of NPs to SiO_2 surfaces. Biotinylated and non-biotinylated iron oxide NPs were exposed to the resulting neutravidin presenting surface. While biotinylated iron oxide NPs bound quickly and specifically, non-biotinylated PEG(1.5)-nitroDOPA stabilized iron oxide NPs did not bind (Figure 9.1). Negligible non-specific NP adsorption to neutravidin presenting surfaces confirmed the high NP stability under physiologic conditions measured with DLS (see *e.g.* Figure 6.3). The low QCM-D response upon addition of biotinylated NPs might be assigned to ultrasmall NPs which were also functionalized with biotinylated dispersants. They might have blocked the majority of the biotin binding sites of the neutravidin presenting surfaces before the larger cores reached these sites.

9.2.3 Neutravidin Quantification

Biotinylated functionalities can be immobilized on biotinylated NPs via an intermediate avidin layer (Figure 9.2). All studies were conducted using neutravidin as an intermediate layer despite that the same principles hold for all avidin derivatives that have more

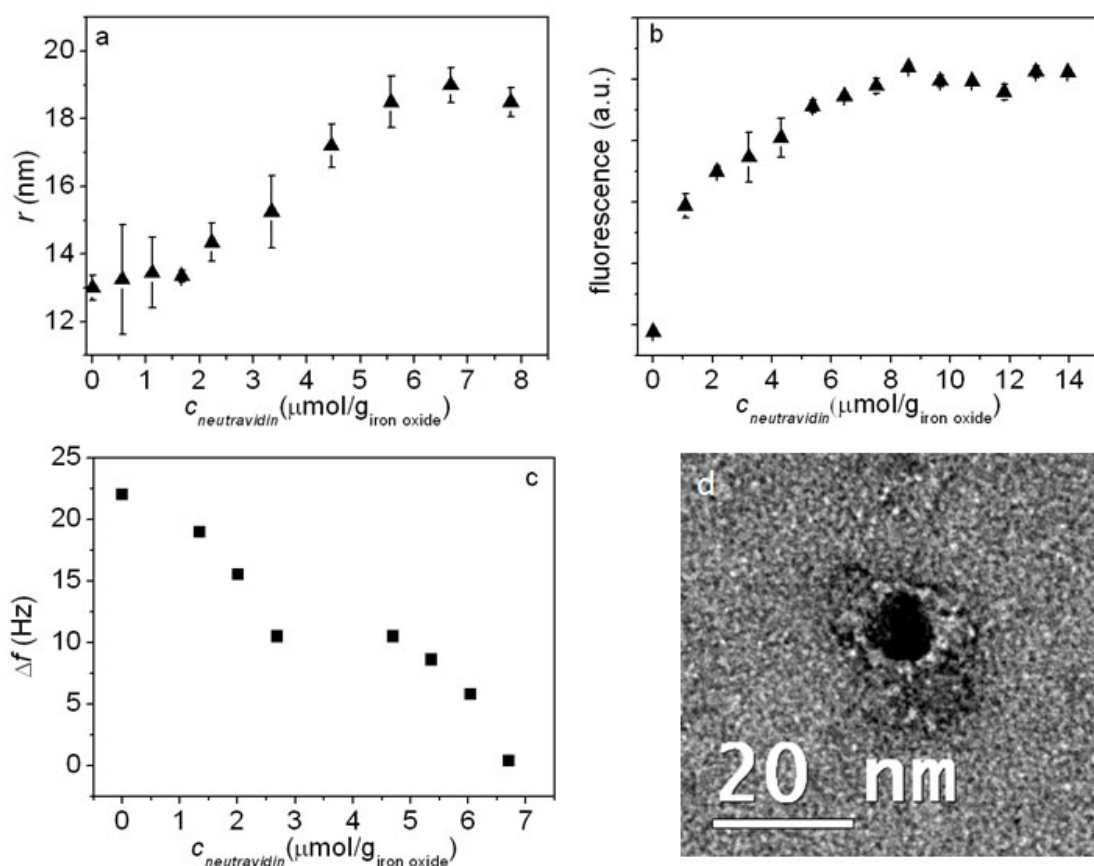


Figure 9.2: Quantification of neutravidin adsorbed on biotinylated NPs synthesized by aqueous precipitation. The neutravidin saturation concentration of mPEG(0.55)-gallol stabilized iron oxide NPs synthesized by aqueous precipitation was determined by (a) DLS where an increase in hydrodynamic radius of NPs bearing increasing amounts of neutravidin was measured up to the neutravidin saturation concentration. Statistics was done on 8 independent samples. (b) FACS measurements revealing an increase in fluorescence of NPs coated with increasing amounts of FITC-labeled neutravidin up to the neutravidin saturation concentration. Statistics was done on 3 independent samples. (c) QCM-D measurements demonstrating NP binding towards a neutravidin monolayer. Binding decreased with increasing amount of neutravidin bound to the biotinylated NPs. The neutravidin monolayer was immobilized onto SiO_2 -coated sensors through non-fouling supported lipid bilayers (SLBs) containing biotinylated lipids. All three techniques showed that maximally $\approx 7 \mu\text{mol}$ neutravidin/g(iron oxide) can be bound to the biotin-bearing NPs, corresponding to 8 neutravidin molecules per particle. (d) TEM micrograph of biotinylated NPs coated with neutravidin. NPs have been stained with uranyl acetate which renders neutravidin white on TEM images.

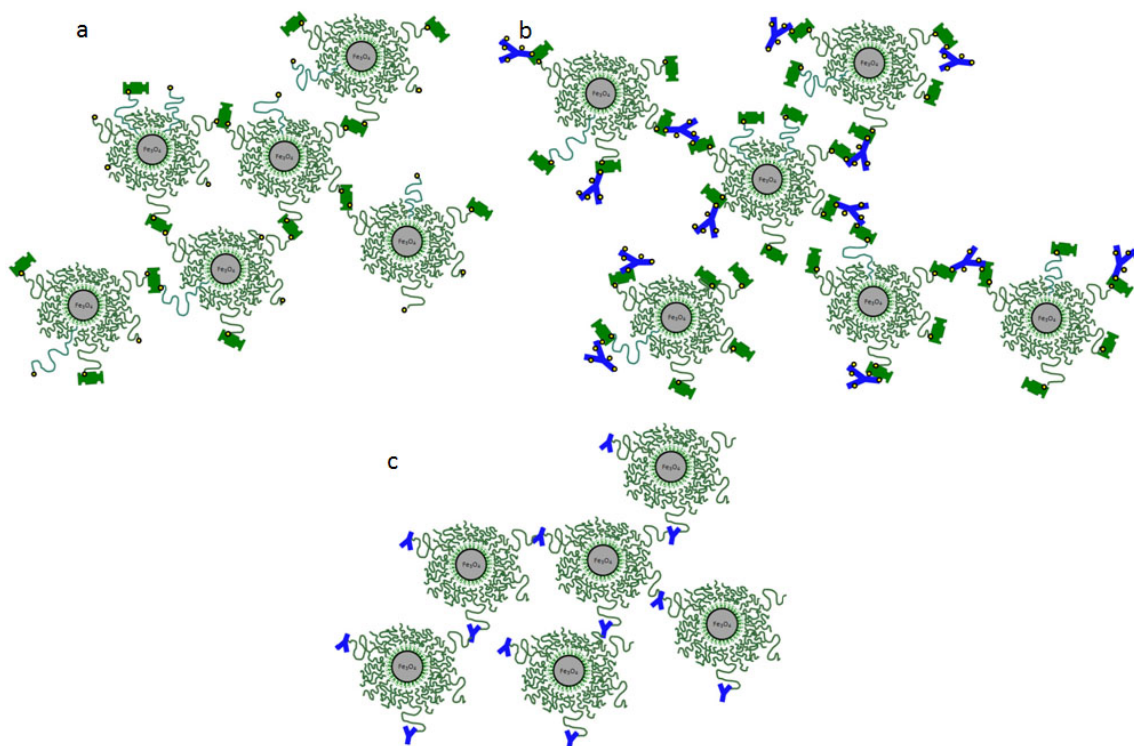


Figure 9.3: *Cartoon of crosslinked functionalized NPs.* Cartoon of crosslinking of (a) biotinylated NPs partially coated with neutravidin, (b) biotinylated NPs saturated with neutravidin and further functionalized with antibodies carrying multiple biotins and (c) acrylate functionalized NPs where antibodies are covalently attached to the acrylate.

than one biotin binding site per protein. Because neutravidin has four biotin binding sites, different biotinylated NPs can bind to the same neutravidin (Figure 9.3a). Therefore, biotinylated NPs tend to agglomerate if exposed to an insufficient amount of neutravidin. This is in analogy to what had been reported for biotinylated liposomes that formed dense agglomerates upon addition of streptavidin [525].

To prevent agglomeration of biotinylated NPs, the maximum number of neutravidins adsorbed per NP was quantified. The neutravidin saturation concentration of these biotinylated NPs was determined with DLS (Figure 9.2a), fluorescence activated cell sorting (FACS) (Figure 9.2b), and QCM-D (Figure 9.2c) by adding different amounts of neutravidin to PBS containing biotin-PEG(3.4)-gallol/mPEG(0.55)-gallol stabilized iron oxide NPs. The hydrodynamic radius of neutravidin-coated NPs increased with increasing neutravidin concentration up to a protein concentration of $7 \mu\text{mol}$ neutravidin/g(iron oxide). This yielded an increase in hydrodynamic radius of 6 nm (Figure 9.2a). Streptavidin, another avidin derivative of similar M_w as neutravidin [519], has a thickness of ≈ 5 nm [526]. The observed increase in hydrodynamic radius was close to the thickness of an

adsorbed neutravidin and thus agrees well with NPs surrounded by a neutravidin monolayer. This was additionally supported by the negative stained TEM micrographs where NPs were surrounded by a white rim that can be assigned to negatively stained neutravidin (Figure 9.2d). The increased fluorescence signal of NPs with increasing addition of FITC-labeled neutravidin up to a concentration of $7 \mu\text{mol}$ neutravidin/g(iron oxide) further supported the findings from DLS (Figure 9.2b). Lastly, SiO_2 -coated QCM-D sensors were used to form a neutravidin monolayer on top of a non-fouling SLB containing biotinylated lipids. NP binding to the neutravidin monolayer decreased as the surface coverage of neutravidin on the NPs increased. No binding was observed at $7 \mu\text{mol}$ neutravidin/g(iron oxide) (Figure 9.2), which corresponds to 8 neutravidins per NP assuming an iron oxide density of 5.18 g/cm^3 [379]. If one considers that at least 2 biotin binding sites per neutravidin are accessible, this would correspond to close to full saturation of the average 20 biotin binding sites per NP estimated from our TGA-FTIR data. Based on these results, it is unlikely that any free biotin site was still accessible after saturating the NP shell with neutravidin. This was supported by the observed plateau in both the DLS and FACS curves, indicating that there was no NP aggregation.

9.2.4 Functionalization with Biotinylated Antibodies

Functionalization with VCAM-1 Antibodies

Real-time binding kinetics and binding specificity of functionalized NPs was investigated using QCM-D. Recombinant human VCAM-1 chimera was immobilized via protein A onto SiO_2 QCM-D sensor crystals (schematically shown in Figure 9.4). Neutravidin pre-coated NPs were further functionalized with biotinylated human anti-VCAM-1 antibodies at iron oxide NP concentrations of $\approx 100 \mu\text{g/ml}$. Upon exposure of such-functionalized NPs to the sensor, fast and specific binding was observed. Only minimal frequency and dissipation shifts (-1.5 Hz and 1.2×10^{-6} , respectively) were measured 2 h after NP injection for NPs lacking the anti-VCAM-1 antibody. Corresponding shifts in frequency (-30 Hz) and dissipation (18.7×10^{-6}) for NPs functionalized with biotinylated human anti-VCAM-1 antibody demonstrated that the binding was specific (Figure 9.4b). Neither neutravidin pre-coated NPs bearing biotinylated anti-E-selectin antibodies nor PEGylated iron oxide NPs or bovine serum albumin (BSA) adsorbed significantly on surfaces presenting recombinant human VCAM-1 chimeras. Specificity of the observed binding interaction was further demonstrated by the fact, that NPs functionalized with anti-VCAM-1

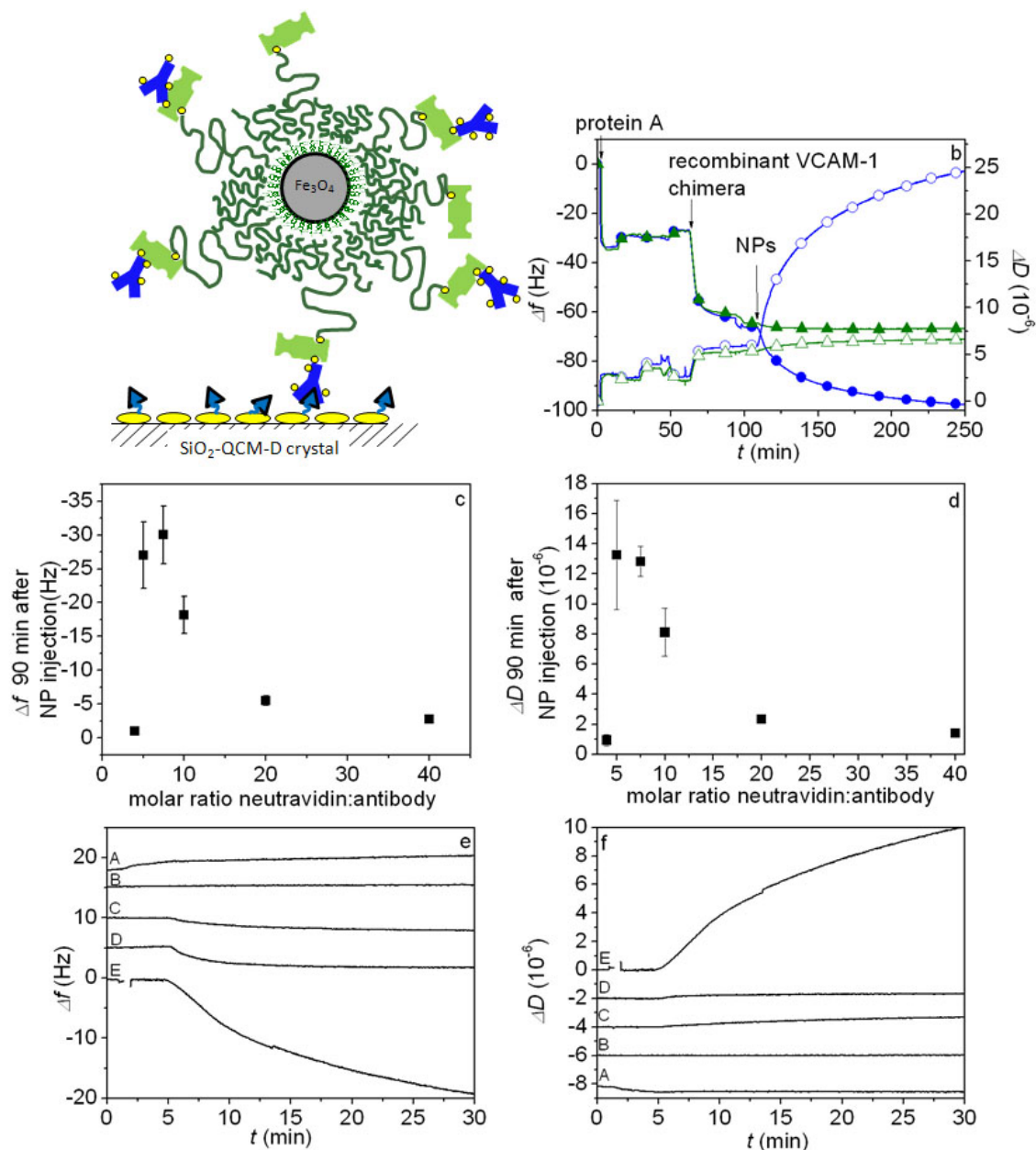


Figure 9.4: Functionalization of PEG-gallol stabilized iron oxide NPs synthesized by the aqueous precipitation method. (a) Cartoon of iron oxide NPs synthesized by the aqueous precipitation method. They were stabilized with 10 mol% biotin-PEG(3.4)-gallol and back-filled with mPEG(0.55)-gallol. Subsequently, they were functionalized with biotinylated anti-VCAM-1 antibodies through the neutravidin linkage. Their binding towards recombinant VCAM-1 antibody presenting surfaces was measured *in situ* with QCM-D. (b) Frequency (filled symbols) and dissipation shifts (empty symbols) of neutravidin coated ($-\Delta-$) and anti-VCAM-1 antibody functionalized NPs ($-\circ-$) towards VCAM-1 chimera presenting surfaces were measured with QCM-D. (c) Frequency and (d) dissipation shifts 90 min after anti-VCAM-1 functionalized NPs were adsorbed on VCAM-1 chimera presenting surfaces as measured with QCM-D as a function of the molar ratio of neutravidin : anti-VCAM-1 antibody added to the NPs where NPs were always coated with equivalent amounts of neutravidin. Control measurements of the response of the (e) frequency and (f) dissipation upon addition of (A) anti-VCAM-1 functionalized NPs to serum presenting surfaces, and (B) cadherin E presenting surfaces, (C) biotinylated, unfunctionalized, (D) anti-E-selectin functionalized and (E) anti-VCAM-1 antibody functionalized NPs to VCAM-1 chimera presenting surfaces. Statistics was done on 2-5 independent samples.

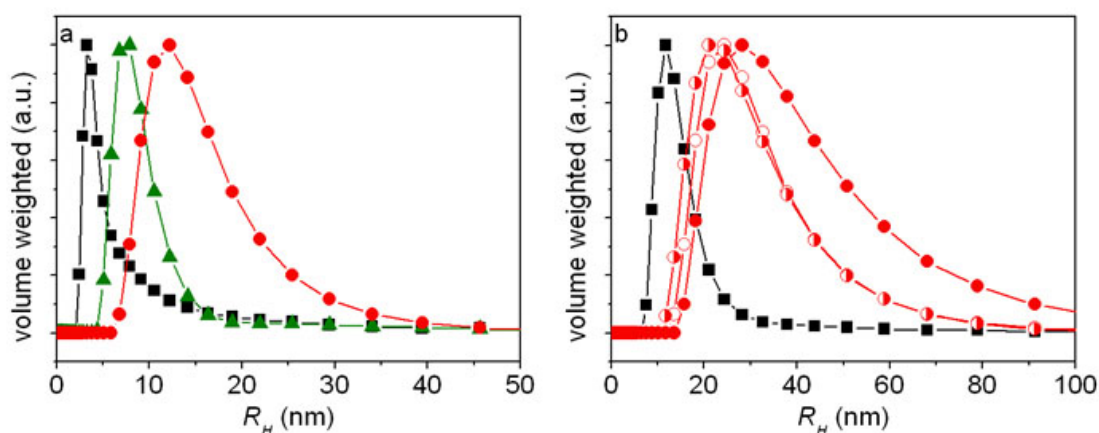


Figure 9.5: DLS of antibody functionalized iron oxide NPs synthesized in the MW. (a) Iron oxide NPs synthesized in the MW have been stabilized with a mixture of 10 mol% biotin-PEG(3.4)-nitroDOPA and 90 mol% PEG(1.5)-nitroDOPA (-■-) and were further functionalized with 2 wt% neutravidin (-▲-) and biotinylated HSP60-antibodies (-●-) (b) The size of unfunctionalized NPs (□) is compared to that of iron oxide NPs functionalized with HSP60-antibodies using 2 wt% (-○-), 3 wt% (-◐-) and 4 wt % neutravidin (-●-) to immobilize the antibodies on the NP surface. The wt % corresponds to the weight neutravidin added to the total mass of stabilized iron oxide NPs (dispersant + iron oxide cores). The molar ratio of neutravidin to HSP60-antibody was kept constant at 4 : 1.

antibodies did not bind to cadherins nor to human serum. However, binding of functionalized NPs was highly dependent on the amount of anti-VCAM-1 antibodies added to neutravidin pre-coated NPs and peaked at a molar ratio of neutravidin : antibodies $\approx 7 : 1$ (Figure 9.4c).

Functionalization with HSP60 Antibodies

Assembly of Nanoparticles

Similar results as described for iron oxide NPs synthesized by aqueous precipitation and functionalized with VCAM-1 antibodies were obtained for NPs synthesized by the non-aqueous sol-gel route. These NPs were functionalized with 10 mol% biotin-PEG(3.4)-nitroDOPA and back-filled with mPEG(1.5)-nitroDOPA. The gradual increase in the hydrodynamic radius of biotinylated NPs further functionalized with neutravidin and biotinylated heat shock protein 60 (HSP60) antibodies shown in Figure 9.5 demonstrates the advantages of the layer-by-layer assembly of these NPs. Each layer of the NP shell can, to a certain extent, be independently tailored. HSP60 antibodies were chosen as ligands because they are up-regulated at atherosclerotic and cancerogenic sites and thus serve as early markers for different diseases such as atherosclerosis and cancer [527].

As was detailed earlier in this chapter, biotinylated NPs have to be saturated with neutravidin to prevent NP crosslinking. However, excessive neutravidin has to be removed prior to the addition of biotinylated ligands. This is required not only to prevent that biotinylated ligands bind to free neutravidins, decreasing the ligand density at the NP surface, but more importantly to prevent NP crosslinking through the multiple biotin sites that high M_w ligands such as antibodies typically have (cf. Figure 9.5b). However, even if excessive neutravidin was removed, neutravidin coated NPs can crosslink through the multiple binding sites of biotinylated antibodies if the NP concentration is sufficiently high or the functionalized NPs are stored for several hours (Figure 9.3b).

DLS measurements performed on biotinylated NPs functionalized with more than 4 wt% neutravidin revealed low count rates, yielding poor correlation functions that could not be properly analyzed, after samples were kept at RT for 4 h. This result was a strong indication that although NPs did not crosslink while being coated with neutravidin, they were crosslinked through the multiple biotin sites of HSP antibodies. Thus, NPs have to be thoroughly purified after the addition of each layer, namely after stabilization to remove excessive biotinylated dispersants, after functionalization with neutravidin to avoid crosslinking through biotinylated ligands and after ligand addition to prevent that free ligands block receptor sites before the functionalized NPs reach these locations. During each purification step, the yield of NPs decreases. Furthermore, purification often involves up-concentrating dispersions *e.g.* through centrifugation. During centrifugation the risk that NPs crosslink is high due to short interparticle distances which increase the likelihood that two NPs bind to the same neutravidin or biotinylated ligand (Figure 9.3a and b). Thus, especially if larger quantities and high concentrations of functionalized NPs are required, the biotin-avidin coupling strategies has several severe shortcomings.

Binding of HSP60-functionalized Nanoparticles

Binding of HSP60-antibody functionalized NPs to HSP60 receptors was measured with QCM-D. HSP60 receptors were directly immobilized on SiO_2 QCM-D crystals before these surfaces were passivated with poly-(L-lysine)-g(3.5)-PEG(2) (PLL-g(3.5)-PEG(2)), for which PEG(2) was on average coupled to every 3.5th amine group of the PLL. However, as can be seen by the non-specific binding of biotinylated NPs in Figure 9.1b, surface passivation was incomplete. Nevertheless, shifts in frequency (Δf) and dissipation (ΔD) of NPs functionalized with HSP60 antibodies were higher compared to NPs coated with a neutravidin monolayer (Figure 9.1b). Thus, the affinity of HSP60 antibody function-

alized NPs to the HSP60 ligand presenting surfaces was higher compared to unfunctionalized NPs. This is similar to what has been seen for anti-VCAM-1 functionalized NPs, illustrating the versatility of this functionalization approach.

9.2.5 Shortcomings of the Biotin-Avidin Coupling Strategy

One of the main disadvantages of the NP functionalization through the biotin-avidin coupling strategy is the risk that NPs agglomerate during the layer-by-layer assembly and subsequent purification of such-functionalized NPs. During and after biotinylated NPs are coated with neutravidin (or avidins in general), different biotinylated NPs can bind to the same neutravidin leading to agglomeration. To prevent crosslinking while biotinylated NPs are coated with neutravidin, biotinylated NPs always have to be slowly added to a solution containing an excessive amount of neutravidin before neutravidin functionalized NPs have to be thoroughly washed to remove excessive neutravidin. As a result, biotinylated NPs are surrounded by a neutravidin monolayer.

It is even more difficult to prevent agglomeration of neutravidin coated NPs during functionalization with ligands that bear multiple biotin sites. These ligands typically are expensive. Therefore, they cannot be dispersed at high concentrations. However, the latter would be required to reduce the risk that neutravidin coated NPs are crosslinked by these ligands during functionalization. Therefore, NP agglomeration during this functionalization step is almost unavoidable. It might be possible to reduce the risk of crosslinking by adding free biotin to the ligand NP solution slightly after neutravidin coated NPs have been added. Free biotins block some of the biotin binding sites of neutravidin and thus reduce the crosslinking risk. However, this procedure is not well controlled because it is difficult to quantify the exact NP and therefore neutravidin concentration during functionalization. Only if the neutravidin concentration is known, the number of biotin binding sites, and therefore the biotin concentration required to partially saturate free biotin binding sites, can be estimated.

Furthermore, for most of the applications, functionalized NP solutions typically have to be up-concentrated many times. This adds an additional preparation step and increases the risk for NP crosslinking. Needless to say that if dispersants are reversibly bound to the NP surface, dissociation of biotinylated dispersants that are linked to neutravidins also results in free neutravidin in solution which can be another cause for agglomeration of neutravidin coated NPs functionalized with biotinylated ligands.

In summary, while NP functionalization through the avidin-biotin coupling strategy is ex-

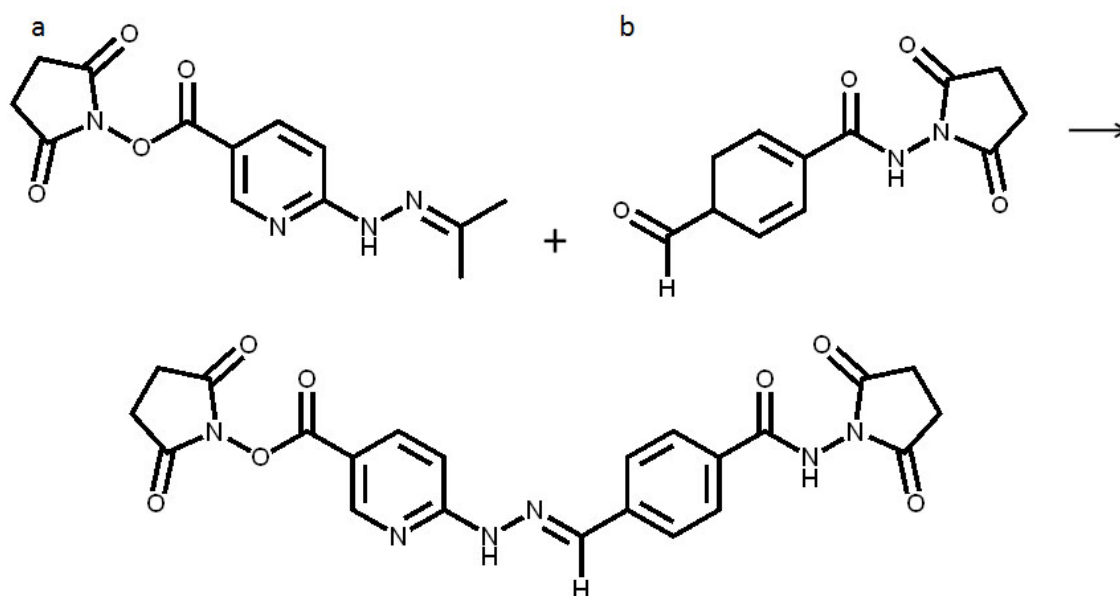


Figure 9.6: Coupling of SANH with SFB. Schematics of the coupling reaction of (a) succinimidyl 6-hydrazinonicotinate acetone hydrazone (SANH) with (b) 4-formylbenzamide (4FB) which results in a stable bis-arylhydrazone.

perimentally easy and versatile, it is only suited for applications that do not require long term NP stability and where NPs are applied under dilute conditions.

9.3 Nanoparticle Functionalization through Covalent Bonds

9.3.1 Succinimide 4-Formylbenzamide (SFB) - Succinimidyl 6-Hydrazinonicotinamide Acetone Hydrazone (SANH) Coupling Strategy

SFB and SANH readily react with each other to a stable bis-arylhydrazone under the formation of a Schiff base (Figure 9.6). This reaction can be conducted under physiologic conditions. This renders it attractive especially for coupling biological entities to NPs. Furthermore, the progression of the reaction can be followed with UV/VIS spectroscopy because the conjugate absorbs at 354 nm. Thus, the ligand density at the NP surface can, in theory, be quantified with UV/VIS spectroscopy. However, because the absorption of the iron oxide cores steadily increases from 800 nm to 200 nm, the absorption of the bis-

arylhydrazone is convoluted with the iron oxide absorption. In practice, the ligand density at the iron oxide NP surface can therefore not be quantified with UV/VIS spectroscopy. Nevertheless, The SFB/SANH coupling strategy is attractive for multiple reasons. SFB and SANH can be coupled to the NPs and ligands separately, before ligands are bound to the NP surface. Additionally, the SFB/SANH coupling can be performed under similar conditions as biotin-avidin coupling. It is therefore an experimentally easy, attractive alternative modification method to the biotin-avidin linkage where the additional protein layer on the NP surface can be avoided.

As detailed in section 3.4.3, NPs were stabilized with PEG(5)-nitroDOPA where 50 mol% of the dispersant had an acrylate end-terminal. Ethan-1,2-diamine was coupled to these NPs before SFB could be bound to the NP shell. SANH was coupled to amine groups of HSP60 antibodies. Because HSP60 antibodies contain multiple amine groups, they were modified with several SANH groups per antibody.

When SFB modified NPs were incubated with SANH modified HSP60 antibodies, NPs started to agglomerate resulting in visible precipitates within 2 h of incubation at RT. Only a small fraction of these NPs passed 200 nm cut-off filters indicating that agglomerates were larger than 200 nm. This is a strong indication that NPs are crosslinked through multiple SANH binding sites of HSP60 antibodies as schematically shown in Figure 9.3c. This is similar to what was observed on neutravidin coated NPs that were incubated with biotinylated antibodies. Thus, unless ligands only have one functional group per ligand, efficient coupling strategies lead to NP crosslinking. They are therefore not suited for NP functionalization in the same way as described for the biotin-avidin coupling strategy.

9.3.2 Functionalization through Michael Addition

A less efficient possibility to covalently couple amine containing ligands to acrylate functionalized NPs compared to the SANH/SFB strategy is the Michael addition. As was reported by Surendra *et al.* [327] amines can be coupled to acrylates in water and RT, conditions many ligands withstand. As a result of the lower coupling efficiency, individually stabilized iron oxide NPs agglomerated significantly slower during functionalization with HSP60 antibodies as compared to the ones functionalized through the SFB/SANH coupling strategy.

NPs functionalized with HSP60 antibodies which passed 200 nm cut-off filters, readily bound to protein A surfaces as was tested with QCM-D experiments (Figure 9.7a). However, if NPs were functionalized at higher NP concentrations (≈ 10 mg/ml), almost all

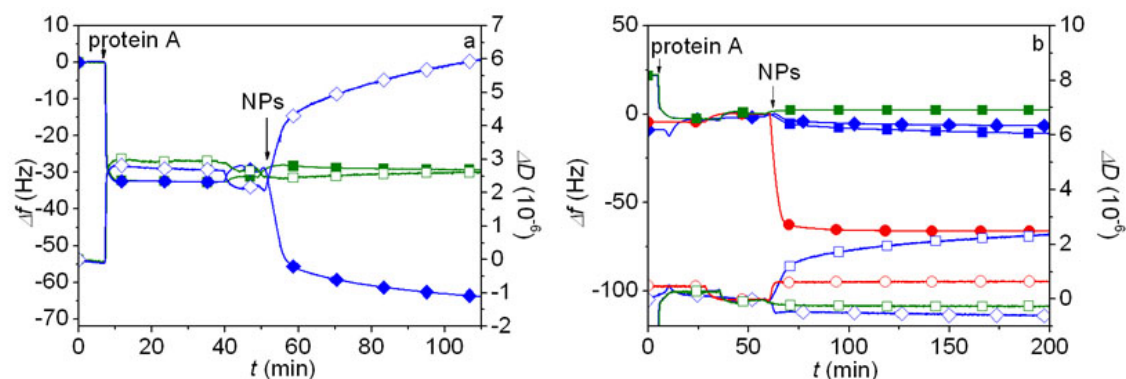


Figure 9.7: *Functionalization of NPs with antibodies.* Iron oxide NPs synthesized in the MW were stabilized with 30 mol% acrylate-PEG(5)-nitroDOPA and 70 mol% PEG(1.5)-nitroDOPA (\square). Binding of these NPs to protein A presenting surfaces was measured with QCM-D by following changes in the frequency (filled symbols) and dissipation (empty symbols). Moreover, such NPs were further functionalized with HSP60 antibodies by coupling the amines of antibodies to acrylates presented at the NPs surface through a Michael addition. Binding of HSP60 antibody functionalized NPs (\diamond) where the functionalization was done at a NP concentration of (a) 0.2 mg(iron oxide)/ml and (b) 10 mg(iron oxide)/ml is shown. In another attempt to functionalize NPs at a concentration of 10 mg(iron oxide)/ml, antibodies were coupled to NPs through an SANH-SFB coupling strategy (\square). As a reference, binding of free HSP60 antibodies, aliquotted at a similar concentration as was used to functionalize NPs with, was measured (\circ).

NPs were removed if they were pushed through 200 nm cut-off filters indicating strong NP agglomeration. NPs that passed the filters likely did not present HSP60 antibodies on their surface. They thus did not crosslink. Consequently, QCM-D response was very low if NPs, that passed 200 nm cut-off filters, but were functionalized at high NP concentrations, were presented to protein A surfaces (Figure 9.7b).

Disadvantages of Antibody Ligands

Functionalization of NPs with antibodies and other ligands of similar sizes is difficult. It requires chemical modifications of the ligands that result in one active linking site per ligand through which the ligand can be coupled to the NP surface. This is challenging especially because the chemical composition of antibodies is often unknown.

Another problem of ligands of the M_w of antibodies is their size. Antibodies are often of similar size as the hydrodynamic diameter of unfunctionalized NPs. Thus, if such NPs are functionalized with antibodies, their hydrodynamic size markedly increases. This can hinder their diffusion [95]. Furthermore, they are thought to decrease the NP circulation time due to non-specific protein adsorption to antibodies. Therefore, functionalization of NPs with antibody fragments such as aptamers and small peptide sequences, that have a known chemical composition, might be more promising [95, 528]. Other potential ligands

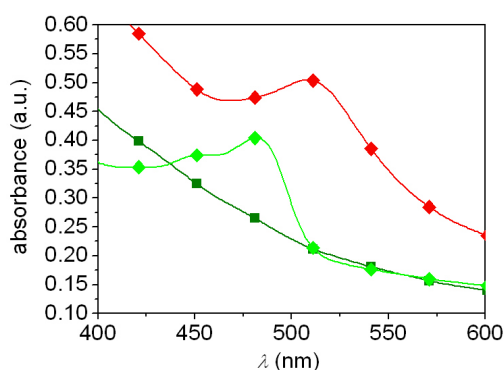


Figure 9.8: UV/VIS spectra of dual labeled iron oxide NPs synthesized in the oil bath. UV/VIS spectra of 5 nm core radius iron oxide NPs synthesized in the oil bath were stabilized with 50 mol% acrylate-PEG(5)-nitroDOPA and back-filled with 50 mol% PEG(5)-nitroDOPA (-■-). These NPs were further labeled with FITC-NH₂ (-◆-) and rhodamine (-◆-) by coupling the fluorophores to acrylates presented at the NP surface through a Michael addition.

where issues such as NP crosslinking during functionalization can be circumvented are DNA and RNA sequences. They can easily be modified with specific end-terminals such as cysteins which allows for controlled covalent coupling of these ligands to NP surfaces without the risk of NP crosslinking.

9.3.3 Functionalization with Fluorophores

PEG-nitroDOPA stabilized NPs crosslinked during functionalized with antibodies leading to a loss of control over their size. Therefore, functionalization of such NPs with antibodies was not successful. However, the same iron oxide NPs, stabilized with PEG(5)-nitroDOPA where 50 mol% of the dispersants were acrylate end-terminated, could be functionalized with a second label such as fluoresceine (FITC) or rhodamine.

Fluorophores containing one NH₂ per molecule were covalently linked to these acrylate presenting iron oxide NPs. NPs were incubated with fluorophores for 3 h in Millipore water at 30 °C before excessive fluorophores were removed by running NPs through a Sephadex column three times to ensure complete removal of unbound molecules.

While PEG-nitroDOPA stabilized iron oxide NPs showed the broad absorption inherent to iron oxide NPs, NPs functionalized with FITC and rhodamine showed additional characteristic absorption peaks at \approx 488 nm and 511 nm respectively (Figure 9.8).

However, a fluorescence peak could only be observed if NPs were functionalized with a high number of fluorophores. The need for high fluorophore concentrations might be assigned to the broad absorption of iron oxide NPs that is convoluted with the absorption

and emission of these fluorophores and to partial fluorophore quenching induced by iron oxide as has been previously reported [112].

In line with this report, NPs functionalized with a mixture of PEG(5)-nitroDOPA and FITC-nitroDOPA, where FITC was directly coupled to nitroDOPA, did not fluoresce unless the FITC-nitroDOPA concentration exceeded 25 mol%. However, at these high FITC-nitroDOPA concentrations, NPs started to visibly agglomerate due to insufficient PEG(5) packing density. No DLS could be measured on these fluorescent NPs because of the interference of fluorescence with the detection of scattered light. Thus, NP stability could only be visually inspected. In summary, stable iron oxide NPs only started to fluoresce, if the fluorophores were separated from the iron oxide core by a sufficiently long PEG-spacer.

9.4 Summary

Motivated by its versatility and experimental ease, biotin-avidin is a well-known, often used NP functionalization method. However, we found that individually stabilized NPs that present biotin at their surface start to agglomerate if they are functionalized with biotinylated ligands either during coating with avidin (if the ratio of avidin : NPs is too low such that NPs cannot be surrounded by an avidin monolayer), or during functionalization with biotinylated ligands (if the ligands bear multiple biotin sites). NP crosslinking becomes especially severe if coupling is performed at high NP concentration and/or during up-concentrating samples.

A promising alternative to the biotin-avidin linkage is to covalently couple functionalities to the NP surface. If ligands are directly covalently bound to the dispersant shell, an additional protein layer, that surrounds the NP core, can be omitted. This reduces the risk for non-specific protein adsorption to the ligands. The large number of well-known, established covalent coupling reactions that can be performed under close to physiologic conditions renders this strategy versatile even though it requires *in situ* chemistry. The high flexibility and close control over the interfacial chemistry and thus ligand density of individually stabilized NPs, ensured by the irreversible binding of nitroDOPA to the Fe_3O_4 NP surface, allows to easily and cost-effectively custom modify resulting multifunctional NPs.

However, irrespective of the coupling strategy, NP crosslinking can only be completely prevented if ligands have exactly one distinct coupling group per molecule through which

they can be linked to the NP surface. This requires a known chemical composition of the functionalities which is often not the case *e.g.* for antibodies. Thus ligands such as DNA, RNA or aptamers that can synthetically be produced, have a known chemical composition and compared to antibodies a low M_w are more promising ligands [528]. They can be engineered to circumvent the crosslinking problem and lead to less non-specific interactions *in vivo*.

Individually stabilized NPs could readily be functionalized with fluorophores that, in contrast to antibodies, contain exactly one NH_2 group per molecule. These fluorophores were covalently attached to acrylate presenting surfaces through a Michael addition. The resulting bimodal contrast agents allow to detect NPs *e.g.* with MRI and fluorescence microscopy. This is often desired especially for *in vitro* biological and biomedical applications [115, 116]. The presented approach can easily be extended to other and more functionalities such as radiotracers [121] and QDs [72, 529].

Assembly of Iron Oxide Nanoparticles into Thermoresponsive Superstructures

10.1 Background

Nanoscale vesicles are crucial not only for drug delivery applications [530–532] but also of high interest to perform *ex vivo* encapsulation, delivery and nanoscale chemistry [140, 533]. Irrespective of the application, it is highly beneficial to externally trigger release of a controlled dose of the encapsulated cargo at a specific time and location [147], as opposed to release that merely relies on passive diffusion or in response to global environmental changes [148].

10.1.1 Liposomes

One of the most researched delivery vehicles are liposomes [530]. Liposomes are assembled from naturally occurring phospholipids, one of the most common building blocks of cells. They are thus naturally compatible with *in vivo* applications. Thus, liposomes are considered to be promising drug delivery vehicles for *in vivo* applications [103, 137, 534]. Their composition and surface presentation of functional units, which determine their properties and performance, can easily be tailored by assembling them from different phospholipids mixtures [137, 530, 535–537]. Furthermore, they can ferry hydrophilic and hydrophobic cargo as hydrophilic species can be loaded in their lumen while hydrophobic compounds can be incorporated into the hydrophobic core of the lipid bilayer

[103] which is $\approx 4 - 5$ nm thick [538–540]. However, due to size restrictions, only a limited amount of cargo can be loaded into liposomes [72]. This is a drawback that becomes especially severe if the liposome size is small.

Liposome Preparation

Liposome size, size distribution and structure are determined by their preparation route. Liposomes are generally prepared from phospholipids or phospholipid mixtures that are dissolved in an organic solvent. The organic solvent is completely evaporated resulting in a thin lipid film. This film is subsequently re-hydrated by adding water or an aqueous buffer that optionally contains hydrophilic cargo. Re-hydration and swelling of multilamellar liposomes is done above the liposome membrane transition temperature T_m where liposomes have been shown to self-assemble without further treatments [538, 541].

To reduce the size and the lamellarity of multilamellar liposomes, they most often are sonicated [535, 538, 542] or extruded after they have been swollen [543].

Compared to sonication, extrusion allows for better control over the size. Thus, this procedure is more reproducible. Sequential extrusion of multilamellar liposomes through polycarbonate filters has been shown to result in unilamellar vesicles with a diameter comparable to the filter pore size used during extrusion if the pore filter size is in the nanometer range [543]. Because of the close control over liposome size and the good reproducibility, liposomes used in this thesis were extruded.

Liposome Biodistribution

If applied *in vivo*, liposomes are cleared through opsonization followed by an uptake by the RES and end up in the liver and spleen [136, 198, 544–546]. Liposome size and charge determine their blood circulation time. Small, unilamellar liposomes circulate significantly longer in the blood compared to multilamellar counterparts. Furthermore, positively charged liposomes are cleared faster than negatively charged ones [547].

In analogy to the PEG-coated NPs, protein adsorption, and thus the recognition of liposomes by the body, can be reduced if they are surrounded by a PEG shell. This significantly increases the liposome blood circulation time [220, 548–552]. Whereas the addition of 5 mol% PEGylated phospholipids with a PEG $M_w > 750$ Da has been shown to efficiently prolonge their blood half life time, similar circulation times could be achieved with higher mol% of PEG(0.12)-DSPG [553]. However, liposomes modified with a low

concentration of PEGylated phospholipids are more prone to enzymatic degradation by lipopolimerases compared to unmodified liposomes [554]. Thus, if good liposome stability and long circulation times are to be achieved, the PEG chains surrounding liposome bilayers have to be in the mushroom to brush or brush regime [554].

Cargo Release

The permeability of liposomes is greatly enhanced around T_m [141] which depends on the lipid composition [142, 143]. Uncharged cargo is released from liposomes as the solution around the liposome membrane is heated above T_m .

If used as drug delivery vehicles, T_m was typically designed to be close to body temperature. This resulted in leakage during circulation [555]. In contrast, if T_m is chosen far above body temperature, release is inefficient [556, 557]. To circumvent the incompatible requirements of simultaneous release efficiency and low passive leakiness, liposomes have been loaded with hydrophilic plasmonic [175] and magnetic [152, 169] NPs to trigger cargo release with light and high frequency alternating magnetic fields (AMF) respectively.

If optical triggers are used, they have to absorb light in the near IR region (≈ 600 nm - 1000 nm). In this region, tissue absorbs least [58, 59] and thus the penetration depth of light is highest. However, even if Au NPs and nanocages are specially engineered, they have to be at least 50 nm in size to absorb in the near IR region [60]. This severely limits their applicability as actuators of superstructure for biomedical applications. In contrast, magnetic NPs only have to be larger than ≈ 2 nm in radius to be magnetically responsive [15].

Very recently, triggered release of liposomes containing oleic acid stabilized iron oxide NPs associated with their membranes was shown. However, these liposomes agglomerated at room temperature and were inherently leaky [176]. Furthermore, oleic acid stabilized NPs agglomerated and therefore are unlikely to efficiently incorporate into liposome bilayer due to size constraints [313]. Thus, the feasibility to incorporate hydrophobic iron oxide NPs into the liposome membrane in a controlled way remains to be shown.

In this chapter, a protocol to assemble PEGylated stealth liposomes with T_m far higher than body temperature and hosting individually stabilized iron oxide NPs in their membranes is established. Emphasis is put on the characterization of the resulting superstructures including the mechanism of cargo release that can be triggered with AMF pulses. Release efficiency and performance of the with iron oxide NP doped liposomes are shown

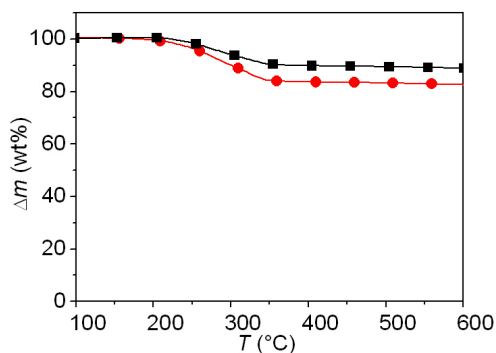


Figure 10.1: TGA of palmityl-nitroDOPA stabilized NPs. TGA was measured on small (●) and large (■) iron oxide NPs stabilized with palmityl-nitroDOPA. Measurements were performed under gas flow consisting of 47.4 sccm Ar and 12.6 sccm O₂.

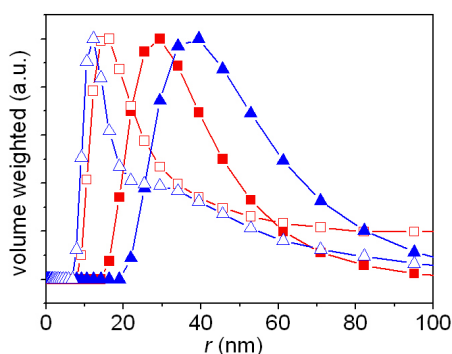


Figure 10.2: DLS of liposomes containing NPs in their membranes. DLS measurements of DSPC liposomes containing 5 mol% PEG(2)-PE. Liposomes prepared by extrusion (filled symbols) and sonication (empty symbols) were loaded with small (●) and large (▲) iron oxide NPs that were stabilized with palmityl nitroDOPA.

to relate directly to the structure and stability of the NP-lipid assemblies. The latter are investigated by small angle neutron scattering (SANS), transmission electron microscopy (TEM), differential scanning calorimetry (DSC), thermogravimetry analysis (TGA) and fluorescence spectroscopy (FS).

10.2 Liposome Assembly

10.2.1 Hydrophobic Iron Oxide Nanoparticles

As was shown in chapters 6 and 7, nitroDOPA is well suited to firmly bind dispersants to iron oxide NP surfaces. However, if NPs are to be assembled into the hydrophobic part of liposomes, they have to be stabilized with a hydrophobic dispersant. For this purpose, nitroDOPA was covalently linked to NHS-activated palmitic acid resulting in palmityl-nitroDOPA (section 3.1.5). Iron oxide NPs synthesized in the oil bath for 24 h at 150 °C, resulting in an average core radius of 2.5 nm, are denoted as small NPs. NPs synthesized at 180 °C, yielding in average core radii of 5 nm, are denoted as large NPs (see section 3.3.2 for details on the NP synthesis). These NPs were stabilized with palmityl-nitroDOPA according to the procedure detailed in section 3.3.3.

According to TGA measurements, the weight percent of palmityl-nitroDOPA adsorbed on small and large iron oxide NPs was 17 wt% and 11 wt%, respectively (Figure 10.1). This yields a dispersant packing density of 1.5 molecules/nm² independent on the core size if the core size distribution determined from TEM micrographs (Figure 5.23) is taken into account.

10.2.2 Assembly of Liposomes

The detailed protocol of the assembly of liposomes containing iron oxide NPs in the hydrophobic core of the lipid bilayer is described in section 3.6.2. In brief, iron oxide NPs surrounded by a palmityl-nitroDOPA shell were dispersed in chloroform and mixed with DSPC lipids containing 5 mol% PEG(2)-PE unless stated otherwise. After chloroform was removed under continuous N₂-flow, lipids were re-dispersed in aqueous media. Sonication yielded in a high concentration of micelles as was shown by the small size of the resulting objects measured with DLS (Figure 10.2). Liposomes that were extruded resulted in significantly larger objects indicating that less micelles were formed (Figure 10.2). To minimize the risk for micelle formation and to be able to control the liposome size, liposomes were prepared by extrusion. Therefore, the MLVs formed after rehydration were sequentially extruded 10 and 31 times through polycarbonate filters with 200 nm and 100 nm pore sizes respectively.

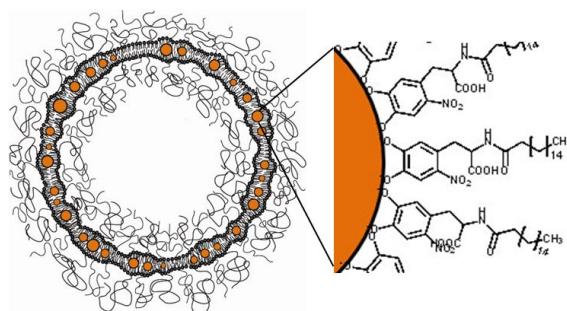


Figure 10.3: Cartoon of liposomes containing iron oxide NPs in their bilayer. NitroDOPA-palmitoyl stabilized iron oxide NPs are embedded in liposome membranes. The liposome membranes contain 5 mol% PEGylated lipids to prevent liposome agglomeration if stored in the gel phase ($T < T_m$).

10.3 Characterization of Liposomes

10.3.1 Influence of Dispersant

Individually palmityl-nitroDOPA stabilized iron oxide NPs spontaneously incorporated into the liposome bilayer (as schematically shown in Figure 10.3). To analyze the morphology of liposomes hosting iron oxide NPs in their membranes, liposome dispersions were frozen in liquid ethane and investigated with cryo-TEM under liquid N_2 temperatures (Figure 10.4a, c, d). According to cryo-TEM images, the vesicular, spherical structure of liposomes was retained also when iron oxide NPs were embedded in their membranes. However, due to the small size of iron oxide NPs, yielding poor contrast in TEM, and the background-contrast from vitrified ice, it was difficult to visualize NPs with cryo-TEM. To unequivocally unravel the presence iron oxide NPs in liposomes, liposomes were fixed with trehalose, air-dried and imaged with conventional TEM. If fixed with trehalose, liposomes should collapse during drying resulting in a 2D projection of their natural 3D shape. Trehalose further prevents re-distribution of phospholipids and iron oxide NPs during drying.

As can be seen in Figure 10.5, well-dispersed iron oxide NPs were associated with these liposomes. If palmityl-nitroDOPA stabilized, hydrophobic NPs were loaded in the liposome lumen, they would instantaneously agglomerate upon addition of water or buffer. Therefore, these NPs have to be embedded in the liposome membrane. The observation that palmityl-nitroDOPA stabilized NPs were well dispersed and embedded in the liposome membrane was in strong contrast to oleic acid stabilized NPs. The latter agglomerated and formed micelles as revealed by cryo-TEM (Figure 10.4b) and by the much darker color seen by optical inspection (Figure 10.6a) of as-extruded liposomes.

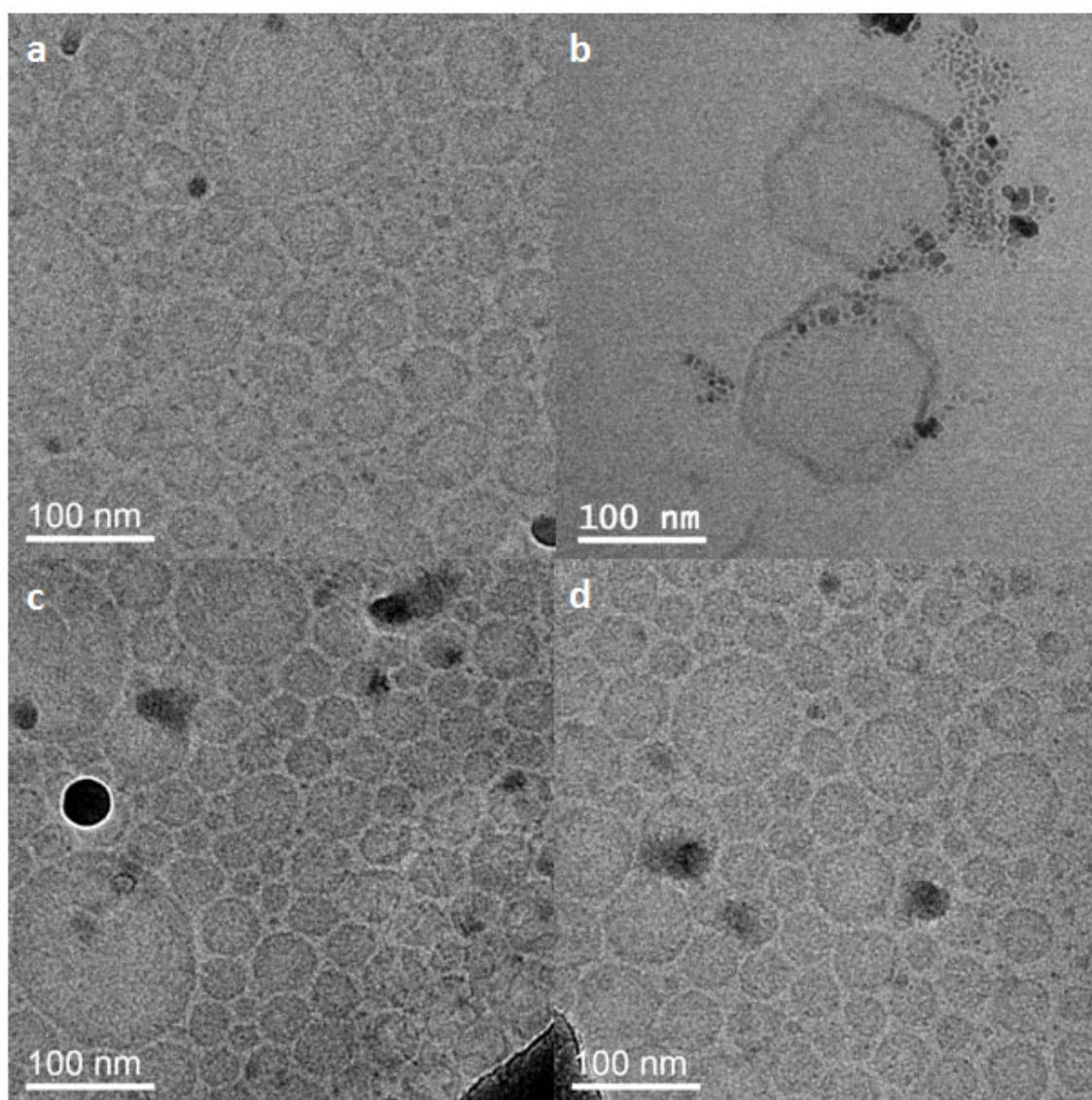


Figure 10.4: Cryo-TEM of DSPC liposomes containing 5 mol% PEG(2)-PE lipids. Cryo-TEM images of DSPC liposomes containing 5 mol% PEG(2)-PE that were (a) unmodified, incorporated (b) oleic acid coated small iron oxide NPs, palmityl-nitroDOPA stabilized (c) small and (d) large iron oxide NPs.

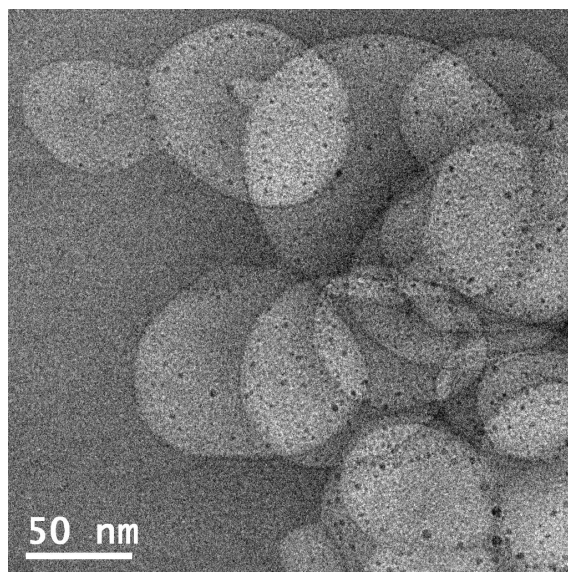


Figure 10.5: DSPC liposomes doped with small palmityl-nitroDOPA stabilized NPs. TEM image of DSPC liposomes containing small palmityl-nitroDOPA stabilized iron oxide NPs in their membrane. Liposomes were fixed with trehalose and air-dried on a carbon film supported TEM grid.

Palmityl-nitroDOPA Stabilized Nanoparticles

To further characterize the structure of liposomes hosting palmityl-nitroDOPA stabilized small NPs in their membranes, liposomes were freeze-dried on a carbon supported TEM grid and analyzed with STEM. Freeze-drying should result in a 2D projection of the 3D shape of vesicles and prevent re-distribution of phospholipids and iron oxide NPs during drying, similar to trehalose. Trehalose fixation did not work for STEM analysis because trehalose contaminated the vesicular structures immediately upon exposure to the STEM beam resulting in a thick hydrocarbon film. This hydrocarbon film prevented a detailed chemical analysis with STEM. Therefore, liposomes were freeze-dried.

Images were acquired using a secondary electron (SE) and a high angle annular dark field (HAADF) detector. Additionally, chemical analysis was performed using electron dispersive X-ray (EDX) spectroscopy. Because secondary electrons can only escape from locations in close proximity to the surface, structures detected with the SE detector must be localized at the surface. The HAADF detector is sensitive to heavy elements. A comparison of Figures 10.6b and c taken from the same region and considering the chemical analysis of this location (Figure 10.6d), allows assigning the white spots to iron oxide NPs. Furthermore, because these NPs were not seen in Figure 10.6c, they must be covered by a continuous organic film.

According to Figure 10.6d, the organic tube seen in Figures 10.6b and 10.6c consists

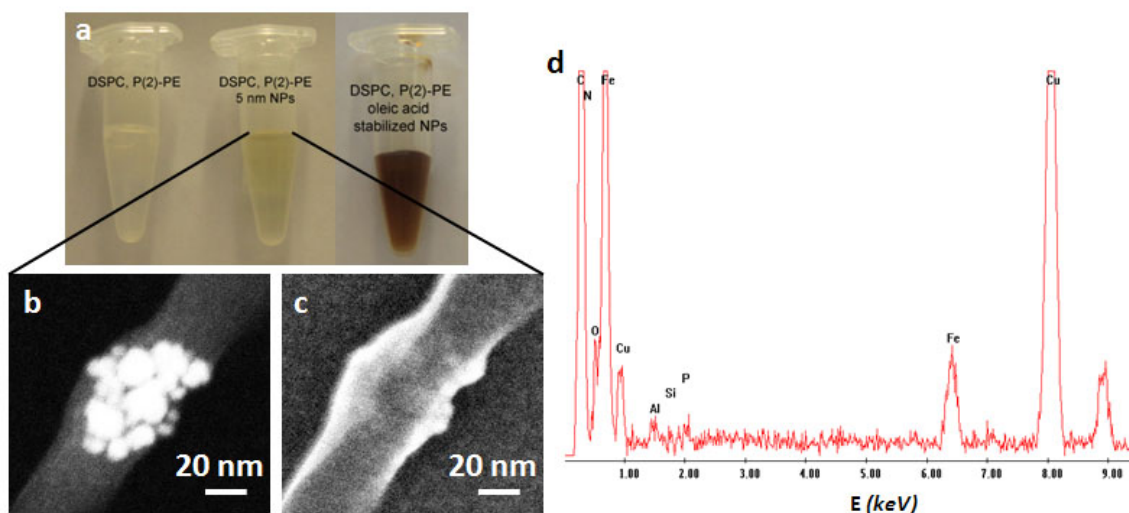


Figure 10.6: TEM analysis of liposomes. (a) Photograph of unmodified DSPC/PEG(2)-PE liposomes and liposome solutions containing palmityl-nitroDOPA and oleic acid surface modified small iron oxide NPs respectively. These liposomes were freeze dried on a carbon supported TEM grid. TEM images of freeze dried DSPC/PEG(2)-PE liposomes containing palmityl-nitroDOPA modified small iron oxide NPs in their membrane. The same location was imaged with the (b) HAADF and (c) SE detector. (d) EDX analysis performed on the structure shown in (b) and (c) confirmed that the white spots seen in Figure (b) are iron oxide NPs covered by a thin organic film consisting of *C*, *N*, *O* and *P*. Thus, the film can be assigned to a phospholipid membrane. *Cu*, *Al* and *Si* signals originate from the holder and TEM grid respectively.

of *C*, *O*, *N* and *P*. It thus can be assigned to phospholipid membranes that most likely deformed either upon adsorption on a glow-discharged, hydrophilic carbon film or upon drying. Hence, iron oxide NPs individually stabilized with palmityl-nitroDOPA must be embedded in phospholipid membranes. This is well in agreement with the observations made with cryo-TEM (Figure 10.4c) and conventional TEM of liposomes embedded in vitrified ice and trehalose fixed liposomes respectively (Figure 10.5).

Effect of Nanoparticle Stability

The striking difference between palmityl-nitroDOPA and oleic acid stabilized NPs can be related to the binding affinity of the dispersant to iron oxide. While nitroDOPA was shown in chapters 6 - 8 to irreversibly bind dispersants to iron oxide surfaces, oleic acid is a reversibly adsorbing dispersant. Reversible dispersant adsorption renders oleic acid stabilized NPs prone to agglomeration. Note that NP aggregation could have occurred either within the lipid membranes or before incorporation of the NPs in liposome membranes. Oleic acid stabilized 3 - 15 nm iron oxide NPs mixed with phospholipids in organic solvents and re-dispersed in aqueous media have been shown to be surrounded by a phos-

pholipid monolayer yielding stable NPs in aqueous media [558, 559]. Thus, the micelles found by cryo-TEM (Figure 10.4b) were likely stabilized by a phospholipid monolayer. That agglomerated NPs cannot be incorporated into liposome membranes is related to their size. Theoretical studies suggest a threshold maximum NP diameter of 6.5 nm [313] for incorporation of neutral NPs [314] into lipid bilayers. Larger or charged cores are preferentially encapsulated in lipid monolayers resulting in micelles.

This size limit is well in agreement with the cryo-TEM images (Figure 10.4c, d). Due to the broad core size distribution, even large NPs (with an average core radius of 5 nm) contain a fraction with cores with radii < 2.75 nm (Figure 5.23). Indeed, TEM images revealed only NP cores with radii < 2.75 nm in liposome membranes irrespective whether liposomes were doped with small or large NPs (Figure 10.4c, d). Similar results have also been observed experimentally for 3 nm trioctyl phosphine (TOPO) stabilized quantum dots (QDs) that could be readily embedded in liposome membranes in contrast to 8 nm QDs [306].

10.3.2 Loading Efficiency

The loading efficiency of iron oxide NPs into liposomes was quantified with TGA. Unilamellar liposomes were found to maximally host 10 ± 4 and 12 ± 2 wt% small and large palmityl-nitroDOPA stabilized iron oxide NPs respectively, corresponding to 2 - 3 vol% iron oxide cores. This yields a loading efficiency of $\approx 30\%$. Iron oxide cores larger than the critical diameter, that were not surrounded by a phospholipid monolayer, most likely started to agglomerate upon contact with aqueous solutions and were removed during extrusion.

10.3.3 Effect of Nanoparticle Size on Liposome Morphology

Only insignificantly lower wt% of small compared to large iron oxide NPs were associated with liposome membranes. Furthermore, TEM images of trehalose fixed liposomes containing small and large NPs in their membranes indicated that no NPs with core radii > 2.75 nm were embedded in liposome membranes (Figure 10.7). Thus, only NPs with core radii < 2.75 nm could assemble in the liposome bilayer. According to TGA, 30% of the NPs added to the lipid/NP dispersion prior to liposome extrusion were present in the liposome dispersion after extrusion (section 10.3.2). However, TEM analysis of the

Table 10.1: SANS characterization of DSPC/PEG(2)-PE liposomes.

NPs	T (°C)	d_{membrane} (nm)	R_G of PEG (nm)	r_{vesicle} (nm)
no	25	4.6	1.8	46 ± 6
small	25	4.6	1.6	23 ± 2
large	25	4.6	1.8	47 ± 6
no	60	4.2	1.7	47 ± 5
small	60	4.5	1.7	22 ± 2
large	60	4.1	1.8	48 ± 5

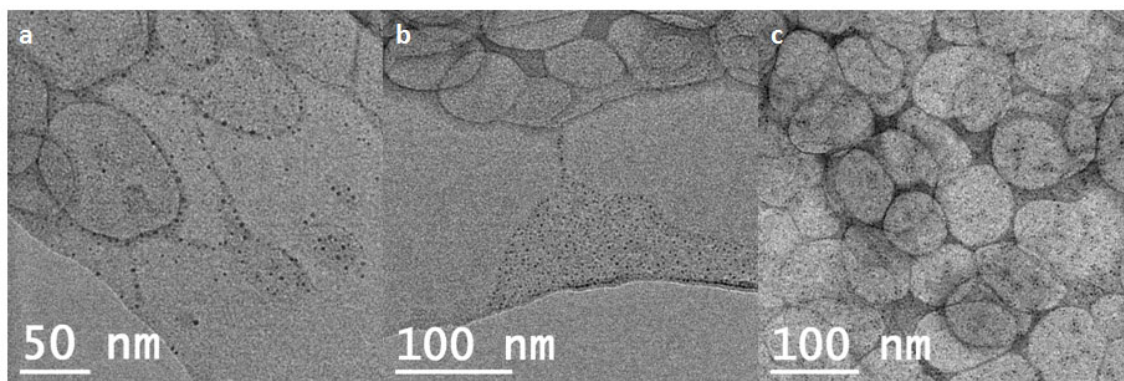


Figure 10.7: TEM of trehalose fixed liposomes doped with iron oxide NPs. DSPC liposomes doped with (a, b) small and (c) large iron oxide NPs stabilized with palmityl-nitroDOPA were fixed with trehalose and air-dried on a carbon film supported TEM grid. In (b) liposomes partially ruptured and formed films that contained densely packed NPs.

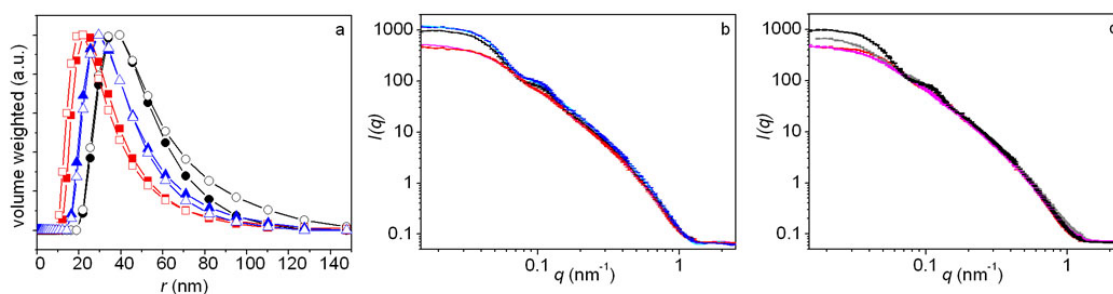


Figure 10.8: DSPC liposomes containing 5 mol% PEG(2)-PE characterized by scattering techniques. (a) DLS curves of DSPC liposomes containing 5 mol% PEG(2)-PE as-extruded (filled symbols) and after 4 weeks storage at 4 °C (empty symbols) of unmodified (●), with palmityl-nitroDOPA surface modified small (■) and large (▲) iron oxide NPs. (b) SANS measurements of unmodified DSPC/PEG(2)-PE liposomes (black), DSPC/PEG(2)-PE liposomes containing small (red) and large (blue) iron oxide NPs in their membranes are shown. These data were fitted with a form factor for bilayer vesicles that was extended to account for the PEG brush that surrounds the bilayers. (c) SANS data measured on unmodified DSPC/PEG(2) liposomes at RT (black) and 60 °C (gray). Similarly, DSPC/PEG(2)-PE liposomes containing small iron oxide NPs in their membranes were measured at RT (red) and 60 °C (magenta).

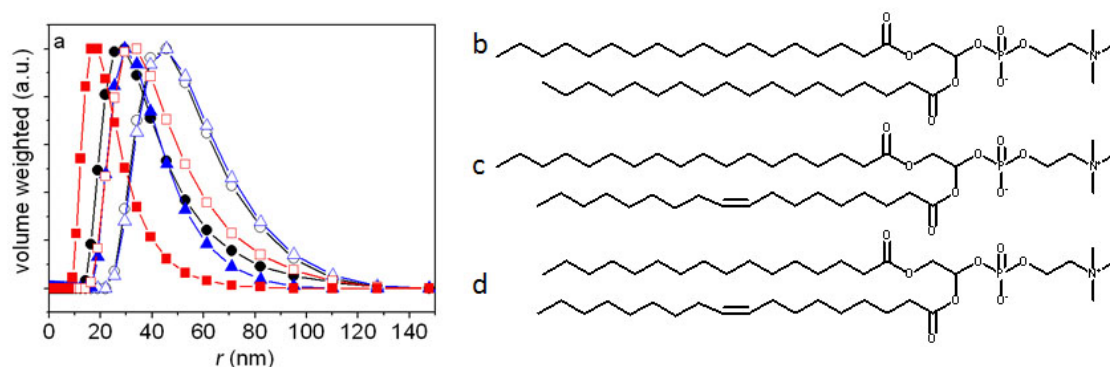


Figure 10.9: Incorporation of small iron oxide NPs into different liposomes. (a) DLS measurements of liposomes containing 5 mol% PEG(2)-PE lipids. Unmodified liposomes (empty symbols) were compared to liposomes that hosted small palmitoyl-nitroDOPA stabilized iron oxide NPs in their membranes (filled symbols). Liposomes consisted of DSPC (-■-) ($T_m = 55$ °C), SOPC (-▲-) ($T_m = 6$ °C) and POPC (-●-) ($T_m = -2$ °C). The chemical structure of (b) DSPC (18:0 PC), (c) SOPC (18:0-18:1 PC) and (d) POPC (16:0-18:1 PC) is shown.

core size distribution of the large NPs revealed, that far less than 30% of these cores have a radius < 2.75 nm (Figure 5.23). Therefore, not all large NPs present in the liposome dispersions could be embedded in the liposome membrane.

NPs with radii > 2.75 nm likely formed micelles similar to oleic acid coated agglomerated NPs. If these larger NPs are surrounded by a phospholipid monolayer, they are stable in solution and thus pass filters during extrusion. The fact, that not all NPs > 2.75 nm in radius were surrounded by a phospholipid monolayer and thus colloidally stable under physiologic conditions might be caused by incomplete lipid coverage of some of the hydrophobic NPs during re-hydration and extrusion.

DSPC liposomes containing 5 mol% PEG(2)-PE loaded with small NPs were significantly smaller compared to liposomes loaded with large NPs and unmodified liposomes when extruded with the same pore size of the extrusion membranes (Figure 10.9 and Table 10.1). Because of the size cut-off above which NPs cannot get embedded in the liposome membrane any more, liposomes functionalized with small NPs likely hosted more NPs in their membranes compared to liposomes functionalized with large NPs. The smallest size of liposomes functionalized with small NPs thus indicates that liposomes get smaller with increasing amount of iron oxide NPs embedded in their membranes (Figure 10.8 and Table 10.1).

Table 10.2: Quantification of the amount of NPs in liposomes determined by TGA.

lipid	NPs	amount of NPs in liposomes (wt%)	amount of NPs in liposomes (vol%)	number of NPs per liposome
DSPC	small	3	0.6	18
DSPC	large	6	1.2	38
DSPC/PEG(2)-PE	small	10 ± 2	2.1	66
DSPC/PEG(2)-PE	large	12 ± 1	2.6	81
SOPC/PEG(2)-PE	small	14	3.1	97
POPC/PEG(2)-PE	small	8 ± 0	1.7	52

10.3.4 Effect of Lipid Composition

To elucidate the influence of the lipid tail length and configuration on the loading efficiency of NPs and its relation to the effect of NPs on the liposome size, small NPs stabilized with palmityl-nitroDOPA were embedded into liposomes consisting of DSPC (18:0 PC), SOPC (18:0 -18:1 PC) and POPC (16:0 -18:1 PC) (Figure 10.9). All liposomes contained 5 mol% PEG(2)-PE. Small NPs could, within experimental error, be loaded equally efficiently into all investigated liposomes (Table 10.2). Interestingly, irrespective of the lipid composition, all liposomes containing small iron oxide NPs in their membranes were significantly smaller than the respective reference liposomes (Figure 10.9a). This indicates that the NP incorporation efficiency and the change in liposome size upon loading with NPs are not critically affected by unsaturated bonds in the lipid tail and the lipid tail length (*cf.* Figure 10.9b-d).

A similar observation concerning decreased size of polymersomes after incorporation of hydrophobic QDs into the membrane was made by Binder *et al.* [312]. While the reason for the reduced size remains to be determined, it might be simply due to a reduced effective pore size of the extrusion membranes determining the liposome size [543], as NPs clearly clogged the filter membranes. As shown below, NPs also affected the curvature of liposome membranes which, although less likely, could lead to a smaller equilibrium size.

10.3.5 Membrane Distortions Caused by Nanoparticles

DSPC Liposomes

To elucidate membrane distortions caused by NPs embedded in the liposome membrane, SANS measurements were performed on DSPC liposomes at RT and 60 °C (Figure 10.10a

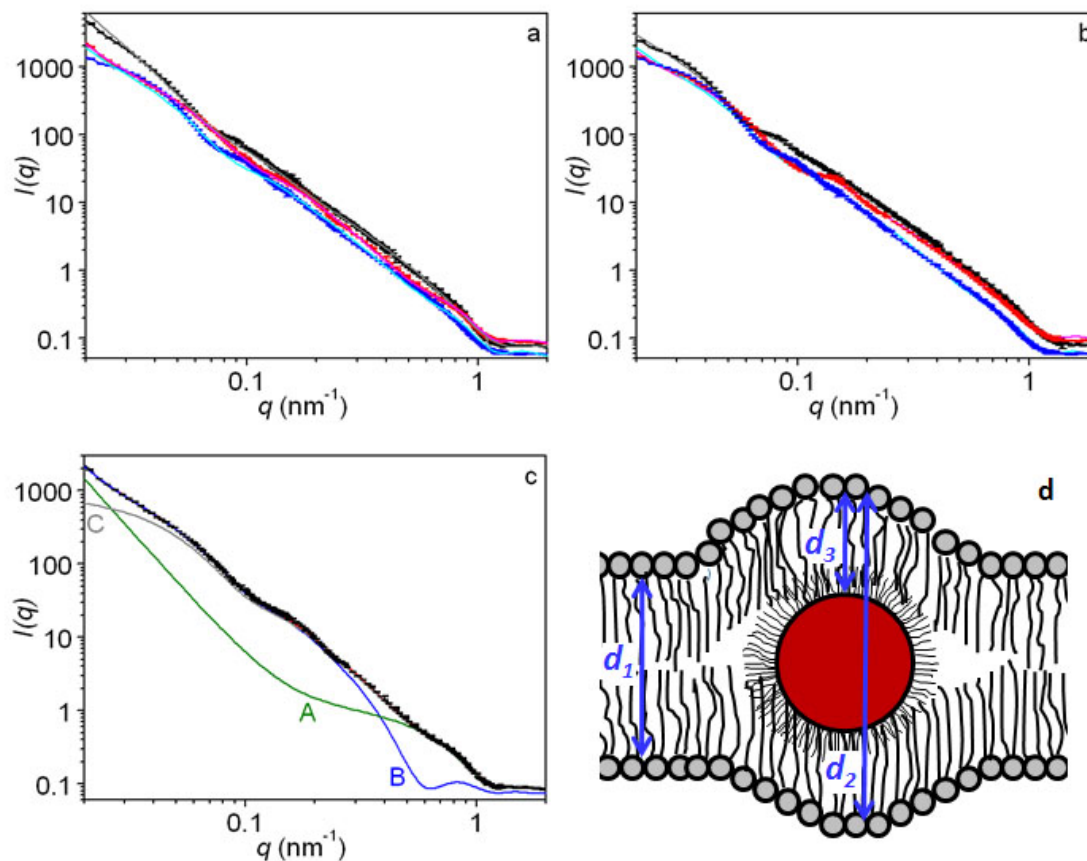


Figure 10.10: SANS measurements of DSPC liposomes. SANS data and the corresponding fits of DSPC liposomes acquired at (a) RT and (b) 60 °C are shown. DSPC liposomes were unmodified (black), functionalized with palmitoyl-nitroDOPA stabilized small (red) and large (blue) iron oxide NPs. Liposomes were dispersed in D_2O . (c) The contributions from the form factor of (A) core-shell NPs (green), (B) bilayer vesicle (blue) and the (C) constantly increasing background (gray) to the fit (red) are shown for DSPC liposomes doped with small NPs, measured at RT. (d) Cartoon of distortions in the liposome membrane caused by iron oxide NPs.

Table 10.3: Quantification of DSPC liposomes based on SANS data shown in Figure 10.10.

NPs	d , RT (nm)	d , 60 °C (nm)	r_{vesicle} RT (nm)	r_{vesicle} 60 °C (nm)
no	3.8	3.4	44	50
small	9.7	8.1	24	31
large	10.4	9.3	47	33

and b). These data were analyzed using a combination of a form factor for bilayer vesicles and core-shell NPs (Figure 10.10c). The thickness of the hydrophobic core of the membrane was extracted from the change in slope at $0.24 \text{ nm}^{-1} < q < 1.20 \text{ nm}^{-1}$. It was quantified using a combination of a form factor for bilayer vesicles and one for core-shell NPs.

Because of the weak scattering contrast of the phosphocholine head group ($\eta_{\text{head}} = 2.78 \times 10^{10} \text{ cm}^{-2}$ relative to $\eta_{\text{D}_2\text{O}} = 6.33 \times 10^{10} \text{ cm}^{-2}$), it is mainly the hydrophobic core of the membrane ($\eta_{\text{tail}} = -5.74 \times 10^9 \text{ cm}^{-2}$) that contributes to the scattering of the phospholipid membrane. The phosphocholine head was simulated to be $\approx 0.5 \text{ nm}$ in size [540]. Thus, considering the fitted values for d_1 (Table 10.3), the total thickness of DSPC liposomes of 4.8 nm at RT and 4.4 nm at 60°C is well in agreement with literature values [560].

If iron oxide NPs are embedded in the liposome membrane, they force the bilayer to open up (Figure 10.10d) [305, 313]. The radius of the NPs (core + shell) (r_{NP}) was according to SANS fits $\approx 3.5 \text{ nm}$. Fully stretched palmityl has a length of $\approx 1.7 \text{ nm}$, assuming a C-C bond length of 0.154 nm [540]. Assuming palmityl-nitroDOPA is close to stretched if adsorbed at the iron oxide NPs at a packing density of $1.5 \text{ molecules/nm}^2$ (section 10.2.1), the iron oxide cores are approximately 1.8 nm in radius. This core size is well in agreement with TEM images (Figures 10.5 and 10.7). r_{NP} is slightly larger than the cut-off radius of 3.25 nm [313]. However, the palmityl-nitroDOPA shell might allow some interpenetration of the hydrophobic phospholipid tails. Thus, NPs with r_{NP} slightly larger than the critical value might still be incorporated into the liposome membrane (Figure 10.10d). However, because scattering from the hydrophobic tail yields the same contrast as scattering of the palmityl-chains, the shell of these NPs with $r_{\text{NP}} \approx 3.5 \text{ nm}$ could also be a bilayer consisting of a palmityl-nitroDOPA and phospholipid monolayer (such that the shell is defined by d_3 in Figure 10.10d). According to Table 10.3, d_1 at RT is 3.8 nm yielding a thickness of the DSPC monolayer of $d_1/2 = 1.9 \text{ nm}$. A complete interpenetration of phospholipids into the palmityl-nitroDOPA shell is unlikely as this would require a drastic change in density and therefore massively change membrane properties such as membrane fluidity and T_m which was, as will be shown below, not the case. Thus, even if one assumes phospholipids can interpenetrate the palmityl-nitroDOPA monolayer by 50%, which seems to be unrealistically high, the NP core radius would be $< 1 \text{ nm}$. This is in disagreement with TEM micrographs (Figures 10.5 and 10.7). Therefore, scattering seen between $0.3 \text{ nm}^{-1} < q < 1.2 \text{ nm}^{-1}$ likely comes from iron oxide cores surrounded by the palmityl-nitroDOPA monolayer.

The sum of the different contributions to d_2 ($d_2 = 2 r_{\text{NP}} + d_1$) yields an upper limit of 10.8

nm. The thickness of liposomes hosting NPs in their membranes quantified with SANS is an intensity weighted average of the membrane thicknesses d that has to be in the range of $d_1 \leq d \leq d_2$. The membrane thicknesses quantified with SANS at RT and 60 °C are with 9.7 nm and 8.1 nm within this range (Table 10.3). From the latter values, the area fraction of liposome membranes that were opened up because NPs were localized in the membrane core can be estimated. The scattering intensity scales with V^2 where V is the volume defined as $V = Ad$ with A the area and d the membrane thickness. If the spherical membrane curvature around NPs is averaged and converted into a step-profile, the upper limit of the area fraction of the membrane, that is opened up (x) can be estimated as

$$xd_2^2A^2 + (1-x)d_1^2A^2 = d_{\text{measured}}^2A^2. \quad (10.1)$$

According to these calculations, $\approx 78\%$ of the membranes are opened up. This indicates a high coverage of NPs in the liposome membrane. It further hints to the fact that the hydrophobic phospholipid tails do not significantly interpenetrate the palmityl-nitroDOPA monolayer presented on the iron oxide NP surface. This supports the theory described above that scattering seen between $0.3 \text{ nm}^{-1} < q < 1.2 \text{ nm}^{-1}$ is caused by the iron oxide core surrounded by a palmityl-nitroDOPA monolayer and does not include contributions from the surrounding phospholipid leaflets.

The high NP coverage indicated by SANS seems to be in contradiction to the NP loading found with TGA (section 10.3.2). However, especially the high NP coverage seen in the film formed from ruptured vesicles upon drying the liposome in the presence of trehalose (Figure 10.7b) supports the high NP loading found with SANS. The very small mass of liposomes analyzed with TGA decreased the accuracy of these measurements. Furthermore, organic contaminations, introduced during drying of liposome dispersions, that contributed to the weight loss measured with TGA, were solely assigned to phospholipids. Thus, TGA provides a lower limit of the NP loading.

DSPC liposomes agglomerated if stored at $T < T_m$ as the continued increase in Figure 10.10 at low q -values (Figure 10.10) and the visible turbidity of these dispersions indicate. In the SANS analysis, this agglomeration was accounted for by assuming a constantly increasing background with a slope of -3.5, indicating densely packed agglomerates. These agglomerates could be disagglomerated with time when heated to $T > T_m$. That liposomes stored in the gel phase ($T < T_m$) agglomerate is well in agreement with literature reports [309].

DSPC Liposomes Containing 5 mol% PEG(2)-PE

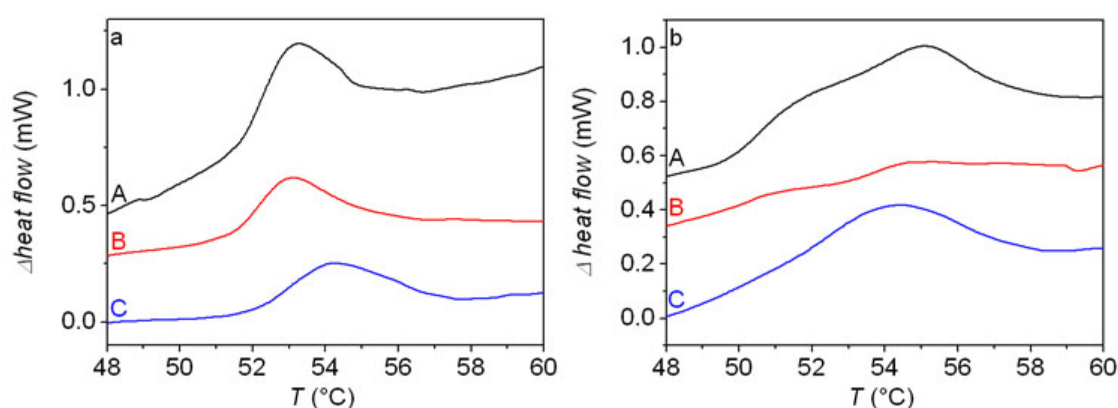
The membrane distortions caused by iron oxide NPs embedded in DSPC/PEG(2)-PE liposome membrane could not be similarly extracted from SANS fits of DSPC liposomes containing 5 mol% PEG(2)-PE as could be done for DSPC liposomes. Scattering caused by PEG was convoluted by the scattering of the DSPC/PEG(2)-PE membrane ($0.7 \text{ nm}^{-1} < q < 1.2 \text{ nm}^{-1}$). No significant difference in the membrane thickness of liposomes hosting iron oxide NPs in their bilayers could thus be extracted at RT. However, the membrane thickness of liposomes containing small iron oxide NPs remained almost unaltered if liposomes were heated to 60°C in contrast to control liposomes and liposomes hosting large iron oxide NPs in their membranes (Table 10.1). The membrane thickness of the latter decreased by $\approx 10\%$, well in agreement with what was seen for DSPC liposomes (Table 10.3) and theoretical calculations [561]. Despite the changes in the membrane thickness of unmodified liposomes and liposomes containing large iron oxide NPs in their membrane, the liposome size and shape did not change significantly upon heating to 60°C (Figure 10.8c and Table 10.1) indicating qualitative differences between unfunctionalized liposomes and liposomes hosting small NPs in their membranes. Well in agreement with DLS results, liposomes functionalized with small iron oxide NPs stabilized with palmityl-nitroDOPA were found to be about two times smaller compared to unmodified liposomes also by SANS (Table 10.1).

In contrast to DSPC liposomes, DSPC liposomes containing 5 mol% PEG(2)-PE were colloidally stable at RT for at least 4 weeks. This was observed by DLS (Figure 10.8a) and supported by SANS results where SANS curves leveled off at low q -values (Figure 10.8b). PEG(2)-PE has been shown to be in the mushroom to brush transition regime if incorporated at 5 mol% into liposomes with a radii of $\approx 50 \text{ nm}$ [562]. Thus, these liposomes were surrounded by a dense PEG-brush that sterically stabilized liposomes.

Incorporation of PEGylated lipids into liposomes favors micelle formation. In fact, the likelihood that micelles are formed increases with increasing amount of PEGylated lipids in the liposomes [563]. Thus, the concentration of PEGylated lipids in liposomes should be high enough to provide good liposome stability but below the threshold where micelles are formed.

Table 10.4: Determination of T_m of DSPC liposomes by DSC.

lipid	NPs	T_m ($^{\circ}\text{C}$)
DSPC	no	53.0 ± 0.2
DSPC	small	53.5 ± 1.0
DSPC	large	54.7 ± 0.5
DSPC/PEG(2)-PE	no	54.6 ± 0.7
DSPC/PEG(2)-PE	small	55.0 ± 0.2
DSPC/PEG(2)-PE	large	54.6 ± 0.3

**Figure 10.11:** DSC investigations of liposomes. DSC spectra of (a) DSPC liposomes and (b) DSPC liposomes containing 5 mol% PEG(2)-PE lipids. The liposomes were (A) unmodified, or contained palmityl-nitroDOPA stabilized (B) small and (C) large iron oxide NPs in their membrane.

10.3.6 Influence of Nanoparticles on T_m

Despite the considerable distortion of the membrane caused by NP incorporation, no significant change in T_m could be measured with DSC (Table 10.4, Figure 10.11b). Furthermore, DSC performed on liposomes that did not contain PEG(2)-PE revealed that the addition of PEG(2)-PE only slightly increased T_m (Table 10.4, Figure 10.11a), well in agreement with literature [564].

That T_m remains unchanged upon loading iron oxide NPs into the liposome membrane indicates that these NPs do not alter membrane properties that determine T_m such as the ordering of the hydrophobic tails. Thus, palmityl-nitroDOPA stabilized NPs are likely localized in the middle of a lipid membrane that is opened up by these NPs and the palmityl-nitroDOPA shell does not heavily interact with the hydrophobic regions of the two liposome monolayers.

However, it also could be that T_m changed only locally at the sites of the NPs. If the volume fraction of these perturbed areas is small compared to the total liposome volume,

the sensitivity of DSC might be too low to detect such changes. However, given the high membrane thickness of DSPC liposomes doped with small NPs quantified with SANS (Table 10.4), a high fraction of the liposome membrane has to be opened up. Therefore, the sensitivity of DSC should be sufficient to detect changes in T_m in these areas. If T_m in areas NPs are accumulated would be different, two DSC peaks would be expected. This, however, was not seen with DSC (Figure 10.11a).

The influence of NPs on T_m is disputed in literature. In agreement with our observation, TOPO stabilized 5 nm CdSe quantum dots (QDs) [306] and decanethiol stabilized 5.7 nm Ag NPs with a lipid : NP ratio > 73 : 1 [309] did not influence T_m if embedded in zwitterionic membranes. In contrast, oleic acid coated iron oxide NPs embedded in zwitterionic liposome membranes have been reported to increase T_m [176] whereas TOPO stabilized CdSe/ZnS QDs decreased and broadened T_m of cationic liposomes [310].

Reversibly adsorbed dispersants, such as oleic acid, that dissociate from the NP surface, diffuse into the membrane. Organic solvents and amphiphiles are well known to influence membrane properties such as membrane fluidity and T_m . A reason for the contradictory literature on the influence of NPs on membrane fluidity and T_m might thus be a varying degree of ligand dissociation in addition to differences in NP loading and core sizes. Thus, irreversibly adhering hydrophobic dispersants are likely not only crucial to prevent NP agglomeration but also to avoid that membrane properties are altered in an uncontrolled way.

10.4 Triggered Release

To probe permeation and actuation of liposomes containing iron oxide NPs in their membranes, they were loaded with calcein, a self-quenching, membrane impermeable dye. At the calcein loading concentration, fluorescence was suppressed through self-quenching. Unencapsulated calcein was removed by running the liposome dispersions through a Sephadex column (section 3.6.2). Therefore, the fluorescence of liposome dispersions increased if calcein diffused through the liposome membrane into bulk solution. As can be seen in Figure 10.12a and b, calcein loaded DSPC/PEG(2)-PE liposomes containing iron oxide NPs in their membranes readily released cargo if exposed to six subsequent 5 min lasting 230 kHz AMF pulses. The system was equilibrated for 1 min in between every AMF pulse (the 5 min AMF pulse followed by 1 min equilibration is denoted as AMF sequence 1). No additional release was observed after these solutions had been ex-

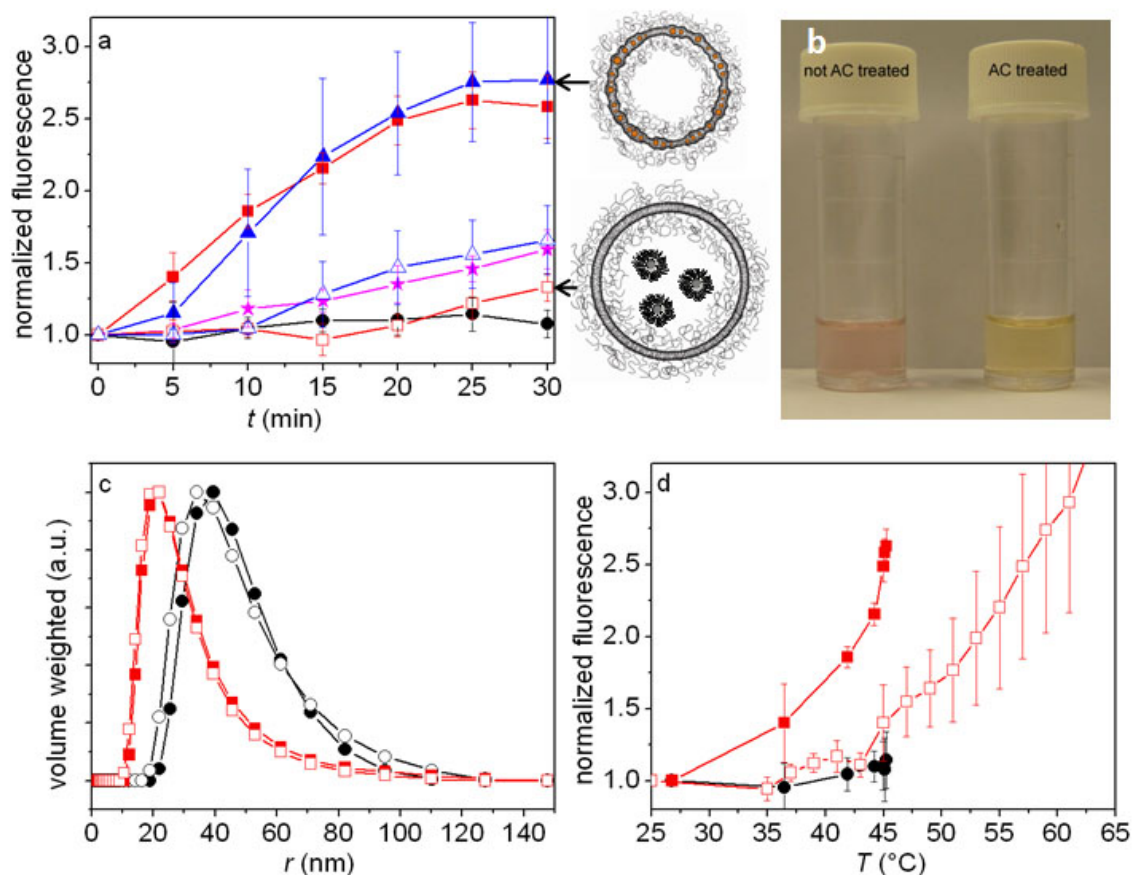


Figure 10.12: Alternating magnetic field triggered release. Release from DSPC liposomes containing 5 mol% PEG(2)-PE loaded with self-quenched calcein was measured by monitoring the fluorescence. (a) AMF treatment for 6×5 min followed by 1 min equilibration between every AMF exposure did not release calcein from unmodified DSPC liposomes containing 5 mol% PEG(2)-PE (\bullet). However, liposomes hosting small (\blacksquare) and large (\blacktriangle) palmityl-nitroDOPA stabilized iron oxide NPs in their membranes efficiently released their cargo. The release from liposomes functionalized with palmityl-nitroDOPA stabilized iron oxide NPs was 180% more efficient compared to that of liposomes prepared with oleic acid coated NPs (\blackstar) or liposomes that were loaded with hydrophilic PEG(1.5)-nitroDOPA stabilized small (\square) and large (\triangle) iron oxide NPs. (b) Photograph of dispersions containing DSPC/PEG(2)-PE liposomes that hosted palmityl-nitroDOPA stabilized small iron oxide NPs in their membranes before and after they were treated 6×5 min with an AMF. The system was equilibrated for 1 min in between the AMF pulses. (c) DLS measurements of DSPC/PEG(2)-PE liposomes (\bullet) and DSPC/PEG(2)-PE liposomes functionalized with palmityl-nitroDOPA stabilized small NPs (\blacksquare) before (filled) and after (empty) AMF exposure are shown. They reveal that the liposome structure is retained upon AMF treatment indicating that cargo is released by the enhanced permeability of liposomes close to T_m . (d) DSPC/PEG(2)-PE liposomes functionalized with small palmityl-nitroDOPA stabilized NPs only started to release significant amounts of calcein at $T > 50$ °C if externally heated (\square). As a comparison, the normalized fluorescence of liposomes that were exposed to an AMF as a function of T is shown for unmodified liposomes (\bullet) and liposomes hosting small palmityl-nitroDOPA stabilized NPs in their membranes (\blacksquare).

posed to 5 subsequent AMF pulses using sequence 1 (Figure 10.12a and 10.13a). This was interpreted as complete release. Furthermore, calcein release ceased when the AMF was turned off. This allowed to closely control the released dose.

10.4.1 Release Mechanism

The unchanged hydrodynamic radius of liposomes loaded with iron oxide NPs before and after AMF treatment (Figure 10.12c) demonstrates that liposomes remained intact during this treatment. Hence, cargo release relies on the increased liposome permeability around T_m .

During exposure of liposomes to AMF sequence 1, the bulk water temperature increased to 45°C after repeated exposure (Figure 10.13b). The largest release occurred already during the first pulse for which the temperature increased to 36 °C (Figure 10.13). Control experiments where liposomes containing iron oxide NPs were externally heated resulted in release only when the temperature was above 50°C which is ≈ 5 °C below T_m (Figure 10.12d).

In contrast to what has been reported previously [176], liposomes without NPs in their membranes also did not leak when subjected to AMF sequence 1 (Figure 10.12a). The much reduced leakiness of the liposomes investigated here can be explained by the higher stability of liposomes sterically shielded with PEG(2)-PE compared to the results reported for dipalmitylphosphocholine (DPPC) liposomes by Chen *et al.* [176].

10.4.2 Effect of AMF Sequence

If the AMF sequence was altered such that the system was exposed to 5 min AMF pulses but equilibrated for 5 min between each AMF pulse (AMF sequence 2), the temperature increase stabilized at 38 °C (Figure 10.13b). Although release efficiency was lower than for sequence 1, repeated cargo release was demonstrated over 12 subsequent AMF cycles (Figure 10.13a).

The slower but continued release is likely related to the effective time, a sufficiently large area of the membrane has a temperature close to T_m . Release of liposome cargo was not observed if liposome dispersions were exposed to 10 subsequent AMF pulses that lasted 1 min followed by 1 min equilibration (AMF sequence 3). This indicates that the local heat generated by the iron oxide NPs during the first minute of AMF treatment is insufficient

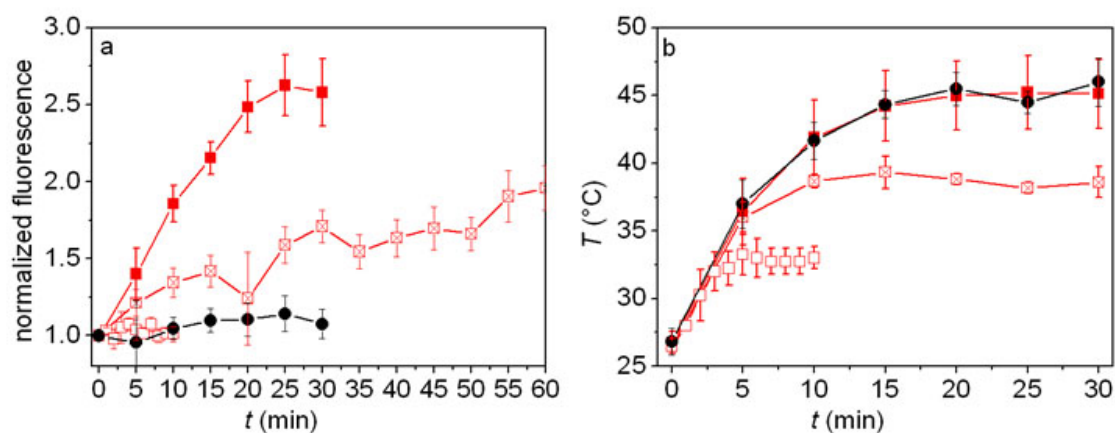


Figure 10.13: Heating of bulk water. (a) Calcein release of DSPC/PEG(2)-PE liposomes functionalized with small iron oxide NPs stabilized with palmitoyl-nitroDOPA was tested for different sequences of the AMF. Release was less efficient if the system was equilibrated for 5 min (-□-) in between each 5 min long AMF cycle (AMF sequence 2) compared to the release of liposomes equilibrated only for 1 min (AMF sequence 1) (-■-) but still significantly above the zero release of unmodified liposomes (-●-) treated with the AMF pulse sequence 1. Furthermore, release of NP modified liposomes was insignificant if these liposomes were subjected to 10 cycles of 1 min AMF pulses followed by 1 min equilibration time (AMF sequence 3) (-□-). (b) Bulk temperatures of liposome dispersions subjected to the respective AMF sequence used in (a).

to increase the temperature inside the bilayer close to the $T_m \approx 55$ °C of DSPC. If cargo is released in pulses, where the system is equilibrated in between AMF pulses, a significant time in the beginning of every pulse is required to locally raise the temperature to T_m . Only after this temperature is reached is cargo released. Thus, the overall time liposomes have to be exposed to an AMF to release the same amount of cargo increases with decreasing length of an AMF pulse due to an increased ratio of time required to locally raise T to T_m to the effective time cargo can be released. Furthermore, it is expected, that if T was much higher than T_m , release would again be halted.

Importantly, the possibility to release cargo with pulsed AMF sequences paves the way to not only trigger release but also to control the dose of released cargo and to slowly release cargo over prolonged times. It additionally allows preventing bursts that could lead to a temporary and local overdose of cargo when this is not desired.

10.4.3 Release Efficiency

The release efficiency of liposomes doped with palmitoyl-nitroDOPA stabilized small and large iron oxide cores was comparable. However, they both exceeded the release efficiency of liposome dispersions containing oleic acid stabilized iron oxide NPs by 180

% (Figure 10.13a). The release efficiency of liposomes containing oleic acid stabilized NPs, however, was comparable to that of magnetoliposomes incorporating hydrophilic, PEG(1.5)-nitroDOPA stabilized iron oxide NPs (described in chapter 8) in their lumen (Figure 10.13a). This indicates that few oleic acid stabilized NPs were incorporated into the liposome membranes in good agreement with cryo-TEM images (Figure 10.4b).

The greatly improved release efficiency of liposomes containing individually stabilized hydrophobic iron oxide NPs in their membranes can be assigned to a direct transfer of heat, generated by the iron oxide NPs upon subjection to an AMF [15], into the liposome membrane. In contrast, hydrophilic and with oleic acid coated agglomerated iron oxide NPs have to heat bulk water to temperatures approaching T_m to release cargo. The need to strongly heat bulk water prevents that thermally sensitive chemicals, drugs and proteins can be incorporated into such magnetoliposomes without risking thermal degradation and loss of functionality of the cargo during release. It would also preclude the use in cell cultures and tissue where heating of the bulk liquid would damage or kill surrounding cells.

10.5 Summary

Iron oxide NPs with core radii < 2.75 nm individually stabilized with palmityl-nitroDOPA spontaneously embedded into liposome membranes. According to TGA, up to ≈ 12 wt% iron oxide NPs could be loaded into liposome membranes. However, SANS results indicate an even higher NP loading. In contrast, iron oxide NPs stabilized with commonly used oleic acid resulted in severe aggregation and poor integration into lipid membranes. DSPC/PEG(2)-PE liposomes hosting iron oxide NPs in their membranes showed long-term stability and low passive permeability at room temperature. AMF treatment of these liposomes resulted in direct injection of heat into the lipid membrane through local heating of embedded iron oxide NPs. This allowed increased permeability by increasing the local temperature to the T_m without bulk water heating. Because the liposome structure was retained during AMF treatment, content could be repeatedly and non-destructively released from liposomes at bulk temperatures significantly below T_m of the liposomes. Consequently, cargo can be released in bursts or over prolonged times allowing a close control over the released dose. Furthermore, the presence of iron oxide NPs in liposome bilayers allows to visualize these vesicles on T_2 - or T_2^* -weighted MR images. Thus such liposomes are non-leaky delivery systems that are easy to assemble and allow to be tracked

with MRI and to trigger content release if subjected to an AMF. They are thus promising drug delivery vehicles and nanoreactors that can locally release thermally sensitive cargo with AMF without risking cargo deactivation during release or heat induced damage to the environment.

Conclusions

Magnetic properties of iron oxide NPs mainly depend on their composition, size and size distribution. However, the performance of iron oxide NPs is also greatly influenced by the NP stability and surface-presentation of functionalities. Control over the surface chemistry is of pivotal importance especially for biomedical applications, where size, protein resistance and surface functionality of NPs determine their circulation time, clearance route and specificity.

Characterization Techniques

To closely control the assembly of NPs and fully exploit the resulting properties, a thorough characterization of these systems is essential. In the course of this thesis, a combination of scattering techniques such as DLS, SAXS and SANS with direct imaging techniques (*e.g.* TEM) and model independent quantification methods (*e.g.* TGA) were especially valuable.

While scattering techniques reveal intensity weighted sizes ($\propto r^6$) of objects dispersed solutions, TEM allows to directly visualize number weighted ($\propto r$) structures that had been dried or frozen prior to analysis. However, in TEM the required sample preparation might introduce artifacts. Different weightings of the NP sizes become especially apparent for broad and bimodal size distributions. Therefore, it is highly beneficial to establish protocols for assembling NPs that allow to closely control size and size distribution. This significantly facilitates data analysis, allows to directly compare results obtained from different techniques and extract more detailed information from scattering data.

However, the analysis of scattering data is model dependent. It therefore is advantageous,

if systems are additionally characterized with complementary techniques yielding quantitative (*e.g.* TGA and for magnetic NPs VSM) and qualitative (*e.g.* TEM) information. These complementary techniques allow to check the suitability of models used to evaluate scattering data.

A major drawback of SANS and SAXS experiments is that they require special infrastructure and large facilities which are not generally available. In contrast, DLS, TGA and TEM, are techniques often readily available to many people. Especially if performed at elevated temperatures, DLS analysis was proven to be a valuable technique for doing standard analysis of NP stability. Furthermore, with an appropriate sample preparation, TEM allowed not only to extract information on the morphology of NPs of expected sizes, but also to reveal information about the presence of electron dense impurities, nuclei and minuscule NPs. This was especially beneficial for optimizing parameters of the core synthesis that required a readily available, comparably high throughput analysis technique to screen different synthesis parameters. Furthermore, even though it is not straight forward to extract quantitative information on bimodally distributed NPs with TEM, TEM can reveal quantitative information about NP size distributions of monomodal NPs, provided statistics is done on several 1'000 NPs. The latter is easily done if TEM samples are prepared such that NPs are densely packed but do not agglomerate and micrographs are analyzed by an image analysis software.

To study more fundamental aspects of chemical interactions between organic molecules and magnetic NPs, EPR turned out to be a well suited characterization method. While the magnetic moment of Fe_3O_4 NPs hampered a standard chemical analysis of anchors adsorbed on the NP surface with NMR, EPR elicited detailed information on the electronic interactions between anchors and Fe_3O_4 NPs. Especially because the signal of magnetically decoupled Fe^{3+} is highly sensitive to the ligand field of said ion, EPR not only revealed information on delocalized electrons but also allowed to investigate changes and distortions of surface bound Fe(III) upon chelation of anchors.

However, while EPR reveals detailed information on electronic interactions, it lacks information about molecular changes. Signals of electrons that were delocalized through strong interactions cannot be distinguished from signals of radical containing decomposition products. Thus, FTIR is a valuable complementary technique that reveals information on molecular vibrations and thus allows to trace degradation reactions potentially taking place at the NP surface. While EPR and FTIR analysis can be done on NPs coated with anchors, iron oxide NPs absorb a significant amount of light in the UV/VIS region. This hampers detailed UV/VIS investigations of electronic transition upon adsorption of an-

chors on NP surfaces. Similar studies can be conducted on anchor/iron ion complexes. However, the relevance of such complexation studies on the interaction of anchors with iron oxide surfaces is unknown due to changed properties of iron atoms in iron oxides compared to freely dispersed iron ions.

In summary, a thorough characterization requires a combination of different, complementary techniques. Only if results obtained with different techniques are consistent can the system be claimed to be well characterized.

Surface Modification of Iron Oxide Nanoparticles

The extent NP core size and size distribution could be controlled was greatly dependent on the synthesis route. Control over the iron oxide core size was poor when synthesized by aqueous precipitation. However, non-aqueous sol-gel routes allowed for tuning of the core size by adjusting the synthesis temperature and time. While iron oxide NPs synthesized in the MW were bimodally distributed, the size distribution of iron oxide NPs synthesized in the oil bath was monomodal. Therefore, the non-aqueous sol gel route using an oil bath as the energy source yielded best control over NP size and size distribution. As a consequence, magnetic properties of NPs synthesized by this method were superior to those of NPs synthesized in the MW or by aqueous precipitation. Therefore, NPs synthesized by the non-aqueous sol-gel route in the oil bath were found to be best suited for fundamental studies and applications.

As-synthesized iron oxide NPs were surface modified with low M_w dispersants consisting of a suitable anchor covalently linked to a spacer. It became clear that the binding affinity of anchors has to be optimized for efficient stabilization of NPs. Too low binding affinity lead to reversible dispersant adsorption and too high binding affinity to gradual dissolution of the cores. Nitrocatechols were proven to have a close to optimal binding affinity towards Fe_3O_4 surfaces. The firm bond between nitrocatechols and iron oxide surfaces was found to be a result of strong electron delocalization between nitrocatechols and Fe(II). The strong electron delocalization resulted in an increased electron density at the nitrocatechol ring and electron depletion at the iron center which was detected as rhombohedrally distorted Fe^{3+} signal in EPR studies. The essentially irreversible bond of nitrocatechols to Fe_3O_4 surfaces allows to closely control NP size and stability e.g. by tailoring the core size and dispersant shell thickness independently.

The dispersant shell thickness was found to depend directly on the PEG M_w of PEG-nitroDOPA dispersants. PEG M_w s between 5 kDa and 10 kDa were found to be optimal

to achieve good NP stability for cores with radii between 2.5 nm and 5 nm. The shell thickness of NPs stabilized with dispersants consisting of PEG M_w 's ≤ 1.5 kDa were too thin to prevent NP agglomeration especially at elevated temperatures. These experimental findings were well in agreement with theoretical interparticle potential calculations. If the PEG M_w , however, was > 10 kDa, the dispersant packing density was too low resulting in instantaneous NP agglomeration. In fact, SANS data indicate a decrease of the dispersant packing density with increasing PEG M_w . Furthermore, these data point to an exponentially decreasing dispersant density profile that is strongly dependent on the dispersant packing density.

Different methods to link antibodies to NP surfaces were explored. It was shown that a controlled assembly of multifunctional NPs presenting functionalities at the surface is only possible if functionalities contain exactly one chemically active group per molecule through which they can be coupled to the NP surface. Ligands that have multiple chemically active binding groups per molecule start to crosslink NPs leading to NP agglomeration. This was observed for two different antibodies, irrespective whether they were bound to the NP surface through the biotin-avidin coupling strategy or by a covalent linkage. However, individually stabilized acrylate presenting iron oxide NPs could be readily functionalized with fluorophores that contained one amine group per molecule.

Close control over the NP surface chemistry is also crucial if NPs are to be embedded into vesicular superstructures and smart materials. For this purpose, iron oxide NPs were surface-modified with a hydrophobic shell consisting of palmityl-nitroDOPA. The resulting individually stabilized hydrophobic NPs with core radii < 2.75 nm spontaneously assembled into liposome membranes. This was in stark contrast to NPs stabilized with reversibly adsorbing oleic acid.

Release from liposomes functionalized with palmityl-nitroDOPA stabilized NPs could be triggered with an alternating magnetic field (AMF). The high release efficiency of liposomes hosting iron oxide NPs in their membrane was assigned to the direct heat transfer from the iron oxide NPs to the liposome membrane if subjected to an AMF. Release relied on the increased liposome permeability at $T \approx T_m$ and ceased upon removal of the AMF. Because the liposome structure was retained during release, content could be repeatedly released over prolonged times, allowing to control the released dose.

Liposomes with hydrophilic NPs in their lumen showed much less efficient release under the same conditions. Thus, good control over the NP surface chemistry, stability and presentation of ligands not only allows for designing multifunctional, ultra-stable hydrophilic NPs but is also directly related to the performance of smart materials actuated

through magnetic NPs.

Key for all these applications are anchors that allow to firmly bind spacers and functionalities to the NP surface. Nitrocatechols met these requirements and proved to be well suited anchors for modifying Fe_3O_4 surfaces under biomedically and biotechnologically relevant conditions. Such anchors pave the way to custom modify NP surfaces in a flexible, experimentally easy, cost-effective and versatile way.

13.1 Outlook

13.1.1 Fe_3O_4 Nanoparticles

The close control over the surface chemistry of Fe_3O_4 NPs opens up the possibility to design new materials. If the PEG shell would be replaced with a thermoresponsive polymer such as poly(N-isopropylacrylamide) (PNIPAM) [565, 566], I would expect NPs to reversibly agglomerate if externally heated or when subjected to an AMF.

Applications, such as the use of NPs as MR contrast agents and for cell separation purposes, require good NP stability and a strong magnetic response. Magnetic NPs become more responsive to magnetic fields upon agglomeration [108] due to an increased magnetic moment of larger agglomerates [15]. I therefore expect these applications to greatly benefit from NPs coated with a thermoresponsive dispersant shell. Such individually stabilized NPs could be targeted to the desired location and subsequently agglomerated by heating above the lower critical solution temperature (LCST) of the polymer shell.

The thermoresponsive shell could *e.g.* be grown at the Fe_3O_4 NP surface. For this, an initiator could be firmly bound to the NP surface through nitroDOPA. The shell could subsequently be grown by adding monomers of a thermoresponsive polymer such as NI-PAM to Fe_3O_4 NPs coated with initiators. I foresee the main difficulty in this approach to be preventing NP agglomeration during *in situ* growth of the dispersants. Agglomeration, however, can potentially be prevented by stabilizing NPs in solvents compatible with reaction conditions needed to grow dispersants but in which unstabilized NPs do not instantaneously agglomerate.

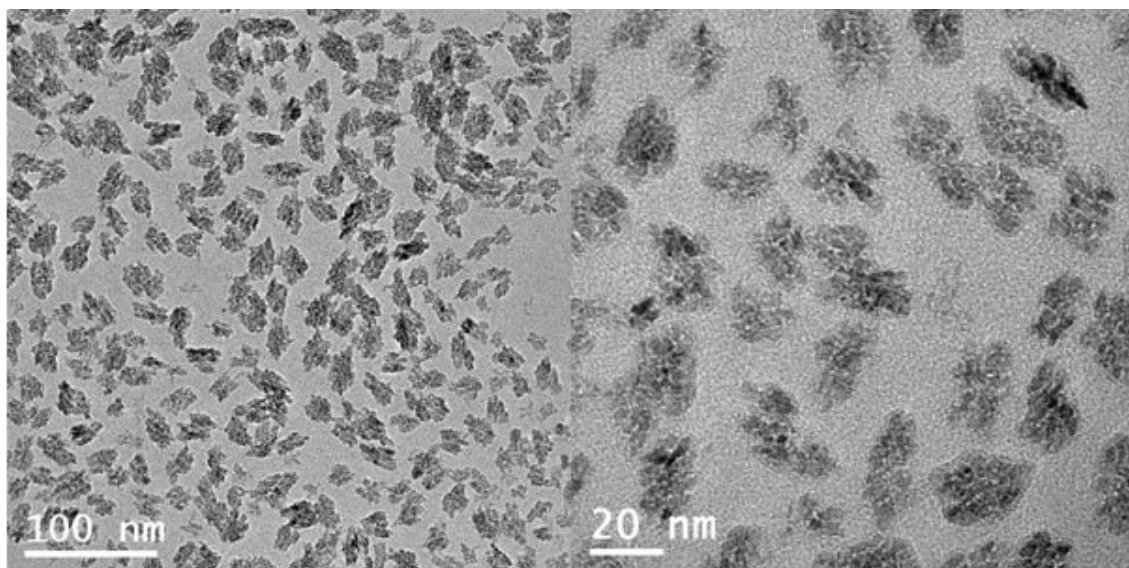


Figure 13.1: TEM of PEG(5)-nitroDOPA stabilized TiO_2 NPs. TEM of PEG(5)-nitroDOPA stabilized TiO_2 NPs dispersed in Millipore water and air dried on a carbon supported Cu TEM-grid.

13.1.2 Oxide Nanoparticles

Catechols are known to have high affinity towards a broad range of oxides, semiconductors, noble metals and polymers [465, 567, 568]. In this context, preliminary results from experiments performed during my PhD have shown that nitrocatechols not only are superior anchors to stabilize Fe_3O_4 NPs compared to catechols, but that they also have an enhanced affinity towards other oxides (Figures 13.2, 13.3 and 13.4). Even though the TiO_2 NPs I used for preliminary experiments had an ill defined shape (Figure 13.1), clear trends towards superior NP stability of PEG(5)-nitroDOPA compared to PEG(5)-dopamine stabilized NPs were observed in temperature dependent DLS experiments (Figure 13.2). The good NP stability likely is due to strong electron delocalization between nitrocatechols and surface bound Ti ions measured with EPR (Figure 13.4).

To explore the suitability of nitroDOPA as anchor to stabilize different oxide NPs, I compared count rates of NPs dispersed in physiologic buffers before and after NPs were pushed through 200 nm cut-off filters. If NPs heavily agglomerate, they will be cleared by the filters resulting in a decrease in the count rate quantified with DLS. Preliminary results indicate that NP stability increases with decreasing band gap of oxides (Figure 13.3). I expect electrons from the conduction band to be more easily delocalized upon binding of nitrocatechols compared to valence band electrons. The likelihood that electrons are in the conduction band increases with decreasing band gap of oxides. I therefore would expect the band gap to be a good indicator to predict the likelihood that nitrocatechols

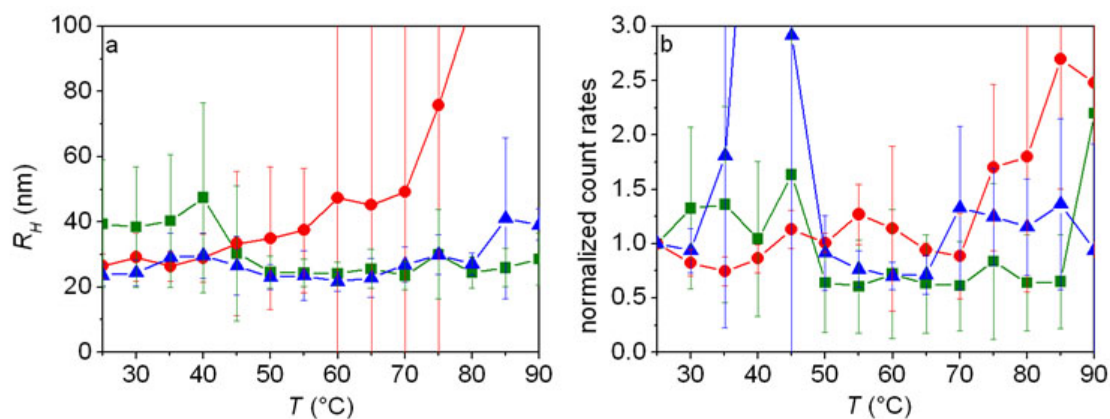


Figure 13.2: Temperature dependent TiO_2 NP stability analyzed with DLS. The (a) hydrodynamic radius and (b) normalized count rate of TiO_2 NPs stabilized with PEG(5)-nitroDOPA (■-), PEG(5)-dopamine (●-) and PEG(5)-mimosine (▲-) dispersed in Tris containing 160 mM NaCl as a function of time. Statistics was done on 9 independent samples.

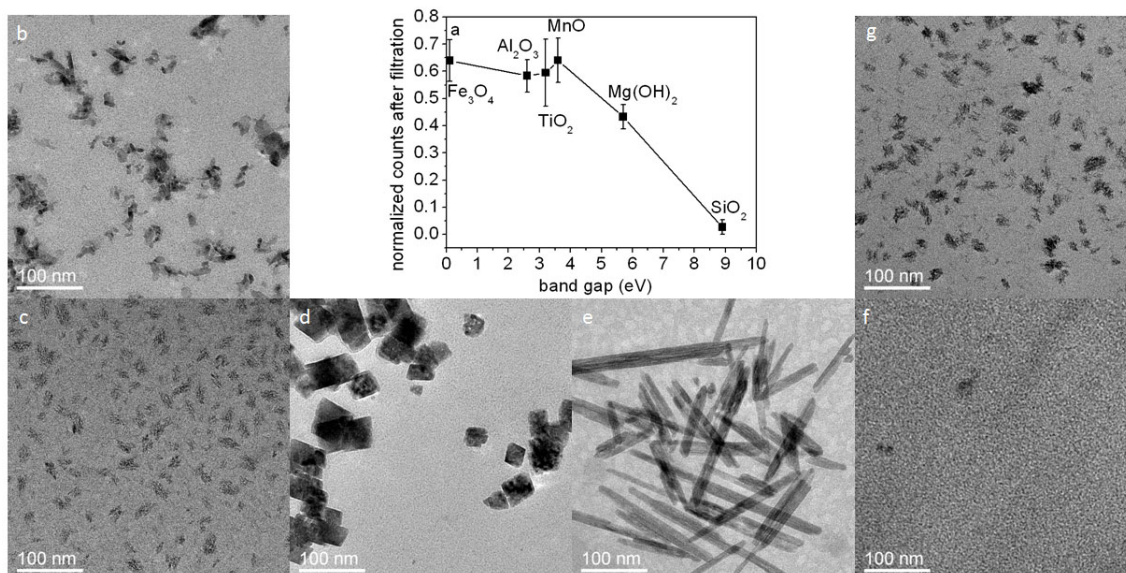


Figure 13.3: Stability of PEG(5)-nitroDOPA coated oxide NPs. (a) The stability of oxide NPs coated with PEG(5)-nitroDOPA was evaluated with DLS where the ratio of the count rates before and after NPs were passed once through 200 nm cut-off filters was measured. NP stability was related to the band gap of the oxides. The morphology of (b) commercially available Al_2O_3 , (c) TiO_2 , (d) MnO synthesized starting from $Mn(ac)_2$, (e) MnO_2 , (f) $Mg(OH)_2$ and (g) SiO_2 NPs was visualized with TEM. Statistics was done on 5-10 independent samples.

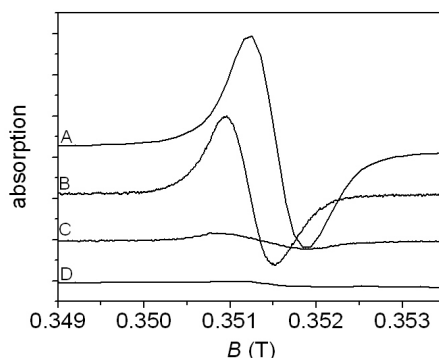


Figure 13.4: EPR measurements on oxide NPs stabilized with PEG(5)-nitroDOPA. EPR was measured on (A) TiO_2 , (B) $Mg(OH)_2$, (C) Al_2O_3 and (D) SiO_2 NPs stabilized with PEG(5)-nitroDOPA. The peak measured at ≈ 0.35 mT can be assigned to delocalized electrons.

would firmly bind to a given oxide. Unfortunately, the morphology of different oxides NPs I investigated in this thesis greatly differed (Figure 13.3). Therefore, more thorough studies on NPs with a defined morphology are warranted to decouple effects of the NP morphology from those of the oxide composition on the binding affinity of nitroDOPA. Furthermore, a comparison of the binding affinity of nitroDOPA to MnO and MnO_2 would allow to tell apart effects of the IEP of oxides, that were shown to be critical for the adsorption of catechol anchored molecules on flat surfaces [301], from those of the band gap of the respective oxide. MnO and MnO_2 NPs have similar IEPs (≈ 5 [569] and 6 [570]) but very different energy band gaps (3.6 eV [571] and 1.3 eV [572]). However, such studies require NPs of comparable size and shape.

In summary, I would be interested to check the hypothesis that binding affinity of nitrocatechols is related to the band gap of oxides. If this was true, the suitability of nitrocatechols to anchor dispersants to certain oxides could be theoretically predicted. This would greatly facilitate the choice of oxides that can be modified using nitrocatechols.

Nanoparticle Assembly

We have shown that PEG-nitroDOPA stabilized core-shell iron oxide NPs can be assembled at liquid-liquid interfaces [573]. Furthermore, preliminary results proved nitroDOPA well suited to surface-modify high refractive index oxides such as TiO_2 (Figures 13.2 and 13.3) and ZrO . I consider these high refractive oxide NPs potent as sensors and actuators. If such high refractive NPs can be individually stabilized, it is conceivable to co-assemble them with magnetic NPs into 2D and 3D structures (Figure 13.5). I expect

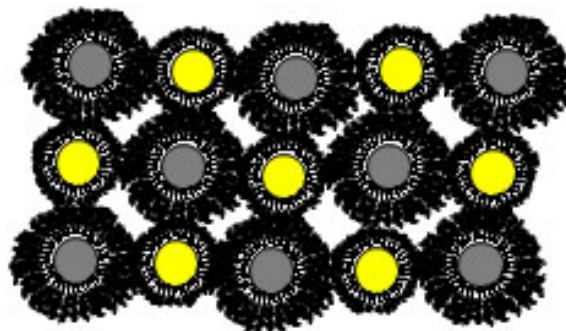


Figure 13.5: *Cartoon of assembled NPs.* Cartoon of assembled individually sterically stabilized magnetic (gray) and optically active (yellow) NPs. Such assemblies could be fixed by crosslinking adjacent dispersant shells such that the 2D or 3D structure is retained upon drying.

these structures, if fixed prior to drying *e.g.* by crosslinking NPs through reactive groups presented at the NP surface, to yield in optically and magnetically responsive films and bulk materials. Especially if the dispersants are thermoresponsive, I would consider these materials to be potent valves, filters, responsive sponges and optically and/or magnetically active coatings.

13.1.3 Liposomes

I have shown that individually stabilized hydrophobic NPs with core radii below ≈ 2.5 nm spontaneously incorporate into the liposome membrane. The overall membrane properties such as T_m and liposome leakiness were not significantly altered by the presence of NPs in the liposome membrane. However, because of a broad NP size distribution, I could not unequivocally determine the effect of NP size on the liposome morphology and membrane properties. It would be of high interest to me to better understand the assembly and mobility of NPs in the liposome membrane and how NPs locally influence the liposome membrane. A better understanding of the influence of NPs on the membranes and overall liposome size and shape, likely would enable us to design liposomes and NPs such that the NP loading and therefore the magnetic response of the resulting liposomes could be increased. Furthermore, I consider the exchange of iron oxide NPs with NPs that have a higher net magnetic moment and thus a higher SAR, such as *Co* NPs, highly beneficial especially for applications not directly related to the biomedical field.

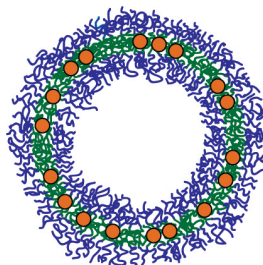


Figure 13.6: Cartoon of polymersomes bearing iron oxide NPs in their membrane. A cartoon of hydrophobic iron oxide NPs embedded in the hydrophobic core of a polymersome membrane. If the hydrophilic block of polymersomes is thermoresponsive, the heat locally generated by iron oxide NPs upon exposure to an AMF, might disassemble these polymersomes leading to cargo release.

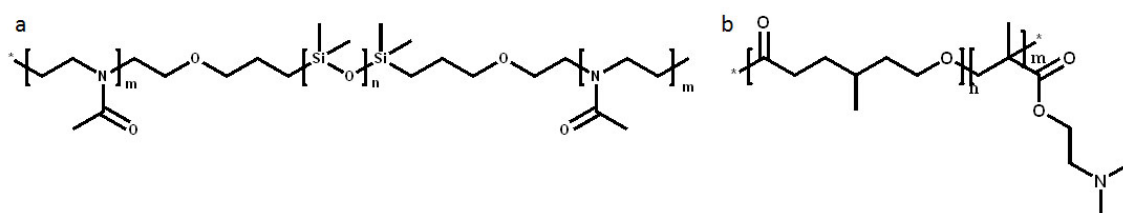


Figure 13.7: Chemical structures of polymersomes. The chemical structure of a) P(MOXA)-b-PDMS-b-P(MOXA) and b) P(MCL)-b-P(DMAEMA) from which polymersomes were extruded.

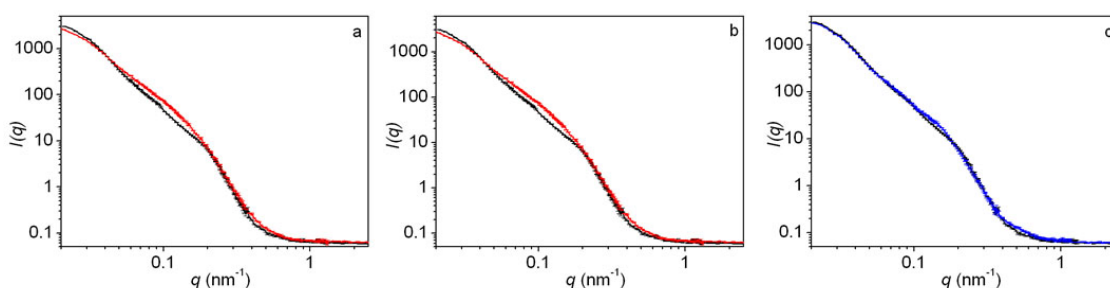


Figure 13.8: SANS measurements of polymersomes. SANS was measured on (a) P(MOXA)-b-PDMS-b-P(MOXA) and (b) P(MCL)-b-P(DMAEMA) polymersomes with (red) and without (black) 5 nm core radius NPs. (c) SANS measured on P(MCL)-b-P(DMAEMA) polymersomes at RT (black) and 60 °C (blue). While NPs seem to distort the polymersome membrane, P(MCL)-b-P(DMAEMA) polymersomes do not respond greatly to temperature changes even though PDMAEMA is thermoresponsive in this temperature range.

13.1.4 Polymersomes

A major drawback of liposomes is that they cannot be stored for a prolonged time. This reduces the attractiveness of liposomes for many applications especially in biotechnology and medicine. Furthermore, liposomes are only stable in aqueous solutions in a limited pH range. An attractive alternative to liposomes are polymersomes. They consist of block-co-polymers that comprise of typically two to three blocks where at least one of the blocks has to be hydrophilic and another one hydrophobic [574–576]. Such block-co-polymers were shown to form vesicles if swollen in aqueous solutions. Their membrane thickness can be tuned by varying the number of repeat units of the hydrophobic block [575, 577]. They are more robust and versatile than liposomes as they are less prone to disassemble if small amounts of detergents are added. Additionally, their shell and membrane thickness can independently be varied [576, 577]. Different blocks of these block-co-polymers can be designed such that the hydrophilic part is *e.g.* thermo- or pH-responsive which adds responsiveness to such vesicles. However, the attractiveness of polymersomes as drug delivery vehicles is limited because block-co-polymers are of synthetic nature and generally not FDA approved.

Iron oxide NPs have been embedded into hollow polystyrene (PS) microspheres resulting in magnetic [578–580] or if QDs were co-encapsulated in multifunctional microspheres [581]. However, to the best of my knowledge, magnetic NPs have not been incorporated into membranes of thermoresponsive polymersomes.

I have performed preliminary SANS experiments which indicate that hydrophobic 5 nm core radii NPs stabilized with palmityl-nitroDOPA can be incorporated into the hydrophobic part of poly(2-methyl-2-oxazoline)-*b*-polydimethylsiloxane-*b*-poly(2-methyl-2-oxazoline) (PMOXA-*b*-PDMS-*b*-PMOXA) and poly(4-methyl- ϵ -carpolactone)-poly(dimethyl aminoethyl methacrylate) (PMCL-PDMAEMA) (Figures 13.7) polymersome vesicle membranes (Figure 13.6 and 13.8).

However, even though PDMAEMA is thermoresponsive in this temperature range [582, 583], no clear changes in the polymersome morphology could be seen (Figure 13.8c). Temperature dependent structural changes of PDMAEMA might be slow or weak such that the polymersome shape is not instantaneously changed if the dispersion is externally heated. However, fast, pronounced changes of the conformation of the thermoresponsive block(s) would be required if cargo should be released upon the application of an AMF. Thus the tested polymersome systems are not optimal for these applications. However, I would be highly interested to add hydrophobic magnetic NPs into polymer-

somes which comprise thermoresponsive blocks that meet the requirements of fast responsiveness to temperature changes. I expect such polymersomes to respond to AMFs either by changes in shape or even to disassemble. Thus, I consider these vehicles promising nanoreactors.

13.1.5 Concluding Remarks

I expect the demand for functionalized, custom adjusted, individually stabilized NPs and NPs embedded in smart materials to rapidly increase in the near future. Key to face and meet these challenges is a close control over the NP surface chemistry and functionality. One way to gain this control is by firmly binding spacers and functionalities to NP surfaces through suitable anchors. Thus, although nitrocatechols are well suited to modify Fe_3O_4 surfaces, I foresee a continued interest to find and optimize new, even better suited anchors to modify different (oxide) surfaces.

Additionally, due to the rapidly increasing demand for responsive materials, I expect high activities in the controlled assembly of responsive NPs used to actuate smart materials. High NP stability is the base to build such superstructures and thus essentially is one of the keys determining the success and speed with which new smart materials comprising NPs can be developed.

References

- [1] A. S. Goldmann, C. Schodel, A. Walther, J. Y. Yuan, K. Loos and A. H. E. Muller, *Macromolecular Rapid Communications*, 2010, **31**, 1608–1615.
- [2] K. L. Kelly, E. Coronado, L. L. Zhao and G. C. Schatz, *Journal of Physical Chemistry B*, 2003, **107**, 668–677.
- [3] L. J. Gauckler, T. Graule and F. Baader, *Materials Chemistry and Physics*, 1999, **61**, 78–102.
- [4] U. T. Gonzenbach, A. R. Studart, E. Tervoort and L. J. Gauckler, *Angewandte Chemie-International Edition*, 2006, **45**, 3526–3530.
- [5] A. R. Studart, E. Amstad, M. Antoni and L. J. Gauckler, *Journal of the American Ceramic Society*, 2006, **89**, 2418–2425.
- [6] U. T. Gonzenbach, A. R. Studart, D. Steinlin, E. Tervoort and L. J. Gauckler, *Journal of the American Ceramic Society*, 2007, **90**, 3407–3414.
- [7] J. Cho, M. S. Joshi and C. T. Sun, *Composites Science and Technology*, 2006, **66**, 1941–1952.
- [8] R. F. Gibson, *Composite Structures*, 2010, **92**, 2793–2810.
- [9] S. Alayoglu, A. U. Nilekar, M. Mavrikakis and B. Eichhorn, *Nature Materials*, 2008, **7**, 333–338.
- [10] A. Schatz, O. Reiser and W. J. Stark, *Chemistry-a European Journal*, 2010, **16**, 8950–8967.
- [11] S. Shylesh, V. Schunemann and W. R. Thiel, *Angewandte Chemie-International Edition*, 2010, **49**, 3428–3459.

- [12] C. Lee, *Gold, Glass and Nanotechnology*, [2010].
- [13] C. Rinaldi, A. Chaves, S. Elborai, X. W. He and M. Zahn, *Current Opinion in Colloid & Interface Science*, 2005, **10**, 141–157.
- [14] A. N. Goldstein, C. M. Echer and A. P. Alivisatos, *Science*, 1992, **256**, 1425–1427.
- [15] K. M. Krishnan, *Magnetics, IEEE Transactions on*, 2010, **46**, 2523–2558.
- [16] G. Binning, H. Rohrer, C. Gerber and E. Weibel, *Physical Review Letters*, 1982, **49**, 57–61.
- [17] M. L. Steigerwald and L. E. Brus, *Accounts of Chemical Research*, 1990, **23**, 183–188.
- [18] G. L. Hornyak, S. Peschel, T. Sawitowski and G. Schmid, *Micron*, 1998, **29**, 183–190.
- [19] R. Costi, A. E. Saunders and U. Banin, *Angewandte Chemie-International Edition*, 2010, **49**, 4878–4897.
- [20] R. C. Ashoori, *Nature*, 1996, **379**, 413–419.
- [21] A. P. Alivisatos, *Science*, 1996, **271**, 933–937.
- [22] U. Banin, Y. W. Cao, D. Katz and O. Millo, *Nature*, 1999, **400**, 542–544.
- [23] J. Aizpurua, G. W. Bryant, L. J. Richter, F. J. G. de Abajo, B. K. Kelley and T. Malouk, *Physical Review B*, 2005, **71**, 235420–1.
- [24] A. Henglein, *Chemical Reviews*, 1989, **89**, 1861–1873.
- [25] L. E. Brus, *Journal of Chemical Physics*, 1984, **80**, 4403–4409.
- [26] H. Gleiter, *Nanostructured Materials*, 1995, **6**, 3–14.
- [27] Y. M. Ma, W. Luo, P. J. Quinn, Z. D. Liu and R. C. Hider, *Journal of Medicinal Chemistry*, 2004, **47**, 6349–6362.
- [28] R. Hergt and S. Dutz, *Journal of Magnetism and Magnetic Materials*, 2007, **311**, 187–192.
- [29] A. Figuerola, R. Di Corato, L. Manna and T. Pellegrino, *Pharmacological Research*, 2010, **62**, 126–143.

- [30] X. Batlle and A. Labarta, *Journal of Physics D-Applied Physics*, 2002, **35**, R15–R42.
- [31] A. H. Lu, E. L. Salabas and F. Schuth, *Angewandte Chemie-International Edition*, 2007, **46**, 1222–1244.
- [32] C. P. Bean and J. D. Livingston, *Journal of Applied Physics*|*Journal of Applied Physics*, 1959, 120S–129S.
- [33] A. Berkowitz, W. J. Schuele and P. J. Flanders, *Journal of Applied Physics*, 1968, **39**, 1261–.
- [34] M. P. Morales, S. Veintemillas-Verdaguer, M. I. Montero, C. J. Serna, A. Roig, L. Casas, B. Martinez and F. Sandiumenge, *Chemistry of Materials*, 1999, **11**, 3058–3064.
- [35] J. Vidal-Vidal, J. Rivas and M. A. Lopez-Quintela, *Colloids and Surfaces a-Physicochemical and Engineering Aspects*, 2006, **288**, 44–51.
- [36] K. L. Krycka, R. A. Booth, C. R. Hogg, Y. Ijiri, J. A. Borchers, W. C. Chen, S. M. Watson, M. Laver, T. R. Gentile, L. R. Dedon, S. Harris, J. J. Rhyne and S. A. Majetich, *Physical Review Letters*, 2010, **104**, 207203–1.
- [37] Q. A. Pankhurst, J. Connolly, S. K. Jones and J. Dobson, *Journal of Physics D-Applied Physics*, 2003, **36**, R167–R181.
- [38] W. F. Brown, *Physical Review*, 1963, **1**, 1677–.
- [39] J. Geshev, O. Popov, V. Masheva and M. Mikhov, *Journal of Magnetism and Magnetic Materials*, 1990, **92**, 185–190.
- [40] M. I. Shliomis, A. F. Pshenichnikov, K. I. Morozov and I. Y. Shurubor, *Journal of Magnetism and Magnetic Materials*, 1990, **85**, 40–46.
- [41] P. C. Fannin and S. W. Charles, *Journal of Physics D-Applied Physics*, 1991, **24**, 76–77.
- [42] M. Hanson, *Journal of Magnetism and Magnetic Materials*, 1991, **96**, 105–113.
- [43] R. Hergt, W. Andra, C. G. d’Ambly, I. Hilger, W. A. Kaiser, U. Richter and H. G. Schmidt, *Ieee Transactions on Magnetism*, 1998, **34**, 3745–3754.

- [44] P. Buffat and J. P. Borel, *Physical Review A*, 1976, **13**, 2287–2298.
- [45] H. Reiss and I. B. Wilson, *Journal of Colloid Science*, 1948, **3**, 551–561.
- [46] J. M. McHale, A. Auroux, A. J. Perrotta and A. Navrotsky, *Science*, 1997, **277**, 788–791.
- [47] R. C. Garvie, *Journal of Physical Chemistry*, 1965, **69**, 1238–.
- [48] G. Baldinozzi, D. Simeone, D. Gosset and M. Dutheil, *Physical Review Letters*, 2003, **90**, 216103/1–4.
- [49] J. A. Nuth, *Nature*, 1987, **329**, 589–589.
- [50] Y. Zhao, K. Thorkelsson, A. J. Mastroianni, T. Schilling, J. M. Luther, B. J. Rancatore, K. Matsunaga, H. Jinnai, Y. Wu, D. Poulsen, J. M. J. Frechet, A. P. Alivisatos and T. Xu, *Nature Materials*, 2009, **8**, 979–985.
- [51] W. Zhao and J. M. Karp, *Nat Mater*, 2009, **8**, 453–454.
- [52] G. von Maltzahn, A. Centrone, J. H. Park, R. Ramanathan, M. J. Sailor, T. A. Hatton and S. N. Bhatia, *Advanced Materials*, 2009, **21**, 3175–3180.
- [53] I. Nabiev, A. Rakovich, A. Sukhanova, E. Lukashev, V. Zagidullin, V. Pachenko, Y. P. Rakovich, J. F. Donegan, A. B. Rubin and A. O. Govorov, *Angewandte Chemie International Edition*, 2010, **49**, 7217–7221.
- [54] S. Lal, S. Link and N. J. Halas, *Nature Photonics*, 2007, **1**, 641–648.
- [55] E. Cubukcu, N. F. Yu, E. J. Smythe, L. Diehl, K. B. Crozier and F. Capasso, *Ieee Journal of Selected Topics in Quantum Electronics*, 2008, **14**, 1448–1461.
- [56] P. Diagaradjane, A. Shetty, J. C. Wang, A. M. Elliott, J. Schwartz, S. Shentu, H. C. Park, A. Deorukhkar, R. J. Stafford, S. H. Cho, J. W. Tunnell, J. D. Hazle and S. Krishnan, *Nano Letters*, 2008, **8**, 1492–1500.
- [57] S. Lal, S. E. Clare and N. J. Halas, *Accounts of Chemical Research*, 2008, **41**, 1842–1851.
- [58] R. RichardsKortum and E. SevickMuraca, *Annual Review of Physical Chemistry*, 1996, **47**, 555–606.

- [59] B. Chance, M. Cope, E. Gratton, N. Ramanujam and B. Tromberg, *Review of Scientific Instruments*, 1998, **69**, 3457–3481.
- [60] S. E. Skrabalak, J. Y. Chen, Y. G. Sun, X. M. Lu, L. Au, C. M. Cobley and Y. N. Xia, *Accounts of Chemical Research*, 2008, **41**, 1587–1595.
- [61] S. H. Sun, C. B. Murray, D. Weller, L. Folks and A. Moser, *Science*, 2000, **287**, 1989–1992.
- [62] G. Reiss and A. Hutten, *Nature Materials*, 2005, **4**, 725–726.
- [63] K. Raj and R. Moskowitz, *Journal of Magnetism and Magnetic Materials*, 1990, **85**, 233–245.
- [64] N. Pamme, *Lab on a Chip*, 2006, **6**, 24–38.
- [65] J. Hu, I. M. C. Lo and G. H. Chen, *Langmuir*, 2005, **21**, 11173–11179.
- [66] S. Wittmann, A. Schatz, R. N. Grass, W. J. Stark and O. Reiser, *Angewandte Chemie-International Edition*, 2010, **49**, 1867–1870.
- [67] V. I. Shubayev, T. R. Pisanic and S. H. Jin, *Advanced Drug Delivery Reviews*, 2009, **61**, 467–477.
- [68] M. A. Dobrovolskaia and S. E. McNeil, *Nature Nanotechnology*, 2007, **2**, 469–478.
- [69] A. Nel, T. Xia, L. Madler and N. Li, *Science*, 2006, **311**, 622–627.
- [70] R. Weissleder, D. D. Stark, B. L. Engelstad, B. R. Bacon, C. C. Compton, D. L. White, P. Jacobs and J. Lewis, *American Journal of Roentgenology*, 1989, **152**, 167–173.
- [71] N. Lewinski, V. Colvin and R. Drezek, *Small*, 2008, **4**, 26–49.
- [72] A. Louie, *Chemical Reviews*, 2010, **110**, 3146–3195.
- [73] H. B. Na, I. C. Song and T. Hyeon, *Advanced Materials*, 2009, **21**, 2133–2148.
- [74] G. Beaune, B. Dubertret, O. Clement, C. Vayssettes, V. Cabuil and C. Menager, *Angewandte Chemie-International Edition*, 2007, **46**, 5421–5424.
- [75] Y. W. Jun, J. H. Lee and J. Cheon, *Angewandte Chemie-International Edition*, 2008, **47**, 5122–5135.

- [76] M. Namdeo, S. Saxena, R. Tankhiwale, M. Bajpai, Y. M. Mohan and S. K. Bajpai, *Journal of Nanoscience and Nanotechnology*, 2008, **8**, 3247–3271.
- [77] R. Sharma and C. J. Chen, *Journal of Nanoparticle Research*, 2009, **11**, 671–689.
- [78] S. W. Zielhuis, J. F. W. Nijssen, J. H. Seppenwoolde, B. A. Zonnenberg, C. J. G. Bakker, W. E. Hennink, P. P. van Rijk and A. D. van het Schip, *Current Medicinal Chemistry - Anti-Cancer Agents*, 2005, **5**, 303–313.
- [79] R. Weissleder, *Nature Reviews Cancer*, 2002, **2**, 11–18.
- [80] J. K. Raty, T. Liimatainen, M. U. Kaikkonen, O. Grohn, K. J. Airene and S. Yla-Herttuala, *Molecular Therapy*, 2007, **15**, 2052–2052.
- [81] W. B. Cai and X. Y. Chen, *Frontiers in Bioscience*, 2007, **12**, 4267–4279.
- [82] L. M. Kornmann, K. D. Reesink, R. S. Reneman and A. P. G. Hoeks, *Ultrasound in Medicine and Biology*, 2010, **36**, 181–191.
- [83] M. Lecchi, P. Fossati, F. Elisei, R. Orecchia and G. Lucignani, *European Journal of Nuclear Medicine and Molecular Imaging*, 2008, **35**, 821–837.
- [84] B. J. Pichler, H. F. Wehrl and M. S. Judenhofer, *Journal of Nuclear Medicine*, 2008, **49**, 5S–23S.
- [85] F. Hallouard, N. Anton, P. Choquet, A. Constantinesco and T. Vandamme, *Biomaterials*, 2010, **31**, 6249–6268.
- [86] A. L. Rogach and M. Ogris, *Current Opinion in Molecular Therapeutics*, 2010, **12**, 331–339.
- [87] S. K. Basiruddin, A. Saha, N. Pradhan and N. R. Jana, *Journal of Physical Chemistry C*, 2010, **114**, 11009–11017.
- [88] W. S. Hinshaw, P. A. Bottomley and G. N. Holland, *Nature*, 1977, **270**, 722–723.
- [89] J. B. Haun, T. J. Yoon, H. Lee and R. Weissleder, *Wiley Interdisciplinary Reviews-Nanomedicine and Nanobiotechnology*, 2010, **2**, 291–304.
- [90] F. A. Jaffer, P. Libby and R. Weissleder, *Journal of the American College of Cardiology*, 2006, **47**, 1328–1338.

- [91] D. A. Sipkins, D. A. Cheresh, M. R. Kazemi, L. M. Nevin, M. D. Bednarski and K. C. P. Li, *Nature Medicine*, 1998, **4**, 623–626.
- [92] J. H. Lee, Y. M. Huh, Y. Jun, J. Seo, J. Jang, H. T. Song, S. Kim, E. J. Cho, H. G. Yoon, J. S. Suh and J. Cheon, *Nature Medicine*, 2007, **13**, 95–99.
- [93] E. A. Waters and S. A. Wickline, *Basic Research in Cardiology*, 2008, **103**, 114–121.
- [94] D. E. Sosnovik, M. Nahrendorf and R. Weissleder, *Basic Research in Cardiology*, 2008, **103**, 122–130.
- [95] J. R. McCarthy and R. Weissleder, *Advanced Drug Delivery Reviews*, 2008, **60**, 1241–1251.
- [96] J. Cheon and J. H. Lee, *Accounts of Chemical Research*, 2008, **41**, 1630–1640.
- [97] J. L. Abraham and C. Thakral, *European Journal of Radiology*, 2008, **66**, 200–207.
- [98] R. Agarwal, S. M. Brunelli, K. Williams, M. D. Mitchell, H. I. Feldman and C. A. Umscheid, *Nephrology Dialysis Transplantation*, 2009, **24**, 856–863.
- [99] V. Mani, K. C. Briley-Saebo, V. V. Itskovich, D. D. Samber and Z. A. Fayad, *Magnetic Resonance in Medicine*, 2006, **55**, 126–135.
- [100] S. Laurent, D. Forge, M. Port, A. Roch, C. Robic, L. V. Elst and R. N. Muller, *Chemical Reviews*, 2008, **108**, 2064–2110.
- [101] Y. Matsumura and H. Maeda, *Cancer Research*, 1986, **46**, 6387–6392.
- [102] H. Maeda, *Advances in Enzyme Regulation, Vol 41*, 2001, **41**, 189–207.
- [103] M. E. Gindy and R. K. Prud'homme, *Expert Opinion on Drug Delivery*, 2009, **6**, 865–878.
- [104] K. A. Kelly, J. R. Allport, A. Tsourkas, V. R. Shinde-Patil, L. Josephson and R. Weissleder, *Circulation Research*, 2005, **96**, 327–336.
- [105] J. Lee, J. Yang, H. Ko, S. J. Oh, J. Kang, J. H. Son, K. Lee, S. W. Lee, H. G. Yoon, J. S. Suh, Y. M. Huh and S. Haam, *Advanced Functional Materials*, 2008, **18**, 258–264.

- [106] Y. Matsumoto and A. Jasanoff, *Magnetic Resonance Imaging*, 2008, **26**, 994–998.
- [107] K. A. Brown, C. C. Vassiliou, D. Issadore, J. Berezovsky, M. J. Cima and R. M. Westervelt, *Journal of Magnetism and Magnetic Materials*, 2010, **322**, 3122–3126.
- [108] L. Josephson, J. M. Perez and R. Weissleder, *Angewandte Chemie-International Edition*, 2001, **40**, 3204–+.
- [109] S. H. Koenig and K. E. Kellar, *Magnetic Resonance in Medicine*, 1995, **34**, 227–233.
- [110] H. W. Duan, M. Kuang, X. X. Wang, Y. A. Wang, H. Mao and S. M. Nie, *Journal of Physical Chemistry C*, 2008, **112**, 8127–8131.
- [111] J. M. Perez, L. Josephson, T. O’Loughlin, D. Hogemann and R. Weissleder, *Nature Biotechnology*, 2002, **20**, 816–820.
- [112] L. Josephson, M. F. Kircher, U. Mahmood, Y. Tang and R. Weissleder, *Bioconjugate Chemistry*, 2002, **13**, 554–560.
- [113] O. Veiseh, C. Sun, J. Gunn, N. Kohler, P. Gabikian, D. Lee, N. Bhattarai, R. Ellenbogen, R. Sze, A. Hallahan, J. Olson and M. Q. Zhang, *Nano Letters*, 2005, **5**, 1003–1008.
- [114] A. N. Pande, R. H. Kohler, E. Aikawa, R. Weissleder and F. A. Jaffer, *Journal of Biomedical Optics*, 2006, **11**, –.
- [115] M. J. Pittet, F. K. Swirski, F. Reynolds, L. Josephson and R. Weissleder, *Nature Protocols*, 2006, **1**, 73–79.
- [116] Z. Medarova, N. V. Evgenov, G. Dai, S. Bonner-Weir and A. Moore, *Nature Protocols*, 2006, **1**, 429–435.
- [117] M. Nahrendorf, H. W. Zhang, S. Hembrador, P. Panizzi, D. E. Sosnovik, E. Aikawa, P. Libby, F. K. Swirski and R. Weissleder, *Circulation*, 2008, **117**, 379–387.
- [118] A. Natarajan, C. Y. Xiong, C. Gruettner, G. L. DeNardo and S. J. DeNardo, *Cancer Biotherapy and Radiopharmaceuticals*, 2008, **23**, 82–91.
- [119] H. Y. Lee, Z. Li, K. Chen, A. R. Hsu, C. J. Xu, J. Xie, S. H. Sun and X. Y. Chen, *Journal of Nuclear Medicine*, 2008, **49**, 1371–1379.

- [120] J. S. Choi, J. C. Park, H. Nah, S. Woo, J. Oh, K. M. Kim, G. J. Cheon, Y. Chang, J. Yoo and J. Cheon, *Angewandte Chemie-International Edition*, 2008, **47**, 6259–6262.
- [121] B. R. Jarrett, B. Gustafsson, D. L. Kukis and A. Y. Louie, *Bioconjugate Chemistry*, 2008, **19**, 1496–1504.
- [122] R. Weissleder, K. Kelly, E. Y. Sun, T. Shtatland and L. Josephson, *Nature Biotechnology*, 2005, **23**, 1418–1423.
- [123] T. A. Larson, J. Bankson, J. Aaron and K. Sokolov, *Nanotechnology*, 2007, **18**, 325101.
- [124] G. H. Du, Z. L. Liu, D. Wang, X. Xia, L. H. Jia, K. L. Yao, Q. Chu and S. M. Zhang, *Journal of Nanoscience and Nanotechnology*, 2009, **9**, 1304–1307.
- [125] H. He, M. Y. Xie, Y. Ding and X. F. Yu, *Applied Surface Science*, 2009, **255**, 4623–4626.
- [126] Y. Jin, C. Jia, S.-W. Huang, M. O'Donnell and X. Gao, *Nat Commun*, 2010, **1**, 41.
- [127] B. C. Giovanella, J. S. Stehlin and A. C. Morgan, *Cancer Research*, 1976, **36**, 3944–3950.
- [128] S. B. Field and N. M. Bleehen, *Cancer Treatment Reviews*, 1979, **6**, 63–94.
- [129] G. M. Hahn, J. Braun and I. Harkedar, *Proceedings of the National Academy of Sciences of the United States of America*, 1975, **72**, 937–940.
- [130] P. K. Sneed, P. R. Stauffer, M. W. McDermott, C. J. Diedrich, K. R. Lamborn, M. D. Prados, S. Chang, K. A. Weaver, L. Spry, M. K. Malec, S. A. Lamb, B. Voss, R. L. Davis, W. M. Wara, D. A. Larson, T. L. Phillips and P. H. Gutin, *International Journal of Radiation Oncology Biology Physics*, 1998, **40**, 287–295.
- [131] R. H. Johnson, M. P. Robinson, A. W. Preece, J. L. Green, N. M. Potheary and C. J. Railton, *Physics in Medicine and Biology*, 1993, **38**, 1023–1034.
- [132] A. Jordan, P. Wust, H. Fahling, W. John, A. Hinz and R. Felix, *International Journal of Hyperthermia*, 1993, **9**, 51–68.
- [133] R. E. Rosensweig, *Journal of Magnetism and Magnetic Materials*, 2002, **252**, 370–374.

- [134] A. Senyei, K. Widder and G. Czerlinski, *Journal of Applied Physics*, 1978, **49**, 3578–3583.
- [135] S. K. Sahoo and V. Labhasetwar, *Drug Discovery Today*, 2003, **8**, 1112–1120.
- [136] M. D. Howard, M. Jay, T. D. Dziublal and X. L. Lu, *Journal of Biomedical Nanotechnology*, 2008, **4**, 133–148.
- [137] Y. Malam, M. Loizidou and A. M. Seifalian, *Trends in Pharmacological Sciences*, 2009, **30**, 592–599.
- [138] S. D. Xiang, C. Selomulya, J. Ho, V. Apostolopoulos and M. Plebanski, *Wiley Interdisciplinary Reviews-Nanomedicine and Nanobiotechnology*, 2010, **2**, 205–218.
- [139] T. Y. Liu, S. H. Hu, D. M. Liu, S. Y. Chen and I. W. Chen, *Nano Today*, 2009, **4**, 52–65.
- [140] K. T. Kim, S. A. Meeuwissen, R. J. M. Nolte and J. C. M. van Hest, *Nanoscale*, 2010, **2**, 844–858.
- [141] Papahadj.D, K. Jacobson, S. Nir and T. Isac, *Biochimica Et Biophysica Acta*, 1973, **311**, 330–348.
- [142] K. Inoue, *Biochimica Et Biophysica Acta*, 1974, **339**, 390–402.
- [143] M. C. Phillips, Ladbrook.Bd and D. Chapman, *Biochimica Et Biophysica Acta*, 1970, **196**, 35–.
- [144] S. Mabrey and J. M. Sturtevant, *Proceedings of the National Academy of Sciences of the United States of America*, 1976, **73**, 3862–3866.
- [145] M. H. Gaber, K. L. Hong, S. K. Huang and D. Papahadjopoulos, *Pharmaceutical Research*, 1995, **12**, 1407–1416.
- [146] J. Zhang and R. D. K. Misra, *Acta Biomaterialia*, 2007, **3**, 838–850.
- [147] M. B. Yatvin, J. N. Weinstein, W. H. Dennis and R. Blumenthal, *Science*, 1978, **202**, 1290–1293.
- [148] D. Needham and M. W. Dewhirst, *Advanced Drug Delivery Reviews*, 2001, **53**, 285–305.

- [149] J. H. Park, G. von Maltzahn, E. Ruoslahti, S. N. Bhatia and M. J. Sailor, *Angewandte Chemie-International Edition*, 2008, **47**, 7284–7288.
- [150] V. Roullier, F. Grasset, F. Boulmedais, F. Artzner, O. Cador and V. Marchi-Artzner, *Chemistry of Materials*, 2008, **20**, 6657–6665.
- [151] E. R. Cintra, F. S. Ferreira, J. L. Santos, J. C. Campello, L. M. Socolovsky, E. M. Lima and A. F. Bakuzis, *Nanotechnology*, 2009, **20**, 045103.
- [152] L. A. Tai, P. J. Tsai, Y. C. Wang, Y. J. Wang, L. W. Lo and C. S. Yang, *Nanotechnology*, 2009, **20**, –.
- [153] J. Connor, M. B. Yatvin and L. Huang, *Proceedings of the National Academy of Sciences of the United States of America-Biological Sciences*, 1984, **81**, 1715–1718.
- [154] H. Ellens, J. Bentz and F. C. Szoka, *Biochemistry*, 1984, **23**, 1532–1538.
- [155] J. L. Thomas and D. A. Tirrell, *Accounts of Chemical Research*, 1992, **25**, 336–342.
- [156] J. Davidsen, C. Vermehren, S. Frokjaer, O. G. Mouritsen and K. Jorgensen, *Advances in Colloid and Interface Science*, 2001, **89**, 303–311.
- [157] D. Needham and R. M. Hochmuth, *Biophysical Journal*, 1989, **55**, 1001–1009.
- [158] V. C. Anderson and D. H. Thompson, *Biochimica Et Biophysica Acta*, 1992, **1109**, 33–42.
- [159] B. Bondurant and D. F. O'Brien, *Journal of the American Chemical Society*, 1998, **120**, 13541–13542.
- [160] S. L. Huang and R. C. MacDonald, *Biochimica Et Biophysica Acta-Biomembranes*, 2004, **1665**, 134–141.
- [161] S. Giri, B. G. Trewyn, M. P. Stellmaker and V. S. Y. Lin, *Angewandte Chemie-International Edition*, 2005, **44**, 5038–5044.
- [162] J. N. Weinstein, R. L. Magin, M. B. Yatvin and D. S. Zaharko, *Science*, 1979, **204**, 188–191.
- [163] S. H. Hu, S. Y. Chen, D. M. Liu and C. S. Hsiao, *Advanced Materials*, 2008, **20**, 2690–+.

- [164] S. H. Hu, T. Y. Liu, H. Y. Huang, D. M. Liu and S. Y. Chen, *Langmuir*, 2008, **24**, 239–244.
- [165] D. Muller-Schulte and T. Schmitz-Rode, *Journal of Magnetism and Magnetic Materials*, 2006, **302**, 267–271.
- [166] T. Hoare, J. Santamaria, G. F. Goya, S. Irusta, D. Lin, S. Lau, R. Padera, R. Langer and D. S. Kohane, *Nano Letters*, 2009, **9**, 3651–3657.
- [167] J. W. M. Bulte, L. D. Ma, R. L. Magin, R. L. Kamman, C. E. Hulstaert, K. G. Go, T. H. The and L. Deleij, *Magnetic Resonance in Medicine*, 1993, **29**, 32–37.
- [168] C. Faure, M. E. Meyre, S. Trepout, O. Lambert and E. Lebraud, *Journal of Physical Chemistry B*, 2009, **113**, 8552–8559.
- [169] M. Babincova, P. Cicmanec, V. Altanero, C. Altaner and P. Babinec, *Bioelectrochemistry*, 2002, **55**, 17–19.
- [170] M. Decuyper and M. Joniau, *European Biophysics Journal with Biophysics Letters*, 1988, **15**, 311–319.
- [171] C. Menager and V. Cabuil, *Colloid and Polymer Science*, 1994, **272**, 1295–1299.
- [172] S. Mann and J. P. Hannington, *Journal of Colloid and Interface Science*, 1988, **122**, 326–335.
- [173] G. Beaune, C. Menager and V. Cabuil, *Journal of Physical Chemistry B*, 2008, **112**, 7424–7429.
- [174] S. Nappini, F. B. Bombelli, M. Bonini, B. Norden and P. Baglioni, *Soft Matter*, 2010, **6**, 154–162.
- [175] L. Paasonen, T. Laaksonen, C. Johans, M. Yliperttula, K. Kontturi and A. Urth, *Journal of Controlled Release*, 2007, **122**, 86–93.
- [176] Y. J. Chen, A. Bose and G. D. Bothun, *Acs Nano*, 2010, **4**, 3215–3221.
- [177] F. Caruso, H. Lichtenfeld, M. Giersig and H. Mohwald, *Journal of the American Chemical Society*, 1998, **120**, 8523–8524.
- [178] F. Caruso, R. A. Caruso and H. Mohwald, *Science*, 1998, **282**, 1111–1114.

- [179] F. Caruso and H. Mohwald, *Langmuir*, 1999, **15**, 8276–8281.
- [180] A. A. Antipov, G. B. Sukhorukov, Y. A. Fedutik, J. Hartmann, M. Giersig and H. Mohwald, *Langmuir*, 2002, **18**, 6687–6693.
- [181] A. S. Angelatos, B. Radt and F. Caruso, *Journal of Physical Chemistry B*, 2005, **109**, 3071–3076.
- [182] A. G. Skirtach, A. M. Javier, O. Kreft, K. Kohler, A. P. Alberola, H. Mohwald, W. J. Parak and G. B. Sukhorukov, *Angewandte Chemie-International Edition*, 2006, **45**, 4612–4617.
- [183] Z. H. Lu, M. D. Prouty, Z. H. Guo, V. O. Golub, C. Kumar and Y. M. Lvov, *Langmuir*, 2005, **21**, 2042–2050.
- [184] D. A. Gorin, S. A. Portnov, O. A. Inozemtseva, Z. Luklinska, A. M. Yashchenok, A. M. Pavlov, A. G. Skirtach, H. Mohwald and G. B. Sukhorukov, *Physical Chemistry Chemical Physics*, 2008, **10**, 6899–6905.
- [185] S. B. Lecommandoux, O. Sandre, F. Checot, J. Rodriguez-Hernandez and R. Perzynski, *Advanced Materials*, 2005, **17**, 712–+.
- [186] S. H. Hu, C. H. Tsai, C. F. Liao, D. M. Liu and S. Y. Chen, *Langmuir*, 2008, **24**, 11811–11818.
- [187] F. Caruso, A. S. Sussha, M. Giersig and H. Mohwald, *Advanced Materials*, 1999, **11**, 950–+.
- [188] A. Voigt, N. Buske, G. B. Sukhorukov, A. A. Antipov, S. Leporatti, H. Lichtenfeld, H. Baumler, E. Donath and H. Mohwald, *Journal of Magnetism and Magnetic Materials*, 2001, **225**, 59–66.
- [189] F. Caruso, M. Spasova, A. Sussha, M. Giersig and R. A. Caruso, *Chemistry of Materials*, 2001, **13**, 109–116.
- [190] D. V. Andreeva, D. A. Gorin, D. G. Shchukin and G. B. Sukhorukov, *Macromolecular Rapid Communications*, 2006, **27**, 931–936.
- [191] E. J. W. Verwey and J. T. G. Overbeek, *Theory of the Stability of Lyophobic Colloids*, Elsevier Publishing Company, 1948.

- [192] A. H. Lu, E. L. Salabas and F. Schuth, *Angewandte Chemie-International Edition*, 2007, **46**, 1222–1244.
- [193] C. Sun, J. S. H. Lee and M. Q. Zhang, *Advanced Drug Delivery Reviews*, 2008, **60**, 1252–1265.
- [194] M. M. Lin, D. K. Kim, A. J. El Haj and J. Dobson, *Ieee Transactions on Nanobiotechnology*, 2008, **7**, 298–305.
- [195] B. Vincent, J. Edwards, S. Emmett and A. Jones, *Colloids and Surfaces*, 1986, **18**, 261–281.
- [196] A. P. Gast, *Langmuir*, 1996, **12**, 4060–4067.
- [197] A. Mori, A. L. Klibanov, V. P. Torchilin and L. Huang, *Febs Letters*, 1991, **284**, 263–266.
- [198] D. E. Owens and N. A. Peppas, *International Journal of Pharmaceutics*, 2006, **307**, 93–102.
- [199] S. I. Jeon, J. H. Lee, J. D. Andrade and P. G. Degennes, *Journal of Colloid and Interface Science*, 1991, **142**, 149–158.
- [200] R. Bhat and S. N. Timasheff, *Protein Science*, 1992, **1**, 1133–1143.
- [201] K. Feldman, G. Hahner, N. D. Spencer, P. Harder and M. Grunze, *Journal of the American Chemical Society*, 1999, **121**, 10134–10141.
- [202] R. L. C. Wang, H. J. Kreuzer and M. Grunze, *Journal of Physical Chemistry B*, 1997, **101**, 9767–9773.
- [203] S. Pasche, S. M. De Paul, J. Voros, N. D. Spencer and M. Textor, *Langmuir*, 2003, **19**, 9216–9225.
- [204] J. L. Dalsin, L. J. Lin, S. Tosatti, J. Voros, M. Textor and P. B. Messersmith, *Langmuir*, 2005, **21**, 640–646.
- [205] R. Michel, S. Pasche, M. Textor and D. G. Castner, *Langmuir*, 2005, **21**, 12327–12332.
- [206] J. N. Israelachvili, *Intermolecular and Surface Forces*, Academic press, London, 2nd edn., 1992.

- [207] G. Strobl, *The Physics of Polymers*, Springer, Berlin, 2nd edn., 1996.
- [208] P. G. Degennes, *Macromolecules*, 1980, **13**, 1069–1075.
- [209] G. Storm, S. O. Belliot, T. Daemen and D. D. Lasic, *Advanced Drug Delivery Reviews*, 1995, **17**, 31–48.
- [210] S. J. Sofia, V. Premnath and E. W. Merrill, *Macromolecules*, 1998, **31**, 5059–5070.
- [211] J. K. Gbadamosi, A. C. Hunter and S. M. Moghimi, *Febs Letters*, 2002, **532**, 338–344.
- [212] S. E. Dunn, A. Brindley, S. S. Davis, M. C. Davies and L. Illum, *Pharmaceutical Research*, 1994, **11**, 1016–1022.
- [213] I. Szleifer, *Biophysical Journal*, 1997, **72**, 595–612.
- [214] V. C. F. Mosqueira, P. Legrand, J. L. Morgat, M. Vert, E. Mysiakine, R. Gref, J. P. Devissaguet and G. Barratt, *Pharmaceutical Research*, 2001, **18**, 1411–1419.
- [215] A. S. Zahr, C. A. Davis and M. V. Pishko, *Langmuir*, 2006, **22**, 8178–8185.
- [216] A. Gessner, B. R. Paulke, R. H. Muller and T. M. Goppert, *Pharmazie*, 2006, **61**, 293–297.
- [217] M. Vittaz, D. Bazile, G. Spenlehauer, T. Verrecchia, M. Veillard, F. Puisieux and D. Labarre, *Biomaterials*, 1996, **17**, 1575–1581.
- [218] R. Gref, M. Luck, P. Quellec, M. Marchand, E. Dellacherie, S. Harnisch, T. Blunk and R. H. Muller, *Colloids and Surfaces B-Biointerfaces*, 2000, **18**, 301–313.
- [219] K. Maruyama, T. Yuda, A. Okamoto, C. Ishikura, S. Kojima and M. Iwatsuru, *Chemical & Pharmaceutical Bulletin*, 1991, **39**, 1620–1622.
- [220] A. L. Klibanov, K. Maruyama, V. P. Torchilin and L. Huang, *Febs Letters*, 1990, **268**, 235–237.
- [221] R. Gref, Y. Minamitake, M. T. Peracchia, V. Trubetskoy, V. Torchilin and R. Langer, *Science*, 1994, **263**, 1600–1603.
- [222] L. X. Tiefenauer, A. Tschirky, G. Kuhne and R. Y. Andres, *Magnetic Resonance Imaging*, 1996, **14**, 391–402.

- [223] A. K. Gupta and S. Wells, *Ieee Transactions on Nanobioscience*, 2004, **3**, 66–73.
- [224] K. Bergstrom, E. Osterberg, K. Holmberg, A. S. Hoffman, T. P. Schuman, A. Kozlowski and J. M. Harris, *Journal of Biomaterials Science-Polymer Edition*, 1994, **6**, 123–132.
- [225] A. H. Latham and M. E. Williams, *Accounts of Chemical Research*, 2008, **41**, 411–420.
- [226] P. F. Renshaw, C. S. Owen, A. E. Evans and H. S. J. Leigh, *Magnetic Resonance Imaging*, 1986, **4**, 351–358.
- [227] L. X. Tiefenauer, G. Kuhne and R. Y. Andres, *Bioconjugate Chemistry*, 1993, **4**, 347–352.
- [228] J. K. Zhou, C. Leuschner, C. Kumar, J. F. Hormes and W. O. Soboyejo, *Biomaterials*, 2006, **27**, 2001–2008.
- [229] X. Montet, M. Funovics, K. Montet-Abou, R. Weissleder and L. Josephson, *Journal of Medicinal Chemistry*, 2006, **49**, 6087–6093.
- [230] C. F. Zhang, M. Jugold, E. C. Woenne, T. Lammers, B. Morgenstern, M. M. Mueller, H. Zentgraf, M. Bock, M. Eisenhut, W. Semmler and F. Kiessling, *Cancer Research*, 2007, **67**, 1555–1562.
- [231] J. Liu and Y. Lu, *Nature Protocols*, 2006, **1**, 246–252.
- [232] P. Decuzzi, R. Pasqualini, W. Arap and M. Ferrari, *Pharmaceutical Research*, 2009, **26**, 235–243.
- [233] A. K. Gupta and A. S. G. Curtis, *Biomaterials*, 2004, **25**, 3029–3040.
- [234] L. M. Lacava, V. A. P. Garcia, S. Kuckelhaus, R. B. Azevedo, N. Sadeghiani, N. Buske, P. C. Morais and Z. G. M. Lacava, *Journal of Magnetism and Magnetic Materials*, 2004, **272**, 2434–2435.
- [235] R. Weissleder, P. F. Hahn, D. D. Stark, E. Rummeny, S. Saini, J. Wittenberg and J. T. Ferrucci, *American Journal of Roentgenology*, 1987, **149**, 723–726.
- [236] R. Weissleder, G. Elizondo, J. Wittenberg, C. A. Rabito, H. H. Bengel and L. Josephson, *Radiology*, 1990, **175**, 489–493.

- [237] A. Halbreich, J. Roger, J. N. Pons, D. Geldwerth, M. F. Da Silva, M. Roudier and J. C. Bacri, *Biochimie*, 1998, **80**, 379–390.
- [238] M. Lewin, N. Carlesso, C. H. Tung, X. W. Tang, D. Cory, D. T. Scadden and R. Weissleder, *Nature Biotechnology*, 2000, **18**, 410–414.
- [239] D. S. Wang, J. B. He, N. Rosenzweig and Z. Rosenzweig, *Nano Letters*, 2004, **4**, 409–413.
- [240] J. H. Gao, H. W. Gu and B. Xu, *Accounts of Chemical Research*, 2009, **42**, 1097–1107.
- [241] J. Yang, J. Gunn, S. R. Dave, M. Q. Zhang, Y. A. Wang and X. H. Gao, *Analyst*, 2008, **133**, 154–160.
- [242] J. Park, M. K. Yu, Y. Y. Jeong, J. W. Kim, K. Lee, V. N. Phan and S. Jon, *Journal of Materials Chemistry*, 2009, **19**, 6412–6417.
- [243] A. F. Thunemann, D. Schutt, L. Kaufner, U. Pison and H. Mohwald, *Langmuir*, 2006, **22**, 2351–2357.
- [244] H. Pardoe, W. Chua-anusorn, T. G. St Pierre and J. Dobson, *Journal of Magnetism and Magnetic Materials*, 2001, **225**, 41–46.
- [245] H. L. Ma, X. T. Qi, Y. Maitani and T. Nagai, *International Journal of Pharmaceutics*, 2007, **333**, 177–186.
- [246] A. Chastellain, A. Petri and H. Hofmann, *Journal of Colloid and Interface Science*, 2004, **278**, 353–360.
- [247] L. F. Gamarra, E. Amaro, S. Alves, D. Soga, W. M. Pontuschka, J. B. Mamani, S. M. Carneiro, G. E. S. Brito and A. M. F. Neto, *Journal of Nanoscience and Nanotechnology*, 2010, **10**, 4145–4153.
- [248] M. A. Morales, P. V. Finotelli, J. A. H. Coaquira, M. H. M. Rocha-Leao, C. Diaz-Aguila, E. M. Baggio-Saitovitch and A. M. Rossi, *Materials Science & Engineering C-Biomimetic and Supramolecular Systems*, 2008, **28**, 253–257.
- [249] B. Schopf, T. Neuberger, K. Schulze, A. Petri, M. Chastellain, M. Hofmann, H. Hofmann and B. von Rechenberg, *Journal of Magnetism and Magnetic Materials*, 2005, **293**, 411–418.

- [250] S. Santra, C. Kaittanis, J. Grimm and J. M. Perez, *Small*, 2009, **5**, 1862–1868.
- [251] M. C. Bautista, O. Bomati-Miguel, X. Zhao, M. P. Morales, T. Gonzalez-Carreno, R. P. de Alejo, J. Ruiz-Cabello and S. Veintemillas-Verdaguer, *Nanotechnology*, 2004, **15**, S154–S159.
- [252] O. Lunov, T. Syrovets, B. Buchele, X. E. Jiang, C. Rucker, K. Tron, G. U. Nienhaus, P. Walther, V. Mailander, K. Landfester and T. Simmet, *Biomaterials*, 2010, **31**, 5063–5071.
- [253] J. C. Neal, S. Stolnik, E. Schacht, E. R. Kenawy, M. C. Garnett, S. S. Davis and L. Illum, *Journal of Pharmaceutical Sciences*, 1998, **87**, 1242–1248.
- [254] L. Josephson, C. H. Tung, A. Moore and R. Weissleder, *Bioconjugate Chemistry*, 1999, **10**, 186–191.
- [255] D. Hogemann, L. Josephson, R. Weissleder and J. P. Bacion, *Bioconjugate Chemistry*, 2000, **11**, 941–946.
- [256] C. J. Xu, K. M. Xu, H. W. Gu, R. K. Zheng, H. Liu, X. X. Zhang, Z. H. Guo and B. Xu, *Journal of the American Chemical Society*, 2004, **126**, 9938–9939.
- [257] H. W. Gu, Z. M. Yang, J. H. Gao, C. K. Chang and B. Xu, *Journal of the American Chemical Society*, 2005, **127**, 34–35.
- [258] H. W. Gu, K. M. Xu, Z. M. Yang, C. K. Chang and B. Xu, *Chemical Communications*, 2005, 4270–4272.
- [259] J. Xie, C. J. Xu, Z. C. Xu, Y. L. Hou, K. L. Young, S. X. Wang, N. Pourmond and S. H. Sun, *Chemistry of Materials*, 2006, **18**, 5401–5403.
- [260] M. K. Corbierre, N. S. Cameron and R. B. Lennox, *Langmuir*, 2004, **20**, 2867–2873.
- [261] Y. Sahoo, H. Pizem, T. Fried, D. Golodnitsky, L. Burstein, C. N. Sukenik and G. Markovich, *Langmuir*, 2001, **17**, 7907–7911.
- [262] M. D. Butterworth, L. Illum and S. S. Davis, *Colloids and Surfaces a-Physicochemical and Engineering Aspects*, 2001, **179**, 93–102.
- [263] Y. Zhang, N. Kohler and M. Q. Zhang, *Biomaterials*, 2002, **23**, 1553–1561.

- [264] N. Kohler, G. E. Fryxell and M. Q. Zhang, *Journal of the American Chemical Society*, 2004, **126**, 7206–7211.
- [265] J. H. Waite and M. L. Tanzer, *Science*, 1981, **212**, 1038–1040.
- [266] J. Xie, C. Xu, N. Kohler, Y. Hou and S. Sun, *Advanced Materials*, 2007, **19**, 3163–+.
- [267] J. H. Gao, G. L. Liang, J. S. Cheung, Y. Pan, Y. Kuang, F. Zhao, B. Zhang, X. X. Zhang, E. X. Wu and B. Xu, *Journal of the American Chemical Society*, 2008, **130**, 11828–11833.
- [268] K. Somaskandan, T. Veres, M. Niewczas and B. Simard, *New Journal of Chemistry*, 2008, **32**, 201–209.
- [269] M. W. Lynch, M. Valentine and D. N. Hendrickson, *Journal of the American Chemical Society*, 1982, **104**, 6982–6989.
- [270] R. H. Heistand, A. L. Roe and L. Que, *Inorganic Chemistry*, 1982, **21**, 676–681.
- [271] D. Zirong, R. C. Haltiwanger, S. Bhattacharya and C. G. Pierpont, *Inorganic Chemistry*, 1991, **30**, 4288–4290.
- [272] A. S. Attia, S. Bhattacharya and C. G. Pierpont, *Inorganic Chemistry*, 1995, **34**, 4427–4433.
- [273] V. A. Grillo, G. R. Hanson, D. M. Wang, T. W. Hambley, L. R. Gahan, K. S. Murray, B. Moubaraki and C. J. Hawkins, *Inorganic Chemistry*, 1996, **35**, 3568–3576.
- [274] J. J. Girerd, M. L. Boillot, G. Blain and E. Riviere, *Inorganica Chimica Acta*, 2008, **361**, 4012–4016.
- [275] J. T. Weisser, M. J. Nilges, M. J. Sever and J. J. Wilker, *Inorganic Chemistry*, 2006, **45**, 7736–7747.
- [276] M. J. Sever, J. T. Weisser, J. Monahan, S. Srinivasan and J. J. Wilker, *Angewandte Chemie-International Edition*, 2004, **43**, 448–450.
- [277] R. B. Lauffer, R. H. Heistand and L. Que, *Inorganic Chemistry*, 1983, **22**, 50–55.

- [278] A. P. S. Citadini, A. P. A. Pinto, A. P. U. Araujo, O. R. Nascimento and A. J. Costa, *Biophysical Journal*, 2005, **88**, 3502–3508.
- [279] P. C. A. Bruijninx, M. Lutz, A. L. Spek, W. R. Hagen, B. M. Weckhuysen, G. van Koten and R. Gebbink, *Journal of the American Chemical Society*, 2007, **129**, 2275–2286.
- [280] B. Kalyanaraman, C. C. Felix and R. C. Sealy, *Environmental Health Perspectives*, 1985, **64**, 185–198.
- [281] D. D. Cox and L. Que, *Journal of the American Chemical Society*, 1988, **110**, 8085–8092.
- [282] H. G. Jang, D. D. Cox and L. Que, *Journal of the American Chemical Society*, 1991, **113**, 9200–9204.
- [283] W. Linert, R. F. Jameson and E. Herlinger, *Inorganica Chimica Acta*, 1991, **187**, 239–247.
- [284] U. ElAyaan, E. Herlinger, R. F. Jameson and W. Linert, *Journal of the Chemical Society-Dalton Transactions*, 1997, 2813–2818.
- [285] T. Funabiki, A. Fukui, Y. Hitomi, M. Higuchi, T. Yamamoto, T. Tanaka, F. Tani and Y. Naruta, *Journal of Inorganic Biochemistry*, 2002, **91**, 151–158.
- [286] J. P. Emerson, E. G. Kovaleva, E. R. Farquhar, J. D. Lipscomb and L. Que, *Proceedings of the National Academy of Sciences of the United States of America*, 2008, **105**, 7347–7352.
- [287] M. D. Shultz, J. U. Reveles, S. N. Khanna and E. E. Carpenter, *Journal of the American Chemical Society*, 2007, **129**, 2482–2487.
- [288] Q. X. Liu, Z. H. Xu, J. A. Finch and R. Egerton, *Chemistry of Materials*, 1998, **10**, 3936–3940.
- [289] D. Nagao, M. Yokoyama, N. Yamauchi, H. Matsumoto, Y. Kobayashi and M. Konno, *Langmuir*, 2008, **24**, 9804–9808.
- [290] K. Woo, J. Hong and J. P. Ahn, *Journal of Magnetism and Magnetic Materials*, 2005, **293**, 177–181.

- [291] Y. B. Sun, X. B. Ding, Z. H. Zheng, X. Cheng, X. H. Hu and Y. X. Peng, *European Polymer Journal*, 2007, **43**, 762–772.
- [292] J. R. Galpin, L. G. M. Tielens, G. A. Veldink, J. F. G. Vliegthart and J. Boldingh, *Febs Letters*, 1976, **69**, 179–182.
- [293] C. A. Tyson, *Journal of Biological Chemistry*, 1975, **250**, 1765–1770.
- [294] A. Avdeef, S. R. Sofen, T. L. Bregante and K. N. Raymond, *Journal of the American Chemical Society*, 1978, **100**, 5362–5370.
- [295] L. Que and R. M. Epstein, *Biochemistry*, 1981, **20**, 2545–2549.
- [296] T. Kawabata, V. Schepkin, N. Haramaki, R. S. Phadke and L. Packer, *Biochemical Pharmacology*, 1996, **51**, 1569–1577.
- [297] D. Vasudevan and A. T. Stone, *Journal of Colloid and Interface Science*, 1998, **202**, 1–19.
- [298] S. T. Martin, J. M. Kesselman, D. S. Park, N. S. Lewis and M. R. Hoffmann, *Environmental Science & Technology*, 1996, **30**, 2535–2542.
- [299] G. Crisponi and M. Remelli, *Coordination Chemistry Reviews*, 2008, **252**, 1225–1240.
- [300] V. M. Nurchi, T. Pivetta, J. I. Lachowicz and G. Crisponi, *Journal of Inorganic Biochemistry*, 2009, **103**, 227–236.
- [301] B. Malisova, S. Tosatti, M. Textor, K. Gademann and S. Zurcher, *Langmuir*, 2010, **26**, 4018–4026.
- [302] A. K. Gupta and M. Gupta, *Biomaterials*, 2005, **26**, 3995–4021.
- [303] W. T. Al-Jamal, K. T. Al-Jamal, B. Tian, L. Lacerda, P. H. Bornans, P. M. Frederik and K. Kostarelos, *Acs Nano*, 2008, **2**, 408–418.
- [304] S. H. Park, S. G. Oh, J. Y. Mun and S. S. Han, *Colloids and Surfaces B-Biointerfaces*, 2005, **44**, 117–122.
- [305] M. R. Rasch, E. Rossinyol, J. L. Hueso, B. W. Goodfellow, J. Arbiol and B. A. Korgel, *Nano Letters*, 2010, **10**, 3733–3739.

- [306] G. Gopalakrishnan, C. Danelon, P. Izewska, M. Prummer, P. Y. Bolinger, I. Geissbuhler, D. Demurtas, J. Dubochet and H. Vogel, *Angewandte Chemie-International Edition*, 2006, **45**, 5478–5483.
- [307] H. Jang, L. E. Pell, B. A. Korgel and D. S. English, *Journal of Photochemistry and Photobiology a-Chemistry*, 2003, **158**, 111–117.
- [308] S. H. Park, S. G. Oh, J. Y. Mun and S. S. Han, *Colloids and Surfaces B-Biointerfaces*, 2006, **48**, 112–118.
- [309] G. D. Bothun, *Journal of Nanobiotechnology*, 2008, 27 pp.
- [310] G. D. Bothun, A. E. Rabideau and M. A. Stoner, *Journal of Physical Chemistry B*, 2009, **113**, 7725–7728.
- [311] A. Tardieu, V. Luzzati and F. C. Reman, *Journal of Molecular Biology*, 1973, **75**, 711–.
- [312] W. H. Binder, R. Sachsenhofer, D. Farnik and D. Blaas, *Physical Chemistry Chemical Physics*, 2007, **9**, 6435–6441.
- [313] H. S. Wi, K. Lee and H. K. Pak, *Journal of Physics-Condensed Matter*, 2008, **20**, 494211.
- [314] V. V. Ginzburg and S. Balijepailli, *Nano Letters*, 2007, **7**, 3716–3722.
- [315] A. Napolitano, M. Dischia, C. Costantini and G. Prota, *Tetrahedron*, 1992, **48**, 8515–8522.
- [316] Z. D. Liu, S. Piyamongkol, D. Y. Liu, H. H. Khodr, S. L. Lu and R. C. Hider, *Bioorganic & Medicinal Chemistry*, 2001, **9**, 563–573.
- [317] J. A. Durden, H. A. Stansburry and W. Catlette, *Correspondence-The Reaction of Azidoorganic Compounds with Acetylenes*, [1964].
- [318] J. G. Atkinson, Y. Girard, J. Rokach, C. S. Rooney, C. S. Mcfarlane, A. Rackham and N. N. Share, *Journal of Medicinal Chemistry*, 1979, **22**, 99–106.
- [319] S. Zurcher, D. Wackerlin, Y. Bethuel, B. Malisova, M. Textor, S. Tosatti and K. Gademann, *Journal of the American Chemical Society*, 2006, **128**, 1064–1065.
- [320] R. Massart, *Ieee Transactions on Magnetics*, 1981, **17**, 1247–1248.

- [321] I. Bilecka, I. Djerdj and M. Niederberger, *Chemical Communications*, 2008, 886–888.
- [322] T. Kotsokechagia, F. Cellesi, A. Thomas, M. Niederberger and N. Tirelli, *Langmuir*, 2008, **24**, 6988–6997.
- [323] A. van Blaaderen and A. Vrij, *Colloidal Silica: Fundamentals and Applications*, 2006, **131**, 65–80.
- [324] J. D. Busbee, A. T. Juhl, L. V. Natarajan, V. P. Tongdilia, T. J. Bunning, R. A. Vaia and P. V. Braun, *Advanced Materials*, 2009, **21**, 3659–+.
- [325] R. N. Deguzman, Y. F. Shen, E. J. Neth, S. L. Suib, C. L. Oyoung, S. Levine and J. M. Newsam, *Chemistry of Materials*, 1994, **6**, 815–821.
- [326] M. Olla, G. Navarra, B. Elsener and A. Rossi, *Surface and Interface Analysis*, 2006, **38**, 964–974.
- [327] K. Surendra, N. S. Krishnaveni, R. Sridhar and K. R. Rao, *Tetrahedron Letters*, 2006, **47**, 2125–2127.
- [328] M. Cullen, *Atomic spectroscopy in elemental analysis*, Sheffield Academic Press, Sheffield, 2003.
- [329] M. Hesse, H. Meier and B. Zeeh, *Spektroskopische Methoden in der organischen Chemie*, Thieme, Stuttgart, 6th edn., 2002.
- [330] M. Pulfer and R. C. Murphy, *Mass Spectrometry Reviews*, 2003, **22**, 332–364.
- [331] R. Knochenmuss, *Analyst*, 2006, **131**, 966–986.
- [332] T. Castner, G. S. Newell, W. C. Holton and C. P. Slichter, *Journal of Chemical Physics*, 1960, **32**, 668–673.
- [333] L. R. Bickford, *Physical Review*, 1950, **78**, 449–457.
- [334] J. Wertz and J. Bolton, *Electron spin resonance: elementary theory and practical applications*, Pergamon Press, Oxford, 1986.
- [335] H. H. Wickman, M. P. Klein and D. A. Shirley, *Journal of Chemical Physics*, 1965, **42**, 2113–.

- [336] V. K. Sharma and F. Waldner, *Journal of Applied Physics*, 1977, **48**, 4298–4302.
- [337] G. Horlick, *Applied Spectroscopy*, 1968, **22**, 617–.
- [338] S. Rao and C. R. Houska, *Acta Crystallographica Section A*, 1986, **42**, 6–13.
- [339] W. Kleber, H.-J. Bautsch and J. Bohm, *Einführung in die Kristallographie*, Verlag Technik GmbH, Berlin, 1998.
- [340] J. F. Banfield, P. J. Wasilewski and D. R. Veblen, *American Mineralogist*, 1994, **79**, 654–667.
- [341] J. Tang, M. Myers, K. A. Bosnick and L. E. Brus, *Journal of Physical Chemistry B*, 2003, **107**, 7501–7506.
- [342] R. M. Cornell and U. Schwertmann, *The Iron Oxides*, Wiley-VCH, Weinheim, 2nd edn., 2003.
- [343] D. B. Williams and C. B. Carter, *Transmission Electron Microscopy*, Plenum Press, 1996.
- [344] B. Fultz and J. M. Howe, *Transmission Electron Microscopy and Diffractometry of Materials*, Springer, 2008.
- [345] L. Reimer and H. Kohl, *Transmission Electron Microscopy*, Springer, 2008.
- [346] D. C. Joy and D. M. Maher, *Journal of Physics E-Scientific Instruments*, 1980, **13**, 260–270.
- [347] E. Majorovits, B. Barton, K. Schultheiss, F. Perez-Willard, D. Gerthsen and R. R. Schroder, *Ultramicroscopy*, 2007, **107**, 213–226.
- [348] J. V. Vickermann, *Surface Analysis, The Principal Techniques*, John Wiley & Sons, 1997.
- [349] D. Q. Yang, J. N. Gillet, M. Meunier and E. Sacher, *Journal of Applied Physics*, 2005, **97**, –.
- [350] J. H. Scofield, *Journal of Electron Spectroscopy and Related Phenomena*, 1976, **8**, 129–137.
- [351] M. P. Seah and W. A. Dench, *Surface and Interface Analysis* | *Surface and Interface Analysis*, 1979, **1**, 2–11.

- [352] S. Tosatti, R. Michel, M. Textor and N. D. Spencer, *Langmuir*, 2002, **18**, 3537–3548.
- [353] C. Y. Li, M. J. Birnkrant, L. V. Natarajan, V. P. Tondiglia, P. F. Lloyd, R. L. Sutherland and T. J. Bunning, *Soft Matter*, 2005, **1**, 238–242.
- [354] T. J. Park, S. Sambasivan, D. A. Fischer, W. S. Yoon, J. A. Misewich and S. S. Wong, *Journal of Physical Chemistry C*, 2008, **112**, 10359–10369.
- [355] J. Stohr, *NEXAFS Spectroscopy*, Springer-Verlag, 1992.
- [356] G. Hahner, *Chemical Society Reviews*, 2006, **35**, 1244–1255.
- [357] B. Watts, L. Thomsen and P. C. Dastoor, *Synthetic Metals*, 2005, **152**, 21–24.
- [358] S. Foner, *Review of Scientific Instruments*, 1956, **27**, 548–548.
- [359] S. Foner, *Journal of Applied Physics*, 1996, **79**, 4740–4745.
- [360] P. S. K. Murthy, Y. M. Mohan, J. Sreeramulu and K. M. Raju, *Reactive & Functional Polymers*, 2006, **66**, 1482–1493.
- [361] C. Henoumont, S. Laurent and L. V. Elst, *Contrast Media & Molecular Imaging*, 2009, **4**, 312–321.
- [362] D. C. F. Chan, D. B. Kirpotin and P. A. Bunn, *Journal of Magnetism and Magnetic Materials*, 1993, **122**, 374–378.
- [363] R. Hergt, R. Hiergeist, M. Zeisberger, G. Glockl, W. Weitschies, P. Ramirez, I. Hilger and W. A. Kaiser, *Journal of Magnetism and Magnetic Materials*, 2004, **280**, 358–368.
- [364] S. A. Rovers, R. Hoogenboom, M. F. Kemmere and J. T. F. Keurentjes, *Journal of Physical Chemistry C*, 2008, **112**, 15643–15646.
- [365] R. Richardson, *Colloid Science*, Blackwell Publishing, 2005.
- [366] N. Dejaeger, H. Demeyere, R. Finsy, R. Sneyers, J. Vanderdeelen, P. Vandermeeren and M. Vanlaethem, *Particle & Particle Systems Characterization*, 1991, **8**, 179–186.
- [367] D. E. Koppel, *Journal of Chemical Physics*, 1972, **57**, 4814–.

- [368] G. Mie, *Annalen Der Physik*, 1908, **25**, 377–445.
- [369] W. J. Wiscombe, *Applied Optics*, 1980, **19**, 1505–1509.
- [370] R. Finsy, N. Dejaeger, R. Sneyers and E. Gelade, *Particle & Particle Systems Characterization*, 1992, **9**, 125–137.
- [371] R. Finsy, *Advances in Colloid and Interface Science*, 1994, **52**, 79–143.
- [372] A. Sanchez-Ferrer and R. Mezzenga, *Macromolecules*, 2010, **43**, 1093–1100.
- [373] T. Narayanan, *Current Opinion in Colloid & Interface Science*, 2009, **14**, 409–415.
- [374] M. Reufer, H. Dietsch, U. Gasser, A. Hirt, A. Menzel and P. Schurtenberger, *Journal of Physical Chemistry B*, 2010, **114**, 4763–4769.
- [375] J. Kohlbrecher and W. Wagner, *Modern Techniques for Characterizing Magnetic Materials*, Kluwer Academic Publishers, Boston, Dordrecht, London, 2005.
- [376] J. S. Pedersen and M. C. Gerstenberg, *Macromolecules*, 1996, **29**, 1363–1365.
- [377] J. S. Pedersen, *Journal of Applied Crystallography*, 2000, **33**, 637–640.
- [378] J. Kohlbrecher, *Sasfit manual*, [2009].
- [379] D. R. Linde and H. Frederikse, *Handbook of Chemistry and Physics, 75th edition*, CRC, 75th edn., 1995.
- [380] H. G. McAdie, *Analytical Chemistry*, 1967, **39**, 543–.
- [381] C. B. Murphy, *Analytical Chemistry*, 1974, **46**, R451–R459.
- [382] M. Rodahl, F. Hook, A. Krozer, P. Brzezinski and B. Kasemo, *Review of Scientific Instruments*, 1995, **66**, 3924–3930.
- [383] G. Sauerbrey, *Zeitschrift Fur Physik*, 1959, **155**, 206–222.
- [384] M. V. Voinova, M. Rodahl, M. Jonson and B. Kasemo, *Physica Scripta*, 1999, **59**, 391–396.
- [385] D. Johannsmann, I. Reviakine, E. Rojas and M. Gallego, *Analytical Chemistry*, 2008, **80**, 8891–8899.
- [386] C. A. Keller and B. Kasemo, *Biophysical Journal*, 1998, **75**, 1397–1402.

- [387]
- [388] A. G. Roca, R. Costo, A. F. Rebolledo, S. Veintemillas-Verdaguer, P. Tartaj, T. Gonzalez-Carreno, M. P. Morales and C. J. Serna, *Journal of Physics D-Applied Physics*, 2009, **42**, –.
- [389] S. Mornet, S. Vasseur, F. Grasset, P. Veverka, G. Goglio, A. Demourgues, J. Portier, E. Pollert and E. Duguet, *Progress in Solid State Chemistry*, 2006, **34**, 237–247.
- [390] B. L. Cushing, V. L. Kolesnichenko and C. J. O'Connor, *Chemical Reviews*, 2004, **104**, 3893–3946.
- [391] R. Massart and V. Cabuil, *Journal De Chimie Physique Et De Physico-Chimie Biologique*, 1987, **84**, 967–973.
- [392] N. M. Griбанov, E. E. Bibik, O. V. Buzunov and V. N. Naumov, *Journal of Magnetism and Magnetic Materials*, 1990, **85**, 7–10.
- [393] L. Vayssieres, C. Chaneac, E. Tronc and J. P. Jolivet, *Journal of Colloid and Interface Science*, 1998, **205**, 205–212.
- [394] M. Niederberger and G. Garnweitner, *Chemistry-a European Journal*, 2006, **12**, 7282–7302.
- [395] S. H. Sun, H. Zeng, D. B. Robinson, S. Raoux, P. M. Rice, S. X. Wang and G. X. Li, *Journal of the American Chemical Society*, 2004, **126**, 273–279.
- [396] I. Bilecka, P. Elser and M. Niederberger, *Acs Nano*, 2009, **3**, 467–477.
- [397] J. Rockenberger, E. C. Scher and A. P. Alivisatos, *Journal of the American Chemical Society*, 1999, **121**, 11595–11596.
- [398] T. Hyeon, S. S. Lee, J. Park, Y. Chung and H. Bin Na, *Journal of the American Chemical Society*, 2001, **123**, 12798–12801.
- [399] N. Pinna, S. Grancharov, P. Beato, P. Bonville, M. Antonietti and M. Niederberger, *Chemistry of Materials*, 2005, **17**, 3044–3049.
- [400] A. L. Rogach, D. Nagesha, J. W. Ostrander, M. Giersig and N. A. Kotov, *Chemistry of Materials*, 2000, **12**, 2676–2685.
- [401] W. Y. Yu, W. X. Tu and H. F. Liu, *Langmuir*, 1999, **15**, 6–9.

- [402] I. Pastoriza-Santos and L. M. Liz-Marzan, *Langmuir*, 2002, **18**, 2888–2894.
- [403] A. B. Panda, G. Glaspell and M. S. El-Shall, *Journal of the American Chemical Society*, 2006, **128**, 2790–2791.
- [404] M. Tsuji, M. Hashimoto and T. Tsuji, *Chemistry Letters*, 2002, 1232–1233.
- [405] F. K. Liu, Y. C. Chang, F. H. Ko and T. C. Chu, *Materials Letters*, 2004, **58**, 373–377.
- [406] A. Michailovski, R. Kiebach, W. Bensch, J. D. Grunwaldt, A. Baiker, S. Komarneni and G. R. Patzke, *Chemistry of Materials*, 2007, **19**, 185–197.
- [407] R. Kerner, O. Palchik and A. Gedanken, *Chemistry of Materials*, 2001, **13**, 1413–1419.
- [408] G. Buehler and C. Feldmann, *Angewandte Chemie-International Edition*, 2006, **45**, 4864–4867.
- [409] W. W. Wang and Y. J. Zhu, *Inorganic Chemistry Communications*, 2004, **7**, 1003–1005.
- [410] S. Baldassari, S. Komarneni, E. Mariani and C. Villa, *Materials Research Bulletin*, 2005, **40**, 2014–2020.
- [411] A. V. Murugan, V. Samuel and V. Ravi, *Materials Letters*, 2006, **60**, 479–480.
- [412] K. L. Ding, Z. J. Miao, Z. M. Liu, Z. F. Zhang, B. X. Han, G. M. An, S. D. Miao and Y. Xie, *Journal of the American Chemical Society*, 2007, **129**, 6362–+.
- [413] J. M. Lee, D. P. Amalnerkar, Y. K. Hwang, S. H. Jhung, J. S. Hwang and J. S. Chang, *Journal of Nanoscience and Nanotechnology*, 2007, **7**, 952–959.
- [414] A. Bee, R. Massart and S. Neveu, *Journal of Magnetism and Magnetic Materials*, 1995, **149**, 6–9.
- [415] J. Park, K. J. An, Y. S. Hwang, J. G. Park, H. J. Noh, J. Y. Kim, J. H. Park, N. M. Hwang and T. Hyeon, *Nature Materials Marcus iron oxide nanoparticle nanoparticle synthesis synthesis*, 2004, **3**, 891–895.
- [416] Z. Li, L. Wei, M. Y. Gao and H. Lei, *Advanced Materials*, 2005, **17**, 1001–+.

- [417] A. Barbieri, W. Weiss, M. A. Vanhove and G. A. Somorjai, *Surface Science*, 1994, **302**, 259–279.
- [418] C. R. Brundle, T. J. Chuang and K. Wandelt, *Surface Science*, 1977, **68**, 459–468.
- [419] T. Fujii, F. M. F. de Groot, G. A. Sawatzky, F. C. Voogt, T. Hibma and K. Okada, *Physical Review B-Condensed Matter*, 1999, **59**, 3195–3202.
- [420] S. Pal, P. Dutta, N. Shah, G. P. Huffman and M. S. Seehra, *Ieee Transactions on Magnetics*, 2007, **43**, 3091–3093.
- [421] P. Dutta, S. Pai, M. S. Seehra, N. Shah and G. P. Huffman, *Journal of Applied Physics*, 2009, **105**, 236–244.
- [422] D. M. L. Goodgame, D. J. Williams and R. E. P. Winpenny, *Inorganica Chimica Acta*, 1989, **166**, 159–162.
- [423] D. B. Dadyburjor and E. Ruckenstein, *Journal of Crystal Growth*, 1977, **40**, 279–290.
- [424] I. Baker, Q. Zeng, W. D. Li and C. R. Sullivan, *Journal of Applied Physics*, 2006, **99**, 08H10.
- [425] M. Gonzales-Weimuller, M. Zeisberger and K. M. Krishnan, *Journal of Magnetism and Magnetic Materials*, 2009, **321**, 1947–1950.
- [426] Z. Li, Q. Sun and M. Y. Gao, *Angewandte Chemie-International Edition*, 2005, **44**, 123–126.
- [427] J. Park, E. Lee, N. M. Hwang, M. S. Kang, S. C. Kim, Y. Hwang, J. G. Park, H. J. Noh, J. Y. Kini, J. H. Park and T. Hyeon, *Angewandte Chemie-International Edition*, 2005, **44**, 2872–2877.
- [428] I. M. Lifshitz and V. V. Slyozov, *Journal of Physics and Chemistry of Solids*, 1961, **19**, 35–50.
- [429] C. Wagner, *Zeitschrift fur Elektrochemie*, 1961.
- [430] M. Kahlweit, *Advances in Colloid and Interface Science*, 1975, **5**, 1–35.
- [431] T. Sugimoto, *Journal of Colloid and Interface Science*, 1978, **63**, 16–26.

- [432] B. Zhao and W. J. Brittain, *Progress in Polymer Science*, 2000, **25**, 677–710.
- [433] A. L. Willis, N. J. Turro and S. O'Brien, *Chemistry of Materials*, 2005, **17**, 5970–5975.
- [434] T. K. Jain, M. A. Moralles, S. K. Sahoo, D. L. Lesllie-Pellecky and V. Labhasetwar, *Molecular Pharmaceutics*, 2005, **2**, 194–205.
- [435] J. Xie, K. Chen, H.-Y. Lee, C. Xu, A. R. Hsu, S. Peng, X. Chen and S. Sun, *Journal of the American Chemical Society*, 2008, **130**, 7542–7543.
- [436] M. I. Shukoor, F. Natalio, M. N. Tahir, M. Divekar, N. Metz, H. A. Therese, P. Theato, V. Ksenofontov, H. C. Schroder, W. E. G. Muller and W. Tremel, *Journal of Magnetism and Magnetic Materials*, 2008, **320**, 2339–2344.
- [437] K. Herve, L. Douziech-Eyrolles, E. Munnier, S. Cohen-Jonathan, M. Souce, H. Marchais, P. Limelette, F. Warmont, M. L. Saboungi, P. Dubois and I. Chourpa, *Nanotechnology*, 2008, 465608 (7 pp.).
- [438] Y. Zhang, C. Sun, N. Kohler and M. Q. Zhang, *Biomedical Microdevices*, 2004, **6**, 33–40.
- [439] E. A. Boucher and P. M. Hines, *Journal of Polymer Science Part B-Polymer Physics*, 1976, **14**, 2241–2251.
- [440] E. Florin, R. Kjellander and J. C. Eriksson, *Journal of the Chemical Society-Faraday Transactions I*, 1984, **80**, 2889–2910.
- [441] A. Kira, H. Kim and K. Yasuda, *Langmuir*, 2009, **25**, 1285–1288.
- [442] R. I. Gelb, D. A. Laufer, L. M. Schwartz and K. Wairimu, *Journal of Chemical and Engineering Data*, 1989, **34**, 82–83.
- [443] K. S. Rajan and J. M. Davis, *Journal of Inorganic & Nuclear Chemistry*, 1976, **38**, 897–905.
- [444] T. Ishimitsu, S. Hirose and H. Sakurai, *Chemical & Pharmaceutical Bulletin*, 1978, **26**, 74–78.
- [445] T. Kiss and A. Gergely, *Inorganica Chimica Acta*, 1979, **36**, 31–36.
- [446] C. Gerard, H. Chehhal and R. P. Hugel, *Polyhedron*, 1994, **13**, 591–597.

- [447] P. Z. Araujo, P. J. Morando and M. A. Blesa, *Langmuir*, 2005, **21**, 3470–3474.
- [448] L. K. Charkoudian and K. J. Franz, *Inorganic Chemistry*, 2006, **45**, 3657–3664.
- [449] M. Andjelkovic, J. Van Camp, B. De Meulenaer, G. Depaemelaere, C. Socaciu, M. Verloo and R. Verhe, *Food Chemistry*, 2006, **98**, 23–31.
- [450] M. M. Noginov, N. Noginova, O. Amponsah, R. Bah, R. Rakhimov and V. A. Atsarkin, *Journal of Magnetism and Magnetic Materials*, 2008, **320**, 2228–2232.
- [451] W. J. Barreto, S. R. G. Barreto, I. Moreira and Y. Kawano, *Quimica Nova*, 2006, **29**, 1255–1258.
- [452] A. U. Gehring, R. Karthein and A. Reller, *Naturwissenschaften*, 1990, **77**, 177–179.
- [453] S. L. Jewett, S. Egging and L. Geller, *Journal of Inorganic Biochemistry*, 1997, **66**, 165–173.
- [454] A. Abragam and B. Bleaney, *Electron paramagnetic resonance of transition ions*, 1970, xiv+911.
- [455] H. Schmitt, R. Altenburger, B. Jastorff and G. Schuurmann, *Chemical Research in Toxicology*, 2000, **13**, 441–450.
- [456] D. C. Harris and P. Aisen, *Biochimica Et Biophysica Acta*, 1973, **329**, 156–158.
- [457] G. W. Bates, E. F. Workman and Schlabac.Mr, *Biochemical and Biophysical Research Communications*, 1973, **50**, 84–90.
- [458] J. P. Cornard, C. Lapouge and J. C. Merlin, *Chemical Physics*, 2007, **340**, 273–282.
- [459] C. Floriani, R. Henzi and Calderaz.F, *Journal of the Chemical Society-Dalton Transactions*, 1972, 2640–2642.
- [460] S. R. Sofen, S. R. Cooper and K. N. Raymond, *Inorganic Chemistry*, 1979, **18**, 1611–1616.
- [461] H. Suzuki, M. Nagasaka, M. Sugiura and T. Noguchi, *Biochemistry*, 2005, **44**, 11323–11328.
- [462] M. Higuchi, Y. Hitomi, H. Minami, T. Tanaka and T. Funabiki, *Inorganic Chemistry*, 2005, **44**, 8810–8821.

- [463] H. Stunzi, R. L. N. Harris, D. D. Perrin and T. Teitei, *Australian Journal of Chemistry*, 1980, **33**, 2207–2220.
- [464] J. Moser, S. PUNCHIHewa, P. P. Infelta and M. Gratzel, *Langmuir*, 1991, **7**, 3012–3018.
- [465] R. Rodriguez, M. A. Blesa and A. E. Regazzoni, *Journal of Colloid and Interface Science*, 1996, **177**, 122–131.
- [466] T. Rajh, L. X. Chen, K. Lukas, T. Liu, M. C. Thurnauer and D. M. Tiede, *Journal of Physical Chemistry B*, 2002, **106**, 10543–10552.
- [467] P. C. Redfern, P. Zapol, L. A. Curtiss, T. Rajh and M. C. Thurnauer, *Journal of Physical Chemistry B*, 2003, **107**, 11419–11427.
- [468] L. G. C. Rego and V. S. Batista, *Journal of the American Chemical Society*, 2003, **125**, 7989–7997.
- [469] P. Hakkinen, *Finnish Chemical Letters*, 1984, 59–62.
- [470] B. L. Ellis, A. K. Duhme, R. C. Hider, M. B. Hossain, S. Rizvi and D. van der Helm, *Journal of Medicinal Chemistry*, 1996, **39**, 3659–3670.
- [471] F. M. F. Degroot, M. Grioni, J. C. Fuggle, J. Ghijsen, G. A. Sawatzky and H. Petersen, *Physical Review B*, 1989, **40**, 5715–5723.
- [472] Wu, Stanley, Mutucumarana and Stafford, *Thrombosis and Haemostasis*, 1997, **78**, 1530–1530.
- [473] S. Giovannini, F. Boscherini, R. Carboni, L. Signorini, L. Pasquini, N. Mahne, A. Giglia, M. Pedio, S. Nannarone, M. Benfatto and S. Della Longa, *Physica Scripta/Physica Scripta*, 2005, 4 pp.
- [474] J. Hong, D. M. Xu, J. H. Yu, P. J. Gong, H. J. Ma and S. D. Yao, *Nanotechnology*, 2007, **18**, –.
- [475] F. X. Hu, K. G. Neoh, L. Cen and E. T. Kang, *Biomacromolecules*, 2006, **7**, 809–816.
- [476] G. Maris, O. Shklyarevskii, L. Jdira, J. G. H. Hermesen and S. Speller, *Surface Science*, 2006, **600**, 5084–5091.

- [477] T. A. Witten and P. A. Pincus, *Macromolecules*, 1986, **19**, 2509–2513.
- [478] S. T. Milner, T. A. Witten and M. E. Cates, *Macromolecules*, 1988, **21**, 2610–2619.
- [479] E. B. Zhulina, O. V. Borisov and V. A. Priamitsyn, *Journal of Colloid and Interface Science*, 1990, **137**, 495–511.
- [480] N. Dan and M. Tirrell, *Macromolecules*, 1992, **25**, 2890–2895.
- [481] S. T. Milner, T. A. Witten and M. E. Cates, *Europhysics Letters*, 1988, **5**, 413–418.
- [482] A. F. Miller, R. W. Richards and J. R. P. Webster, *Macromolecules*, 2001, **34**, 8361–8369.
- [483] D. F. K. Shim and M. E. Cates, *Journal De Physique*, 1989, **50**, 3535–3551.
- [484] T. L. Li and K. N. Park, *Computational and Theoretical Polymer Science*, 2001, **11**, 133–142.
- [485] R. Toral and A. Chakrabarti, *Physical Review E*, 1993, **47**, 4240–4246.
- [486] L. Zhang, J. Lin and S. Lin, *Macromolecules*, 2007, **40**, 5582–5592.
- [487] E. K. Lin and A. P. Gast, *Macromolecules*, 1996, **29**, 390–397.
- [488] S. Alexander, *Journal De Physique*, 1977, **38**, 977–981.
- [489] T. M. Birshtein and E. B. Zhulina, *Polymer*, 1984, **25**, 1453–1461.
- [490] H. Li and T. A. Witten, *Macromolecules*, 1994, **27**, 449–457.
- [491] R. C. Ball, J. F. Marko, S. T. Milner and T. A. Witten, *Macromolecules*, 1991, **24**, 693–703.
- [492] J. I. Martin and Z. G. Wang, *Journal of Physical Chemistry*, 1995, **99**, 2833–2844.
- [493] C. M. Wijmans, F. A. M. Leermakers and G. J. Fleer, *Langmuir*, 1994, **10**, 1331–1333.
- [494] G. Fritz, V. Schadler, N. Willenbacher and N. J. Wagner, *Langmuir*, 2002, **18**, 6381–6390.
- [495] U. Genz, B. Daguanno, J. Mewis and R. Klein, *Langmuir*, 1994, **10**, 2206–2212.

- [496] K. A. Cogan, A. P. Gast and M. Capel, *Macromolecules*, 1991, **24**, 6512–6520.
- [497] J. S. Pedersen and C. Svaneborg, *Current Opinion in Colloid & Interface Science*, 2002, **7**, 158–166.
- [498] J. S. Pedersen and M. C. Gerstenberg, *Colloids and Surfaces a-Physicochemical and Engineering Aspects*, 2003, **213**, 175–187.
- [499] Q. A. Zhang, M. S. Thompson, A. Y. Carmichael-Baranauskas, B. L. Caba, M. A. Zalich, Y. N. Lin, O. T. Mefford, R. M. Davis and J. S. Riffle, *Langmuir*, 2007, **23**, 6927–6936.
- [500] O. T. Mefford, M. L. Vadala, J. D. Goff, M. R. J. Carroll, R. Mejia-Ariza, B. L. Caba, T. G. S. Pierre, R. C. Woodward, R. M. Davis and J. S. Riffle, *Langmuir*, 2008, **24**, 5060–5069.
- [501] J. K. Lim, S. A. Majetich and R. D. Tilton, *Langmuir*, 2009, **25**, 13384–13393.
- [502] D. A. Sverjensky and N. Sahai, *Geochimica Et Cosmochimica Acta*, 1998, **62**, 3703–3716.
- [503] M. A. Bevan, S. N. Petris and D. Y. C. Chan, *Langmuir*, 2002, **18**, 7845–7852.
- [504] R. Tadmor and J. Klein, *Journal of Colloid and Interface Science*, 2002, **247**, 321–326.
- [505] M. Mohsen-Nia, H. Modarress and H. Rasa, *Journal of Chemical and Engineering Data*, 2005, **50**, 1662–1666.
- [506] C. N. Likos, H. Lowen, M. Watzlawek, B. Abbas, O. Jucknischke, J. Allgaier and D. Richter, *Physical Review Letters*, 1998, **80**, 4450–4453.
- [507] F. Kienberger, V. P. Pastushenko, G. Kada, H. J. Gruber, C. Riener, H. Schindler and P. Hinterdorfer, *Single Molecules|Single Molecules*, 2000, **1**, 123–8.
- [508] H. Lee, R. M. Venable, A. D. MacKerell and R. W. Pastor, *Biophysical Journal*, 2008, **95**, 1590–1599.
- [509] B. Zhu, T. Eurell, R. Gunawan and D. Leckband, *Journal of Biomedical Materials Research*, 2001, **56**, 406–416.

- [510] Y. X. J. Wang, S. M. Hussain and G. P. Krestin, *European Radiology*, 2001, **11**, 2319–2331.
- [511] C. W. Jung and P. Jacobs, *Magnetic Resonance Imaging*, 1995, **13**, 661–674.
- [512] Y. W. Jun, Y. M. Huh, J. S. Choi, J. H. Lee, H. T. Song, S. Kim, S. Yoon, K. S. Kim, J. S. Shin, J. S. Suh and J. Cheon, *Journal of the American Chemical Society*, 2005, **127**, 5732–5733.
- [513] L. E. W. LaConte, N. Nitin, O. Zurkiya, D. Caruntu, C. J. O'Connor, X. P. Hu and G. Bao, *Journal of Magnetic Resonance Imaging*, 2007, **26**, 1634–1641.
- [514] J. W. M. Bulte, Y. Hoekstra, R. L. Kamman, R. L. Magin, A. G. Webb, R. W. Briggs, K. G. Go, C. E. Hulstaert, S. Miltenyi, T. H. The and L. Deleij, *Magnetic Resonance in Medicine*, 1992, **25**, 148–157.
- [515] D. Artemov, N. Mori, B. Okollie and Z. M. Bhujwalla, *Magnetic Resonance in Medicine*, 2003, **49**, 403–408.
- [516] E. Y. Sun, L. Josephson and R. Weissleder, *Molecular Imaging*, 2006, **5**, 122–128.
- [517] S. Boutry, S. Laurent, L. Vander Elst and R. N. Muller, *Contrast Media & Molecular Imaging*, 2006, **1**, 15–22.
- [518] N. M. Green, *Methods in Enzymology*, 1990, **184**, 51–67.
- [519] S. C. Meyer, T. Gaj and I. Ghosh, *Chemical Biology & Drug Design*, 2006, **68**, 3–10.
- [520] A. B. Lowe, *Polymer Chemistry*, 2010, **1**, 17–36.
- [521] W. Linert, E. Herlinger, R. F. Jameson, E. Kienzl, K. Jellinger and M. B. H. Youdim, *Biochimica Et Biophysica Acta-Molecular Basis of Disease*, 1996, **1316**, 160–168.
- [522] Y. Nakashima, E. W. Raines, A. S. Plump, J. L. Breslow and R. Ross, *Arteriosclerosis Thrombosis and Vascular Biology*, 1998, **18**, 842–851.
- [523] M. I. Cybulsky, K. Iiyama, H. M. Li, S. N. Zhu, M. Chen, M. Iiyama, V. Davis, J. C. Gutierrez-Ramos, P. W. Connelly and D. S. Milstone, *Journal of Clinical Investigation*, 2001, **107**, 1255–1262.

- [524] S. Brunauer, P. H. Emmett and E. Teller, *Journal of the American Chemical Society*, 1938, **60**, 309–319.
- [525] E. T. Kisak, M. T. Kennedy, D. Trommeshauser and J. A. Zasadzinski, *Langmuir*, 2000, **16**, 2825–2831.
- [526] S. A. Darst, M. Ahlers, P. H. Meller, E. W. Kubalek, R. Blankenburg, H. O. Ribi, H. Ringsdorf and R. D. Kornberg, *Biophysical Journal*, 1991, **59**, 387–396.
- [527] F. Cappello, E. C. de Macario, V. Di Felice, G. Zummo and A. J. L. Macario, *Plos Pathogens*, 2009, **5**, e1000552.
- [528] C. Giovannoli, C. Baggiani, L. Anfossi and G. Giraudi, *Electrophoresis*, 2008, **29**, 3349–3365.
- [529] C. Fang and M. Q. Zhang, *Journal of Materials Chemistry*, 2009, **19**, 6258–6266.
- [530] D. Peer, J. M. Karp, S. Hong, O. C. Farokhzad, R. Margalit and R. Langer, *Nature Nanotechnology*, 2007, **2**, 751–760.
- [531] P. Y. Bolinger, D. Stamou and H. Vogel, *Angewandte Chemie-International Edition*, 2008, **47**, 5544–5549.
- [532] R. R. Sawant and V. P. Torchilin, *Soft Matter*, 2010, **6**, 4026–4044.
- [533] B. Stadler, R. Chandrawati, A. D. Price, S. F. Chong, K. Breheney, A. Postma, L. A. Connal, A. N. Zelikin and F. Caruso, *Angewandte Chemie-International Edition*, 2009, **48**, 4359–4362.
- [534] S. Simoes, J. N. Moreira, C. Fonseca, N. Duzgunes and M. C. P. de Lima, *Advanced Drug Delivery Reviews*, 2004, **56**, 947–965.
- [535] F. Szoka and D. Papahadjopoulos, *Annual Review of Biophysics and Bioengineering*, 1980, **9**, 467–508.
- [536] S. Ebrahim, G. A. Peyman and P. J. Lee, *Survey of Ophthalmology*, 2005, **50**, 167–182.
- [537] V. P. Torchilin, *Nature Reviews Drug Discovery*, 2005, **4**, 145–160.
- [538] Papahadj.D and N. Miller, *Biochimica Et Biophysica Acta*, 1967, **135**, 624–.

- [539] Y. K. Levine, A. I. Bailey and M. H. F. Wilkins, *Nature*, 1968, **220**, 577–.
- [540] J. F. Nagle and S. Tristram-Nagle, *Biochimica Et Biophysica Acta-Reviews on Biomembranes*, 2000, **1469**, 159–195.
- [541] A. D. Bangham, M. M. Standish and J. C. Watkins, *Journal of Molecular Biology*, 1965, **13**, 238–.
- [542] H. O. Hauser, *Biochemical and Biophysical Research Communications*, 1971, **45**, 1049–.
- [543] F. Olson, C. A. Hunt, F. C. Szoka, W. J. Vail and D. Papahadjopoulos, *Biochimica Et Biophysica Acta*, 1979, **557**, 9–23.
- [544] Gregoria.G and Neerunju.De, *European Journal of Biochemistry*, 1974, **47**, 179–185.
- [545] H. K. Kimelberg, *Biochimica Et Biophysica Acta*, 1976, **448**, 531–550.
- [546] S. M. Moghimi and H. M. Patel, *Advanced Drug Delivery Reviews*, 1998, **32**, 45–60.
- [547] R. L. Juliano and D. Stamp, *Biochemical and Biophysical Research Communications*, 1975, **63**, 651–658.
- [548] G. Blume and G. Cevc, *Biochimica Et Biophysica Acta*, 1990, **1029**, 91–97.
- [549] D. Papahadjopoulos, T. M. Allen, A. Gabizon, E. Mayhew, K. Matthay, S. K. Huang, K. D. Lee, M. C. Woodle, D. D. Lasic, C. Redemann and F. J. Martin, *Proceedings of the National Academy of Sciences of the United States of America*, 1991, **88**, 11460–11464.
- [550] J. Senior, C. Delgado, D. Fisher, C. Tilcock and G. Gregoriadis, *Biochimica Et Biophysica Acta*, 1991, **1062**, 77–82.
- [551] D. D. Lasic, F. J. Martin, A. Gabizon, S. K. Huang and D. Papahadjopoulos, *Biochimica Et Biophysica Acta*, 1991, **1070**, 187–192.
- [552] D. D. Lasic and D. Needham, *Chemical Reviews*, 1995, **95**, 2601–2628.
- [553] M. C. Woodle, K. K. Matthay, M. S. Newman, J. E. Hidayat, L. R. Collins, C. Redemann, F. J. Martin and D. Papahadjopoulos, *Biochimica Et Biophysica Acta*, 1992, **1105**, 193–200.

- [554] C. Vermehren, K. Jorgensen and S. Frokjaer, *International Journal of Pharmaceutics*, 1999, **183**, 13–16.
- [555] I. V. Zhigaltsev, N. Maurer, Q. F. Akhong, R. Leone, E. Leng, J. Wang, S. C. Semple and P. R. Cullis, *Journal of Controlled Release*, 2005, **104**, 103–111.
- [556] W. C. Zamboni, A. C. Gervais, M. J. Egorin, J. H. M. Schellens, E. G. Zuhowski, D. Pluim, E. Joseph, D. R. Hamburger, P. K. Working, G. Colbern, M. E. Tonda, D. M. Potter and J. L. Eiseman, *Cancer Chemotherapy and Pharmacology*, 2004, **53**, 329–336.
- [557] K. M. Laginha, S. Verwoert, G. J. R. Charrois and T. M. Allen, *Clinical Cancer Research*, 2005, **11**, 6944–6949.
- [558] G. A. F. van Tilborg, W. J. M. Mulder, N. Deckers, G. Storm, C. P. M. Reutelingsperger, G. J. Strijkers and K. Nicolay, *Bioconjugate Chemistry*, 2006, **17**, 741–749.
- [559] Y. Namiki, T. Namiki, H. Yoshida, Y. Ishii, A. Tsubota, S. Koido, K. Nariai, M. Mitsunaga, S. Yanagisawa, H. Kashiwagi, Y. Mabashi, Y. Yumoto, S. Hoshina, K. Fujise and N. Tada, *Nat Nano*, 2009, **4**, 598–606.
- [560] P. Balgavy, M. Dubnickova, N. Kucerka, M. A. Kiselev, S. P. Yaradaikin and D. Uhrikova, *Biochimica Et Biophysica Acta-Biomembranes*, 2001, **1512**, 40–52.
- [561] S. S. Qin, Z. W. Yu and Y. X. Yu, *Journal of Physical Chemistry B*, 2009, **113**, 8114–8123.
- [562] S. Kaufmann, G. Papastavrou, K. Kumar, M. Textor and E. Reimhult, *Soft Matter*, 2009, **5**, 2804–2814.
- [563] A. K. Kenworthy, S. A. Simon and T. J. McIntosh, *Biophysical Journal*, 1995, **68**, 1903–1920.
- [564] P. Pradhan, J. Giri, F. Rieken, C. Koch, O. Mykhaylyk, M. Doblinger, R. Banerjee, D. Bahadur and C. Plank, *Journal of Controlled Release*, 2010, **142**, 108–121.
- [565] K. Kubota, S. Fujishige and I. Ando, *Polymer Journal*, 1990, **22**, 15–20.
- [566] H. Uludag, B. Norrie, N. Kousinioris and T. J. Gao, *Biotechnology and Bioengineering*, 2001, **73**, 510–521.

- [567] J. L. Dalsin, B. H. Hu, B. P. Lee and P. B. Messersmith, *Journal of the American Chemical Society*, 2003, **125**, 4253–4258.
- [568] H. Lee, S. M. Dellatore, W. M. Miller and P. B. Messersmith, *Science*, 2007, **318**, 426–430.
- [569] I. ulHaq and E. Matijevic, *Journal of Colloid and Interface Science*, 1997, **192**, 104–113.
- [570] T. W. Healy, A. P. Herring and Fuersten.Dw, *Journal of Colloid and Interface Science*, 1966, **21**, 435–.
- [571] V. I. Anisimov, M. A. Korotin and E. Z. Kurmaev, *Journal of Physics-Condensed Matter*, 1990, **2**, 3973–3987.
- [572] G. Tao, M. Glerup, F. Krumeich, R. Nesper, H. Fjellvag and P. Norby, *Journal of Physical Chemistry C*, 2008, 13134–40.
- [573] L. Isa, E. Amstad, M. Textor and E. Reimhult, *Chimia*, 2010, **64**, 145–149.
- [574] B. M. Discher, H. Bermudez, D. A. Hammer, D. E. Discher, Y. Y. Won and F. S. Bates, *Journal of Physical Chemistry B*, 2002, **106**, 2848–2854.
- [575] H. Bermudez, A. K. Brannan, D. A. Hammer, F. S. Bates and D. E. Discher, *Macromolecules*, 2002, **35**, 8203–8208.
- [576] D. E. Discher and F. Ahmed, *Annual Review of Biomedical Engineering*, 2006, **8**, 323–341.
- [577] B. M. Discher, D. A. Hammer, F. S. Bates and D. E. Discher, *Current Opinion in Colloid & Interface Science*, 2000, **5**, 125–131.
- [578] S. Yang and H. R. Liu, *Journal of Materials Chemistry*, 2006, **16**, 4480–4487.
- [579] S. Yang, H. R. Liu and Z. C. Zhang, *Journal of Polymer Science Part a-Polymer Chemistry*, 2008, **46**, 3900–3910.
- [580] S. Yang, H. R. Liu, H. F. Huang and Z. C. Zhang, *Journal of Colloid and Interface Science*, 2009, **338**, 584–590.
- [581] S. Yang, H. R. Liu and Z. C. Zhang, *New Journal of Chemistry*, 2009, **33**, 620–625.

- [582] F. A. Plamper, M. Ruppel, A. Schmalz, O. Borisov, M. Ballauff and A. H. E. Muller, *Macromolecules*, 2007, **40**, 8361–8366.
- [583] D. Fournier, R. Hoogenboom, H. M. L. Thijs, R. M. Paulus and U. S. Schubert, *Macromolecules*, 2007, **40**, 915–920.
- [584] L. M. Bronstein, X. L. Huang, J. Retrum, A. Schmucker, M. Pink, B. D. Stein and B. Dragnea, *Chemistry of Materials*, 2007, **19**, 3624–3632.
- [585] P. Kingshott, H. Thissen and H. J. Griesser, *Biomaterials*, 2002, **23**, 2043–2056.
- [586] S. Yu and G. M. Chow, *Journal of Materials Chemistry*, 2004, **14**, 2781–2786.
- [587] S. Mornet, J. Portier and E. Duguet, *Journal of Magnetism and Magnetic Materials*, 2005, **293**, 127–134.
- [588] E. Taboada, E. Rodriguez, A. Roig, J. Oro, A. Roch and R. N. Muller, *Langmuir*, 2007, **23**, 4583–4588.
- [589] A. R. Studart, E. Amstad and L. J. Gauckler, *Langmuir*, 2007, **23**, 1081–1090.
- [590] J. F. Lutz, S. Stiller, A. Hoth, L. Kaufner, U. Pison and R. Cartier, *Biomacromolecules*, 2006, **7**, 3132–3138.

Curriculum Vitae

ESTHER AMSTAD

Date of birth: 6th of June 1983
Place of birth: Walenstadt, Switzerland
Nationality: Swiss
Marital status: single
Hobbies: sports in general, playing the piano



EDUCATION

May 2007 - December 2010: PhD studies at the Laboratory for Surface Science and Technology (Department of Materials), ETH Zurich, Switzerland, supervised by Prof. Dr. Erik Reimhult and Prof. Dr. Marcus Textor

October 2005 - April 2007: Master in material science at ETH Zurich, Switzerland

October 2002 - June 2005: Bachelor in material science at ETH Zurich, Switzerland

August 1996 - June 2002: High school degree in mathematics and physics at Kantonale Mittelschule Uri, Switzerland

EXPERIENCE

- September 2006 - April 2007: Master thesis at Boston University, USA; Title: "Targeted Magnetic Resonance (MR) Contrast Agents for Molecular Imaging of Atherosclerosis", supervised by Prof. Dr. Joyce Y. Wong (Boston University, MA, USA), Prof. Dr. Erik Reimhult (ETH Zurich, Switzerland), Prof. Dr. Marcus Textor (ETH Zurich, Switzerland)
- July 2006 - September 2006: Master project at ETH Zurich, Switzerland; Title: "Iron Oxide Nanoparticles as Contrast Agents for MR Imaging"
- February 2006 - April 2006: Master project at ETH Zurich, Switzerland; Title: "Micro-Tribology of Graphite-Reinforced Vit 105", supervised by Dr. Marco Siegrist, Prof. Dr. Jörg Löffler (ETH Zurich, Switzerland)
- July 2005 - August 2005: Bachelor thesis at ETH Zurich, Switzerland; Title: "Dispersion of Nanoparticles in Colloidal Suspensions", supervised by Prof. Dr. André R. Studart, Prof. Dr. Ludwig J. Gauckler (ETH Zurich, Switzerland)
- July 2005 - September 2005: Internship at Aerosol-Service AG, Möhlin, Switzerland
- March 2004: Internship at Metallbau Brand AG, Schattdorf, Switzerland

AWARDS

- 2010 Dorothy M. and Earl S. Hoffman award at 57th AVS International Symposium and Exhibition in Albuquerque (NM), USA
- 2009 Soft Matter poster prize from the Royal Chemical Society (RCS) at the European Colloid and Interface Science (ECIS) conference in Antalya, Turkey
- 2008 ETH Medial for outstanding Master thesis: "Targeted Magnetic Resonance (MR) Contrast Agents for Molecular Imaging of Atherosclerosis", ETH Zurich, Switzerland

STUDENT PROJECT SUPERVISION

- 2010 **Post-diploma work**, *Deborah Studer*, Iron Oxide Nanoparticle Functionalized Supported Lipid Bilayers
- 2009 **Semester project**, *Ali Arefi*, Synthesis and Stabilization of Au Nanorods
- 2009 **Semester project**, *Sandro Bidler*, ZnO Nanorod Synthesis and Characterization
- 2009 **Semester project**, *Fabian Fischer*, Dimerization of Nanoparticles
- 2008 **Master thesis**, *Roman Kontic*, Dual Labeled Contrast Agents

SCIENTIFIC PAPERS

- 2010 E. Amstad, A. U. Gehring, H. Fischer, V. V. Nagaiyanallur, G. Hähner, M. Textor, E. Reimhult. *The Influence of Electronegative Substituents on the Binding Affinity of Catechol Derived Anchors to Fe₃O₄ Surfaces*, accepted in Journal of Physical Chemistry C.
- 2010 M. Baumann, E. Amstad, A. Mashaghi, M. Textor, E. Reimhult. *Characterization of supported lipid bilayers incorporating the phosphoinositides phosphatidylinositol 4,5-biphosphate and phosphoinositol-3,4,5-triphosphate by complementary techniques*, Biointerphases, 5, online available.
- 2010 L. Isa, E. Amstad, M. Textor, E. Reimhult. *Nanoparticles at Liquid-Liquid Interfaces*, Chimia, 64.
- 2010 I. Bilecka, M. Kubli, E. Amstad, M. Niederberger. *Simultaneous Formation of Ferrite Nanocrystals and Deposition of Thin Films via a Microwave-assisted Nonaqueous Sol-gel Process*, Journal of Sol-Gel Science and Technology, accepted.
- 2009 E. Amstad, T. Gillich, I. Bilecka, M. Textor, E. Reimhult. *Controlled Surface Modification of Superparamagnetic Iron oxide nanoparticles (SPIONs)*, AIChE conference paper.
- 2009 E. Amstad, T. Gillich, I. Bilecka, M. Textor, E. Reimhult. *Ultrastable Iron Oxide Nanoparticle Colloidal Suspensions Using Dispersants with Catechol-Derived Anchor Groups*, Nano Letters, 9, 4042.
- 2009 E. Amstad, S. Zurcher, A. Mashaghi, J.Y. Wong, M. Textor, E. Reimhult. *Surface Functionalization of Single Superparamagnetic Iron Oxide Nanoparticles for Targeted Magnetic Resonance Imaging*, Small, 5, 1334
- 2009 B.S. Yeo, E. Amstad, T. Schmid, J. Stadler, R. Zenobi. *Nanoscale Probing of a Polymer-Blend Thin Film with Tip-Enhanced Raman Spectroscopy*, Small, 5, 952.

- 2007 M. E. Siegrist, E. Amstad, J.F. Löffler. *Tribological Properties of Graphite- and ZrC-Reinforced Bulk Metallic Glass Composites*, *Intermetallics*, 15, 1228.
- 2007 A.R. Studart, E. Amstad, L.J. Gauckler. *Colloidal Stabilization of Nanoparticles in Concentrated Suspensions*, *Langmuir*, 23, 1081.
- 2006 A.R. Studart, E. Amstad, M. Antoni, L.J. Gauckler. *Rheology of Concentrated Suspensions Containing Weakly Attractive Alumina Nanoparticles*, *Journal of the American Ceramic Society*, 89, 2418.

SCIENTIFIC PAPERS IN PREPARATION

- ▷ E. Amstad, H. Fischer, A. U. Gehring, M. Textor, E. Reimhult. *Magnetic Decoupling of Surface Fe^{3+} in Magnetite Nanoparticles upon Nitrocatechol Anchored Dispersant Binding*, *submitted*.
- ▷ E. Amstad, J. Kohlbrecher, E. Müller, T. Schweizer, M. Textor, E. Reimhult. *Magnetically Triggered Release of Liposomes Bearing Iron Oxide Nanoparticles in their Membranes*, *submitted*.
- ▷ E. Amstad, M. Textor, E. Reimhult. *Stabilization and Functionalization of Iron Oxide Nanoparticles for Biomedical Applications*, *in preparation*.

EXPERIENCE WITH SYNTHESIS AND CHARACTERIZATION METHODS

- ▷ Synthesis and surface modification of iron oxide nanoparticles
- ▷ Transmission electron microscopy (TEM) including high resolution TEM (HRTEM), scanning TEM (STEM) and cryo-TEM
- ▷ X-ray diffraction (XRD)
- ▷ Dynamic light scattering (DLS)
- ▷ Small angle neutron scattering (SANS)
- ▷ X-ray photoelectron spectroscopy (XPS)
- ▷ Quartz crystal microbalance with dissipation monitoring (QCM-D)
- ▷ Fourier transform infrared spectroscopy (FTIR)

M.1 Effect of Adsorption Conditions on Nanoparticle Stability

NPs synthesized in organic solvents contain organic residues on their surface that need to be replaced by anchors if good NP stability is to be achieved. To test, if the binding affinity of nitroDOPA is high enough to replace these residues and whether stabilization is facilitated if NP surfaces were partially cleaned before adsorption of PEG-nitroDOPA, NPs were washed with organic solvents that have different polarities, namely ethanol, isopropanol and acetone, and subsequently stabilized with PEG-nitroDOPA.

M.1.1 Effect of Solvent Nanoparticles are Washed With

As can be seen in Figures M.1 and M.2, no difference in NP stability and dispersant packing density was measured irrespective on the solvent NPs were washed with. This indicates that nitroDOPA can replace organic residues. However, acetone washed NPs appeared red, in contrast to NPs washed with ethanol and isopropanol. This hints to an oxidation of Fe_3O_4 NPs during washing with acetone. The yield of with acetone washed NPs was considerably lower compared to NPs washed with ethanol and isopropanol. It hints to lower NP stability of NPs washed with acetone compared to counterparts washed with ethanol or isopropanol, as unstable NPs were lost during purification. Thus, only the stable fraction of NPs was analyzed with DLS and TGA. This result corroborates EPR results that showed enhanced binding affinity of nitroDOPA to Fe_3O_4 compared to

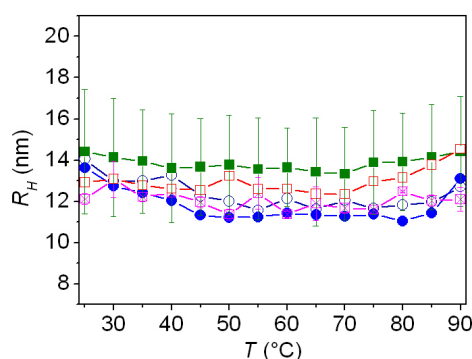


Figure M.1: DLS of iron oxide NPs stabilized with PEG(5)-nitroDOPA. DLS of iron oxide NPs washed with ethanol (-■-), isopropanol (-▣-) and acetone (-□-) before they were stabilized with PEG(5)-nitroDOPA at 50 °C under constant mechanic stirring. Additionally, iron oxide NPs were stabilized statically at 50 °C (-●-) and RT (-○-) respectively. Statistics was done on 14 independent samples for NPs washed with ethanol, while it was done on one and two independent samples for NPs washed with isopropanol and acetone respectively.

oxidized iron oxide surfaces (see chapter 7). Based on this comparison and because NPs were stabilized in ethanol, iron oxide NPs studied in this thesis were washed twice with ethanol before they were stabilized.

M.1.2 Adsorption Conditions

Whether ethanol washed NPs were stabilized with 6 mg dispersant/mg(NP) at 50 °C under constant mechanical stirring, under static conditions at 50 °C or room temperature did not seem to influence NP stability and dispersant packing density of the stable NP fraction. However, the yield of NPs stabilized at room temperature was lower compared to NPs stabilized at 50 °C. The latter could be due to an increased desorption rate of organic contaminations physisorbed at the iron oxide NP surface or a facilitated electron delocalization between nitroDOPA and Fe(II) at elevated temperatures.

Constant mechanic stirring of NPs during stabilization considerably slowed down sedimentation of as-synthesized NPs. This might ease dispersant adsorption because NP surfaces are more readily accessible if they are dispersed in ethanol as compared to sedimented NPs. However, as shown in Figures M.1 and M.2, mechanical stirring did not influence NP stability nor dispersant packing density of the stable NP fraction. To increase the likelihood to achieve a homogeneous dispersant coating on the NP surface, NPs were stabilized at 50 °C under constant mechanic stirring in this thesis even though no influence of mechanic stirring on NP stability could be observed here.

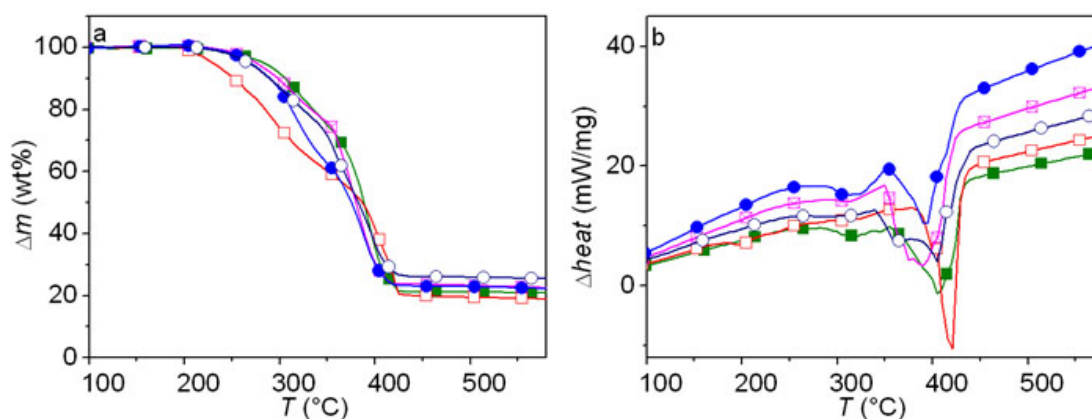


Figure M.2: Influence of the dispersant packing density on the adsorption conditions. (a) TGA and (b) DSC of PEG(5)-nitroDOPA stabilized 5 nm core radius iron oxide NPs synthesized in the oil bath. Iron oxide NPs have been washed with ethanol (-■-), isopropanol (-◻-) and acetone (-◻-) prior to stabilization at 50 °C under constant mechanical stirring. Furthermore, ethanol washed iron oxide NPs have been stabilized without mechanical stirring at 50 °C (-●-) and at room temperature (-○-).

M.2 Replacing Oleic Acid with nitroDOPA

Most of the monodisperse Fe_3O_4 NPs reported today are synthesized using oleic acid as a capping agent during the synthesis of iron oxide NPs. Oleic acid facilitates control over the core shape, size and size distribution [395]. Especially applications, that require good stability of monodisperse Fe_3O_4 NPs in aqueous environments, would benefit from anchors that can displace oleic acid with a dense sterically stabilizing polymer shell.

To test, if the close to optimal binding affinity of nitroDOPA to Fe_3O_4 and its low desorption rate allows to replace oleic acid, Fe_3O_4 NPs were synthesized in the oil bath in the presence of oleic acid. These NPs were washed with ethanol according to the standard protocol described in section 3.3.2. Washed NPs were incubated with nitroDOPA in ethanol at 50 °C under constant mechanical mixing. FTIR peaks at $\approx 1280\text{ cm}^{-1}$ and 1496 cm^{-1} assigned to C-O stretch vibration and C-C ring vibrations of nitroDOPA [447] appeared after NPs were incubated with nitroDOPA for at least 1 d. The intensities of these peaks increased for NPs incubated with nitroDOPA for 2 d (Figure M.3). Furthermore, the peak around 1444 cm^{-1} assigned to the COO^- and CH_2 stretch vibration [584] disappeared after iron oxide NPs were incubated with nitroDOPA for at least 1 d. This indicated that the binding affinity of nitroDOPA is high enough to replace oleic acid within 24 h to 48 h if ligand exchange is performed in ethanol.

However, despite that nitroDOPA can replace oleic acid if NPs are incubated in ethanol for at least 2 d at 50 °C (Figure M.3), iron oxide NPs synthesized in the presence of oleic

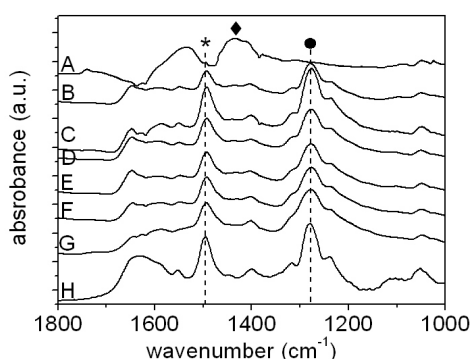


Figure M.3: FTIR spectra of Fe_3O_4 NPs synthesized in the presence of oleic acid. FTIR spectra of Fe_3O_4 NPs synthesized in the oil bath using oleic acid as a capping agent were (A) not incubated with nitroDOPA and NPs incubated with nitroDOPA for (B) 1 d, (C) 2 d, (D) 3 d, (E) 6 d, (F) 8 d, (G) 2 weeks. (H) As a reference nitroDOPA coated Fe_3O_4 NPs synthesized in the absence of oleic acid are shown. The pronounced peaks of the C-O stretch vibration (●) and C-C ring vibration (*) [447] clearly show the presence of nitroDOPA. Furthermore, the peak at 1444 cm^{-1} (◆) assigned to the COO^- and CH_2 stretch vibration [584] indicate that oleic acid is bound on as-synthesized NPs.

acid could not be sterically stabilized with PEG(5)-nitroDOPA even if they were incubated with PEG(5)-nitroDOPA at $50\text{ }^\circ\text{C}$ in ethanol for 2 weeks.

The molar concentration of PEG(5)-nitroDOPA was 5 times lower compared to that of nitroDOPA. Furthermore, PEG(5) might sterically hinder PEG(5)-nitroDOPA to adsorb on the iron oxide NP surface despite that it is collapsed if dispersed in ethanol. Therefore, exchange of oleic acid by PEG(5)-nitroDOPA might have been hindered. However, good NP stability requires a high packing density of PEG-nitroDOPA (see chapter 6). Therefore, inefficient and incomplete exchange of oleic acid by PEG-nitroDOPA negatively affects the NP stability in aqueous media.

Ligand exchange might be more efficient if NPs are stabilized in solvents such as chloroform, where the hydrophobic tail of oleic acid is well soluble in. However, the packing density of PEG on flat surfaces is known to be higher, if PEG is adsorbed in a partially collapsed state under cloud point conditions [301, 567, 585]. Therefore, it is expected that a high packing density of PEG-nitroDOPA on NPs can only be obtained if it is adsorbed from solvents in which PEG is at the most moderately soluble. Thus, it is questionable, whether good NP stability would be achieved if exchange of oleic acid to PEG-nitroDOPA is performed in chloroform where PEG is well soluble.

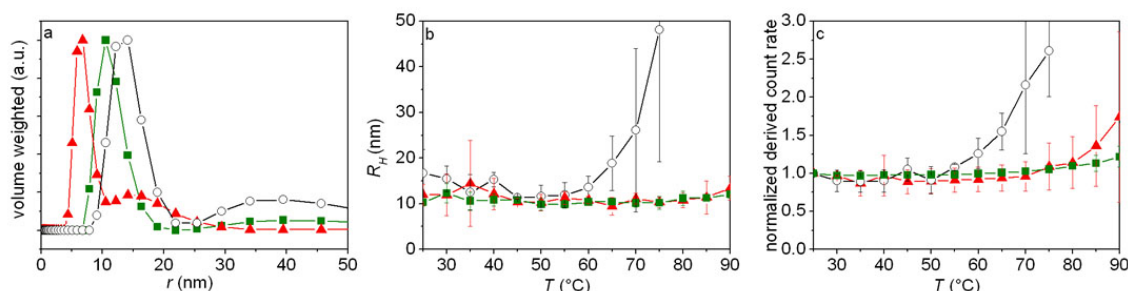


Figure M.4: Temperature dependent DLS of PEG-nitroDOPA stabilized iron oxide NPs synthesized in the MW. The (a) hydrodynamic radius at RT, the temperature dependent (b) hydrodynamic radius and (c) normalized count rate of iron oxide cores heated in the MW to 180 °C and grown at this temperature for 3 min, stabilized with PEG(5)-nitroDOPA (-■-), PEG(1.5)-nitroDOPA (-▲-) and PEG(0.8)-nitroDOPA (-○-). Iron oxide NPs were dispersed in HEPES containing 160 mM NaCl. Statistics was done on 4-5 independent samples.

M.3 Effect of PEG M_w on the Stability of Bimodally Distributed Iron Oxide Nanoparticles

The effect of the PEG M_w on the hydrodynamic radius, dispersant packing density and NP stability was also investigated for iron oxide NPs synthesized in the MW which were shown in chapter 5 to be bimodally distributed.

M.3.1 Effect of PEG M_w on Iron Oxide Nanoparticle Stability

Similar to what was seen in DLS measurements of the unstable fraction of PEG-nitroDOPA stabilized NPs synthesized in the oil bath (Figure 8.18), the volume weighted hydrodynamic radius did not increase with increasing PEG-nitroDOPA M_w . Additionally, a second broad peak centered around 40 nm was measured for PEG-nitroDOPA stabilized NPs synthesized in the MW (Figure M.4a). However, PEG(1.5)-nitroDOPA and PEG(0.8)-nitroDOPA stabilized iron oxide NPs synthesized in the MW (where the large fraction of these bimodally distributed cores was ≈ 2.5 nm - 3 nm in core radius) remained stable up to 80 °C and 60 °C respectively (Figure M.4). Thus, these bimodally distributed NPs stabilized with PEG(0.8)-nitroDOPA and PEG(1.5)-nitroDOPA started to agglomerate at higher temperatures compared to unimodally distributed NPs of similar core sizes. This might be related to the presence of numerous ultrasmall NPs in the former batches. Ultrasmall NPs were surrounded by a high amount of dispersants. Thus, the probability that two NPs of the larger fraction meet and agglomerate is much lower in case of bimodally compared to unimodally distributed NPs.

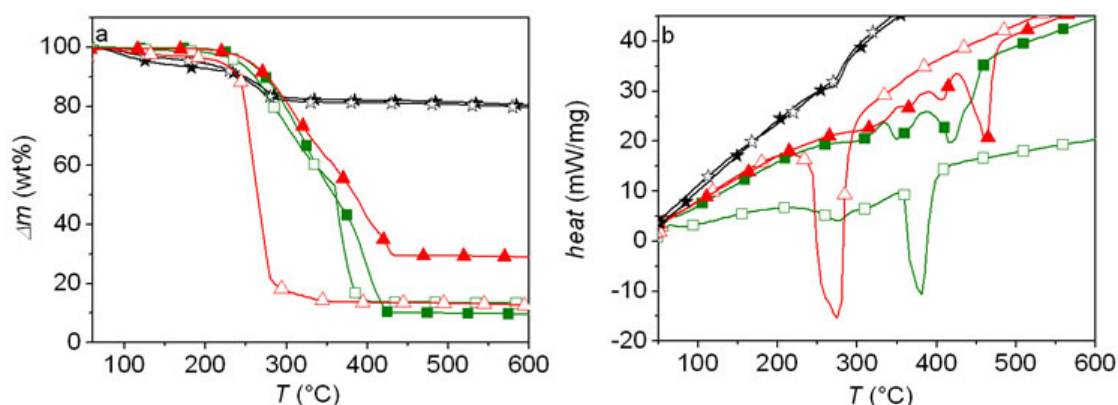


Figure M.5: DSC and TGA measurements of PEG(5)-nitroDOPA stabilized iron oxide NPs synthesized in the MW. (a) TGA and (b) DSC measurements of iron oxide NPs synthesized in the MW by heating them to 180 °C where they were kept for 3 min were stabilized with PEG(5)-nitroDOPA (■) and PEG(1.5)-nitroDOPA (▲) in DMF (□) and ethanol (●) respectively. As a control, unstabilized NPs (☆) incubated in DMF and ethanol for 24 h are shown.

M.3.2 Effect of PEG M_w on the Dispersant Packing Density

Quantification of the dispersant packing density on bimodally distributed NPs is difficult because of the unknown ratio between the two size fractions. However, a comparison between DSC results of these bimodally distributed NPs stabilized with PEG(5)-nitroDOPA, where PEG(5)-nitroDOPA was adsorbed in ethanol and DMF respectively, showed that the main endothermic reactions were shifted towards lower temperatures if NPs had been stabilized in DMF compared to ethanol (Figure M.5). This shift towards lower temperatures was particularly pronounced for PEG(1.5)-nitroDOPA stabilized NPs. As described in chapter 6 and previously in this chapter, the endothermic peak around 250 °C was assigned to the decomposition of organic contaminants. Therefore, the shift of the DSC peak towards lower temperatures was interpreted as a higher amount of organic species adsorbed on iron oxide cores for NPs stabilized in DMF compared to counterparts stabilized in ethanol.

M.3.3 Effect of PEG M_w on the Zeta Potential

Irrespective of the PEG M_w , the zeta potential of these iron oxide NPs dispersed in Millipore water was close to zero if at least 20 mM NaCl was added. Therefore, these NPs were almost exclusively sterically stabilized. However, the zeta potential was more negative if the NPs were dispersed in D_2O . For the latter, PEG(0.8)-nitroDOPA stabilized NPs had,

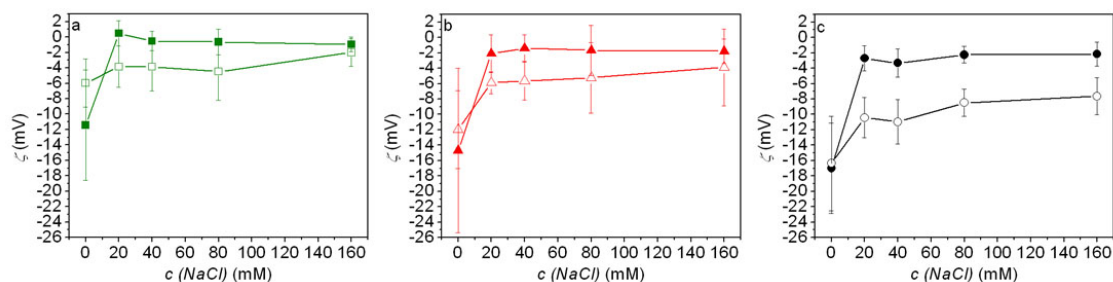


Figure M.6: Zeta potential measurements of iron oxide NPs synthesized in the MW and stabilized with PEG-nitroDOPA. Zeta potential measurements of iron oxide NPs heated in the MW to 180 °C for 3 min and stabilized with (a) PEG(5)-nitroDOPA, (b) PEG(1.5)-nitroDOPA and (c) PEG(0.8)-nitroDOPA. The zeta potential of these NPs was measured as a function of the NaCl concentration if dispersed in Millipore water (filled symbols) and D_2O (empty symbols) respectively. Statistics was done on 6-12 independent samples.

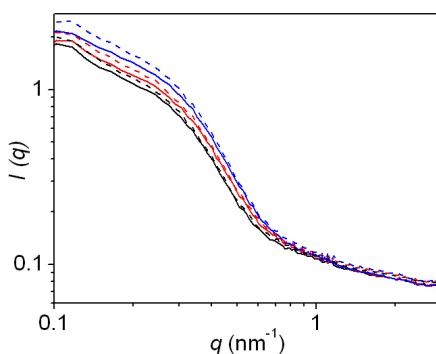


Figure M.7: SANS measurements of NPs synthesized in the MW. SANS was measured on PEG(5)-nitroDOPA stabilized iron oxide NPs which had been synthesized in the MW as a function of temperature. NPs were dispersed in D_2O (solid line) and D_2O containing 160 mM NaCl (dashed line). SANS measurements were conducted at 25 °C (black), 40 °C (red) and 60 °C (blue).

with ≈ -12 mV, a slightly more negative zeta potential compared to PEG(1.5)-nitroDOPA and PEG(5)-nitroDOPA stabilized NPs (Figure M.6). This can be attributed to the thinner dispersant shell of PEG(0.8)-nitroDOPA compared to PEG(1.5)- and PEG(5)-nitroDOPA stabilized NPs.

M.3.4 Influence of Solvent Conditions on the Dispersant Layer Thickness

To investigate the dependence of temperature and NaCl concentration on the extension of the PEG brush and thus scattering of PEG(5)-nitroDOPA stabilized NPs, SANS was measured on PEG(5)-nitroDOPA stabilized NPs dispersed in D_2O . D_2O rather than H_2O

Table M.1: Hydrodynamic diameter of PEG(5)-nitroDOPA stabilized iron oxide NPs synthesized in the MW.

temperature (°C)	NaCl concentration (mM)	R_G (nm)	I_0
25	0	5.4	1.5
40	0	5.3	1.7
60	0	5.2	2.0
25	160	5.5	1.6
40	160	5.4	1.8
60	160	5.4	2.2

was chosen as a solvent to maximize neutron scattering contrast of PEG. Based on these measurements, R_G was quantified by fitting SANS curves in the q -range of $0.15 \text{ nm}^{-1} < q < 0.45 \text{ nm}^{-1}$ using a Guinier approximation. The theoretically calculated R_G of PEG(5) is 2.9 nm. Fitting results are summarized in Table M.1. The decrease of the solvent quality of water for PEG with increasing temperature and salt concentration [301, 585] is well in agreement with the decreased R_G values found both with increasing temperature and by adding 160 mM NaCl. The increased forward scattering I_0 with increasing temperature and salt concentration might be assigned to NP agglomeration that was driven by the gradual collapse of the PEG brush surrounding the iron oxide cores with increasing temperature and salt concentration.

However, R_G values measured by SANS for PEG(5)-nitroDOPA adsorbed on iron oxide NPs were considerably higher compared to the value calculated for free PEG(5) chains in solution. This might be because of steric inter-chain repulsion of adjacent PEG(5) chains if adsorbed on iron oxide NPs. Steric inter-chain repulsion interactions cause PEG(5) to stretch resulting in higher R_G values measured with SANS if adsorbed on NPs.

M.4 Iron Oxide Nanoparticles Synthesized by Aqueous Precipitation

As described in chapter 5, aqueous precipitation resulted in larger iron oxide cores and a broader core size distribution compared to iron oxide NPs synthesized by the non-aqueous sol-gel methods. However, before we synthesized NPs by non-aqueous sol-gel methods, NPs were synthesized by aqueous precipitation. Therefore, initial stabilization and functionalization studies were done on NPs synthesized using the latter method. To test NP stability without the aim to do fundamental studies *e.g.* on the shell thickness or disper-

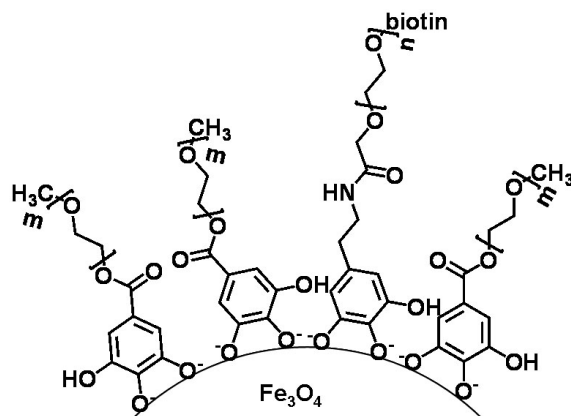


Figure M.8: Cartoon of iron oxide NPs stabilized with PEG-gallol. Cartoon of iron oxide NPs stabilized with a mixture of biotinylated and unfunctionalized PEG-gallol.

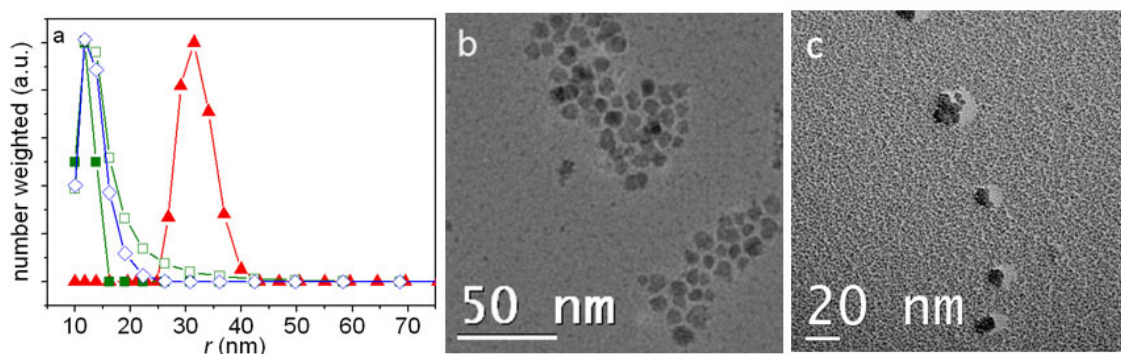


Figure M.9: Size of PEG(0.55)-gallol stabilized iron oxide NPs synthesized by aqueous precipitation. (a) DLS of PEG(0.55)-gallol stabilized iron oxide NPs synthesized by aqueous precipitation freshly dispersed (-■-), stored for 20 months in HEPES containing 160 mM NaCl (-□-), stored for 1 year in PBS (-◇-) and as a comparison Feridex (-▲-). (b) TEM of PEG(0.55)-nitroDOPA stabilized iron oxide NPs dispersed in Millipore water and air-dried on a carbon film supported Cu TEM-grid. (c) PEG(0.55)-gallol stabilized NPs were coated with tungsten under a shallow angle revealing the e* structure of NPs.

sant density profile, NP size distribution is less important. Nevertheless, the fact, that NPs have been synthesized by different methods requires some care by comparing results described in the following to results obtained for NPs synthesized by the non-aqueous sol-gel methods.

M.4.1 Effect of Dispersant on Nanoparticle Stability

Dispersant Type

A comparison of the hydrodynamic radius of PEG-gallol stabilized NPs, schematically shown in Figure M.8, and Feridex revealed a considerably smaller hydrodynamic radius

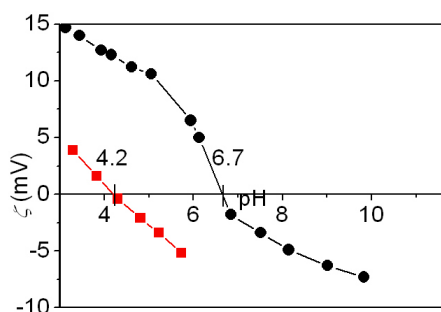


Figure M.10: Zeta potential measurements of iron oxide NPs synthesized by aqueous precipitation. The zeta potential was measured in Millipore based solutions containing 160 mM NaCl for unstabilized (●) and PEG(0.55)-gallol stabilized iron oxide NPs (▲) as a function of pH. The pH was shifted by adding 1 M HCl and NaOH respectively.

and narrower size distribution for the former NPs. Moreover, PEG-gallol stabilized iron oxide NPs were stable even after 20 months storage at room temperature in HEPES containing 160 mM NaCl (Figure M.9).

Feridex consists of multiple iron oxide cores with an average radius of 2.4 nm embedded in a dextran matrix [510] resulting in a hydrodynamic radius of 32 ± 11 nm. However, NPs stabilized with a mixture of PEG(0.55)-gallol and biotin-PEG(3.4)-gallol had a hydrodynamic radius of 14 ± 1 nm (Figure M.9a), well in agreement with X-ray disc centrifuge (XDC) measurements (hydrodynamic radius = 13 ± 1 nm). Furthermore, Figure M.9b indicates that NPs, previously filtered using syringe filters with a cut-off of 200 nm, were well separated even if dried on a carbon film. However, only very few assembled NPs were found for PEG-gallol stabilized NPs whereas PEG-nitroDOPA stabilized NPs synthesized in the oil bath formed μm large films without that they agglomerated (cf. Figures 6.4 and 5.19). This points to a higher NP stability of PEG-nitrocatechol as compared to PEG-gallol stabilized NPs, well in agreement with what has been described in chapter 6.

Next to the inferior anchor used to stabilize NPs synthesized by aqueous precipitation, the PEG length of PEG(0.55)-gallol stabilized NPs was, as shown in chapter 8, below the threshold where good NP stability can be assured. Thus, the NP stability of PEG(0.55)-gallol compared to PEG(5)-nitrocatechol stabilized NPs is, for two reasons, considerably lower.

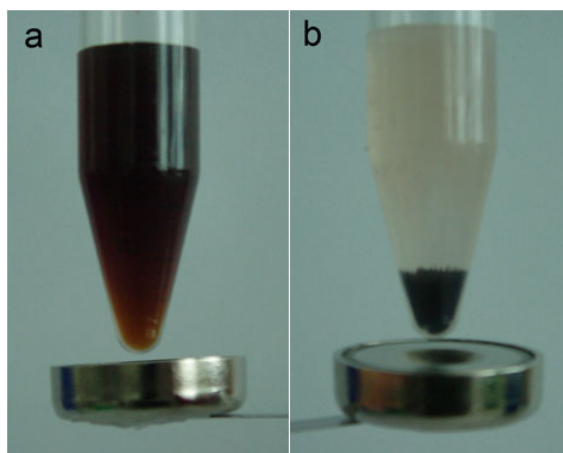


Figure M.11: *Stability of PEG(0.55)-gallol coated iron oxide NPs.* (a) The biotin-PEG(3.4)-gallol/mPEG(0.55)-gallol dispersant layer surrounding the iron oxide NP cores is stable and thick enough to prevent particle agglomeration in the presence of a small external magnet, even after particles have been dispersed in PBS for more than one year. (b) In the absence of the dispersant layer, iron oxide cores agglomerate and thus sediment instantaneously upon approaching a small external magnet.

Surface Charge

These NPs might be, in addition to the steric repulsion introduced through PEG(0.55)-gallol, electrostatically stabilized at physiologic pH as zeta potential measurements revealed (Figure M.10). The point of zero charge (PZC) of 6.7 measured for uncoated iron oxide NPs is in good agreement with what other groups have reported [586–588]. The IEP of NPs stabilized with mPEG(0.55)-gallol and dialyzed for 24 hours against Millipore water, was shifted to 4.2 (Figure M.10). The difference between the PZC of non-stabilized and the IEP of mPEG(0.55)-gallol stabilized NPs was assumed to result from the adsorption of at least partially deprotonated gallol, as was reported by Studart and co-workers for Al_2O_3 NPs [589].

Magnetic Separation

A widely used test for NP stability is their performance upon approaching a small external magnet. However, individually stabilized iron oxide NPs of core radii < 5 nm stay in solution even in the presence of a small external magnetic field due to the low magnetic moment of individual cores (Figure M.11a). This is contrasted by unstabilized iron oxide NPs as illustrated in Figure M.11b. They agglomerated and sedimented within seconds after approaching a small external magnet. This is due to the many times higher magnetic moment of agglomerates as compared to individually stabilized iron oxide cores.

Similarly, iron oxide NPs stabilized with high M_w dispersants might agglomerate upon approaching an external magnet and can be magnetically separated from solution. That iron oxide NPs with core radii < 5 nm can be magnetically separated can be taken as a sign of poor NP stability.

M.4.2 Characterization of Nanoparticle Stability

Figure M.11 exemplifies the apparent high NP stability of mPEG(0.55)-gallol stabilized iron oxide NPs even after storing them for more than one year in PBS at RT. This good NP stability was measured despite that NPs were stabilized with a reversibly binding anchor that was covalently linked to PEG that had a too low M_w . Even though PEG(0.55)-gallol is a suboptimal dispersant for two reasons, PEG(0.55)-gallol modified NPs showed good stability if stored and analyzed at RT, conditions which are usually used in literature to claim good NP stability [590]. Thus, characterization techniques such as DLS at RT or TEM analysis, which are typically used to claim good NP stability, might not reveal potential deficiencies in NP stability. These deficiencies potentially become detrimental during *in vivo* applications. However, once injected into a living body, agglomeration of NPs is difficult to assess because NP size cannot easily be measured any more. Additionally, *in vivo*, NP agglomeration is convoluted with other effects such as exposure to many different proteins that potentially adsorb on the NP surface or even replace dispersants if dispersants are insufficiently anchored to the NP surface. This illustrates the necessity to characterize NPs more stringently especially if they are intended for biomedical applications.

M.5 Chemical analysis of PEG(5)-anchors

M.5.1 MALDI-ToF

The m/z values measured by MALDI-TOF of the main mass distribution measured by MS (marked with * in Figure M.12) could all be assigned to [anchor-PEG-CH₃-H]⁺ and [anchor-PEG-CH₃-2H]²⁺ respectively. m/z was 44 Da, which is the M_w of an ethylene glycol (C₂H₄O) r.u., for all investigated dispersants. The polydispersity indices (PDI) calculated from the MALDI-ToF measurements for the different dispersants varied be-

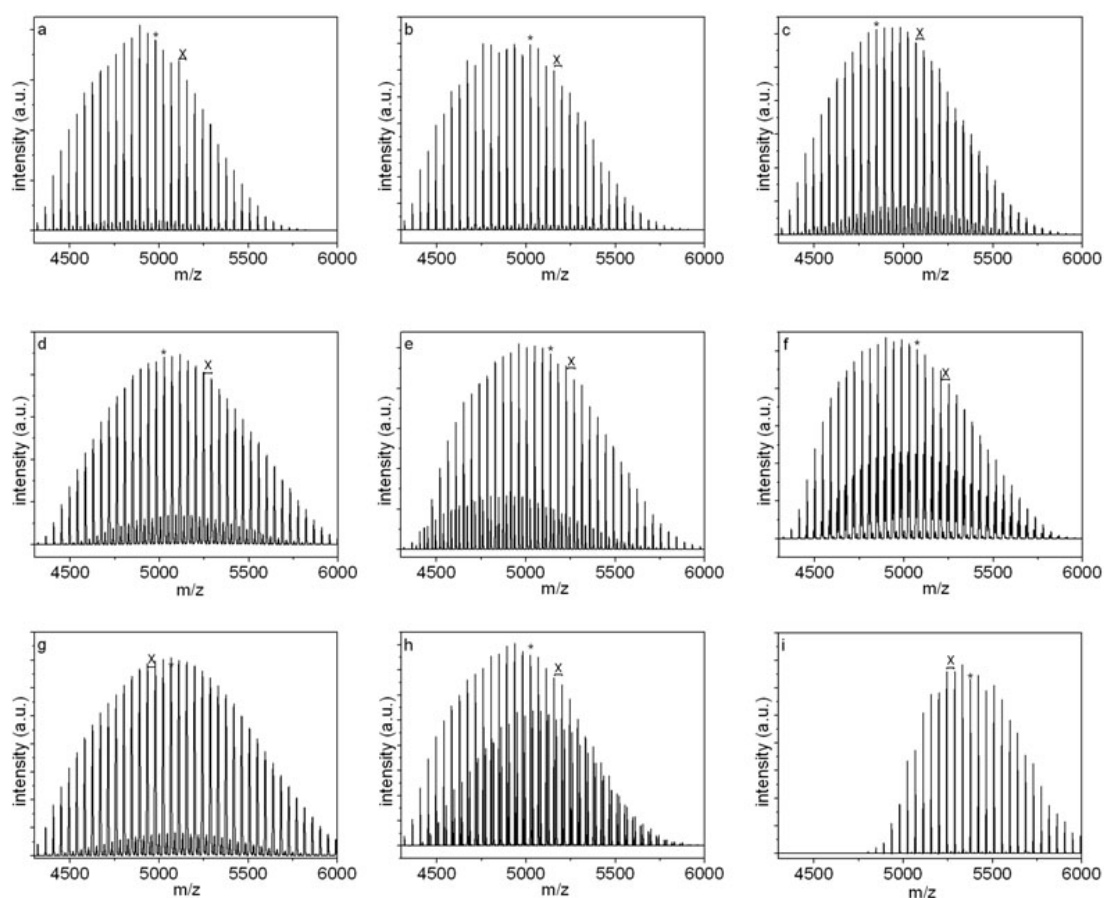


Figure M.12: MALDI-tof of PEG(5)-anchor dispersants. MALDI-tof of (a) PEG(5)-nitroDOPA, (b) PEG(5)-nitrodopamine, (c) PEG(5)-mimosine, (d) PEG(5)-DOPA, (e) PEG(5)-dopamine, (f) PEG(5)-hydroxypyridine, (g) PEG(5)-hydroxydopamine, (h) PEG(5)-hydroxypyrrone and (i) PEG(5)-COOH. m/z values of peaks indicated with * are reported in Table M.2. $m/z(x) = 44$ Da, corresponding to the ethylene glycol repeat unit.

tween 1.001 and 1.004. The second, smaller, M_w distribution seen in Figure M.12 was assigned to hydrolyzed PEG.

M.5.2 Microelement Analysis

Table M.2: *m/z* values of in Figure M.12 with * indicated peaks.

dispersant	<i>m/z</i>
PEG(5)-nitroDOPA	4979
PEG(5)-nitrodopamine	5023
PEG(5)-mimosine	4848
PEG(5)-DOPA	5022
PEG(5)-dopamine	5135
PEG(5)-hydroxydopamine	5073
PEG(5)-hydroxypyridine	5067
PEG(5)-hydroxypyronone	5135
PEG(5)-COOH	5375

Table M.3: *m/z* values of in Figure M.12 with * indicated peaks.

dispersant	C_{measured} (at%)	$C_{\text{calculated}}$ (at%)	O_{measured} (at%)	$O_{\text{calculated}}$ (at%)	N_{measured} (at%)	$N_{\text{calculated}}$ (at%)
PEG(5)-nitroDOPA	53.9	53.9	36.6	36.7	0.4	0.5
PEG(5)-nitrodopamine	54.2	54.1	36.3	36.4	0.3	0.5
PEG(5)-mimosine	54.1	54.2	36.4	36.3	0.4	0.5
PEG(5)-DOPA	53.6	54.5	36.5	36.3	0.2	0.3
PEG(5)-dopamine	54.5	45.7	36.0	36.0	0.2	0.3
PEG(5)-hydroxydopamine	54.0	54.4	36.4	36.3	0.5	0.3
PEG(5)-hydroxypyridine	53.5	54.6	36.0	35.9	0.4	0.5
PEG(5)-hydroxypyrrone	54.3	54.4	36.3	36.4	0.2	0.3
PEG(5)-COOH	54.4	54.3	36.8	36.6	0.0	0.0

M.5.3 NMR

As already seen in the MS analysis, $^1\text{H-NMR}$ analysis of dispersants confirmed the presence of hydrolyzed PEG in dispersants. Moreover, the presence of hydrolyzed PEG was also responsible for the lower percentage of N measured in microelemental analysis compared to the theoretical value (Table M.3).

However, control experiments where PEG(5)-NHS and, as shown in chapter 6, PEG(5)-COOH do not adsorb on flat Fe_3O_4 surfaces and particles respectively. Thus, hydrolyzed PEG did not seem to influence the adsorption of PEG-anchors. This was confirmed by the similar stability of NPs stabilized with different batches of PEG(5)-mimosine, containing different amounts of hydrolyzed PEG. Therefore, these dispersants have not been further purified prior to their adsorption on iron oxide NPs.

PEG(5)-nitroDOPA

$^1\text{H NMR}$ (500 MHz, D_2O): δ 7.56 (s, 1H), 6.76 (s, 1H), 2.98-4.70 (m, 777H)

$^{13}\text{C NMR}$ (500 MHz, D_2O): δ 175.9, 171.8, 150.4, 143.5, 140.6, 127.5, 119.3, 113.2, 67.7-71.9, 58.2, 53.5, 35.2.

PEG(5)-nitrodopamine

$^1\text{H NMR}$ (500 MHz, D_2O): δ 7.44 (s, 1H), 6.70-6.74 (d, $J=22.0$ Hz, 1H), 3.85-3.91 (m, 6H), 3.47-3.74 (m, 1127H), 3.29 (s, 9H), 3.07 (m, 2H), 3.02 (d, $J=5.6$ Hz, 2H)

$^{13}\text{C NMR}$ (500 MHz, D_2O): δ 293.9, 177.9, 172.5, 150.6, 119.0, 113.3, 69.7-71.1, 58.2, 39.0, 32.5.

PEG(5)-mimosine

$^1\text{H NMR}$ (500 MHz, D_2O): δ 7.47-7.75 (m, 2H), 6.74-6.75 (d, $J=6.6$ Hz, 1H), 4.24-4.29 (q, $J=8.6$ Hz, 1H), 4.07 (s, 1H), 3.90-3.99 (q, $J=15.9$ Hz, 2H), 3.29-3.74.29 (m, 648H)

$^{13}\text{C NMR}$ (500 MHz, D_2O): δ 175.1, 172.7, 166.8, 146.2, 139.0, 128.0, 121.2, 113.9, 68.2-71.1, 59.0, 58.2, 54.1.

PEG(5)-DOPA

$^1\text{H NMR}$ (500 MHz, D_2O): δ 6.73-6.78 (d, $J=7.9$ Hz, 1H), 6.67 (s, 1H), 6.59-6.60 (d, $J=7.9$ Hz, 1H), 4.42 (m, 1H), 3.96 (s, 2 H), 3.83-3.87 (d, $J=15.8$, 2H), 3.47-3.75 (m, 655 H), 3.29 (s, 5H)

$^{13}\text{C NMR}$ (500 MHz, D_2O): δ 176.6, 171.8, 144.1, 143.0, 129.7, 121.6, 117.0, 116.2, 69.1-71.1, 58.2, 55.0, 36.5

PEG(5)-dopamine

$^1\text{H NMR}$ (500 MHz, D_2O): δ 6.74-6.75 (d, $J=7.3$ Hz, 1H), 6.69 (s, 1H), 6.60-6.61 (d, $J=6.3$ Hz, 1H), 3.28-3.97 (m, 517 H), 2.64 (s, 3H)

$^{13}\text{C NMR}$ (500 MHz, D_2O): δ 172.3, 144.2, 142.7, 131.7, 121.2, 116.7, 116.3, 69.0-71.1, 58.2, 40.4, 33.9

PEG(5)-hydroxydopamine

$^1\text{H NMR}$ (500 MHz, D_2O): δ 6.33 (s, 1H), 6.29, (s, 1H), 4.15-4.16 (t, $J=6.6$ Hz, 1H) 3.91-3.92 (d, $J=3.8$ Hz, 1H), 3.29-3.68 (m, 362H)

$^{13}\text{C NMR}$ (500 MHz, D_2O): δ 176.5, 172.6, 145.7, 131.5, 128.9, 108.6, 68.1-71.1, 64.0, 62.3, 53.3, 40.7, 32.4

PEG(5)-hydroxypyridine

$^1\text{H NMR}$ (500 MHz, D_2O): δ 7.49 (s, 1H), 6.45 (s, 1H), 4.11 (s, 2H), 3.29-3.92 (m, 765H), 2.35 (s, 3H)

$^{13}\text{C NMR}$ (500 MHz, D_2O): δ 173.2, 173.2, 115.8, 144.9, 142.1, 115.8, 68.2-71.1, 58.2, 52.9, 38.2, 18.4.

PEG(5)-hydroxypyrrone

$^1\text{H NMR}$ (500 MHz, D_2O): δ 4.11 (s, 2H), 3.11-3.96 (m, 478H)

$^{13}\text{C NMR}$ (500 MHz, D_2O): δ 176.5, 173.2, 165.8, 144.9, 142.1, 115.8, 68.2-71.1, 58.2, 52.9, 38.2, 18.4.

Table M.4: *m/z* values of in Figure M.13 with * indicated peaks.

dispersant	<i>m/z</i>
PEG(20)-nitroDOPA	22284
PEG(10)-nitroDOPA	10945
PEG(5)-nitroDOPA	5377
PEG(1.5)-nitroDOPA	2117
PEG(0.8)-nitroDOPA	707
palmityl-nitroDOPA	523

PEG(5)-COOH

¹H NMR (500 MHz, D₂O): δ 4.70 (s, 1H), 6.41 (s, 1H), 4.31 (s, 3H), 4.07 (s, 3H), 4.02 (s, 4H), 3.29-3.74 (m, 977H)

¹³C NMR (500 MHz, D₂O): δ 174.8, 68.1-71.2, 58.2.

M.6 Chemical Analysis of Dispersants Containing NitroDOPA as Anchor

M.6.1 MALDI-tof

Identical to the MALDI-tof spectra shown for PEG-anchor dispersants, one of the *m/z* values per dispersant shown in Figure M.13 indicated with * is listed in Table M.4.

M.6.2 Microelement Analysis

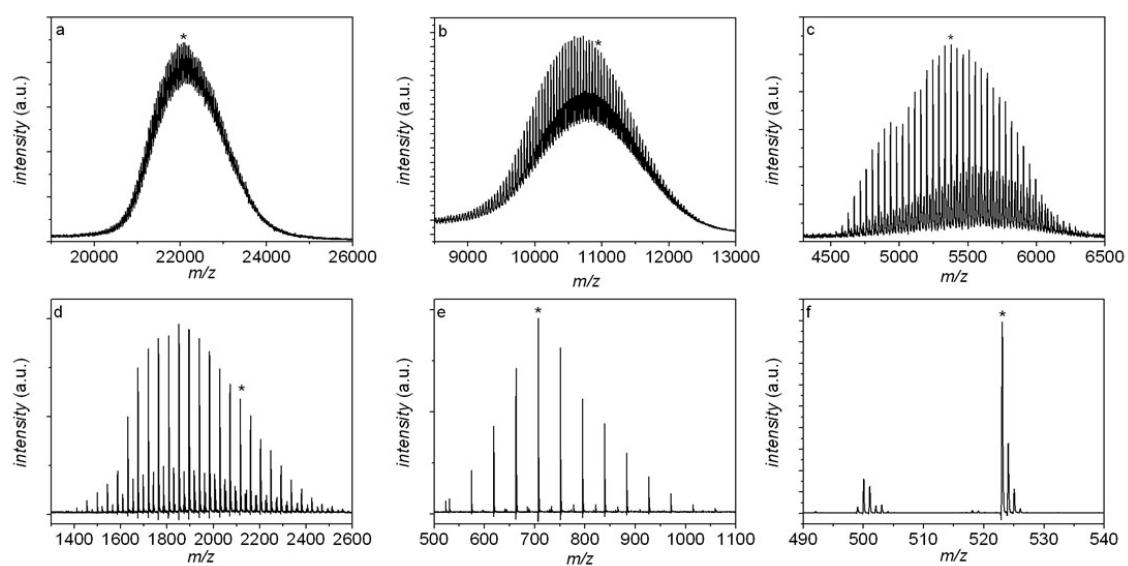


Figure M.13: MALDI-tof of PEG-nitroDOPA and palmityl-nitroDOPA dispersants. MALDI-tof of (a) PEG(20)-nitroDOPA, (b) PEG(10)-nitroDOPA, (c) PEG(5)-nitroDOPA, (d) PEG(1.5)-nitroDOPA, (e) PEG(0.8)-nitroDOPA and (f) palmityl-nitroDOPA.

Table M.5: *m/z* values of in Figure M.12 with * indicated peaks.

dispersant	C_{measured} (at%)	$C_{\text{calculated}}$ (at%)	O_{measured} (at%)	$O_{\text{calculated}}$ (at%)	N_{measured} (at%)	$N_{\text{calculated}}$ (at%)	H_{measured} (at%)	$H_{\text{calculated}}$ (at%)
palmityl-nitroDOPA	61.3	62.5		23.3	6.1	5.8	8.3	8.3
PEG(20)-nitroDOPA	54.1	54.5	36.5	36.3	0.3	0.1	8.8	9.1
PEG(10)-nitroDOPA	53.5	54.4	36.2	36.3	0.1	0.3	8.8	9.1
PEG(5)-nitroDOPA	53.7	54.2	36.9	36.2	0.4	0.6	8.6	9.0
PEG(1.5)-nitroDOPA	52.6	53.5	36.7	35.7	0.9	1.8	8.3	8.9
PEG(0.8)-nitroDOPA	45.1	52.7		35.1	2.5	3.4	6.9	8.8

M.6.3 NMR

Palmityl-nitroDOPA

$^1\text{H NMR}$ (500 MHz, DOCH_3): δ 8.00 (s, 1H), 7.58 (s, 1H), 3.65 (split d, 1H), 3.33 (s, 1H), 3.06 (split d, 1H), 2.23 (t, 1H), 1.22-1.50 (m, 25H), 0.92 (t, 3H);

$^{13}\text{C NMR}$ (500 MHz, DOCH_3): δ 175.1, 173.8, 151.2, 144.6, 140.7, 126.6, 118.9, 112.5, 66.8, 35.5, 35.4, 32.1, 29.2-29.8, 25.9, 22.8.

PEG(20)-nitroDOPA

$^1\text{H NMR}$ (500 MHz, D_2O): δ 7.61 (s, 1H), 6.79 (s, 1H), 1.44-6.79 (m, 4523H)

$^{13}\text{C NMR}$ (500 MHz, D_2O): δ 174.7, 172.2, 127.0, 119.4, 113.3, 58.2-73.1, 52.4, 29.9.

PEG(10)-nitroDOPA

$^1\text{H NMR}$ (500 MHz, D_2O): δ 7.59 (s, 1H), 6.77 (s, 1H), 3.29-4.11 (m, 1107H)

$^{13}\text{C NMR}$ (500 MHz, D_2O): δ 174.5, 172.2, 150.6, 143.8, 140.5, 127.0, 119.4, 113.3, 67.8-71.9, 58.2, 52.4, 34.8.

PEG(5)-nitroDOPA

$^1\text{H NMR}$ (500 MHz, D_2O): δ 7.58 (s, 1H), 6.76 (s, 1H), 3.46-4.04 (m, 651H), 3.28 (s, 4H)

$^{13}\text{C NMR}$ (500 MHz, D_2O): δ 172.3, 150.7, 143.8, 140.9, 127.5, 119.6, 113.6, 69.8-71.4, 58.5, 53.3, 35.3.

PEG(1.5)-nitroDOPA

$^1\text{H NMR}$ (500 MHz, D_2O): δ 7.58 (s, 1H), 6.68 (s, 1H), 4.11 (s, 4H), 3.43-3.74 (m, 503H), 3.28 (s, 10H)

$^{13}\text{C NMR}$ (500 MHz, D_2O): δ 172.4, 150.8, 143.9, 140.8, 127.3, 119.7, 113.6, 78.2, 69.7-71.4, 68.3, 66.4, 58.4, 52.8, 35.2.

PEG(0.8)-nitroDOPA

¹H NMR (500 MHz, D₂O): δ 7.58 (s, 1H), 6.75 (s, 1H), 3.37-3.73 (m, 710H), 3.37 (s, 39H)

¹³C NMR (500 MHz, D₂O): δ 176.8, 175.1, 70.0-71.4, 68.3, 58.4, 25.6.